OSCILLATIONS, WAVES AND PATTERNS IN THE PHYSICAL AND LIFE SCIENCES

EDITED BY: Rabih Sultan, Nobuhiko J. Suematsu, Federico Rossi and Istvan Lagzi

PUBLISHED IN: Frontiers in Physics and Frontiers in Chemistry

frontiers Research Topics

frontiers

ISSN 1664-8714
ISBN 978-2-83250-657-8
DOI 10.3389/978-2-83250-657-8

About Frontiers

Frontiers is more than just an open-access publisher of scholarly articles: it is a pioneering approach to the world of academia, radically improving the way scholarly research is managed. The grand vision of Frontiers is a world where all people have an equal opportunity to seek, share and generate knowledge. Frontiers provides immediate and permanent online open access to all its publications, but this alone is not enough to realize our grand goals.

Frontiers Journal Series

The Frontiers Journal Series is a multi-tier and interdisciplinary set of open-access, online journals, promising a paradigm shift from the current review, selection and dissemination processes in academic publishing. All Frontiers journals are driven by researchers for researchers; therefore, they constitute a service to the scholarly community. At the same time, the Frontiers Journal Series operates on a revolutionary invention, the tiered publishing system, initially addressing specific communities of scholars, and gradually climbing up to broader public understanding, thus serving the interests of the lay society, too.

Dedication to Quality

Each Frontiers article is a landmark of the highest quality, thanks to genuinely collaborative interactions between authors and review editors, who include some of the world's best academicians. Research must be certified by peers before entering a stream of knowledge that may eventually reach the public - and shape society; therefore, Frontiers only applies the most rigorous and unbiased reviews.
Frontiers revolutionizes research publishing by freely delivering the most outstanding research, evaluated with no bias from both the academic and social point of view. By applying the most advanced information technologies, Frontiers is catapulting scholarly publishing into a new generation.

What are Frontiers Research Topics?

Frontiers Research Topics are very popular trademarks of the Frontiers Journals Series: they are collections of at least ten articles, all centered on a particular subject. With their unique mix of varied contributions from Original Research to Review Articles, Frontiers Research Topics unify the most influential researchers, the latest key findings and historical advances in a hot research area! Find out more on how to host your own Frontiers Research Topic or contribute to one as an author by contacting the Frontiers Editorial Office: frontiersin.org/about/contact

OSCILLATIONS, WAVES AND PATTERNS IN THE PHYSICAL AND LIFE SCIENCES

Topic Editors:
Rabih Sultan, American University of Beirut, Lebanon
Nobuhiko J. Suematsu, Meiji University, Japan
Federico Rossi, University of Siena, Italy
Istvan Lagzi, Budapest University of Technology and Economics, Hungary

Citation: Sultan, R., Suematsu, N. J., Rossi, F., Lagzi, I., eds. (2022). Oscillations, Waves and Patterns in the Physical and Life Sciences. Lausanne: Frontiers Media SA. doi: 10.3389/978-2-83250-657-8

Table of Contents

frontiers | Frontiers in Physics

TYPE Editorial
PUBLISHED 18 October 2022
DOI 10.3389/fphy.2022.1051493

OPEN ACCESS

EDITED AND REVIEWED BY
Malgorzata Biczysko,
Shanghai University, China

*CORRESPONDENCE
Rabih Sultan,
rsultan@aub.edu.lb

SPECIALTY SECTION
This article was submitted to Physical Chemistry and Chemical Physics, a section of the journal Frontiers in Physics

RECEIVED 22 September 2022
ACCEPTED 05 October 2022
PUBLISHED 18 October 2022

CITATION
Lagzi I, Rossi F, Suematsu N and Sultan R (2022), Editorial: Oscillations, waves and patterns in the physical and life sciences. *Front. Phys.* 10:1051493.
doi: 10.3389/fphy.2022.1051493

Editorial: Oscillations, waves and patterns in the physical and life sciences

Istvan Lagzi[1,2], Federico Rossi[3], Nobuhiko Suematsu[4] and Rabih Sultan[5]*

[1]Department of Physics, Institute of Physics, Budapest University of Technology and Economics, Budapest, Hungary, [2]ELKH-BME Condensed Matter Research Group, Budapest University of Technology and Economics, Budapest, Hungary, [3]Department of Earth, Environmental and Physical Sciences, DEEP Sciences, University of Siena, Siena, Italy, [4]School of Interdisciplinary Mathematical Sciences, Graduate School of Advanced Mathematical Sciences, Meiji Institute for Advanced Study of Mathematical Sciences (MIMS), Meiji University, Nakano, Japan, [5]Department of Chemistry, American University of Beirut (AUB), Beirut, Lebanon

KEYWORDS

oscillations, pattern formation, chaos and complexity, particles and droplets, networks, self-assembly and self-organization, chemo-hydrodynamics, biological and ecological complexity

Editorial on the Research Topic
Oscillations, waves and patterns in the physical and life sciences

This special issue of *Frontiers in Physics* explores the vast field of nonlinear dynamical phenomena, manifested notably by oscillatory behavior and exotic pattern formation, both periodic and aperiodic. The contributions treated a broad variety of problems from physics, chemistry, biology, economics, engineering and medicine.

The development of wave mechanics continues to lie at the basis of quantum physics and chemistry. Frontiers research spans a wide range of wave studies encompassing gravitational, magnetic, convective waves, touching on the physics of dark matter, and black holes, and ranging from subatomic axions to new (HFR) waves discovered in the Sun. The physics of particles is visited here in a number of contributions, with a focus on interactions, collisions, undulatory swimming as well as mechano-chemical effects. “Liquid particles” or droplets have widely and tremendously important industrial applications and usages. Their study is also of pivotal importance to prevent or control infection and disease spread (such as the recent Covid-19 pandemic), whenever they are contaminated and harmful. The motion of droplets and clusters of droplets is treated here, considering mechanical, dynamic and thermodynamic aspects.

Oscillations in biology are ubiquitous and their applications fall in a broad spectrum of categories. From attractive patterns on butterflies and the pelt of many animals, to the dynamics of populations evolution, to the cycle of sleep (circadian), and to a huge multitude of biochemical processes in living organisms, the study of biological/biochemical oscillations lies at the heart of the understanding of various aspects of life on our planet.

In chemistry, over 300 chemical oscillators (oscillating chemical reactions) are known and classified. Oscillations are dynamic, but the resulting patterns can often be locked in space, such as in periodic precipitation (Liesegang) patterns and, typically, the geological stratigraphic scenery. We conclude with a study of oscillations in the economy and complex market systems. Besides this diversity across those disciplines, the richness of the contributions also lies in a harmonious balance between theory and experiment.

The quantum world is the central area in physics for the study of oscillations, spanning the properties of light waves with a wide spectrum of applications. In a paper by Choi, quantum light waves studied formerly by the same author in a static environment in the q-quadrature space were extended to an investigation in the p-quadrature space, along with an inquiry of the coupling between the two. The conjecture of nonstatic waves can be applied to interferometers, gravitational-wave detection, quantum information processing, high-precision measurements, and nano-quantum dots.

From light waves to the Physics of particles, objects and droplets. Two articles analyze the evolution of the motion of self-propelled objects. Kitahata and Koyano reported a mathematical approach to uncover fundamental behaviors of a cluster of two or three self-propelled particles. One of the common self-propelled particle changes its surrounding chemical concentration profile and succeeds to get driving force.

Mechano-chemical effects were studied by Fujita et al. in a nonlinear science context. Self-propelled objects in nonlinear multi-dimensional motion on an aqueous surface exhibit a so-called undulatory "swimming". Experimental implementation was tested on two systems: a filament on water and a floating camphor disc.

The filament exhibits periodic pendulum motion horizontally with an oscillation phase propagated in the opposite direction of the motion, a regime (or module) coined undulatory swimming. In a camphor disc on a water surface submerged with a nervonic acid condensed fluid phase layer, different modes of motion were determined, with both lateral and vertical oscillations at the air-water interface.

Polo et al. analyzed mechanical forcing transferred to a milling ball within two reactors with slightly different geometries: rectangular with flat bases, and rectangular with semi-circular bases. The oscillations amplitude, the number of collisions and the mean square velocity per collision were monitored by varying two essential parameters: the disc radius and the restitution coefficient. Those parameters critically control the transition from periodic to chaotic regimes *via* period doubling-like routes. The geometry of the reactor governs the dynamics of the milling body and hence the powder dragging and mixing, and the transfer of mechanical energy.

The present special issue extrapolates the interest in the motion of solid particles, to the study of liquid droplets and their clustering properties.

Itatani and Nabika reported novel chemical systems in which droplets spontaneously moved with interfacial chemical reaction. They carefully measured interfacial tension depending on the concentration of surfactant and related to the droplet motion, in particular movement length.

Particle physics using a coarse-grained model could be extended to biological systems, notably that autonomous oscillatory dynamics are ubiquitous at every level in biology. At the cellular level, one of the most relevant and well-characterized examples of periodic behavior is the cyclic assembly and disassembly of actomyosin networks. Hernández-Del-Valle et al. recently proposed that this cyclic behavior arises as a system's property from the competition between the cooperative assembly and the tension-induced disassembly of actin networks. In their contribution to this special issue, the authors perform experiments and simulations to characterize the properties of the actomyosin oscillations and how they depend on different features of the system.

This research collection touches on widely diverse aspects and perspectives of applications of nonlinear dynamics in biology and medicine. The behavior of ant colonies, the formation of Turing patterns on zebra fish and the diagnosis of schizophrenia.

Yamanaka et al. clearly showed characteristic collective behavior of ants, namely ants use two different tactic behaviors. One is to follow pheromone and the other is to use visual information. To show such complex behaviors, they prepared a circular-shaped pheromone road connecting between nest and food and observed much amount of ants' behaviors. Stochastic analysis of the data indicated that ants switched between the two different tactic behaviors. This paper provides a biological strategy for the special issue. It is expected to inspire chemical and physical experimentalists of nonlinear sciences.

In the paper by Nakamasu, pattern formation on a zebrafish skin was mathematically investigated by introducing a three-variable nonlinear reaction–diffusion model. The main objective of this study was to link the parameters in the reaction–diffusion model and connexin (gap junction protein in the cells) functions during the Turing pattern formation. Higher diffusivity of the chemical species was implemented by using channels in the membranes of pigment cells.

Bose and Gorecki describe a method that can be used in the diagnosis of schizophrenia based on the analysis by networks of chemical oscillators. The networks were constructed by using a 2-variable mathematical model (Oregonator), which describes the kinetics of the Belousov-Zhabotinsky reaction. The overall accuracy of schizophrenia diagnosis can be improved when using the majority decision from a network consisting of three oscillators.

The experimental and theoretical characterization of some novel properties discovered in the well-known Belousov-Zhabotinsky oscillating chemical reaction, was also the focus of two further contributions. Okamoto et al. exploited the nonlinear behavior of the Belousov-Zhabotinsky reaction to relate the degree of homogeneity of a reactive mixture with the characteristics of the travelling waves that may form in a reaction-diffusion system. In particular, they found that the wavelength and the wavenumber of a BZ pulse-train depend on the mixing state of the solution.

Wodlei et al. thoroughly reinvestigated the transient chaotic dynamics generally observed in unstirred Belousov-Zhabotinsky media. They discovered that periodic bulk motions, in form of convective cells, appeared during the aperiodic regime. Single and double convection cells were observed and they were found to be related to the duration of the chaotic transient.

Precipitation patterns are perhaps the earliest observed manifestation of self-organization in chemical systems after the discovery of the Liesegang phenomenon in 1896. Hayashi explored a wide diversity of such patterns with the Prussian blue (PB) reagent and its analogs (PBA) in agarose hydrogel as the supporting anion, and a variety of metal cations in the presence of an applied electric field (both constant and alternating voltages). A wealth of colorful patterns is obtained and displayed, along with the generation of Liesegang bands in the cyclic voltage mode experiments with the Cu–Fe PBA system.

The coupling of simple chemical reaction schemes to transport and hydrodynamic effects can result in complex behavior engendering oscillations. Tiani and Rongy, describe a mechanism for the emergence of spatial and temporal oscillations of the surface tension and of the velocity field in a bimolecular system (A+ B → C reaction-type) with no chemical instability involved. Such oscillations emerge as the result of the interplay between differential diffusion of chemical species and chemically driven Marangoni stresses at the air/liquid interface.

Last but not least, nonlinear dynamics and chaos theory transcended beyond the natural sciences reaching out to the social sciences, notably in population dynamics and the study of uncertainty in economic systems.

Economy and market are prototypical complex systems that influence (and are influenced by) life styles, well-being and behaviors of human societies all over the world. In their contribution, Yesiltas et al. constructed an economic index based on data from social media (Twitter) to track out and somehow predict market fluctuations and economic risks at a country level. By using macroeconomic modeling techniques, the authors developed a set of key financial indicators for tracking financial developments in Turkey, the country chosen as a benchmark.

Author contributions

All authors listed have made a substantial, direct, and intellectual contribution to the work and approved it for publication.

Conflict of interest

The authors declare that the research was conducted in the absence of any commercial or financial relationships that could be construed as a potential conflict of interest.

Publisher's note

frontiers in Physics

ORIGINAL RESEARCH
published: 12 January 2022
doi: 10.3389/fphy.2021.789652

Clarifying Nonstatic-Quantum-Wave Behavior Through Extending Its Analysis to the p-Quadrature Space: Interrelation Between the q- and p-Space Wave-Nonstaticities

Jeong Ryeol Choi *

Department of Nanoengineering, Kyonggi University, Suwon, South Korea

If electromagnetic parameters of a medium vary in time, quantum light waves traveling in it become nonstatic. A recent report shows that such nonstatic waves can also appear even when the environment is static where the parameters of the medium do not vary. In this work, the properties of nonstatic waves in a static environment are investigated from their *p*-space analysis, focusing on the interrelation between the *q*- and *p*-space nonstatic waves. The probability densities in *p*-space (as well as in *q*-space) for both the nostatic Fock and Gaussian states evolve in a periodic manner, i.e., they constitute belly and node in turn successively as time goes by. If we neglect the displacement of waves, the *q*- and *p*-space wave phases are opposite each other. Since the intensity of the wave in each space is relatively large whenever the wave forms a belly, such a phase difference indicates that periodical intensity exchange between the *q*- and *p*-component waves takes place through their nonstatic evolutions. This is the novel reciprocal optical phenomenon arisen on account of the wave nonstaticity.

Keywords: nonstatic light wave, wave function, measure of nonstaticity, Fock state, Gaussian state, quantum optics

OPEN ACCESS

Edited by:
Rabih Sultan,
American University of Beirut, Lebanon

Reviewed by:
Youbin Yu,
Zhejiang Sci-Tech University, China
Q. H. Liu,
Hunan University, China

***Correspondence:**
Jeong Ryeol Choi
choiardor@hanmail.net

Specialty section:
This article was submitted to Physical Chemistry and Chemical Physics, a section of the journal Frontiers in Physics

Received: *05 October 2021*
Accepted: *10 November 2021*
Published: *12 January 2022*

Citation:
Choi JR (2022) Clarifying Nonstatic-Quantum-Wave Behavior Through Extending Its Analysis to the p-Quadrature Space: Interrelation Between the q- and p-Space Wave-Nonstaticities. Front. Phys. 9:789652. doi: 10.3389/fphy.2021.789652

INTRODUCTION

If the characteristics of a medium vary in time by external perturbations, quantum light waves propagating through it may exhibit nonstatic properties [1–8]. Then, the shapes of the waves would be modified through the change of parameters. The dissipation and amplification of the wave amplitudes are also classified as the phenomena of wave nonstaticity. The light waves in such cases are usually described by time-dependent Hamiltonians, where their mathematical treatment is somewhat complicated.

Owing to the temporal and/or spatial variations of electromagnetic parameters in media, nonstatic quantum waves exhibit many novel physical properties that are absent in common light waves. As a noticeable consequence of wave nonstaticity, highly rapid periodic or arbitrary modulations of the wave phases and amplitudes are possible under appropriate conditions [8–13]. Such ultrafast modulations at a weak photon level can be applied to a time-resolved optical heterodyne detection in nano quantum dots [8, 11]. On one hand, temporal modulation of a driving electromagnetic field can be used in enhancing the entanglement between a microwave mode and a mechanical resonator [12, 13]. Another main consequence achieved through wave nonstaticity

is a frequency shift [7, 14] in subwavelength optics. Frequency shifts are potential tools for producing millimeter-waves and terahertz signals whose generations can hardly be realized by other technological means.

In a previous work [15], we showed a notable feature in optics, which is that nonstatic waves can also appear even in a static environment, i.e., without changes of the parameter values in media. The properties of such nonstatic waves have been studied in a rigorous way from the fundamental quantum-mechanical point of view in that work. Through this, we confirmed that the width of the waves varies periodically in time as a consequence of their nonstaticity. The related quantitative measure of nonstaticity, resulting from the modification of the waveform, was defined. Further, the mechanism of wave expansion and collapse was elucidated in Ref. [16].

However, the above mentioned research was in principle confined in q-quadrature space only. In this work, we will investigate such nonstatic waves especially on their p-quadrature space characteristics. The behavior of nonstatic waves described in p-space will be compared to that in q-space; through this, we clarify how they are mutually connected, as well as demonstrate the differences and similarities between them. A rigorous analysis of the relation between the two conjugate space evolutions of the nonstatic waves is necessary in understanding the peculiar wave behavior caused by its nonstaticity as a whole. Our analyses will be carried out separately for the Fock state waves and the Gaussian ones.

RESULTS AND DISCUSSION

Nonstatic Waves in the Fock States

We investigate the properties of nonstatic waves in the Fock states in a static environment through the p-space analysis in this section. As a preliminary step for understanding the theory of wave nonstaticity along this line, the readers may need to know its previous research consequence in q-quadrature space, reported in Ref. [15]. For the convenience of readers, the research of Ref. [15] including its outcome is briefly introduced in **Supplementary Material**.

Let us consider a medium where the electric permittivity ϵ and the magnetic permeability μ do not vary in time, whereas the electric conductivity σ is zero. The vector potential relevant to the light-wave propagation in that medium can be written as $\mathbf{A}(\mathbf{r}, t) = \mathbf{u}(\mathbf{r})q(t)$, where $\mathbf{r}$ is a position in three dimensions. Whereas $\mathbf{u}(\mathbf{r})$ follows position boundary conditions, the time function $q(t)$ exhibits an oscillatory behavior. In order to describe the light waves from quantum mechanical point of view, we need to change $q(t)$ into an operator $\hat{q}$. Then, the waves that propagate through the static medium is described by a simple Hamiltonian of the form $\hat{H} = \hat{p}^2/(2\epsilon) + \epsilon\omega^2\hat{q}^2/2$, where $\hat{p}$ is the conjugate variable of $\hat{q}$, which is defined as $\hat{p} = -i\hbar\partial/\partial q$. According to a previous report [15], quantum waves that have nonstatic properties in q-space can appear even in this static situation as mentioned in the introductory part.

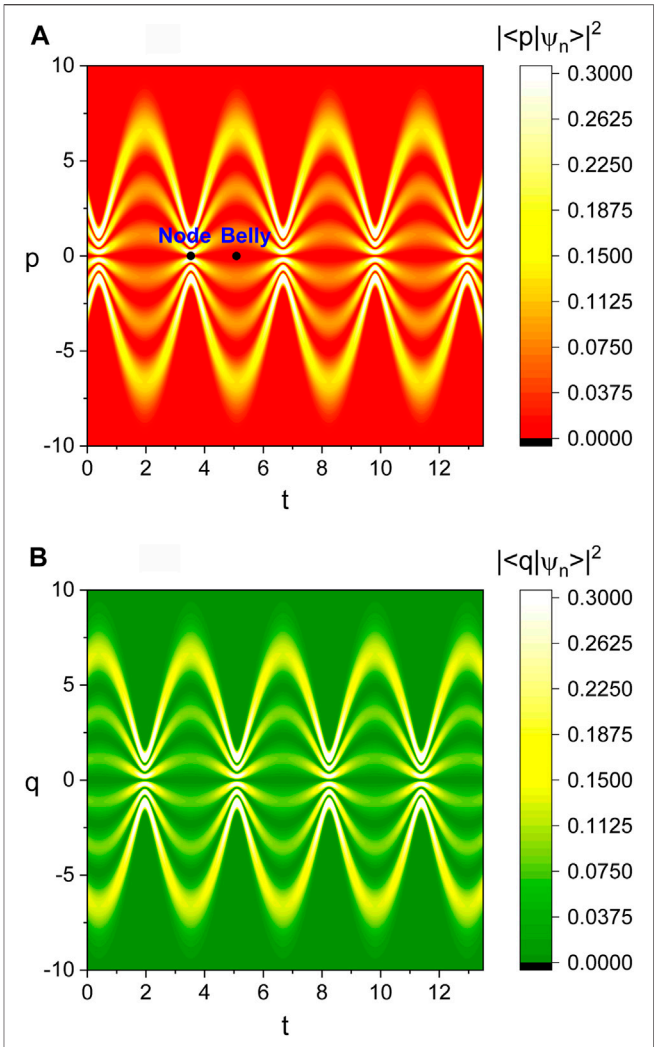

FIGURE 1 | (A) is the density plot of the probability density in p-space, $|\langle p|\psi_n(t)\rangle|^2$, as a function of p and t. For comparison purposes, we have also represented the probability density in q-space, $|\langle q|\psi_n(t)\rangle|^2$, in **(B)** as a function of q and t. The values that we used are $A = 1, B = 5, C = 2, \omega = 1, n = 5, \hbar = 1, \epsilon = 1, t_0 = 0$, and $\varphi = 0$. All values are taken to be dimensionless for convenience; this convention will also be used in all subsequent figures.

The nonstatic waves propagating in the static environment can be represented in terms of a time function of the form

$$W(t) = W_{\mathrm{R}}(t) + iW_{\mathrm{I}}(t), \tag{1}$$

where $W_{\mathrm{R}}(t)$ and $W_{\mathrm{I}}(t)$ are its real and imaginary parts, respectively (i.e., both $W_{\mathrm{R}}(t)$ and $W_{\mathrm{I}}(t)$ are real). The formulae of the real and imaginary parts are given by [15].

$$W_{\mathrm{R}}(t) = \frac{\epsilon\omega}{\hbar f(t)}, \qquad W_{\mathrm{I}}(t) = -\frac{\epsilon \dot{f}(t)}{2\hbar f(t)}, \tag{2}$$

where

$$f(t) = A\sin^2\tilde{\varphi}(t) + B\cos^2\tilde{\varphi}(t) + C\sin[2\tilde{\varphi}(t)], \tag{3}$$

$$\tilde{\varphi}(t) = \omega(t - t_0) + \varphi, \tag{4}$$

with a constant phase φ and a constant time t_0. In **Eq. 3**, A, B, and C are real values that obey the conditions $AB - C^2 = 1$ and $AB \geq 1$. We note that **Eq. 3** is a general solution of the nonlinear equation [15]

$$\ddot{f} - \left(\dot{f}\right)^2/(2f) + 2\omega^2\left(f - 1/f\right) = 0. \tag{5}$$

The wave functions in p-space, which exhibit nonstatic properties, may also be represented in terms of the time function given in **Eq. 1**. An exact evaluation of the wave functions for such waves in the Fock states results in (see **Appendix A**)

$$\langle p|\psi_n(t)\rangle = \langle p|\phi_n(t)\rangle \exp\left[i\gamma_n(t)\right], \tag{6}$$

where

$$\langle p|\phi_n\rangle = (-i)^n \left(\frac{W_R(t)}{\pi\hbar^2}\right)^{1/4} \sqrt{\frac{[W^*(t)]^n}{[W(t)]^{n+1}}}\, \frac{1}{\sqrt{2^n n!}} \times H_n\left(\sqrt{\frac{W_R(t)}{W_R^2(t) + W_I^2(t)}}\, \frac{p}{\hbar}\right) \exp\left[-\frac{W_p(t)}{2}p^2\right], \tag{7}$$

$$\gamma_n(t) = -\omega(n + 1/2)\int_{t_0}^{t} f^{-1}(t')dt' + \gamma_n(t_0), \tag{8}$$

with

$$W_p(t) = \frac{W_R(t) - iW_I(t)}{\hbar^2\left[W_R^2(t) + W_I^2(t)\right]} \equiv W_{p,R}(t) + iW_{p,I}(t). \tag{9}$$

Here, H_n are nth order Hermite polynomials, whereas $W_{p,R}(t)$ and $W_{p,I}(t)$ are real and imaginary parts of $W_p(t)$, respectively. We can also represent **Eq. 9** simply as $W_p(t) = 1/[\hbar^2 W(t)]$.

Now it is possible to analyze quantum optical phenomena associated with the nonstatic waves on the basis of the wave functions given in **Eq. 6**, **Figure 1** shows the temporal evolution of the probability density which is defined as $|\langle p|\psi_n(t)\rangle|^2$. We see from **Figure 1A** that there are bellies and nodes in the p-space wave evolution like the q-space evolution represented in **Figure 1B**. While the period of such evolutions is π/ω for both $|\langle p|\phi_n\rangle|^2$ and $|\langle q|\phi_n\rangle|^2$, the corresponding wave phases associated with wave nonstaticity are different from each other. We confirm, from the comparison of **Figure 1A** and **Figure 1B**, that such a phase difference between the two probability densities is π, i.e., the phases are opposite each other. Notice that the phase of nonstatic evolution that we use here is the one that emerges due to nonstatic characteristics of the wave: this concept of the phase is essentially different from the generally used quantum phase which is composed of the dynamical and geometric phases as shown, for example, in Ref. [17]. Since the wave intensity is strong at a belly and weak at a node, the π difference between the q- and p-space wave phases implies the exchange of the wave intensity between the two conjugate components of the wave.

As stated in **Supplementary Material**, it was shown in the previous work [15] that the non-zero value of $W_I(t)$ is responsible for the appearance of the nonstatic properties of the waves in q-space. In addition, the quantitative measure of nonstaticity in q-space was defined in the same reference as the root-mean-square (RMS) value of $W_I(t)/W_R(t)$.

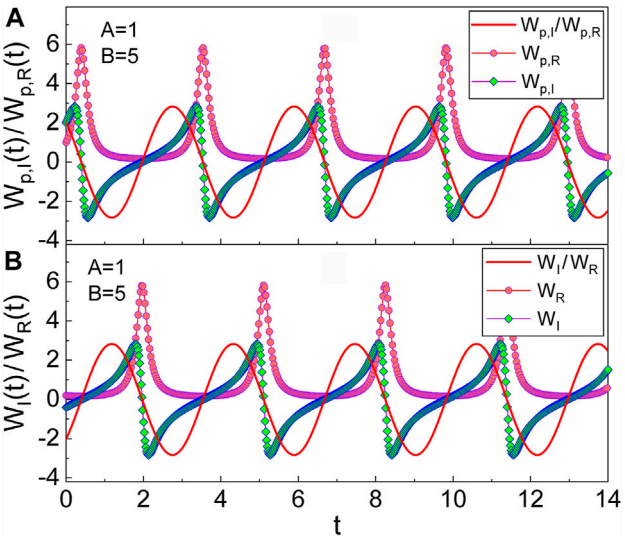

FIGURE 2 | (A) is the evolution of $W_{p,I}/W_{p,R}$ and its components $W_{p,R}$ and $W_{p,I}$, relevant to p-space, with the choice of $A = 1$, $B = 5$, and $C = 2$. **(B)** is the evolution of W_I/W_R and its components relevant to q-space (comparison purpose). The values that we have taken are $\omega = 1$, $\hbar = 1$, $\epsilon = 1$, $t_0 = 0$, and $\varphi = 0$.

For the case of the wave description in p-space, the associated wave nonstaticity originates from the non-zero value of $W_{p,I}$. Hence, the nonstaticity measure in p-space can also be defined as the RMS value of $W_{p,I}/W_{p,R}$. We see from **Figure 2** that the evolution of $W_{p,I}/W_{p,R}$ exhibits sinusoidal behavior as that of W_I/W_R. However, there is a phase difference π between them. This difference is responsible for the phase difference between the evolutions of $|\langle p|\psi_n\rangle|^2$ and $|\langle q|\psi_n\rangle|^2$. From a minor evaluation, we can easily confirm that

$$\frac{W_{p,I}}{W_{p,R}} = \frac{1}{2}\sqrt{(A + B)^2 - 4}\cos\left[2\tilde{\varphi}(t) + \delta\right], \tag{10}$$

where $\delta = \text{atan}(2C, B - A)$. Here, $\theta \equiv \text{atan}(x, y)$ is the two-arguments inverse function of $\tan\theta = y/x$, which is defined in the range $0 \leq \theta < 2\pi$. We have depicted the temporal evolution of $W_{p,I}/W_{p,R}$ and its components $W_{p,R}$ and $W_{p,I}$ in **Figure 2**. While $W_{p,I}/W_{p,R}$ varies sinusoidally, $W_{p,R}$ and $W_{p,I}$ vary abruptly at certain instants of time where the p-space probability density constitutes nodes. By taking the RMS value of **Eq. 10** for a cycle, we have the measure of nonstaticity in p-space as

$$D_{p,F} = \frac{\sqrt{(A + B)^2 - 4}}{2\sqrt{2}}. \tag{11}$$

This is exactly the same as the measure of nonstaticity in q-space, which was previously evaluated in Ref. [15]. Thus, the definition of the measure of nonstaticity shown above, can be generally used irrespective of the given space. For instance, we confirm that the measure of nonstaticity for the wave given in **Figure 2** is 2.0 from a simple calculation using $A = 1$ and $B = 5$.

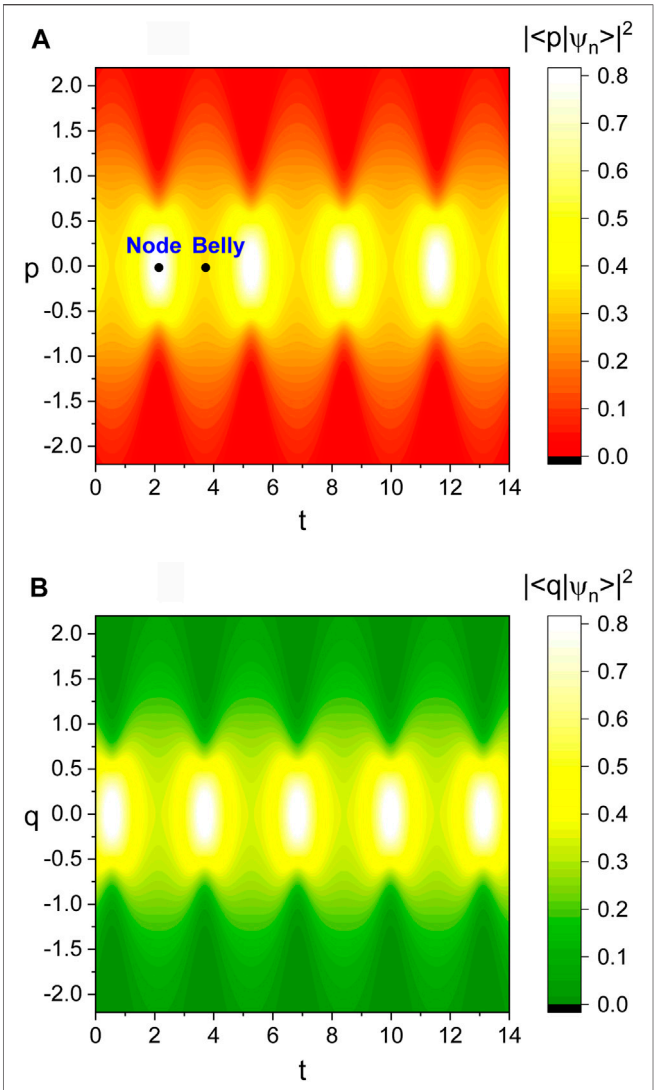

FIGURE 3 | (A) is the density plot of the probability density $|\langle p|\phi_n\rangle|^2$ given as a function of p and t. **(B)** is the density plot of $|\langle q|\phi_n\rangle|^2$ given as a function of q and t (comparison purpose). The values that we have taken are $K_R = 1$, $K_I = 1$, $A = 1$, $B = 5$, $C = 2$, $\xi = 0$, $\omega = 1$, $\hbar = 1$, $\epsilon = 1$, $t_0 = 0$, and $\varphi = 0$.

Nonstatic Waves in the Gaussian States

Our theory for the evolution of nonstatic waves can be extended to a more general case which is the Gaussian wave. To see the nonstatic properties of a Gaussian wave that evolves in a static environment, we take an initial waveform as

$$\langle q|\psi(0)\rangle = \sqrt[4]{\frac{K_R}{\pi}} e^{-\frac{1}{2}K(q-\xi)^2}, \tag{12}$$

where ξ is a displacement and $K = K_R + iK_I$. Here, K_R and K_I mean real and imaginary parts, respectively. The existence of K_I is responsible for the nonstatic evolution of the wave in this case [15]. To see the evolution of this Gaussian quantum wave in p-space, it is necessary to evaluate the wave function $\langle p|\psi(t)\rangle$ at an arbitrary time t from **Eq. 12**. We have provided the method of evaluating the analytical formula for such a wave function in **Appendix B**, and the result is given by

$$\langle p|\psi(t)\rangle = \frac{N(t)}{\sqrt{\hbar\mathcal{W}(t)}} \exp\left(-\frac{\mathcal{W}_p(t)}{2}[p + i\hbar R(t)]^2\right), \tag{13}$$

where

$$N(t) = \left(\frac{W_R(0)W_R(t)}{\pi}\right)^{1/4} \left(\frac{2K_R^{1/2}}{g(t)\exp[-2i\Theta(t)]}\right)^{1/2} \exp\left[-\frac{1}{2}\left(K\xi^2 + i\Theta(t)\right)\right] \times \exp\left[\frac{K^2\xi^2}{K + W^*(0)}\left(\frac{1}{2} - \frac{W_R(0)}{g(t)}\right)\right], \tag{14}$$

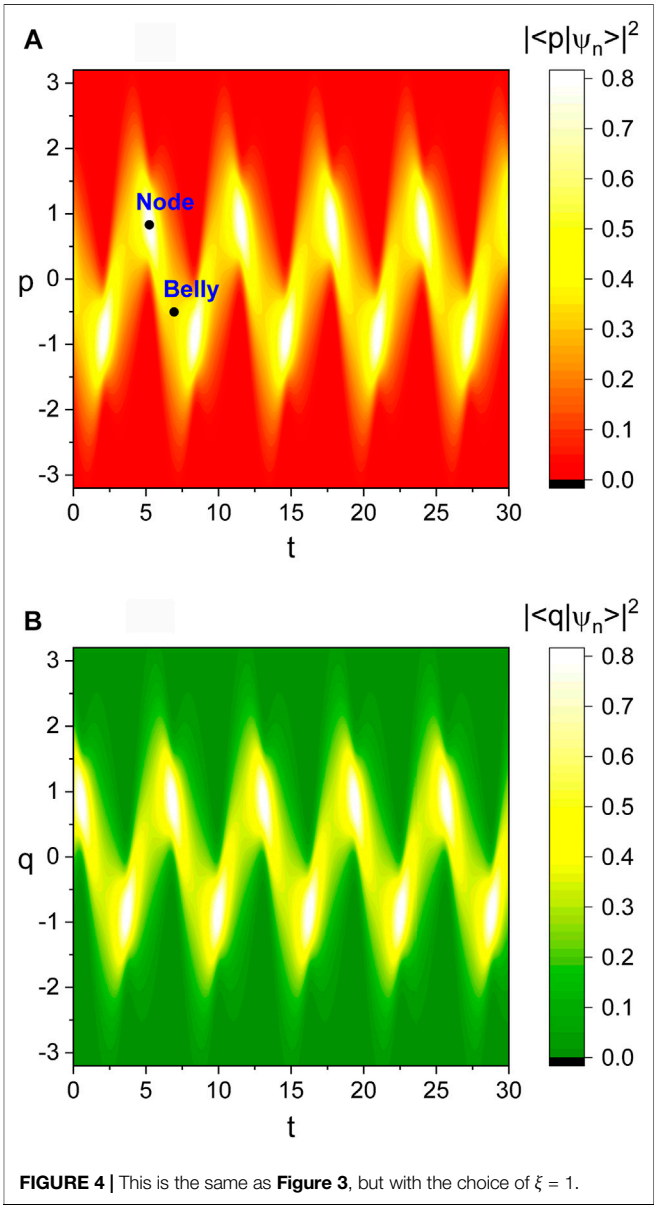

FIGURE 4 | This is the same as **Figure 3**, but with the choice of $\xi = 1$.

$$\mathcal{W}(t) = W(t) + \frac{2W_{\mathrm{R}}(t)[K - W(0)]}{g(t)} \equiv \mathcal{W}_{\mathrm{R}}(t) + i\mathcal{W}_{\mathrm{I}}(t), \tag{15}$$

$$\mathcal{W}_p(t) = \frac{\mathcal{W}_{\mathrm{R}}(t) - i\mathcal{W}_{\mathrm{I}}(t)}{\hbar^2\left[\mathcal{W}_{\mathrm{R}}^2(t) + \mathcal{W}_{\mathrm{I}}^2(t)\right]} \equiv \mathcal{W}_{p,\mathrm{R}}(t) + i\mathcal{W}_{p,\mathrm{I}}(t), \tag{16}$$

$$R(t) = \frac{2K\xi\sqrt{W_{\mathrm{R}}(0)W_{\mathrm{R}}(t)}}{g(t)\exp[-i\Theta(t)]}, \tag{17}$$

with

$$\Theta(t) = \omega\int_0^t f^{-1}(t')dt', \tag{18}$$

$$g(t) = [K + W^*(0)]\exp[2i\Theta(t)] - [K - W(0)]. \tag{19}$$

We have illustrated the probability density that corresponds to **Eq. 13** in **Figures 3**, **4**. **Figure 3** is the case where the displacement ξ is zero, whereas **Figure 4** corresponds to the case of the displaced Gaussian wave. We see from **Figure 3** that the width of the probability density varies periodically over time with the period 3.14 (= π/ω), which is the same period as that of the Fock-state wave functions that we have already seen. The comparison of **Figure 3A** and **Figure 3B** shows that the phase difference between $|\langle p|\psi(t)\rangle|^2$ and $|\langle q|\psi(t)\rangle|^2$ is π, which is also the same as that between the Fock-state probability densities $|\langle p|\psi_n(t)\rangle|^2$ and $|\langle q|\psi_n(t)\rangle|^2$.

On the other hand, the period of wave evolution (oscillation) in the case of **Figure 4** is not 3.14 but 6.28 (= $2\pi/\omega$). This means that the wave evolves a one-cycle (2π rad) during $T = 6.28$. Based on this, we can conclude that the phase difference between **Figure 4A** and **Figure 4B** is $\pi/2$ which is different from the previous cases. The difference of the period in this case from that in the previous cases is responsible for such an inconsistency in the phase differences (p-space wave phase minus q-space wave phase) between them. However, if we neglect the oscillation of the Gaussian wave in **Figure 4**, the period of its evolution reduces to π and as a consequence, the phase difference between $|\langle p|\psi(t)\rangle|^2$ and $|\langle q|\psi(t)\rangle|^2$ becomes π which is identical to the previous two cases (**Figures 1**, **3**).

The displaced Gaussian wave that can be seen from **Figure 4** oscillates back and forth like a classical state. However, the shape of the wave varies in an abnormal manner in time due to its nonstatic properties. The value of the probability density is highly peaked whenever the value of p becomes one of certain two values (one is plus and the other is minus) just after the turning points of the oscillation in p-space. Such peaks are in fact nodes as designated in the figure. Because the Gaussian nonstatic wave also exhibits node and belly in turn regularly, the intensity exchange between the q- and p-space waves occurs.

We can define the measure of nonstaticity for the Gaussian wave in a similar manner as that of the previous section. It is the RMS value of $\mathcal{W}_{p,\mathrm{I}}(t)/\mathcal{W}_{p,\mathrm{R}}(t)$. The temporal evolution of $\mathcal{W}_{p,\mathrm{I}}(t)/\mathcal{W}_{p,\mathrm{R}}(t)$ has been represented in **Figure 5** with its comparison to the evolution of the counterpart q-space value $\mathcal{W}_{\mathrm{I}}(t)/\mathcal{W}_{\mathrm{R}}(t)$. The amplitude of both $\mathcal{W}_{p,\mathrm{I}}(t)/\mathcal{W}_{p,\mathrm{R}}(t)$ and $\mathcal{W}_{\mathrm{I}}(t)/\mathcal{W}_{\mathrm{R}}(t)$ in **Figure 5** is 2.83. From this, the corresponding measure of nonstaticity is 2.0 and this value is the same as that of the wave shown in **Figure 2**. We can confirm that the patterns of the

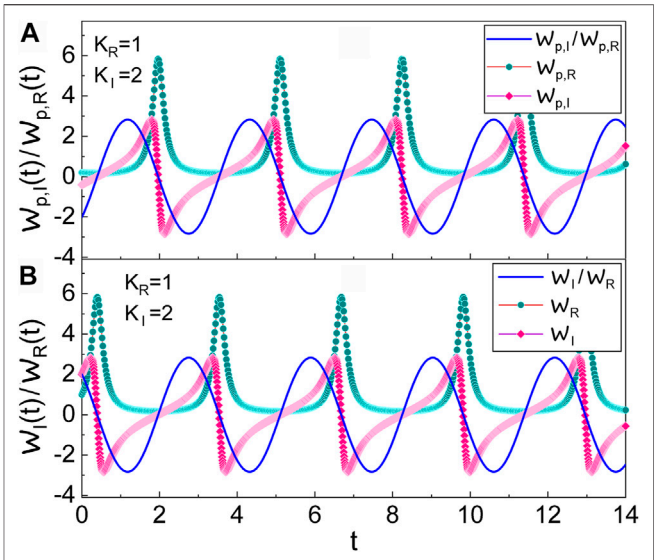

FIGURE 5 | (A) is the evolution of $\mathcal{W}_{p,\mathrm{I}}/\mathcal{W}_{p,\mathrm{R}}$ with the components $\mathcal{W}_{p,\mathrm{R}}$ and $\mathcal{W}_{p,\mathrm{I}}$, where $K_{\mathrm{R}} = 1$ and $K_{\mathrm{I}} = 2$. **(B)** is the evolution of $\mathcal{W}_{\mathrm{I}}/\mathcal{W}_{\mathrm{R}}$ and its relevant components (comparison purpose). The values that we have used are $A = 1$, $B = 5$, $C = 2$, $\omega = 1$, $\hbar = 1$, $\epsilon = 1$, $t_0 = 0$, and $\varphi = 0$.

evolutions of $\mathcal{W}_{p,\mathrm{R}}(t)$ and $\mathcal{W}_{p,\mathrm{I}}(t)$ given in **Figure 5** are the same as those of $W_{p,\mathrm{R}}(t)$ and $W_{p,\mathrm{I}}(t)$ given in **Figure 2**, respectively, except for the phases in their evolutions. From this, we can conclude that if the measure of nonstaticity is the same as each other, the patterns of their temporal evolutions are also the same. On the other hand, we can confirm by comparing panels of Fig. 3 and Fig. 6 in Ref. [15] each other that, if the measure of nonstaticity is different, the patterns of their evolutions are no longer the same. However, $\mathcal{W}_{p,\mathrm{I}}(t)/\mathcal{W}_{p,\mathrm{R}}(t)$ and $W_{p,\mathrm{I}}(t)/W_{p,\mathrm{R}}(t)$ always undergo sinusoidal evolution in any case in the static environment.

CONCLUSION

Through the extension of the research in q-space nonstatic-wave phenomena to its conjugate p-space ones, we pursued better understanding of wave nonstaticity including the interaction of the two component waves. Our analysis was carried out purely on the basis of analytical methods, where we did not use any approximation.

We have shown that bellies and nodes appear in the p-space evolution of the Fock and Gaussian state quantum-waves as a manifestation of their nonstaticity, like in the case of q-space evolution. The evolving pattern of the p-space wave caused by its nonstaticity is in general out of phase by π with the q-space evolution of the wave. This implies that the two wave components are reciprocally linked. Because the wave intensity is large when it constitutes a belly, the wave in each space gives and receives intensity from the conjugate wave-component periodically. If there is an initial displacement in the Gaussian wave, the wave in p-space oscillates back and forth like the q-space wave. This behavior very much resembles classical waves. However, the waveform in such an oscillation was altered due to the appearance of bellies and nodes.

Whenever the wave in q-space (p-space) poses a node, the uncertainty of q (p) reduces below its standard quantum level. From this, we can conclude that the nonstatic wave treated here is a kind of squeezed state. Several methods of generating squeezed states are known until now [18–22]. Likewise, the nonstatic wave may also be generated by using the technique of squeezed-state generation. The nonstatic wave can be used in physical disciplines where the squeezed state plays a major role, such as interferometers in gravitational-wave detection [23–25], quantum information processing [26–28], and high-precision measurements [29, 30].

It may be noticeable that nonstatic waves can arise without temporal changes of the electromagnetic parameters in media. However, we can never say that we know wave nonstaticity well if our related knowledge is limited to only q–space behavior of the light waves. The outcome of this research complements previous q-quadrature analyses in this context [15]. Based on this research, we can outline the entire aspect of wave nonstaticity including the integral connection between the q- and p-space wave behaviors.

DATA AVAILABILITY STATEMENT

The original contributions presented in the study are included in the article/**Supplementary Material**, further inquiries can be directed to the corresponding author.

AUTHOR CONTRIBUTIONS

JRC wrote the paper and approved it.

FUNDING

This work was supported by the National Research Foundation of Korea(NRF) grant funded by the Korea government(MSIT) (No.: NRF-2021R1F1A1062849).

ACKNOWLEDGMENTS

This work is focused on the behavior of p-quadrature wave functions, but we also provide the graphics of the physical quantities associated with q-quadrature for comparison purposes. The graphics that belong to q-quadrature were depicted using the analytical evaluations given in Ref. [15].

SUPPLEMENTARY MATERIAL

The Supplementary Material for this article can be found online at: https://www.frontiersin.org/articles/10.3389/fphy.2021.789652/full#supplementary-material

REFERENCES

1. Dodonov VV, Klimov AB, Nikonov DE. Quantum Phenomena in Nonstationary Media. *Phys Rev A* (1993) 47(5):4422–9. doi:10.1103/physreva.47.4422
2. Akhmanov SA, Sukhorukov AP, Chirkin AS. Nonstationary Phenomena and Space-Time Analogy in Nonlinear Optics. *Soviet Phys JETP* (1969) 28(4):748–57.
3. Vorgul I. On Maxwell's Equations in Non-Stationary Media. *Phil Trans R Soc A* (2008) 366(1871):1781–8. doi:10.1098/rsta.2007.2186
4. Dodonov AV. Photon Creation from Vacuum and Interactions Engineering in Nonstationary Circuit QED. *J Phys Conf Ser* (2009) 161(1):012029. doi:10.1088/1742-6596/161/1/012029
5. Portí JA, Salinas A, Morente JA, Rodri´guez-Sola M, Nerukh AG. Time-Varying Electromagnetic-Media Modelling with TLM Method. *Electron Lett* (2003) 39(6):505–7. doi:10.1049/el:20030390
6. Bakunov MI, Grachev IS. Energetics of Electromagnetic Wave Transformation in a Time-Varying Magnetoplasma Medium. *Phys Rev E* (2002) 65(3):036405. doi:10.1103/PhysRevE.65.036405
7. Shvartsburg AB, Petite G. Instantaneous Optics of Ultrashort Broadband Pulses and Rapidly Varying Media. *Prog Opt* (2002) 44:143–214. doi:10.1016/S0079-6638(02)80016-6
8. Moody G, McDonald C, Feldman A, Harvey T, Mirin RP, Silverman KL. Quadrature Demodulation of a Quantum Dot Optical Response to Faint Light fields. *Optica* (2016) 3(12):1397–403. doi:10.1364/OPTICA.3.001397
9. Bogatov AP, D'yachkov NV, Drakin AE, Gushchik TI. Amplitude and Phase Modulation of Radiation in a Travelling-Wave Amplifier Based on a Laser Diode. *Quan Electron.* (2013) 43(8):699–705. doi:10.1070/QE2013v043n08ABEH015166
10. Waarts RG, Friesem AA, Hefetz Y. Frequency-modulated to Amplitude-Modulated Signal Conversion by a Brillouin-Induced Phase Change in Single-Mode Fibers. *Opt Lett* (1988) 13(2):152–4. doi:10.1364/OL.13.000152
11. Liu B, Li X, Zhang Y, Xin X, Yu J. Probabilistic Shaping for ROF System with Heterodyne Coherent Detection. *APL Photon* (2017) 2(5):056104. doi:10.1063/1.4981393
12. Mari A, Eisert J. Opto- and Electro-Mechanical Entanglement Improved by Modulation. *New J Phys* (2012) 14:075014. doi:10.1088/1367-2630/14/7/075014
13. Averchenko V, Sych D, Schunk G, Vogl U, Marquardt C, Leuchs G. Temporal Shaping of Single Photons Enabled by Entanglement. *Phys Rev A* (2017) 96(4):043822. doi:10.1103/PhysRevA.96.043822
14. Savage RL, Jr., Joshi C, Mori WB. Frequency Upconversion of Electromagnetic Radiation upon Transmission into an Ionization Front. *Phys Rev Lett* (1992) 68(7):946–9. doi:10.1103/PhysRevLett.68.946
15. Choi JR. On the Possible Emergence of Nonstatic Quantum Waves in a Static Environment. *Nonlinear Dyn* (2021) 103(3):2783–92. doi:10.1007/s11071-021-06222-8
16. Choi JR. Characteristics of Nonstatic Quantum Light Waves: the Principle for Wave Expansion and Collapse. *Photonics* (2021) 8(5):158. doi:10.3390/photonics8050158
17. Choi JR. Quadrature Squeezing and Geometric-Phase Oscillations in Nano-Optics. *Nanomaterials* (2020) 10(7):1391. doi:10.3390/nano10071391
18. Han Y, Wen X, Liu J, He J, Wang J. Generation of Polarization Squeezed Light with an Optical Parametric Amplifier at 795 nm. *Opt Commun* (2018) 416:1–4. doi:10.1016/j.optcom.2018.01.038
19. Ma L, Guo H, Sun H, Liu K, Su B, Gao J. Generation of Squeezed States of Light in Arbitrary Complex Amplitude Transverse Distribution. *Photon Res* (2020) 8(9):1422–7. doi:10.1364/PRJ.388956
20. Li Y-q., Xiao M. Generation and Applications of Amplitude-Squeezed States of Light from Semiconductor Diode Lasers. *Opt Express* (1998) 2(3):110–7. doi:10.1364/OE.2.000110
21. Raizen MG, Orozco LA, Xiao M, Boyd TL, Kimble HJ. Squeezed-State Generation by the Normal Modes of a Coupled System. *Phys Rev Lett* (1987) 59(2):198–201. doi:10.1103/PhysRevLett.59.198
22. Yurke B. Use of Cavities in Squeezed-State Generation. *Phys Rev A* (1984) 29(1):408–10. doi:10.1103/PhysRevA.29.408
23. Grote H, Danzmann K, Dooley KL, Schnabel R, Slutsky J, Vahlbruch H. First Long-Term Application of Squeezed States of Light in a Gravitational-Wave Observatory. *Phys Rev Lett* (2013) 110(18):181101. doi:10.1103/PhysRevLett.110.181101

24. Aasi J, Abadie J, Abbott BP, Abbott R, Abbott TD, Abernathy MR, et al. The LIGO Scientific Collaboration. Enhanced Sensitivity of the LIGO Gravitational Wave Detector by Using Squeezed States of Light. *Nat Photon* (2013) 7(8): 613–9. doi:10.1038/nphoton.2013.177
25. Abadie J, Abbott BP, Abbott R, Abbott TD, Abernathy M, Adams C, et al. The LIGO Scientific Collaboration. A Gravitational Wave Observatory Operating beyond the Quantum Shot-Noise Limit. *Nat Phys* (2011) 7:962–5. doi:10.1038/nphys2083
26. Appel J, Figueroa E, Korystov D, Lobino M, LLvovsky AI. Quantum Memory for Squeezed Light. *Phys Rev Lett* (2008) 100(9):093602. doi:10.1103/PhysRevLett.100.093602
27. Honda K, Akamatsu D, Arikawa M, Yokoi Y, Akiba K, Nagatsuka S, et al. Storage and Retrieval of a Squeezed Vacuum. *Phys Rev Lett* (2008) 100(9): 093601. doi:10.1103/PhysRevLett.100.093601
28. Hétet G, Buchler BC, Glöeckl O, Hsu MTL, Akulshin AM, Bachor HA, et al. Delay of Squeezing and Entanglement Using Electromagnetically Induced Transparency in a Vapour Cell. *Opt Express* (2008) 16(10):7369–81. doi:10.1364/OE.16.007369
29. Liu K, Cai C, Li J, Ma L, Sun H, Gao J. Squeezing-enhanced Rotating-Angle Measurement beyond the Quantum Limit. *Appl Phys Lett* (2018) 113(26): 261103. doi:10.1063/1.5066028
30. Smithey DT, Beck M, Raymer MG, Faridani A. Measurement of the Wigner Distribution and the Density Matrix of a Light Mode Using Optical Homodyne Tomography: Application to Squeezed States and the Vacuum. *Phys Rev Lett* (1993) 70(9):1244–7. doi:10.1103/PhysRevLett.70.1244

Conflict of Interest: The author declares that the research was conducted in the absence of any commercial or financial relationships that could be construed as a potential conflict of interest.

APPENDIX A
EVALUATION OF THE FOCK-STATE WAVE FUNCTIONS IN *p*-SPACE

The wave functions which exhibit nonstatic properties in p-space can be obtained from the Fourier transformation of the wave functions in q-space. The wave functions for the nonstatic waves in q-space, which propagate in a static environment, are given by [15].

$$\langle q|\psi_n(t)\rangle = \langle q|\phi_n(t)\rangle \exp[i\gamma_n(t)], \tag{A1}$$

where $\langle q|\phi_n\rangle$ are eigenstates of the form

$$\langle q|\phi_n\rangle = \left(\frac{W_R(t)}{\pi}\right)^{1/4} \frac{1}{\sqrt{2^n n!}} H_n\left(\sqrt{W_R(t)}\, q\right) \exp\left[-\frac{W(t)}{2} q^2\right]. \tag{A2}$$

Let us carry out the Fourier transformation of these waves, such that

$$\langle p|\psi_n(t)\rangle = \frac{1}{\sqrt{2\pi\hbar}} \int_{-\infty}^{\infty} \langle q|\psi_n(t)\rangle e^{-ipq/\hbar} dq. \tag{A3}$$

By evaluating the above equation using **Eqs. A1**, **A2** straightforwardly, we easily have the p-space wave functions, which are given in **Eq. 6** with **Eqs. 7**-**9** in the text.

APPENDIX B
THE GAUSSIAN WAVE IN *p*-SPACE

The Gaussian wave in q-space, that exhibits nonstatic properties, was suggested in Ref. [15]. From that reference, the corresponding wave function is given by

$$\langle q|\psi(t)\rangle = N(t) \exp\left[-\frac{\mathcal{W}(t)}{2} q^2 + R(t) q\right], \tag{B1}$$

where $N(t)$, $\mathcal{W}(t)$, and $R(t)$ are defined in the text. From the Fourier transformation of this, we have the exact wave function for the Gaussian wave in p-space, which is given in **Eq. 13** with **Eqs. 14**-**19**.

frontiers in Physics

ORIGINAL RESEARCH
published: 18 January 2022
doi: 10.3389/fphy.2021.805659

Correspondences Between Parameters in a Reaction-Diffusion Model and Connexin Functions During Zebrafish Stripe Formation

Akiko M. Nakamasu *

International Research Organization for Advanced Science and Technologies, Kumamoto University, Kumamoto, Japan

Different diffusivities among interacting substances actualize the potential instability of a system. When these elicited instabilities manifest as forms of spatial periodicity, they are called Turing patterns. Simulations using general reaction-diffusion (RD) models demonstrate that pigment patterns on the body trunk of growing fish follow a Turing pattern. Laser ablation experiments performed on zebrafish reveal apparent interactions among pigment cells, which allow for a three-component RD model to be derived. However, the underlying molecular mechanisms responsible for Turing pattern formation in this system remain unknown. A zebrafish mutant with a spotted pattern was found to have a defect in Connexin41.8 (Cx41.8) which, together with Cx39.4, exists in pigment cells and controls pattern formation. Here, molecular-level evidence derived from connexin analyses is linked to the interactions among pigment cells described in previous RD modeling. Channels on pigment cells are generalized as "gates," and the effects of respective gates were deduced. The model uses partial differential equations (PDEs) to enable numerical and mathematical analyses of characteristics observed in the experiments. Furthermore, the improved PDE model, including nonlinear reaction terms, enables the consideration of the behavior of components realistically.

Keywords: pattern formation, turing pattern, mathematical model, reaction-diffusion system, connexin, fish pigmentation

OPEN ACCESS

Edited by:
Istvan Lagzi,
Budapest University of Technology and Economics, Hungary

Reviewed by:
Daishin Ueyama,
Musashino University, Japan
Qingyu Gao,
China University of Mining and Technology, China
István Szalai,
Eötvös Loránd University, Hungary

***Correspondence:**
Akiko M. Nakamasu
nakamasu@kumamoto-u.ac.jp

Specialty section:
This article was submitted to Physical Chemistry and Chemical Physics, a section of the journal Frontiers in Physics

Received: *30 October 2021*
Accepted: *25 November 2021*
Published: *18 January 2022*

Citation:
Nakamasu AM (2022) Correspondences Between Parameters in a Reaction-Diffusion Model and Connexin Functions During Zebrafish Stripe Formation. Front. Phys. 9:805659. doi: 10.3389/fphy.2021.805659

1 INTRODUCTION

In 1952, Alan Turing postulated that two substrates interacting with each other show instability when they diffuse at different speeds. He explained this diffusion-driven instability by utilizing a linear reaction-diffusion (RD) model. This model demonstrates that spatial inhomogeneity (i.e., the Turing pattern) could be generated by such conditions. This relationship is known to generate patterns though the components remain to be explored.

More than two decades ago, [1] reported that pigment stripes on the bodies of growing marine angel fish behave as a Turing pattern. The research focus then shifted mainly to zebrafish (*Danio rerio*) as a model organism for pattern-formation studies [2–4]. Zebrafish have a pattern of stripes on their body and fins (**Figure 1A**). The pattern is generated by three types of pigment cells: complementarily distributed black melanophores and yellow xanthophores (**Figure 1C**) plus iridescent iridophores. Numerous zebrafish pigment-pattern mutants were artificially generated [5], and the corresponding genes were identified. One of the most important mutants is leopard, which produces a spotted pattern that is representative of Turing patterns (**Figure 1B**) [6] identifies

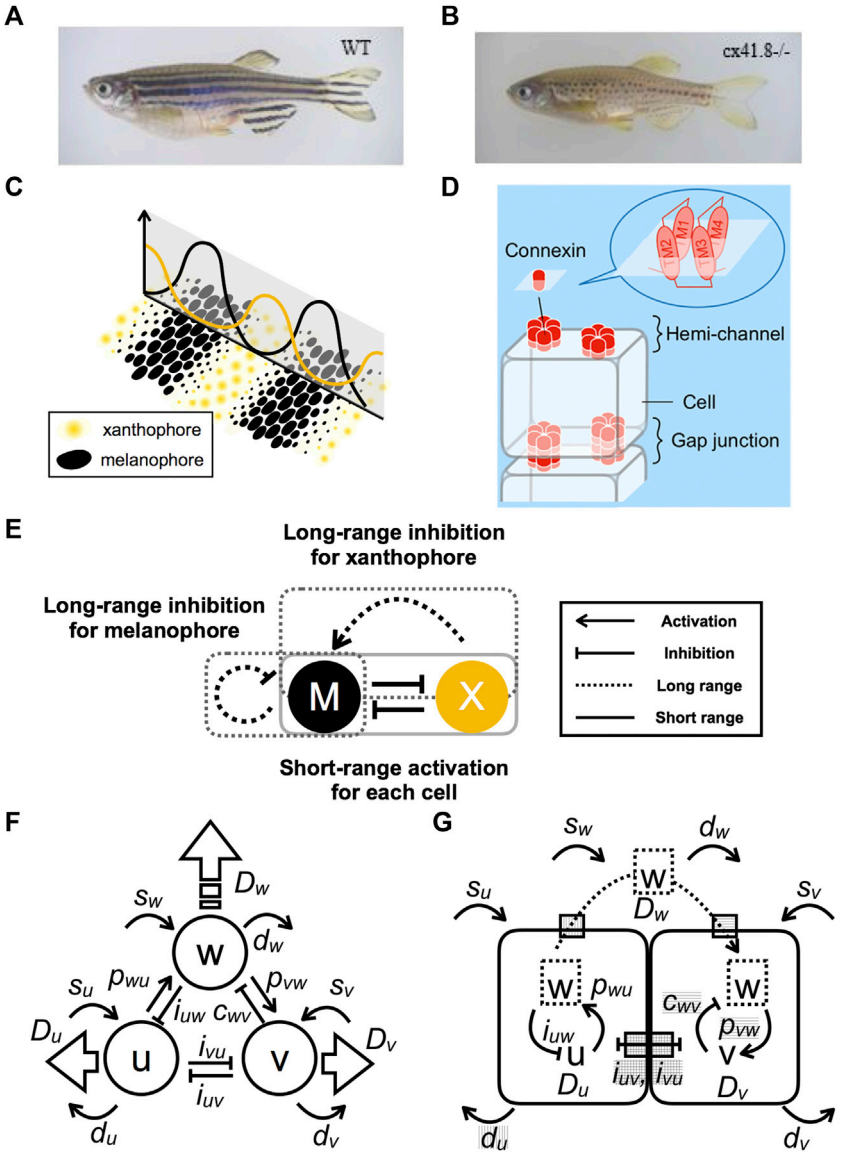

FIGURE 1 | Model-based prediction of defects in channels and interactions. **(A)** Striped wild-type (WT) zebrafish. **(B)** Spotted leopard mutant zebrafish. **(C)** Schematic representation of the relationship between the distribution of pigment cells and the numerical result of the continuous model. **(D)** Schematic representation of channels composed of connexin complexes. Hemi-channels are open to the outside of a cell, whereas gap junctions form by the docking of hemi-channel connecting to adjacent cells. **(E)** Apparent interactions of pigment cells as revealed by laser ablation experiments. **(F)** Schematic diagram of a three-component PDE model composed of components *U* or *V*, which correspond to melanophores or xanthophores, respectively, and component *w*, which represents a highly diffusible molecule. Interactions are indicated by fine arrows, diffusion coefficients (the motility of the components) are indicated by wide arrows, and corresponding parameters are indicated. **(G)** Schematic diagram of the effect of channels on pigment cells according to the mathematical model. Parameters related to the function of each gate are indicated by hatchings.

connexin41.8 (cx41.8) as the gene responsible for the leopard mutation [6]. Besides Cx41.8, other connexins, such as Cx39.4, exist in pigment cells and affect pigment-pattern formation. Six connexins form a hemi-channel (or "connexon"), which connects intracellular and extracellular spaces (**Figure 1D**). Docking of two hemi-channels from adjacent cells give rise to a gap junction, which mediates intercellular signal transfer [7]. The minimal connexin network required to originate a striped pattern was recently revealed by regulating connexin expression in each pigment cell [8]. Therefore, these channels are important for pigment-pattern formation.

Interactions among pigment cells and their molecular mechanisms involved in pattern formation are summarized in [9]. However, the molecular mechanisms leading to Turing instability remain mostly unresolved. Mosaic fish experiments indicate that both leopard/cx41.8 and jaguar/obelix/kcnj13 genes

are required for segregation of melanophores and xanthophores. Such segregation is proposed to involve local interactions between adjacent pigment cells [10]. Xanthophore ablation using a temperature-sensitive csf1ra allele led to the gradual death of melanophores in both the body trunk and fins of adult fish [11]. Accordingly, melanophore survival requires continuous signaling from xanthophores. Laser ablation of stripe and interstripe areas has revealed the mutual interactions between melanophores and xanthophores [12]. The interactions comply with the requirements for Turing pattern formation (**Figure 1E**). Specifically, both types of pigment cells activate their own types at a single-cell distance (short range) by inhibitions of other types and then inhibit their own types beyond the width of the stripe (long range). The difference in reaction distances achieves the "local activation and lateral inhibition" condition needed for pattern formations [13]. It should be noted, however, that the distinction between iridophores and xanthophores is sometimes unclear in those experiments.

To explain the opposing actions at long vs. short distance, a model that includes a highly diffusible molecule (i.e., long-range factor) and two cells (regarded as short-range factors with low diffusivity) was constructed [12]. This three-component RD model with its linear reaction terms and upper and lower limits describes the apparent interactions obtained experimentally. Then, the different diffusibilities and the interactions in the model achieved diffusion-driven instability (Turing instability).

Further investigations reveal that the interactions are mediated by cell projections [14]. The interaction mediated by gap junctions on the tip of the projection is considered to be a long-range effect observed in the previous experiments [15]. The researchers mention the possibility that the pattern formation might not require actual diffusion. Later, a Turing model based on an integral kernel was suggested [16] though the link between parameter and molecular function was ambiguous. Most other models for pigment-pattern formation are based on interactions at a cellular level. These models implement different effects depending on the distance from each pigment cell by agent-based models [17, 18] and by minimal lattice models [19, 20]. Several attempts were made to explain the observed patterns in zebrafish mutants by a general Turing model [21, 22]; however, they were not supported experimentally even though there are several paths to cause the expected pattern changes in mutants.

Here, the interactions in a three-component model, including a hypothetical highly diffusible factor, are developed to attempt to link the molecular functions of connexins in zebrafish. Channels thought to be important for pattern formation are generalized as "gates" of pigment cells. These gates enable transport of the diffusible molecule across the membrane. The parameters affected by each gate are deduced; then, the effects on pattern selection and size are analyzed. Finally, the model is improved to an analogous model with nonlinear terms. These models together enable reasonable explanations of detailed behavior of the components that relate to the pattern formation.

2 MATERIALS AND METHODS

2.1 Numerical Simulations

For the linear model, d_u was increased from 0 to 0.2 within limits of the reaction term along the x-axis (**Figures 4A, D–H**). It can change the distance between the equilibrium point of u and the upper limitation [23] without shifting the maximum of the limit, and the parameters p_{vw} and c_{wv} were decreased linearly from 1 to 0 (**Figures 4B,D–H**) for investigation of the effect of gates on each cell. For short-range effects, i_{uv} and i_{vu} were decreased linearly from 1 to 0.6 in **Figure 4C**. Accordingly, the arbitrary parameter set generating stripes (wild type) was placed in the right top of the phase plane (**Figures 4D–I**). Partial differential equations (PDEs) were calculated with 20,000 and 40,000 iterations with $dt = 0.1$ and $dt = 0.05$ in fields sized $xl = 56.25$, $yl = 225$ with $dx = 0.75$, and $xl = yl = 200$ with $ds = 0.5$ for **Figures 4A–C** and **Figures 4D–H**, respectively. These conditions satisfy each CLF condition. In **Figure 4I**, to investigate the simultaneous gap-junction effects with hemi-channels $s_d(x, y) = 1 - 0.002 \max\{x, y\}$, $u_d(x) = 0.0004x$, and $v_d(y) = 1 - 0.002y$ were utilized in the field sized $x = y = 300\,(dx = 0.75)$ and $dt = 0.1$ for 20,000 iterations.

For the nonlinear improved model with nonlinear terms, the parameters d_u, i_{uv}, and i_{vu} were decreased linearly from 1 to 0.6. $\boldsymbol{c_{wv}}$ and $\boldsymbol{p_{vw}}$ were decreased linearly from 0.5 to 0.1 in Figures 5A–C and decreased by $s_d(x, y) = 1 - 0.002 \max\{x, y\}$ simultaneously in **Figure 5D**. Accordingly, the arbitrary parameter set generating stripes (wild type) was placed in the right top of the phase plane. PDEs were calculated in fields sized $xl = 10$, $yl = 40$ in **Figures 5A–C** and $xl = yl = 50$ with $ds = 0.25$ in **Figure 5D**. Then, after 500,000 iterations calculated with $dt = 0.01$, we obtained the result.

Calculations were performed in the language Full BASIC ver. 8.1 with no-diffusion boundary conditions with difference calculus; then, results are shown as density plots of u. Parameters utilized in this study are summarized in **Table 1**.

2.2 Quantification of Simulated Color Patterns

Color pattern complexity and overall tone were quantified from binarized images using ImageJ as described in [24]. Briefly, the pattern simplicity score (PSS) is defined as the area weighted mean isoperimetric quotient of the contours extracted from each image. The overall color tone (OCT) of a pattern is defined and calculated as the ratio of white pixels in the binarized image. Analyzed images were prepared by the quaternary connection of a numerical result (100×100 individual fields with periodic boundary conditions) of u in each parameter.

TABLE 1 | Parameter set utilized in this paper.

	D_u, D_v	d_u	i_{uv}	i_{uw}	s_u	i_{vu}	d_v	p_{vw}	s_v	D_w	p_{wu}	c_{wv}	d_w	s_w	f_{max}, g_{max}	h_{max}
Figure 2	0.01	–)0.01	0.05	0.05	0.05	0.05	0.01	0.05	0	1	0.05	0.07	0.05	0.02	0.01	0.05
Figures 4A–D																
Figure 4E	0.01	–)0.01	0.04	0.05	0.05	0.04	0.01	0.05	0	1	0.05	0.07	0.05	0.02	0.01	0.05
Figure 4F	0.01	–)0.01	0.03	0.05	0.05	0.03	0.01	0.05	0	1	0.05	0.07	0.05	0.02	0.01	0.05
Figure 4G	0.01	–)0.01	0.02	0.05	0.05	0.02	0.01	0.05	0	1	0.05	0.07	0.05	0.02	0.01	0.05
Figure 4H	0.01	–)0.01	0.01	0.05	0.05	0.01	0.01	0.05	0	1	0.05	0.07	0.05	0.02	0.01	0.05
Figures 5A–D	0.01	1	0.5	0.5	0.1	1	0.1	1	0.2	1	1	0.5	0.0	—	—	—

3 RESULTS

3.1 Linear RD Model for Pigment-Pattern Formation

Previous laser ablation experiments reveal that the presence of mutual interactions between two types of pigment cells are necessary to generate Turing patterns (**Figure 1E**). Briefly, the density of melanophore existing and newly generated in a stripe decreases when the xanthophores in adjacent interstripes are ablated. On the other hand, that of xanthophore was not drastically changed. Then, two types of pigment cell inhibit each other at a one-cell distance even though the inhibition from xanthophore is inapparent until melanophores in adjacent stripes are eliminated. A mathematical model is derived from these apparent interactions in [12] although the details of the relationship between the experimental results and the model are not described. This model is based on the following set of RD equations:

$$\begin{cases} \dfrac{\partial u}{\partial t} = D_u \nabla^2 u + f(v, w) - d_u u \\ \dfrac{\partial v}{\partial t} = D_v \nabla^2 v + g(u, w) - d_v v \\ \dfrac{\partial w}{\partial t} = D_w \nabla^2 w + h(u, v) - d_w w \end{cases} . \tag{1}$$

Here the alternative distribution of two types of pigment cells (**Figure 1C**) is expressed by two factors (U, V) of the three components. Then, u and v are each volume (viability). The numerical simulation of this model results in a Turing pattern in which u and v are distributed with antiphase, and a concentration of third factor $W(w)$ presents peaks synchronized with u (**Figure 2**). It should be noted that cell divisions of differentiated melanophores contribute only minimally to the pigment-pattern formation in fish (**Figure 1F**). Therefore, the number of melanophores is changed by 1) the supply of new cells from randomly scattered precursor cells, 2) the death of existing pigment cells, or 3) the migration from a position close to the skin surface [25]. In the case of melanophores, it is known that cell movements and cell deaths are complementary to each other [26]. Even though they are inhibited, xanthophores are found in the stripe region, where they exist with a pale color [27–29]. Xanthophores do not move actively *in vivo* as may be the case for iridophores. As detailed in **Figure 1F**, motilities of the cells are approximated by small diffusion coefficients (D). The rapidly diffusing factor W is assumed to have a large diffusion coefficient

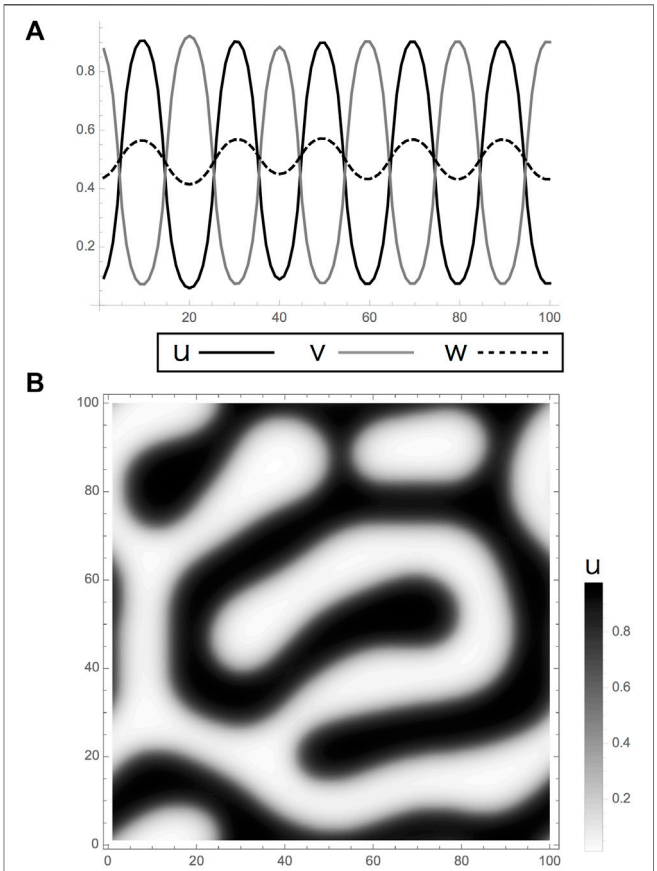

FIGURE 2 | Turing pattern obtained by a reaction-diffusion model in **Eqs 1**, **2**. **(A,B).** Calculation results of the model had linear terms with limits. **(A)** One and **(B)** two dimensions. Results indicate Turing patterns in which the variables u and v are distributed complementarily, and the highly diffusible molecule W peaks at high u.

1 in the outer region of the cells based on the results of electrophysiological experiments [30–32].

In the reaction, rather than it should be called an interaction, formulae, the dimension-less parameters are chosen arbitrarily from the sets that bring diffusion-driven instability. They are positive constants as shown in **Table 1**. Each formula is composed of a set of linear terms with upper and lower limits as utilized in the two-component system mentioned by [1] as follows:

$$\begin{cases} f(v,w) = \begin{pmatrix} 0; -i_{uv}v - i_{uw}w + s_u < 0 \\ -i_{uv}v - i_{uw}w + s_u; 0 < -i_{uv}v - i_{uw}w + s_u < f_{max} \\ f_{max}; -i_{uv}v - i_{uw}w + s_u > f_{max} \end{pmatrix} \\ g(u,w) = \begin{pmatrix} 0; -i_{vu}u + p_{vw}w + s_v < 0 \\ -i_{vu}u + p_{vw}w + s_v; 0 < -i_{vu}u + p_{vw}w + s_v < g_{max} \\ g_{max}; -i_{vu}u + p_{vw}w + s_v > g_{max} \end{pmatrix} \\ h(u,v) = \begin{pmatrix} 0; p_{wu}u - c_{wv}v + s_w < 0 \\ p_{wu}u - c_{wv}v + s_w; 0 < p_{wu}u - c_{wv}v + s_w < h_{max} \\ h_{max}; p_{wu}u - c_{wv}v + s_w > h_{max} \end{pmatrix} \end{cases}. \tag{2}$$

These equations simply indicate negative or positive interactions among two cells and molecules by the coefficients with different signs. They are derived from the interaction network obtained by the experimental results in [12]. The cells are assumed to be inhibiting mutually ($-i_{uv}, -i_{vu}$), and then W is assumed to be produced by U (p_{wu}) and consumed by V ($-c_{wv}$). Accordingly, W is assumed to inhibit pigment cells of the producer ($-i_{uw}$) and produce (or preserve) the consumer (p_{vw}). The self-coupling parameters $-d_u$, $-d_v$, $-d_w$ corresponded to degradation (or death) coefficients, whereas s's represent constants related to the supply (also called "support sustainability") of each component. The producer U activates V but then inhibits itself at long range via W. By consuming W, V also indirectly inhibits itself but then is activating U by double inhibition at long range. As a result, U and V exhibit no difference in apparent interactions, making it difficult to identify which factor corresponds to which cell type. Besides melanophores, xanthophores also show self-inhibition at long range. In laser ablation experiments, melanophore elimination in adjacent stripes causes pale-colored xanthophores in an interstripe region. Therefore, the pale color reflects xanthophore inhibition even without a change in cell number.

The three-component model in **(1)** is somewhat complex though it can be roughly regarded as a combination of two-component systems originally suggested by [33] as follows. For ease of mathematical analyses, I use the following two-component system that shares a component with high-diffusivity.

$$\begin{cases} \dfrac{\partial x}{\partial t} = f_x x + f_y y + D_x \nabla^2 x \\ \dfrac{\partial y}{\partial t} = g_x x + g_y y + D_y \nabla^2 y \end{cases}. \tag{3}$$

There are two different cases that bring diffusion-driven instabilities, i.e., activator–inhibitor type (**Figure 3A**) or activator–substrate–depletion type (**Figure 3B**), characterized by different signs of the parameters [34, 35]. Both conditions are included in the three-component model sharing with the high-diffusible component (**Figure 3C**). Therefore, each parameter in the model can be regarded as part of a two-component system. The first and second reaction **Eq. 2** include mutual inhibitions ($-i_{uv}v, -i_{vu}u$), each of which corresponds to the respective self-activation ($f_x > 0$ for x) though it cannot be realized without each partner. Recent experiments reveal that xanthophores are generated from division of other xanthophores [29]. Therefore, at least one self-reaction parameter; $-d$ for u or v in **Eq. 2** cannot be a degradation coefficient; i.e., it might be a nonnegative parameter.

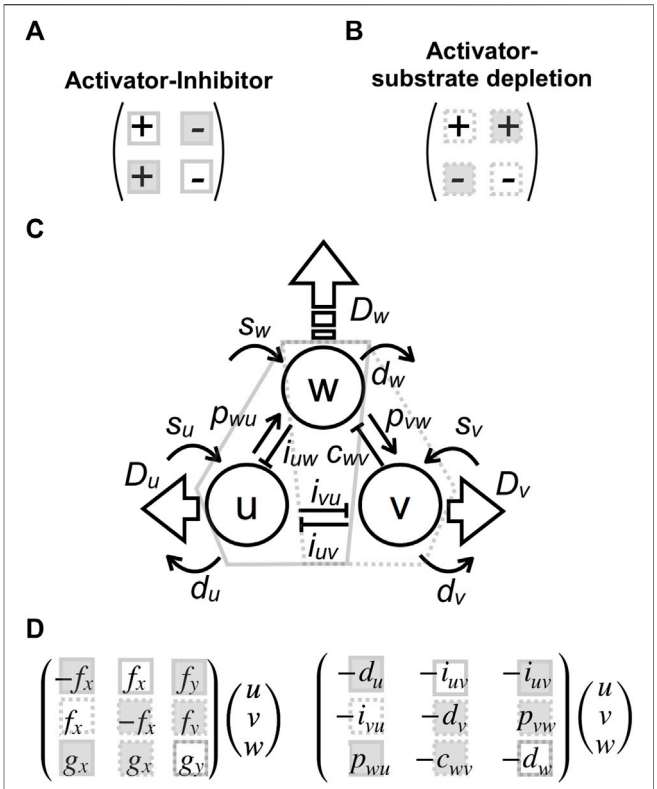

FIGURE 3 | Parameter correspondences to two-component systems and effects on pattern size. **(A,B)** Two conditions that generate a Turing pattern: activator–inhibitor type **(A)** or activator–substrate–depletion type **(B)** with different signs of reaction parameters. **(C)** Correspondence between parameters in the present tree-component model and the two-component systems. Interactions included in conditions **(A)** and **(B)** are enclosed by solid and dashed polygons, respectively. **(D)** Matrix forms of reaction terms corresponding to the two-component system: the filled squares indicate the parameter that increases pattern size when the absolute value is decreased, and the open squares denote the opposite; the solid squares correspond to condition **(A)**, and the dashed ones correspond to condition **(B)**.

3.2 Effects of the Parameters on the Component Proportion and the Characteristic Wavelength of a Pattern.

Variation in patterns observed in most zebrafish mutants is explained by changes in the types and sizes of patterns. The former is defined by pattern selection [23, 36] and manifests as a general variation of the Turing pattern from spots to stripes to reverse spots. The latter is dictated by the characteristic wavelength of the pattern [37]. The following sections analytically describe the effect of parameters in the model (1)–(2) on these characteristics.

3.2.1 Effects of Parameter on Pattern Size

The characteristic wavelength of a pattern can be analytically obtained from the dispersion relation of linear stability [37]. The wavelength of a two-component RD system in **(3)** is given by the following equations of which derivation was mentioned in detail in [37]:

$$\frac{2\pi}{k_{max}} = \sqrt{\frac{\sqrt{D_x D_y}\left(D_y - D_x\right)}{\left(D_x + D_y\right)\sqrt{-f_y g_x} - \sqrt{D_x D_y}\left(f_x - g_y\right)}}. \quad (4)$$

$k_{\max}$ is a preferable wave number in a system. As mentioned, each parameter in the model can be regarded as a two-component system (**Figure 3C**). The mutual inhibitions ($-i_{uv}v$, $-i_{vu}u$) in the three-component system correspond to self-activation though they are inversely related; i.e., the sign of the parameters is different from f_x in two-component systems. The increase in the absolute values of the parameters reinforces the self-activation. At the same time, the effects of $-d_u$ and $-d_v$ are the opposite of f_x. The effect on pattern size when the absolute value of each parameter is decreased (i.e., the decline of each interaction) is shown in **Figure 3D** and indicates correspondence with two-component systems (**Figures 3A,B**).

3.2.2 Effects of Parameter on Pattern Selection

In zebrafish, pattern selection is determined mainly by the proportion of two types of pigment cells with complementary distribution. The relative position of the equilibrium from the limits of the reaction terms provides an index for pattern selection [23] as that is the origin of diffusion-driven instability.

Considering the differential equations, the decrease in each absolute value of parameter (i.e., the decline of each interaction) with a positive effect decreases the population volume of respective cells; then that of the parameter with a negative effect increases the population of the respective cells. Here, the component W with high diffusivity represses u and promotes v; therefore, the decrease in the positive parameter in the differential equations of w increases u and decreases v, respectively. The opposite can apply to negative parameters. From this aspect, however, it is difficult to refer about the combined effect of parameters with different signs.

3.3 Correspondence Between the Mathematical Model and Connexin Defects in Zebrafish Estimated from Molecular Function

Next, correspondence between this model and molecular functions is assumed (**Figure 1G**). In zebrafish, leopard mutants are known to have an aberrant pigment pattern, whereby stripes are changed to spots [6] (**Figures 1A,B**). The gene responsible for the leopard mutation is a connexin cx41.8, which encodes a four trans-membrane connexin protein. Additionally, mutation of connexin cx39.4 results in wavy stripes. Recent analyses of connexin activity reveal different functions associated with hemi-channels and gap junctions [30, 31]. Hemi-channels are open to the extracellular environment, whereas gap junctions form connections between cells to allow the exchange of small molecules (**Figure 1D**). Accordingly, connexins may be involved in both long- and short-range interactions. These channels may function as gates for the transport of molecule W across the membrane (**Figure 1G**). Accordingly, producer U produces W, which then diffuses outside the cell into the extracellular space via some kind of gate. Therefore, gate defects affect survival of the producer by preventing the release of harmful W (i.e., d_u of $-d_u$ is increased). I consider two other possibilities, i.e., the effect of the gate defect on D_w and/or i_{uw}. If D_w is changed, W outside of the cells is also e affected. A u-dependent decrease in D_w might be more appropriate for the assumption of enclosed W though it gives difficulties in the analytical approach and both finally result in an increase in the death of U. Then, the degree of harmful effect on U by the same concentration of w does not change. Therefore, D_w and i_{uw} are not affected. w has peaks with the peaks of producer U, and gates on cells assume passive effects on W movements. Defects of gate on a U cell will enclose W into the cell, then the production of W from U, i.e., p_{wu}, other than d_u will also be affected. If p_{wu} is decreased, v cells will be affected to decrease. However, the supply of w from other than u cells to the system will absorb the negative effects on v, even though the s_w in **Table 1** is 0.0. Then the increase in d_u itself has the effect to decrease the concentration of W. Consumer V is assumed to incorporate beneficial W into the cell across the gates and then to consume it, indicating that the gate defects decrease the parameters c_{vw} of $-c_{vw}$ and p_{wv}. Both parameters are assumed to be related to intracellular events; therefore, higher w is needed for the same rate of consumption and V production compared with the case of intact hemi-channels. At the same time, parameters for mutual inhibitions i_{uv} and i_{vu} seem to be decreased by the leopard mutation [38] through gap junctions (combination of gates) at short range. They are simultaneously affected, linking with the hemi-channel defect on the corresponding cell. In **Figure 1G**, these parameters linked to different gates are indicated by different hatchings.

3.4 Comparisons of Results Obtained by Simulation and Experiments.

First, the independent effects of the gate on each cell were analyzed numerically. When an arbitrary stripe is set as a starting point, only gates that open to the outside on U and V cells were removed along the x- and y-axes. Numerical simulation of this model yielded a spot pattern of u in the case in which gates on U cells have defects as expected by the sign of the parameter (**Figure 4A**). Reversed u spots are yielded in V cell defects (**Figure 4B**) though the change is not strong because it includes opposite effects on V volume. PSS increases in both cases, and then OCT are decreased and increased by respective defects. That is, the asymmetry of changes in pattern selection can be observed by the removals of gates on respective cell types.

Defects on short-range inhibition do not have drastic effects on pattern selection though the pattern does finally disappear (**Figure 4C**). On the 2-D plane, the stripe region is recessive together with the defect in short-range effects by gap junctions (**Figures 4D–H,J**) though the tendency to shift the pattern selection is not changed. In **Figure 4I**, short-range effects are simultaneously decreased by respective x or y values that link with U or V defects as shown in the right panel in **Figure 4J**. This

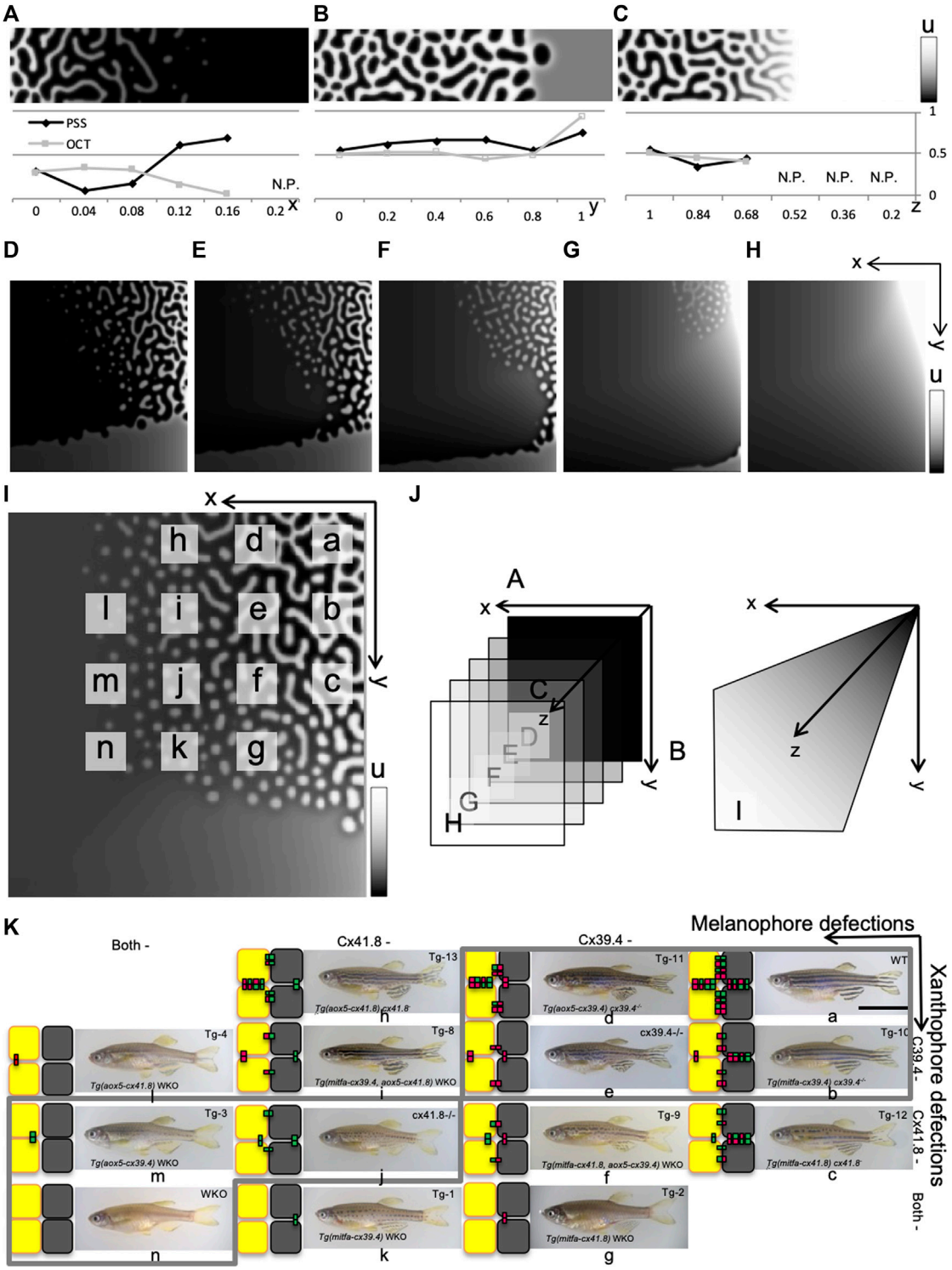

FIGURE 4 | Numerical results of gate effects and comparison with experiments. **(A–I)** Numerical results obtained from a model of linear reaction terms with limits. Pattern shifts were observed when the effects of gate defects on both cells were changed. Defects of gates on *U* and *V* cells and between the cells become larger along the *x*– , *y*–, and *z* (or *x*, *y*)–axes, respectively. **(A–C)** Each defect was analyzed independently with quantification of patterns. **(A)** *U* defect, **(B)** *V* defect, and **(C)** short-range defects. PPS and OCT were obtained quantitatively. The short-range effects by gap junctions were eliminated from arbitral wild-type condition **(D)** 0.05 to **(E)** 0.04, **(F)** 0.03, **(G)** 0.02, and **(H)** 0.01. **(I)** Numerical result of linear terms with limits in which the short-range effects were spontaneously changed along the *x*– and *y*–axes with increasing u_d and decreasing v_d. Each small letter indicates the corresponding fish with connexin conditions. **(J)** Schematics of this analyses utilizing the present linear model. *U* defect, **(B)** *V* defect, and **(C)** short-range defects were changed along with the axes in each panel as shown in the figures. **(K)** Pigmentation pattern on connexin-manipulated fish slightly changed from [8], with permission to use the figures from Dr. M. Watanabe. Gray flamed fish had correspondence to numerical results.

also keeps the same tendency to shift the pattern selection with individual cases.

The results mostly consist of the positive effects of connexin additions to WKO that increase the respective pigment cells [8]. However, experimental eliminations of the gate on each wild-type pigment cell lead to an increase in the rate of respective pigment cells; melanophore defects generate net (or rather wavy stripe) patterns of melanophores, and the xanthophore defects result in dot patterns of melanophores (i.e., net patterns of xanthophore). Therefore, the simulation results are partly inconsistent with experimental results in [8] in which the effects of connexins on each or both pigment cells are investigated in detail (**Figure 4K**).

From the electro-physiological experiments in [30]; each type of connexin can be considered to have different strengths of the (hemi-) channel functions on the two types of cells. Deduced patterns of respective transgenic fish are indicated by small letters on the phase plane in **Figure 4I**. Even though the differences in the strengths of channels are taken into account, the removal of hemi-channels on wild-type xanthophores tends to increase the proportion of xanthophores; then a faint increase of proportion in melanophore is brought in the case of connexin on melanophores (**Figure 4K**). If cell U is a melanophore, other than that the gray-framed patterns shown in **Figure 4K** do not seem to correspond to **Figure 4I**, all of the experimentally obtained patterns exist in the simulation.

From the analyses of wavelength mentioned above, defects to the gates on cell U (increasing in d_u of $-d_u$) or cell V (decreasing in p_{vw} and c_{wv}) cause a decrease or an increase in pattern size, respectively. In numerical simulations, the pattern size tends to be decreased and increased by the hemi-channel defects on both U and V cells as expected (**Figures 3A,B**). The characteristic thinning of u stripes and widening of v interstripes are observed in the simulation of U-cell defects though it is not explained by the analyses. From the characteristic thinning of the u stripe, each cell corresponding to one of two short-range factors may be deduced. However, the thinning is observed on melanophore stripe in the case of a defect in the xanthophore. Inconsistent with the U defect, the melanophore defect tends to result in wide melanophore stripes in the experiment.

3.5 Improvements to the Model with Nonlinear Terms.

To describe the detailed behavior of the components in the system, the model is changed to a model including nonlinear terms as shown in **(5)**.

$$\begin{cases} \dfrac{\partial u}{\partial t} = D\nabla^2 u - i_{uv}uv - i_{uw}uw + d_u u + \dfrac{s_u}{1+u+v} \\ \dfrac{\partial v}{\partial t} = D\nabla^2 v - i_{vu}vu + p_{vw}vw - d_v v + \dfrac{s_v}{1+u+v} \\ \dfrac{\partial w}{\partial t} = \nabla^2 w + p_{wu}u - c_{wv}wv - d_w w + s_w \end{cases} \quad (5)$$

The qualitative relationships for pattern formation shown in **Figure 1F** are not changed from model (1) and (2). That is, mutual inhibitions between U and V ($-i_{uv}uv$, $-i_{vu}vu$) are assumed; then, substance W with high diffusivity is assumed to inhibit the producer U ($-i_{uw}uw$) and to promote consumer V ($p_{vw}vw$). Considering the interactions between different types of cells and between cells and molecules, the inhibitions were given by multiplication terms (e.g., the inhibition of U by W was described as uw and so on). These multiple terms are based on the description of the second order reaction in the chemical kinetic equation or dimer reactions by [39]; it enables only limited reaction by the contacts between the components. W is needed for maintenance of cell V, so this reaction is also given by a multiplication term of their volume. On the other hand, production of W by U only occurs u-dependently, and degradation (and death) is also w-dependent. Therefore, those terms are linearly related to each component. This model as an example of possible improvements also generated Turing patterns (**Figure 5**). These improvements can identify the functions on existing cells or newly differentiating cells. Then, new generations of pigment cells occur only with eliminations of existing cells [40]. Therefore, mature cells would inhibit the new generation of cells. The sign of d_u seemed preferably to be positive for the starting point of pattern selection corresponding to zebrafish, i.e., the start from stripe. Even though the sign was opposite to the linear model, total u change may become minus with relation to other components (i.e., $-i_{uv}v - i_{uw}w + d_u < 0$ in the deformed reaction terms $((-i_{uv}v - i_{uw}w + d_u)u + s_u/(1+u+v))$. Therefore, the self-productivity can be small enough to agree with the low proliferation rate of melanophores. Similarly, concerns about the self-productivity of xanthophores mentioned above, $\partial v/\partial t$ in **(Eq. 5)** already have self-productivity by the multiplication term vw regardless of the sign of d_v (i.e., $-i_{vu}u + p_{vw}w - d_v > 0$ in deformed reaction terms $(-i_{vu}u + p_{vw}w - d_v)v + s_v/(1+u+v)$). The sign of d_v can be inverted though the change is not expected to substantially affect pattern characteristics.

Next, numerical calculations of the nonlinear model are performed to consider the condition in which respective gates on U and V cells and both-gate defects are added (**Figures 5A–C**). Again, numerical results consistent with the linear model can be obtained from an arbitrary parameter set generating a stripe pattern. A biased pattern shift can also be obtained by simulations, partly corresponding to connexin-mutation experiments. When gates on the U cell are deleted, it results in a u dot pattern (**Figure 5A**). Simultaneous decreases in p_{vw} and c_{wv} by increasing the gate defect on V cells generate a net of u though not so drastic (**Figure 5B**). A defect in the gap junction by decreasing i_{vu} and i_{uv} has a minimal effect though the stripe region became recessive with a combination of defects on each outer gate (**Figures 5C,D**). The thinning of the u population is not clear because of the thin stripe at the start.

4 DISCUSSION

In the present study, to confirm the potency of diffusion-driven instability in determining fish pigmentation patterns, channels on

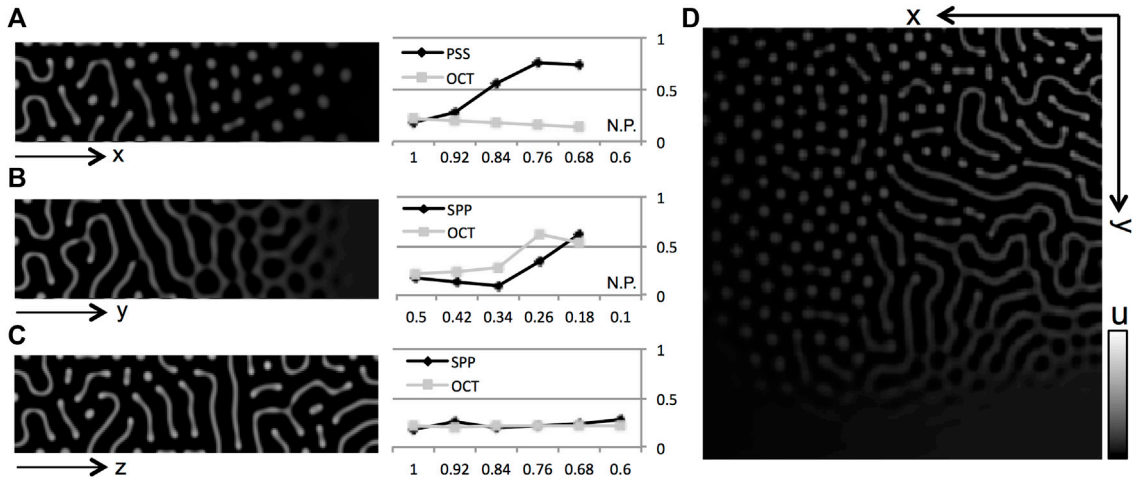

FIGURE 5 | Numerical results of gate effects by nonlinear model. **(A–D)** Numerical results obtained from a model with nonlinear reaction terms. Pattern shifts were observed when the effects of gate defects on both cells were changed. **(A)** U defect, **(B)** *V* defect, and (C) short-range defects, and between the cells, became larger along the *x*–, *y*–, and *z* (or *x*, *y*)-axes, respectively. Pattern quantification by PSS and OCT are shown on the right. Then, the short-range inhibitions were decreased along both axes, spontaneously. All results are shown as density plots of *u*.

pigment cells are generalized as gates (**Figure 1**). The three-component RD model (1) is shown to be composed of two-component RD systems bringing diffusion-driven instabilities (**Figures 2**, **3**). The proposed qualitative models help to understand the relationship between pigment cells as well as between cells and molecules even when their identity is unknown. The terms of the theoretical model are connected with the functions of each channel on different cells. Parameters affected by the gate defects were deduced (**Figure 1G**); then, the effects of such defects are simulated from a parameter set that generates an arbitrary stripe as a benchmark (**Figures 4**, **5**). Then, dots and thinning of the *U* cell population can be obtained by a defect of the gate on it in numerical simulations. The identities of melanophores and xanthophores are deduced from the change of pattern selection and the wavelengths though the identify of important substance *W* is still missing. Then, improvements to the nonlinear model enable a description of the detailed behaviors of components that are related to pattern formation. Though the numerical analyses cannot strictly explain the pattern obtained by experimental manipulation of connexins by [8]; the present study can help to interpret the mechanism underlying the leopard mutation as a Turing system.

The determination of the signs of self-reaction terms for *U* and *V* is difficult. The signs of d_u prefer to invert for a desirable range of pattern selection starting from the stripe in the improved model though the total changes for *U* (= melanophore) correspond to experimental observations. The increase in existing melanophores brought by positive d_u are visible by the laser ablation of adjacent xanthophores or deletion of stripes in the experiments in [12]. Each manipulation decreases $-i_{uv}vu$ or $-i_{uw}wu$ inhibitions, respectively. On the other hand, the self-productivity of xanthophores in the nonlinear model can be achieved even with the negative coefficient of self-reaction. The combination of two cases of diffusion-driven instability in the three-component model indicates the capacity to make a pattern without melanophores by the self-productivity of xanthophores if sufficient *W* is added externally. On the other hand, if melanophores have strong self-productivity, they are also able to make a pattern without xanthophores by the removal of extra *W*.

Connexins are related to both hemi-channels and gap junctions. Hemi-channels are considered less important in physiology although it was recently revealed that the aberrant activity of hemi-channels can change the proportion of vertebrae [31] and are related to the pigment-pattern formation in zebrafish [30, 32]. Laser ablation experiments show that the interactions between xanthophores and melanophores differ depending on the distance. In the present model, the highly diffusible molecule *W* has a positive effect on *V*. Hence, the inhibition of *V* via gap junctions is inconsistent. Outflow of harmful *W* from *via* gap junctions is also inconsistent with the inhibition. Furthermore, generation of a new gap junction between two cells takes more than 30 min [41] (Watanabe personal communication). This elicits a different signal transduction cascade as cell depolarization [42] and incorporation of functions for molecules other than connexin should be envisioned. Then, the inverted function may be derived from an observed rectified current in the gap junction. It is observed that quail melanocytes interact with each other via filopodia *in vivo* and *in vitro* [43]. Therefore, gap junctions may have functions on interactions not only between other types of cells but among the same populations though the obtained simulation results included several collisions with experimental results. Similar discords are also in experiments. The results of [8] indicate that either Cx41.8 or Cx39.4 is needed on melanophores; then, Cx41.8 is necessary and sufficient on xanthophore for (stripe) pattern formation. As plotted in **Figure 6A**, the proportion of pigment cells is drastically changed in the case of the

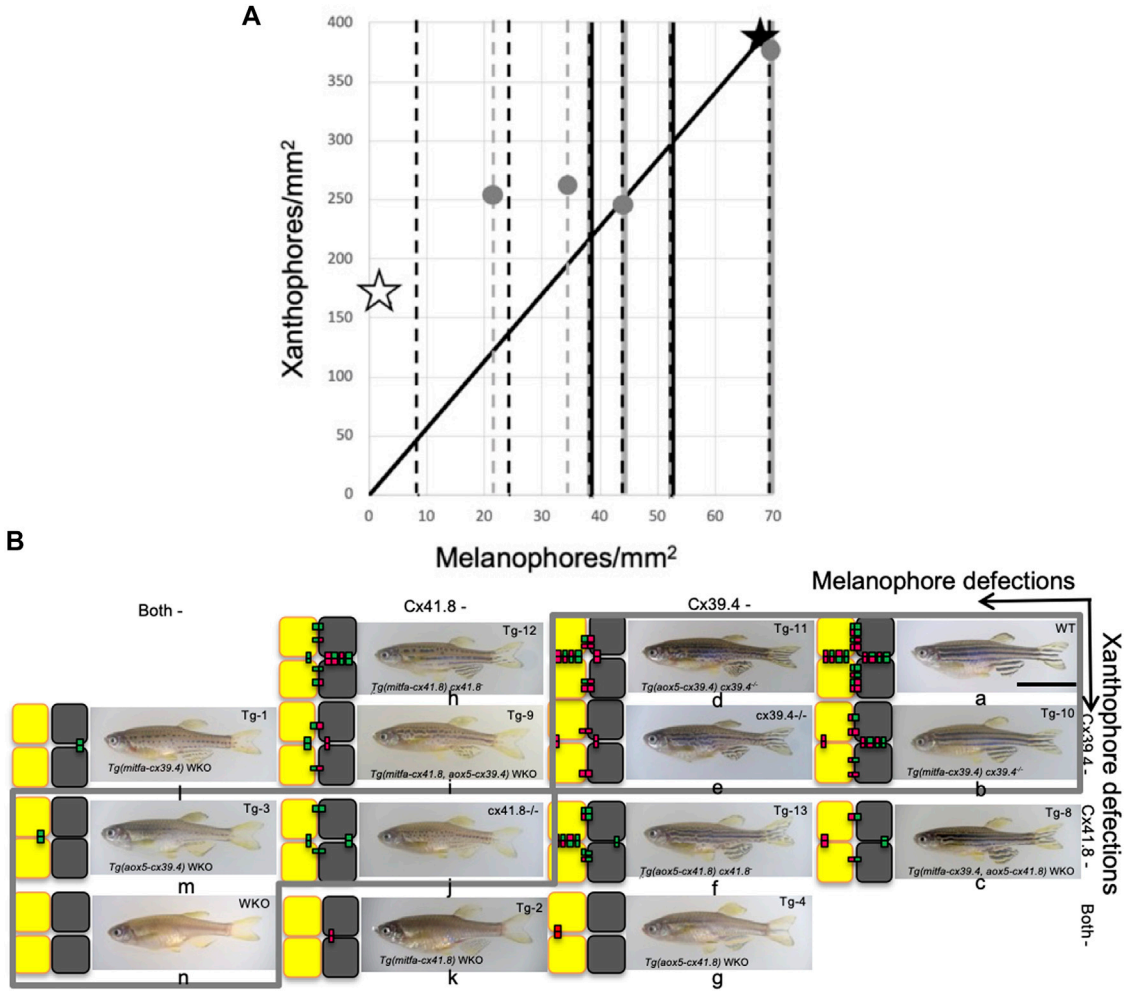

FIGURE 6 | Shuffle of mutant fish that gives accordance with numerical results. **(A)** A scatterplot of two types of pigment cells. Stars and dots indicate shifts of proportion of pigment cells caused by experimental manipulations of connexin by [8]. However, most data can be obtained only about melanophores, so changes in melanophore number are indicated by broken lines. Simple broken lines indicate the addition of connexins to double knockout (WKO); black ones are "on melanophore," and gray ones are "on xanthophore," and broken lines with solid lines on the back denote deletion of connexon from WT; black dot on gray corresponds to "from melanophore" and gray dot on black "from xanthophore." Solid lines indicate the proportion of WT. Open stars and filled ones indicate the values of WKO and WT, respectively. **(B)** Mutant fish are shuffled for accordance with numerical results in **Figure 3I**. Each small letter indicates the corresponding fish with simulation in the aspect of pattern selection.

manipulation of the gate on xanthophores though asymmetry of change in color tones of simulated pattern in **Figures 4A–C** indicate the gate on melanophores is effective. Shuffle of mutant fish further supports the numerical results shown in **Figure 6B**. In this case, expected "Cx41.8" manipulations show the "necessary and sufficient" trait on melanophores.

Similar effects of connexin mutations (i.e., shift from stripe to dots) can be observed on both the body and fins. Because the fins lack iridophores, the effect on the pigment pattern formation depends on the relationship between melanophores and xanthophores. Even though pattern formation is achieved by the two types of cells, details on the role of iridophores in cellular interactions are revealed [10]. The evaluation of the iridophore function in similar modeling is also possible and should be attempted.

Using such a model with PDEs will lead to various mathematical analyses. For example, pattern size was mathematically analyzed with regard the model as combination of two-component systems here. This method cannot yet describe the independent pattern sizes of each type of pigment cell that are observed experimentally [22] and predicted numerically in this paper. Therefore, more sophisticated analyses are required in the future.

DATA AVAILABILITY STATEMENT

The raw data supporting the conclusion of this article will be made available by the authors, without undue reservation.

AUTHOR CONTRIBUTIONS

The author confirms being the sole contributor of this work and has approved it for publication.

FUNDING

This research was supported from Grant-in-Aid for Scientific Research on Innovative Areas (The Japan Society for the Promotion of Science), Periodicity and its modulation in plant No. 20H05421 and Research grant from Shimadzu Science Foundation.

ACKNOWLEDGMENTS

The author thanks Masakatsu Watanabe and Masafumi Inaba for stimulating discussions and important comments as well as members of the Higaki lab for providing a suitable environment to concentrate on this investigation. I also thank Editage (www.editage.com) for English language editing and the IROAST Proofreading/Publication Support Program. I would like to thank to S. Kondo.

REFERENCES

1. Kondo S, Asai R. A Reaction-Diffusion Wave on the Skin of the marine Angelfish Pomacanthus. *Nature* (1995) 376:765–8. doi:10.1038/376765a0
2. Johnson SL, Africa D, Horne S, Postlethwait JH. Half-tetrad Analysis in Zebrafish: Mapping the Ros Mutation and the Centromere of Linkage Group I. *Genetics* (1995) 139:1727–35. doi:10.1093/genetics/139.4.1727
3. Johnson SL, Africa D, Walker C, Weston JA. Genetic Control of Adult Pigment Stripe Development in Zebrafish. *Develop Biol* (1995) 167:27–33. doi:10.1006/dbio.1995.1004
4. Kelsh RN. Genetics and Evolution of Pigment Patterns in Fish. *Pigment Cel Res* (2004) 17:326–36. doi:10.1111/j.1600-0749.2004.00174.x
5. Haffter P, Granato M, Brand M, Mullins MC, Hammerschmidt M, Kane DA, et al. The Identification of Genes with Unique and Essential Functions in the Development of the Zebrafish, *Danio rerio*. *Development* (1996) 123:1–36. doi:10.1242/dev.123.1.1
6. Watanabe M, Iwashita M, Ishii M, Kurachi Y, Kawakami A, Kondo S, et al. Spot Pattern Ofleopard Daniois Caused by Mutation in the zebrafishconnexin41.8gene. *EMBO Rep* (2006) 7:893–7. doi:10.1038/sj.embor.7400757
7. Kumar NM, Gilula NB. The gap junction Communication Channel. *Cell* (1996) 84:381–8. doi:10.1016/s0092-8674(00)81282-9
8. Usui Y, Aramaki T, Kondo S, Watanabe M. The Minimal gap-junction Network Among Melanophores and Xanthophores Required for Stripe Pattern Formation in Zebrafish. *Development* (2019) 146:dev181065. doi:10.1242/dev.181065
9. Volkening A. Linking Genotype, Cell Behavior, and Phenotype: Multidisciplinary Perspectives with a Basis in Zebrafish Patterns. *Curr Opin Genet Develop* (2020) 63:78–85. doi:10.1016/j.gde.2020.05.010
10. Maderspacher F, Nüsslein-Volhard C. Formation of the Adult Pigment Pattern in Zebrafish Requiresleopardandobelixdependent Cell Interactions. *Development* (2003) 130:3447–57. doi:10.1242/dev.00519
11. Parichy DM, Turner JM. Temporal and Cellular Requirements for Fms Signaling during Zebrafish Adult Pigment Pattern Development. *Development* (2003) 130:817–33. doi:10.1242/dev.00307
12. Nakamasu A, Takahashi G, Kanbe A, Kondo S. Interactions between Zebrafish Pigment Cells Responsible for the Generation of Turing Patterns. *Proc Natl Acad Sci* (2009) 106:8429–34. doi:10.1073/pnas.0808622106
13. Meinhardt H, Gierer A. Application of a Theory of Biological Pattern Formation Based on Lateral Inhibition. *J Cel Sci.* (1974) 15:132–46. doi:10.1242/jcs.15.2.321
14. Hamada H, Watanabe M, Lau HE, Nishida T, Hasegawa T, Parichy DM, et al. Involvement of Delta/Notch Signaling in Zebrafish Adult Pigment Stripe Patterning. *Development* (2014) 141:318–24. doi:10.1242/dev.099804
15. Watanabe M, Kondo S. Comment on "Local Reorganization of Xanthophores fine-tunes and Colors the Striped Pattern of Zebrafish". *Science* (2015) 348:297. doi:10.1126/science.1261947
16. Kondo S. An Updated Kernel-Based Turing Model for Studying the Mechanisms of Biological Pattern Formation. *J Theor Biol* (2017) 414:120–7. doi:10.1016/j.jtbi.2016.11.003
17. Volkening A, Sandstede B. Iridophores as a Source of Robustness in Zebrafish Stripes and Variability in Danio Patterns. *Nat Commun* (2018) 9:3231. doi:10.1038/s41467-018-05629-z
18. Owen JP, Kelsh RN, Yates CA. A Quantitative Modelling Approach to Zebrafish Pigment Pattern Formation. *eLife* (2020) 9:E52998. doi:10.7554/eLife.52998
19. Bullara D, De Decker Y. Pigment Cell Movement Is Not Required for Generation of Turing Patterns in Zebrafish Skin. *Nat Commun* (2015) 6:6971. doi:10.1038/ncomms7971
20. Konow C, Li Z, Shepherd S, Bullara D, Epstein IR. Influence of Survival, Promotion, and Growth on Pattern Formation in Zebrafish Skin. *Sci Rep* (2021) 11:9864. doi:10.1038/s41598-021-89116-4
21. Asai R, Taguchi E, Kume Y, Saito M, Kondo S. Zebrafish Leopard Gene as a Component of the Putative Reaction-Diffusion System. *Mech Develop* (1999) 89:87–92. doi:10.1016/s0925-4773(99)00211-7
22. Watanabe M, Kondo S. Changing Clothes Easily: connexin41.8 Regulates Skin Pattern Variation. *Pigment Cel Melanoma Res* (2012) 25:326–30. doi:10.1111/j.1755-148x.2012.00984.x
23. Shoji H, Iwasa Y, Kondo S. Stripes, Spots, or Reversed Spots in Two-Dimensional Turing Systems. *J Theor Biol* (2003) 224:339–50. doi:10.1016/s0022-5193(03)00170-x
24. Miyazawa S, Okamoto M, Kondo S. Blending of Animal Colour Patterns by Hybridization. *Nat Commun* (2010) 1:66–6. doi:10.1038/ncomms1071
25. Takahashi G, Kondo S. Melanophores in the Stripes of Adult Zebrafish Do Not Have the Nature to Gather, but Disperse when They Have the Space to Move. *Pigment Cel Melanoma Res* (2008) 21:677–86. doi:10.1111/j.1755-148x.2008.00504.x
26. Sawada R, Aramaki T, Kondo S. Flexibility of Pigment Cell Behavior Permits the Robustness of Skin Pattern Formation. *Genes Cells* (2018) 23:537–45. doi:10.1111/gtc.12596
27. Hirata M, Nakamura K-i., Kanemaru T, Shibata Y, Kondo S. Pigment Cell Organization in the Hypodermis of Zebrafish. *Dev Dyn* (2003) 227:497–503. doi:10.1002/dvdy.10334
28. Hirata M, Nakamura K-I, Kondo S. Pigment Cell Distributions in Different Tissues of the Zebrafish, with Special Reference to the Striped Pigment Pattern. *Dev Dyn* (2005) 234:293–300. doi:10.1002/dvdy.20513
29. Mahalwar P, Walderich B, Singh AP, Nüsslein-Volhard C. Local Reorganization of Xanthophores fine-tunes and Colors the Striped Pattern of Zebrafish. *Science* (2014) 345:1362–4. doi:10.1126/science.1254837
30. Watanabe M, Sawada R, Aramaki T, Skerrett IM, Kondo S. The Physiological Characterization of connexin41.8 and connexin39.4, Which Are Involved in the Striped Pattern Formation of Zebrafish. *J Biol Chem* (2016) 291:1053–63. doi:10.1074/jbc.m115.673129
31. Misu A, Yamanaka H, Aramaki T, Kondo S, Skerrett IM, Iovine MK, et al. Two Different Functions of Connexin43 Confer Two Different Bone Phenotypes in Zebrafish. *J Biol Chem* (2016) 291:12601–11. doi:10.1074/jbc.m116.720110
32. Watanabe M. Gap junction in the Teleost Fish Lineage: Duplicated Connexins May Contribute to Skin Pattern Formation and Body Shape Determination. *Front Cel Dev. Biol.* (2017) 5:13. doi:10.3389/fcell.2017.00013

33. Turing AM. The Chemical Basis of Morphogenesis. *Philos Trans R Soc Lond B* (1952) 462:27–73.
34. Gierer A, Meinhardt H. A Theory of Biological Pattern Formation. *Kybernetik* (1972) 12:30–9. doi:10.1007/bf00289234
35. Murray JD. *Mathematical Biology II – Spatial Models and Biomedical Applications*. Seattle, WA: University of Washington (2003).
36. Ermentrout B. Stripes or Spots? Nonlinear Effects in Bifurcation of Reaction-Diffusion Equations on the Square. *Proc R Soc A* (1991) 434(1891). doi:10.1098/rspa.1991.0100
37. Miura T, Maini PK. Speed of Pattern Appearance in Reaction-Diffusion Models: Implications in the Pattern Formation of Limb Bud Mesenchyme Cells. *Bull Math Biol* (2004) 66(4):627–49. doi:10.1016/j.bulm.2003.09.009
38. Yamanaka H, Kondo S. *In Vitro* analysis Suggests that Difference in Cell Movement during Direct Interaction Can Generate Various Pigment Patterns *In Vivo*. *Proc Natl Acad Sci U S A* (2013) 111:1867–72. doi:10.1073/pnas.1315416111
39. Meinhardt H. Chapter 11. Cell Determination. In: PK Maini HG Othmer, editors. *Models of Biological Pattern Formation*. London: Academic Press (1982). p. 107–17.
40. Yamaguchi M, Yoshimoto E, Kondo S. Pattern Regulation in the Stripe of Zebrafish Suggests an Underlying Dynamic and Autonomous Mechanism. *Proc Natl Acad Sci* (2007) 104(12):4790–3. doi:10.1073/pnas.0607790104
41. Usui Y, Watanabe M. Role of the Connexin C-Terminus in Skin Pattern Formation of Zebrafish. *BBA Adv* (2021) 1:100006. doi:10.1016/j.bbadva.2021.100006
42. Inaba M, Yamanaka H, Kondo S. Pigment Pattern Formation by Contact-dependent Depolarization. *Science* (2012) 335:677. doi:10.1126/science.1212821
43. Inaba M, Jiang T-X, Liang Y-C, Tsai S, Lai Y-C, Widelitz RB, et al. Instructive Role of Melanocytes during Pigment Pattern Formation of the Avian Skin. *Proc Natl Acad Sci USA* (2019) 116:6884–90. doi:10.1073/pnas.1816107116

Conflict of Interest: The authors declare that the research was conducted in the absence of any commercial or financial relationships that could be construed as a potential conflict of interest.

Publisher's Note: All claims expressed in this article are solely those of the authors and do not necessarily represent those of their affiliated organizations, or those of the publisher, the editors and the reviewers. Any product that may be evaluated in this article, or claim that may be made by its manufacturer, is not guaranteed or endorsed by the publisher.

frontiers in Physics

CORRECTION
published: 23 March 2022
doi: 10.3389/fphy.2022.874424

Corrigendum: Correspondences Between Parameters in a Reaction-Diffusion Model and Connexin Function During Zebrafish Stripe Formation

Akiko M. Nakamasu *

International Research Organization for Advanced Science and Technologies, Kumamoto University, Kumamoto, Japan

Keywords: pattern formation, turing pattern, mathematical model, reaction -diffusion system, pigmentation pattern, connexin

OPEN ACCESS

Edited by:
Istvan Lagzi,
Budapest University of Technology and Economics, Hungary

Reviewed by:
Daishin Ueyama,
Musashino University, Japan
István Szalai,
Eötvös Loránd University, Hungary

***Correspondence:**
Akiko M. Nakamasu
nakamasu@kumamoto-u.ac.jp

Specialty section:
This article was submitted to Physical Chemistry and Chemical Physics, a section of the journal Frontiers in Physics

Received: *12 February 2022*
Accepted: *28 February 2022*
Published: *23 March 2022*

Citation:
Nakamasu AM (2022) Corrigendum: Correspondences Between Parameters in a Reaction-Diffusion Model and Connexin Function During Zebrafish Stripe Formation. Front. Phys. 10:874424. doi: 10.3389/fphy.2022.874424

A corrigendum on

Correspondences Between Parameters in a Reaction-Diffusion Model and Connexin Function During Zebrafish Stripe Formation
by Nakamasu A. M. (2022). Front. Phys. 9:805659. doi: 10.3389/fphy.2021.805659

In the original article, there are errors. Interpretation of the parameter corresponding to the connexin defect in this model was incomplete.

A correction has been made on page 6 to the section **3 RESULTS**, "3.3 Correspondence Between the Mathematical Model and Connexin Defects in Zebrafish Estimated from Molecular Function":

"w has peaks with the peaks of producer U, and gates on cells assume passive effects on W movements. Defects of gate on a U cell will enclose W into the cell, then the production of W from U, i.e., p_{wu}, other than d_u will also be affected. If p_{wu} is decreased, v cells will be affected to decrease. However, the supply of w from other than u cells to the system will absorb the negative effects on v, even though the s_w in **Table 1** is 0.0. Then the increase in d_u itself has the effect to decrease the concentration of W."

Then parameters in **Table 1**, **Figures 5A–D** is as follows, 0.01, 1, 0.5, 0.5, 0.1, 1, 0.1, 1, 0.2, 1, 1, 0.5, 0.0.

The authors apologize for this error and state that this does not change the scientific conclusions of the article in any way. The original article has been updated.

frontiers in Chemistry

ORIGINAL RESEARCH
published: 16 February 2022
doi: 10.3389/fchem.2022.848685

Computing With Networks of Chemical Oscillators and its Application for Schizophrenia Diagnosis

Ashmita Bose and Jerzy Gorecki *

Institute of Physical Chemistry, Polish Academy of Sciences, Warsaw, Poland

OPEN ACCESS

Edited by:
IstvanLagzi,
Budapest University of Technology and Economics, Hungary

Reviewed by:
Ben Costello,
University of the West of England, United Kingdom
Ágota Tóth,
University of Szeged, Hungary
Tamas Bansagi,
University of Bath, United Kingdom

***Correspondence:**
Jerzy Gorecki
jgorecki@ichf.edu.pl

Specialty section:
This article was submitted to Physical Chemistry and Chemical Physics, a section of the journal Frontiers in Chemistry

Received: *04 January 2022*
Accepted: *03 February 2022*
Published: *16 February 2022*

Citation:
Bose A and Gorecki J (2022) Computing With Networks of Chemical Oscillators and its Application for Schizophrenia Diagnosis. Front. Chem. 10:848685. doi: 10.3389/fchem.2022.848685

Chemical reactions are responsible for information processing in living organisms, yet biomimetic computers are still at the early stage of development. The bottom-up design strategy commonly used to construct semiconductor information processing devices is not efficient for chemical computers because the lifetime of chemical logic gates is usually limited to hours. It has been demonstrated that chemical media can efficiently perform a specific function like labyrinth search or image processing if the medium operates in parallel. However, the number of parallel algorithms for chemical computers is very limited. Here we discuss top-down design of such algorithms for a network of chemical oscillators that are coupled by the exchange of reaction activators. The output information is extracted from the number of excitations observed on a selected oscillator. In our model of a computing network, we assume that there is an external factor that can suppress oscillations. This factor can be applied to control the nodes and introduce input information for processing by a network. We consider the relationship between the number of oscillation nodes and the network accuracy. Our analysis is based on computer simulations for a network of oscillators described by the Oregonator model of a chemical oscillator. As the example problem that can be solved with an oscillator network, we consider schizophrenia diagnosis on the basis of EEG signals recorded using electrodes located at the patient's scalp. We demonstrated that a network formed of interacting chemical oscillators can process recorded signals and help to diagnose a patient. The parameters of considered networks were optimized using an evolutionary algorithm to achieve the best results on a small training dataset of EEG signals recorded from 45 ill and 39 healthy patients. For the optimized networks, we obtained over 82% accuracy of schizophrenia detection on the training dataset. The diagnostic accuracy can be increased to almost 87% if the majority rule is applied to answers of three networks with different number of nodes.

Keywords: chemical computing, oscillations, Oregonator model, networks, genetic optimization, schizophrenia, EEG signal

1 INTRODUCTION

It is known that chemical reactions are responsible for acquiring information, transmitting it, and decision-making in living organisms. However, the number of man-written algorithms that can be efficiently executed using a chemical medium Adleman, (1994); Kuhnert (1986), Kuhnert et al. (1989); Steinbock et al. (1995); Agladze et al. (1997); Vazquez-Otero et al. (2012) is quite limited. We believe that the difficulties in practical applications of chemical computers are mainly caused by the fact that an efficient strategy for signal coding using a chemical medium has not been developed yet. The most popular approach to chemical computing imitates information processing with semiconductor devices. In semiconductor devices, information is binary coded in different values of electric potentials.

The success of semiconductor technology came as the consequence of the highly efficient realization of semiconductor binary logic gates. Such gates are characterized by a long time of error-free operation. The semiconductor gates can be assembled together inside an integrated circuit, producing more complicated information processing devices. The bottom-up design strategy Feynman et al. (2000) perfectly matches the technology; complex devices are made as a concatenation of simpler ones. On the contrary, chemical logic gates Toth and Showalter (1995); Steinbock et al. (1996); Sielewiesiuk and Gorecki (2001); Adamatzky et al. (2002) are not small nor fast. The time of their reliable operation is measured in hours, not in years. It seems very hard to make a chemical medium where millions of gates are combined together and work as planned for a long time.

Here we describe and discuss an example of chemical computation based on non-binary information coding. The presented results are based on numerical simulations of the time evolution of the considered computing medium. Such an approach has been motivated by similarities between nerve signals and propagating pulses in a spatially distributed medium in which Belousov-Zhabotinsky (BZ) reaction proceeds Gorecki (2015). The BZ-reaction is catalytic oxidation of an organic substrate in an acidic environment Belousov (1959); Zhabotinsky (1964); Field and Burger (1985); Epstein and Pojman (1994). Two stages of BZ reaction can be visually identified. One of these stages is the fast oxidation of the catalyst. The other is a slow reduction by an organic substrate. The color of the solution of BZ-medium reflects concentrations of catalyst in the oxidized and reduced forms. Therefore, the nonlinear behavior of the medium as oscillations between reduced and oxidized states, propagation of the region characterized by a high concentration of oxidized catalyst, or appearance of spatio-temporal patterns can be easily observed. In a spatially distributed medium, where BZ-reaction proceeds, a local excitation corresponding to the high concentration of $HBrO_2$ can propagate in space in the form of the concentration pulse. This type of behavior resembles the propagation of nerve impulses in living organisms. As a result, the BZ-reaction has attracted attention as a medium for experiments with neuron-like chemical computing Adamatzky et al. (2005); Gorecka and Gorecki (2006). Within the most popular approach to chemical computing with BZ-medium, it is assumed that information is transmitted by propagating pulses of the oxidized form of catalyst. For a binary coding, the presence of a pulse represents the logic TRUE state, and the state with a low concentration of the catalyst in the oxidized form is the logic FALSE state Field and Burger (1985); Epstein and Pojman (1994).

If the ruthenium complex $(Ru(bpy)_3^{2+})$ is used as the reaction catalyst, then BZ-reaction becomes photosensitive Kadar et al. (1997). Oscillations can be inhibited by light. For the same initial concentrations of reagents, the medium can oscillate at dark and show an excitable behavior at a low light intensity. And it converges to a steady-state when it is strongly illuminated.

In a medium with photosensitive BZ-reaction excitable channels in which signals can propagate can be formed by specific illumination of a spatially distributed medium. Using a suitable geometry of excitable and non-excitable channels, one can force an appropriate type of interactions between excitations and, for example, make a signal diode Agladze et al. (1996), a memory cell, or logic gates Adamatzky et al. (2005); Yoshikawa et al. (2009). However, in typical applications, such gates are big (with an area of about 1 cm^2), and a single operation takes more than 10 s Epstein and Pojman (1994). Therefore, the bottom-up approach from gates to complex information processing tasks does not look promising if the binary is used with BZ-medium.

Recent studies have demonstrated that an oscillating BZ-reaction can be efficiently applied for information processing Smelov and Vanag (2018); Vanag VK. (2019); Proskurkin et al. (2020); Egbert, (2019); Duenas-Diez and Perez-Mercader (2019); Duenas-Diez and Perez-Mercader (2020). For example, it has been shown that a network of interacting chemical oscillators can be trained to perform classification tasks with a reasonable accuracy Gruenert et al. (2015); Gizynski and Gorecki (2017a). To illustrate the problem, let us consider a database D_A composed of N records:

$$D_A = \left\{\left(p_n^1, p_n^2, \ldots, p_n^k, q_n\right), n = 1, N\right\}. \tag{1}$$

The records have a form of $(k + 1)$ tuples $(p_n^1, p_n^2, \ldots, p_n^k, q_n)$, where the first k elements are predictors and the last element (q_n) is the discrete record type. A classifier of D_A is supposed to return the correct data type if the predictor values are used as the input.

We can easily define the predictor values and the corresponding record type for many life-inspired classification problems, but usually we do not know how to relate both quantities. For example, the needs of medical diagnostic belong to such class of problems. The input information (the predictor values $(p_n^1, p_n^2, \ldots, p_n^k)$) are collected from several medical tests on the patient $^{\#}$n. On this ground, we are expected to conclude if the patient is healthy or not (the value of q_n). Our knowledge of the relationship between input (results of medical tests) and output (patient's health condition) is based on previously accumulated examples. For such problems, the top-down design strategy Gizynski et al. (2016) of a chemical computing medium seems to be more beneficial than the bottom-up one.

Let us assume we have selected a classification problem to be solved. In the following text, it is the determination if a

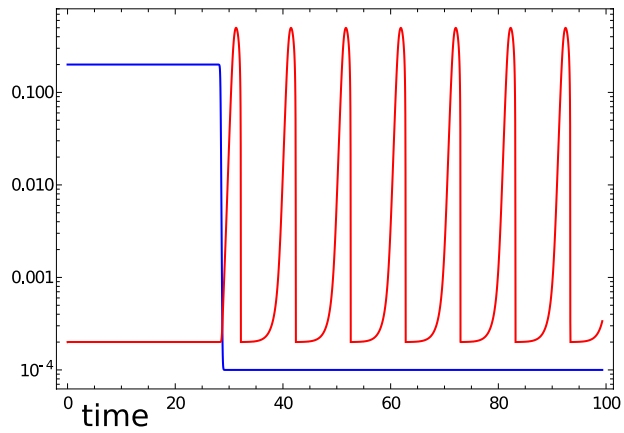

FIGURE 1 | Illumination $\phi_i(t)$ (blue curve) and time evolution of $u_1(t)$ (red curve) in the time interval [0,99.3] predicted by **Eqs 2**, **3** with the considered Oregonator parameters and t_{illum} (1)=28.4.

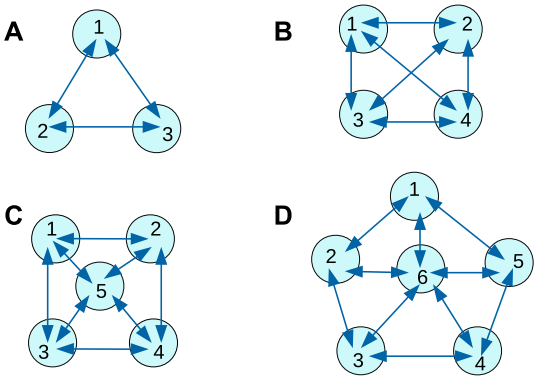

FIGURE 2 | Geometries of oscillator networks considered for the schizophrenia diagnosis. The disks represent individual oscillators that can act as input oscillators or normal ones. Arrows show interactions among the oscillators. The numbers are used to mark individual oscillators in the following description of results. **(A)** 3-oscillator network, **(B)** 4-oscillator network, **(C)** 5-oscillator network, **(D)** 6-oscillator network.

patient has schizophrenia or not. To apply the top-down strategy, we should decide about the medium that is supposed to perform the classification. Here we assume that a network of interacting chemical oscillators can approximately solve the determination of schizophrenia problem. We do not know which network is the best for this task, so we considered a few simple networks illustrated in **Figure 2**. We selected these particular networks because our previous studies indicated that for a fixed number of modes, a large number of connections in increases the accuracy. All networks can include nodes (oscillators) of two types Gizynski and Gorecki (2017a); Gizynski et al. (2016); Gizynski and Gorecki (2016). The input nodes belong to the first type. They are used to introduce the values of predictors into the network. If a node is assigned as the input of the *i*th predictor, then its oscillations are suppressed for the time interval of length related to the value of p_i. There are also so-called normal oscillators that are inhibited for a fixed time that is not related to the predictor value. These normal oscillators moderate interactions between oscillators in the medium and optimize the network to solve a specific problem. The time intervals during which their activity is suppressed do not depend on the input. These time intervals define the program executed by the network. For the analysis presented below, we assume that the output information is coded in the number of oscillation cycles observed on a given node. The choice of the output oscillator follows directly from the network optimization. The complete definition of a computing network includes the number of oscillators in the network, their types, locations, the information about the time intervals they are active, and the information about interactions between oscillators.

Obviously, a network with randomly selected parameters has a small chance to work as a good classifier. We have to optimize its parameters (i.e., to teach a network) to perform the selected function. Teaching means that we need a teacher, and in our optimization, it is a specific database T_A that contains diagnostic results and information if a patient is ill or healthy EEG (n. d.). In the following, we do not change the number of oscillators in a network nor modify the geometry of interactions between them.

The application of the top-down strategy to the considered networks means that the parameters such as locations of the input and normal oscillators, inhibition times for the normal oscillators, the method for inputting the values of predictors, or the parameters of reactions responsible for interactions between oscillators are the subjects of optimization. The optimization is supposed to achieve the best match with a representative (training) dataset of cases T_A. We have found Gruenert et al. (2015); Gizynski and Gorecki (2017a); Gizynski et al. (2016); Gizynski and Gorecki (2016) that evolutionary optimization oriented on obtaining the best classifier for a representative training dataset of the problem can lead to a computing network that performs the anticipated task with reasonable accuracy.

In previous papers on chemical database classifiers Gruenert et al. (2015); Gizynski and Gorecki (2017a); Gizynski et al. (2016); Gizynski and Gorecki (2016) an oversimplified event-based-model reflecting the basic features of the oscillator time evolution and of interactions between oscillators coupled by mutual activations was used. The event-based-model divides an oscillation cycle into three phases: excitation, refractory and responsive phase. It also assumes a sharp difference between these phases. An oscillator in the refractory phase is not susceptible to stimulations by interacting oscillations. However, the event-based-model allows for the excitation of an oscillator in the responsive phase that is in contact with an excited oscillator. In this paper, we consider a more realistic model. We represent the time evolution of an individual oscillator using the two-variable Oregonator model I. R. Epstein and Pojman (1994); Field and Noyes (1974) of the photosensitive Belousov-Zhabotinsky (BZ) reaction.

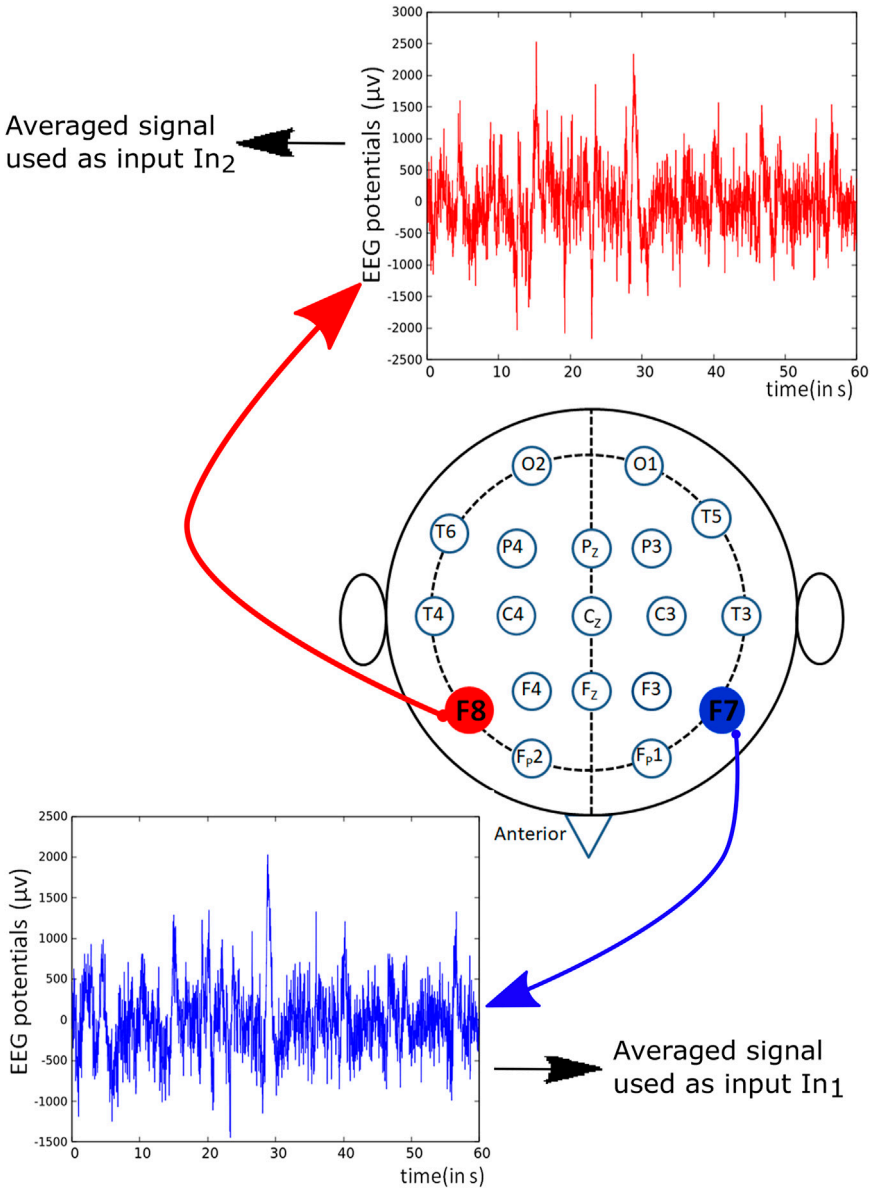

FIGURE 3 | Schematic representation of positions of different electrodes used for recording EEG potentials. The potentials derived from the marked red channels were used to generate predictors in the training dataset T_S.

If we neglect interactions with the other oscillators of the network, then equations describing the time evolution of jth oscillator are:

$$\frac{du_j}{dt} = \frac{1}{\varepsilon}\left(u_j - u_j^2 - \left(fv_j + \phi_j(t)\right)\frac{u_j - q}{u_j + q}\right) \tag{2}$$

$$\frac{dv_j}{dt} = u_j - v_j \tag{3}$$

Where the variables u_j and v_j represent concentrations of an activator (U_j) and an inhibitor (V_j) for proceeding reactions. The parameter ε sets up the ratio of time scales for variables u and v, q is a scaling constant, and f is the stoichiometric coefficient. We used the same values of model parameters for all oscillators in the network in our simulations: $\varepsilon = 0.2$, $q = 0.0002$, and $f = 1.1$. The parameters of the Oregonator model were fixed and did not undergo optimization.

If we assume that the time evolution of oscillators is described by a model of photosensitive BZ-reaction, then oscillators can be individually controlled by illumination, and we include this feature into the considered model as the time-dependent function $\phi_j(t)$ in **Eq. 2**. The time-dependent function $\phi_j(t)$ that describes the influence of illumination on an oscillator is proportional to the light intensity. We considered $\phi_j(t)$ in the form:

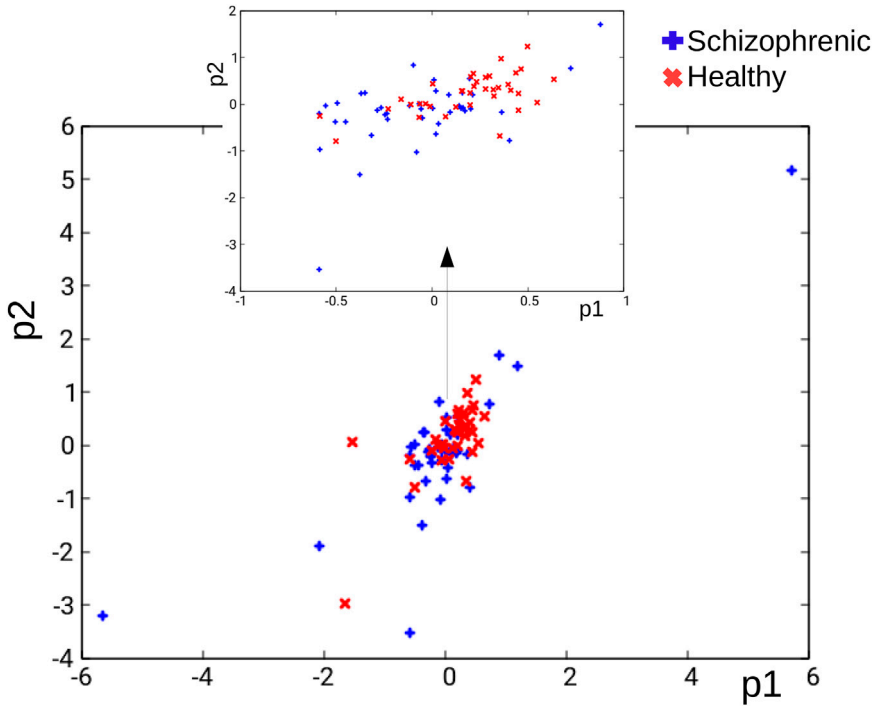

FIGURE 4 | The distribution of records in the T_S database in the (p_1, p_2) coordinates. Blue and red crosses correspond to schizophrenic and healthy cases, respectively.

$$\phi_j(t) = 0.1 \cdot \left(1.001 + \tanh\left(-10 \cdot \left(t - t_{illum}(j)\right)\right)\right) \quad (4)$$

In this definition $t_{illum}(j) > 0$ defines illumination of the jth oscillator. In the time interval $[0, t_{illum}(j) - \delta]$ ($\delta = 0.1$) the value of $\phi_j(t)$ is high (~ 0.2). The Oregonator model with parameters given above predicts a stable steady state corresponding to $u_j = 0.0002$ and $v_j = 0.0002$. For long times ($t > t_{illum}(j) + \delta$) the value of $\phi_j(t)$ approaches 0.0001 what corresponds to oscillations with the period of approximately 10.8 time units. The value of δ describing the speed of transition between the steady state and oscillations can be reduced by increasing the multiplier under tanh () function. In order to extract the answer of a classifier we consider the number of activator maxima within the time interval $Z = [0, t_{\max}]$. It can be noticed that **Eq. (4)** has a physical meaning for any value of $t_{illum}(j)$. If $t_{illum}(i) < 0$ then $\phi_i(t)$ is small and the oscillator $^{\#}i$ is active during the whole observation interval. When $t_{illum}(k) > t_{\max}$ than $\phi_k(t)$ is large and the oscillator $^{\#}k$ is blocked within Z and does not oscillate. **Figure 1** shows the time evolution of activator $u_1(t)$ predicted by **Eqs 2** and **3** with $t_{\max} = 99.3$ and $t_{illum}(1) = 28.4$ (cf. **Table 3**). As seen for such parameters, oscillations restart just after $t_{illum}(1)$, and the system produces seven activator maxima within the observation time interval.

In the investigated networks the values of $t_{illum}(j)$ for normal oscillators were fixed. On the other hand, if an oscillator was considered as the input of p^i ($i = 1, 2$) then $t_{illum}(j)$ was an affine function of p^i (cf. **Eq. 7**). Such function is defined by two parameters t_{start} and t_{end} and it has the form:

$$t_{illum}(j) = t_{start} + (t_{end} - t_{start}) \cdot p^i \quad (5)$$

We assumed that t_{start} and t_{end} are the same for all predictors in the considered schizophrenia records (p^1 and p^2).

It was demonstrated that even a small network composed of 16 or fewer oscillators, with the time evolution of mutual excitations described by the event-based-model could be used to diagnose if a cancer cell is malignant or benign Gizynski and Gorecki (2017a). In this report, we concentrate on designing a network of oscillators that can determine whether the patient has schizophrenia. Schizophrenia is one of the most common forms of psychotic behavior. The patients experience hallucinations, delusion, or disorganized speech. However, schizophrenia is difficult to detect Siebenhuhner et al. (2013). It is believed that the analysis of EEG signals recording brain activity can help to verify if a patient is ill or healthy Ben et al. (2007). The relevant EEG signals were recorded from electrodes placed in different parts of the scalp (see **Figure 3**). We postulate that a network of interacting chemical oscillators in the form presented in **Figure 2** can process the information extracted from the EEG signals and help diagnose schizophrenia. Preliminary results obtained using the network illustrated in **Figure 2D** were reported in the extended abstract of the ASPAI 2020 Conference Bose and Gorecki (2020). For the database T_A, available on the web EEG (n. d.) containing signals recorded on $N = 84$ patients, out of which $N_h = 39$ were healthy and the other had symptoms of schizophrenia ($N_s = 45$) the optimized classifier returned 82% correct answers.

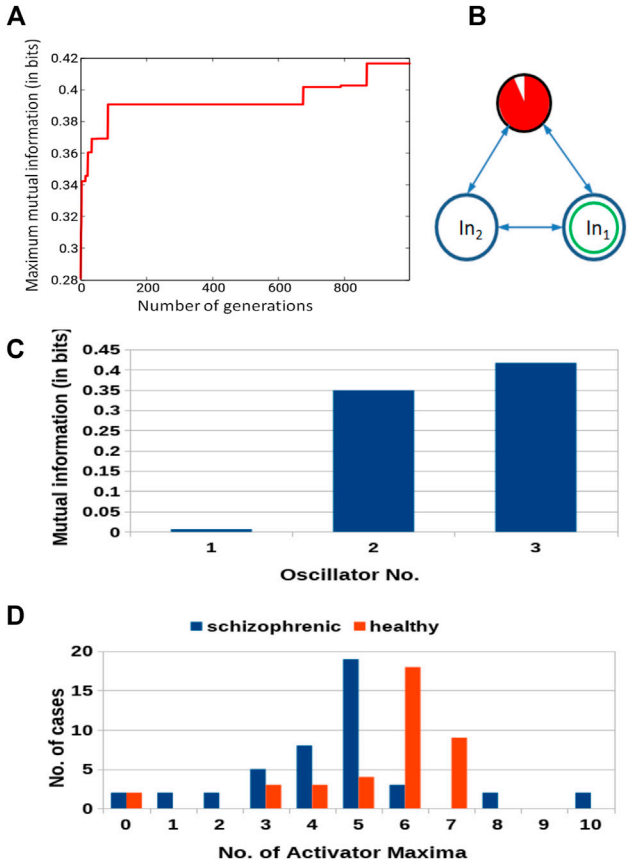

FIGURE 5 | Results for 3-oscillator network (cf. **Figure 2A**): **(A)** The progress of optimization; the *Fitness* as a function of generation number. **(B)** The structure of the optimized network. The disk within a black circle is the normal oscillator. The ratio between the surface of the red shaded part and the disk surface represents the ratio between t^j_{illum} and t_{max}. In_1 and In_2 mark inputs for p^1 and p^2. The disk with the green circle inside is the output oscillator. **(C)** The mutual information $I(G; O_j)$ for $j \in \{1,2,3\}$. The mutual information has the maximum at the oscillator $^{\#}3$. **(D)** The distribution of the numbers of cases for which a given number of activator maxima was observed on oscillator $^{\#}3$. Colors indicate records representing schizophrenic and healthy patients.

The extended study on the schizophrenia classifier in the network's pentagon geometry (**Figure 2D**) was published in the International Journal of Unconventional Computing (IJUC) Bose and Gorecki (2021). In this IJUC paper, we also studied if the classification accuracy can be improved by dividing the whole recorded signal into 3 shorter (20 s long) parts and processing these shorter signals separately. Separated networks with **Figure 2D** geometry were optimized for each time subinterval within 500 generations of evolution. Next, the majority procedure was applied to obtain the final classification results. Such a method increased the classification accuracy of records in T_A to 90%. In the current report, we investigate if the classification accuracy can be improved by the network geometry. The results of schizophrenia diagnosis using classifiers with geometries illustrated in **Figures 2A–C** are new and have not been previously reported. Moreover, the presented results for the pentagon geometry differ from those published because the genetic optimization was performed for 260 more steps than in Bose and Gorecki (2021) and a new maximum of fitness was achieved during these additional steps. Therefore the pentagon-shaped classifier has a different structure than previously reported.

TABLE 1 | Parameters of the optimized 3-oscillator network.

Parameter	Value
t_{max}	99.8
t_{start}	42.5
t_{end}	6.3
α	0.89
β	0.36
t_{illum} (1)	92.5

The manuscript is organized as follows. *Transformation of EEG Signals Into the Input Data* describes how the input data are extracted from the EEG signals. In *Numerical Model of Information Processing Network*, we present a numerical model for the simulation of network time evolution. *Network Optimization and Results* gives details of network optimization. The conclusions and suggestions for the future development of the networks for schizophrenia diagnosis are presented in the following *Conclusion and Discussion*.

2 TRANSFORMATION OF EEG SIGNALS INTO THE INPUT DATA

The considered networks were small, and there was no room for too many input variables because each predictor requires its input oscillator. We used the signals recorded from F7 and F8 channels marked red in **Figure 3** as the inputs for schizophrenia detecting networks described below. Such choice is motivated by previous studies indicating that the signals obtained from the frontal lobe of the brain reveal the difference in the brain activity between a schizophrenic patient and a healthy subject Ben et al. (2007).

The EEG signals were recorded with a sampling rate of 128 Hz for 1 min. The medical EEG test of each patient produced 16 data files corresponding to signals recorded on different electrodes. Each data file contained $K = 7{,}680$ values of recorded potential (in μV). The time between consecutive potential values is $\Delta t = 7.812\ 5\ ms$. Let $V^l(n, k)$ denote the potential recorded for nth patient, on the lth electrode and at the time $t_k = k \cdot \Delta t$. To reduce the size of input data, we averaged the recorded signals. Therefore, each signal was trimmed to a single number. We assumed that time average signals provide us with a sufficient amount of information to diagnose schizophrenia. The averaged potentials were defined as:

$$x^l_n = \sum_{k=0}^{K} V^l(n,k) \tag{6}$$

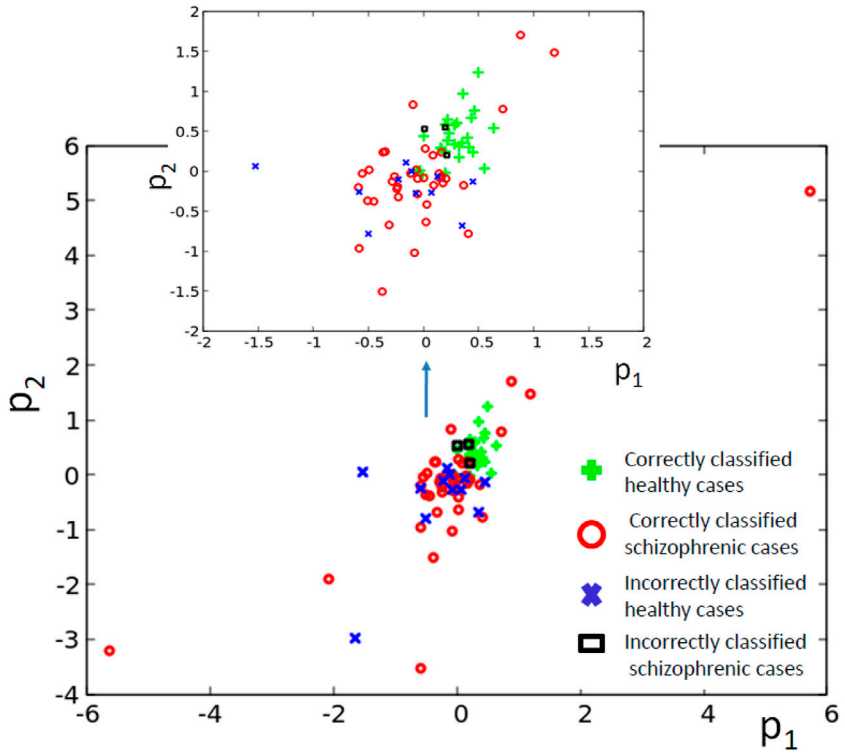

FIGURE 6 | The distribution of correctly and incorrectly classified cases for 3-oscillator network (cf. **Figure 2A**) in the phase space (p_1, p_2).

Next, the time averaged potentials recorded for the whole set of patients were normalized. We introduced:

$$\mu^l = \frac{1}{N}\sum_{n=1}^{N} x_n^l$$

and

$$\sigma^l = \sqrt{\frac{1}{N-1}\sum_{i=1}^{N}\left(x_n^l - \mu^l\right)^2}$$

The values of predictors p_n^1 and p_n^2 for the patient n were defined as:

$$p_n^1 = \frac{x_n^{F7} - \mu^{F7}}{\sigma^{F7}}, p_n^2 = \frac{x_n^{F8} - \mu^{F8}}{\sigma^{F8}} \tag{7}$$

In the above equations $\mu^{F7} = 7.724\,\mu V$, $\mu^{F8} = 2.46\,\mu V$, $\sigma^{F7} = 20.3\,\mu V$ and $\sigma^{F8} = 15.10\,\mu V$.

As a result, the problem of schizophrenia diagnosis is reduced to the best classification of the training dataset: $T_S = \{(p_n^1, p_n^2, q_n), n = 1, N\}$where the record type $q_n = 0$ for a schizophrenic patient and $q_n = 1$ for a healthy subject. The distribution of records in the T_s database in the (p_1, p_2) coordinates is illustrated in **Figure 4**. Blue and red crosses correspond to schizophrenic and healthy cases, respectively. It can be seen that the points corresponding to different cases are not separated, which makes their classification difficult.

In our study, we also considered predictors generated using combinations of signals recorded on other electrodes, but for those, the classification accuracies on corresponding datasets were lower.

3 NUMERICAL MODEL OF INFORMATION PROCESSING NETWORK

The time evolution of reactions proceeding in a single oscillator was described by the two-variable Oregonator model (**Eqs 2** and **3**). We assumed that interactions between the oscillators $^{\#}$k and $^{\#}$j appeared as the results of reactions involving the activators U_k and U_j of these oscillators:

$$U_j + B_j \rightarrow U_k + C_k \tag{8}$$

$$U_k + B_k \rightarrow U_j + C_j \tag{9}$$

with identical reaction rate constant k_B.

We also assumed that the activator of each reaction could spontaneously decay in the binary reaction:

$$U_j + D_j \rightarrow products \tag{10}$$

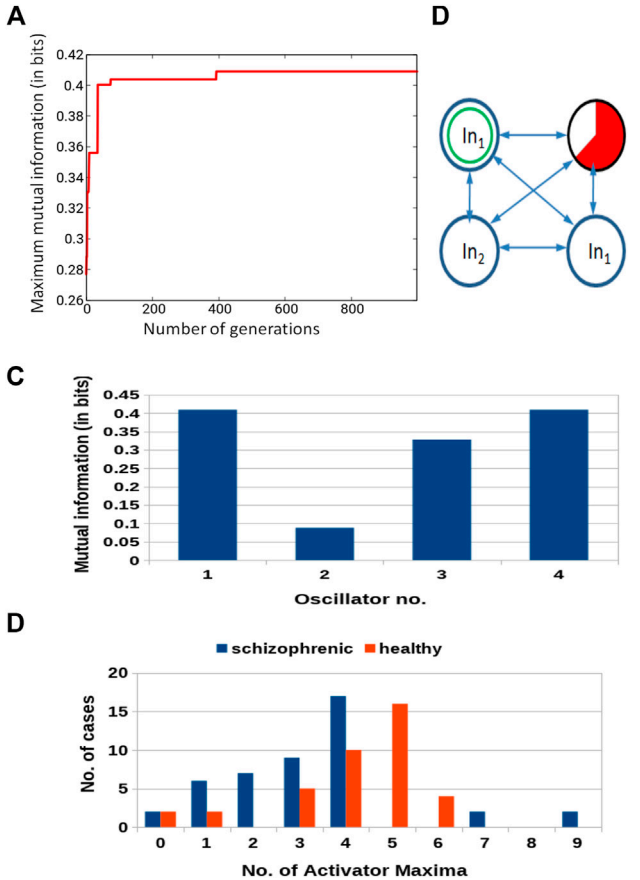

FIGURE 7 | Results for 4-oscillator network (cf. **Figure 2B**): **(A)** The progress of optimization; the *Fitness* as a function of generation number. **(B)** The structure of the optimized network. Notation as in **Figure 5B**. **(C)** The mutual information $I\,(G;\,O_j)$ for $j \in \{1,2,3,4\}$. The function $j \rightarrow I\,(G;\,O_j)$ has the maximum at $j = 1$. **(D)** The distribution of the numbers of cases for which a given number of activator maxima was observed on oscillator $^{\#}1$ for records representing schizophrenic and healthy patients.

with the rate constant k_D. In the equations above symbols B, C and D denote other molecules involved in these reactions. Reactions (8–10) involving species B, C and D are formally introduced to explain chemical communication between nodes and to justify the mathematical description of it.

Therefore, the changes in concentrations of U_k and U_j as the result of reactions (8 and 9) are:

$$\frac{du_j}{dt} = -k_B b_j u_j \tag{11}$$

$$\frac{du_k}{dt} = -k_B b_k u_k \tag{12}$$

and the changes in concentration of U_j as the result of reaction (10) is:

$$\frac{du_j}{dt} = -k_D d_j u_j \tag{13}$$

In **Eqs 11–13** b_j, b_k and d_j denote concentrations of B_j, B_k and D_j, respectively. We assume that these concentrations

TABLE 2 | Parameters of the optimized 4-oscillator network.

Parameter	Value
t_{max}	94.1
t_{start}	57.7
t_{end}	11.5
α	0.61
β	0.36
t_{illum} (1)	59.6

were high with respect to concentrations of activators involved and the same for all oscillators. Therefore, the concentrations of B, C, and D were regarded as constant during the network evolution, and there is no need to include them in the model of network evolution. Let us introduce symbols α and β defined as: $\alpha = k_D d_j$ and $\beta = k_B b_j$. Keeping in mind that values of α and β can be modified by concentrations of B_j and D_j, we can treat them as free parameters that can be easily adjusted. Therefore, the values of α and β can be included in the optimization procedure. The same mathematical description of interactions between nodes applies for controlled exchange of reaction mixtures between nodes and outflow of activator in a system with immobilized catalyst.

Within our model the time evolution of the network is described by the following set of kinetic equations:

$$\frac{du_j}{dt} = \frac{1}{\varepsilon}\left(u_j - u_j^2 - \left(f v_j + \phi_j(t)\right)\frac{u_j - q}{u_j + q}\right) - (\alpha + \beta \sum_{i=1,m} s_{j,i})u_j + \beta(\sum_{i=1,m} s_{j,i}u_i) \tag{14}$$

$$\frac{dv_j}{dt} = u_j - v_j \tag{15}$$

The last two terms in **Eq. 14** represent the coupling in between ith and jth oscillators and the activator decay. The symbols $s_{j,i}$ are defined as:

$s_{j,i} = 0$ if $j = i$ or if $j \neq i$ and oscillators $^{\#}j$ and $^{\#}i$ do not interact,
$s_{j,i} = 1$ if $j \neq i$ and oscillators $^{\#}j$ and $^{\#}i$ do interact.

The set of **Eqs 14** and **15** describes the network evolution after all parameters characterizing the medium including t_{illum} for all oscillators are known.

A classifier is supposed to produce an answer within a finite time. However we do not know it. Therefore, the time t_{max} that defines the interval of time for which the network evolution is observed $[Z = (0, t_{max})]$ is one of the optimized parameters of a classifier. We postulate that information about patient health is extracted from the number of activator maxima recorded on a selected oscillator of the network, during the time interval Z. In order to find which oscillator should be used as the output one we calculate the mutual information $I\,(G;\,O_j)$ Cover and Thomas (2006) between the discrete random variable G of record types in the training dataset T_S $(G = \{q_n,\, n = 1,\, N\})$ and the discrete random variable O_j of the number of activator u_j maxima $o_j(n)$ observed on the jth oscillator in the network when the predictors of nth database record are used as the network

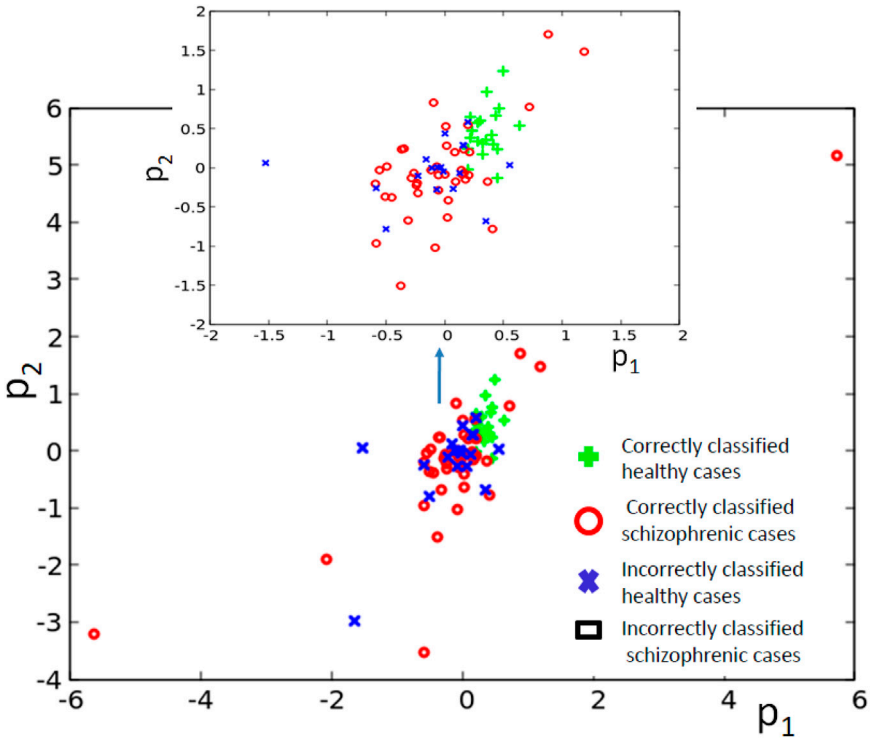

FIGURE 8 | The distribution of correctly and incorrectly classified cases for 4-oscillator network (cf. **Figure 2B**) in the phase space (p_1, p_2).

input ($O_j = \{o_j(n), n = 1, N\}$). The mutual information $I(G; O_j)$ can be calculated as:

$$I(G;O_j) = H(G) + H(O_j) - H(G,O_j) \tag{16}$$

where $H()$ is the Shannon information entropy Shannon (1948) and the discrete random variable $(G, O_j) = \{(q_n, o_j(n)), n = 1, N\}$. The oscillator $^{\#}i$ for which the mutual information between G and O_i is maximal is used as the network output. The mutual information calculated for the output oscillator was considered as the measure of network fitness:

$$Fitness = max_j I(G;O_j) \tag{17}$$

It can be expected that in the majority of cases the optimization based on the mutual information leads to a classifier with the highest accuracy Gorecki (2020).

4 NETWORK OPTIMIZATION AND RESULTS

4.1 Network Optimization

The network parameters as locations of input and normal oscillators, $t_{\max}$, t_{start}, t_{end}, the values of $t_{illum}(j)$ for normal oscillators and the rates α, β were subject of optimization. Following the idea of information coded in spikes Quiroga et al. (2009); Ghosh-Dastidar and Adeli (2009); Vidybida (2011) and the design of chemical classifiers described in Gruenert et al (2015) we optimized the system parameters using an evolutionary algorithm Koza (1989); Fogel (1994). In our calculations, the population of 200 networks was considered. In the beginning, the population of networks was randomly generated. The fitness of each network was calculated using the whole training dataset T_S as defined in **Eq. 17**.

The next generation of classifiers also consisted of 200 elements. It included 2% of the fittest networks from the previous generation that were copied without changes. The remaining 98% elements of the next generation were offsprings created by recombination and mutation operations applied to oscillators from the top 40% networks of the previous population. For recombination, two networks were selected and randomly separated into two parts. The separation into parts was identical for both networks. Next, an offspring was generated by combining one part of the first network with the other part of the second one. At this step, the function of an oscillator (input, normal) and illumination times of normal oscillators were copied to the offspring. The values of $t_{\max}$, t_{start}, t_{end}, α and β were randomly selected from the parent oscillators and copied to the offspring.

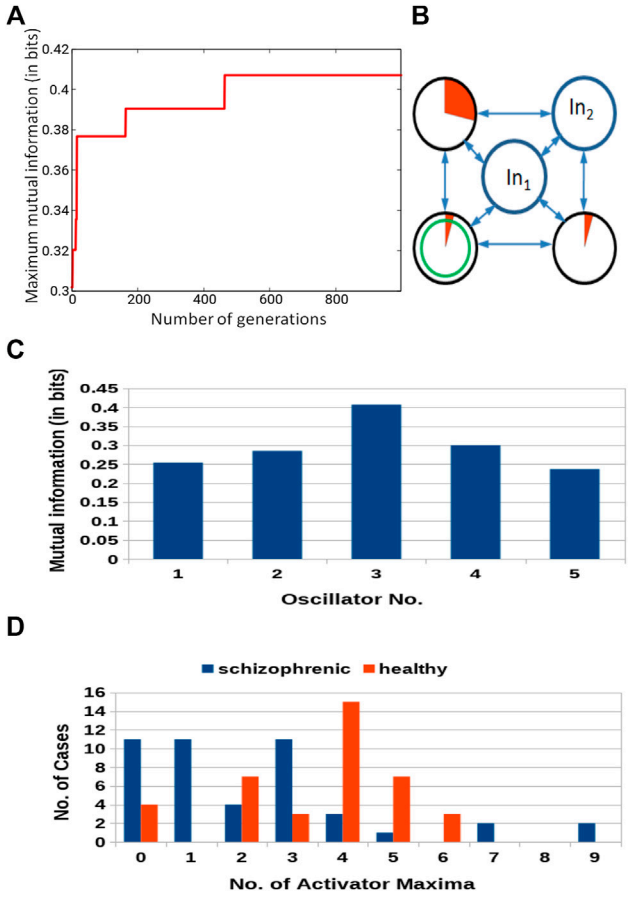

FIGURE 9 | Results for 5-oscillator network (cf. **Figure 2C**): **(A)** The progress of optimization; the *Fitness* as a function of generation number. **(B)** The structure of the optimized network. Notation as in **Figure 5B**. **(C)** The mutual information $I\,(G;\,O_j)$ for $j\,\epsilon\{1,2,3,4,5\}$. The function $j \rightarrow I\,(G;\,O_j)$ has the maximum at j =3. **(D)** The distribution of the numbers of cases for which a given number of activator maxima was observed on oscillator $^{\#}3$ for records representing schizophrenic and healthy patients.

As the next step, mutation of the parameters of the newborn offspring was considered. We allowed for mutation on the rate of coupling between oscillators (β) and the rate of formation of product(α). The probability of mutation rate was 0.5 per step. The mutated values of α and β were the sum of a half of their old values and a random number.

We introduced no constraints on the oscillator types. The recombination procedure could produce an offspring without any input oscillators. It was also possible there were no normal oscillators in the offspring. The fate of such pathological offsprings was decided by its *Fitness*. If it was lower, then the offspring did not qualify into the 40% of networks, and the information about it was not used when the next generation of the networks was created.

The procedure described above was repeated for 1,000 generations. The classifiers discussed in the following were the fittest ones after completing the optimization.

TABLE 3 | Parameters of the optimized 5-oscillator network.

Parameter	Value
t_{max}	99.3
t_{start}	72.5
t_{end}	13.8
α	1.11
β	0.23
t_{illum} (1)	28.4
t_{illum} (3)	4.64
t_{illum} (4)	4.64

4.2 Optimized Networks With Different Numbers of Chemical Oscillators for Schizophrenia Diagnosis

Now, let us present the optimized classifiers of geometries illustrated in **Figure 2**. We studied the time evolution of the networks by numerical solution of **Eqs 14** and **15** using Cash-Karp R-K45 method William press et al (1992) with $h = 10^{-3}$ time steps. The number of activator maxima $o_j(n)$ was calculated as the number of $u_j(t)$ maxima larger than 0.05, observed when the predictors p_n^1, p_n^2 were used as the input.

Figure 5A shows the progress of optimization as the function of number of generations for the network composed of three oscillators. The increase in *Fitness* is fast for the first few generations. Next, it changes into randomly distributed jumps with decreasing amplitude and frequency. Such dependence of the *Fitness* is typical for genetic optimization of classifiers Gruenert et al. (2015); Gizynski and Gorecki (2017a). The *Fitness* observed after 1,000 optimization steps was 0.417 bit. The parameters describing the best classifier are given in **Table 1**.

Figure 5B illustrates the structure of the optimized classifier. It is interesting to notice that the normal oscillator remained non-active for the majority of the time when the network evolution was observed. This feature is reflected by the values of $I\,(G;\,O_j)$ shown in **Figure 5C**. The value of $I\,(G;\,O_1)$ is very small, which means that the activity of the oscillator $^{\#}1$ gives little information about the patient health. The value of $I\,(G;\,O_3)$ = 0.417 is the maximum one; thus, the oscillator $^{\#}3$ was selected as the output one. **Figure 5D** shows the distribution of numbers of activator maxima observed on the oscillator $^{\#}3$ for schizophrenic and healthy patients. This result suggests the following classification rule: a patient is healthy if the number of

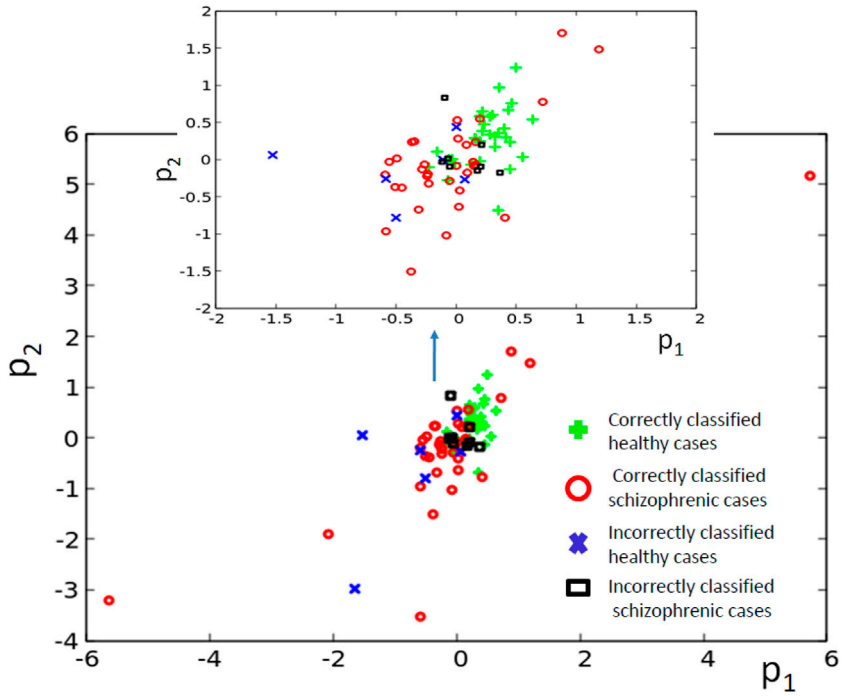

FIGURE 10 | The distribution of correctly and incorrectly classified cases for 5-oscillator network (cf. **Figure 2C**) in the phase space (p_1, p_2).

activator maxima is six or seven. The observation of any other number of maxima diagnoses schizophrenia. The application of this rule gives 15 errors for 84 cases included in T_S (82% accuracy). Only three schizophrenic patients (of 45) are diagnosed as the healthy ones. It gives over 93% accuracy in detecting the illness. On the other hand, 12 healthy people (of 39) are diagnosed as schizophrenic ones (30% error). If these results are confirmed using a large dataset of cases, then the 3-oscillator classifier can detect healthy people with high accuracy, because the "healthy" answer of the classifier is incorrect in three of the total 30 answers (10%). On the other hand, if a person is diagnosed as "ill", then such diagnosis can be wrong in 12 of 54 answers (over 22%). Therefore, the "ill" diagnosis requires further investigation. Positions of correctly and incorrectly classified cases for 3-oscillator network (cf.1a) in the phase space (p_1, p_2) are shown in **Figure 6**.

Similar results for optimization of the 4-oscillator classifier are illustrated in **Figure 7A**. The *Fitness* observed after 1,000 optimization steps was 0.409 bit. The parameters describing the best classifier are given in **Table 2**.

Figure 7B illustrates the structure of the optimized classifier. There are two oscillators that act as inputs of the predictor p^1 and a single input for predictor p^2. Due to the network symmetry I (G; O_1) = I (G; O_4) (**Figure 7C**). These values (0.409 bit) are the maximum ones; thus, both oscillators $^{\#}1$ and $^{\#}4$ can be selected as the output one. In **Figure 7B**, we marked the first of them. **Figure 7D** shows the distribution of numbers of activator maxima observed on the oscillator $^{\#}1$ for schizophrenic and healthy patients. The classification rule based on the majority of cases for a given number of activator maxima is: a patient is healthy if the number of activator maxima is five or six. The observation of any other number of maxima diagnoses schizophrenia. The application of this rule gives 19 errors for 84 cases included in T_S (77% accuracy). All incorrectly diagnosed patients are the healthy ones who are diagnosed as being schizophrenic. On the other hand, ALL schizophrenic patients were correctly diagnosed. **Figure 8** presents locations of correctly and incorrectly classified cases for 4-oscillator network in the phase space (p_1, p_2).

The results for optimization of the 5-oscillator classifier are illustrated in **Figure 9A**. The *Fitness* observed after 1,000 optimization steps was 0.407 bit. The parameters describing the best classifier are given in **Table 3**. **Figure 9B** illustrates the structure of the optimized classifier. It is highly asymmetric and includes three normal oscillators. There are two oscillators that act as inputs of the predictor p^1 and a single input for predictor p^2. The highest value of I (G; O_j) was observed for the oscillator $^{\#}3$ (**Figure 9C**) that has no direct contact with the input of predictor p^2. **Figure 9D** shows the distribution of numbers of activator maxima observed on the oscillator $^{\#}3$. As for the three- and four-oscillator cases the output oscillator does not generate small

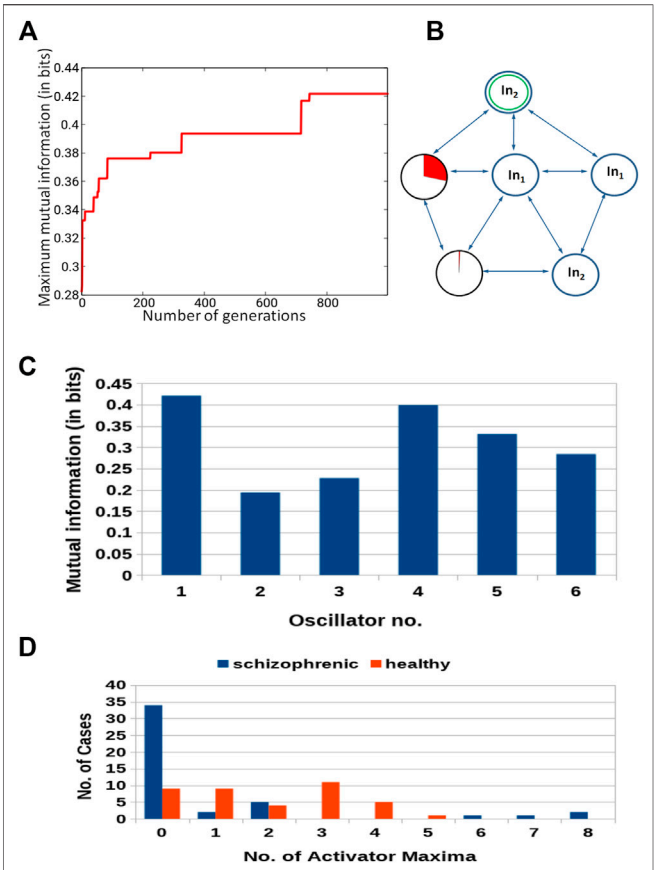

FIGURE 11 | Results for 6-oscillator network (cf. **Figure 2D**): **(A)** The progress of optimization; the *Fitness* as a function of generation number. **(B)** The structure of the optimized network. Notation as in **Figure 5B**. **(C)** The mutual information $I(G; O_j)$ for $j \in \{1,2,3,4,5,6\}$.The function $j \rightarrow I(G; O_j)$ has the maximum at $j = 1$. **(D)** The distribution of the numbers of cases for which a given number of activator maxima was observed on oscillator #1 for records representing schizophrenic and healthy patients.

nor large numbers of activator maxima for healthy patients. The 5-oscillator network diagnoses a patient as a healthy one if the number of activator maxima is 2, 4, 5, or 6. The observation of any other number of maxima diagnoses schizophrenia. The application of this rule gives 15 errors for 84 cases included in T_S (82% accuracy). The schizophrenic patients are diagnosed with very similar accuracy as the healthy ones (82.2 vs. 82.1%). Correctly and incorrectly classified cases for 5-oscillator network are located in the phase space (p_1, p_2), as shown if **Figure 10**.

The classifier made of six oscillators arranged in the geometry illustrated in **Figure 2D** was discussed in our abstract for the ASPAI 2020 Conference Bose and Gorecki (2020) and in Bose and Gorecki (2021). In both publications, the classifier was optimized for 740 generations, and the maximum *Fitness* was 0.416 bit. **Figure 11** shows the results of optimization for 1,000 generations. The *Fitness* observed after 1,000 optimization steps was 0.422 bit. The

TABLE 4 | Parameters of the optimized 6-oscillator network.

Parameter	Value
t_{max}	79.5
t_{start}	72.1
t_{end}	4.9
α	0.25
β	0.77
t_{illum} (2)	22.5
t_{illum} (3)	0.57

parameters of the best classifier are given in **Table 4**. **Figure 11B** illustrates the structure of the optimized classifier. It is similar to that of the classifier reported in Bose and Gorecki (2020, 2021). In all optimized classifiers, there are two normal oscillators, two oscillators that act as inputs of the predictor p^1, and two oscillators representing inputs of p^2. In all classifiers, the input of p^2 was also the classifier output. Moreover, in the central oscillator was the input of p^1. However, there are also differences. In previously reported classifiers, inputs of p^2 were directly interconnected. In the structure shown in **Figure 11B**, they are separated by inputs of p^1. **Figure 11D** shows the distribution of numbers of activator maxima observed on the oscillator $^{\#}1$. On its basis, we can deduce the following classification rule: a patient is healthy if the number of activator maxima is 1, 3, 4, or 5. The observation of any other number of activator maxima indicates that the patient is ill. Application of this rule gives 15 errors for 84 cases included in T_S (82% accuracy); thus, the accuracy is exactly the same as for the classifier reported in Bose and Gorecki (2021). For both classifiers, the structures of errors were similar. The previously reported classifier diagnosed incorrectly 12 of 39 healthy patients and three schizophrenic ones. The classifier reported in this paper diagnosed incorrectly 13 of 39 healthy patients and two who were ill. It is worth noticing that for the majority of schizophrenic cases, the optimized classifier in the geometry in **Figure 11D** did not produce a single activator maximum at the output oscillator. **Figure 12** illustrates the positions of correctly and incorrectly classified cases for 6-oscillator network in the phase space (p_1, p_2).

Using our optimization method, we could not increase the classification accuracy above 82% for any considered geometry within 1,000 optimization steps. However, the accuracy can be increased if one combines answers of different classifiers using the voting strategy. We considered three classifiers that showed the highest accuracy. They were based on 3, 5, and 6 oscillators. The same record was processed by all classifiers, and the majority verdict was taken as the answer. Such a method gave only one mistakenly diagnosed case for 45 schizophrenic records from T_S. The classification accuracy for healthy patients (39 records in T_S) was lower, and 10 such cases were misdiagnosed. Therefore, the overall accuracy of classification increased to 86.9%.

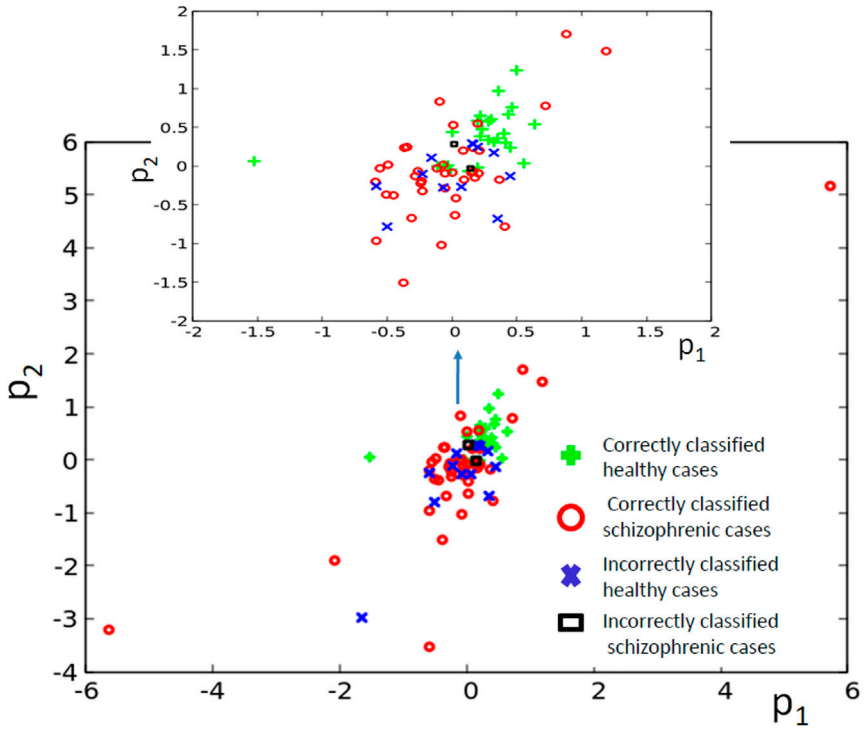

FIGURE 12 | The distribution of correctly and incorrectly classified cases for 6-oscillator network (cf. **Figure 2D**) in the phase space (p_1, p_2).

5 CONCLUSION AND DISCUSSION

One of the most significant challenges of civilization is how to use Artificial Intelligence (AI) for various life-inspired problems AI (2022). AI techniques can be beneficial for medical applications where the knowledge is accumulated as information on previously cured cases. To diagnose a new patient, one should search for similarities with the previous ones. Here we presented an application of AI methods for designing a system that can help to diagnose schizophrenia. We assumed that schizophrenia could be detected by a chemical oscillator network that analyses EEG signals recorded from electrodes located on a patient scalp.

We considered a few information processing networks characterized by different numbers of nodes (c.f. **Figure 2**). We think that networks of interacting chemical oscillators represent more realistic models of biological neural computing than typical artificial neural networks with arbitrarily selected activity rules Kay (2003). Their time evolution is described by realistic kinetic equations that model specific nonlinear chemical reactions. Here we used the Oregonator model for the Belousov-Zhabotinsky reaction. We believe that other, more realistic models Vanag and Epstein (2009) of chemical evolution lead to qualitatively similar results. It seems that oscillator networks require a smaller number of nodes than standard neural networks to achieve the same accuracy. The results presented in Gorecki and Bose (2020) indicate that just three oscillators can solve a geometrical problem of how a point from a unit square is located with respect to a disk placed at the square center with 95% accuracy. The fact that just a few oscillators can perform a complex information processing function, confirmed by the results for schizophrenia diagnostics reported in this paper, opens the door for experimental realization of chemical instant machines with systems of interacting oscillators reported in the literature Juan Manuel et al. (2020); Vanag and Yasuk (2018); Vanag. (2019a); Proskurkin et al. (2019); Gizynski and Gorecki (2017b).

We expected that the schizophrenia diagnosis accuracy increases with the network size. However, the networks formed of 3, 5, and 6 oscillators gave 82% of correct answers for cases included in the training dataset. On the other hand, this number is much higher than given by standard classification methods included as options in the Clasiffy procedure of the Mathematica program Mathematica (2021). If we apply this procedure to the training dataset T_S, the highest classification accuracy (76.2%) is obtained for the GradientBoostedTrees method, whereas the NeuralNetwork option leads to 73.8% accuracy. The accuracy of schizophrenia diagnosis using chemical oscillator networks increased to 86.9% if three networks process a case and the majority rule is used to select the final answer. The fact that larger networks did not produce better results than the small ones could be related to inefficient optimization for a large number of parameters that were taken into account. The problem can be overcome by a larger population of classifiers and a larger number of optimization steps. However, both methods increase the numerical complexity of the optimization. It is also worth mentioning that the recent study on the application of machine learning methods for schizophrenia detection from textual input Wawer et al.

(2022) reported ~ 80% accuracy on a sample of 94 people (47 ill and 47 healthy).

Although the presented results are encouraging, datasets with a larger number of patient data are important for further studies. A dataset with a large number of patient records can be separated into a training dataset of a few thousand cases and much larger testing ones Gorecki and Bose (2020) that is independent of the training one. The separation of records between the training and the testing datasets can be done in many different ways. By selecting different training datasets, one can verify the stability of the schizophrenia diagnostic classifier with respect to different training. The observation that classifiers with similar parameters are obtained for different training datasets confirms that the diagnostics are unbiased by selecting a training dataset.

The presented classification method is based on many assumptions. All of them can be lifted in search of the best network for the schizophrenia diagnosis.

The optimization of interactions in the medium can be directly included in the optimization program. The presented results were obtained assuming that interactions between oscillators were fixed, as shown in **Figure 2**. The information about interactions was included in equations describing the time evolution of oscillators as the binary parameters $s_{i,j}$ in **Eq. 14**. The values of these parameters can be included in classifier optimization. The network model includes the activatory coupling between oscillators. It means that an excited oscillator can speed up the excitations of the other oscillators that interact with it. Such coupling is observed, for example, in droplets containing reagents of BZ reaction. Alternatively, one can consider a medium with inhibitory coupling where excitation of one oscillator slows down the activity of those oscillators that interact with it Vanag and Yasuk (2018); Vanag. (2019b); Proskurkin et al. (2019). Allowing for different types of coupling within a single network can help to identify the best medium for a given computing task.

We assumed that the output could be related to the number of activator maxima observed at a specific oscillator. However, one can consider alternative methods of extracting information from network evolution Borst and Theunissen (1999); Zhang et al. (2014). For example, the output can be related to a pair of numbers of activator excitations recorded on two selected oscillators Gorecki (2020).

It is anticipated that the accuracy of diagnosis should improve if the information on signals recorded on more than two electrodes is included in the input. The presented optimization algorithm can be easily modified to do this if one includes input oscillators of any important signal into the network. If additional signals do not increase the *Fitness*, then networks with the inputs of irrelevant signals will vanish from the population. Moreover, to improve the accuracy of a large oscillator network, one should consider different decay rates α at different oscillators and different activator transfer rates β for individual couplings. Of course, it results in a significant increase in the number of parameters undergoing optimization.

Future studies should reveal if the generalizations of classifiers as described above can significantly increase their accuracy of schizophrenia diagnosis if compared with the classifiers presented in this paper. After a successful classifier optimization is completed, its application does not require significant computing power. There are just two steps of the algorithm: 1) normalization of patient data with parameters (μ, σ) obtained for the training dataset and 2) numerical solution of differential **Eqs 14** and **15** and activator maxima counting. A modern laptop needs a few seconds to execute these tasks. The whole procedure can be incorporated into EEG equipment software or distributed as a laptop or smartphone application.

DATA AVAILABILITY STATEMENT

The original contributions presented in the study are included in the article/Supplementary Material, further inquiries can be directed to the corresponding author.

AUTHOR CONTRIBUTIONS

All authors listed have made a substantial, direct, and intellectual contribution to the work and approved it for publication.

FUNDING

This publication is part of a project that has received funding from the European Union's Horizon 2020 research and innovation programm under the Marie Skłodowska-Curie grant agreement No. 711859. Scientific work funded from the financial resources for science in the years 2017–2022 awarded by the Polish Ministry of Science and Higher Education for the implementation of an international co-financed project.

REFERENCES

Adamatzky, A., De Lacy Costello, B., and Benjamin, K. (2002). Experimental Logical gates in a Reaction-Diffusion Medium: the XOR Gate and beyond. *Phys. Rev. E Stat. Nonlin Soft Matter Phys.* 66, 046112. doi:10.1103/PhysRevE.66.046112

Adamatzky, A., De Lacy Costello, B., and Asai, T. (2005). *Reaction-diffusion Computers*. New York: Elsevier.

Adleman, L. M. (1994). Molecular Computation of Solutions to Combinatorial Problems. *Science* 266 (5187), 1021–1024. doi:10.1126/science.7973651

Agladze, K., Magome, N., Aliev, R., Yamaguchi, T., and Yoshikawa, K. (1997). Finding the Optimal Path with the Aid of Chemical Wave. *Physica D: Nonlinear Phenomena* 106 (3), 247–254. doi:10.1016/s0167-2789(97)00049-3

Agladze, K., Aliev, R., and Yamaguchi, T. (1996). Chemical Diode. *J. Phys. Chem.* 100 (08), 13895–13897. doi:10.1021/jp9608990

Ai (2022). *https://en.wikipedia.org/wiki/Artificial_intelligence*.

Belousov, B. P. 1959. *Collection of Short Papers on Radiation Medicine*. Moscow: Medgiz.

Ben, Dzh., Kaplan, A., Vstovs, G., and Pak, B. (2007). Variability of the EEG Autocorrelation Structure in Adolescents with Schizophrenia Spectrum Disorders. *Fiziologiia cheloveka* 33 (02), 138

Borst, A., and Theunissen, F. E. (1999). Information Theory and Neural Coding. *Nat. Neurosci.* 2 (11), 947–957. doi:10.1038/14731

Bose, A., and Gorecki, J. 2020. Determination of Psychotic Behaviour Using a Network of Chemical Oscillators. ASPAI 2020 Conference Proceedings.

Bose, A., and Gorecki, J. (2021). Can a Network of Chemical Oscillators Help to Diagnose Schizophrenia? *Int. J. Unconventional Comput.* 16, 1.

Cover, T. M., and Thomas, J. A. (2006). *Elements of Information Theory*. New York: Wiley-Interscience.

Duenas-Dez, M., and Perez-Mercader, J. (2019). How Chemistry Computes: Language Recognition by Non-biochemical Chemical Automata. From Finite Automata to Turing Machines. *iScience* 19, 514. doi:10.1016/j.isci.2019.08.007

Dueñas-Díez, M., and Pérez-Mercader, J. (2020). *In-vitro* Reconfigurability of Native Chemical Automata, the Inclusiveness of Their Hierarchy and Their Thermodynamics. *Sci. Rep.* 10, 6814. doi:10.1038/s41598-020-63576-6

EEG *EEG of Healthy Adolescents and Adolescents with Symptoms of Schizophrenia*. http://brain.bio.msu.ru/eeg_schizophrenia.htm.

Egbert, M., Gagnonn, J. S., and Pérez-Mercader, J. (2019). From Chemical Soup to Computing Circuit: Transforming a Contiguous Chemical Medium into a Logic Gate Network by Modulating its External Conditions. *J. R. Soc. Interf.* 16, 20190190. doi:10.1098/rsif.2019.0190

Epstein, I. R., and Pojman, J. A. (1994). *Introduction to Nonlinear Chemical Dynamics: Oscillations, Waves, patterns, and Chaos.* New York: Oxford University Press.

Feynman, R. P., Hey, T., and Allen, R. W. (2000). *Feynman Lectures on Computation*. Boulder, Colorado USA: CRC Press.

Field, R. J., and Burger, M. (1985). *Oscillations and Traveling Waves in Chemical Systems*. New York: Wiley.

Field, R. J., and Noyes, R. M. (1974). Oscillations in Chemical Systems. IV. Limit Cycle Behavior in a Model of a Real Chemical Reaction. *J. Chem. Phys.* 60 (5), 1877–1884. doi:10.1063/1.1681288

Fogel, D. B. (1994). An Introduction to Simulated Evolutionary Optimization. *IEEE Trans. Neural Netw.* 5 (1), 3–14. doi:10.1109/72.265956

Ghosh-Dastidar, S., and Adeli, H. (2009). Spiking Neural Networks. *Int. J. Neural Syst.* 19 (08), 295–308. doi:10.1142/s0129065709002002

Gizynski, K., and Gorecki, J. (2017a). Cancer Classification with a Network of Chemical Oscillators. *Phys. Chem. Chem. Phys.* 19 (10), 28808–28819. doi:10.1039/c7cp05655a

Gizynski, K., Gruenert, G., Dittrich, P., and Gorecki, J. (2016). Evolutionary Design of Classifiers Made of Droplets Containing a Nonlinear Chemical Medium. *Evol. Comput.* 25 (10), 643–671. doi:10.1162/EVCO_a_00197

Gizynski, K., and Gorecki, J. (2017b). Chemical Memory with States Coded in Light Controlled Oscillations of Interacting Belousov-Zhabotinsky Droplets. *Phys. Chem. Chem. Phys.* 19 (9), 6519–6531. doi:10.1039/c6cp07492h

Gizynski, K., and Gorecki, J. (2016). A Chemical System that Recognizes the Shape of a Sphere. *Comput. Methods Sci. Techn.* 22 (12), 167. doi:10.12921/cmst.2016.0000057

Gorecka, J., and Gorecki, J. (2006). Multiargument Logical Operations Performed with Excitable Chemical Medium. *J. Chem. Phys.* 124, 084101. doi:10.1063/1.2170076

Gorecki, J. (2020). Applications of Information Theory Methods for Evolutionary Optimization of Chemical Computers. *Entropy (Basel)* 22 (03), 313. doi:10.3390/e22030313

Gorecki, J., and Bose, A. (2020). How Does a Simple Network of Chemical Oscillators See the Japanese Flag? *Front. Chem.* 8, 580703. doi:10.3389/fchem.2020.580703

Gorecki, J., Gizynski, K., Guzowski, J., Gorecka, J. N., Garstecki, P., Gruenert, G., et al. (2015). Chemical Computing with Reaction-Diffusion processesChemical Computing with Reaction - Diffusion Processes. *Phil. Trans. R. Soc. A. Soc.* 373, 20140219. doi:10.1098/rsta.2014.0219

Gruenert, G., Gizynski, K., Escuela, G., Ibrahim, B., Gorecki, J., and Dittrich, P. (2015). Understanding Networks of Computing Chemical Droplet Neurons Based on Information Flow. *Int. J. Neur. Syst.* 25, 1450032. doi:10.1142/s0129065714500324

Kádár, S., Amemiya, T., and Showalter, K. (1997). Reaction Mechanism for Light Sensitivity of the Ru(bpy)32+-Catalyzed Belousov–Zhabotinsky Reaction. *J. Phys. Chem. A.* 101 (44), 8200–8206. doi:10.1021/jp971937y

Kay, David. J. C. (2003). *Information Theory, Inference and Learning Algorithms*. USA: University Press

Koza, J. R. (1989). "Hierarchical Genetic Algorithms Operating on Populations of Computer Programs," in *Proc. Eleventh Int. Joint Conf. Artificial Intelligence IJCAI-89*.

Kuhnert, L. (1986). A New Optical Photochemical Memory Device in a Light-Sensitive Chemical Active Medium. *Nature* 319 (Jan.), 393–394. doi:10.1038/319393a0

Kuhnert, L., Agladze, K. I., and Krinsky, V. I. (1989). Image Processing Using Light-Sensitive Chemical Waves. *Nature* 337, 244–247. doi:10.1038/337244a0

Mathematica (2021). *https://www.wolfram.com/mathematica/*.

Parrilla-Gutierrez, J. M., Sharma, A., Tsuda, S., Cooper, G. J. T., Aragon-Camarasa, G., Donkers, K., et al. (2020). A Programmable Chemical Computer with Memory and Pattern Recognition. *Nat. Commun.* 11, 1442. doi:10.1038/s41467-020-15190-3

Proskurkin, I. S., Smelov, P. S., and Vanag, V. K. (2019). Experimental Investigation of the Dynamical Modes of Four Pulse-Coupled Chemical Micro-Oscillators. *ChemPhysChem* 20 (17), 2162–2165. doi:10.1002/cphc.201900421

Proskurkin, I. S., Smelov, P. S., and Vanag, V. K. (2020). Experimental Verification of an Opto-Chemical "neurocomputer". *Phys. Chem. Chem. Phys.* 22, 19359–19367. doi:10.1039/d0cp01858a

Quian Quiroga, R., Panzeri, S., and Panzeri, D. (2009). Extracting Information from Neuronal Populations: Information Theory and Decoding Approaches. *Nat. Rev. Neurosci.* 10, 173–185. doi:10.1038/nrn2578

Shannon, C. E. (1948). A Mathematical Theory of Communication. *Bell Syst. Tech. J.* 27 (3), 379–423. doi:10.1002/j.1538-7305.1948.tb01338.x

Shennan, A., Daniel, R., and Bassett, D. S. (2013). Intra- and Inter-frequency Brain Network Structure in Health and Schizophrenia. *PLOS ONE* 8 (8), 1. doi:10.1371/journal.pone.0072351

Siebenhuhner, F., Weiss, S. A., Coppola, R., Weinberger, D. R., and Bassett, D. S.(2013). Intra- and Inter- Frequency Brain Network Structure in Health and Schizophrenia. *PLos ONE* 8 (8), e72351. doi:10.1371/journal.pone.0072351

Sielewiesiuk, J., and Gorecki, J. (2001). Logical Functions of a Cross Junction of Excitable Chemical Media. *J. Phys. Chem. A* 105 (08), 8189–8195. doi:10.1021/jp011072v

Smelov, P. S., and Vanag, V. K. (2018). A 'reader' Unit of the Chemical Computer. *R. Soc. Open Sci.* 5 (01), 171495. doi:10.1098/rsos.171495

Steinbock, O., Kettunen, P., and Showalter, K. (1996). Chemical Wave Logic Gates. *J. Phys. Chem.* 100 (49), 18970–18975. doi:10.1021/jp961209v

Steinbock, O., Tóth, Á., and Showalter, K. (1995). Navigating Complex Labyrinths: Optimal Paths from Chemical Waves. *Science* 267 (5199), 868–871. doi:10.1126/science.267.5199.868

Tóth, Á., and Showalter, K. (1995). Logic gates in Excitable media. *J. Chem. Phys.* 103 (6), 2058–2066. doi:10.1063/1.469732

Vanag, V. K. (2019a). Hierarchical Network of Pulse Coupled Chemical Oscillators with Adaptive Behavior: Chemical Neurocomputer. *Chaos* 29, 083104. doi:10.1063/1.5099979

Vanag, V. K. (2019b). "Cognitive" Modes in Small Networks of Almost Identical Chemical Oscillators with Pulsatile Inhibitory Coupling. *Chaos* 29, 033106. doi:10.1063/1.5063322

Vanag, V. K., and Yasuk, V. O. (2018). Dynamic Modes in a Network of Five Oscillators with Inhibitory All-To-All Pulse Coupling. *Chaos* 28, 033105. doi:10.1063/1.5004015

Vanag, Vr., and Epstein, I (2009). A Model for Jumping and Bubble Waves in the Belousov-Zhabotinsky-Aerosol OT System. *J. Chem. Phys.* 131 (09), 104512. doi:10.1063/1.3231488

Vazquez-Otero, A., Faigl, J., and Munuzuri, A. 2012). *Path Planning Based on Reaction-Diffusion Process*.doi:10.1109/iros.2012.6385592

Vidybida, A. (2011). Testing of Information Condensation in a Model Reverberating Spiking Neural Network. *Int. J. Neur. Syst.* 21, 187–198. doi:10.1142/s0129065711002742

Wawer, Ar., Chojnicka, I., Okruszek, L., and Sarzynska-Wawer, J. (2022). Single and Cross-Disorder Detection for Autism and Schizophrenia. *Cogn. Comput.* 14 (01), 461–473. doi:10.1007/s12559-021-09834-9

William Press, H., SaulTeukolsky, A., and WilliamVetterling, T. (1992). *Numerical Recipes in C ,the Art of Scientific Computing, 2nd Edn*. USA: Cambridge University Press.

Yoshikawa, K., Motoike, I. N., Ichino, T., Yamaguchi, T., Igarashi, Y., Górecki, J., et al. (2009). Basic Information Processing Operations with Pulses of Excitation in a Reaction-Diffusion System. *Int. J. Unconventional Comput.* 5 (1), 3

Zhabotinsky, A. M. (1964). Periodic Liquid Phase Reactions. *Proc. Acad. Sci. USSR* 157, 392

Zhang, G., Rong, H., Neri, F., and Pérez-Jiménez, M. J. (2014). An Optimization Spiking Neural P System for Approximately Solving Combinatorial Optimization Problems. *Int. J. Neural Syst.* 24 (08), 1440006. doi:10.1142/S0129065714400061

Conflict of Interest: The authors declare that the research was conducted in the absence of any commercial or financial relationships that could be construed as a potential conflict of interest.

frontiers in Physics

ORIGINAL RESEARCH
published: 07 March 2022
doi: 10.3389/fphy.2022.849111

Self-Propelled Motion of an Oil Droplet Containing a Phospholipid and its Stability in Collectivity

Masaki Itatani[1] *and Hideki Nabika*[2]*

[1]Graduate School of Science and Engineering, Yamagata University, Yamagata, Japan, [2]Faculty of Science, Yamagata University, Yamagata, Japan

Collective cell migration (CCM) is a universal process that is responsible for various biological phenomena in living organisms. Therefore, unraveling the mechanism of CCM is critical for understanding the principles underlying such processes and for their application in biomaterials and biomedical science. Among these phenomena, unjamming/jamming transitions are particularly intriguing as they are controlled by three factors: cell motility, cell density, and cell–cell adhesion. However, there is no experimental system to independently demonstrate and control these effects. In this study, we added 1,2-dimyristoyl-*sn*-glycero-3-phosphocholine (DMPC) to a nitrobenzene droplet containing KI and I_2 to develop a prototype system that shows self-propelled motion in an aqueous trimethylstearylammonium chloride (TSAC) solution. First, we explored the relationship between the motility of the droplet and experimental parameters, namely, the concentrations of TSAC, I_2, and DMPC and droplet size. The droplet showed directional motion driven by Marangoni convection owing to a solubilization promoted by the formation of mixed micelles filled with oil between DMPC and TSA^+; notably, droplet motility could be controlled by each parameter. Furthermore, the interfacial tension (γ) at the oil–water interface, measured using the pendant drop method, indicated that each parameter contributed to changes in γ. Based on our experimental results, we inferred that the dynamics of the insertion of TSA^+ in the aqueous phase into the self-assembled DMPC membrane covering the nitrobenzene droplet, as well as the solubilization, are important factors that trigger Marangoni convection and lead to controlled droplet motility. Furthermore, the developed droplets remained stable in a confluent state, wherein they were in contact with each other and exhibited various polygonal shapes depending on their size and density because they were protected by a robust self-assembled DMPC membrane layer. The results indicated that the density and the morphology of the droplets are controllable in this system, and that they indirectly altered droplet adhesion. Thus, we procured a prototype system that could be controlled independently using three parameters to elucidate phase transition for CCM. This system can be biomodified through the combination of phospholipids with any biomolecule and can enable a more precise evaluation of the CCM exhibited by living cells.

Keywords: nonlinear science, active matter, phospholipid, self-propelled motion, oil droplet, surface chemistry

OPEN ACCESS

Edited by:
Nobuhiko J. Suematsu, Meiji University, Japan

Reviewed by:
Taisuke Banno, Keio University, Japan
Ryan McGorty, University of San Diego, United States

***Correspondence:**
Hideki Nabika
nabika@sci.kj.yamagata-u.ac.jp

Specialty section:
This article was submitted to Physical Chemistry and Chemical Physics, a section of the journal Frontiers in Physics

Received: *05 January 2022*
Accepted: *21 February 2022*
Published: *07 March 2022*

Citation:
Itatani M and Nabika H (2022) Self-Propelled Motion of an Oil Droplet Containing a Phospholipid and its Stability in Collectivity. Front. Phys. 10:849111. doi: 10.3389/fphy.2022.849111

Abbreviations: CCM, collective cell migration; DMPC, 1,2-dimyristoyl-sn-glycero-3-phosphocholine; TSAC, trimethylstearylammonium chloride; CMC, critical micellar concentration; PEG, polyethylene glycol; potassium iodide, KI.

INTRODUCTION

Cell migration plays a central role in the development and maintenance of the morphologies and functions of cells in multicellular organisms, wherein cells move toward and between tissue compartments either individually or collectively [1, 2]. In particular, it has been reported that collective cell migration (CCM) [3, 4] is involved in embryo development [5], wound healing [6], and cancer infiltration and metastasis [7, 8]. Therefore, elucidating the mechanism underlying CCM would not only lead to a better understanding of the basis of life science phenomena but also to a wide range of applications, including the development of drugs that utilize this mechanism. However, it is difficult to study the underlying mechanism of CCM because interactions during this process are usually complex. Previous studies of single cell migration have provided fundamental insights into cell migration. According to these studies, the motion of a cell is induced by the following factors: the generation of differences in intracellular tensions for directed movement (cell polarization) through competitive actin polymerization and formation of actomyosin networks [9–11], and the development of chemical and/or physical factor gradients [12–14]. Therefore, the mechanism of single cell migration has been clarified sufficiently. On the other hand, cell–cell interactions, namely, adhesion and interaction through fields, should be considered in CCM, in addition to the above-mentioned factors [3–5, 15–17]. With the recent developments in measurement technologies [15, 18, 19], biological studies have become much more effective for understanding single cell migration. However, it is difficult to investigate the complex interactions between cells using only biological studies for understanding CCM. To solve this issue, experimental studies and mathematical modeling are crucial, because by using this approach each interaction can be investigated independently.

Unjamming/jamming transitions are one of the most important phenomena in CCM under confluent conditions for cells such as epithelial cells [8, 20–22]. The unjamming phase is a fluid phase in which cell motility is guaranteed and individual cells can alter their positions, while the jamming phase is a solid phase in which cell motility is lost and the positions of individual cells are locked. Some previous biological experiments and numerical simulations have suggested that mutual relationships among single cell motility, cell density in an ensemble of cells, and cell–cell adhesion dominate the unjamming/jamming transitions [23–25]. However, there is a lack of methods that can control these factors to demonstrate their effects independently; therefore, the involvement of these factors in CCM remains speculative. However, as such transitions are also observed in spherical colloidal particle systems [26, 27], these systems have been used as models [28]. However, movements in such systems are randomly governed by Brownian motion, unlike the directional motion of cells, and these systems do not exhibit the polygonal adhesion morphology of cells [5, 29] owing to the robustness of their spherical morphology. Therefore, the development of soft matter showing spontaneous self-propelled motion, namely, active soft matter, is important for developing a practical experimental system to demonstrate the unjamming/jamming transitions in CCM.

This study focused on a self-propelled oil droplet of nitrobenzene containing I^- and I_2 in a water phase containing trimethylstearylammonium chloride (TSAC) as the surfactant, as an attractive experimental system that satisfies the above-mentioned requirements [30–33]. This oil droplet shows self-propelled motion driven by Marangoni convection on a glass substrate due to symmetry breaking of interfacial tension owing to the competition between the adsorption of TSA^+ onto the glass surface and its uptake by the droplet. Although other self-propelled oil droplets have been reported, some of them move at the air–water interface [34]. In contrast, self-propelled oil droplets developed in this study can move on a glass substrate in a manner similar to the two-dimensional movement of cells on the extracellular matrix. This is because the density of the oil phase is higher than that of the water phase. Furthermore, as the related mechanism has been studied well both experimentally and numerically [33], it is feasible to consider and control the motility of the droplet. Therefore, this system could potentially serve as a practical model for CCM. However, when droplets meet each other in the same batch, they immediately coalesce; that is, they are very unstable in collectivity. This is because these droplets are not covered with a robust self-assembled membrane, as in the case of cells enclosed by a phospholipid bilayer membrane.

To improve the stability of oil droplets in contact, previously, silicon oil droplets in which the water–oil interface contained a monolayer of a self-assembled lipid and surfactant, were prepared by emulsifying the phospholipid-containing oil phase with a surfactant-containing aqueous solution [35, 36]. In these studies, two types of lipids, egg L-α-phosphatidylcholine lipids and polyethylene glycol (PEG) biotinylated lipids, were used, and then streptavidin was added to the system with emulsion droplets. This resulted in biotin–streptavidin–biotin complex bridging, leading to crosslinking of the droplets with streptavidin [37, 38], resulting in the development of adhesive properties similar to the molecular crosslinking mechanism of cells. Therefore, combining a self-propelled droplet with a phospholipid could not only improve the stability of droplets in collectivity but also result in the creation of a practical model with cell-like adhesiveness upon further biomodification (for example, using the above biotin–streptavidin interaction).

The objective of this study was to develop a prototype experimental system using a self-propelled active soft matter with independently controllable motility, density, and adhesiveness as a model of CCM; this system is suitable for further biomodification in the future. For developing this system, we included 1,2-dimyristoyl-*sn*-glycero-3-phosphocholine (DMPC) as a phospholipid in the aforementioned self-propelling nitrobenzene oil droplet. This study is based on two considerations: 1) exploring the factors controlling droplet motility and probing the mechanism of self-propelled motion in the presence of the phospholipid, and 2) investigating whether droplets maintain their form in collectivity without coalescing and whether their density is controllable. For consideration 1), we explored the dependence of the motion speed (V) of the droplet on the experimental parameters (the concentrations of TSAC, I_2,

and DMPC, and droplet diameter). We found that the motion was driven by Marangoni convection induced in a droplet by a solubilization of the oil droplet promoted by a formation of mixed DMPC/TSA^+ micelle filled with oil and symmetry breaking of interfacial tension (γ) owing to their departure from the oil–water interface. Furthermore, V could be controlled by changing these parameters, and the results are discussed from the perspective of changes in the γ of a droplet. In addition, for consideration 2), the droplet stability was evaluated. The droplets existed stably in collectivity without coalescing for ~200 s, and they showed unique morphology depending on confluency and density.

MATERIALS AND METHODS

Reagents

TSAC (>98.0%) and iodine (I_2, >98.0%) were purchased from Tokyo Chemical Industry (Tokyo, Japan). Nitrobenzene and potassium iodide (KI) were purchased from FUJIFILM Wako Pure Chemical Industries (Osaka, Japan). DMPC (25 mg/ml in chloroform) was purchased from Sigma-Aldrich Co. LLC (St. Louis, MS, United States). All reagents were used without further purification.

Exploration of the Self-Propelled Motion of a Nitrobenzene Droplet in an Aqueous TSAC Solution

The lipid DMPC (5 mg) was first dried by blowing Ar gas and then dried overnight under vacuum. Subsequently, 1.0 ml of nitrobenzene saturated with KI was added to the dried lipid. The resulting mixture was sonicated for 60 min and then heated at 50°C for 3 h to dissolve the lipid in nitrobenzene. Subsequently, I_2 was dissolved in this mixture to a predetermined concentration (0–10 mM) through sonication, followed by heating at 50°C. The concentration of DMPC was changed by mixing DMPC-containing nitrobenzene with DMPC-free nitrobenzene, both containing the same [I_2]. Before the self-propelled motion experiment, 10 ml of an aqueous TSAC solution of known concentration (0–1.0 mM) was prepared in a glass Petri dish (Ø = 47 mm). Subsequently, a known volume of DMPC-containing nitrobenzene was pipetted (2.0–15.0 µl per droplet) into the TSAC solution. This motion experiment was carried out at room temperature (26 ± 0.4°C). The droplet motion was monitored and the corresponding images were captured using a digital camera.

Measurement of Interfacial Tension (γ) at the Oil–Water Interface Using the Pendant Drop Method

The interfacial tension, γ, at the oil–water interface (oil droplet surface) was measured using the pendant drop method [39]. The aqueous TSAC solution was poured into a glass cell (10 × 10 mm) used for spectrophotometry. Subsequently, a microsyringe (710N PST-5, Hamilton Company, Reno, NV, United States) was used to form a droplet at the tip of the needle in the aqueous solution such that it did not touch wall surface. The droplets were formed at the largest size that allowed them to adhere to the needle tip. The value of γ was calculated using the following equations:

$$\gamma = \Delta\rho g D^2 \frac{1}{H} \quad (1)$$

$$\frac{1}{H} = \frac{B_4}{S^a} + B_3 S^3 - B_2 S^2 + B_1 S - B_0 \quad (2)$$

$$S = \frac{d}{D} \quad (3)$$

Here, $\Delta\rho$, g, and D are the density difference between the water and oil phases, gravitational acceleration, and maximum diameter of a droplet, respectively. H is a correction factor calculated using the characteristic coefficients (B_n) in **Eq. 2**; these coefficients are determined depending on the ratio (S) between D and the diameter at a distance D from the bottom of a droplet (d) [39]. The value of $\Delta\rho$ was calculated from the average of three measurements of the weight per milliliter of the aqueous TSAC solution and DMPC-containing nitrobenzene, respectively, at room temperature (26 ± 0.4°C). γ was evaluated under the same condition.

Demonstration of Droplet Stability in Collectivity

First, we prepared DMPC-containing nitrobenzene saturated with 5.0 mg/ml DMPC and 10 mM I_2 as the oil phase, according to the above-described procedures. Then, 5.0 ml of water was added to a glass Petri dish (Ø = 21 mm). Subsequently, a silicon ring (Ø = 10 mm) was submerged in the water. Subsequently, the oil phase, nitrobenzene mixture was pipetted into the silicon ring several times with 5.0 or 10.0 µl per droplet. After multiple droplets were pipetted, pipetting was stopped, and the coalescence behavior of the droplets was observed.

Statistical Analysis

All error bars of experimental results in this study were obtained from replicates of at least three times, which were calculated using p-values < 0.05.

RESULTS AND DISCUSSION

Self-Propelled Motion of a Single Droplet

Figure 1A shows the self-propelled locomotion under the typical conditions of [DMPC] = 1.0 mg/ml, [I_2] = 10 mM, and [TSAC] = 1.0 mM. After the nitrobenzene droplet was dispensed (t = 0 s) into the aqueous phase, it exhibited a random spontaneous movement for a few seconds, and then the motion was stabilized, i.e., the droplet showed self-propelled directional motion from the center of the Petri dish to its edge (t ~ 20 s). The direction of motion was different for each droplet and not controllable. In addition, as shown later, this directed motion was also observed for droplets with much smaller diameters (~1.8 mm) than the height of the aqueous phase (~5.4 mm). Therefore, this motion is independent of meniscus effects, and the

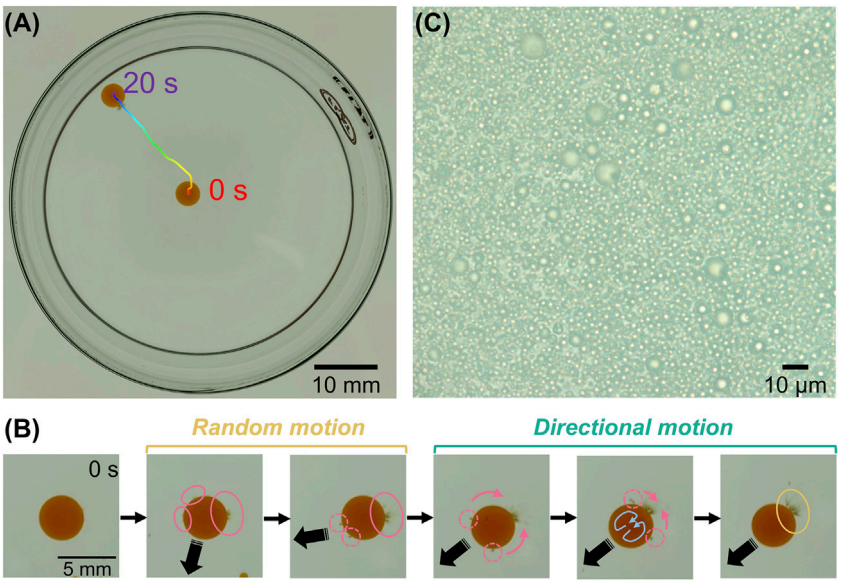

FIGURE 1 | (A) Top-view image illustrating the self-propelled locomotion of a droplet for 20 s ([DMPC] = 1.0 mg/ml, [I_2] = 10 mM, and [TSAC] = 1.0 mM). **(B)** Successive snapshots of a self-propelled droplet under the same condition as in **(A)**. Pink and yellow circles show ejection points of aggregates at the beginning and final stages, respectively. Blue arrows represent Marangoni convection inside the droplet. **(C)** Enlarged image of an ejected aggregate.

driving force originates from the droplet itself. To investigate the principle of this self-propulsion, we carefully observed the droplets under magnification (**Figure 1B**). Immediately after it was dispensed (t = 0 s), there was no change in the droplet appearance and it did not move. However, after a few seconds, the droplet ejected brown aggregates from several parts of its surface (regions enclosed by pink circles in **Figure 1B**) and began to move concurrently. This aggregate ejection event occurred repeatedly, and the droplet showed random motion during this period. However, after a certain time, the weak ejection point (dashed pink circle) moved along the interface toward a strong ejection point (solid pink circle), and the ejection points began to converge to one position. After several repetitions of this concentrating event, the ejection point was completely fixed in one position (yellow circle). During this period, the motion was maintained in the direction opposite to this strong ejection point; that is, the random motion switched to directional motion. We could observe that Marangoni convection (blue arrow) occurred inside the droplet because ejection points were transported along the interface. Therefore, we inferred that this convection, which has been identified as the primary driving force in many self-propelled droplet systems, was the cause of the self-propulsion of the droplet in this system [40–46]. In general, Marangoni convection occurs when the interfacial tension γ at the droplet interface becomes unbalanced. **Figure 1C** shows an enlarged image of the ejected aggregates, which consisted of many microemulsion units. Therefore, the emergence of droplet motility, which was attributed to Marangoni convection, can be linked to the ejection of aggregates. It was found that the ejection of such emulsion units induced a change in γ, suggesting that the emulsion was formed by the desorption of materials that can alter γ, namely, DMPC and TSA^+. Some previous studies have shown that the formation and ejection of molecular aggregates of the surfactant induce unbalanced γ, following which Marangoni convection occurs and propels the motion of the droplet [42, 43]. In these systems, aggregates were suggested to form by the aggregation of products generated by the hydrolysis of surfactant molecules at the droplet interface with unhydrolyzed surfactant molecules. However, our system does not contain hydrolysable surfactants. On the other hand, it has been reported that phospholipids and surfactants form aggregates, in a process that is well known as the solubilization of lipid membranes by surfactants into the solution [47]. In this phenomenon, surfactant molecules first enter the lipid membrane with an increasing surfactant concentration, and aggregates of the surfactant and lipid molecules are formed as surfactant concentration is increased further. Furthermore, another study showed that solubilization, namely micellization of surfactants with oil, and ejection of solubilized emulsions proceed when the concentration of the surfactant at the droplet interface exceeds a threshold value [46]. Therefore, we infer that, in this study, TSA^+ is first inserted into the self-assembled DMPC monolayer surrounding the droplet, and aggregated emulsions are formed and ejected them owing to the solubilization promoted by the micellization among TSA^+, DMPC, and nitrobenzene oil when the concentration of the inserted TSA^+ exceeds a threshold value. Accordingly, we assume that Marangoni convection is generated inside the droplet due to the unbalanced γ between the solubilized and non-solubilized regions, and finally the droplet shows self-propelled motion.

If our system follows the above-mentioned mechanism, TSAC plays an important role because the solubilization might depend on a concentration of TSA^+. We therefore explored the effect of

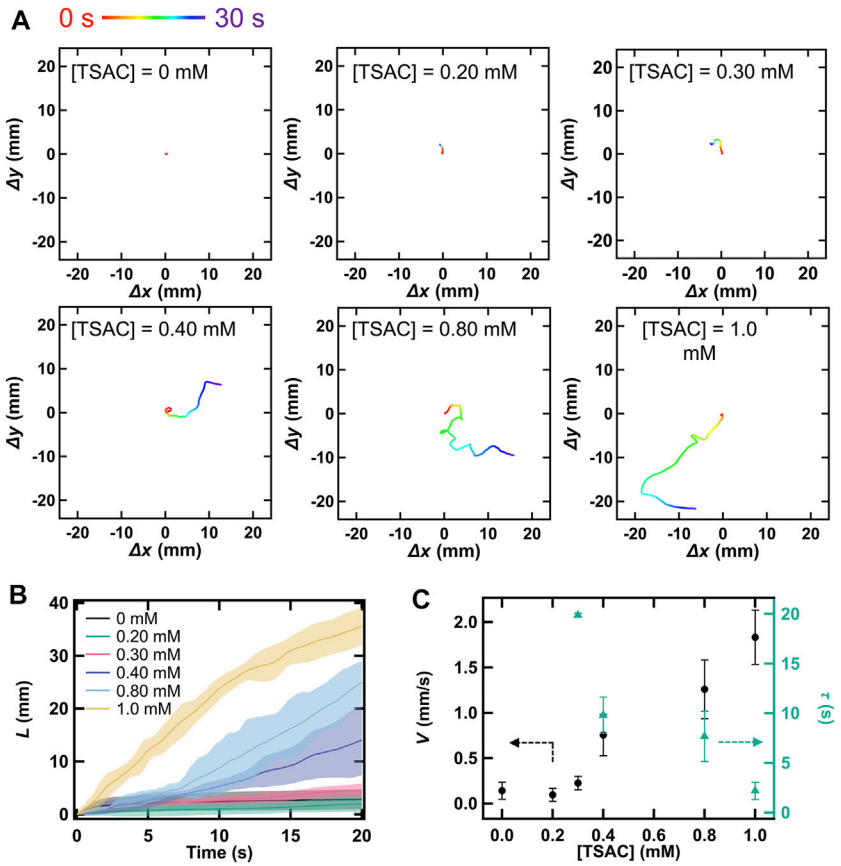

FIGURE 2 | (A) Locomotion of a droplet over 20 s owing to its self-propelled motion at different TSAC concentrations in the range of 0–1.0 mM ([DMPC] = 2.0 mg/ml and $[I_2]$ = 10 mM). Quantity of motion with respect to the *x*- or *y*-direction is calculated as a displacement value with respect to an initial pipetted position. **(B)** Relationship between time and the total path length of droplet movement during 20 s (*L*) at different TSAC concentrations, where $t = 0$ represents the time of pipetting. **(C)** Variation in the mean motion speed of the droplet (*V*) and induction period (τ) at different TSAC concentrations.

TSAC concentration on the motility of the droplet. **Figure 2A** shows the droplet locomotion for 30 s at different initial TSAC concentrations in the range of 0–1.0 mM. At [TSAC] = 0 mM, the droplets did not exhibit motility. Although the droplet moved slightly at [TSAC] = 0.20 and 0.30 mM, the final position was almost anchored at the center. However, droplet motility improved remarkably when TSAC concentration was increased further. With an increase in TSAC concentration from 0.40 to 1.0 mM, the droplet moved toward the edge of the glass Petri dish, and the total path length of movement during this observation (*L*) increased. In particular, the sudden change in direction after ~20 s at [TSAC] = 1.0 mM indicated that the droplet collided with the glass wall and continued its motion along the wall. To clarify the effect of TSAC concentration, we evaluated the relationship between *L* and time from the initiation of their locomotion (**Figure 2B**). Note that *L* was evaluated from 0 s (pipetting a droplet) until after 20 s to eliminate the effect of collision on the glass wall. For [TSAC] = 0–0.30 mM, *L* was almost the same during the entire period, without any significant differences in the changes in *L*. However, *L* increased significantly from 15 to 35 mm with an increase in [TSAC] from 0.40 to 1.0 mM. Furthermore, the increasing trend of *L* with time was noted for each condition. Although *L* increased immediately after the dispensation of the droplet in the case of [TSAC] = 1.0 mM, the increase in *L* began after a certain duration in the cases of [TSAC] = 0.40 and 0.80 mM, indicating an induction period (τ) for the propulsion of this system. Then, we evaluated the dependence of the mean motion speed (*V*) and τ as a function of TSAC concentration (**Figure 2C**); in this evaluation, τ was defined as the time taken until *L* became greater than 5 mm, and *V* was calculated from the slope of the *L* vs. time plot obtained after τ. Similar to the above-mentioned results, *V* increased remarkably at [TSAC] ≥ 0.30 mM (black circle). The value of τ decreased from 20 to 2 s with an increase in [TSAC] (green triangle). Thus, we found that TSAC not only controlled the emergence of motility but also improved the motility of the droplet. Furthermore, the critical micellar concentration (CMC) of TSAC is ~0.3 mM at room temperature [48]. Although solubilization could occur at TSAC concentrations lower than the CMC, the motility of the droplet only emerged when the TSAC concentration approached the CMC of our system. Therefore, this strongly suggests that the solubilization process that induces droplet motility is related to the micellization of TSA^+.

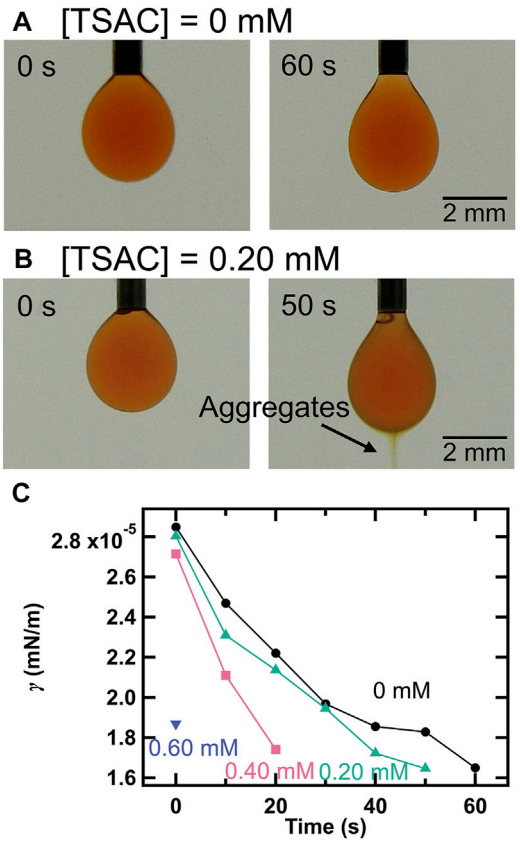

FIGURE 3 | Snapshots of the droplet at the tip of a needle when **(A)** [TSAC] = 0 mM and **(B)** [TSAC] = 0.20 mM ([DMPC] = 0.25 mg/ml and [I_2] = 10 mM). **(C)** Variation in the interfacial tension (γ) with time at different TSAC concentrations (the concentrations of DMPC and I_2 were the same as those in the cases of **(A)** and **(B)**).

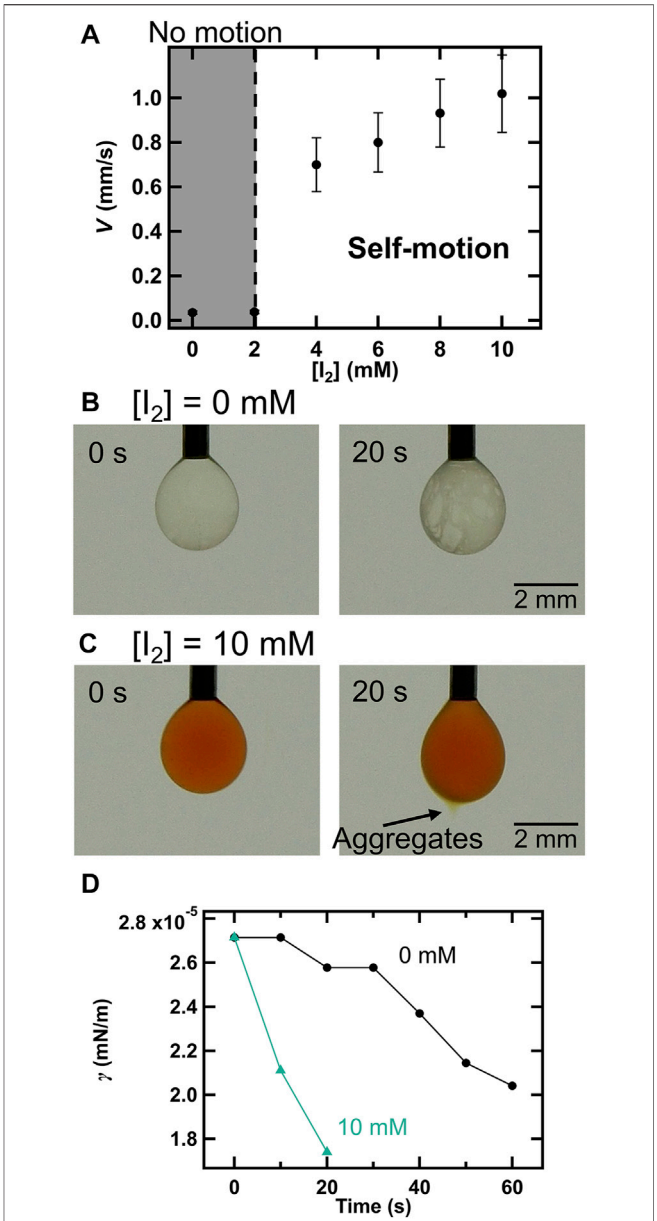

FIGURE 4 | (A) Effects of I_2 concentration (0–10 mM) on V ([DMPC] = 1.0 mg/ml and [TSAC] = 1.0 mM). Snapshots of the droplet when **(B)** [I_2] = 0 mM and **(C)** [I_2] = 10 mM. **(D)** Changes in γ with time at different I_2 concentrations (the concentrations of DMPC and I_2 were the same as those in the cases of **(B)** and **(C)**).

To further investigate the influence of TSAC concentration on droplet motility, we measured the changes in γ with time using the pendant drop method. **Figures 3A,B** present the changes in the appearance of droplets at [TSAC] = 0 and 0.20 mM. Under both conditions, the appearance of the droplets was almost the same immediately after their formation (t = 0 s). However, some differences were observed in their evolution with time. Whereas the droplet stretched slightly and then simply broke off and fell after 60 s in the absence of TSAC, apparent aggregates were formed at the bottom of the droplet in addition to the above-mentioned changes in the presence of TSAC (0.20 mM). Therefore, it is clear that γ changed with the formation of aggregates in the presence of TSA^+. Furthermore, **Figure 3C** shows the changes in γ with time at different TSAC concentrations; in this evaluation, γ was calculated using **Eqs. 1–3**, and the measurement was continued until the droplets fell from the tip of the needle. In the absence of TSAC, γ decreased with time (data represented by •). This could be ascribed to the self-assembly of DMPC at the oil–water interface. Then, the droplet fell when γ decreased below ~1.8 mN/m. Under all the conditions, the droplets fell at this critical value of γ. However, the rate of decrease in γ was different in the presence of TSA^+ (data represented by▲–▼). At [TSAC] = 0.20 mM, the droplets fell after 50 s following their formation, and the time taken for their fall shortened with increasing TSAC concentration. Finally, the droplets fell immediately after being formed at [TSAC] = 0.60 mM. These results indicated that a higher TSAC concentration promoted faster TSA^+ insertion into the droplet interface and the solubilization. Marangoni convection in this study is triggered by the unbalancing of γ between the front (direction of motion) and rear parts of the droplet owing to the increase in γ at the rear where TSA^+ and DMPC leave the

interface (owing to the solubilization). As shown clearly by the above-described experiments, a higher TSAC concentration led to the faster formation of aggregates and their ejection. That is, the time required for γ imbalance was shortened with increasing TSAC concentration; thus, τ decreased with increasing TSAC concentration, leading to self-propelled motion. Therefore, we can analyze the improvement in motility from the perspective of the change in the equilibrium γ value. In general, the distribution ratio between surfactant molecules in the water phase and lipid membrane depends on the concentration of the surfactant in the water phase [49–51]. It is also known that the value of γ at equilibrium at the air–water interface decreases with an increase in the amount of the adsorbed surfactant [52, 53], which is generally observed in the cases of oil–water interfaces. Therefore, the increase in TSAC concentration caused a decrease in γ at equilibrium, in addition to affecting the kinetics of the solubilization. The possible scenarios are as follows: although the equilibrium γ value could not be measured with the pendant drop method because the droplet fell, the equilibrium γ at the oil (nitrobenzene-DMPC)–water (aqueous TSAC solution) interface decreased with increasing TSAC concentration because the surfactant distribution ratio increased. Owing to the lowered equilibrium γ value, the difference between γ ($\Delta\gamma$) before and after the ejection DMPC/TSA^+/oil aggregates increase. This enhances the Marangoni convection, and improves the motility.

According to a previous study [33, 54], anionic I_3^- generated by the complexation of I_2 and I^- made ion pairs with cationic TSA^+ both at the oil–water interface and in the oil phase, and thus the incorporation (dissolution) of TSA^+ into the oil phase is promoted, leading to improved droplet motility. The authors suggested that I_2 is the primary source of self-propelled energy. Therefore, we explored the role of I_2 in droplet motility (**Figure 4A**). Interestingly, while V was almost 0 at $[I_2]$ = 0 and 2.0 mM (i.e., no motion), the motility emerged abruptly at $[I_2]$ exceeding 4.0 mM and then V increased linearly with increasing I_2 concentration. This result suggests that a certain amount of I_2 present in the droplet is required for the emergence of self-propelled motion. To investigate this aspect, we evaluated the changes in γ with iodine concentration (**Figures 4B–D**). In the absence of I_2, the surface of the droplet, which was clear immediately after droplet formation, became cloudy after 20 s (**Figure 4B**). This is probably due to structural disruption and the formation of small aggregates owing to TSA^+ insertion into the DMPC layer. In contrast, yellow aggregates, which were similar to those observed in earlier experiments, were formed and ejected from the droplet after 20 s at $[I_2]$ = 10 mM (**Figure 4C**). Furthermore, γ decreased rapidly in the case of $[I_2]$ = 10 mM, compared to that in the case of $[I_2]$ = 0 mM (**Figure 4D**). This behavior is similar to that observed with an increase in TSAC concentration. Thus, we found that I_2 promoted the insertion of TSA^+ into the DMPC membrane and thus aided the solubilization process. That is, I_2 played an important role in the dissolution of more TSA^+ into the droplet and TSA^+ insertion at the interface to overcome the energy barrier required to break the stable DMPC membrane structure and promote the solubilization depending on the micelle formation.

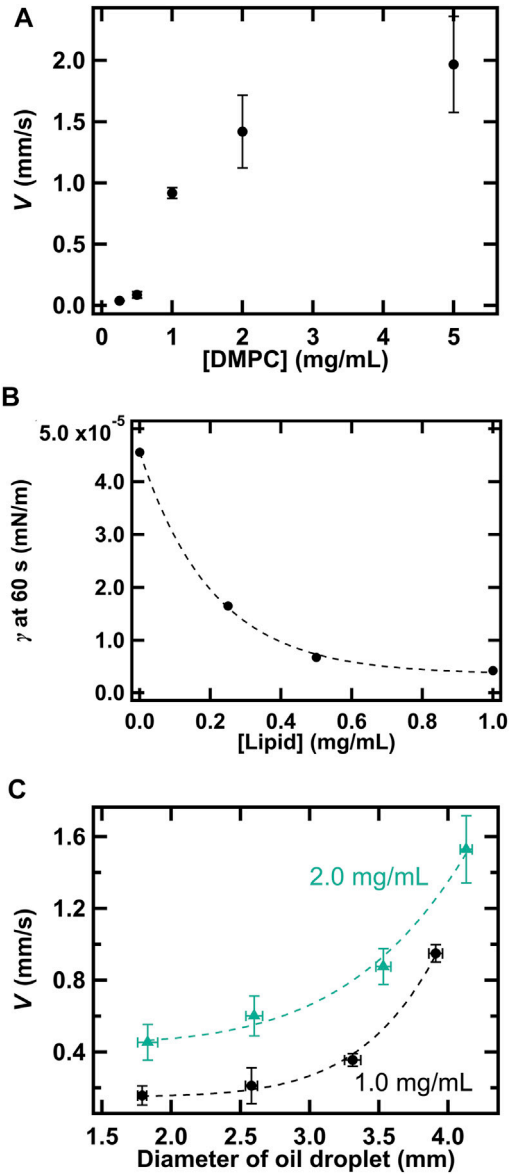

FIGURE 5 | (A) Effects of DMPC concentration (0–5.0 mg/ml) on V ($[I_2]$ = 1.0 mM and [TSAC] = 1.0 mM). **(B)** Measured γ at 60 s for droplets with different DMPC concentrations ($[I_2]$ = 1.0 mM and [TSAC] = 0 mM). **(C)** Variation in V with the diameter of the droplet at [DMPC] = 1.0 and 2.0 mg/ml.

Furthermore, we explored the influence of DMPC concentration on droplet motility (**Figure 5A**). V increased substantially with DMPC concentration between 0.50 and 1.0 mg/ml and then increased gently until DMPC concentration reached 5.0 mg/ml. In addition, we studied the variation in γ value in water with the changes in DMPC concentration (**Figure 5B**). The value of γ decreased exponentially with an increase in DMPC concentration. Thus, the increase in V can be explained based on the change in γ, as in the case of TSAC concentration. That is, $\Delta\gamma$ increases as the concentration of DMPC increases. In addition, we studied the effect of droplet diameter, another factor that affects droplet motility in this system

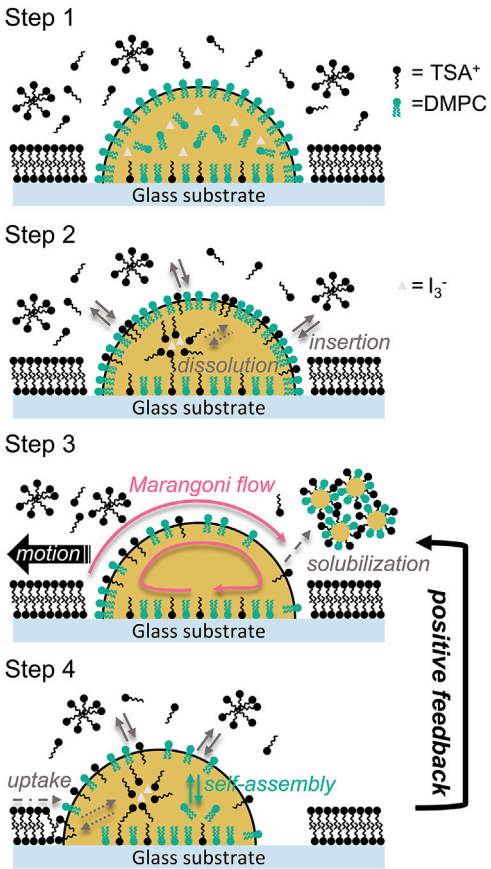

FIGURE 6 | Mechanism of the self-propelled motion of the nitrobenzene droplet observed in this study. **Step 1**: Initial state of the oil phase (the droplet) and water phase containing TSAC, corresponding to the situation immediately after the droplet was dispensed. **Step 2**: Insertion of TSAC into the DMPC membrane layer and dissolution of TSAC in the oil phase assisted by I_3^-. **Step 3**: Symmetry breaking of the interfacial tension at the oil–water interface owing to the solubilization by the formation and ejection of DMPC/TSA^+/nitrobenzene aggregates, and then the self-propelled motion. **Step 4**: Recovery of the droplet condition owing to following processes: the uptake of TSA^+ from the front of the droplet and from the solution (reinsertion), and the self-assembly of DMPC at the interface.

(**Figure 5C**), by changing the pipetted liquid volume for tuning the diameter. At both [DMPC] = 1.0 and 2.0 mg/ml, V increased with an increase in droplet diameter, as observed in other studies [45, 55, 56]. In some of the previous studies, the motion behavior was found to change, for example, from random to directional motion; however, our system did not show such a transition. The effect of droplet diameter on V in our system can be explained by following reason: As the diameter of the droplet decreases, the distinction between front and rear parts of the droplet becomes blurred. Therefore, $\Delta\gamma$ became smaller and V decreased.

According to the results of the dependence of droplet motility on TSAC, I_2, and DMPC concentrations and droplet diameter, the complete mechanism of the self-propelled motion of the droplet is depicted in **Figure 6**. Immediately after the oil phase (DMPC-containing nitrobenzene) is dispensed into the water phase, a droplet covered with a self-assembled DMPC monolayer membrane is formed on the glass substrate (step 1). At this time, TSA^+ present in the water phase is adsorbed on the glass surface and exists both in molecular and micellar forms in the solution. Subsequently, TSA^+ enters the self-assembled layer and dissolves in the oil phase, assisted by ion pairing between TSA^+ and I_3^-, a complex formed between I^- and I_2 (step 2). The concentration of TSA^+ in the self-assembled layer increases because of this process. When the concentration finally exceeds the CMC of TSAC, the solubilization process is promoted drastically, which is combination of the formation of emulsions formation among TSA^+, DMPC, and nitrobenzene followed by the ejection of their aggregates. In the beginning, ejection points exist all over the surface of the droplet, and each point induces an increase in γ. Therefore, the Marangoni effect is induced, and the droplet exhibits random self-propelled motion. After a certain duration, the scattered points that proceed the solubilization eventually coalesce into a single point (this final point depends on the initial fluctuation of γ) owing to Marangoni convection. That is, complete symmetry breaking occurs and a unified Marangoni convection is induced in the droplet (step 3). Thus, the mode of movement (random) switches to directional motion. Furthermore, because TSA^+ is adsorbed to the glass surface in the forward part of the droplet in the direction of motion, γ is always maintained at a low value in the front of the droplet owing to TSA^+ insertion from the surface of a glass substrate (step 4). In addition, the direct insertion of TSA^+ from the solution plays the same role in maintaining a lower γ. Furthermore, the oil–water interface of the entire droplet is continuously supplied with DMPC molecules because DMPC continues to self-assemble from the inside of the droplet. This process (step 4) causes the droplet to recover to step 3, and the directional self-propelled motion continues; that is, step 4 provides positive feedback for this mechanism. Therefore, the motility of the droplet can be rationalized from the perspective of the change in γ, droplet motility, which is one of the important parameters that govern the unjamming/jamming phase transition, can be controlled by controlling these experimental parameters.

Stability of Droplets in Collectivity

Figure 7 shows the variation in the number of droplets (N) with time in cases where the pipetted volume per droplet was 10.0 μl (**Figure 7A**) and 5.0 μl (**Figure 7B**). The confluency was calculated from the ratio between the total area occupied by all the droplets and the area surrounded by the silicon ring, wherein the vertical axis corresponding to confluency has been inverted for comparison with N. The droplet boundaries required for this calculation were determined by segmentation image processing using an arbitrary color threshold. In these figures, the increase in N indicates that droplets were added within the silicon ring by pipetting, and the time when the increase stops indicates that the addition of droplets was stopped. Furthermore, **Figures 7C,D** shows a collection of actual droplets under several N conditions; their state can be distinguished into two types: non-confluent and confluent. At 10.0 μl/droplet, N increased monotonically with the regular addition of droplets (•), and the confluency decreased accordingly (▲), reaching the confluent state at N = 9 (confluency is ~100%) (**Figure 7A**). Thereafter, N increased with the addition of droplets, while maintaining the confluent state, and the addition was continued

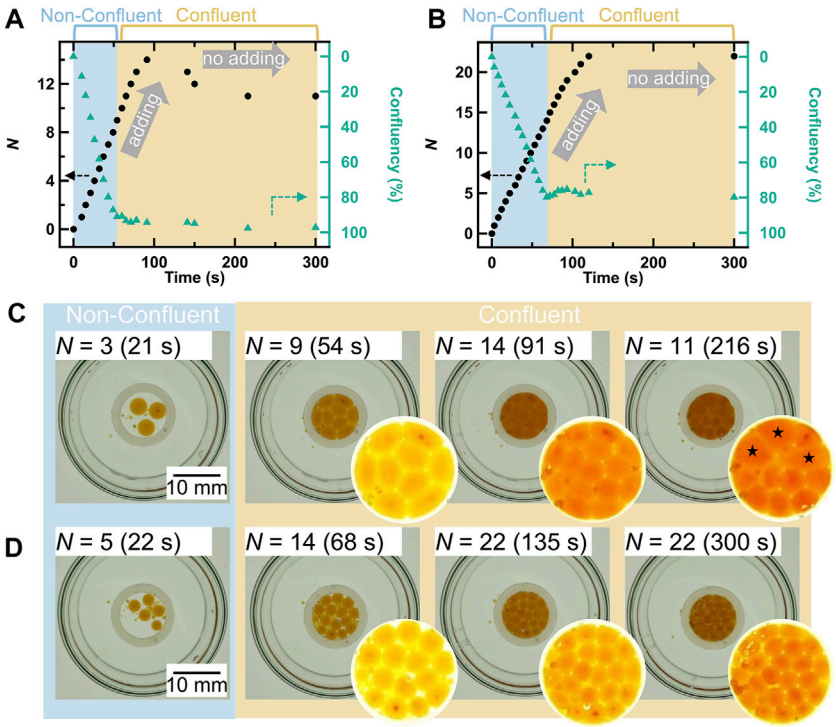

FIGURE 7 | Changes in the total number of droplets within the silicon ring (*N*) and confluency with time in the cases of **(A)** 10.0 μl/droplet and **(B)** 5.0 μl/droplet. Confluency was calculated as the ratio between the total area occupied by all the droplets and the area surrounded by the silicon ring. The axis of confluency is inverted. The increasing *N* indicates that droplets were added, and stopping means that droplet addition was stopped. Top-view snapshots of the droplets and enlarged images showing the interior of the silicon ring in the cases of **(C)** 10.0 μl/droplet and **(D)** 5.0 μl/droplet. The ★ symbol represents coalescing droplets.

until the maximum *N* of 14 was reached. The monotonic increase in *N* with each addition indicated that the droplets did not coalesce and maintained their individual morphologies. That is, the droplets remained stable with an increase in *N*, which suggests that they maintained their stability with an increase in droplet density. This result indicates that droplet density, which is another important parameter for CCM, is controllable. On the other hand, *N* decreased at $t = 150$ s because of droplet coalescence, which began after 50 s following the termination of addition. Subsequently, intermittent droplet coalescence finally reduced the *N* to 11 at $t = 300$ s. However, this instability was not an issue in our experiments because the time taken for this coalescence process to start (~50 s) was less compared to the observation time of the self-propelled motion (~30 s). Furthermore, the morphology of each droplet in the ensemble was also observed, as shown in **Figure 7C**. Under non-confluent conditions ($N = 3$), each droplet had a clear spherical morphology because the droplets did not contact each other. On the other hand, linear contact surfaces were formed under confluent conditions ($N = 9$) because the droplets contacted each other, and each droplet showed a characteristic polygonal shape depending on the number of surface contacts. As the density increased ($N = 14$), the area occupied by each droplet decreased, while the polygonal shape remained intact. As the droplets coalesced (★ in $N = 11$), the morphology of each droplet changed slightly. The observed polygonal morphology is similar to the cell morphologies of confluent cells, such as epithelial cells. In most previous studies that examined the collective motion of self-collective droplets, each droplet had a relatively small specific surface area, thus maintaining a small contact area and a spherical shape [34, 57]. Therefore, our results are superior to those of previous studies because the droplets could stably adopt a characteristic polygonal shape. Although the details are not provided here, we have also experimentally confirmed that these droplets exhibit self-propelled motion in collectivity. In addition, the same experiment was also conducted under the condition of 5.0 μl/droplet (**Figures 7B,D**). In contrast to that in the case of 10.0 μl/droplet, the maximum *N* increased significantly to 22 and the droplets were highly stable (without coalescing over the entire period), but the confluency saturated at ~80% (**Figure 7B**). This is because of two reasons: 1) many miniscule droplets were formed due to pipetting when the droplets were added and 2) each droplet had a high spherical retention and large vacancy between contacting points because the droplets were smaller than those created with 10.0 μl/droplet (**Figure 7D**). Thus, we found that it is possible to alter the adhesion of droplets in terms of the size of the contact area depending on the rigidity by adjusting the droplet size, which is different from the adhesion mechanism in cells. As such, this control of adhesiveness is considered indirect. However, this droplet system has potential to be possibility of biomodification in order to further improve the controllability of adhesion, as mentioned in the introduction section. These results clarify the second consideration of this study, which is the stability of the droplets in collectivity. Thus, we succeeded in developing a prototype experimental self-propelled

droplet system for demonstrating the unjamming/jamming phase transition in CCM.

CONCLUSION

In this study, we developed an improved prototype of a self-propelled droplet system by combining self-propelling nitrobenzene oil on a glass surface with a robust self-assembled DMPC membrane. This system can potentially be used for demonstrating the unjamming/jamming phase transitions in CCM. The main driving force of the self-propelled motility of this system is the Marangoni convection induced by the following processes: The insertion of TSAC into the DMPC membrane layer and the solubilization promoted by the combination of DMPC/TSA^+/nitrobenzene aggregate formation. The controllability of motility was explored in terms of the concentrations of TSAC, I_2, and DMPC, as well as the droplet size. Furthermore, the effects of these parameters were discussed based on the changes in the interfacial tension and its unbalancing owing to the chemical dynamics at the oil–water surface under each condition because the change in interfacial tension was the main factor driving the Marangoni convection. We found that droplet motility could be controlled well by altering these conditions, and the related mechanism was explained adequately. In addition, the developed system showed high stability in collectivity, regardless of the conditions (non-confluent or confluent conditions). Therefore, the cell density could also be controlled for this system. Furthermore, each droplet in collectivity showed characteristic polygonal shapes depending on the droplet size because of the difference in the contact area between the droplets owing to their rigidity. Thus, the adhesive force could be controlled experimentally. In fact, this controlling mechanism is different from the molecular adhesion mechanism operating in living cells. This issue can be overcome by modifying the system for implementing interactions such as those between biomodified lipid molecules and proteins as in the case of biotin–streptavidin–biotin complex bridging. As described above, the developed system is highly attractive because it can control three important aspects of CCM: the motility, density, and adhesion of cells. The CCM exhibited by cells is unique, but the underlying mechanisms are extremely complex. Therefore, a simple understanding of this phenomenon through experiments and mathematical modeling is essential. The system developed in this study has the potential to address this challenge. Accordingly, we expect that this prototype experimental model can be applied in various modeling studies of the unjamming/jamming phase transitions in CCM, and that it can bridge the gap between modeling studies and real biochemical phenomena.

DATA AVAILABILITY STATEMENT

The original contributions presented in the study are included in the article/Supplementary Material, further inquiries can be directed to the corresponding author.

AUTHOR CONTRIBUTIONS

In this study, all experiments and data analyses were performed by MI. Both the authors contributed to the preparation of the final manuscript.

FUNDING

This work was supported by JSPS KAKENHI (Grant Number 19H02668) and JSPS Fellows (Grant Number 19J23178).

REFERENCES

1. Lauffenburger DA, Horwitz AF. Cell Migration: A Physically Integrated Molecular Process. *Cell* (1996) 84:359–69. doi:10.1016/s0092-8674(00)81280-5
2. Ridley AJ, Schwartz MA, Burridge K, Firtel RA, Ginsberg MH, Borisy G, et al. Cell Migration: Integrating Signals from Front to Back. *Science* (2003) 302: 1704–9. doi:10.1126/science.1092053
3. Friedl P, Gilmour D. Collective Cell Migration in Morphogenesis, Regeneration and Cancer. *Nat Rev Mol Cel Biol* (2009) 10:445–57. doi:10.1038/nrm2720
4. Haeger A, Wolf K, Zegers MM, Friedl P. Collective Cell Migration: Guidance Principles and Hierarchies. *Trends Cel Biol* (2015) 25:556–66. doi:10.1016/j.tcb.2015.06.003
5. Montell DJ. Morphogenetic Cell Movements: Diversity from Modular Mechanical Properties. *Science* (2008) 322:1502–5. doi:10.1126/science.1164073
6. Staddon MF, Bi D, Tabatabai AP, Ajeti V, Murrell MP, Banerjee S. Cooperation of Dual Modes of Cell Motility Promotes Epithelial Stress Relaxation to Accelerate Wound Healing. *Plos Comput Biol* (2018) 14: e1006502. doi:10.1371/journal.pcbi.1006502
7. Friedl P, Wolf K. Tumour-cell Invasion and Migration: Diversity and Escape Mechanisms. *Nat Rev Cancer* (2003) 3:362–74. doi:10.1038/nrc1075
8. Spatarelu C-P, Zhang H, Nguyen DT, Han X, Liu R, Guo Q, et al. Biomechanics of Collective Cell Migration in Cancer Progression: Experimental and Computational Methods. *ACS Biomater Sci Eng* (2019) 5:3766–87. doi:10.1021/acsbiomaterials.8b01428
9. Rappel W-J, Edelstein-Keshet L. Mechanisms of Cell Polarization. *Curr Opin Syst Biol* (2017) 3:43–53. doi:10.1016/j.coisb.2017.03.005
10. Pellegrin S, Mellor H. Actin Stress Fibres. *J Cel Sci* (2007) 120:3491–9. doi:10.1242/jcs.018473
11. Ananthakrishnan R, Ehrlicher A. The Forces behind Cell Movement. *Int J Biol Sci* (2007) 3:303–17. doi:10.7150/ijbs.3.303
12. Van Haastert PJM, Devreotes PN. Chemotaxis: Signalling the Way Forward. *Nat Rev Mol Cel Biol* (2004) 5:626–34. doi:10.1038/nrm1435
13. Cai P, Layani M, Leow WR, Amini S, Liu Z, Qi D, et al. Bio-Inspired Mechanotactic Hybrids for Orchestrating Traction-Mediated Epithelial Migration. *Adv Mater* (2016) 28:3102–10. doi:10.1002/adma.201505300
14. Chen Y-C, Allen SG, Ingram PN, Buckanovich R, Merajver SD, Yoon E. Single-cell Migration Chip for Chemotaxis-Based Microfluidic Selection of Heterogeneous Cell Populations. *Sci Rep* (2015) 5:9980. doi:10.1038/srep09980
15. Trepat X, Wasserman MR, Angelini TE, Millet E, Weitz DA, Butler JP, et al. Physical Forces during Collective Cell Migration. *Nat Phys* (2009) 5:426–30. doi:10.1038/nphys1269
16. Pegoraro AF, Fredberg JJ, Park J-A. Problems in Biology with many Scales of Length: Cell-Cell Adhesion and Cell Jamming in Collective Cellular Migration. *Exp Cel Res* (2016) 343:54–9. doi:10.1016/j.yexcr.2015.10.036
17. Angelini TE, Hannezo E, Trepat X, Fredberg JJ, Weitz DA. Cell Migration Driven by Cooperative Substrate Deformation Patterns. *Phys Rev Lett* (2010) 104:168104. doi:10.1103/physrevlett.104.168104
18. Hu B, Leow WR, Cai P, Li Y-Q, Wu Y-L, Chen X. Nanomechanical Force Mapping of Restricted Cell-To-Cell Collisions Oscillating between

Contraction and Relaxation. *ACS Nano* (2017) 11:12302–10. doi:10.1021/acsnano.7b06063
19. Brugués A, Anon E, Conte V, Veldhuis JH, Gupta M, Colombelli J, et al. Forces Driving Epithelial Wound Healing. *Nat Phys* (2014) 10:683–90. doi:10.1038/nphys3040
20. Szabó B, Szöllösi GJ, Gönci B, Jurányi Z, Selmeczi D, Vicsek T. Phase Transition in the Collective Migration of Tissue Cells: Experiment and Model. *Phys Rev E* (2006) 74:061908. doi:10.1103/PhysRevE.74.061908
21. Sadati M, Taheri Qazvini N, Krishnan R, Park CY, Fredberg JJ. Collective Migration and Cell Jamming. *Differentiation* (2013) 86:121–5. doi:10.1016/j.diff.2013.02.005
22. Park JA, Atia L, Mitchel JA, Fredberg JJ, Butler JP. Collective Migration and Cell Jamming in Asthma, Cancer and Development. *J Cel Sci* (2016) 129:3375–83. doi:10.1242/jcs.187922
23. Doxzen K, Vedula SRK, Leong MC, Hirata H, Gov NS, Kabla AJ, et al. Guidance of Collective Cell Migration by Substrate Geometry. *Integr Biol* (2013) 5:1026–35. doi:10.1039/c3ib40054a
24. Bi D, Yang X, Marchetti MC, Manning ML. Motility-Driven Glass and Jamming Transitions in Biological Tissues. *Phys Rev X* (2016) 6:021011. doi:10.1103/PhysRevX.6.021011
25. Bi D, Lopez JH, Schwarz JM, Manning ML. A Density-independent Rigidity Transition in Biological Tissues. *Nat Phys* (2015) 11:1074–9. doi:10.1038/nphys3471
26. Liu AJ, Nagel SR. The Jamming Transition and the Marginally Jammed Solid. *Annu Rev Condens Matter Phys* (2010) 1:347–69. doi:10.1146/annurev-conmatphys-070909-104045
27. Pusey PN, Van Megen W. Phase Behaviour of Concentrated Suspensions of Nearly Hard Colloidal Spheres. *Nature* (1986) 320:340–2. doi:10.1038/320340a0
28. Zhou EH, Trepat X, Park CY, Lenormand G, Oliver MN, Mijailovich SM, et al. Universal Behavior of the Osmotically Compressed Cell and its Analogy to the Colloidal Glass Transition. *Proc Natl Acad Sci* (2009) 106:10632–7. doi:10.1073/pnas.0901462106
29. Kim S, Pochitaloff M, Stooke-Vaughan GA, Campàs O. Embryonic Tissues as Active Foams. *Nat Phys* (2021) 17:859–66. doi:10.1038/s41567-021-01215-1
30. Magome N, Yoshikawa K. Nonlinear Oscillation and Ameba-like Motion in an Oil/Water System. *J Phys Chem* (1996) 100:19102–5. doi:10.1021/jp9616876
31. Sumino Y, Magome N, Hamada T, Yoshikawa K. Self-Running Droplet: Emergence of Regular Motion from Nonequilibrium Noise. *Phys Rev Lett* (2005) 94:068301. doi:10.1103/PhysRevLett.94.068301
32. Sumino Y, Kitahata H, Yoshikawa K, Nagayama M, Nomura SM, Magome N, et al. Chemosensitive Running Droplet. *Phys Rev E Stat Nonlin Soft Matter Phys* (2005) 72:041603. doi:10.1103/PhysRevE.72.041603
33. Sumino Y, Yoshikawa K. Self-motion of an Oil Droplet: A Simple Physicochemical Model of Active Brownian Motion. *Chaos* (2008) 18:026106. doi:10.1063/1.2943646
34. Kichatov B, Korshunov A, Sudakov V, Gubernov V, Yakovenko I, Kiverin A. Crystallization of Active Emulsion. *Langmuir* (2021) 37:5691–8. doi:10.1021/acs.langmuir.1c00630
35. Pontani L-L, Jorjadze I, Viasnoff V, Brujic J. Biomimetic Emulsions Reveal the Effect of Mechanical Forces on Cell-Cell Adhesion. *Proc Natl Acad Sci* (2012) 109:9839–44. doi:10.1073/pnas.1201499109
36. Golovkova I, Montel L, Pan F, Wandersman E, Prevost AM, Bertrand T, et al. Adhesion as a Trigger of Droplet Polarization in Flowing Emulsions. *Soft Matter* (2021) 17:3820–8. doi:10.1039/d1sm00097g
37. Fattaccioli J, Baudry J, Henry N, Brochard-Wyart F, Bibette J. Specific Wetting Probed with Biomimetic Emulsion Droplets. *Soft Matter* (2008) 4:2434. doi:10.1039/b806635c
38. Bourouina N, Husson J, Waharte F, Pansu RB, Henry N. Formation of Specific Receptor-Ligand Bonds between Liquid Interfaces. *Soft Matter* (2011) 7:9130–9. doi:10.1039/c1sm05659j
39. Hubbard AT. *Encyclopedia of Surface and Colloid Science*. USA: CRC Press (2002).
40. Suematsu NJ, Saikusa K, Nagata T, Izumi S. Interfacial Dynamics in the Spontaneous Motion of an Aqueous Droplet. *Langmuir* (2019) 35:11601–7. doi:10.1021/acs.langmuir.9b01866
41. Suematsu NJ, Mori Y, Amemiya T, Nakata S. Spontaneous Mode Switching of Self-Propelled Droplet Motion Induced by a Clock Reaction in the Belousov-Zhabotinsky Medium. *J Phys Chem Lett* (2021) 12:7526–30. doi:10.1021/acs.jpclett.1c02079
42. Toyota T, Maru N, Hanczyc MM, Ikegami T, Sugawara T. Self-Propelled Oil Droplets Consuming "Fuel" Surfactant. *J Am Chem Soc* (2009) 131:5012–3. doi:10.1021/ja806689p
43. Banno T, Kuroha R, Toyota T. pH-Sensitive Self-Propelled Motion of Oil Droplets in the Presence of Cationic Surfactants Containing Hydrolyzable Ester Linkages. *Langmuir* (2012) 28:1190–5. doi:10.1021/la2045338
44. Banno T, Asami A, Ueno N, Kitahata H, Koyano Y, Asakura K, et al. Deformable Self-Propelled Micro-object Comprising Underwater Oil Droplets. *Sci Rep* (2016) 6:31292. doi:10.1038/srep31292
45. Ban T, Yamagami T, Nakata H, Okano Y. pH-Dependent Motion of Self-Propelled Droplets Due to Marangoni Effect at Neutral pH. *Langmuir* (2013) 29:2554–61. doi:10.1021/la3047164
46. Babu D, Scanes RJH, Plamont R, Ryabchun A, Lancia F, Kudernac T, et al. Acceleration of Lipid Reproduction by Emergence of Microscopic Motion. *Nat Commun* (2021) 12:2959. doi:10.1038/s41467-021-23022-1
47. Aguirre-Ramírez M, Silva-Jiménez H, Banat IM, Díaz De Rienzo MA. Surfactants: Physicochemical Interactions with Biological Macromolecules. *Biotechnol Lett* (2021) 43:523–35. doi:10.1007/s10529-020-03054-1
48. Sumino Y, Kitahata H, Seto H, Nakata S, Yoshikawa K. Spontaneous Deformation of an Oil Droplet Induced by the Cooperative Transport of Cationic and Anionic Surfactants through the Interface. *J Phys Chem B* (2009) 113:15709–14. doi:10.1021/jp9037733
49. Ueno M. Partition Behavior of a Nonionic Detergent, Octyl Glucoside, between Membrane and Water Phases, and its Effect on Membrane Permeability. *Biochemistry* (1989) 28:5631–4. doi:10.1021/bi00439a044
50. Levy D, Gulik A, Seigneuret M, Rigaud JL. Phospholipid Vesicle Solubilization and Reconstitution by Detergents. Symmetrical Analysis of the Two Processes Using Octaethylene Glycol Mono-N-Dodecyl Ether. *Biochemistry* (1990) 29:9480–8. doi:10.1021/bi00492a022
51. Schurtenberger P, Mazer N, Kaenzig W. Micelle to Vesicle Transition in Aqueous Solutions of Bile Salt and Lecithin. *J Phys Chem* (1985) 89:1042–9. doi:10.1021/j100252a031
52. Chang H-C, Hsu C-T, Lin S-Y. Adsorption Kinetics of C10E8 at the Air−Water Interface. *Langmuir* (1998) 14:2476–84. doi:10.1021/la970923g
53. Touhami Y, Rana D, Neale GH, Hornof V. Study of Polymer-Surfactant Interactions via Surface Tension Measurements. *Colloid Polym Sci* (2001) 279:297–300. doi:10.1007/s003960000455
54. Yoshikawa K, Matsubara Y. Spontaneous Oscillation of pH and Electrical Potential in an Oil-Water System. *J Am Chem Soc* (1983) 105:5967–9. doi:10.1021/ja00357a001
55. Ueno N, Banno T, Asami A, Kazayama Y, Morimoto Y, Osaki T, et al. Self-Propelled Motion of Monodisperse Underwater Oil Droplets Formed by a Microfluidic Device. *Langmuir* (2017) 33:5393–7. doi:10.1021/acs.langmuir.7b00092
56. Suga M, Suda S, Ichikawa M, Kimura Y. Self-propelled Motion Switching in Nematic Liquid crystal Droplets in Aqueous Surfactant Solutions. *Phys Rev E* (2018) 97:062703. doi:10.1103/PhysRevE.97.062703
57. Herminghaus S, Maass CC, Krüger C, Thutupalli S, Goehring L, Bahr C. Interfacial Mechanisms in Active Emulsions. *Soft Matter* (2014) 10:7008–22. doi:10.1039/c4sm00550c

Conflict of Interest: The authors declare that the research was conducted in the absence of any commercial or financial relationships that could be construed as a potential conflict of interest.

frontiers in Physics

PERSPECTIVE
published: 07 March 2022
doi: 10.3389/fphy.2022.854892

Multidimensional Self-Propelled Motion Based on Nonlinear Science

*Risa Fujita, Muneyuki Matsuo and Satoshi Nakata**

Department of Mathematical and Life Sciences, Graduate School of Integrated Sciences for Life, Hiroshima University, Higashihiroshima, Japan

Self-propelled objects, which exhibit characteristic features of motion, are proposed based on nonlinear science. At first, a self-propelled object with length like undulatory swimming is designed, i.e., the phase of oscillation at several points on the object is propagated in the opposite direction of motion. Second, the vertical oscillation of a camphor disk is created at an amphiphilic molecular layer developed on water. The proposed systems suggest that nonlinearity can enhance the autonomy of self-propelled objects as multidimensional motion.

Keywords: nonlinear, oscillation, self-propelled object, camphor, nonequilibrium, autonomy

OPEN ACCESS

Edited by:
Rabih Sultan, American University of Beirut, Lebanon

Reviewed by:
Charles Reichhardt, Los Alamos National Laboratory (DOE), United States

****Correspondence:***
Satoshi Nakata
nakatas@hiroshima-u.ac.jp

Specialty section:
This article was submitted to Physical Chemistry and Chemical Physics, a section of the journal Frontiers in Physics

Received: *14 January 2022*
Accepted: *04 February 2022*
Published: *07 March 2022*

Citation:
Fujita R, Matsuo M and Nakata S (2022) Multidimensional Self-Propelled Motion Based on Nonlinear Science. Front. Phys. 10:854892. doi: 10.3389/fphy.2022.854892

INTRODUCTION

Several types of inanimate self-propelled objects such as nano wires and Janus particles have been developed for environmental, industrial, and medical applications [1–4]. In general, self-propelled objects exhibit random motion or unidirectional motion which is determined by their shape or the external force [1–7]. On the other hand, animate self-propelled objects such as bacteria exhibit characteristic features of motion depending on the information of the environment. These facts suggest that the autonomy of animate self-propelled objects is significantly higher than that of the inanimate ones [5–7].

We introduced nonlinear science into systems to enhance their autonomy, and as a result, characteristic nonlinear phenomena such as oscillation, bifurcation, synchronization, hysteresis, and pattern formation could be reproduced experimentally [5–7]. Several types of self-propelled objects, which exhibit characteristic features of motion from the viewpoint of nonlinear science, have been reported [5–18]. Among them, the objects composed of camphor or camphor derivatives, of which the driving force is the difference in surface tension, have been investigated as a simple experimental system [5–7, 19–35]. For example, a camphor disk placed on a linear water channel, reciprocating motion along the channel, was observed [5, 6]. When a camphor disk attached to the bottom of a larger plastic circular plate was placed on water, oscillatory motion between rest and motion was observed, and the bifurcation between the continuous and oscillatory motion was determined by the location of the camphor disk [5, 6, 23, 27]. The period of oscillatory motion and bifurcation between continuous and oscillatory motion was observed coupled with chemical reactions [5–8, 36, 37]. When two or more camphor disks or boats were placed in the same circular water channel, synchronized swimming or collective motion was observed [5–7]. Motion with memory, i.e., future motion expected by previous motion, could be realized by using a camphor disk and plastic plate [22, 28, 35]. Recently, the catch and release type of chemotaxis was realized using 6-methylcoumarin as a self-propelled object and sodium phosphate as a chemical stimulus [38]. These characteristic features of motion could be qualitatively reproduced by numerical calculations based on reaction–diffusion equations and the equation of motion [5–7, 28, 31–35, 39].

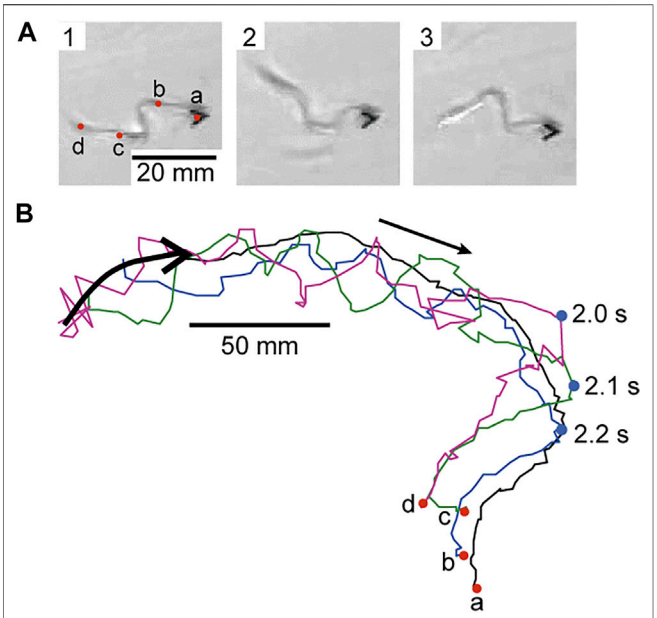

FIGURE 1 | (A) Snapshots of the self-propelled filament (time interval: 0.2 s) and **(B)** outline of the points a, b, c, and d on the filament from top view. The arrow around the middle of the outline denotes the direction of motion. The object around the left side of the outline denotes the schematic illustration of the filament. [See the actual movies in the supporting information as **Supplementary Movie S1** (10× speed)]. 2.2, 2.1, and 2.0 s on the blue circles in **(A)** denote the time at one of the maximum values of the oscillation on the outlines of the points b, c, and d.

In this article, we propose novel self-propelled objects which exhibit multidimensional motion at the air–water interface under nonequilibrium: one is a self-propelled object with length like undulatory swimming and the other exhibits vertical oscillation of a camphor disk on an amphiphilic molecular layer developed on water. The proposed systems suggest that nonlinearity can further enhance the autonomy of self-propelled objects.

SELF-PROPELLED FILAMENT LIKE UNDULATORY SWIMMING

In this section, we introduce a self-propelled filament placed on water. The filament is produced from a commercial adhesive (consisting mainly of nitrocellulose and acetone), and the energy source is acetone and the driving force of motion is the difference in the surface tension around the filament since acetone reduces the surface tension. As the shape of the filament is deformed and oscillated periodically, information of wave propagation along the filament is added as characteristic features of motion in addition to information of mass movement [40]. When one of the end points of the single filament is fixed on the edge of the chamber, periodic pendulum motion is produced and the phase of the filament near the fixed edge progresses faster in comparison with the phase of the free edge for the pendulum motion. When two filaments are coupled together, in-phase and out-phase synchronizations are produced depending on the distance between them and the initial floating state.

We propose a self-propelled filament of which one of the end points is adhered to the free plastic film with V-shape to introduce heterogeneity. **Figure 1** shows (a) snapshots of the filament and (b) outline of points a, b, c, and d on the filament. The filament moves in the direction of the plastic film while oscillating except for point a, i.e., the head of the filament. The phase of oscillation was propagated from b to d, i.e., in the opposite direction of the motion. The propagation of the phase oscillation in the animate undulatory swimming is the same as the direction of motion. Thus, the direction of the phase propagation of our inanimate meandering filament is opposite to the animate undulatory swimming like "moon walk" by MJ. The opposite direction of phase propagation suggests that our inanimate filament is passive on the motion since the Marangoni flow occurs in the opposite direction of motion. The shape and size of the head of the filament should be improved to make the direction of the phase propagation the same as animate undulatory swimming.

VERTICAL OSCILLATORY MOTION OF A CAMPHOR DISK PLACED ON AN AMPHIPHILIC MOLECULAR LAYER DEVELOPED AT THE AIR–WATER INTERFACE

In this chapter, we introduce vertical oscillatory motion of a camphor disk placed on an amphiphilic molecular layer developed at the air–water interface. Here, nervonic acid is used as an amphiphilic substance [24]. The surface pressure *vs.* area isotherm exhibits a transition point corresponding to a phase transition between the fluid and fluid/condensed phases of nervonic acid. The characteristic features of motion, i.e., no motion, oscillatory motion, and continuous motion, are determined by not only the value of the surface pressure but also the nature of the phase in the nervonic acid molecular layer. These results suggest that the characteristic features of motion can be designed based on the chemical structure of an amphiphilic molecule.

We propose vertical oscillation of a camphor disk (diameter: 3 mm, thickness: 1 mm) placed at the air–water interface. Here, nervonic acid which is developed on water is in the fluid/condensed phase. **Figure 2** shows (a1) snapshots of one cycle of vertical oscillation and (a2) time-variation of the lateral location of a camphor disk. The camphor disk exhibited not only lateral oscillation but also vertical oscillation even at the air–water interface. The vertical oscillation may be generated by the following mechanism. As the surface pressure of the nervonic acid molecular layer (Π_{na} ~ 8 mN m^{-1} at 293 K and 40 Å molecule^{-1}) is similar to that of the camphor (Π_c, the saturated value of Π_c ~ 17 mN m^{-1}), repetition between the resting and motion states is possible since no motion at $\Pi_{na} \geq \Pi_c$ and motion at $\Pi_{na} \leq \Pi_c$ occur. The periodicity and

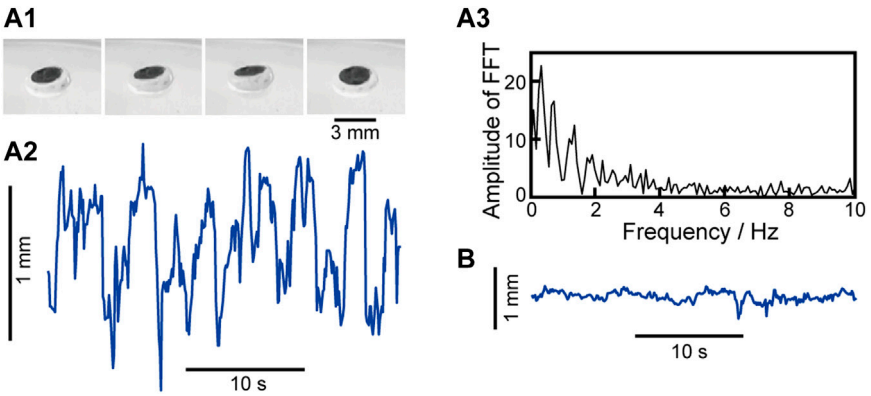

FIGURE 2 | (A1) Snapshots of vertical oscillation of a camphor disk (time interval: 0.2 s, view from an angle) and **(A2)** time-variation of the location of the camphor disk on the vertical axis, **(A3)** linear spectrum of FFT for **(A2)** at 293 K and 40 Å molecule^{-1} and **(B)** time-variation of the location of the camphor disk on the vertical axis at 298 K and 40 Å molecule^{-1}. A black circle on the camphor disk was marked to measure the vertical location using the laser displacement meter. [See the actual movies in the supporting information as **Supplementary Movie S2** (10× speed)].

nonlinearity of the oscillation were observed as the fundamental frequency (~0.3 Hz) and the higher harmonics in the linear spectrum of the fast Fourier transformation (FFT) for **Figure 2A2**, respectively (see **Figure 2A3**). Vertical oscillation may occur due to the repetition of fluid and fluid/condensed phases since the development and sublimation of the camphor molecules at the air–water interface induces the phase transition from the fluid/condensed to the fluid phase and *vice versa*, respectively. No oscillation was observed at 298 K and 40 Å molecule^{-1}, i.e., the fluid phase, as shown in **Figure 2B**. The change in the surface pressure around the disk induces the change in the meniscus at the camphor solid/water interface including nervonic acid, and as a result, the vertical oscillation occurs.

CONCLUSION AND OUTLOOK

In this article, we proposed novel types of self-propelled objects which exhibit multidimensional motion from the viewpoint of nonlinear science. Further multidimensional motion, such as translation including rotation like drill and pattern formation coupled with motion like collective motion, will be created in the near future by enhancing autonomy.

DATA AVAILABILITY STATEMENT

The data that support the findings of this study are available from the corresponding author, SN, upon reasonable request.

AUTHOR CONTRIBUTIONS

RF performed the examination, analyzed the experimental results, and prepared the manuscript. MM analyzed the data and edited the manuscript. SN planned the experimental system and edited the manuscript.

FUNDING

This study was supported by JSPS KAKENHI (Grant Nos. JP20H02712, JP20H01871, and JP21H00996), the Cooperative Research Program of "Network Joint Research Center for Materials and Devices" (No. 20211061) to SN, JSPS Bilateral Joint Research Project between Japan and the Polish Academy of Sciences (JPJSBP120204602), and JSPS Japan–Hungary Bilateral Joint Research Project (JPJSBP120213801).

ACKNOWLEDGMENTS

We acknowledge Mr. Katsuhiko Kayahara for his technical support on the examination.

SUPPLEMENTARY MATERIAL

The Supplementary Material for this article can be found online at: https://www.frontiersin.org/articles/10.3389/fphy.2022.854892/full#supplementary-material

REFERENCES

1. Soto F, Karshalev E, Zhang F, Esteban Fernandez de Avila B, Nourhani A, Wang J. *Smart Materials for Microrobots*. Chem Rev (2021). doi:10.1021/acs.chemrev.0c00999
2. Wang H, Pumera M. Coordinated Behaviors of Artificial Micro/Nanomachines: From Mutual Interactions to Interactions with the Environment. *Chem Soc Rev* (2020) 49:3211–30. doi:10.1039/c9cs00877b
3. Huang Z, Chen P, Zhu G, Yang Y, Xu Z, Yan L-T. Bacteria-Activated Janus Particles Driven by Chemotaxis. *ACS Nano* (2018) 12(7):6725–33. doi:10.1021/acsnano.8b01842

4. Bechinger C, Di Leonardo R, Löwen H, Reichhardt C, Volpe G, Volpe G. Active Particles in Complex and Crowded Environments. *Rev Mod Phys* (2016) 88(4):45006–150. doi:10.1103/RevModPhys.88.045006
5. Nakata S, Pimienta V, Lagzi I, Kitahata H, Suematsu NJ. *Self-Organized Motion, Physicochemical Design Based on Nonlinear Dynamics*. Cambridge: RSC-ebook (2018). doi:10.1039/9781788013499
6. Nakata S, Nagayama M, Kitahata H, Suematsu NJ, Hasegawa T. Physicochemical Design and Analysis of Self-Propelled Objects that Are Characteristically Sensitive to Environments. *Phys Chem Chem Phys* (2015) 17:10326–38. doi:10.1039/C5CP00541H
7. Suematsu NJ, Nakata S. Evolution of Self-Propelled Objects: From the Viewpoint of Nonlinear Science. *Chem Eur J* (2018) 24:6308–24. doi:10.1002/chem.201705171
8. Suematsu NJ, Mori Y, Amemiya T, Nakata S. Spontaneous Mode Switching of Self-Propelled Droplet Motion Induced by a Clock Reaction in the Belousov-Zhabotinsky Medium. *J Phys Chem Lett* (2021) 12(31):7526–30. doi:10.1021/acs.jpclett.1c02079
9. Kitahata H, Yoshinaga N, Nagai KH, Sumino Y. Spontaneous Motion of a Droplet Coupled with a Chemical Wave. *Phys Rev E* (2011) 84(1):015101. doi:10.1103/PhysRevE.84.015101
10. Tanaka S, Nakata S, Nagayama M. A Surfactant Reaction Model for the Reciprocating Motion of a Self-Propelled Droplet. *Soft Matter* (2021) 17:388–96. doi:10.1039/d0sm01500h
11. Banno T, Asami A, Ueno N, Kitahata H, Koyano Y, Asakura K, et al. Deformable Self-Propelled Micro-object Comprising Underwater Oil Droplets. *Sci Rep* (2016) 6:31292–19. doi:10.1038/srep31292
12. Banno T, Kuroha R, Toyota T. pH-Sensitive Self-Propelled Motion of Oil Droplets in the Presence of Cationic Surfactants Containing Hydrolyzable Ester Linkages. *Langmuir* (2012) 28(2):1190–5. doi:10.1021/la2045338
13. Ban T, Matsumoto K, Nanzai B, Mori Y, Nabika H. Bifurcation of Chemically Driven Self-Propelled Droplets on a Surfactant-Adsorbed Surface Based on Spreading Coefficients. *Colloids Surf A: Physicochemical Eng Aspects* (2021) 620(5):126563. doi:10.1016/j.colsurfa.2021.126563
14. Sharma J, Tiwari I, Das D, Parmananda P, Akella VS, Pimienta V. Rotational Synchronization of Camphor Ribbons. *Phys Rev E* (2019) 99(1):012204. doi:10.1103/PhysRevE.99.012204
15. Čejková J, Novák M, Štěpánek F, Hanczyc MM. Dynamics of Chemotactic Droplets in Salt Concentration Gradients. *Langmuir* (2014) 30(40):11937–44. doi:10.1021/la502624f
16. Zhou C, Chen X, Han Z, Wang W. Photochemically Excited, Pulsating Janus Colloidal Motors of Tunable Dynamics. *ACS Nano* (2019) 13(4):4064–72. doi:10.1021/acsnano.8b08276
17. Holló G, Suematsu NJ, Ginder E, Lagzi I. Electric Field Assisted Motion of a Mercury Droplet. *Sci Rep* (2021) 11:2753–111. doi:10.1038/s41598-020-80375-1
18. Yamamoto D, Maeno J, Manabe Y, Okamoto Y, Nawa-Okita E, Shioi A. Mode Bifurcation on Contact Line Dynamics at Oil/Water Interface Depending on the Contact Line Length. *Front Chem* (2021) 9:708633–18. doi:10.3389/fchem.2021.708633
19. Tomlinson C. On the Motions of Camphor on the Surface of Water. *Proc R Soc Lond* (1860) 11:575–7.
20. Rayleigh L. Measurements of the Amount of Oil Necessary in Order to Check the Motions of Camphor upon Water. *Proc R Soc Lond* (1890) 47:364–7.
21. Nakata S, Iguchi Y, Ose S, Kuboyama M, Ishii T, Yoshikawa K. Self-Rotation of a Camphor Scraping on Water: New Insight into the Old Problem. *Langmuir* (1997) 13(16):4454–8. doi:10.1021/la970196p
22. Fujita R, Matsufuji T, Matsuo M, Nakata S. Alternate Route Selection of Self-Propelled Filter Papers Impregnated with Camphor for Two-Branched Water Channels. *Langmuir* (2021) 37(23):7039–42. doi:10.1021/acs.langmuir.1c00644
23. Xu Y, Takayama N, Er H, Nakata S. Oscillatory Motion of a Camphor Object on a Surfactant Solution. *J Phys Chem B* (2021) 125(6):1674–9. doi:10.1021/acs.jpcb.0c09314
24. Nakata S, Fujita R. Self-Propelled Motion of a Camphor Disk on a Nervonic Acid Molecular Layer and its Dependence on Phase Transition. *J Phys Chem B* (2020) 124(26):5525–9. doi:10.1021/acs.jpcb.0c03044
25. Nakata S, Matsufuji T, Gorecki J, Kitahata H, Nishimori H. Inversion Probability of Three-Bladed Self-Propelled Rotors after Forced Stops of Different Durations. *Phys Chem Chem Phys* (2020) 22:13123–8. doi:10.1039/d0cp00746c
26. Nakata S, Nasu K, Irie Y, Hatano S. Self-Propelled Motion of a Camphor Disk on a Photosensitive Amphiphilic Molecular Layer. *Langmuir* (2019) 35(12):4233–7. doi:10.1021/acs.langmuir.8b04285
27. Tenno R, Gunjima Y, Yoshii M, Kitahata H, Gorecki J, Suematsu NJ, et al. Period of Oscillatory Motion of a Camphor Boat Determined by the Dissolution and Diffusion of Camphor Molecules. *J Phys Chem B* (2018) 122(6):2610–5. doi:10.1021/acs.jpcb.7b11903
28. Nakata S, Kayahara K, Yamamoto H, Skrobanska P, Gorecki J, Awazu A, et al. Reciprocating Motion of a Self-Propelled Rotor Induced by Forced Halt and Release Operations. *J Phys Chem C* (2018) 122(6):3482–7. doi:10.1021/acs.jpcc.7b12089
29. Matsuo M, Hashishita H, Nakata S. Self-Propelled Motion Sensitive to the Chemical Structure of Amphiphilic Molecular Layer on an Aqueous Phase. *Membranes* (2021) 11(11):885. doi:10.3390/membranes11110885
30. Löffler RJG, Hanczyc MM, Gorecki J. A Hybrid Camphor-Camphene Wax Material for Studies on Self-Propelled Motion. *Phys Chem Chem Phys* (2019) 21:24852–6. doi:10.1039/C9CP04722K
31. Koyano Y, Kitahata H, Nakata S, Gorecki J. On a Simple Model that Explains Inversion of a Self-Propelled Rotor under Periodic Stop-And-Release-Operations. *Chaos* (2020) 30:023105–1. doi:10.1063/1.5140626
32. Nagayama M, Nakata S, Doi Y, Hayashima Y. A Theoretical and Experimental Study on the Unidirectional Motion of a Camphor Disk. *Physica D: Nonlinear Phenomena* (2004) 194:151–65. doi:10.1016/j.physd.2004.02.003
33. Koyano Y, Gryciuk M, Skrobanska P, Malecki M, Sumino Y, Kitahata H, et al. Relationship between the Size of a Camphor-Driven Rotor and its Angular Velocity. *Phys Rev E* (2017) 96:012609. doi:10.1103/PhysRevE.96.012609
34. Koyano Y, Suematsu NJ, Kitahata H. Rotational Motion of a Camphor Disk in a Circular Region. *Phys Rev E* (2019) 99:022211. doi:10.1103/PhysRevE.99.022211
35. Nakata S, Hata M, Ikura YS, Heisler E, Awazu A, Kitahata H, et al. Motion with Memory of a Self-Propelled Object. *J Phys Chem C* (2013) 117(46):24490–5. doi:10.1021/jp409172m
36. Nakata S, Irie Y, Suematsu NJ. Self-Propelled Motion of a Coumarin Disk Characteristically Changed in Couple with Hydrolysis on an Aqueous Phase. *J Phys Chem B* (2019) 123(19):4311–7. doi:10.1021/acs.jpcb.8b11534
37. Xu Y, Ji L, Izumi S, Nakata S. pH-Sensitive Oscillatory Motion of a Urease Motor on the Urea Aqueous Phase. *Chem Asian J* (2021) 16(13):1762–6. doi:10.1002/asia.202100336
38. Yasugahira Y, Tatsumi Y, Yamanaka O, Nishimori H, Nagayama M, Nakata S. Catch and Release Chemotaxis. *ChemSystemsChem* (2021) 3:e202100031–16. doi:10.1002/syst.202100031
39. Kim M, Okamoto M, Yasugahira Y, Tanaka S, Nakata S, Kobayashi Y, et al. A Reaction-Diffusion Particle Model for Clustering of Self-Propelled Oil Droplets on a Surfactant Solution. *Physica D: Nonlinear Phenomena* (2021) 425:132949–113. doi:10.1016/j.physd.2021.132949
40. Nakata S, Kayahara K, Kuze M, Ginder E, Nagayama M, Nishimori H. Synchronization of Self-Propelled Soft Pendulums. *Soft Matter* (2018) 14:3791–8. doi:10.1039/c8sm00517f

Conflict of Interest: The authors declare that the research was conducted in the absence of any commercial or financial relationships that could be construed as a potential conflict of interest.

Publisher's Note: All claims expressed in this article are solely those of the authors and do not necessarily represent those of their affiliated organizations, or those of the publisher, the editors, and the reviewers. Any product that may be evaluated in this article, or claim that may be made by its manufacturer, is not guaranteed or endorsed by the publisher.

frontiers | Frontiers in Physics

ORIGINAL RESEARCH
published: 01 April 2022
doi: 10.3389/fphy.2022.828444

Precipitation Patterns in Reaction–Diffusion–Reaction Systems of Prussian Blue and Cu–Fe-Based Prussian Blue Analogs

*Hisashi Hayashi**

Department of Chemical and Biological Sciences, Faculty of Science, Japan Women's University, Tokyo, Japan

In agarose gel containing $[Fe(CN)_6]^{3-}$ ions and sandwiched between two metal rods (Ti, Fe, or Cu) with a voltage of 1–5 V applied for 20–100 h, reaction–diffusion–reaction (RDR) processes (that is, electrochemical reactions at metal rods to generate reactant ions, diffusion of the reactant ions influenced by the electric field in agarose gel, and reactions of the reactant ions to form/decompose precipitates) were coupled to generate diverse precipitation patterns of Prussian blues (PB) or Cu–Fe-based Prussian blue analogs (Cu–Fe PBA). These patterns strongly depended on the type of metal electrode, applied voltage, initial $[Fe(CN)_6]^{3-}$ concentration, and elapsed time after voltage application. Under the application of 2 V for 20/50 h, the PB/Cu–Fe PBA formed a discrete precipitation band on the anode/cathode side in an agarose gel containing 0.050 M $[Fe(CN)_6]^{3-}$ ions. In the Cu–Fe PBA system, a relatively long precipitation band of $Cu(OH)_2$ was also generated on the anode side by OH^- ions produced on the cathode as a byproduct. Longer voltage applications promoted propagation of the Cu–Fe PBA band to the anode side and caused the discrete PB band to disappear. Higher initial $[Fe(CN)_6]^{3-}$ concentrations deepened the color of the generated patterns. Higher voltage applications suppressed the propagation of the Cu–Fe PBA band to the anode side and caused the PB band to disappear. Experiments using a Ti cathode suggested that the formation and subsequent decomposition of PB or Cu–Fe PBA at the cathode surface are important for forming precipitation band(s) in the gel near the cathode. The application of cyclic alternating voltages (particularly, 4 V for 1 h and 1 V for 4 h) was effective in generating Liesegang-band-like periodic bands, particularly for the Cu–Fe PBA system.

Keywords: precipitation pattern, periodic band structure, Prussian blue analog (PBA), reaction-diffusion system, electrochemical reaction (ECR)

Edited by:
Rabih Sultan, American University of Beirut, Lebanon

Reviewed by:
Ivan L'Heureux, University of Ottawa, Canada
Byungchan Han, Yonsei University, South Korea

***Correspondence:**
Hisashi Hayashi
hayashih@fc.jwu.ac.jp

Specialty section:
This article was submitted to Physical Chemistry and Chemical Physics, a section of the journal Frontiers in Physics

Received: *03 December 2021*
Accepted: *28 February 2022*
Published: *01 April 2022*

Citation:
Hayashi H (2022) Precipitation Patterns in Reaction–Diffusion–Reaction Systems of Prussian Blue and Cu–Fe-Based Prussian Blue Analogs. Front. Phys. 10:828444. doi: 10.3389/fphy.2022.828444

1 INTRODUCTION

Liesegang bands [1, 2], which are the periodic precipitation bands of slightly soluble compounds *via* reaction–diffusion (RD) processes in hydrogels, have been continuously investigated [3] since their discovery by Liesegang in 1896 [4, 5]. Liesegang banding continues to attract considerable scientific interest as a self-organization phenomenon [6, 7] that is potentially applicable to micro- and nanofabrication [1,8–10]. In conventional experiments to observe Liesegang bands, two electrolytes are loaded into separate columns in a single sample tube. The

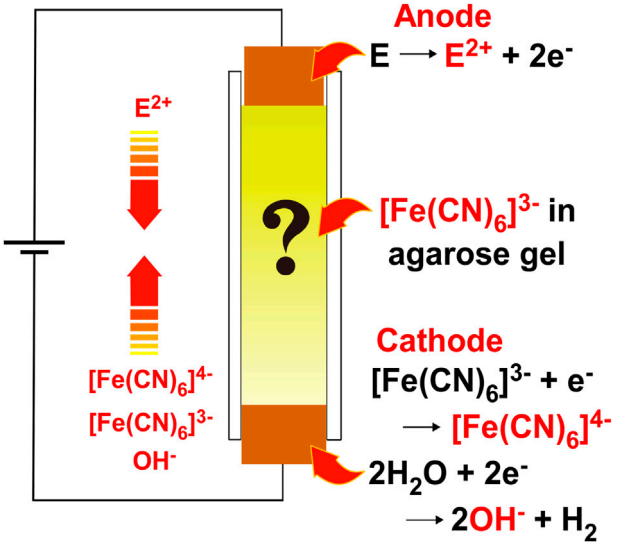

FIGURE 1 | A schematic illustration of the reaction–diffusion–reaction (RDR) setup in which electrochemical reactions to generate reactant ions, diffusion of the reactant ions influenced by an electric field, and reactions of the reactant ions to form precipitates are coupled to generate precipitation patterns of PB or PBA in agarose hydrogel. The arrows indicate the movement directions of reactant ions in the electric field.

shorter column on top (in the form of a gel or aqueous solution) has a higher electrolyte concentration, and the longer gel column is placed at the bottom, in which a continuous precipitation zone and/or Liesegang bands form. Because only limited systems have been reported to form Liesegang bands [1], it is scientifically interesting and technologically important to widely explore systems in which Liesegang-band-like precipitation patterns could form.

Recently, we proposed a new class of systems to stochastically form Liesegang-band-like, periodic precipitation bands of Cu–Fe-based Prussian blue analogs (Cu–Fe PBA) in agarose gel through the coupled processes of 1) electrochemical reactions to generate reactant ions, 2) diffusion of the reactant ions influenced by the electric field in the gel, and 3) reactions of the reactant ions to form precipitates, that is, reaction–diffusion–reaction (RDR) processes [11]. The proposed system is illustrated in **Figure 1**.

The setup in **Figure 1** is simple: it consists only of agarose gel with $[Fe^{III}(CN)_6]^{3-}$ ions in a plastic straw sandwiched between two metal rods for voltage application. However, the chemical processes that occur within this system are considerably complicated. The reactant metal ions (E^{2+}: E = Fe or Cu in this study) and reactant $[Fe^{II}(CN)_6]^{4-}$ ions are generated at the anode and cathode by reactions (**1**) and (**2**), respectively, when the applied voltage exceeds the sum of the overpotential of the electrodes and the potentials of the electrode reactions (typically ~1 V [11])

$$E \rightarrow E^{2+} + 2e^{-} \quad (1)$$

$$2\left[Fe^{III}(CN)_6\right]^{3-} + 2e^{-} \rightarrow 2\left[Fe^{II}(CN)_6\right]^{4-} \quad (2)$$

For E = Fe, because aqueous Fe^{2+} ions are easily oxidized by dissolved oxygen in the hydrogel, Fe^{3+} ions are generated by

$$4Fe^{2+} + 4H^{+} + O_2 \rightarrow 4Fe^{3+} + 2H_2O \quad (3)$$

Additionally, side reactions that form H^+ and OH^- ions are also possible at the anode and cathode, respectively

$$2H_2O \rightarrow O_2 + 4H^{+} + 4e^{-} \quad (4)$$

$$2H_2O + 2e^{-} \rightarrow H_2 + 2OH^{-} \quad (5)$$

The ions generated by reactions **(1–5)** are transported under the influence of the electric field and thermal diffusion and react with each other to form precipitates of Prussian blues (PB) or Prussian blue analogs (PBA), which are generally represented by the formula $A_xE_y\,[E'(CN)_6]_z\square_{1-z}{\cdot}nH_2O$ [A is an alkali metal element, and E (= Mg, V, Cr, Mn, Fe, Co., Ni, Cu, Zn, Ag, Ce, Sm, Bi, etc.) and E′ (= V, Cr, Mn, Fe, Co., Ru, etc.) are specific (mainly transition) metal elements; A = K and E′ = Fe in this study]. Here, if E = E′ = Fe, the compounds are generally called "PB; " if not, they are called "E–E′-based PBA" (for example, for E = Cu and E′ = Fe, they are called "Cu–Fe-based PBA"). The symbol □ indicates $E'(CN)_6$ vacancies, that is, defects resulting from missing $E'(CN)_6$ moieties. For most PBA, $0 \le x \le 2$, $y = 1$, and $0 < z \le 1$; for example, $x = y = z = 1$ for Cu^{II}-Fe^{III} PBA with no $Fe(CN)_6$ vacancies. Thus, the possible reactions to form PB/Cu–Fe PBA precipitates in the proposed system can be expressed as

$$xK^{+} + yE^{2+} + z\left[Fe^{III}(CN)_6\right]^{3-} + nH_2O \rightarrow K_xE^{II}_y\left[Fe^{III}(CN)_6\right]_z\square_{1-z}\cdot nH_2O \quad (6)$$

$$xK^{+} + yE^{2+} + z\left[Fe^{II}(CN)_6\right]^{4-} + nH_2O \rightarrow K_xE^{II}_y\left[Fe^{II}(CN)_6\right]_z\square_{1-z}\cdot nH_2O \quad (7)$$

$$xK^{+} + yE^{3+} + z\left[Fe^{III}(CN)_6\right]^{3-} + nH_2O \rightarrow K_xFe^{III}_y\left[Fe^{III}(CN)_6\right]_z\square_{1-z}\cdot nH_2O \quad (8)$$

$$xK^{+} + yE^{3+} + z\left[Fe^{II}(CN)_6\right]^{4-} + nH_2O \rightarrow K_xFe^{III}_y\left[Fe^{II}(CN)_6\right]_z\square_{1-z}\cdot nH_2O \quad (9)$$

Note that 1) the compounds $K_xFe^{II}_y[Fe^{III}(CN)_6]_z\square_{1-z}{\cdot}nH_2O$, which are generated by reaction (**6**) for E = Fe, are unstable and readily transformed into $K_xFe^{III}_y[Fe^{II}(CN)_6]_z\square_{1-z}{\cdot}nH_2O$:

$$K_xFe^{II}_y\left[Fe^{III}(CN)_6\right]_z\square_{1-z}\cdot nH_2O \rightarrow K_xFe^{III}_y\left[Fe^{II}(CN)_6\right]_z\square_{1-z}\cdot nH_2O \quad (10)$$

2) the compounds $K_xFe^{III}_y\,[Fe^{III}(CN)_6]_z\square_{1-z}{\cdot}nH_2O$, which are historically called "Berlin green (BG)," are soluble and do not form precipitates [12]. Thus, for E = Fe, two types of precipitates, $K_xFe^{III}_y\,[Fe^{II}(CN)_6]_z\square_{1-z}{\cdot}nH_2O$ and $K_xFe^{II}_y\,[Fe^{II}(CN)_6]_z\square_{1-z}{\cdot}nH_2O$, are expected. The former is "PB" in the strict sense, and the latter is historically called "Prussian white (PW)" [12]. For E = Cu, two types of precipitates, $K_xCu^{II}_y\,[Fe^{III}(CN)_6]_z\square_{1-z}{\cdot}nH_2O$ and $K_xCu^{II}_y\,[Fe^{II}(CN)_6]_z\square_{1-z}{\cdot}nH_2O$, are possible, which are generated by reactions (**6**) and (**7**), respectively.

Because the surfaces of the E metal are generally reactive to $[Fe^{III}(CN)_6]^{3-}$and $[Fe^{II}(CN)_6]^{4-}$ ions [11], precipitates of PB and PBA can also form on the surfaces of the electrodes [if they consist of E metal(s)]. For example, reactions (**1**) and (**2**) can occur at the metal surface and the gel surface in contact with the metal, respectively,

even without voltage application. At the cathode/anode of the E metal, the $E^{2+}/[Fe^{II}(CN)_6]^{4-}$ ions generated at these surfaces can react with the $[Fe^{II}(CN)_6]^{4-}/E^{2+}$ ions generated electrochemically to produce precipitates of $K_xE^{II}_y\,[Fe^{II}(CN)_6]_z\square_{1-z}{\cdot}nH_2O$. At the anode, direct electrochemical production of $K_xE^{II}_y\,[Fe^{II}(CN)_6]_z\square_{1-z}{\cdot}nH_2O$ is also possible through

$$xK^+ + yE + z\left[Fe^{III}(CN)_6\right]^{3-} + nH_2O \rightarrow K_xE^{II}_y\left[Fe^{II}(CN)_6\right]_z\square_{1-z}\cdot nH_2O \tag{11}$$

Note also that the OH^- ions generated by reaction (**5**) can form precipitates of metal hydroxides through

$$E^{2+} + 2OH^- \rightarrow E^{II}(OH)_2 \tag{12}$$

$$Fe^{3+} + 3OH^- \rightarrow Fe^{III}(OH)_3 \tag{13}$$

Here, $Fe^{II}(OH)_2$ [E = Fe in reaction (**12**)] is relatively unstable in aqueous solutions or hydrogels and is rapidly oxidized by

$$Fe^{II}(OH)_2 + OH^- \rightarrow Fe^{III}(OH)_3 + e^- \tag{14}$$

Thus, three types of colored precipitates, which provide multicolored precipitation patterns in gels, are expected to form in the RDR system shown in **Figure 1**: for E = Cu, these are $K_xCu^{II}_y\,[Fe^{II}(CN)_6]_z\square_{1-z}{\cdot}nH_2O$ (Cu^{II}–Fe^{II} PBA), $K_xCu^{II}_y\,[Fe^{III}(CN)_6]_z\square_{1-z}{\cdot}nH_2O$ (Cu^{II}–Fe^{III} PBA), and $Cu^{II}(OH)_2$; for E = Fe, these are $K_xFe^{II}_y\,[Fe^{II}(CN)_6]_z\square_{1-z}{\cdot}nH_2O$ (PW), $K_xFe^{III}_y\,[Fe^{II}(CN)_6]_z\square_{1-z}{\cdot}nH_2O$ (PB), and $Fe^{III}(OH)_3$.

Furthermore, OH^- ions can dissolve the precipitates of PB and PBA [13] (both at the surface of electrodes and in agarose gel) through

$$K_xE^{II}_y\left[Fe^{II}(CN)_6\right]_Z\square_{1-Z}\cdot nH_2O + 2yOH^- \rightarrow xK^+ + yE^{II}(OH)_2 + z\left[Fe^{II}(CN)_6\right]^{4-} + nH_2O \tag{15}$$

$$K_xE^{II}_y\left[Fe^{III}(CN)_6\right]_Z\square_{1-Z}\cdot nH_2O + 2yOH^- \rightarrow xK^+ + yE^{II}(OH)_2 + z\left[Fe^{III}(CN)_6\right]^{3-} + nH_2O \tag{16}$$

$$K_xFe^{III(II)}_y\left[Fe^{II}(CN)_6\right]_Z\square_{1-Z}\cdot nH_2O + 3yOH^- \rightarrow xK^+ + yFe^{III}(OH)_3 + z\left[Fe^{II}(CN)_6\right]^{4-} + nH_2O \tag{17}$$

As shown above, the chemistry of the proposed RDR system is considerably complicated; hence, the generated precipitation patterns may strongly depend on the preparation conditions. In this paper, we comprehensively report the diverse precipitation patterns of PB and Cu–Fe PBA observed in the RDR system. This is an extension of a previous study [11] exploring the experimental conditions under which periodic patterns are observed with high probability. Because very little is currently known about RDR patterning (only for Cu–Fe PBA system [11]), the present study (although qualitative) is useful for outlining this novel class of macroscopic patterning.

Additionally, the RDR patterning of PB and PBA is also interesting from the perspective of applications in material science because PB and PBA have attracted significant interest as multifunctional platforms for various applications [14] such as magnets [15, 16], batteries [13, 17, 18], catalysts [19], gas adsorbents [20–22], and radioactive-Cs adsorbents [20,23–25] owing to their characteristic crystal structures. Generally, PB/PBA properties are strongly influenced by the $Fe(CN)_6$ vacancies (or the value of z), the amount of which depends considerably on the preparation process [13, 15, 17]. Therefore, if we could prepare gels containing PB/PBA with position-dependent variation of $Fe(CN)_6$ vacancies using RDR processes in the future, the RDR patterning may be used to simultaneously obtain PB/PBA with different functional properties [11].

2 MATERIALS AND METHODS

2.1 Materials

Analytical reagent-grade $K_3\,[Fe^{III}(CN)_6]$ (≥99.0%), $K_4\,[Fe^{II}(CN)_6]{\cdot}3H_2O$ (≥99.5%), $Fe^{II}SO_4{\cdot}7H_2O$ (≥99.0%), $Fe^{III}Cl_3{\cdot}6H_2O$ (≥99.0%), and $Cu^{II}Cl_2{\cdot}2H_2O$ (≥99.0%) were obtained from Wako Pure Chemical Industries (Osaka, Japan). Agarose for electrophoresis (gel strength: 1,800–2300 g/cm^3) was purchased from Kanto Chemical (Tokyo, Japan). All chemicals were used without further purification. All aqueous solutions were prepared using deionized water that had been purified from tap water using a cartridge water purifier (G-10: Organo, Tokyo, Japan). For the electrodes, Ti (≥99.5%), Fe (≥99.5%), and Cu (≥99.9%) rods were obtained from Nilaco (Tokyo, Japan).

2.2 Preparation of the Sample for the RDR Experiment

A sample tube filled with agarose gel containing $[Fe^{III}(CN)_6]^{3-}$ ions was prepared as described below. Appropriate amounts of $K_3\,[Fe^{III}(CN)_6]$ powder were dissolved in deionized water at 25°C to form a $[Fe^{III}(CN)_6]^{3-}$ solution (30 ml) with a concentration of 0.050–0.100 M. After adding 2.0 mass% agarose, the mixture was stirred vigorously at 98°C for 30 s to produce a uniform $[Fe^{III}(CN)_6]^{3-}$agarose sol. Note that the density of the employed agarose sol was relatively high to suppress gel shrinkage when a voltage was applied. Using a Pasteur pipette, the prepared sol was transferred to plastic straws (4 mm in diameter and 50 mm long), the bottoms of which were plugged with a metal (Ti, Fe, or Cu) rod with a diameter of 4 mm and length of ~20 mm, which was used as the cathode. Because the sol was viscous and solidified within 1000 s, it did not leak from the bottom of the straws. Plastic straws were employed as sample holders because they are simple to process and use, low-cost, and enable the easy introduction of viscous samples [26]. The hot sol in the straw was left to cool to 25°C, thus forming a solidified gel. The height of the gel column in the sample tube was ~40 mm.

Another metal rod (Fe or Cu; 3 mm in diameter and ~20 mm long) was placed atop the gel as the anode. This metal rod was narrower than that at the bottom of the tube. Because it did not fit tightly inside the straw, the metal anode maintained contact with the gel surface even when the electric field caused the gel sample to contract. The cathode and anode were connected to a programmable power supply (1696B, B&K Precision, Yorba

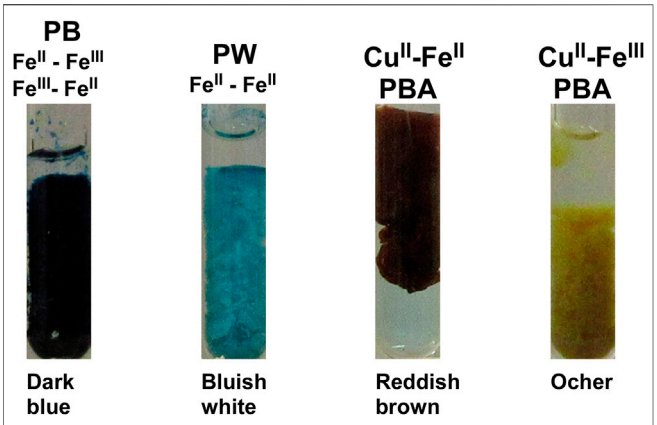

FIGURE 2 | Precipitates of PB, PW, and Cu–Fe PBA formed at 25°C in aqueous solutions. The types of precipitates are indicated at the top. The colors of these precipitates are labeled at the bottom.

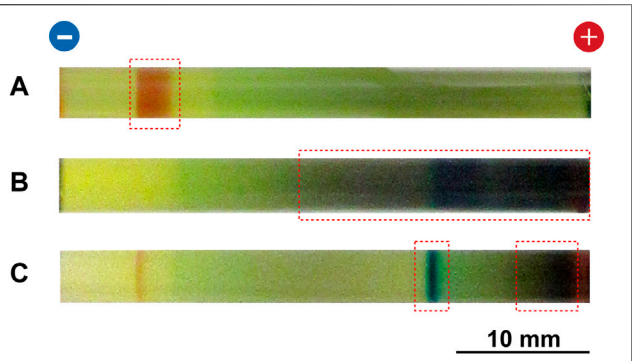

FIGURE 3 | Typical multicolored patterns formed at 25°C in the RDR system of **(A)** Cu–Fe PBA and **(B)** PB under an applied voltage of 2 V for 50 h. For the PB system, **(C)** the pattern formed under an applied voltage of 2 V for 20 h is also depicted. The initial $[Fe^{III}(CN)_6]^{3-}$concentration and the initial agarose density were 0.050 M and 2.0 mass%, respectively. The regions in which a precipitation band of PB or Cu–Fe PBA was formed are indicated by red squares. The charges of the electrodes and a scale bar are provided at the top and bottom of the images, respectively.

Linda, CA, United States). During voltage application at 25°C for 20–100 h (current <1 mA), the precipitation patterns formed in the sample tube were monitored using a digital camera (IXY650, Canon, Japan). In some experiments, not only constant voltage application, but also cyclic alternating voltage application [11] were examined. After these voltage applications, several gel samples were removed from the straws and repeatedly immersed in deionized water (~200 ml) for 3 days to remove unreacted $[Fe^{III}(CN)_6]^{3-}$ ions and soluble compounds (these ions and compounds were spontaneously eluted from the gels into water). Without such immersion, the precipitation patterns in the gel occasionally changed (within 50 h), implying that precipitation reactions in the gel can proceed even without voltage application; however, such changes were not significant [11].

For comparison, precipitates of PB and Cu–Fe PBA were formed in aqueous solutions as follows: 0.050 M $[Fe^{III}(CN)_6]^{3-}$/$[Fe^{II}(CN)_6]^{4-}$ aqueous solutions (0.1 ml) were prepared in glass tubes (4 mm in diameter and 60 mm long) by dissolving $K_3[Fe^{III}(CN)_6]$/$K_4[Fe^{II}(CN)_6]\cdot 3H_2O$ powder in deionized water at 25°C. Separately, 0.250 M aqueous solutions of Fe^{2+}, Fe^{3+}, and Cu^{2+} (0.1 ml) were prepared by dissolving powders of $Fe^{II}SO_4\cdot 7H_2O$, $Fe^{III}Cl_3\cdot 6H_2O$, and $Cu^{II}Cl_2\cdot 2H_2O$, respectively, in deionized water at 25°C and were mixed with the 0.050 M $[Fe^{III}(CN)_6]^{3-}$/$[Fe^{II}(CN)_6]^{4-}$ solutions. Precipitates of PB or Cu–Fe PBA formed immediately in the mixed solutions.

3 RESULTS

3.1 Colors of Precipitates of PB and Cu–Fe PBA

The precipitates of PB and PBA are known to exhibit various colors depending on the types of E^{2+} ions and the oxidation states of Fe [27]. **Figure 2** shows the precipitates of PB and Cu–Fe PBA formed in aqueous solutions with labeled precipitate colors. The characteristic colors of these precipitates are useful for assigning the types of PB and Cu–Fe PBA formed in the RDR systems, as described later.

3.2 Precipitation Patterns under Constant Voltage

3.2.1 Basic Features

Figures 3A,B show typical multicolored patterns formed at 25°C in the RDR system of the Cu–Fe PBA and PB, respectively, under an applied voltage of 2 V for 50 h. The initial $[Fe^{III}(CN)_6]^{3-}$ concentration was 0.050 M. Despite its intrinsic stochasticity, the pattern shown in **Figure 3A** was primarily the same as that previously reported [11].

As reported previously [11], in the Cu–Fe PBA system, a relatively short reddish-brown band formed on the cathode side (**Figure 3A**), suggesting the accumulation of Cu^{II}–Fe^{II} PBA after 50 h of voltage application. Meanwhile, a wide region on the anode side became green, which is the color of aqueous Cu^{2+} ions (providing a blue color) that were mixed with $[Fe^{III}(CN)_6]^{3-}$ ions (providing a yellow color) [11]. Thus, the green color suggests the accumulation of aqueous Cu^{2+} ions without generating Cu^{II}–Fe^{III} PBA, which are typically ocher (**Figure 2**). These findings suggest that precipitation reaction (**7**) is more dominant than reaction (**6**) in the agarose gel. Note that significant amounts of reddish-brown deposits accumulated at the cathode and anode surfaces [11], suggesting that at the electrode surfaces reaction (**7**) [as well as reaction (**11**)] is again more dominant than reaction (**6**).

Interestingly, the pattern observed in the PB system (**Figure 3B**) was completely different from that of the Cu–Fe PBA system. Here, a relatively long dark-blue (characteristic color of PB; **Figure 2**) band with graduations in color was observed on the anode side, suggesting the accumulation of PB precipitates. The PB accumulation on the anode side was considered to be due to the extremely low solubility of PB: for example, at 25°C, the base 10 logarithm of the solubility constant for PB (−40.52) is much lower than that for Mn^{II}–Fe^{II}-based PBA (−12.10), Co^{II}–Fe^{II}-based PBA (−14.74), Ni^{II}–Fe^{II}-based PBA (−14.89), and Cu^{II}–Fe^{II} PBA (−15.89) [28]. Owing to this property, the Fe^{2+} ions produced at the anode could readily form PB

FIGURE 4 | Typical multicolored patterns formed at 25°C in the RDR system of **(A)** Cu–Fe PBA and **(B)** PB under an applied voltage of 2 V for 100 h. The initial $[Fe^{III}(CN)_6]^{3-}$concentration and the initial agarose density were 0.050 M and 2.0 mass%, respectively. The charges of the electrodes and a scale bar are provided at the top and bottom of the images, respectively.

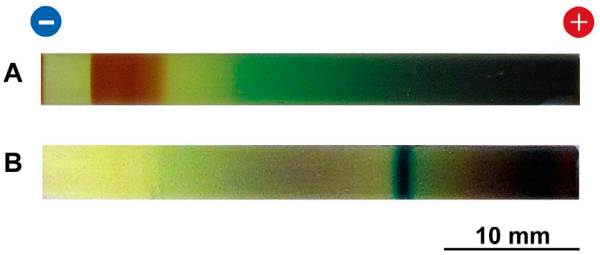

FIGURE 5 | (A) Typical multicolored pattern formed at 25°C in the Cu–Fe PBA system under an applied voltage of 2 V for 50 h. **(B)** Typical precipitation pattern formed at 25°C in the PB system under an applied voltage of 2 V for 20 h. The initial $[Fe^{III}(CN)_6]^{3-}$concentration and the initial agarose density were 0.100 M and 2.0 mass%, respectively. The charges of the electrodes and a scale bar are provided at the top and bottom of the images, respectively.

precipitates *via* reaction (**6**) with the initially loaded $[Fe^{III}(CN)_6]^{3-}$ ions [and the subsequent reaction (**10**)]. Additionally, significant amounts of dark-blue deposits accumulated at the cathode and anode surfaces. Note that bluish-white PW precipitates could not be clearly observed anywhere in this system. The lack of PW (Fe^{II}–Fe^{II}) precipitates suggests that in the PB system, precipitation reaction (**6**) to produce PB was more dominant than reaction (**7**) to produce PW. This opposite trend to the Cu–Fe PBA system can be explained by two factors: 1) generally, the reduced species $[Fe^{II}(CN)_6]^{4-}$ ions, are less abundant around the anode and 2) Fe^{2+} ions are easily oxidized to Fe^{3+} ions in the hydrogel through reaction (**3**).

As shown in **Figure 3C**, until ~20 h of voltage application, the dark-blue PB band was located away from the anode surface and its bandwidth was significantly narrow. The color around the anode surface was dark brown which is the color of the BG (and possibly Fe^{3+} ion-related compounds including $Fe^{III}(OH)_3$). This observation suggests that, around the anode, side reactions (**3**), (**8**), and/or (**12**–**14**) were competitive with the PB-forming reaction (**6**). Here, competitive $Fe^{III}(OH)_3$ formation is possible because the base 10 logarithm of the solubility constant for $Fe^{III}(OH)_3$ (−36.35) is comparable to that for PB (−40.52) at 25°C [28]. Additionally, **Figure 3C** shows a thin brown band near the cathode, which was occasionally (not always) observed in the PB system. The existence of this band suggests that the aforementioned side reactions can also contribute to band formation on the cathode side.

3.2.2 Effects of Long-Time Voltage Application

Figure 4 shows typical multicolored patterns formed at 25°C in the RDR system of the Cu–Fe PBA and PB under an applied voltage of 2 V for 100 h. Here, the initial $[Fe^{III}(CN)_6]^{3-}$ concentration was 0.050 M.

For Cu–Fe PBA (**Figure 4A**), the reddish-brown band broadened toward the anode with color fading, suggesting a decrease in the amount of Cu^{II}–Fe^{II} PBA. This observation can be explained as follows. Under long-time voltage application, Cu^{II}–Fe^{II} PBA precipitates in the precipitation band were partially decomposed by OH^- ions [increasingly generated from the cathode by side reaction (**5**)] through reaction (**15**). Owing to the diffusion and

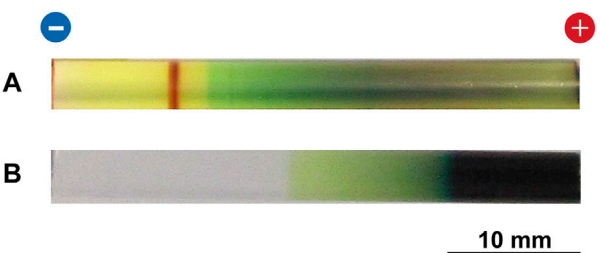

FIGURE 6 | (A) Typical multicolored pattern formed at 25°C in the Cu–Fe PBA system under an applied voltage of 4 V for 50 h. **(B)** Typical precipitation pattern formed at 25°C in the PB system under an applied voltage of 4 V for 20 h. The initial $[Fe^{III}(CN)_6]^{3-}$concentration and the initial agarose density were 0.050 M and 2.0 mass%, respectively. The charges of the electrodes and a scale bar are provided at the top and bottom of the images, respectively.

electric field, the decomposed $[Fe^{II}(CN)_6]^{4-}$ ions drifted to the anode side, where the green color deepened, suggesting the accumulation of Cu^{2+} ions [increasingly generated from the anode by reaction (**1**)]. Thus, these two types of reactant ions reacted on the anode side to reproduce Cu^{II}–Fe^{II} PBA, which resulted in the broadening of the Cu^{II}–Fe^{II} PBA band toward the anode. Meanwhile, for the PB system, the long-time voltage application broadened the almost-continuous dark-blue (PB) band toward the cathode side with a deepening color (compare **Figures 3B**, **4B**), suggesting the continuous accumulation of PB precipitates with time. Thus, long-time voltage application was effective in broadening the precipitation band of PB and Cu^{II}–Fe^{II} PBA but not in forming their periodic bands.

3.2.3 Effects of Higher-Concentration $[Fe^{III}(CN)_6]^{3-}$ Ions

Figure 5 shows typical multicolored patterns formed at 25°C in the RDR system of the Cu–Fe PBA and PB under an applied voltage of 2 V. Here, the initial $[Fe^{III}(CN)_6]^{3-}$concentration was 0.100 M.

A comparison between **Figures 3**, **5** suggests a common effect of increasing $[Fe^{III}(CN)_6]^{3-}$ ions (0.050 M → 0.100 M) on the two systems: higher $[Fe^{III}(CN)_6]^{3-}$ concentrations significantly deepened the color of the generated patterns. For the Cu–Fe PBA system, an

FIGURE 7 | (A) Typical multicolored pattern formed at 25 °C in the Cu–Fe PBA system using a Ti rod as a cathode under an applied voltage of 2 V for 50 h. **(B)** Typical precipitation pattern formed at 25°C in the PB system using the Ti cathode under an applied voltage of 2 V for 20 h. The initial $[Fe^{III}(CN)_6]^{3-}$concentration and the initial agarose density were 0.050 M and 2.0 mass%, respectively. The charges of the electrodes and a scale bar are provided at the top and bottom of the images, respectively.

increase in the concentration broadened the reddish-brown (Cu^{II}–Fe^{II} PBA) band. These findings are consistent with the expectation that the increase in $[Fe^{III}(CN)_6]^{3-}$ ions promotes the generation of reactant $[Fe^{II}(CN)_6]^{4-}$ ions [*via* reaction (**2**)] and the precipitation of PB [*via* reaction (**9**)] and Cu^{II}–Fe^{II} PBA [*via* reaction (**7**)]. Interestingly, the comparison between **Figures 3**, **5** also suggests that higher $[Fe^{III}(CN)_6]^{3-}$ concentrations only slightly influenced the number and position of the PB/Cu^{II}–Fe^{II} PBA band; in other words, higher concentrations did not lead to periodic banding or a large shift in the band position. Based on these observations, the 0.050 M $[Fe^{III}(CN)_6]^{3-}$ concentration was primarily employed in this study because the multicolored patterns were generally most clearly observable at this concentration.

3.2.4 Influence of Applied Voltage

Figure 6 shows typical multicolored patterns formed at 25°C in the RDR system of the Cu–Fe PBA and PB under an applied voltage of 4 V. Here, the initial $[Fe^{III}(CN)_6]^{3-}$concentration was 0.050 M.

For the Cu–Fe PBA system, a comparison between **Figures 3A**, **6A** indicates that the propagation of the reddish-brown Cu^{II}–Fe^{II} PBA band to the anode side was considerably suppressed at 4 V, and the bandwidth was narrower than that at 2 V. Meanwhile, the Cu^{II}–Fe^{II} PBA band did not increase in number upon the application of 4 V. These observations suggest that increasing the applied voltage is effective in restricting the broadening of the Cu^{II}–Fe^{II} PBA band but not in the formation of periodic bands.

In the PB system under the application of 4 V, only a relatively long, thick dark-blue band was formed in the region close to the anode, followed by a thin green region (**Figure 6B**). The yellow color of $[Fe^{III}(CN)_6]^{3-}$ ions disappeared near the cathode, indicating that the anode strongly attracted $[Fe^{III}(CN)_6]^{3-}$ions. The relatively narrow, discrete, dark-blue PB band that formed at 2 V (observed in **Figure 3C**) disappeared. Thus, for the PB system, the 4 V application hindered periodic banding or even the formation of a discrete PB band.

In addition, the application of a constant voltage of 4 V or higher occasionally resulted in several experimental problems, particularly for long-time observations (≥50 h). For example, the agarose gel occasionally shrank during the application of a constant voltage of 4 V, primarily on the cathode side. At higher voltages, such shrinkage occurred more frequently and prevented detailed observation. Furthermore, at voltages greater than 4 V, contact between the cathode and gel was frequently lost, possibly because of the formation of H_2 bubbles generated by reaction (**5**) on the cathode surface (although the bubbles were not observed in the gels by the naked eye). At less than 2 V (such as 1.5 V), the precipitation bands of PB and Cu^{II}–Fe^{II} PBA were not clearly observed, even after 100 h (not shown here). Thus, in this study, the applied constant voltages for examining precipitation patterns in detail were limited to 2–4 V.

3.2.5 Influence of the Ti Cathode

The multicolored patterns shown in **Figures 3–6** were obtained when the same metal was used as the anode and cathode. If the precipitates of PB and PBA formed only through the precipitation reactions (**6**), (**7**), or (**9**) of the reactant ions that were simply produced by reactions (**1**) and (**2**) at the electrodes and were subsequently moved by diffusion and the electric field in the gel (**Figure 1** is depicted according to this simple model), the substitution of the cathode metal is expected to hardly change the precipitation pattern because any metal, in principle, can operate as a cathode to reduce $[Fe^{III}(CN)_6]^{3-}$ ions.

Figure 7 shows typical multicolored patterns formed at 25°C in the RDR system of the Cu–Fe PBA and PB commonly using a Ti cathode under an applied voltage of 2 V. Here, the initial $[Fe^{III}(CN)_6]^{3-}$concentration was 0.050 M, and the voltage application periods were set to be the same as those employed to observe the patterns in **Figures 3A,C**: 50 and 20 h. Ti metal was selected as the cathode because it can generate $[Fe^{II}(CN)_6]^{4-}$ ions but cannot provide PB or Cu–Fe-PBA at its surface.

As shown in **Figure 7A**, substitution into the Ti cathode clearly blocked the formation of the Cu^{II}–Fe^{II} PBA band, and a narrow, reddish-brown band was barely observed on the cathode side, but its color was very light, indicating that the amount of Cu^{II}–Fe^{II} PBA in the band was very low. This observation suggests that the Cu^{II}–Fe^{II} PBA precipitates generated at the Cu cathode surface considerably contributed to the Cu^{II}–Fe^{II} PBA band in the agarose gel. The Cu^{II}–Fe^{II} PBA precipitates at the cathode surface can be decomposed through reaction (**15**) by OH^- ions generated at the cathode by reaction (**5**). The $[Fe^{II}(CN)_6]^{4-}$ ions and charged

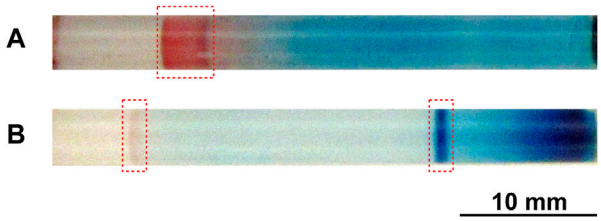

FIGURE 8 | (A) Typical precipitation pattern (formed at 25°C under an applied voltage of 2 V for 50 h) after removing unreacted ions and soluble compounds from the Cu–Fe PBA system. **(B)** Typical precipitation pattern (formed at 25°C under an applied voltage of 2 V for 20 h) after removing unreacted ions and soluble compounds from the PB system. The initial $[Fe^{III}(CN)_6]^{3-}$concentration and the initial agarose density were 0.050 M and 2.0 mass%, respectively. The regions in which a precipitation band was formed are indicated by red squares. A scale bar is provided at the bottom of the images.

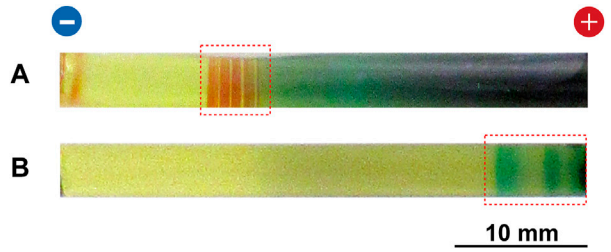

FIGURE 9 | Typical multicolored patterns formed at 25°C in the RDR system of **(A)** Cu–Fe PBA and **(B)** PB under cyclic alternating voltages of 4 V (1 h) and 1 V (4 h). The Cu–Fe PBA pattern was obtained by 20 cycles (100 h), and the PB pattern was obtained by four cycles (20 h). The initial $[Fe^{III}(CN)_6]^{3-}$concentration and the initial agarose density were 0.050 M and 2.0 mass%, respectively. The regions in which periodic precipitation bands were formed are indicated by red squares. The charges of the electrodes and a scale bar are provided at the top and bottom of the images, respectively.

fragments of the precipitates thus generated can disperse owing to diffusion and an electric field to re-produce Cu^{II}–Fe^{II} PBA precipitates in the agarose gel.

The above mechanism is expected to be less effective for the PB system because the PB band formed on the anode side, suggesting that the reactions with the initially loaded $[Fe^{III}(CN)_6]^{3-}$ ions near the anode were dominant in forming the band patterns. Indeed, a comparison between **Figures 3C**, **7B** indicates that the substitution of the cathode from Fe to Ti only slightly affected the dark-blue PB band on the anode side. Interestingly, a thin brown band on the cathode side, which was occasionally observed using the Fe cathode (**Figure 3C**), always disappeared completely through this cathode substitution. This finding suggests that the formation of the thin brown (not PB) band requires several fragments generated from PB at the Fe cathode surface through reaction (**17**). Thus, we deduced that the formation and decomposition of PB or Cu^{II}–Fe^{II} PBA precipitates at the Fe or Cu cathode surfaces, respectively, are important for the formation of precipitate band(s) in the gel near the cathode.

3.2.6 Precipitation Patterns after Removing Unreacted Ions and Soluble Compounds

Figure 8A shows a typical precipitation pattern (formed at 25°C under an applied voltage of 2 V for 50 h) after the removal of the unreacted ions and soluble compounds from the Cu–Fe PBA system. The initial $[Fe^{III}(CN)_6]^{3-}$concentration was 0.050 M. As expected, the characteristic yellow color of the $[Fe^{III}(CN)_6]^{3-}$ ions disappeared and the reddish-brown Cu^{II}–Fe^{II} PBA band persisted. Note that the ocher color of the Cu^{II}–Fe^{III} PBA was not observed in **Figure 8A**. Interestingly, the blue color remained over a wide area on the anode side (right side of **Figure 8A**). This finding suggests that the Cu^{2+} ions formed sparingly soluble $Cu^{II}(OH)_2$ on the anode side through side reactions (**12**) and/or (**15**) with OH^- ions that migrated to the anode side under the influence of a constant 2 V application. These observations confirm the suggestion provided by **Figure 3A** that in the Cu–Fe PBA system $[Fe^{III}(CN)_6]^{3-}$ ions are less reactive with aqueous Cu^{2+} ions than $[Fe^{II}(CN)_6]^{4-}$ and OH^- ions; in other words, reaction (**6**) is less active than reactions (**7**) and (**12**).

Figure 8B shows a typical precipitation pattern (formed at 25°C under an applied voltage of 2 V for 20 h) after the removal of the unreacted ions and soluble compounds from the PB system. The initial $[Fe^{III}(CN)_6]^{3-}$concentration was 0.050 M. As expected, the characteristic yellow color of the $[Fe^{III}(CN)_6]^{3-}$ ions and the dark-brown color of the BG disappeared, and the discrete dark-blue PB band persisted. Interestingly, the dark-blue color remained in the region near the anode, although it was not very clear before the removal process (see **Figures 3C**, **5B**, **7B**), possibly because of the overlap with unreacted Fe^{3+} (yellow brown) and $[Fe^{III}(CN)_6]^{3-}$ ions (yellow) and the generated BG (dark brown). Furthermore, the bluish-white color of PW is not observed in **Figure 8B**. These observations confirm the suggestion provided by **Figure 3B** that, in the PB system, reaction (**7**) is less active than reaction (**6**). Additionally, it is interesting that a thin brown band on the cathode side, which was occasionally observed using the Fe cathode (**Figure 3C**) but not using the Ti cathode (**Figure 7B**), persisted. This finding suggests that the thin brown band did not consist of soluble BG, but sparingly soluble $Fe^{III}(OH)_3$; hence, the PB fragments required for its generation were $Fe^{III}(OH)_3$-related fragments, possibly provided by reaction (**17**) at the cathode surface.

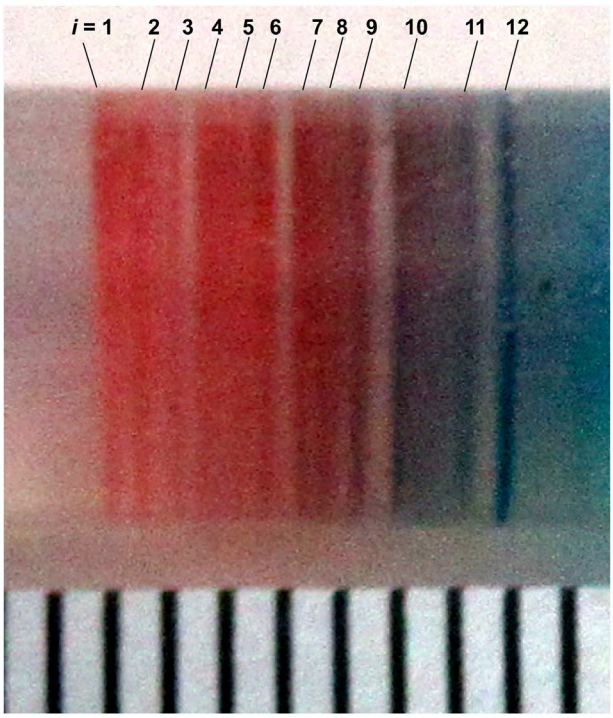

FIGURE 10 | Enlarged image of the periodic bands shown in **Figure 9A** after removing unreacted ions and soluble compounds. The bands are numbered from 1 (the cathode side) to 12 (the anode side). For comparison, 1 mm graduations are also shown at the bottom of the image.

3.3 Precipitation Patterns under Cyclic Alternating Voltages

3.3.1 Influence of Cyclic Alternating Voltages

Figure 9 shows typical multicolored patterns formed in the RDR system under cyclic alternating voltages of 4 V for 1 h and then 1 V for 4 h per cycle (the initial $[Fe^{III}(CN)_6]^{3-}$concentration was 0.050 M). In

this cyclic voltage sequence, fewer reactant ions are produced at 1 V, and more reactant ions are produced at 4 V. Furthermore, the diffusion contribution to their transportation is more important at 1 V, and the drift contribution due to the electric field is more important at 4 V.

In the Cu–Fe PBA system (**Figure 9A**), several periodic (that is, Liesegang-band-like), short reddish-brown Cu^{II}–Fe^{II} PBA bands (which were not observed under constant voltage; see **Figures 3A–7A**) were observed within a relatively narrow region (<8 mm) near the cathode. **Figure 10** shows an enlarged image of the periodic bands in **Figure 9A** after removing unreacted ions and soluble compounds; 1 mm graduations are shown for ease of comparison. These periodic bands were numbered from i = 1 (cathode side) to 12 (anode side). Because of the stochastic nature, the periodic pattern shown in **Figure 10** was not completely the same as the pattern previously reported [11]; however, it exhibited similar basic features, including a band number of ~12 and the existence of the blue band.

As reported previously [11], these periodic bands stochastically formed with a probability of ~50% after 40 h of cyclic voltage application (eight cycles), and the number of bands increased with time (within 12 ± 5 after removing unreacted ions). Here, ~50% formation of periodic bands indicates that when the m gel samples are prepared under the same experimental conditions (in this study, typically m = 24), we may observe periodic banding in ~m/2 samples. In the other ~m/2 samples, an almost continuous band with several lengths was formed, implying an overlap of the periodic bands [11]. The periodic bands maintained their positions during the observation period, and several bands were blue (for example, the band with i = 12 in **Figure 10**), strongly suggesting the presence of $Cu^{II}(OH)_2$ [11].

It is well known that Liesegang bands tend to follow an empirical scaling law, the so-called spacing law, irrespective of the electrolyte pair and geometry of the system: $X_{i+1}/X_i = 1 + p$, where X_i is the position of the i-th band and $p > 0$ for most systems [1, 2, 5–8]. The spacing law means that the space between adjacent bands increases monotonically with i [11]. Meanwhile, **Figure 10** indicates that the band space obtained in the Cu–Fe PBA system did not increase monotonically with i but remained approximately constant (~0.3 mm) with a broad dispersion (±0.3 mm), thus failing to obey the spacing law. It is not surprising that the periodic banding in **Figure 10** disobeyed the spacing law because the mechanism to form periodic bands in the proposed RDR system fundamentally differs from that in the conventional RD system used to examine Liesegang banding. Currently, no mathematical model is available to explain the periodic banding observed in RDR systems under cyclic alternating voltages. A deeper understanding of this new class of periodic banding is urgently required.

In the PB system (**Figure 9B**), the cyclic alternating voltage application could split a discrete precipitation band (which formed under constant voltage pplications; **Figures 3C**, **5B**, **7B**, **8B**) into a few bands near the anode. Such splitting stochastically occurred with a probability of ~50% after 10 h of cyclic voltage application (two cycles), whereas in the other ~50% of the scenarios, the cyclic alternating voltage application caused the discrete precipitation band to be completely painted out in a continuous band. The observed split bands were broader and more blurred than the periodic bands in the Cu–Fe PBA system, and their numbers were less than three. By combining these findings and the suggestions from **Figures 3B**, **7B**, **8B** that in the PB system, the reactions with the initially loaded $[Fe^{III}(CN)_6]^{3-}$ ions are dominant, we deduced that the cyclic voltage application is more effective for forming periodic precipitation bands when both the anode and cathode can supply the reactant ions of the precipitates.

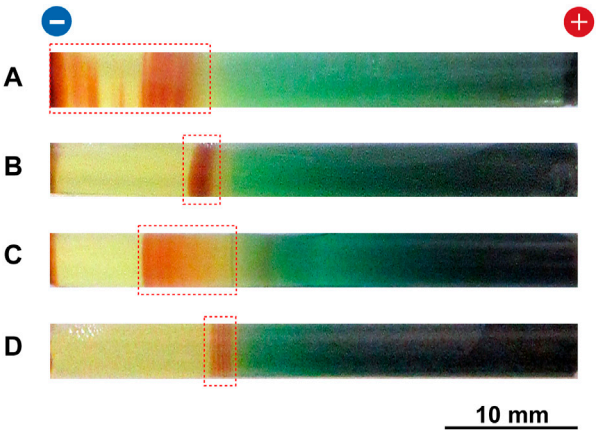

FIGURE 11 | Typical multicolored patterns formed at 25°C in the Cu–Fe PBA system under various cyclic alternating voltage conditions. The initial $[Fe^{III}(CN)_6]^{3-}$concentration and the initial agarose density were 0.050 M and 2.0 mass%, respectively. The multicolored patterns **(A,B)** were obtained by 10 cycles of alternating voltages of 4 V (1 h) and 1 V (9 h) and 40 cycles of alternating voltages of 4 V (1 h) and 1 V (1.5 h), respectively. The multicolored patterns **(C,D)** were obtained by 20 cycles of alternating voltages of 3 V (1 h) and 1 V (4 h) and 5 V (1 h) and 1 V (4 h), respectively. For each sample, the total voltage application time was set to 100 h. The regions in which periodic bands were formed are indicated by red squares. The charges of the electrodes and a scale bar are provided at the top and bottom of the images, respectively.

3.3.2 Effects of Voltage and Period in Cyclic Alternating Voltage Application

Based on the above results, the Cu–Fe PBA system is employed hereafter for more detailed analyses of the factors that form periodic bands under cyclic alternating voltages. Note that the precipitation band formation in the RDR system is stochastic to an extent; hence, we can suggest only the general trend of the patterning, depending on some factors.

Figures 11A,B show typical multicolored patterns formed at 25°C in the Cu–Fe PBA system under 10 cycles of alternating voltages of 4 V for 1 h and 1 V for 9 h per cycle, and 40 cycles of alternating voltages of 4 V for 1 h and 1 V for 1.5 h per cycle, respectively (the initial $[Fe^{III}(CN)_6]^{3-}$concentration was 0.050 M). Compared with the reddish-brown bands shown in **Figure 9A**, the bands in **Figure 11A** are considerably broad, distorted, and defective in shape. These diffusive features suggest the strong influence of diffusion to reactant ions, primarily because of the relatively long period of 1 V application. In contrast, the reddish-brown bands in **Figure 11B** are significantly narrow, thick in color, and overall similar to the corresponding bands observed in **Figure 6A** (obtained under a constant 4 V application). This similarity is not surprising because such a frequently alternating voltage application can be approximated as a constant 4 V application.

Figures 11C,D show typical multicolored patterns formed at 25°C in the Cu–Fe PBA system under 20 cycles of alternating voltages of 3 V for 1 h and 1 V for 4 h per cycle, and 5 V for 1 h and 1 V for 4 h per cycle, respectively (the initial $[Fe^{III}(CN)_6]^{3-}$concentration was 0.050 M). As shown in **Figure 11C**, the alternating voltage application of 3 V (1 h) and 1 V (4 h) broadened the precipitation band, whereas its band shape was almost continuous, unlike that under the 4 V (1 h) and 1 V (4 h) conditions (**Figure 9A**). Thus, this alternating voltage application does not seem to be effective in producing periodic bands. In contrast, as shown in **Figure 11D**, the alternating voltage application of 5 V (1 h) and 1 V (4 h) tended to generate several periodic bands, similar to the 4 V (1 h) and 1 V (4 h) applications, but the regions forming the bands were considerably limited (<3 mm).

Thus, we conclude from the results in **Figure 11** that 1) the voltage and period of alternating voltage application strongly influence the resultant precipitation patterns, and 2) currently, the application of 4 V (1 h) and 1 V (4 h) is the most effective for generating periodic bands over a relatively wide region in the gel.

4 DISCUSSION

As shown in **Figures 3–11**, the RDR system (**Figure 1**) can generate various types of precipitation patterns of PB and Cu^{II}–Fe^{II} PBA with a significant aesthetic appeal, depending on the type of electrode and the conditions of voltage application. Its preparation and operation are simple and low-cost [for example, constant-voltage experiments can be performed within $130: a plastic straw ($ ~0.01), metal rods ($ ~2), agarose ($ ~85), $K_3[Fe^{III}(CN)_6]$ ($ ~40), and two dry cells ($ ~1.5)], but its chemistry is complicated and its physics is interesting. These features make the proposed RDR system a fascinating educational tool for pattern forming. Furthermore, RDR patterning of PB and PBA is potentially applicable in materials science [11]. However, from the perspective of the practical applications of RDR patterning, many challenges remain. For example, in the Cu–Fe PBA system, periodic banding only occurred stochastically (with a probability of ~50%), and some byproducts such as $Cu^{II}(OH)_2$ were present in the bands. These characteristics can hinder its application; hence, better control over RDR patterning is required, including the reproducibility of the obtained patterns and the amounts of PB or PBA and byproducts in the RDR system.

Achieving better control of the RDR patterns requires a deeper understanding of the observations reported in this paper, particularly periodic banding under an alternating voltage application (**Figures 9–11**). As previously mentioned [11], a theoretical framework applicable to the RDR system should be developed. Optimal experimental conditions for producing well-controlled patterns should be further explored. In addition to the initial concentration of $[Fe^{III}(CN)_6]^{3-}$ ions (**Figure 5**), cathode metals (**Figure 7**), applied voltages (**Figures 6**, **11**), and application periods (**Figures 4**, **11**), several factors can change the precipitation patterns: for example, the length and diameter of the gel column, gel type [29], gel density [29], and the presence of magnetic fields [30]. Precipitation patterns, including periodic bands, should be examined while varying these factors. The extension of the RDR experiments to other PBA systems is also interesting; for example, the RDR patterning of Co–Fe-based PBA and Ni–Fe-based PBA can be easily examined using the current setup by substituting for Co and Ni electrodes. It is also important to comprehensively characterize the reaction products, including byproducts, formed in the precipitation band(s), other colored regions in the gel, and anode and cathode surfaces. For example, X-ray absorption fine structure spectroscopy and X-ray diffractometry are useful for investigating the local structure(s) around the metal atoms and the crystallinity of the generated compounds, respectively. Scanning electron microscopy and micro-X-ray fluorescence mapping may be helpful for determining the characteristics and distribution of the byproducts. If possible, effective methods should be developed to remove (or at least suppress) the byproducts. Additionally, electrochemical processes at the boundaries between the metal electrodes and agarose gel should be further investigated. Electrochemical measurements capable of detecting μA levels may provide insights into this issue. Thus, further research across several scientific fields is required.

5 CONCLUSION

In a significantly simple RDR system, diverse precipitation patterns of PB and Cu^{II}–Fe^{II} PBA were generated, depending on the type of metal electrode, applied voltage, initial $[Fe^{III}(CN)_6]^{3-}$ concentration, and elapsed time after voltage application. We observed that 1) cyclic alternating voltage applications (particularly, that of 4 V for 1 h and 1 V for 4 h per cycle) could generate Liesegang-band-like periodic bands (although stochastically with a probability of ~50%); and 2) OH^- ions, a byproduct of the cathode, considerably influence the resultant patterns through the formation of hydroxide precipitates in the gel and the decomposition of the PB/Cu^{II}–Fe^{II} PBA precipitates generated at the cathode surface. Despite these findings, many aspects of the RDR patterning remain unclear. The novelty, simplicity of handling, diversity of the observed patterns, significant aesthetic appeal, and associated potential applications warrant further investigation of the RDR patterning of PB and PBA.

DATA AVAILABILITY STATEMENT

The original contributions presented in the study are included in the article/Supplementary Materials; further inquiries can be directed to the corresponding author.

AUTHOR CONTRIBUTIONS

HH conceived the concept, performed the experiments, analyzed the results, wrote the manuscript, and prepared the figures.

FUNDING

This research was funded by the JSPS KAKENHI (grant number JP19K05409).

ACKNOWLEDGMENTS

The author is grateful to R. Matsumoto, M. Arai, H. Kawakami, M. Shinoda, A. Seimiya, N. Taniguchi, and H. Matsumoto of Japan Women's University for their aid in sample preparation.

REFERENCES

1. Nabika H. Liesegang Phenomena: Spontaneous Pattern Formation Engineered by Chemical Reactions. *Cpc* (2015) 5:5–20. doi:10.2174/1877946805011509081108 39
2. Nabika H, Itatani M, Lagzi I. Pattern Formation in Precipitation Reactions: the Liesegang Phenomenon. *Langmuir* (2020) 36:481–97. doi:10.1021/acs.langmuir.9b03018
3. Sadek S, Sultan R. Liesegang Patterns in Nature: A Diverse Scenery across the Sciences. In: I Lagzi, editor. *Precipitation Patterns in Reaction–Diffusion Systems*. Kerala, India: Research Signpost (2010). p. 1.
4. Liesegang RE. Ueber einige eigenschaften von gallerten. *Naturwiss Wochenschr* (1896) 11:353.
5. Henisch H. *Crystals in Gels and Liesegang Rings*. Cambridge, UK: Cambridge University Press (1988). p. 116.
6. Nakouzi E, Steinbock O. Self-organization in Precipitation Reactions Far from the Equilibrium. *Sci Adv* (2016) 2:e1601144. doi:10.1126/sciadv.1601144
7. Arango-Restrepo A, Barragán D, Rubi JM. Self-Assembling outside Equilibrium: Emergence of Structures Mediated by Dissipation. *Phys Chem Chem Phys* (2019) 21:17475–93. doi:10.1039/c9cp01088b
8. Grzybowski BA. *Chemistry in Motion: Reaction–Diffusion Systems for Micro- and Nanotechnology*. Chichester, UK: John Wiley & Sons (2009). p. 93.
9. Grzybowski BA, Bishop KJM, Campbell CJ, Fialkowski M, Smoukov SK. Micro- and Nanotechnology via Reaction-Diffusion. *Soft Matter* (2005) 1:114. doi:10.1039/b501769f
10. Grzybowski BA, Campbell CJ. Fabrication Using 'programmed' Reactions. *Mater Today* (2007) 10:38–46. doi:10.1016/s1369-7021(07)70131-1
11. Hayashi H, Suzuki T. A Reaction-Diffusion-Reaction System for Forming Periodic Precipitation Bands of Cu-Fe-Based Prussian Blue Analogues. *Appl Sci* (2021) 11:5000. doi:10.3390/app11115000
12. Karyakin AA. Prussian Blue and its Analogues: Electrochemistry and Analytical Applications. *Electroanalysis* (2001) 13:813–9. doi:10.1002/1521-4109(200106)13:10<813::aid-elan813>3.0.co;2-z
13. Li WJ, Han C, Cheng G, Chou SL, Liu HK, Dou SX. Chemical Properties, Structural Properties, and Energy Storage Applications of Prussian Blue Analogues. *Small* (2019) 15:1900470. doi:10.1002/smll.201900470
14. Azhar A, Li Y, Cai Z, Zakaria MB, Masud MK, Hossain MSA, et al. Nanoarchitectonics: A New Materials Horizon for Prussian Blue and its Analogues. *Bcsj* (2019) 92:875–904. doi:10.1246/bcsj.20180368
15. Verdaguer M, Girolami G. Magnetic Prussian Blue Analogs. In: JS Miller M Drillon, editors. *Magnetism: Molecules to Materials V*. Weinheim, Germany: Wiley–VCH Verlag GmbH & Co. KGaA (2004). p. 283.
16. Pajerowski DM, Gardner JE, Frye FA, Andrus MJ, Dumont MF, Knowles ES, et al. Photoinduced Magnetism in a Series of Prussian Blue Analogue Heterostructures. *Chem Mater* (2011) 23:3045–53. doi:10.1021/cm2003337
17. Ma F, Li Q, Wang T, Zhang H, Wu G. Energy Storage Materials Derived from Prussian Blue Analogues. *Sci Bull* (2017) 62:358–68. doi:10.1016/j.scib.2017.01.030
18. Hurlbutt K, Wheeler S, Capone I, Pasta M. Prussian Blue Analogs as Battery Materials. *Joule* (2018) 2:1. doi:10.1016/j.joule.2018.07.017
19. Yu Z-Y, Duan Y, Liu J-D, Chen Y, Liu X-K, Liu W, et al. Unconventional CN Vacancies Suppress Iron-Leaching in Prussian Blue Analogue Pre-catalyst for Boosted Oxygen Evolution Catalysis. *Nat Commun* (2019) 10:2799. doi:10.1038/s41467-019-10698-9
20. Estelrich J, Busquets MA. Prussian Blue: A Safe Pigment with Zeolitic-like Activity. *Ijms* (2021) 22:780. doi:10.3390/ijms22020780
21. Kaye SS, Long JR. Hydrogen Storage in the Dehydrated Prussian Blue Analogues $M_3[Co(CN)_6]_2$ (M = Mn, Fe, Co, Ni, Cu, Zn). *J Am Chem Soc* (2005) 127:6506–7. doi:10.1021/ja051168t
22. Svensson G, Grins J, Eklöf D, Eriksson L, Wardecki D, Thoral C, et al. Influence of the Presence of Different Alkali Cations and the Amount of $Fe(CN)_6$ Vacancies on CO_2 Adsorption on Copper Hexacyanoferrates. *Materials* (2019) 12:3371. doi:10.3390/ma12203371
23. Nielsen P, Dresow B, Heinrich HC. *In Vitro* Study of ^{137}Cs Sorption by Hexacyanoferrates(II). *Z Naturforsch B* (1987) 42:1451–60. doi:10.1515/znb-1987-1114
24. Altagracia-Martínez M, Kravzov-Jinich J, Martínez-Núñez JM, Ríos-Castañeda C, López-Naranjo F. Prussian Blue as an Antidote for Radioactive Thallium and Cesium Poisoning. *Orphan Drugs Res Rev* (2012) 2:13.
25. Sandal N, Mittal G, Bhatnagar A, Pathak DP, Singh AK. Preparation, Characterization, and *In Vivo* Pharmacoscintigraphy Evaluation of an Intestinal Release Delivery System of Prussian Blue for Decorporation of Cesium and Thallium. *J Drug Deliv* (2017) 2017:4875784. doi:10.1155/2017/4875784
26. Hayashi H, Takaishi M. Low-cost, High-Performance Sample Cell for X-ray Spectroscopy of Solutions and Gels Made from Plastic Straw. *Anal Sci* (2019) 35:651–357. doi:10.2116/analsci.18p538
27. Gotoh A, Uchida H, Ishizaki M, Satoh T, Kaga S, Okamoto S, et al. Simple Synthesis of Three Primary Colour Nanoparticle Inks of Prussian Blue and its Analogues. *Nanotechnology* (2007) 18:345609. doi:10.1088/0957-4484/18/34/345609
28. Sillen L. *Stability Constants of Metal-Ion Complexes. Section I: Inorganic Ligands*. London, UK: The Chemical SocietyBurlington House (1964). p. 52.
29. Hayashi H, Abe H. Gel-State Dependencies of Brown Patterns of Mn-Fe-Based Prussian Blue Analogues Studied by Combined X-ray Spectroscopies. *Bcsj* (2017) 90:807–19. doi:10.1246/bcsj.20170080
30. Hayashi H, Aoki S, Abe H. Magnetic-Field-Induced Painting-Out of Precipitation Bands of Mn-Fe-Based Prussian Blue Analogues in Water-Glass Gels. *ACS Omega* (2018) 3:4494–501. doi:10.1021/acsomega.8b00285

Conflict of Interest: The authors declare that the research was conducted in the absence of any commercial or financial relationships that could be construed as a potential conflict of interest.

frontiers | Frontiers in Physics

ORIGINAL RESEARCH
published: 06 April 2022
doi: 10.3389/fphy.2022.858791

Self-Propelled Motion of the Camphor Float With n-Fold Rotational Symmetry

Hiroyuki Kitahata[1]* *and Yuki Koyano*[2]

[1]*Department of Physics, Graduate School of Science, Chiba University, Chiba, Japan,* [2]*Department of Human Environmental Science, Graduate School of Human Development and Environment, Kobe University, Kobe, Japan*

It is known that a camphor particle at a water surface exhibits self-propulsion since it releases camphor molecules at the surface and reduces the surface tension, and the gradient of surface tension drives the camphor particle itself. Such a motion is considered to be driven by the concentration field of the chemicals emitted by the particle itself. It is also known that the shape of the particle seriously affects the mode of motion. In order to understand the universal mechanism on the effect of the shape on such a self-propelled motion, we theoretically investigated the bifurcation structure of the motion of the camphor float with n-fold rotational symmetry, which comprises n camphor disks attached to a rigid light circular plate along a periphery with an equivalent spacing. Here, we mainly studied the cases with $n = 2$ and 3. We found that the camphor float with $n = 2$ moves in the direction perpendicular to the line connecting the two camphor disks, while that with $n = 3$ changes its direction of motion depending on the size of the camphor float.

Keywords: camphor, self-propelled motion, reaction-diffusion system, surface tension, Marangoni effect, spontaneous symmetry breaking

OPEN ACCESS

Edited by:
Nobuhiko J. Suematsu, Meiji University, Japan

Reviewed by:
Hepeng Zhang, Shanghai Jiao Tong University, China
Charles Reichhardt, Los Alamos National Laboratory (DOE), United States

***Correspondence:**
Hiroyuki Kitahata
kitahata@chiba-u.jp

Specialty section:
This article was submitted to Physical Chemistry and Chemical Physics, a section of the journal Frontiers in Physics

Received: *20 January 2022*
Accepted: *14 February 2022*
Published: *06 April 2022*

Citation:
Kitahata H and Koyano Y (2022) Self-Propelled Motion of the Camphor Float With n-Fold Rotational Symmetry. Front. Phys. 10:858791. doi: 10.3389/fphy.2022.858791

1 INTRODUCTION

Self-propelled particles, which can transduce free energy into kinetic energy under nonequilibrium conditions, have been investigated for last decades since they can be a model for the motion of living organisms [1–6]. The relationship between the self-propelled motion and the shape of the particle has attracted much attention, and both experimental and theoretical studies have been intensively reported [7–11]. When we discuss the mechanism of the self-propelled motion, we have to keep in mind that the conservation of momentum should hold rigourously. For example, a self-propelled liquid droplet in the other immisible liquid can be discussed based on the momentum exchange in hydrodynamics. There have been many papers on such self-propelled motions, most of which are considered in the regime of low-Reynolds number [4, 12–15]. In contrast, some systems, such as a self-propelled particle at a liquid surface, a self-propelled droplet on a solid surface, and a living cell on a substrate, can apparently break the momentum conservation [16–18]. It is sure that they exchange momentum with the environment but the momentum conservation is not treated explicitly in their model.

The self-propelled motion of a camphor disk at a water surface is one of the most studied self-propelled motion [19–26]. The camphor disk releases the camphor molecules at a water surface, and the concentration gradient of the camphor molecules induces the surface tension gradient, which drives the disk. Such a camphor disk motion can be discussed based on the hydrodynamics [27–29], but it has also been discussed from the viewpoint of the coupling between the reaction-diffusion field and the disk motion [9, 22, 30, 31]. Based on the latter approach, we have studied the self-propelled motion of a camphor particle with the shape other than a circle, and have discussed the relation between the camphor particle shape and the direction of motion [6, 9, 32–35]. For example, we show that an elliptic camphor particle moves in the dircetion of its minor axis [9, 33–35]. As for a

triangular-shaped camphor particle, the direction of motion depends on the size of the particle; a smaller particle moves in the direction of a corner, while a larger particle moves in the direction of a side [35]. These studies clarify that the symmetric property of the shape is important for determining the preferable direction of the self-propelled motion.

Motivated by these previous studies, here we propose the simpler system with which the relation between the direction of self-propelled motion and symmetric property can be discussed; a camphor float with n-fold rotational symmetry, which comprises a rigid light circular plate attaching n camphor disks along a periphery with an equivalent spacing. From the viewpoint of rotational symmetry, an elliptic camphor particle corresponds to the camphor float with $n = 2$, while the triangular camphor particle corresponds to that with $n = 3$; we mainly discuss these two cases. By considering these camphor floats, we discuss the direction of the self-propelled motion affected by the symmetric properties. In the present paper, we first formulate the mathematical model for them, and then analytically discuss the preferable direction of the self-propelled motion. Finally, we check the validity of the analytical results by numerical simulations.

2 MODEL

We construct a mathematical model that describes the self-propelled motion of the camphor float with n-fold rotational symmetry, which is floating at a water surface. The float comprises a rigid light circular plate attaching n camphor disks along a periphery with an equivalent spacing. We consider the concentration field of camphor molecules $u(\boldsymbol{r}, t)$ on a two-dimensional plane corresponding to the water surface. As for the motion of the camphor float, the position and configureation can be described by the center of mass of the camphor float $\boldsymbol{r}_c$ and the characteristic angle θ_c. For the camphor float with n-fold rotational symmetry, the center position of the k-th camphor disk ($k = 0, 1, \ldots, n-1$) is set as

$$\boldsymbol{r}_k = \boldsymbol{r}_c + \ell \boldsymbol{e}\left(\theta_c + \frac{2\pi k}{n}\right), \tag{1}$$

where $\boldsymbol{e}(\theta)$ is the unit vector defined as

$$\boldsymbol{e}(\theta) = \cos\theta \boldsymbol{e}_x + \sin\theta \boldsymbol{e}_y. \tag{2}$$

Here, $\boldsymbol{e}_x$ and $\boldsymbol{e}_y$ are the unit vectors in x- and y-directions, respectively. The schematic illustrations for the camphor floats with $n = 2$ and 3 are shown in **Figure 1**.

Each camphor disk has a radius of R and supplys the camphor molecules to the water surface at the rate of S_0. The dynamics of $u(\boldsymbol{r}, t)$ is described as

$$\frac{\partial u}{\partial t} = D\nabla^2 u - au + \frac{S_0}{\pi R^2}\sum_{k=0}^{n-1}\Theta(R - |\boldsymbol{r} - \boldsymbol{r}_k|). \tag{3}$$

The first, second, and third terms in the righthand side correspond to the diffusion, sublimation, and supply of the camphor molecules. Here, D is the effiective diffusion coefficient [36, 37], a is the sublimation rate, and $\Theta(\cdot)$ is the Heaviside's step function. It should be noted that the effective diffusion coefficient is introduced to include the effect by the hydrodynamic transport due to the Marangoni effect. The effective diffusion coefficient is estimated from the concentration profile with a resting camphor particle based on the reaction-diffusion-advection equation. Thus, this approxiation works well when the velocity is small.

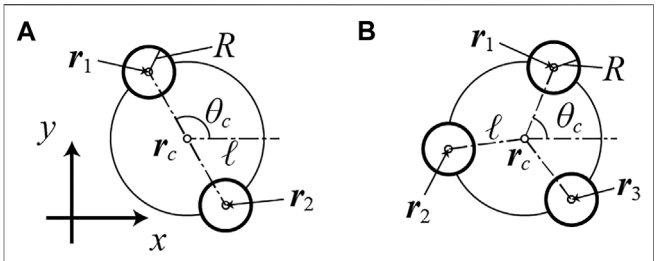

FIGURE 1 | Schematic illustration for the camphor float with n-fold rotational symmetry. **(A)** $n = 2$. **(B)** $n = 3$.

As for the motion of the camphor float, we consider the equation of motion for the k-th camphor disk as

$$m\frac{d^2\boldsymbol{r}_k}{dt^2} = -\eta\frac{d\boldsymbol{r}_k}{dt} + \boldsymbol{F}_k^{(\mathrm{conc})} + \boldsymbol{F}_k^{(\mathrm{int})}, \tag{4}$$

where m is the mass, and η is the viscous friction coefficient of the camphor disk. We assume that they are both proportional to the area of the camphor disk as $m = \pi\rho R^2$ and $\eta = \pi\kappa R^2$. $\boldsymbol{F}_k^{(\mathrm{conc})}$ is the force originating from the surface tension gradient due to the camphor concentration field described as

$$\boldsymbol{F}_k^{(\mathrm{conc})} = \oint_{\partial\Omega_k}\gamma(u(\boldsymbol{r}'))\boldsymbol{n}(\boldsymbol{r}')\,d\ell' \tag{5}$$

$$= \iint_{\Omega_k}(\nabla'\gamma(u(\boldsymbol{r}')))\,dA'. \tag{6}$$

Here, Ω_k is the region of the k-th camphor disk, which is defined as

$$\Omega_k = \{\boldsymbol{r} \,||\, \boldsymbol{r} - \boldsymbol{r}_k| \le R\}, \tag{7}$$

and $\partial\Omega_k$ is the periphery of Ω_k. $d\ell'$ is the line element along the periphery, $\boldsymbol{n}(\boldsymbol{r}')$ is the outward unit normal vector at the periphery, ∇' is the nabla operator with respect to $\boldsymbol{r}'$, and dA' is the area element in the region Ω_k. Here, the relation between the surface tension and camphor concentration is assumed to be

$$\gamma = \Gamma_0 - \Gamma u, \tag{8}$$

where Γ_0 is the surface tension of pure water, and Γ is a positive constant connecting the camphor concentration and surface tension [37–39]. Using this relationship, the force $\boldsymbol{F}_k^{(\mathrm{conc})}$ is described as

$$\boldsymbol{F}_k^{(\mathrm{conc})} = -\Gamma\oint_{\partial\Omega_k}u(\boldsymbol{r}')\boldsymbol{n}(\boldsymbol{r}')d\ell' \tag{9}$$

$$= -\Gamma\iint_{\Omega_k}(\nabla' u(\boldsymbol{r}'))dA'. \tag{10}$$

$\boldsymbol{F}_k^{(\mathrm{int})}$ is the internal force that maintains the configuration of the camphor float. It can be described as the summation of the internal force, $\boldsymbol{f}_{k,j}$, from the j-th disk as

$$\boldsymbol{F}_k^{(\mathrm{int})} = \sum_{j=0}^{n-1} \boldsymbol{f}_{k,j}, \tag{11}$$

where

$$\boldsymbol{f}_{k,j} = -\boldsymbol{f}_{j,k}, \tag{12}$$

and

$$\boldsymbol{f}_{k,j} \propto \boldsymbol{r}_k - \boldsymbol{r}_j. \tag{13}$$

Here, it should be noted that $\boldsymbol{f}_{k,k} = \boldsymbol{0}$.

By summing up the equations of motion for n disks, we obtain the evolution equation for $\boldsymbol{r}_c$ as

$$\begin{aligned}\rho\pi R^2 n\frac{d^2\boldsymbol{r}_c}{dt^2} &= -\kappa\pi R^2 n\frac{d\boldsymbol{r}_c}{dt} + \sum_{k=0}^{n-1}\boldsymbol{F}_k^{(\mathrm{conc})}\\ &= -\kappa\pi R^2 n\frac{d\boldsymbol{r}_c}{dt} + \pi R^2\boldsymbol{\mathcal{F}}^{(n)},\end{aligned} \tag{14}$$

where $\boldsymbol{\mathcal{F}}^{(n)}$ is the force per unit area exerting on the camphor float with n-fold rotational symmetry. By calculating the vector product of the equations of motion with $\boldsymbol{r}_k - \boldsymbol{r}_c$ and then summing up for n disks, we obtain the evolution equation for θ_c as

$$\begin{aligned}\rho\pi R^2\ell^2 n\frac{d^2\theta_c}{dt^2} &= -\kappa\pi R^2\ell^2 n\frac{d\theta_c}{dt} + \sum_{k=0}^{n-1}(\boldsymbol{r}_k - \boldsymbol{r}_c)\times\boldsymbol{F}_k^{(\mathrm{conc})}\\ &= -\kappa\pi R^2\ell^2 n\frac{d\theta_c}{dt} + \pi R^2\mathcal{N}^{(n)},\end{aligned} \tag{15}$$

where $\mathcal{N}^{(n)}$ is the torque per unit area exerting on the camphor float with n-fold rotational symmetry. Here, the operator "×" is defined so that $\boldsymbol{a}\times\boldsymbol{b} = a_x b_y - a_y b_x$ for $\boldsymbol{a} = a_x\boldsymbol{e}_x + a_y\boldsymbol{e}_y$ and $\boldsymbol{b} = b_x\boldsymbol{e}_x + b_y\boldsymbol{e}_y$. It should be noted that the obtained time evolution equations for $\boldsymbol{r}_c$ and θ_c in **Eqs 14**, **15** does not explicitly include the terms originating from the internal force.

Finally, we derive the dimensionless version of our model. The dimensionless variables are defined as

$$\begin{aligned}&\tilde{\boldsymbol{r}} = \frac{\boldsymbol{r}}{\sqrt{D/a}}, \tilde{\boldsymbol{r}}_k = \frac{\boldsymbol{r}_k}{\sqrt{D/a}}, \tilde{\boldsymbol{r}}_c = \frac{\boldsymbol{r}_c}{\sqrt{D/a}}, \quad \tilde{R} = \frac{R}{\sqrt{D/a}}, \tilde{\ell} = \frac{\ell}{\sqrt{D/a}},\\ &\tilde{t} = at, \tilde{u} = \frac{u}{S_0/D}, \tilde{\rho} = \frac{\rho Da}{\Gamma S_0}, \tilde{\kappa} = \frac{\eta D}{\Gamma S_0},\\ &\tilde{\boldsymbol{F}}_k^{(\mathrm{conc})} = \frac{\boldsymbol{F}_k^{(\mathrm{conc})}}{\Gamma S_0/\sqrt{Da}}, \tilde{\boldsymbol{\mathcal{F}}}^{(n)} = \frac{\boldsymbol{\mathcal{F}}^{(n)}}{\Gamma S_0\sqrt{a}/\left(D\sqrt{D}\right)}, \tilde{\mathcal{N}}^{(n)} = \frac{\mathcal{N}^{(n)}}{\Gamma S_0/D},\end{aligned} \tag{16}$$

and our model with dimensionless variables is summarized as

$$\frac{\partial\tilde{u}}{\partial\tilde{t}} = \tilde{\nabla}^2\tilde{u} - \tilde{u} + \sum_{k=0}^{n-1}\frac{1}{\pi\tilde{R}^2}\Theta\left(\tilde{R} - |\tilde{\boldsymbol{r}} - \tilde{\boldsymbol{r}}_k|\right), \tag{17}$$

$$\begin{aligned}\tilde{\rho}\frac{d^2\tilde{\boldsymbol{r}}_c}{d\tilde{t}^2} &= -\tilde{\kappa}\frac{d\tilde{\boldsymbol{r}}_c}{d\tilde{t}} + \frac{1}{n\pi\tilde{R}^2}\sum_{k=0}^{n-1}\tilde{\boldsymbol{F}}_k^{(\mathrm{conc})}\\ &= -\tilde{\kappa}\frac{d\tilde{\boldsymbol{r}}_c}{d\tilde{t}} + \frac{1}{n}\tilde{\boldsymbol{\mathcal{F}}}^{(n)},\end{aligned} \tag{18}$$

$$\begin{aligned}\tilde{\rho}\frac{d^2\theta_c}{d\tilde{t}^2} &= -\tilde{\kappa}\frac{d\theta_c}{d\tilde{t}} + \frac{1}{n\pi\tilde{R}^2\tilde{\ell}^2}\sum_{k=0}^{n-1}(\tilde{\boldsymbol{r}}_k - \tilde{\boldsymbol{r}}_c)\times\tilde{\boldsymbol{F}}_k^{(\mathrm{conc})}\\ &= -\tilde{\kappa}\frac{d\theta_c}{d\tilde{t}} + \frac{1}{n\tilde{\ell}^2}\tilde{\mathcal{N}}^{(n)},\end{aligned} \tag{19}$$

$$\tilde{\boldsymbol{r}}_k = \tilde{\boldsymbol{r}}_c + \tilde{\ell}\boldsymbol{e}\left(\theta_c + \frac{2\pi k}{n}\right), \tag{20}$$

$$\tilde{\boldsymbol{F}}_k^{(\mathrm{conc})} = -\oint_{\partial\tilde{\Omega}_k}\tilde{u}(\tilde{\boldsymbol{r}}')\boldsymbol{n}(\tilde{\boldsymbol{r}}')d\tilde{\ell}' \tag{21}$$

$$= -\iint_{\tilde{\Omega}_k}\left(\tilde{\nabla}'\tilde{u}(\tilde{\boldsymbol{r}}')\right)d\tilde{A}'. \tag{22}$$

$$\tilde{\Omega}_k = \left\{\tilde{\boldsymbol{r}}\middle|\,|\tilde{\boldsymbol{r}} - \tilde{\boldsymbol{r}}_k| \le \tilde{R}\right\}. \tag{23}$$

Hereafter, we adopt this dimensionless model with the tildes omitted.

3 ANALYSIS

In this section, we analyze our model on the camphor float with n-fold rotational symmetry, derived in the previous section. To enable us to analyze our model, we assume that the camphor disk radius R is sufficiently small and that the concentration field of camphor molecules are described as the function of the positions and velocities of the comprising n camphor disks. In this section, we first obtain the expression of the concentration field under the above assumptions, and then calculate the force $\boldsymbol{\mathcal{F}}^{(n)}$ and torque $\mathcal{N}^{(n)}$ originating from the concentration field. Based on the ordinary differential equations obtained under the assumptions, we perform the linear stability anaysis. Finally, we discuss the motion of the camphor float by calculating the force and torque in the case that the camphor float is moving at a constant velocity with a constant characteristic angle θ_c.

3.1 Simplification of the Model

Under the assumption that $R \to +0$, the evolution equation for the concentration field in **Eq. 17** is described as

$$\frac{\partial u}{\partial t} = \nabla^2 u - u + \sum_{k=0}^{n-1}\delta(\boldsymbol{r} - \boldsymbol{r}_k), \tag{24}$$

where $\delta(\cdot)$ is the Dirac's delta function.

The concentration field u is expressed as the summation of the concentration field generated by each camphor disk due to the linearity of the evolution equation for the concentration field. By assuming that the concentration field generated by the k-th camphor disk is expressed as a function of $\boldsymbol{r}_k$ and $\boldsymbol{v}_k$, $u(\boldsymbol{r})$ is expressed as

$$u(\boldsymbol{r}) = \sum_{k=0}^{n-1}U(\boldsymbol{r} - \boldsymbol{r}_k, \boldsymbol{v}_k), \tag{25}$$

where $U(\boldsymbol{r}, \boldsymbol{v})$ is the stationary concentration field in the comoving frame with the camphor disk whose velocity is fixed to $\boldsymbol{v}$. Thus, $U(\boldsymbol{r}, \boldsymbol{v})$ should satisfy the following equation:

$$-\boldsymbol{v}\cdot\nabla U = \nabla^2 U - U + \delta(\boldsymbol{r}), \tag{26}$$

and is explicitly described as [9]

$$U(\boldsymbol{r},\boldsymbol{v}) = \frac{1}{2\pi}\mathcal{K}_0\left(\sqrt{1+\frac{|\boldsymbol{v}|^2}{4}}|\boldsymbol{r}|\right)\exp\left(-\frac{1}{2}\boldsymbol{r}\cdot\boldsymbol{v}\right), \tag{27}$$

where $\mathcal{K}_\nu(\cdot)$ is the second-kind modified Bessel function of the α-th order.

The force $\boldsymbol{F}_k^{(\mathrm{conc})}$ which exerts on the k-th camphor disk originating from the camphor concentration field is represented as the summation of the forces $\boldsymbol{F}_{k,j}^{(\mathrm{conc})}$ originating from the camphor concentration field released from the j-th camphor disk as

$$\boldsymbol{F}_k^{(\mathrm{conc})} = \sum_{j=0}^{n-1}\boldsymbol{F}_{k,j}^{(\mathrm{conc})}. \tag{28}$$

As for $\boldsymbol{F}_{k,j}^{(\mathrm{conc})}$ $(k\neq j)$, the limit of $\boldsymbol{F}_{k,j}^{(\mathrm{conc})}/(\pi R^2)$ with $R\to+0$ is expressed as

$$\begin{aligned}\lim_{R\to+0}\frac{\boldsymbol{F}_{k,j}^{(\mathrm{conc})}}{\pi R^2} &= \lim_{R\to+0}\frac{1}{\pi R^2}\iint_{\Omega_k}\nabla U\left(\boldsymbol{r},\boldsymbol{v}_j\right)\Big|_{\boldsymbol{r}=\boldsymbol{r}_k-\boldsymbol{r}_j}dA'\\ &= -\nabla U\left(\boldsymbol{r},\boldsymbol{v}_j\right)\Big|_{\boldsymbol{r}=\boldsymbol{r}_k-\boldsymbol{r}_j}.\end{aligned} \tag{29}$$

For the linear stability analysis, the concentration field $U(\boldsymbol{r}, \boldsymbol{v})$ is expanded with respect to $\boldsymbol{v}$ as [40]

$$U(\boldsymbol{r},\boldsymbol{v}) = \frac{1}{2\pi}\mathcal{K}_0(|\boldsymbol{r}|) - \frac{1}{4\pi}\mathcal{K}_0(|\boldsymbol{r}|)\boldsymbol{r}\cdot\boldsymbol{v} + \mathcal{O}\left(|\boldsymbol{v}|^2\right), \tag{30}$$

and therefore the force $\boldsymbol{F}_{k,j}^{(\mathrm{conc})}/(\pi R^2)$ $(k\neq j)$ is also described as the expansion with respect to $\boldsymbol{v}_j$ as

$$\begin{aligned}\frac{\boldsymbol{F}_{k,j}^{(\mathrm{conc})}}{\pi R^2} &= \frac{1}{2\pi}\mathcal{K}_1\left(|\boldsymbol{r}_k-\boldsymbol{r}_j|\right)\frac{\boldsymbol{r}_k-\boldsymbol{r}_j}{|\boldsymbol{r}_k-\boldsymbol{r}_j|} + \frac{1}{4\pi}\mathcal{K}_0\left(|\boldsymbol{r}_k-\boldsymbol{r}_j|\right)\boldsymbol{v}_j\\ &\quad -\frac{1}{4\pi}\mathcal{K}_1\left(|\boldsymbol{r}_k-\boldsymbol{r}_j|\right)\left[\left(\boldsymbol{r}_k-\boldsymbol{r}_j\right)\cdot\boldsymbol{v}_j\right]\frac{\boldsymbol{r}_k-\boldsymbol{r}_j}{|\boldsymbol{r}_k-\boldsymbol{r}_j|} + \mathcal{O}\left(R,|\boldsymbol{v}_j|^2\right).\end{aligned} \tag{31}$$

As for the force $\boldsymbol{F}_{k,k}^{(\mathrm{conc})}$, it cannot be calculated from the concentration field under the assumption of $R\to+0$ since the concentration field is not differentiable at $\boldsymbol{r}=\boldsymbol{r}_k$. Thus we calculate the force working on the disk with a finite small radius, and then consider the limit of $R\to+0$. The force working on the camphor disk originating from the camphor concentration field generated by itself is calculated as

$$\begin{aligned}\frac{\boldsymbol{F}_{k,k}^{(\mathrm{conc})}}{\pi R^2} &= -\frac{1}{\pi R^2}\int_0^{2\pi}U(\boldsymbol{r}_k+R\boldsymbol{e}(\theta),\boldsymbol{v}_k)R\boldsymbol{e}(\theta)d\theta\\ &= \frac{1}{\pi R}\mathcal{K}_0\left(\sqrt{1+\frac{|\boldsymbol{v}_k|^2}{4}}R\right)\mathcal{I}_1\left(\frac{R|\boldsymbol{v}_k|}{2}\right)\frac{\boldsymbol{v}_k}{|\boldsymbol{v}_k|}.\end{aligned} \tag{32}$$

By considering the limit of $R\to+0$ and expanding the expression with respect to $\boldsymbol{v}_k$, we obtain

$$\begin{aligned}\frac{\boldsymbol{F}_{k,k}^{(\mathrm{conc})}}{\pi R^2} &= \frac{1}{4\pi}\left(\ln\left(\frac{2}{R}\right)-\gamma_{\mathrm{Euler}}\right)\boldsymbol{v}_k - \frac{1}{32\pi}|\boldsymbol{v}_k|^2\boldsymbol{v}_k + \frac{1}{256\pi}|\boldsymbol{v}_k|^4\boldsymbol{v}_k\\ &\quad + \mathcal{O}\left(R,|\boldsymbol{v}_k|^7\right),\end{aligned} \tag{33}$$

where $\gamma_{\mathrm{Euler}}\simeq 0.577\,21\ldots$ is the Euler's constant. The coefficient of $\boldsymbol{v}_k$ in the first term of the righthand side diverges for $R\to+0$, but it exhibits the logarithmic divergence. Therefore, we introduce an arbitrary positive constant F_0, and consider that $\boldsymbol{F}_{k,k}/(\pi R^2)$ is described as the expansion with respect to $\boldsymbol{v}_k$ as

$$\frac{\boldsymbol{F}_{k,k}^{(\mathrm{conc})}}{\pi R^2} = F_0\boldsymbol{v}_k - \frac{1}{32\pi}|\boldsymbol{v}_k|^2\boldsymbol{v}_k + \frac{1}{256\pi}|\boldsymbol{v}_k|^4\boldsymbol{v}_k + \mathcal{O}\left(|\boldsymbol{v}_k|^7\right). \tag{34}$$

3.2 Linear Stability Analysis

We first consider the motion of a single camphor disk in order to discuss the motion of the camphor float by comparing with the single disk motion. For a single disk system, the equation of motion should be

$$\rho\frac{d\boldsymbol{v}_c}{dt} = -\kappa\boldsymbol{v}_c + F_0\boldsymbol{v}_c - \frac{1}{32\pi}|\boldsymbol{v}_c|^2\boldsymbol{v}_c + \frac{1}{256\pi}|\boldsymbol{v}_c|^4\boldsymbol{v}_c + \mathcal{O}\left(|\boldsymbol{v}_c|^7\right), \tag{35}$$

where $\boldsymbol{v}_c = d\boldsymbol{r}_c/dt$. Note that the characteristic angle θ_c cannot be defined for a single disk system. This system exhibits a supercritical pitchfork bifurcation at $\kappa = F_0$. In other words, the camphor disk does not move for $\kappa > F_0$, while it moves at a constant speed for $\kappa < F_0$. In the latter case, the camphor disk moves at the speed of $\sqrt{32\pi(F_0-\kappa)}$ under the situation close to the bifurcation point [9, 40, 41].

In the case of $n = 2$, the equations of motion for the camphor float up to the first orders of $\boldsymbol{v}_c$ and $\omega_c(= d\theta_c/dt)$ are obtained as

$$\begin{aligned}\rho\frac{d\boldsymbol{v}_c}{dt} &= -\kappa\boldsymbol{v}_c + F_0\boldsymbol{v}_c + \frac{1}{4\pi}\mathcal{K}_0(2\ell)\boldsymbol{v}_c\\ &\quad -\frac{1}{2\pi}\mathcal{K}_1(2\ell)\ell(\boldsymbol{v}_c\cdot\boldsymbol{e}(\theta_c))\boldsymbol{e}(\theta_c).\end{aligned} \tag{36}$$

$$\rho\frac{d\omega_c}{dt} = -\kappa\omega_c + F_0\omega_c - \frac{1}{4\pi}\mathcal{K}_0(2\ell)\omega_c. \tag{37}$$

Note that the representation of the torque is the same for the camphor rotor whose center is fixed [40, 42]. It is obvious that the system has a stationary solution $\boldsymbol{v}_c = \boldsymbol{0}$ and $\omega_c = 0$, which corresponds to the resting camphor float. From the symmetric property of the system, the system should be neutrally stable on the perturbation on the position $\boldsymbol{r}_c$ and characteristic angle θ_c. Thus, we perform the linear stability anaysis around the stationary solution with $\boldsymbol{r}_c = \boldsymbol{0}$ and $\theta_c = 0$, without losing generality. The linaraized equation is obtained by setting $\boldsymbol{v}_c = \delta v_x\boldsymbol{e}_x + \delta v_y\boldsymbol{e}_y$ and $\omega_c = \delta\omega$ as

$$\frac{d}{dt}\begin{pmatrix}\delta v_x\\ \delta v_y\\ \delta\omega\end{pmatrix} = \begin{pmatrix}-\kappa+\kappa_{2,\parallel} & 0 & 0\\ 0 & -\kappa+\kappa_{2,\perp} & 0\\ 0 & 0 & -\kappa+\kappa_{2,r}\end{pmatrix}\begin{pmatrix}\delta v_x\\ \delta v_y\\ \delta\omega\end{pmatrix}, \tag{38}$$

where

$$\kappa_{2,\parallel} = F_0 + \frac{1}{4\pi}\mathcal{K}_0(2\ell) - \frac{1}{2\pi}\ell\mathcal{K}_1(2\ell), \tag{39}$$

$$\kappa_{2,\perp} = F_0 + \frac{1}{4\pi}\mathcal{K}_0(2\ell), \tag{40}$$

$$\kappa_{2,r} = F_0 - \frac{1}{4\pi}\mathcal{K}_0(2\ell). \tag{41}$$

Eqs 38–41 mean that the bifurcation points for the translational motion in the direction parallel to the line connecting the two camphor disks, that pependicular to it, and that for the rotational motion are $\kappa = \kappa_{2,\parallel}$, $\kappa_{2,\perp}$, and $\kappa_{2,r}$, respectively. $\kappa_{2,\parallel}$, $\kappa_{2,\perp}$, and $\kappa_{2,r}$ are expressed as the summation of the bifurcation point for a single camphor disk F_0 and the terms that decay to 0 for $\ell \to +\infty$. Since $\kappa_{2,\parallel} < \kappa_{2,\perp}$ and $\kappa_{2,r} < \kappa_{2,\perp}$ hold for any $\ell > 0$, the translational motion in the direction perpendicular to the line firstly bifurcates from the stationary state, and thus such a motion tends to be realized.

In the case of $n = 3$, the equations of motion up to the first orders on $\boldsymbol{v}_c$ and ω_c are given as

$$\rho\frac{d\boldsymbol{v}_c}{dt} = -\kappa\boldsymbol{v}_c + F_0\boldsymbol{v}_c + \frac{1}{2\pi}\mathcal{K}_0(\sqrt{3}\,\ell)\boldsymbol{v}_c - \frac{\sqrt{3}}{4\pi}\mathcal{K}_1(\sqrt{3}\,\ell)\ell\boldsymbol{v}_c. \tag{42}$$

$$\rho\frac{d\omega_c}{dt} = -\kappa\omega_c + F_0\omega_c - \frac{1}{4\pi}\mathcal{K}_0(\sqrt{3}\,\ell)\omega_c - \frac{\sqrt{3}}{8\pi}\mathcal{K}_1(\sqrt{3}\,\ell)\ell\omega_c. \tag{43}$$

Also in this case, the stationary solution with $\boldsymbol{v}_c = \boldsymbol{0}$ and $\omega_c = 0$ exists, which corresponds to the resting camphor float, and we arbitrarily set $\boldsymbol{r}_c = \boldsymbol{0}$ and $\theta_c = 0$ arbitrarily owing to the system symmetry. The linearized equation around this solution is obtained as

$$\frac{d}{dt}\begin{pmatrix}\delta v_x\\ \delta v_y\\ \delta\omega\end{pmatrix} = \begin{pmatrix}-\kappa+\kappa_{3,t} & 0 & 0\\ 0 & -\kappa+\kappa_{3,t} & 0\\ 0 & 0 & -\kappa+\kappa_{3,r}\end{pmatrix}\begin{pmatrix}\delta v_x\\ \delta v_y\\ \delta\omega\end{pmatrix}, \tag{44}$$

where

$$\kappa_{3,t} = F_0 + \frac{1}{2\pi}\mathcal{K}_0(\sqrt{3}\,\ell) - \frac{\sqrt{3}}{4\pi}\ell\mathcal{K}_1(\sqrt{3}\,\ell), \tag{45}$$

$$\kappa_{3,r} = F_0 - \frac{1}{4\pi}\mathcal{K}_0(\sqrt{3}\,\ell) - \frac{\sqrt{3}}{8\pi}\ell\mathcal{K}_1(\sqrt{3}\,\ell). \tag{46}$$

Eqs 44–46 mean that the bifurcation points for the translational and rotational motions are $\kappa = \kappa_{3,t}$ and $\kappa_{3,r}$, respectively. Considering that the bifurcation point is independent of the direction of translational motion, which is different from the case with $n = 2$, we cannot discuss the preferable direction for the translational motion based on the linear stability analysis for $n = 3$. Note that the bifurcation point for the translational motion in every direction is the same for each $n \geq 3$. $\kappa_{3,t}$ and $\kappa_{3,r}$ are also expressed as the summation of the bifurcation point for a single camphor disk F_0 and the terms that decay to 0 for $\ell \to +\infty$. The sign of $\kappa_{3,t} - \kappa_{3,r}$ changes at $\ell = \ell_{3,tr} \simeq 3.186\,63\ldots$, which satisfies

$$\frac{\ell_{3,tr}\mathcal{K}_1(\sqrt{3}\,\ell_{3,tr})}{\mathcal{K}_0(\sqrt{3}\,\ell_{3,tr})} = 2\sqrt{3}. \tag{47}$$

This means that the translational and rotational motions tend to occur for $\ell < \ell_{3,tr}$ and $\ell > \ell_{3,tr}$, respectively, though the difference between $\kappa_{3,t}$ and $\kappa_{3,r}$ is so small that such tendency may not be clear for $\ell > \ell_{3,tr}$.

3.3 Preferable Direction of Motion

The linear stability analysis indicates the preferable direction for the translational motion for $n = 2$, but it does not work for $n = 3$. In order to discuss the preferable direction of the translational motion of the camphor float with n-fold symmetry, we calculate the force and torque exerting on the camphor float with constant θ_c when it is moving at a constant velocity in a certain direction [35]. Considering the symmetry of the system, the generality is not lost if we set $\boldsymbol{v}_c = V\boldsymbol{e}_x\,(V > 0)$. Under this assumption, the force $\boldsymbol{\mathcal{F}}^{(n)}$ and torque $\mathcal{N}^{(n)}$ working on the camphor float are calculated as a function of the characteristic angle θ_c and the velocity V based on **Eq. 19**.

For $n = 2$, the force $\boldsymbol{\mathcal{F}}^{(2)}(\theta_c)$ and the torque $\mathcal{N}^{(2)}(\theta_c)$ are calculated as

$$\boldsymbol{\mathcal{F}}^{(2)}(\theta_c) = \left[2F_0 + \frac{1}{2\pi}\mathcal{K}_0\left(2\ell\sqrt{1+\frac{V^2}{4}}\right)\cosh(\ell V\cos\theta_c)\right]V\boldsymbol{e}_x - \frac{1}{\pi}\sqrt{1+\frac{V^2}{4}}\mathcal{K}_1\left(2\ell\sqrt{1+\frac{V^2}{4}}\right)\sinh(\ell V\cos\theta_c)\boldsymbol{e}(\theta_c), \tag{48}$$

and

$$\mathcal{N}^{(2)}(\theta_c) = \frac{V\ell}{2\pi}\mathcal{K}_0\left(2\ell\sqrt{1+\frac{V^2}{4}}\right)\sin\theta_c\sinh(\ell V\cos\theta_c), \tag{49}$$

respectively. For sufficiently small V, **Eqs 48**, **49** are expanded with respect to V as

$$\boldsymbol{\mathcal{F}}^{(2)}(\theta_c) = \left[2F_0 + \frac{1}{2\pi}\mathcal{K}_0(2\ell) - \frac{1}{2\pi}\ell\mathcal{K}_1(2\ell) - \frac{1}{2\pi}\ell\mathcal{K}_1(2\ell)\cos(2\theta_c)\right]V\boldsymbol{e}_x - \left[\frac{1}{2\pi}\ell\mathcal{K}_1(2\ell)\sin(2\theta_c)\right]V\boldsymbol{e}_y + \mathcal{O}(V^2), \tag{50}$$

$$\mathcal{N}^{(2)}(\theta_c) = \frac{\ell^2}{4\pi}\mathcal{K}_0(2\ell)V^2\sin(2\theta_c) + \mathcal{O}(V^3). \tag{51}$$

The force works in the negative y-direction for $0 < \theta_c < \pi/2$ and in the positive y-direction for $-\pi/2 < \theta_c < 0$ from **Eq. 50**, while the torque works counterclockwise for $0 < \theta_c < \pi/2$, and clockwise for $-\pi/2 < \theta_c < 0$ from **Eq. 51**. These expressions indicate that both the force and the torque work on the camphor float so that the characteristic angle should approach $\theta_c = \pm\pi/2$. This agrees with the results by the linear stability analysis. Therefore, the camphor float with 2-fold symmetry moves in the direction perpendicular to the line connecting the two camphor disks.

As for $n = 3$, the force $\boldsymbol{\mathcal{F}}^{(3)}(\theta_c)$ is explicitly expressed as

$$\boldsymbol{\mathcal{F}}^{(3)}(\theta_c) = 3F_0\boldsymbol{e}_x + \boldsymbol{g}(\theta_c) + \boldsymbol{g}\left(\theta_c+\frac{\pi}{3}\right) + \boldsymbol{g}\left(\theta_c+\frac{2\pi}{3}\right) + \boldsymbol{g}(\theta_c+\pi) + \boldsymbol{g}\left(\theta_c-\frac{2\pi}{3}\right) + \boldsymbol{g}\left(\theta_c-\frac{\pi}{3}\right), \tag{52}$$

where

$$\boldsymbol{g}(\theta) = \frac{1}{4\pi}\left[V\mathcal{K}_0\left(\sqrt{3}\,\ell\sqrt{1+\frac{V^2}{4}}\right)\exp\left(\frac{\sqrt{3}}{2}\,\ell\sin\theta\right)\right.$$
$$\left.-2\sqrt{1+\frac{V^2}{4}}\mathcal{K}_1\left(\sqrt{3}\,\ell\sqrt{1+\frac{V^2}{4}}\right)\exp\left(\frac{\sqrt{3}}{2}\,\ell V\sin\theta\right)\sin\theta\right]\boldsymbol{e}_x$$
$$+\frac{1}{2\pi}\left[\sqrt{1+\frac{V^2}{4}}\mathcal{K}_1\left(\sqrt{3}\,\ell\sqrt{1+\frac{V^2}{4}}\right)\exp\left(\frac{\sqrt{3}}{2}\,\ell V\sin\theta\right)\cos\theta\right]\boldsymbol{e}_y. \tag{53}$$

Note that $\boldsymbol{\mathcal{F}}^{(3)}(\theta_c)$ has a period of $\pi/3$ since

$$\boldsymbol{\mathcal{F}}^{(3)}(\theta_c) = \boldsymbol{\mathcal{F}}^{(3)}\left(\theta_c + \frac{\pi}{3}\right) \tag{54}$$

is derived from **Eqs 52**, **53**. For sufficiently small V, the expression in **Eqs 52**, **53** is expanded with respect to V as

$$\boldsymbol{\mathcal{F}}^{(3)}(\theta_c)$$
$$= 3\left[F_0 + \frac{1}{2\pi}\mathcal{K}_0(\sqrt{3}\,\ell) - \frac{\sqrt{3}}{4\pi}\ell\mathcal{K}_1(\sqrt{3}\,\ell)\right]V\boldsymbol{e}_x$$
$$-\frac{3}{128\pi}\left[4 - 24\ell^2\mathcal{K}_0(\sqrt{3}\,\ell) + \sqrt{3}\,\ell(8+3\ell^2)\mathcal{K}_1(\sqrt{3}\,\ell)\right]V^3\boldsymbol{e}_x$$
$$+\frac{3}{40\,960\pi}\left[160 + 60\ell^2(8+9\ell^2)\mathcal{K}_0(\sqrt{3}\,\ell)\right.$$
$$\left.+\sqrt{3}\,\ell(320 - 720\ell^2 - 30\ell^4 + 3\ell^4\cos(6\theta_c))\right]V^5\boldsymbol{e}_x$$
$$+\frac{9\sqrt{3}}{40\,960\pi}\left[\ell^5\mathcal{K}_1(\sqrt{3}\,\ell)\sin(6\theta_c)\right]V^5\boldsymbol{e}_y + \mathcal{O}(V^7). \tag{55}$$

This means that the configurations with both $\theta_c = 0$ and $\pi/3$ are stable for the camphor float with 3-fold rotational symmetry moving in the positive x-direction from the consideration of the force exerting on it. It should be noted thtat the above-mentioned force is on the order of V^5, which should be sufficiently weak close to the bifurcation point.

The torque $\mathcal{N}^{(3)}(\theta_c)$ is obtained as

$$\mathcal{N}^{(3)}(\theta_c) = h(\theta_c) + h\left(\theta_c + \frac{2\pi}{3}\right) + h\left(\theta_c - \frac{2\pi}{3}\right), \tag{56}$$

where

$$h(\theta) = -\frac{\ell}{2\pi}\sqrt{1+\frac{V^2}{4}}\mathcal{K}_1\left(\sqrt{3}\sqrt{1+\frac{V^2}{4}}\ell\right)\sinh\left(\frac{\sqrt{3}}{2}\ell V\sin\theta\right)$$
$$-\frac{V\ell}{2\pi}\mathcal{K}_0\left(\sqrt{3}\sqrt{1+\frac{V^2}{4}}\ell\right)\exp\left(-\frac{3}{4}\ell V\cos\theta\right)\cosh\left(\frac{\sqrt{3}}{4}\ell V\sin\theta\right)\sin\theta. \tag{57}$$

Eqs 56, **57** shows that $\mathcal{N}^{(3)}(\theta_c)$ obviously has a period of $2\pi/3$ since

$$\mathcal{N}^{(3)}(\theta_c) = \mathcal{N}^{(3)}\left(\theta_c + \frac{2\pi}{3}\right). \tag{58}$$

For sufficiently small V, **Eq. 56** is also expanded with respect to V as

$$\mathcal{N}^{(3)}(\theta_c) = \frac{3\ell^3}{128\pi}\left[-3\mathcal{K}_0(\sqrt{3}\,\ell) + \sqrt{3}\,\ell\mathcal{K}_1(\sqrt{3}\,\ell)\right]V^3\sin(3\theta_c)$$
$$+\mathcal{O}(V^5). \tag{59}$$

The torque at the order of V^3 works on the camphor float as a leading term. Comparing the orders between $\boldsymbol{\mathcal{F}}^{(3)}$ and $\mathcal{N}^{(3)}$ that affect the rotation of the camphor float, the effect of $\mathcal{N}^{(3)}$ should govern the dynamics for small V, which corresponds to the system close to the pitchfork bifurcation point. As for the case with high velocity, the other effects can be important, and we cannot discuss the selected mode of motion based on the above analysis. Thus, hereafter we consider the case with small V.

The sign of the proportionality coefficient of $\sin 3\theta_c$ in **Eq. 59** is important for the stable direction of the camphor float motion; If the proportionality coefficient is negative, the torque works clockwise for $0 < \theta_c < \pi/3$ and it works counterclockwise for $-\pi/3 < \theta_c < 0$. This indicates that the camphor float rotates so that θ_c approaches 0 or $\pm 2\pi/3$. In contrast, if the proportionality coefficient is positive, the torque works in the opposite directions, which indicates that θ_c approaches π or $\pm\pi/3$. According to our analytical result in **Eq. 59**, the sign of the proportionality coefficient is negative and positive for $\ell < \ell_{3,t}$ and $\ell > \ell_{3,t}$, respectively. Here, $\ell_{3,t} \simeq 1.464\,58\ldots$, which satisfies

$$\frac{\ell_{3,t}\mathcal{K}_1(\sqrt{3}\,\ell_{3,t})}{\mathcal{K}_0(\sqrt{3}\,\ell_{3,t})} = \sqrt{3}. \tag{60}$$

This means that, as far as the camphor float is moving slowly, the small camphor float with $\ell < \ell_{3,t}$ rotates so that it moves with one camphor disk at the front, while the large camphor float with $\ell > \ell_{3,t}$ rotates so that it moves with one camphor disk at the rear.

4 NUMERICAL CALCULATION

In order to confirm the analytical results, we perform the numerical calculation. We used the dimensionless model in **Eqs 17–23**. For the numerical calculation, we used the smoothed function; the source part and the force are changed as

$$\frac{\partial u}{\partial t} = \nabla^2 u - u + \sum_{k=0}^{n-1}\frac{1}{\pi R^2}G(|\boldsymbol{r} - \boldsymbol{r}_k|), \tag{61}$$

$$\boldsymbol{F}_k^{(\mathrm{conc})} = -\iint_{\mathbb{R}^2}(\nabla' u(\boldsymbol{r}'))G(|\boldsymbol{r}' - \boldsymbol{r}_k|)dA'. \tag{62}$$

where

$$G(r) = \frac{1}{2}\left[1 + \tanh\left(\frac{R-r}{\delta}\right)\right]. \tag{63}$$

It should be noted that $G(r)$ converges to $\Theta(R-r)$ for the limit of $\delta \to +0$.

Numerical calculation was performed with the explicit method with the time step $\Delta t = 0.000\,5$, and the spatial mesh $\Delta x = 0.05$. The calculation area for the concentration field is set to 20×20 with periodic boundary conditions. The parameters are fixed as $\rho = 0.01$, $R = 0.2$, and $\delta = 0.05$, and κ and ℓ were varied as parameters. The initial condition for the concentration was $u = 0$ in the whole region. The initial conditions for the velocity, characterisitic angle, and angular velocity were set as $\boldsymbol{v}_c = 0.5\boldsymbol{e}_x + 0.01\boldsymbol{e}_y$, $\theta_c = 0.5$, and $\omega_c = 0.01$. Since the initial condition was set so that the camphor float has a high velocity and

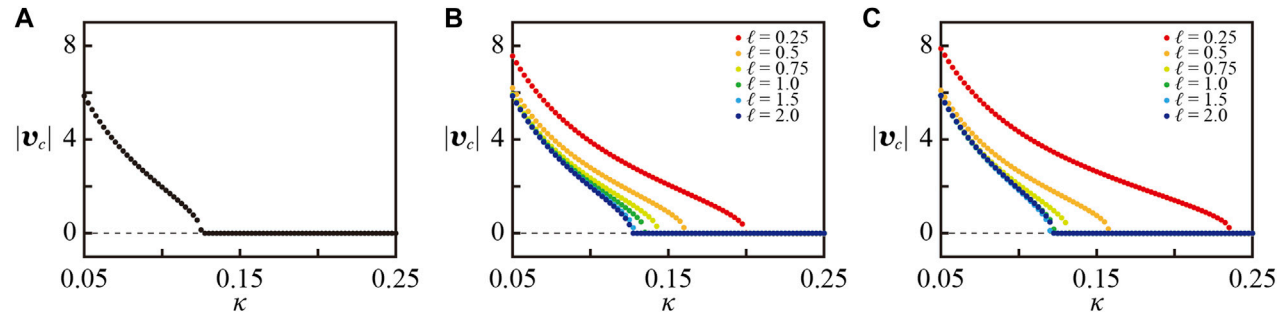

FIGURE 2 | Numerical results on the stationary translational velocity of the camphor float. **(A)** A single camphor disk. **(B)** The camphor float with two camphor disks. **(C)** The camphor float with three camphor disks. For the cases **(B,C)**, the results for various ℓ were represented in different colors.

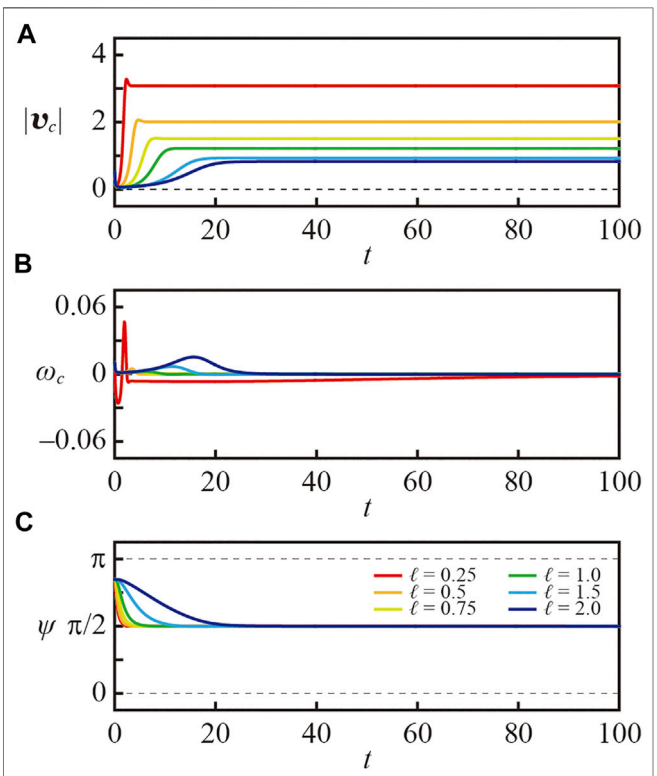

FIGURE 3 | Numerical results on the time series of **(A)** velocity, **(B)** angular velocity, and **(C)** angle difference between the velocity and characteristic angle θ_c for the camphor float with $n = 2$. κ was fixed to 0.12. The results for various ℓ were represented in different colors. It should be noted that ψ has a periodicity of π.

low angular velocity, the float was easy to converge to the translational motion.

In **Figure 2A**, we first plot the stationary translational velocity against κ for a single camphor disk. In this case, we could only consider the translational motion but not the rotational motion. Thus, the initial condition for the velocity was set as $\boldsymbol{v}_c = 0.5\boldsymbol{e}_x + 0.01\boldsymbol{e}_y$. We confirmed that the motion of the single camprhor disk converged to a translational motion with a constant velocity at $t = 100$, even when the initial condition was changed. Thus, we plotted $|\boldsymbol{v}_c|$ at $t = 100$ for the stationary translational velocity. The stationary translational velocity was finite for the smaller κ, while it was almost zero for the larger κ. The bifurcation point with respect to the bifurcation parameter κ for the translational motion was slightly greater than 0.12, where the bifurcation was supposed to be classified into a supercritical pitchfork bifurcation.

We also calculated the cases with $n = 2$ and 3. In **Figures 2B,C**, we plotted the stationary translational velocity for various ℓ. Also in these cases, the velocity at $t = 100$ was adopted as the stationary translational velocity, at which we confirmed that the velocity was converged. For the camphor float with $n = 2$, the bifurcation point was greater for the smaller ℓ as shown in **Figure 2B**. This agrees with the theoretical results in **Eq. 40**. For the camphor float with $n = 3$, the bifurcation point had a minimum value at a certain ℓ around 1.5 as shown in **Figure 2C**. This also corresponds to the theoretical result in **Eq. 45**, which indicates that the bifuracation point has the minimum value at $\ell = 1.377\,98\ldots$.

In **Figure 3**, the time series of the velocity $|\boldsymbol{v}_c|$, angular velocity ω_c, and the angle difference ψ between the direction of velocity and the characteristic angle θ_c are plotted for the camphor float with $n = 2$. The angle difference ψ is defined as

$$\psi = \phi - \theta_c, \tag{64}$$

where ϕ is defined as $\boldsymbol{v}_c = |\boldsymbol{v}_c|(\cos\phi\boldsymbol{e}_x + \sin\phi\boldsymbol{e}_y)$. We set $\kappa = 0.12$ since we wanted to discuss the behavior close to the bifurcation point for the translational motion of a single camphor disk. The convergence to the stationary translational motion was faster for small ℓ, whereas the system almost reached the stationary states around $t = 30$ even in the case of $\ell = 2$. The angular velocity decayed to zero and the angle difference ψ approached $\pi/2$, which corresponds to the translational motion in the direction perpendicular to the line connecting the two camphor disks.

As for the camphor float with $n = 3$, the time series are shown in **Figure 4**. It should be noted that the time range in **Figure 4** is ten times as long as that in **Figure 3**, since the convergence of the angle difference ψ was much slower than the case with $n = 2$, though the convergence of the velocity and angular velocity was as fast as that in the case with $n = 2$. The angle difference ψ converged to zero for $\ell = 0.25$, 0.5, 0.75, and 1.0, while it converged to $-\pi/3$ for $\ell = 2.0$. This agrees with the analytical results in **Eqs 59**, **60**. These results show

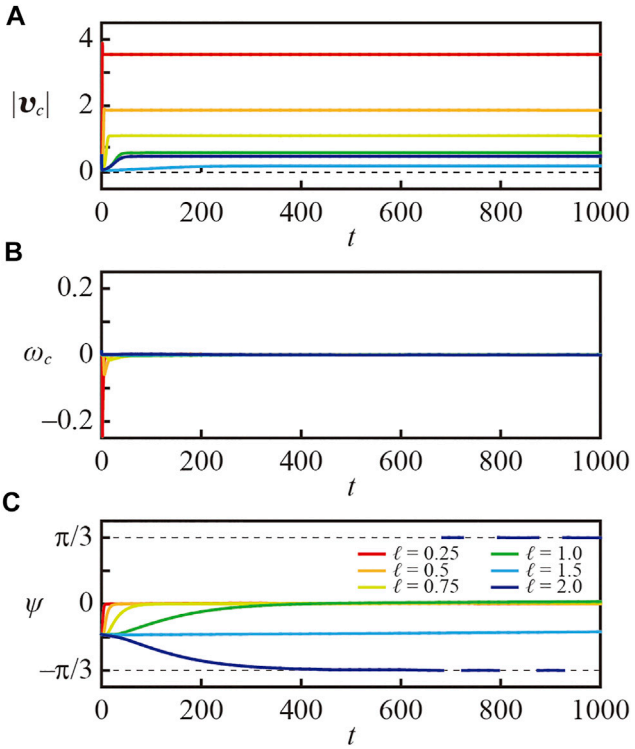

FIGURE 4 | Numerical results on the time series of **(A)** velocity, **(B)** angular velocity, and **(C)** angle difference between the velocity and characteristic angle θ_c for the camphor float with $n = 3$. κ was fixed to 0.12. The results for various ℓ were represented in different colors. It should be noted that ψ has a periodicity of $2\pi/3$.

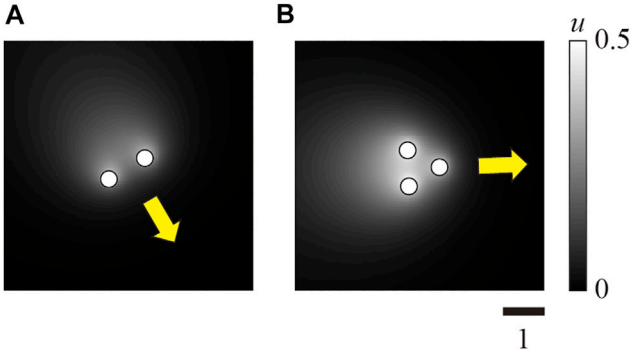

FIGURE 5 | Snapshots of the camphor concentration around the camphor floats. **(A)** Camphor float with $n = 2$ at $t = 100$. **(B)** Camphor float with $n = 3$ at $t = 100$. κ was set to 0.12, and ℓ was set to 0.5. Corresponding videos are avialable as **Supplementary Video S1, S2**.

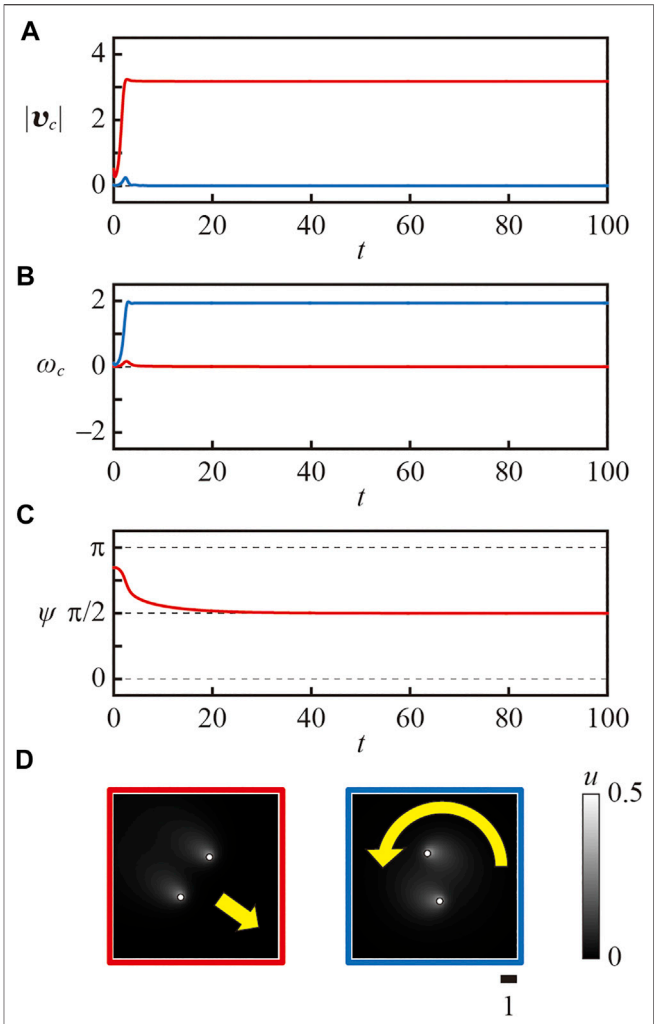

FIGURE 6 | Numerical results on the time series of **(A)** velocity $|\boldsymbol{v}_c|$, **(B)** angular velocity ω_c, and **(C)** angle difference between the velocity and characteristic angle θ_c for the camphor float with $n = 2$. κ was fixed to 0.08 and ℓ was fixed to 1.5. The results from various initial conditions were represented in different colors. Angle difference was plotted only for the case that $|\boldsymbol{v}_c|$ was converged to a non-zero value. It should be noted that ψ has a periodicity of π. **(D)** Snapshots at $t = 100$ from each initial condition indicated in the same color. The initial conditions were (red) $\boldsymbol{v}_c = 0.5\boldsymbol{e}_x + 0.01\boldsymbol{e}_y$, $\omega_c = 0.01$, and (blue) $\boldsymbol{v}_c = 0.02\boldsymbol{e}_x + 0.01\boldsymbol{e}_y$, $\omega_c = 0.1$.

that the smaller camphor float with $n = 3$ moved with one disk at its front, while the larger camphor float moved with one disk at its rear, which agrees with the analytical results. In the case with $\ell = 1.5$, the convergence of ψ was very slow, which can be understood from the fact that $\ell = 1.5$ is close to the threshold value $\ell_{3,t} \simeq 1.464\,58\ldots$. Considering that $1.5 > \ell_{3,t}$, the angle difference should converge to $\pm\pi/3$ but it appeared to approach 0. We consider that the difference between the theoretical and analytical results owes the slight difference in the setting; e.g. the finite size of the camphor disk, etc.

In **Figure 5**, the snapshots of the camphor concentration u together with the camphor disk positions are shown for the cases of the camphor float with $n = 2$ and 3 for $\ell = 0.5$. Considering that the camphor concentration profile has a tail in the opposite direction of the traveling direction, the obtained concentration field also indicated that the angle difference ψ between the velocity and the characteristic angle was $\pi/2$ for the case with $n = 2$, and 0 for the case with $n = 3$.

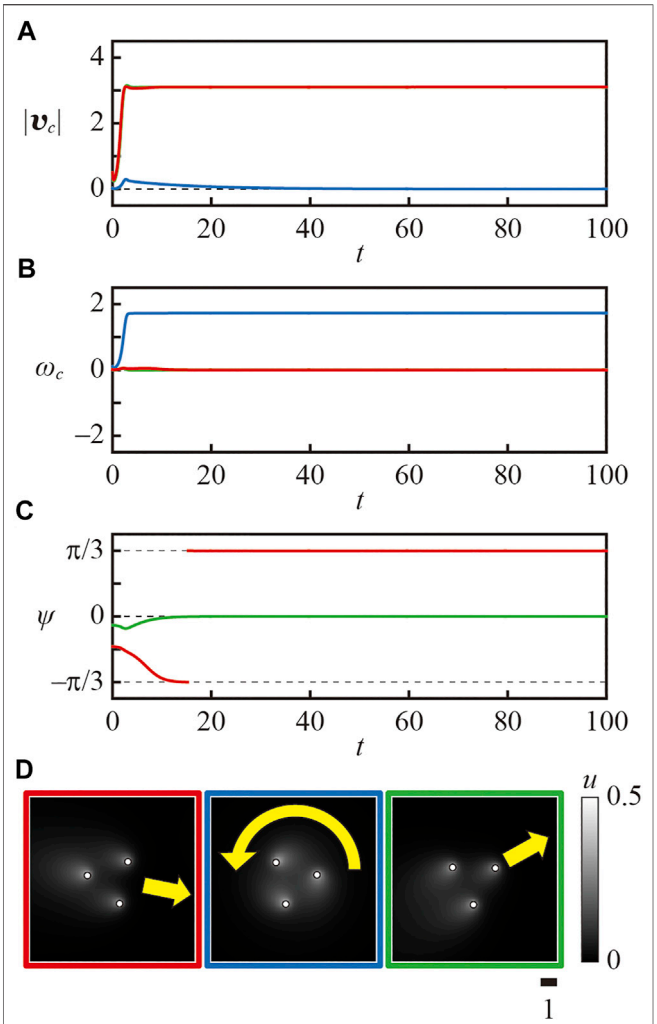

FIGURE 7 | Numerical results on the time series of **(A)** velocity $|\boldsymbol{v}_c|$, **(B)** angular velocity ω_c, and **(C)** angle difference between the velocity and characteristic angle θ_c for the camphor float with $n = 3$. κ was fixed to 0.08 and ℓ was fixed to 1.5. The results from various initial conditions were represented in different colors. Angle difference was plotted only for the case that $|\boldsymbol{v}_c|$ was converged to a non-zero value. It should be noted that ψ has a periodicity of $2\pi/3$. **(D)** Snapshots at $t = 100$ from each initial condition indicated in the same color. The initial conditions were (red) $\boldsymbol{v}_c = 0.5\boldsymbol{e}_x + 0.01\boldsymbol{e}_y$, $\omega_c = 0.01$, and (blue) $\boldsymbol{v}_c = 0.02\boldsymbol{e}_x + 0.01\boldsymbol{e}_y$, $\omega_c = 0.1$, and (green) $\boldsymbol{v}_c = 0.4\boldsymbol{e}_x + 0.15\boldsymbol{e}_y$, $\omega_c = 0.01$.

5 DISCUSSION

In the analysis in **Section 3**, we assume that the system is close to the bifurcation point. In such a situation, our analytical results match the results by numerical calculation; i.e., the camphor float with $n = 2$ moves in the perpendicular direction to the line connecting the two camphor disks. For the case with $n = 3$, the smaller camphor float moves with one disk at its front, while the larger camphor float moves with one disk at its rear. However, in the condition far from the bifurcation point, the system often becomes multistable and one of several modes of motions is selected depending on the initial condition. Actually, the numerical results that exhibit multistability are shown in **Figures 6**, **7** for $n = 2$ and 3, respectively. The parameters were set as $\kappa = 0.08$ and $\ell = 1.5$. In the case with $n = 2$ shown in **Figure 6**, the translational motion and spinning motion were observed depending on the initial conditions. The direction of the translational motion was always perpendicular to the line connecting the two disks. In the case with $n = 3$, the two types of translational motions, i.e., the motion with one disk at its front and that with one disk at its rear, and the spinning motion were observed depending on the initial conditions. Such multistability could be observed in the wider parameter regions for the larger ℓ, but the system was often monostable for the smaller ℓ.

In our model, the concentration field around one camphor disk has the leading term described by the second-kind modified Bessel function as far as the traveling velocity is low. This means that the concentration field decays exponentially. Taking this into consideration, the coupling between the direction of motion and the camphor float configuration should be stronger for the smaller camphor float. Thus, the smaller camphor float can easily change the moving direction and quickly takes the preferable direction. In contrast, for the larger camphor float, the interaction is so small that it takes much time for the camphor float to take the preferable direction. Moreover, the system can often show the multistability for the larger camphor float as discussed in the previous paragraph. Threfore, the present discussion can be adequately adopted for the smaller camphor float.

The analytical results for the cases with $n = 2$ and $n = 3$ are essentially different; the bifurcation point for the translational motion depends on the moving direction for $n = 2$, while it is equivalent for any direction for $n = 3$. Moreover, we calculated the force and torque exerting on the camphor float which is moving at a constant velocity V without rotation. For $n = 2$, the leading terms of the force and torque which depend on the direction of the motion are at the order of V and V^2, respectively. In contrast, for $n = 3$, they are at the order of V^5 and V^3, respectively. This reflects that the linear stability analysis can lead to the nontrivial results for $n = 2$ but not for $n = 3$. Considering the orders of V in the force and torque, the configuration and the velocity of the camphor float are more strongly coupled with each other for $n = 2$ than for $n = 3$ near the bifurcation point as shown in **Figures 3**, **4**. In addition, the force is more greatly affected to the dynamics than the torque for $n = 2$, and thus the preferable configuration is achieved by changing the velocity direction. In contrast, the torque is more greatly affected to the dynamics than the force for $n = 3$, and thus the preferable direction is achieved by changing the configuration by spinning. For the camphor float with $n \geq 4$, we can perform the similar approach. However, for greater n, the effect of the configuration on the translational motion becomes smaller. Therefore, the analysis for the case with smaller n is more important, and here we especially discuss on the cases with $n = 2$ and $n = 3$.

We believe that the present theoretical results can be confirmed by the experiments. In the dimensionless model, the length and time are scaled by the diffusion length $\sqrt{D/a}$ and the characteristic sublimation time $1/a$, respectively. From the previous results [37], they correspond to *ca.* 100 mm and *ca.* 50 s. Using these scale units, the typical size of the camphor float corresponds to *ca.* 100 mm in the actual system, since the dimensionless size of the camphor float adopted in this study

is on the order of 1. As for the velocity, the obtained dimensionless value is on the order of 1 from **Figures 2–7**, which corresponds to *ca.* 2 mm/s. This value is rather slower than the typical velocity observed in experiments, *ca.* 10 mm/s, but these values are of the same order. Considering that the size of the camphor float is difficult to exceed 100 mm, the scale available in the experimental setup should be less than 1. Moreover, as discussed in the previous paragraph, the coupling between the configuration and the translational motion is stronger for the small camphor float. Therefore, we suppose that the experimental confirmation is possible only for the camphor float with small ℓ. Considering that the effect of the shape is stronger for $n = 2$, we suppose that the shape effect due to the 2-fold rotational symmetry can be easily confirmed, but that the effect for $n = 3$ or higher is more difficult to confirm.

In our previous work, we showed that an elliptic camphor particle moves in its minor-axis direction in theoretical analysis, numerical calculation, and experiments [9, 33, 34]. The symmetric property of the distribution of the mass and the camphor molecule source for an elliptic camphor particle is similar to that of the camphor float with 2-fold rotational symmetry discussed in the present study. In our result, it moves in the direction perpendicular to the line connecting the two camphors. Thus, the present results and our previous results show good correspondence. As for the camphor float with 3-fold rotational symmetry, it corresponds to the triangular camphor particle discussed in our previous study [35] from the viewpoint of the symmetric property. In our previous work, we concluded that the smaller triangular camphor particle moves in the direction of the corner for the smaller particle, while it moves in the direction of the side for the larger particle. The present results correspond to our previous ones in that the preferable direction changes depending on the size by considering the deviation of the mass and camphor molecule source. Taking the present analytical results into consideration, we suggest that the low-wave-number modulation from a symmetric circular shape most effectively affects the self-propelled motion, and the high-wave-number modulation is not so important.

6 CONCLUSION

In the present study, we theoretically investigated the self-propulsion of a camphor float with n-fold rotational symmetry, which comprises a rigid light circular plate attached with n camphor disks along a periphery with an equivalent spacing. We constructed a mathematical model for the camphor float, and analyzed it under the assumptions that the camphor disk radius is negligibly small and that the camphor concentration only depends on the positions and velocities of the camphor disks. From the linear stability analysis and the calculation of the force and torque for the situation that a camphor float is moving at a constant velocity with a certain characteristic angle, we concluded that the camphor float with 2-fold rotational symmetry moves in the direction perpendicular to the line connecting the two camphor disks. As for the camphor float with 3-fold rotational symmetry, the smaller float moves with one camphor disk at the front, while the larger float moves with one camphor disk at the rear.

As the extensions of the present study, we consider the particles with an asymmetric configuration. By considering such particles, we can generally discuss the manner of coupling between the motion and the symmtric featrures of self-propelled particles. We are also interested in the collective motion of the particles with n-fold rotational symmetry. In such systems, we expect some interesting structures with a nematic order and/or a hexagonal order can be realized. The symmetric properties embedded in the external condition such as the system boundary and the spatial modulation of the parameters also seem to be interesting. We hope the present results will provide the fundamental knowledge to understand the above-mentioned more complex systems, and moreover, will help understanding the universal mechanism on the shape effect on self-propelled motions driven by the self-generated concentration field.

DATA AVAILABILITY STATEMENT

The original contributions presented in the study are included in the article/**Supplementary Material**, further inquiries can be directed to the corresponding author.

AUTHOR CONTRIBUTIONS

HK and YK contributed to the conception and design of the work. HK performed the analytical and numerical calculations, and YK confirmed the validity of the results. HK and YK prepared the manuscript. All authors contributed to the article and approved the submitted version.

FUNDING

This work was supported by JSPS KAKENHI Grant Nos. JP19K03765, JP19J00365, JP20K14370, JP20H02712, and JP21H01004, and also the Cooperative Research Program of "Network Joint Research Center for Materials and Devices: Dynamic Alliance for Open Innovation Bridging Human, Environment and Materials" (Nos. 20211014 and 20214004). This work was also supported by JSPS and PAN under the Japan-Poland Research Cooperative Program (No. JPJSBP120204602).

ACKNOWLEDGMENTS

The authors acknoweldge Professor Jerzy Gorecki (Polish Academy of Sciences), Professor Masaharu Nagayama (Hokkaido University), and Professor Yutaka Sumino (Tokyo University of Science) for their fruitful discussion.

SUPPLEMENTARY MATERIAL

The Supplementary Material for this article can be found online at: https://www.frontiersin.org/articles/10.3389/fphy.2022.858791/full#supplementary-material

REFERENCES

1. Mikhailov A, Calenbuhr V. *From Cells to Societies: Models of Complex Coherent Action*. Berlin: Springer (2002).
2. Ramaswamy S. The Mechanics and Statistics of Active Matter. *Annu Rev Condens Matter Phys* (2010) 1:323–45. doi:10.1146/annurev-conmatphys-070909-104101
3. Vicsek T, Zafeiris A. Collective Motion. *Phys Rep* (2012) 517:71–140. doi:10.1016/j.physrep.2012.03.004
4. Maass CC, Krüger C, Herminghaus S, Bahr C. Swimming Droplets. *Annu Rev Condens Matter Phys* (2016) 7:171–93. doi:10.1146/annurev-conmatphys-031115-011517
5. Bechinger C, Di Leonardo R, Löwen H, Reichhardt C, Volpe G, Volpe G. Active Particles in Complex and Crowded Environments. *Rev Mod Phys* (2016) 88:045006. doi:10.1103/RevModPhys.88.045006
6. Kitahata H, Yoshikawa K. Chemo-mechanical Energy Transduction through Interfacial Instability. *Physica D: Nonlinear Phenomena* (2005) 205:283–91. doi:10.1016/j.physd.2004.12.012
7. Ohta T, Ohkuma T. Deformable Self-Propelled Particles. *Phys Rev Lett* (2009) 102:154101. doi:10.1103/PhysRevLett.102.154101
8. Ohta T. Dynamics of Deformable Active Particles. *J Phys Soc Jpn* (2017) 86:072001. doi:10.7566/JPSJ.86.072001
9. Kitahata H, Koyano Y, Iida K, Nagayama M. Chapter 2. Mathematical Model and Analyses on Spontaneous Motion of Camphor Particle. In: *Self-organized Motion: Physicochemical Design Based on Nonlinear Dynamics*. Cambridge: The Royal Society of Chemistry (2018). p. 31–62. doi:10.1039/9781788013499-00031
10. Keren K, Pincus Z, Allen GM, Barnhart EL, Marriott G, Mogilner A, et al. Mechanism of Shape Determination in Motile Cells. *Nature* (2008) 453:475–80. doi:10.1038/nature06952
11. Ebata H, Sano M. Swimming Droplets Driven by a Surface Wave. *Sci Rep* (2015) 5:8546. doi:10.1038/srep08546
12. Michelin S, Lauga E, Bartolo D. Spontaneous Autophoretic Motion of Isotropic Particles. *Phys Fluids* (2013) 25:061701. doi:10.1063/1.4810749
13. Yoshinaga N, Nagai KH, Sumino Y, Kitahata H. Drift Instability in the Motion of a Fluid Droplet with a Chemically Reactive Surface Driven by Marangoni Flow. *Phys Rev E* (2012) 86:016108. doi:10.1103/PhysRevE.86.016108
14. Izri Z, van der Linden MN, Michelin S, Dauchot O. Self-propulsion of Pure Water Droplets by Spontaneous Marangoni-Stress-Driven Motion. *Phys Rev Lett* (2014) 113:248302. doi:10.1103/PhysRevLett.113.248302
15. Toyota T, Maru N, Hanczyc MM, Ikegami T, Sugawara T. Self-Propelled Oil Droplets Consuming "Fuel" Surfactant. *J Am Chem Soc* (2009) 131:5012–3. doi:10.1021/ja806689p
16. Sumino Y, Magome N, Hamada T, Yoshikawa K. Self-running Droplet: Emergence of Regular Motion from Nonequilibrium Noise. *Phys Rev Lett* (2005) 94:068301. doi:10.1103/PhysRevLett.94.068301
17. Sumino Y, Kitahata H, Yoshikawa K, Nagayama M, Nomura S-i. M, Magome N, et al. Chemosensitive Running Droplet. *Phys Rev E* (2005) 72:041603. doi:10.1103/PhysRevE.72.041603
18. Shao D, Rappel W-J, Levine H. Computational Model for Cell Morphodynamics. *Phys Rev Lett* (2010) 105:108104. doi:10.1103/PhysRevLett.105.108104
19. Tomlinson C, Miller WA. II. On the Motions of Camphor on the Surface of Water. *Proc R Soc Lond* (1862) 11:575–7. doi:10.1098/rspl.1860.0124
20. Strutt RJ. IV. Measurements of the Amount of Oil Necessary Iu Order to Check the Motions of Camphor upon Water. *Proc R Soc Lond* (1890) 47:364–7. doi:10.1098/rspl.1889.0099
21. Nakata S, Iguchi Y, Ose S, Kuboyama M, Ishii T, Yoshikawa K. Self-rotation of a Camphor Scraping on Water: New Insight into the Old Problem. *Langmuir* (1997) 13:4454–8. doi:10.1021/la970196p
22. Nakata S, Nagayama M, Kitahata H, Suematsu NJ, Hasegawa T. Physicochemical Design and Analysis of Self-Propelled Objects that Are Characteristically Sensitive to Environments. *Phys Chem Chem Phys* (2015) 17:10326–38. doi:10.1039/C5CP00541H
23. Boniface D, Cottin-Bizonne C, Kervil R, Ybert C, Detcheverry F. Self-propulsion of Symmetric Chemically Active Particles: Point-source Model and Experiments on Camphor Disks. *Phys Rev E* (2019) 99:062605. doi:10.1103/PhysRevE.99.062605
24. Nishimori H, Suematsu NJ, Nakata S. Collective Behavior of Camphor Floats Migrating on the Water Surface. *J Phys Soc Jpn* (2017) 86:101012. doi:10.7566/JPSJ.86.101012
25. Morohashi H, Imai M, Toyota T. Construction of a Chemical Motor-Movable Frame Assembly Based on Camphor Grains Using Water-Floating 3d-Printed Models. *Chem Phys Lett* (2019) 721:104–10. doi:10.1016/j.cplett.2019.02.034
26. Sharma J, Tiwari I, Das D, Parmananda P, Akella VS, Pimienta V. Rotational Synchronization of Camphor Ribbons. *Phys Rev E* (2019) 99:012204. doi:10.1103/PhysRevE.99.012204
27. Lauga E, Davis AMJ. Viscous Marangoni Propulsion. *J Fluid Mech* (2012) 705:120–33. doi:10.1017/jfm.2011.484
28. Sur S, Masoud H, Rothstein JP. Translational and Rotational Motion of Disk-Shaped Marangoni Surfers. *Phys Fluids* (2019) 31:102101. doi:10.1063/1.5119360
29. Jafari Kang S, Sur S, Rothstein JP, Masoud H. Forward, Reverse, and No Motion of Marangoni Surfers under Confinement. *Phys Rev Fluids* (2020) 5:084004. doi:10.1103/PhysRevFluids.5.084004
30. Nagayama M, Nakata S, Doi Y, Hayashima Y. A Theoretical and Experimental Study on the Unidirectional Motion of a Camphor Disk. *Physica D: Nonlinear Phenomena* (2004) 194:151–65. doi:10.1016/j.physd.2004.02.003
31. Hayashima Y, Nagayama M, Nakata S. A Camphor Grain Oscillates while Breaking Symmetry. *J Phys Chem B* (2001) 105:5353–7. doi:10.1021/jp004505n
32. Koyano Y, Kitahata H. Imperfect Bifurcation in the Rotation of a Propeller-Shaped Camphor Rotor. *Phys Rev E* (2021) 103:012202. doi:10.1103/PhysRevE.103.012202
33. Kitahata H, Iida K, Nagayama M. Spontaneous Motion of an Elliptic Camphor Particle. *Phys Rev E* (2013) 87:010901. doi:10.1103/PhysRevE.87.010901
34. Iida K, Kitahata H, Nagayama M. Theoretical Study on the Translation and Rotation of an Elliptic Camphor Particle. *Physica D: Nonlinear Phenomena* (2014) 272:39–50. doi:10.1016/j.physd.2014.01.005
35. Kitahata H, Koyano Y. Spontaneous Motion of a Camphor Particle with a Triangular Modification from a circle. *J Phys Soc Jpn* (2020) 89:094001. doi:10.7566/JPSJ.89.094001
36. Kitahata H, Yoshinaga N. Effective Diffusion Coefficient Including the Marangoni Effect. *J Chem Phys* (2018) 148:134906. doi:10.1063/1.5021502
37. Suematsu NJ, Sasaki T, Nakata S, Kitahata H. Quantitative Estimation of the Parameters for Self-Motion Driven by Difference in Surface Tension. *Langmuir* (2014) 30:8101–8. doi:10.1021/la501628d
38. Karasawa Y, Oshima S, Nomoto T, Toyota T, Fujinami M. Simultaneous Measurement of Surface Tension and its Gradient Around Moving Camphor Boat on Water Surface. *Chem Lett* (2014) 43:1002–4. doi:10.1246/cl.140201
39. Karasawa Y, Nomoto T, Chiari L, Toyota T, Fujinami M. Motion Modes of Two Self-Propelled Camphor Boats on the Surface of a Surfactant-Containing Solution. *J Colloid Interf Sci* (2018) 511:184–92. doi:10.1016/j.jcis.2017.09.099
40. Koyano Y, Gryciuk M, Skrobanska P, Malecki M, Sumino Y, Kitahata H, et al. Relationship between the Size of a Camphor-Driven Rotor and its Angular Velocity. *Phys Rev E* (2017) 96:012609. doi:10.1103/PhysRevE.96.012609
41. Koyano Y, Suematsu NJ, Kitahata H. Rotational Motion of a Camphor Disk in a Circular Region. *Phys Rev E* (2019) 99:022211. doi:10.1103/PhysRevE.99.022211
42. Koyano Y, Kitahata H, Gryciuk M, Akulich N, Gorecka A, Malecki M, et al. Bifurcation in the Angular Velocity of a Circular Disk Propelled by Symmetrically Distributed Camphor Pills. *Chaos* (2019) 29:013125. doi:10.1063/1.5061027

Conflict of Interest: The authors declare that the research was conducted in the absence of any commercial or financial relationships that could be construed as a potential conflict of interest.

frontiers | Frontiers in Physics

ORIGINAL RESEARCH
published: 04 May 2022
doi: 10.3389/fphy.2022.895824

Detection of Inhomogeneity After Mixing Solutions by Analyzing the Chemical Wave Pattern in the Belousov-Zhabotinsky Reaction

*Yasunao Okamoto[1], Erika Okita[2], Daigo Yamamoto[3], Satoshi Nakata[4] and Akihisa Shioi[3]**

[1]Organization for Research Initiatives and Development, Faculty of Science and Engineering, Doshisha University, Kyoto, Japan, [2]Department of Chemical Engineering, Osaka Prefecture University, Osaka, Japan, [3]Department of Chemical Engineering and Materials Science, Doshisha University, Kyoto, Japan, [4]Graduate School of Integrated Sciences for Life, Hiroshima University, Hiroshima, Japan

The correlation between BZ reaction and mixing state has been studied for decades, and the researchers are trying to apply it to chemical engineering. We observed a chemical wave pattern in the Belouzov-Zhabotinsky (BZ) reaction based on the inhomogeneity after mixing BZ and ferroin solutions with a mixing method named the rotation-and-stop method. A one-dimensional chemical wave appeared for large inhomogeneity in mixing. The frequency and wavenumber decreased with decreasing degree of inhomogeneity. In an almost perfectly mixed state, the wavenumber significantly reduced and approached the global oscillation. The degree of mixing could be efficiently determined by this reported method. Perfect mixing has never been realized in natural and biological systems. The results of this study can be applied to estimate the degree of mixing in a solution that is not being stirred after the mixing process.

Keywords: Belousov-Zhabotinsky reaction, mixing, chemical oscillation, chemical wave, visualization, nonlinear dynamics, inhomogeneity

OPEN ACCESS

Edited by:
Federico Rossi,
University of Siena, Italy

Reviewed by:
Marcelllo Budroni,
University of Sassari, Italy
Marek Orlik,
University of Warsaw, Poland

****Correspondence:***
Akihisa Shioi
ashioi@mail.doshisha.ac.jp

Specialty section:
This article was submitted to Physical Chemistry and Chemical Physics, a section of the journal Frontiers in Physics

Received: *14 March 2022*
Accepted: *07 April 2022*
Published: *04 May 2022*

Citation:
Okamoto Y, Okita E, Yamamoto D, Nakata S and Shioi A (2022) Detection of Inhomogeneity After Mixing Solutions by Analyzing the Chemical Wave Pattern in the Belousov-Zhabotinsky Reaction. Front. Phys. 10:895824. doi: 10.3389/fphy.2022.895824

1 INTRODUCTION

The correlation between the Belouzov-Zhabotinsky (BZ) reaction and the mixing state has been studied extensively for decades [1–4]. The quality of products in industrial processes depends on the mixing state; therefore, an easy method to quantify the mixing state is essential. The BZ reaction is a nonlinear chemical reaction that shows period oscillations in the concentration of the reaction intermediates. A significant characteristic of the BZ reaction is the amplification of a small initial concentration fluctuation in the excitable system. The oscillation period depends on the stirring rate in the batch reactor; with increasing stirring rate, the period increases and the oscillation suddenly disappears [5–7]. At a low stirring rate, the redox potential in a macroscopic area (average over a larger area) shows a noisy oscillation pattern compared to that of a smaller area [8]. This suggests that the oscillation pattern in a batch reactor is affected by the spatial inhomogeneity of the solution. The oscillation pattern of the BZ reaction in a continuous stirred tank reactor (CSTR) depends on both the stirring speed and reactant supply rate, which causes period-doubling bifurcation and chaotic behavior [9,10]. Using gallic acid as an organic redox agent, the redox potential showed a hysteresis against the stirring speed [11]. These results observed in the CSTR arise from the inhomogeneous distribution of reactant concentrations due to incomplete mixing.

TABLE 1 | Concentrations of constituents of the BZ and ferroin solutions.

Solution	$NaBrO_3$ (M)	NaBr (M)	$CH_2(COOH)_2$ (M)	H_2SO_4 (M)	Ferroin (mM)	Density (g/cm^3)
BZ	0.2	0.01	0.1	0.7		1.06
ferroin					0.96	0.986

The BZ reaction exhibits a chemical wave without stirring [1]. In the studies related to chemical waves, researchers considered perfectly mixed solutions or gels [3]. The role of the convection due to imperfect mixing and chemically-driven inhomogeneity in the BZ reaction is studied with the batch conditions in detail [12,13]. However, the generation of a chemical wave requires concentration fluctuations (inhomogeneity). If the solution in the oscillatory regime is completely homogeneous, the oscillation exhibits a global oscillation. To the best of our knowledge, the effect of inhomogeneity after mixing (hereinafter referred to as "the inhomogeneity") on chemical waves has not been studied. If inhomogeneity affects the characteristics of the chemical wave, the degree of mixing can be estimated from the chemical wave pattern.

Furthermore, the BZ reaction has been studied as a model for cyclic chemical reactions in living systems, such as the tricarboxylic acid cycle [14], rhythmic motion [15–18], synchronization [19–21], and self-organization [22–24]. A living system cannot be stirred mechanically; as a result, perfect mixing has never been realized. Thus, their self-organizations are probably affected by the effect of the imperfect mixing. Therefore, the study of the mixing effect based on the chemical wave pattern is essential for analyzing living systems.

Herein, we demonstrate the effect of inhomogeneity on the chemical wave pattern produced by the BZ reaction. This study leads to a new quantitative method to estimate the degree of mixing and a deeper understanding of pattern formation in living systems.

2 MATERIALS AND METHODS

2.1 Chemicals and Preparation of the BZ and Ferroin Solutions

All the chemicals used in this study were purchased from FUJIFILM Wako Pure Chemical Corporation. We prepared a catalyst-free BZ solution and ferroin solution (catalyst) using the purchased chemicals. Ferroin is oxidized to ferriin by the BZ reaction, which is accompanied by a color change from red to blue. As shown in **Table 1**, constituents of the BZ solution were sodium bromate (Wako Special Grade, 99.5%), sodium bromide (guaranteed reagent grade, 99.5%), malonic acid (Wako Special Grade, 99.5%), and sulfuric acid (64%). Ferroin solution was prepared using iron (II) sulfate heptahydrate (~99.0–102.0%) and 1,10-Phenanthroline monohydrate (guaranteed reagent grade, 99.0%). First, we prepared the BZ solution by mixing the constituents in the following order: 5 ml of 1 M sodium bromate, 0.25 ml of 1 M sodium bromide, 2.5 ml of 1 M malonic acid, 13.75 ml of ultrapure water (PURELAB flex 3, ELGA LabWater), and 3.5 ml of 5 M sulfuric acid. After the addition of sulfuric acid, the color of the mixture changed to brown immediately, and it was mixed for 20 s until the mixture became colorless. In addition, 1.2 ml of 20 mM ferroin solution was diluted in a measuring flask to a volume of 25 ml. Before use in the experiments, the two solutions were bubbled with nitrogen gas for 1 minute, and the capped bottles containing the solutions were placed in a water bath at 20°C for 30 min, which is for avoiding the effects of the oxygen and temperature. The compositions of the BZ and ferroin solutions are shown in **Table 1**. These solutions were prepared before every experiment.

2.2 Preparation of the Two-Layer Solution

The chemical oscillation started after the BZ and ferroin solutions were mixed, and the mixing was carried out in a test tube using the method explained in **section 2.3**. In this study, the initial separation of these two solutions in the test tube was important. As shown in **Figure 1A**, 1 ml of both the BZ and ferroin solutions were poured into a test tube. The inner diameter and length of the test tube were 0.72 and 30 cm, respectively. First, the BZ solution, which has a higher density, was poured into the test tube, followed by the ferroin solution. The ferroin solution was poured carefully onto the BZ solution in the test tube using a silicone tube with an inner diameter of 1 mm, such that the boundary of the two solutions was not violated.

2.3 Mixing Method to Evaluate the Inhomogeneity After Mixing

Figure 1 shows the mixing method of the BZ and ferroin solutions (mentioned in 2.1) in a test tube, which is referred to as the rotation-and-stop method. As shown in **Figures 1A,B**, the test tube was capped and attached to a stirrer machine (IKA, RW 14 basic). The tube slanted to the right side, as shown in **Figure 1A**, because of the mechanical structure of the apparatus (this is the initial state before the rotation). Using this setup, the tube was rotated (center of the test tube was the center of rotation) counterclockwise twice at a rate of approximately one rotation/s, following a sudden stop. The mixing occurs primarily because of this sudden stop, where the two solutions mix near the interface owing to weak convection caused by the inertia. The tube was rotated again approximately 3 s after the rotation was completely stopped. This series was repeated several times and the number of repetitions (also the number of stops) was denoted as n (n = 20–200). The two solutions were mixed slightly at each stop process. After completion of this rotation process, 2 ml of decane was poured onto the surface of the mixed solution to avoid the dissolution of oxygen from the air. The tube was then placed vertically in a water bath at 20°C. More than three experiments were performed under identical conditions. The solution in the test tube was recorded by a video camera for 30 min after the

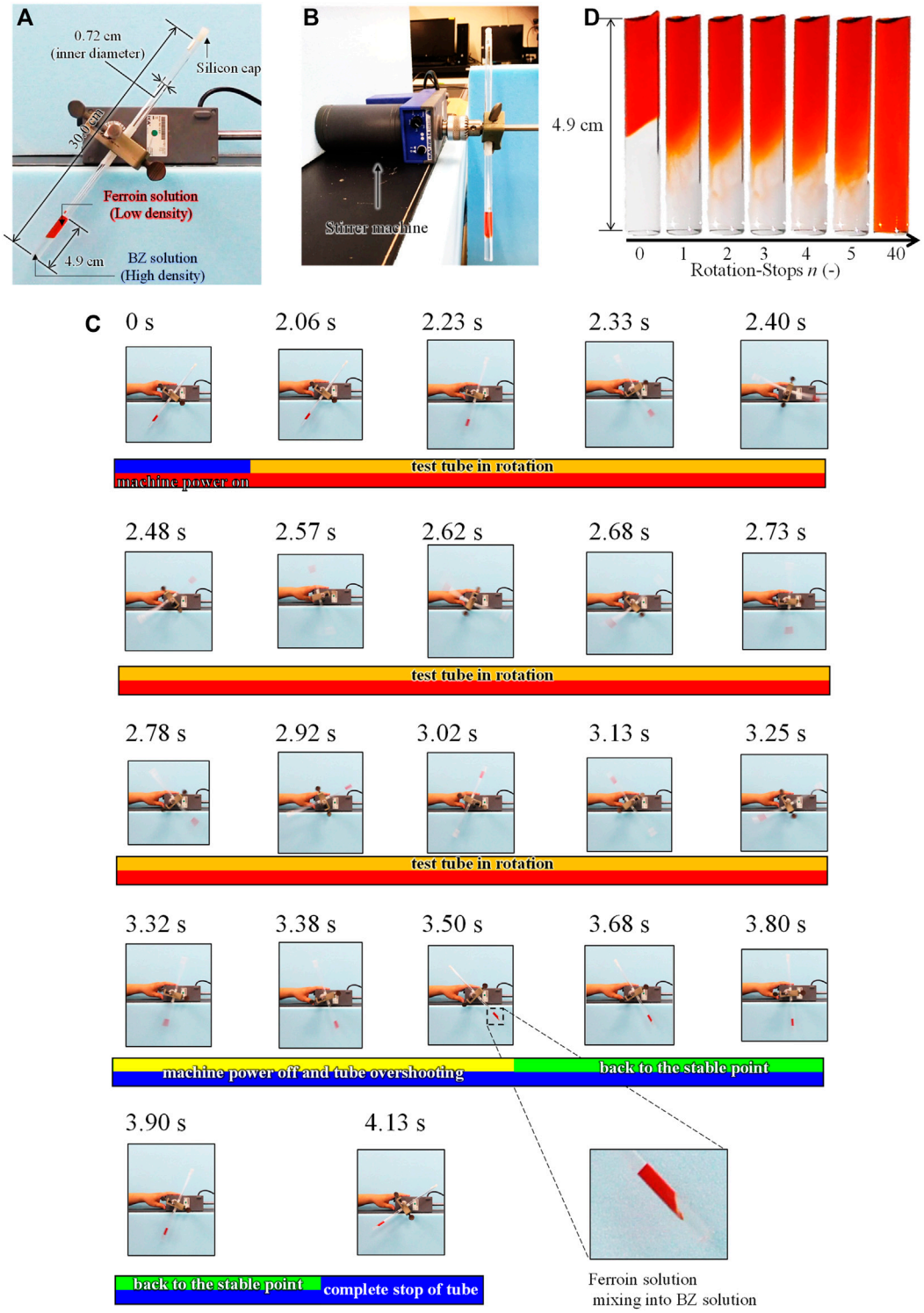

FIGURE 1 | Rotation-and-stop method; **(A)** Front view and **(B)** side view of the experimental setup. **(C)** The behavior of the solutions in a tube during a single rotation-stop cycle. **(D)** The mixing process of between Na_2SO_4 and ferroin solutions in a test tube by rotation-and-stop method. The residual image in the **(C)** is caused by the fast rotation (~90 cm/s) and the slow frame rate (30 frame/s).

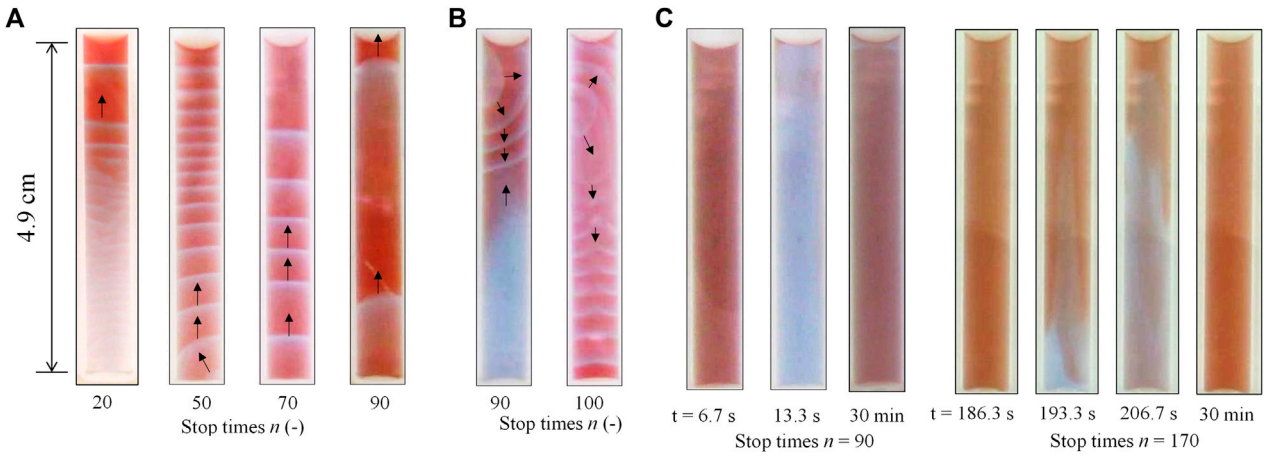

FIGURE 2 | Three different modes of the chemical wave were observed in the tube 30 min after the rotation-and-stop process; **(A)** upward wave, **(B)** complicated pattern, and **(C)** global-oscillation-like pattern. The black arrows (**Figures 2A,B**) indicate the direction of the wave movement.

completion of the rotation-and-stop process, and the movie slices were analyzed using the image analysis software ImageJ.

3 RESULTS AND DISCUSSION

3.1 Mixing of Solutions by Rotation-and-Stop Method

Figure 1C shows a series of snapshots recorded in a single rotation-stop process. In this experiment, the ferroin solution and Na_2SO_4 aqueous solution (0.77 M) were mixed to investigate only mixing process without the BZ reaction. The density of the Na_2SO_4 aqueous solution is approximately the same as that of the BZ solution, however, the BZ reaction did not occur. As shown in **Figure 1C**, the stirrer power was turned on at 0 s, but the rotation started after 2 s. Subsequently, the tube started to rotate counterclockwise. The stirrer was turned off at 3.32 s when two rotations were completed. However, the tube overshot until 3.50 s. After the overshoot, the tube returned to a stable state and stopped completely at 4.13 s. The solutions were mixed only around the boundary region after the two rotations. The mixing occurred at the stop-and-overshoot stages because of the density difference between the two solutions and the small diameter of the test tube which caused the complete separation of the solutions during rotation owing to the centrifugal force. Similarly, the BZ and ferroin solutions mix only at the stop-and-overshoot stages. Thus, the stepwise mixing can be achieved by the stop-and-overshoot stages n.

Figure 1D shows the interface between the two aqueous solutions after n stops. The interface diffused with increasing n. The mixing achieved by a single rotation stop was very weak and the degree of mixing monotonically increased with an increase in n. This result indicates that fine control of the mixing state is possible by controlling the value of n. Solutions with $n \geq 40$ appeared to be homogeneous. Even though inhomogeneity could be present, it is difficult to detect with the naked eye.

3.2 Behavior of Chemical Wave at Different Stop Times (n)

After the completion of the mixing between BZ and ferroin solutions with the rotation-and-stop method, three modes were observed for different values of n. The first was an upward chemical wave, as shown in **Figure 2A**. This type of pattern is likely to appear at relatively smaller n values. This upward chemical wave was generated at the bottom of the solution, then traveled upward and spread in the entire solution. The second pattern was referred to as the complicated pattern as shown in **Figure 2B**. In this pattern, a chemical wave was generated at the top or middle of the solution together with an upward chemical wave or oscillation at the local place. For example, oscillation of color appeared in the lower half of the solution at n = 90 (**Figure 2B**). This complicated pattern, observed 30 min after the rotation-and-stop process, was transient, and one of the local chemical waves or chemical oscillations became dominant over time (see **Supplementary Video S1**). The last pattern was a global-oscillation-like pattern over the entire solution, as shown in **Figure 2C**. In this phenomenon, the color of the entire solution oscillated for at least 30 min after the completion of the rotation-and-stop process. This oscillation is gradually transformed into a one-dimensional chemical wave (primarily into an upward wave) over time. In addition, the bubble growth caused by CO_2 generation was rarely observed in any modes, and so the additional mixing due to this effect can be ignored.

In general, if chemical oscillations with different frequencies exist, the maximum frequency dominates the entire solution [25]. Furthermore, the different profile of the chemical species may cause the different local excitability and thus different patterns [26,27]. Therefore, the oscillation frequencies f at three different

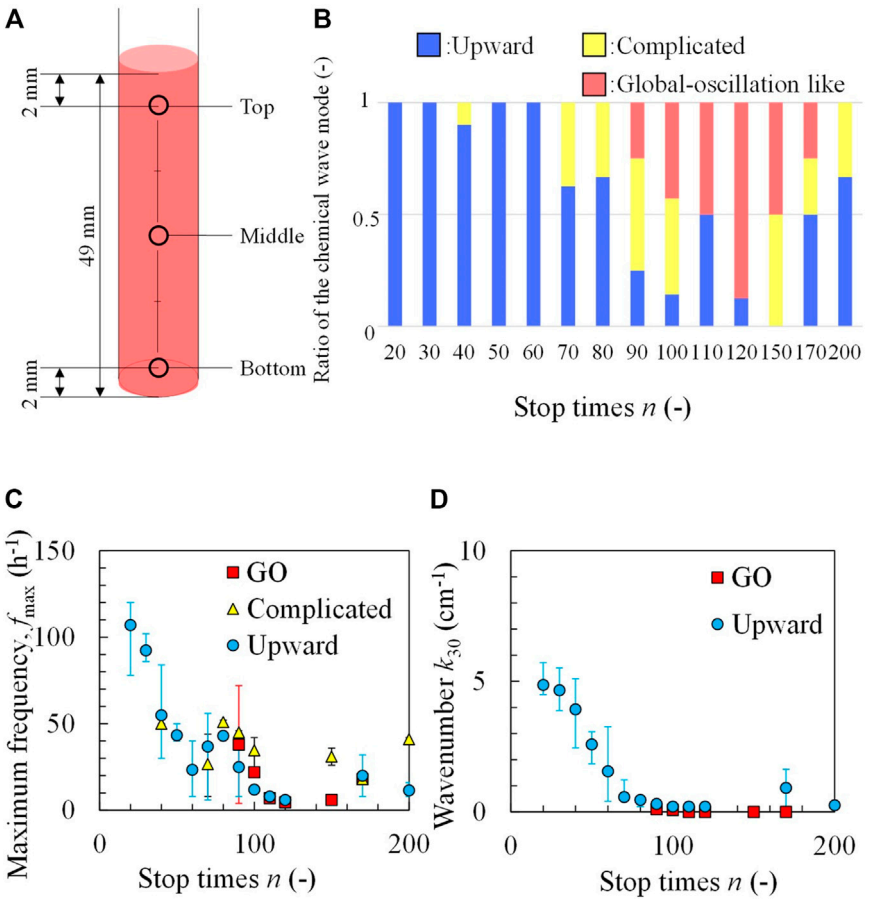

FIGURE 3 | Classification of the wave patterns by measuring the maximum frequency; **(A)** three measuring positions of the test tube, **(B)** ratio of three modes at different values of *n*. **(C)** Maximum frequency and **(D)** wavenumber as a function of *n*. GO indicates a global-oscillation-like pattern. The error bar represents the range covering the results of three times experiments.

points in the test tube as shown in **Figure 3A**, were measured. The results shown in **Figure 2** are presented in **Table 2**. The maximum in the three types of f (f_{max}) was determined (the measurement was performed 30 min after the completion of the rotation-and-stop process with different n values). The patterns were classified by identifying the position where f_{max} was observed; when the position of f_{max} was found at the bottom, the mode was identified as an upward chemical wave. When f_{max} appeared at the middle or top of the tube, the pattern was classified as complicated. A global-oscillation-like pattern appeared when the frequencies of the three points were the same. The classification made by this method was in good agreement with that of visual observation, as shown in **Figure 2**. In this study, the classification of wave patterns was achieved by measuring the f_{max} to avoid human subjectivity. **Figure 3B** shows the ratio of the three modes obtained for each value of n. The upward chemical wave was found to be dominant for $n \leq 60$. Complicated and global-oscillation-like patterns appeared at a higher n value. **Figure 3C** shows the f_{max}, as a function of n. It was observed that f_{max} decreased with increasing n.

TABLE 2 | Frequencies of chemical oscillations, f at three different positions of the tube for n values of 20–170 (**Figure 2**).

n (–)	Top (h^{-1})	Middle (h^{-1})	Bottom (h^{-1})	Mode
20	4	42	114	Upward
50	12	30	40	Upward
70	40	44	52	Upward
90	4	6	8	Upward
90	46	42	42	Complicated
90	72	72	72	Global-oscillation like
100	38	38	24	Complicated
170	18	18	18	Global-oscillation like

These experimental results show that the upward chemical waves with higher f_{max} appeared for lower values of n. The upward chemical wave indicates that the lower part of the test tube is the source of the chemical oscillation. Therefore, at $n \leq 60$ (where the upward wave dominated), the highest frequency oscillator is generated at the lower part of the test tube because the oscillator with the highest frequency dominates the entire solution. At the lower part of the test tube, the ratio

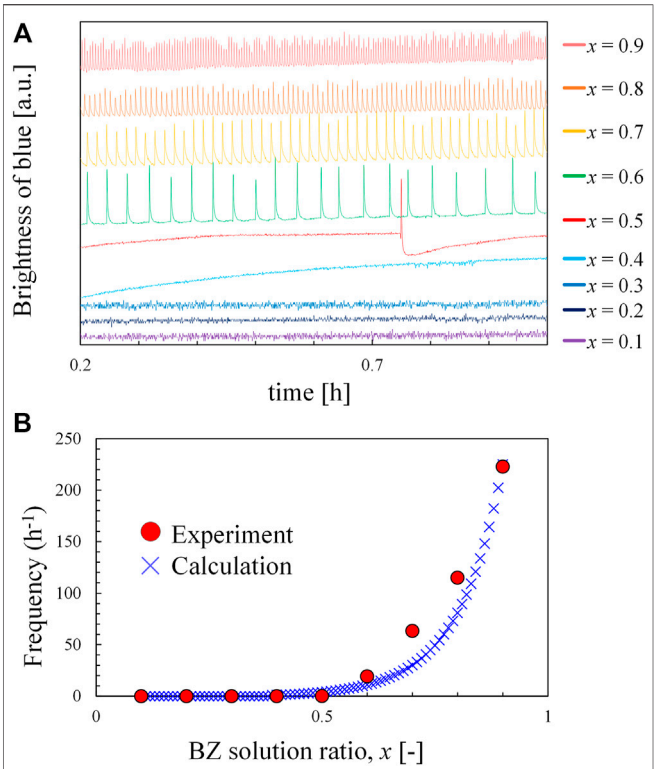

FIGURE 4 | Behavior of the mixture of BZ solution and ferroin solution in a batch reactor; **(A)** time developments of the blue brightness of the mixture with BZ solution ratio, *x* and **(B)** oscillation frequency of mixture as a function of *x*.

of BZ solution to the local solution of the BZ to the ferroin solutions was estimated to be larger owing to the mixing process using the rotation-and-stop method, as shown in **Figure 1D**. The worse the mixing (the smaller the *n* values), the larger the ratio of BZ solution.

To understand the effect of the ratio of BZ solution on the frequency of waves, another experiment was performed, where the oscillation frequency of the *x*: (1-*x*) volumetric mixture of BZ and ferroin solutions was measured in a batch reactor with a magnetic stirrer. **Figure 4A** shows that the global oscillation was observed in the range of $x \geq 0.5$, and **Figure 4B** indicates that the frequency is higher at a larger *x* value (i.e., BZ-rich solution). The BZ-rich portion in the lower part of the test tube generated a chemical wave with a higher frequency to dominate the entire solution. This led to the upward chemical wave in the test tube. The solution approached a uniform mixture with an increase in *n*, and the frequencies at different locations approached each other. BZ reactions with the same frequency in the entire solution form a global oscillation. This phenomenon agrees with our experimental result where a global-oscillation-like pattern appeared at extremely large *n* values. However, in an actual experiment, an imperfection in mixing may exist even at larger *n* values. Owing to this imperfection, the local frequencies may differ slightly and the close frequencies form a complicated pattern. Therefore, complicated and global-oscillation-like patterns appear at a larger *n* value, where f_{max} is small because of better mixing. The *x*-values of the oscillators decreased and approached $x = 0.5$ for larger *n* values. This agrees with the results shown in **Figure 3B**. As shown in **Figure 4A**, the oscillation periods during 1 h batch experiment are almost the same. Furthermore, the time required for 200 times of rotation and stop (the maximum value of in the experiment) is less than 20 min. Therefore, the reactants remain sufficiently after the rotation and stop procedure, and the consumption of the reactants does not affect the result.

Apart from frequency, the wavenumber was also counted (k_{30}) 30 min after the rotation-stop procedure. For the upward wave, the wavenumber was calculated from the number of blue lines at **Figure 2A** divided by the solution height (4.9 cm). For the global-oscillation-like pattern, the number of wave crests was one or zero in the snapshot of 30 min; hence, k_{30} was calculated to be 0.20 or 0 cm^{-1}. For complicated patterns, the wavenumber was not counted because of its complexity. **Figure 3D** shows that k_{30} decreased to an extremely small value with an increase in *n*. Both the frequency and wavenumber exhibited a similar trend. This result suggests that the inhomogeneity in mixing (incompleteness of mixing) can be estimated by the frequency and/or wavenumber of the chemical wave.

4 NUMERICAL CALCULATION USING THE ROVINSKY-ZHABOTINSKY MODEL

The numerical calculation was performed employing the RZ model [2] to study the BZ reaction kinetics. This model has been developed for the ferroin-catalyzed BZ reaction. The solution is not one-dimensional strictly, because the three-dimensional pattern is observed (**Figure 2B** or **Supplementary Video S1B**). However, both the upward wave and the global-oscillation-like pattern may be expressed by the one-dimensional coordinate. Here, therefore, one-dimensional reaction-diffusion equations are used and solved numerically. The original RZ model is proposed in a dimensionless form, where the dimensionless time τ is scaled by the initial concentration of the reactant and reaction rate constants. In the present calculation, each position in a test tube had a different initial concentration of reactants; hence, we used equations with actual dimensions:

$$R_U(U, V) = k_1 H_0 A_0 U - 2k_4 H_0 U^2 - \left\{ \frac{qK_8 B_0 V}{H_0 (F_0 - V)} + \frac{k_{12} B_0}{2} \right\} \frac{k_5 H_0 U - k_7 H_0 A_0}{k_5 H_0 U + k_7 H_0 A_0} \quad (1)$$

$$R_V(U, V) = 2k_1 H_0 A_0 U - \frac{k_8 B_0 V}{H_0 (F_0 - V)} \quad (2)$$

$$\frac{\partial U}{\partial t} = D_U \frac{\partial^2 U}{\partial x^2} + R_U(U, V) \quad (3)$$

$$\frac{\partial V}{\partial t} = D_V \frac{\partial^2 V}{\partial x^2} + R_V(U, V) \quad (4)$$

TABLE 3 | Tuned values of reaction and diffusion constants.

k_1 ($M^{-2}\cdot s^{-1}$)	k_4 ($M^{-2}\cdot s^{-1}$)	k_5 ($M^{-2}\cdot s^{-1}$)	k_7 ($M^{-2}\cdot s^{-1}$)	K_8 ($M\cdot s^{-1}$)	k_{12} (s^{-1})	q (–)	D_U ($cm^2\cdot s^{-1}$)	D_V ($cm^2\cdot s^{-1}$)
9.5	8×10^4	1.5×10^7	5	0.4×10^{-5}	1.5×10^{-6}	0.5	1.5×10^{-5}	0.9×10^{-5}

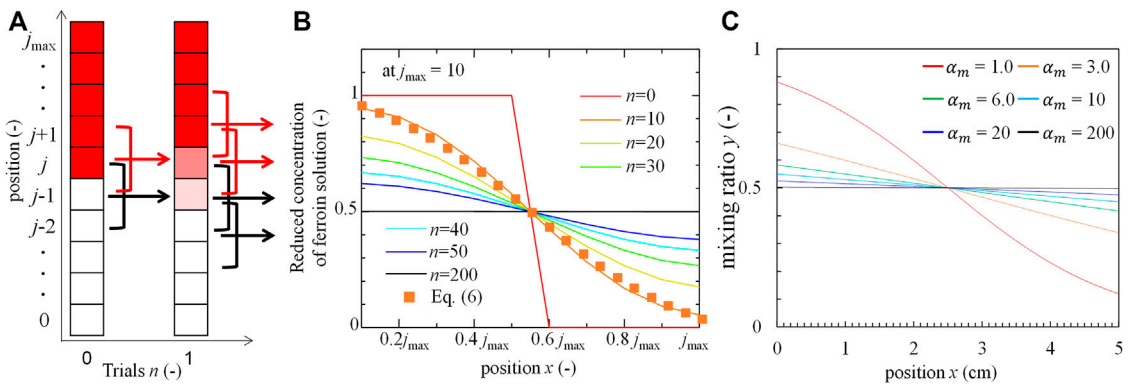

FIGURE 5 | Mixing model and distributions. **(A)** Schematic of the model (the arrows indicate that three portions mix into one region), **(B)** Distribution of ferroin concentration at each trial obtained from the model. **(C)** The ratio of BZ solution to the local solution with s in calculation fit by hyperbolic tangent function.

where U and V correspond to the concentrations of $HBrO_2$ and ferriin, respectively. t and x denote time and position, respectively. D_U and D_V are the diffusion constants for U and V, respectively [3]. k_1, k_4, k_5, k_7, k_{12}, and K_8 are reaction rate constants. The NaBr concentration was maintained at a steady state [2]. A_0, B_0, F_0, and H_0 correspond to the initial concentrations of $NaBrO_3$, malonic acid, ferroin, and protons, respectively, which all were approximated as constants owing to their excess amount in solution throughout the reaction. Actually, A_0, B_0, F_0, and H_0 diffuse obeying their concentration gradient, but the diffusion length within 30 min is approximately 1 mm ($\sim \sqrt{10^{-5} cm^2/s \cdot 1800\, s}$). On the other hand, the small changes in U and V by diffusion dramatically affect the reaction kinetics, because they are directly related to the autocatalytic processes; their diffusion terms are required for the chemical wave generation. Therefore, the diffusion terms only for U and V are taken into account in **Eqs 3**, **4**. A_0, B_0, F_0, and H_0 depend on the height (position) of the test tube. In the present experiment, stock solutions of BZ and ferroin (compositions shown in **Table 1**) were poured into a test tube and mixed gradually. The concentrations of each constituent in the stock solution are defined as notations with subscript S. Therefore, A_S, B_S, and H_S correspond to the concentrations of $NaBrO_3$, malonic acid, and protons in the BZ solution, respectively. F_S corresponds to the ferroin concentration in the ferroin solution. In a batch reactor experiment, the BZ and ferroin solutions were mixed in the volumetric ratio x:(1–x). Then, the initial concentrations A_0, B_0, H_0, and F_0 were calculated by x A_S, x B_S, x H_S, and (1–x) F_S, respectively. The blue curve in **Figure 4B** is the frequency calculated using **Eqs 1–4** using these initial concentrations and ignoring diffusion terms (perfect mixing is assumed). The calculated results were in good agreement with the experimental results. The tuned constant values shown in **Table 3** are in the same order as those reported in the literature [2,3] except k_1, and fine-tuning is provided to obtain a better agreement in **Figure 4B**.

During the rotation-and-stop method, A_0, B_0, H_0 and F_0 in a test tube were calculated by y A_S, y B_S, y H_S, (1- y) F_S, where y is the ratio of BZ solution of the two solutions at a particular height (position) of the test tube for a certain value of n. Thus, to estimate y, the height and n are required.

In the rotation-and-stop method, only the regions close to the interface of the two solutions are mixed by a single rotation-stop cycle. This elementary step was repeated several times. Therefore, the mixing achieved by this procedure can be estimated by integrating the local mixing states. The mixing process in this study can be modelled as shown in **Figure 5A**. The mixing by the single rotation and stop process is restricted within a small region where the collision between the solution element and the tube wall induces the local mixing. Here, the small region is evaluated as approximately one-tenth of the solution height. The volumetric ratio of BZ solution is expressed as $y_{n,\,j}$, where n and j represent the stop times and positions, respectively. In the initial state is expressed by (to express perfect separation): $y_{0,\,j} = 0$ at $j \geq j_{max}/2$ and $y_{0,\,j} = 1$ at $j < j_{max}/2$ (the smaller $y_{n,\,j}$ is colored red in **Figure 5A**). The ratio of BZ solution at position j after a single rotation stop is calculated as

$$y_{n+1,\,j} = \left(y_{n,\,j+1} + y_{n,\,j} + y_{n,\,j-1}\right)/3 \tag{5}$$

Figure 5B shows $y_{n,\,j}$ after n rotations-stop cycles. $y_{n,\,j}$ approached a uniform distribution as n increased. A transient distribution (the dotted curve), which was approximately well correlated to the line of $n = 10$ at **Figure 5B**, is calculated using the hyperbolic tangent function:

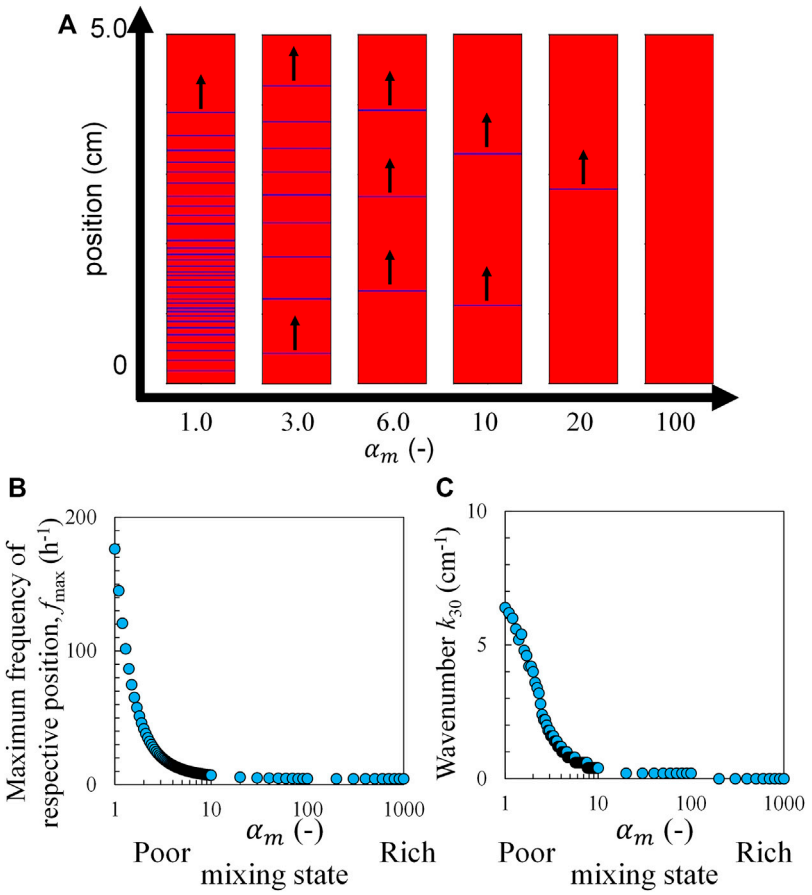

FIGURE 6 | Calculation results based on the RZ model and the concentration distribution with **Eq. 6**, **(A)** the pseudo-colored image of the chemical wave, **(B)** maximum frequency, and **(C)** wavenumber as a function of *s* 30 min after mixing. The black arrows indicate the travel direction.

$$y_{n,j} = y(x) = \frac{1}{2}\left\{1 - tanh\left(\frac{x - \frac{h}{2}}{\alpha_m \cdot \frac{h}{2}}\right)\right\} \tag{6}$$

where x and h (instead of j_{max}) denote the position and length of the system, respectively. The mixing index, α_m expresses the degree of mixing and is correlated with the stop time n in the experiment, where an increase in α_m corresponds to an increase in n. **Figure 5C** shows the concentration distributions of the BZ solution ingredients at each α_m. For example, $\alpha_m \cong 0$ and ∞, indicate that the two solutions are completely separated and mixed, respectively.

In the experiment, a blue color appeared in the ferriin-rich part formed by the oxidation of ferroin. Therefore, in the calculation, the region with the highest V (highest concentration of ferriin) is colored blue. **Figure 6A** shows the pseudo-colored image created by this method at each α_m value 30 min after mixing. The upward chemical wave was reproduced as shown in **Figure 6A** (waves traveling to larger x-values, see **Supplementary Video S2**). **Figures 6B,C** show the calculated f_{max} and k_{30} values, respectively. The calculation was performed using the same method as that applied for the experimental results. The results indicated that f_{max} and k_{30} decreased with an increase in α_m. Because α_m is positively correlated with n, this trend is qualitatively identical to those shown in **Figures 3C,D**. At $\alpha_m > 100$, k_{30} reached zero, and f_{max} took a small non-zero value. This represents the global-oscillation-like pattern. The global-oscillation-like pattern is observed only at a sufficiently large n value in the experiment, which is reproduced by this calculation.

5 CONCLUSION

The stepwise mixing of two solutions in a test tube was achieved using the rotation-and-stop method. The BZ reaction exhibited three modes: upward chemical waves, complex patterns, and global-oscillation-like patterns in this mixing process. These patterns were visible to the naked eye and distinguished by determining the position of the highest oscillation frequency in the test tube. A transition from an upward chemical wave to complicated and global-oscillation-like patterns (which signifies the degree of mixing) was observed with an increase in the number of stops. An improved mixing state was achieved with a relatively low frequency and wavenumber. The results were explained by a numerical calculation using the RZ model and an

appropriate concentration distribution. The relationship between the degree of mixing and the pattern produced in the BZ reaction will help quantify the degree of mixing using the spatiotemporal pattern. It is looking forward that the investigation of the accuracy of measurement with a comparison with the other method and that the developed quantification by the measurement of the chemical wave propagating speed.

DATA AVAILABILITY STATEMENT

The original contributions presented in the study are included in the article/**Supplementary Material**, further inquiries can be directed to the corresponding author.

AUTHOR CONTRIBUTIONS

YO performed all experiments and calculations. YO, EO, DY, and AS conceived the study. YO, DY, and AS used a physicochemical model. YO, EO, DY, SN, and AS have discussed this research.

ACKNOWLEDGMENTS

We thank Mr. Kun Lin for giving an opportunity of this study. YO acknowledges financial support from JSPS KAKENHI Grant Numbers 20K22335.

SUPPLEMENTARY MATERIAL

The Supplementary Material for this article can be found online at: https://www.frontiersin.org/articles/10.3389/fphy.2022.895824/full#supplementary-material

Supplementary Video S1 | Experimental results: **(A)** upward chemical wave, **(B)** complicated pattern, and **(C)** global-oscillation-like pattern. The speed was 200 times faster than the real speed.

Supplementary Video S2 | Calculated pseudo-color image of the chemical wave. The speed was 150 times faster than the real speed.

REFERENCES

1. Zaikin AN, Zhabotinsky AM. Concentration Wave Propagation in Two-Dimensional Liquid-phase Self-Oscillating System. *Nature* (1970) 225: 535–7. doi:10.1038/225535b0
2. Zhabotinsky AM, Rovinsky AB. Mechanism and Nonlinear Dynamics of an Oscillating Chemical Reaction. *J Stat Phys* (1987) 48:959–75. doi:10.1007/bf01009526
3. Miike H, Mori Y, Yamaguchi T. *Hiheikoukeinokagaku* III. Tokyo: Kodansha (1997).
4. Yoshikawa K. *Hisenkeikagaku*. Tokyo: Japan Scientific Societies Press. (1992).
5. Vanag VK, Melikhov DP. *J Phys Chem* (1995) 99:4817372. doi:10.1021/j100048a011
6. Hashimoto S, Chikamochi Y, Inoue Y. Visualization of Partially Mixed Region by Use of Periodical Reaction. *Chem Eng Sci* (2012) 80:30–8. doi:10.1016/j.ces.2012.05.053
7. Ruoff P. Excitations Induced by Fluctuations: an Explanation of Stirring Effects and Chaos in Closed Anaerobic Classical Belousov-Zhabotinskii Systems. *J Phys Chem* (1993) 97(24):6405–11. doi:10.1021/j100126a014
8. Menzinger M, Jankowski P. Heterogeneities and Stirring Effects in the Belusov-Zhabotinskii Reaction. *J Phys Chem* (1986) 90(7):1217–9. doi:10.1021/j100398a001
9. Zong C, Gao Q, Wang Y, Feng J, Mao S, Zhang L. Period-doubling and Chaotic Oscillations in the Ferroin-Catalyzed Belousov-Zhabotinsky Reaction in a CSTR. *Sci China Ser B* (2007) 50(2):205–11. doi:10.1007/s11426-007-0026-8
10. Rachwalska M, Kawczyński AL. Period-Adding Bifurcations in Mixed-Mode Oscillations in the Belousov–Zhabotinsky Reaction at Various Residence Times in a CSTR. *J Phys Chem A* (2001) 105:7885–8. doi:10.1021/jp0108059
11. Dutt AK, Mueller SC. Effect of Stirring and Temperature on the Belousov-Zhabotinskii Reaction in a CSTR. *J Phys Chem* (1993) 97(39):10059–63. doi:10.1021/j100141a027
12. Budroni MA, Masia M, Rustici M, Marchettini N, Volpert V. Bifurcations in Spiral Tip Dynamics Induced by Natural Convection in the Belousov-Zhabotinsky Reaction. *J Chem Phys* (2009) 130(2):024902. doi:10.1063/1.3050356
13. Budroni MA, Calabrese I, Miele Y, Rustici M, Marchettini N, Rossi F. Control of Chemical Chaos through Medium Viscosity in a Batch Ferroin-Catalysed Belousov-Zhabotinsky Reaction. *Phys Chem Chem Phys* (2017) 19(48): 32235–41. doi:10.1039/c7cp06601e
14. Berg JM, Tymoczko JL, Stryer L. *Biochemistry*. 5th ed. New York, NY: W. H. Freeman (2002).
15. Yoshida R. Design of Self-Oscillating Gels and Application to Biomimetic Actuators. *Sensors* (2010) 10:1810–22. doi:10.3390/s100301810
16. Aihara R, Yoshikawa K. Size-Dependent Switching of the Spatiotemporal Structure between a Traveling Wave and Global Rhythm. *J Phys Chem A* (2001) 105:8445–8. doi:10.1021/jp010908r
17. Suematsu NJ, Mori Y, Amemiya T, Nakata S. Oscillation of Speed of a Self-Propelled Belousov-Zhabotinsky Droplet. *J Phys Chem Lett* (2016) 7:3424–8. doi:10.1021/acs.jpclett.6b01539
18. Sumino Y, Kitahata H, Yoshikawa K. Mode Selection in the Spontaneous Motion of an Alcohol Droplet. *Phys Rev E* (2005) 72:4. doi:10.1103/physreve.72.041603
19. Kuze M, Hiranishi Y, Okamoto Y, Shioi A, Nakata S. Construction of Nitrogen-containing Polycyclic Aromatic Compounds by Intramolecular Oxidative C-H/C-H Coupling of Bis(9H-carbazol-9-yl)benzenes and Their Properties. *Chem Lett* (2019) 48:9. doi:10.1246/cl.190292
20. Yoshimoto M, Yoshikawa K, Mori Y. Coupling among three chemical oscillators: Synchronization, phase death, and frustration. *Phys Rev E* (1993) 47:2. doi:10.1103/physreve.47.864
21. Yashin VV, Balazs AC. Chemomechanical synchronization in heterogeneous self-oscillating gels. *Phys Rev E* (2008) 77:046210. doi:10.1103/physreve.77.046210
22. Cherkashin AA, Vanag VK. Self-Organization Induced by Self-Assembly in Microheterogeneous Reaction-Diffusion System. *J Phys Chem B* (2017) 121: 2127–31. doi:10.1021/acs.jpcb.6b12089
23. Suzuki D, Sakai T, Yoshida R. Self-Flocculating/Self-Dispersing Oscillation of Microgels. *Angew Chem* (2008) 120:931–4. doi:10.1002/ange.200703953
24. Lagzi I, Kowalczyk B, Wang D, Grzybowski BA. Nanoparticle Oscillations and Fronts. *Angew Chem Int Edition* (2010) 49:8616–9. doi:10.1002/anie.201004231
25. Matsushita M, Nakata S, Kitahata H. Characteristic Features in the Collision of Chemical Waves Depending on the Aspect Ratio of a Rectangular Field. *J Phys Chem A* (2007) 111(26):5833–8. doi:10.1021/jp068207n

26. Budroni MA, Lemaigre L, Escala DM, Muñuzuri AP, De Wit A. Spatially Localized Chemical Patterns Around an A + B → Oscillator Front. *J Phys Chem A* (2016) 120(6):851–60. doi:10.1021/acs.jpca.5b10802
27. Budron MA. *Phys Rev E* 2016, 93(6):062207.

Conflict of Interest: The authors declare that the research was conducted in the absence of any commercial or financial relationships that could be construed as a potential conflict of interest.

Publisher's Note: All claims expressed in this article are solely those of the authors and do not necessarily represent those of their affiliated organizations, or those of the publisher, the editors and the reviewers. Any product that may be evaluated in this article, or claim that may be made by its manufacturer, is not guaranteed or endorsed by the publisher.

frontiers | Frontiers in Physics

ORIGINAL RESEARCH
published: 09 May 2022
doi: 10.3389/fphy.2022.860419

Spatial and Temporal Oscillations of Surface Tension Induced by an A + B → C Traveling Front

Reda Tiani and Laurence Rongy**

Nonlinear Physical Chemistry Unit, Université libre de Bruxelles (ULB), Brussels, Belgium

This work describes a new mechanism for the emergence of oscillatory dynamics driven by the interaction of hydrodynamic flows and reaction-diffusion processes with no autocatalytic feedback nor prescribed hydrodynamic instability involved. To do so, we study the dynamics of an A+ B → C reaction-diffusion front in the presence of chemically-driven Marangoni flows for arbitrary initial concentrations of reactants and diffusion coefficients of all species. All the species are assumed to affect the solution surface tension thereby inducing Marangoni flows at the air-liquid interface. The system dynamics is studied by numerically integrating the incompressible Navier-Stokes equations coupled to reaction-diffusion-convection equations for the three chemical species. We report spatial and temporal oscillations of surface tension triggered by differential diffusion effects of surfactant species coupled to the chemically-induced Marangoni effect. Such oscillations are related to the discontinuous traveling of the front along the surface leading to the progressive formation of local extrema in the surface tension profiles as time evolves.

Keywords: A + B → C reaction front, bimolecular front, reaction-diffusion-convection system, Marangoni flow, surface tension, differential diffusion, chemo-hydrodynamics

OPEN ACCESS

Edited by:
Federico Rossi,
University of Siena, Italy

Reviewed by:
Philip Trevelyan,
University of South Wales, United Kingdom
Saikat Mukherjee,
University of Minnesota Twin Cities, United States

****Correspondence:***
Reda Tiani
reda.tiani@ulb.be
Laurence Rongy
laurence.rongy@ulb.be

Specialty section:
This article was submitted to Physical Chemistry and Chemical Physics, a section of the journal Frontiers in Physics

Received: *22 January 2022*
Accepted: *02 March 2022*
Published: *09 May 2022*

Citation:
Tiani R and Rongy L (2022) Spatial and Temporal Oscillations of Surface Tension Induced by an A + B → C Traveling Front. Front. Phys. 10:860419. doi: 10.3389/fphy.2022.860419

1 INTRODUCTION

Traveling fronts are recurrent examples of spatio-temporal structures observed in Nature [1–5]. In the context of chemistry, fronts are localized reactive interfaces driven by reaction-diffusion (RD) processes that may exhibit unique dynamical behaviors. For instance, for bimolecular fronts, universal time scaling behaviors of the front properties are noted [6–8] and, for autocatalytic fronts, where a reaction product (the autocatalytic species) catalyzes its own production, spatio-temporal chaos may be observed due to front instabilities [9].

Front propagation is typically influenced by spontaneous hydrodynamic motions, typically buoyancy-driven and/or surface tension-driven (Marangoni) flows, arising from composition (solutal effects) and/or temperature (thermal effects) changes across the front [10, 11]. When such flows are driven across chemical fronts in horizontally oriented-systems (e.g., in Petri dishes or thin layers), many scenarios have been shown to lead to oscillatory phenomena (see Tiani et al. [10] and references therein). In particular, in the presence of Marangoni flows driven across isothermal autocatalytic fronts, transient oscillations of concentration and fluid velocity can be seen before the long-time asymptotic dynamics is reached when the Marangoni number of the autocatalytic species, quantifying its influence on surface tension, is sufficiently large [12]. The antagonistic coupling of surface tension-driven and buoyancy-driven flows can also induce an unsteady periodic behavior of autocatalytic isothermal fronts [13]. Such oscillations, together with oscillations in the temperature field, have also been observed to emerge across exothermal autocatalytic fronts when Marangoni or

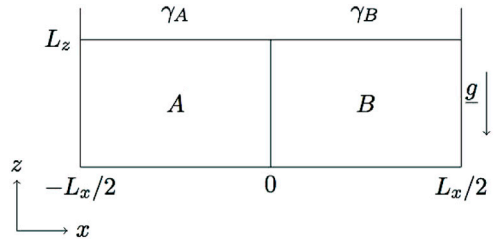

FIGURE 1 | Sketch of the system. Two aqueous solutions of reactants A and B of concentrations a_0 and b_0 and of surface tension γ_A and γ_B, respectively, are initially separated in space in a 2D domain of length L_x and height L_z. The species diffuse at rates D_a and D_b.

buoyancy-driven flows are at play due to antagonistic contribution of thermal and solutal effects [13, 14]. The interplay of the oscillating Belousov-Zhabotinky reaction around an A+ B → oscillator configuration with buoyancy forces can also induce new chemo-hydrodynamic instabilities leading to pulsatile fingering and plumes as well as rising or sinking Turing spots [15]. When the same localized oscillating reaction is assumed to change the viscosity of the solutions involved, viscous fingering instabilities can be triggered by the reaction and can induce oscillations in situations that are stable in the absence of chemo-hydrodynamic coupling [16]. While most works on chemical oscillations focused on autocatalytic systems, Budroni et al. recently showed that a transient oscillatory dynamics can be triggered in the presence of Marangoni-driven flows across A+ B → C bimolecular fronts for equal diffusion coefficients and initial concentrations of all species, provided that the surface tension changes during the reaction are large enough [17–19]. In that case, such oscillations are explained by the competition of Marangoni convection and the vertical RD relaxation of the front. The combination of both Marangoni and buoyancy-driven flows has further been observed to lead to sustained oscillations around such bimolecular fronts [17–19]. In the absence of reaction, spontaneous oscillations can also be observed due to Marangoni instability [20–25]. A simple example is the one of a surfactant droplet dissolving under the air/water interface [22]. A solutal Marangoni instability can develop in this system either as steady convection or as oscillations.

In this work, we report an additional mechanism that may lead to transient oscillations and is a unique property of reactive systems where differential diffusion of chemical species combines with chemically-driven Marangoni convection. The mechanism we describe does not require any feedback loop nor prescribed hydrodynamic instability. As detailed below, it is also fundamentally different from the one described by Budroni et al. when the species diffuse at the same rate [17,18], since it does not involve any competition between Marangoni stresses and RD processes as described by the authors and leads to oscillations in the surface tension profiles.

The article is organized as follows. In **Section 2**, the model system and related governing equations are presented. In **Section 3**, we describe the emergence of spatio-temporal oscillations of surface tension observed by numerically integrating the governing equations for arbitrary diffusion coefficients and initial concentrations of reactants. Next, in **Section 4**, we illustrate the control of the oscillatory dynamics as a function of the model parameters. Eventually, conclusions and prospects are drawn in **Section 5**.

2 MODEL

The model system consists of a horizontally orientated system (see **Figure 1**), in which an aqueous solution containing a reactant A, of concentration a_0, is placed beside an aqueous solution containing a reactant B, of concentration b_0, along a vertical contact line at time $t = 0$. The species A and B diffuse at rates D_a and D_b, respectively. The two miscible reacting solutions meet at $t > 0$ and react according to the isothermal A+ B → C reaction to produce a third species C. The resulting localized region of space where C is produced is called the reaction front. All the species are supposed to affect the surface tension of the solution, therefore inducing gradients of surface tension leading to Marangoni flows. We assume that the air/liquid interface is not deformable and neglect the evaporation processes during the chemical reaction, so that we do not address the dynamics in the air layer. In order to focus on surface tension effects, we also consider the solution density as constant in space and time preventing any buoyancy-driven convection in solution.

The dimensional governing equations for the evolution of the concentrations of the reactants $\hat{a}, \hat{b}$ and of the product $\hat{c}$ in this system are obtained by coupling the reaction-diffusion-convection (RDC) equations for the chemical concentrations to the incompressible Navier-Stokes equations for the dimensional velocity field $\underline{\hat{v}} = (\hat{u}, \hat{w})$, i.e.,

$$\frac{\partial \hat{a}}{\partial \hat{t}} + \underline{\hat{v}}.\underline{\hat{\nabla}}\,\hat{a} = D_a\hat{\nabla}^2\hat{a} - k\hat{a}\hat{b}, \tag{1}$$

$$\frac{\partial \hat{b}}{\partial \hat{t}} + \underline{\hat{v}}.\underline{\hat{\nabla}}\,\hat{b} = D_b\hat{\nabla}^2\hat{b} - k\hat{a}\hat{b}, \tag{2}$$

$$\frac{\partial \hat{c}}{\partial \hat{t}} + \underline{\hat{v}}.\underline{\hat{\nabla}}\,\hat{c} = D_c\hat{\nabla}^2\hat{c} + k\hat{a}\hat{b}, \tag{3}$$

$$\frac{\partial\, \underline{\hat{v}}}{\partial \hat{t}} + \left(\underline{\hat{v}}.\underline{\hat{\nabla}}\right)\underline{\hat{v}} = \nu\hat{\nabla}^2\,\underline{\hat{v}} - \frac{1}{\rho_0}\,\underline{\hat{\nabla}}\,\hat{p} + \underline{g}, \tag{4}$$

$$\mathrm{div}\ \underline{\hat{v}} = 0, \tag{5}$$

or, in dimensionless form,

$$\frac{\partial a}{\partial t} + \underline{v}.\underline{\nabla}\,a = \nabla^2 a - ab, \tag{6}$$

$$\frac{\partial b}{\partial t} + \underline{v}.\underline{\nabla}\,b = \delta_b\nabla^2 b - ab, \tag{7}$$

$$\frac{\partial c}{\partial t} + \underline{v}.\underline{\nabla}\,c = \delta_c\nabla^2 c + ab, \tag{8}$$

$$\frac{\partial\, \underline{v}}{\partial t} + \left(\underline{v}.\underline{\nabla}\right)\underline{v} = S_c\left(\nabla^2\,\underline{v} - \underline{\nabla}\,p\right), \tag{9}$$

$$\mathrm{div}\ \underline{v} = 0, \tag{10}$$

where $\delta_{b,c} = D_{b,c}/D_a$ are the two diffusion coefficient ratios, D_c is the diffusion coefficient of species C, and $S_c = (\nu/D_a)$ is the Schmidt number (fixed to 10^3 as typical for small species at room temperature in water), with $\nu = (\mu/\rho_0)$ the kinematic viscosity, μ the dynamic viscosity and ρ_0 the solution density. To non-dimensionalize the problem, as in Tiani and Rongy [26], we have used the characteristic scales of the reaction-diffusion system: for time, $\tau_c = (1/ka_0)$ (with k the reaction rate constant), length $L_c = \sqrt{D_a\tau_c}$, velocity $U_c = (L_c/\tau_c) = \sqrt{D_a/\tau_c}$, concentration a_0. The pressure is scaled by $p_c = (\mu/\tau_c) = \rho_0 S_c D_a/\tau_c$ and a new dimensionless pressure gradient incorporating the hydrostatic pressure gradient is defined as $\underline{\nabla}\, p = \underline{\nabla}\, \hat{p}/p_c - \rho_0 L_c\, \underline{g}\,/p_c$, with $\underline{g} = (0, -g)$ the gravity acceleration.

The dimensionless initial conditions are separated reactants such that, $\forall z$, $a = 1$, $b = 0$, $c = 0$, for $x < 0$ and $a = 0$, $b = \beta$, $c = 0$, for $x \geq 0$, where $\beta = b_0/a_0$ is the ratio between the initial dimensional concentrations of B and A. The dimensionless conditions at boundaries of **Figure 1** are no-flux boundary conditions (BCs) for the chemical concentrations at each boundary of the domain. The BCs for the fluid velocity field at the rigid boundaries ($x = \pm L_x/2$ and $z = 0$) are no-slip conditions, $u = 0 = w$. At the free surface, we assume $w = 0$ and we use a Marangoni boundary condition for u derived from the tangential stress balance condition of the form, $\mu(\partial\hat{u}/\partial\hat{z}) = \partial\hat{\gamma}/\partial\hat{x}$ at the free surface [21, 27], or in dimensionless form,

$$\frac{\partial u}{\partial z} = -\sum_i M_i \frac{\partial c_i}{\partial x} \quad \text{at } z = L_z, \tag{11}$$

where L_x and L_z represent the dimensionless length and height of the system, respectively. In **Eq. 11**, the dimensionless solutal Marangoni number M_i of species $i = (a, b, c)$ which quantifies the influence of each chemical species on the solution surface tension, is defined as,

$$M_i = -\frac{1}{\mu}\sqrt{\frac{a_0}{D_a k}}\,\frac{\partial\hat{\gamma}}{\partial\hat{c}_i}, \tag{12}$$

where $\hat{\gamma}$ and $\hat{c}_i$ are the dimensional solution surface tension and concentration of solute i.

For sufficiently dilute solutions, the solution surface tension is expected to vary linearly with the concentrations. Then, we can write that $\hat{\gamma} = \hat{\gamma}_0 + \sum(\partial\hat{\gamma}/\partial\hat{c}_i)\hat{c}_i$, with $\hat{\gamma}_0$ the (dimensional) surface tension of the^i solvent ($\hat{c}_i = 0, \forall i$). Using **Eq. 12**, the dimensionless solution surface tension, which is defined as $\gamma = (\hat{\gamma} - \hat{\gamma}_0)/\hat{\gamma}_c$ where $\hat{\gamma}_c = p_c L_c$, therefore reads

$$\gamma(x,t) = -M_a a(x, L_z, t) - M_b b(x, L_z, t) - M_c c(x, L_z, t). \tag{13}$$

In **Eqs 12**, **13**, the Marangoni numbers are assumed positive, i.e., $M_{a,b,c} \geq 0$, to describe surfactants decreasing the surface tension of the solvent with $(\partial\hat{\gamma}/\partial\hat{c}_i) < 0, \forall i$. From **Eq. 13**, the surface tension of the initial pure A and B solutions therefore read, $\gamma_A = -M_a$ and $\gamma_B = -M_b\beta$, respectively.

The system dynamics is then obtained by numerically integrating the complete set of **Eqs 6–10** subjected to initial conditions and BCs specified above, with the numerical procedure described in Rongy and De Wit [12]. The length L_x is chosen sufficiently large so that the results are not affected by lateral boundary effects on the time of interest, typically $L_x = 350$.

3 SPATIO-TEMPORAL OSCILLATIONS OF SURFACE TENSION: MECHANISM

When the species diffuse at different rates, oscillations are found in the surface tension profiles for appropriate values of the model parameters (see **Figure 2**). Such oscillations emerge as local extrema that progressively form at different spatial positions in the surface tension profiles between γ_A and γ_B in the course of time. To explain the mechanism leading to such oscillations, we consider the simplest scenario when species A and B have the same influence on the solution surface tension, i.e. $M_a = M = M_b$, and we assume $\beta > 1$ so that $\gamma_B < \gamma_A$. However, the mechanism described below is universal and does not depend on this particular choice.

In the short-time limit, the concentration of C is negligible so that we can neglect its influence on surface tension and the related profiles are nonmonotonic with a global minimum (see **Figure 2A** at time $t = 1$). In this limit, from the pure diffusion equations, we can predict the profiles to admit two global extrema (a global maximum and a global minimum) (see reference Trevelyan et al. [28] for the analytical derivation of the corresponding RD profiles, along with the change of notation $\rho \leftrightarrow -\gamma$). We note that such a global maximum is also formed in the presence of convection but it cannot be seen on the considered scale in **Figure 2A** due to its negligible amplitude and thus plays no role on the system dynamics. The minimum drives two counterrotating convective rolls, a main convective roll that turns counterclockwise and is of much bigger intensity than the clockwise convective roll on the right (see **Figure 3** at time $t = 1$). Since species A diffuses faster than species B, we note that the main convective roll and surface tension profiles are asymmetric, i.e. more elongated on the side of A than of B. Such an asymmetric convective roll deforms the reaction front across the layer and the maximum production rate of C is found at the surface. As time increases, the effect of species C becomes important. In the reaction zone which is mainly located at the surface, the concentration of C increases. Since $M_c > M_a = M_b$, the reactants are replaced by the more surface-active product, reducing thereby the surface tension locally and leading to the formation of the first two local extrema (a local minimum and a local maximum) in the surface tension profiles (see **Figure 2A** at time $t = 5$). The formation of such extrema locally reduces the intensity of the flow and deforms the inner structure of the main convective roll so that two counterclockwise vortices are formed in the bulk (see **Figure 3** at time $t = 5$). Driven by the vortices, the reactants are transported from their reservoir along the surface at the spatial locations where the flow is the most intense. This generates a new intense reaction zone at the surface (around $x = -10$ in **Figure 3** at time $t = 15$) while the previous one (located around $x = 10$ in **Figure 3** at time $t = 15$) reduces in intensity. Inside the newly generated reaction zone, the concentration of C increases, locally reducing the surface tension and thereby inducing two additional local extrema. This

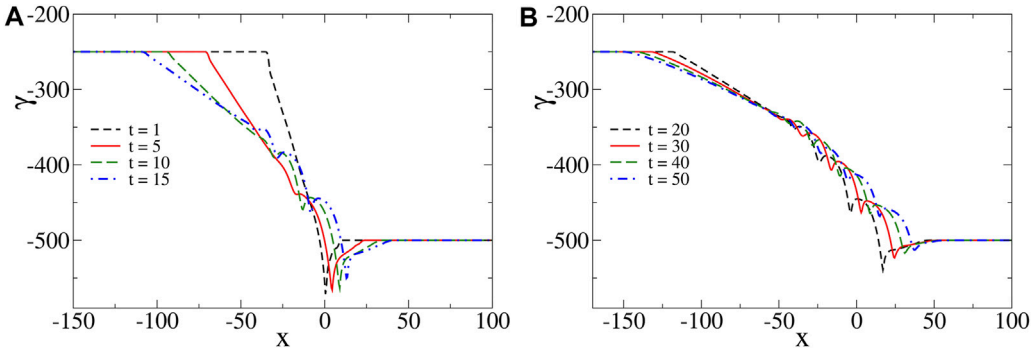

FIGURE 2 | Spatial oscillations of surface tension profiles at different times for $M_a = 250 = M_b$, $M_c = 500$, $\beta = 2$, $\delta_b = 0.25$, $\delta_c = 0.50$ and $L_z = 10$. Such profiles are separated in two plots, **(A,B)**, for clarity.

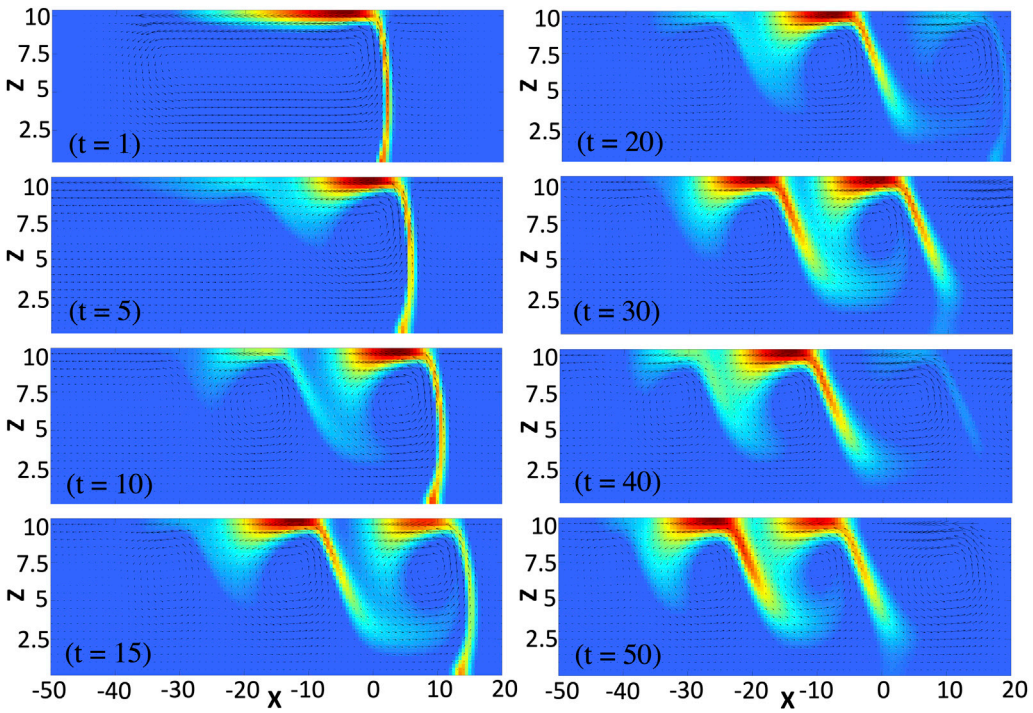

FIGURE 3 | Focus on the convective rolls centered on the reaction front at different times for the same parameters values as in **Figure 2**. The fluid velocity field is superimposed on a 2D plot of the production rate which ranges between its maximum value, $(ab)_{max}$ shown in red, and its minimum value, $(ab)_{min} = 0$, shown in blue. The front is mainly located at the surface and travels in the course of time discontinuously leading to oscillations in the surface tension profiles (cf: **Figure 2**). The velocity vectors are here tripled compared to their effective length to allow for a better visualization.

RDC process repeats itself progressively forming new intense reaction zones further away towards the left (around $x = -20$ and $x = -30$ at times $t = 30$ and $t = 50$, respectively) and leading to the observed oscillations in the surface tension profiles. Since the newly generated local minima in such profiles are less pronounced than the previous ones and that the profiles stretch in the course of time, the corresponding vortices are of weaker intensities. Eventually, this process always stops generating new local extrema after some time. In the long-time limit, when all the gradients of surface tension decrease with time, the monotonic properties of the surface tension profiles as predicted by the analysis of RD profiles are recovered Trevelyan et al. [28], here corresponding to two global extrema between γ_A and γ_B (e.g., when $L_z = 4$ and for same values of the other parameters as in **Figure 2**, the RD profiles properties are recovered numerically after a time of about $t = 40$. This time typically increases with the intensity of convection as detailed in **Section 4**.)

Thus, we deduce that oscillations in the surface tension profiles are the results of the subsequent formation of

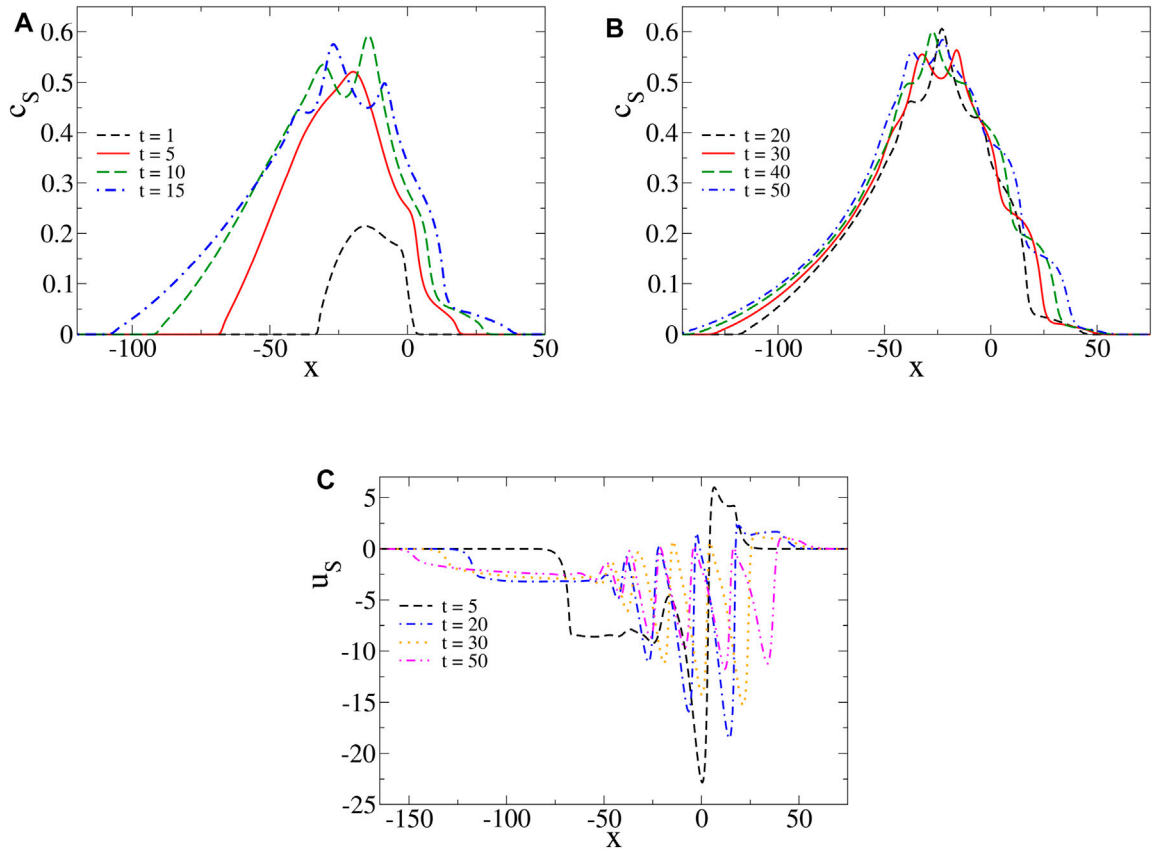

FIGURE 4 | (A,B) Product concentration c_S and **(C)** horizontal component of the fluid velocity field u_S, at the surface, at different times and for the same parameters values as in **Figure 2**. We note wave-like tails in the profiles of c_S and oscillations in the profiles of u_S.

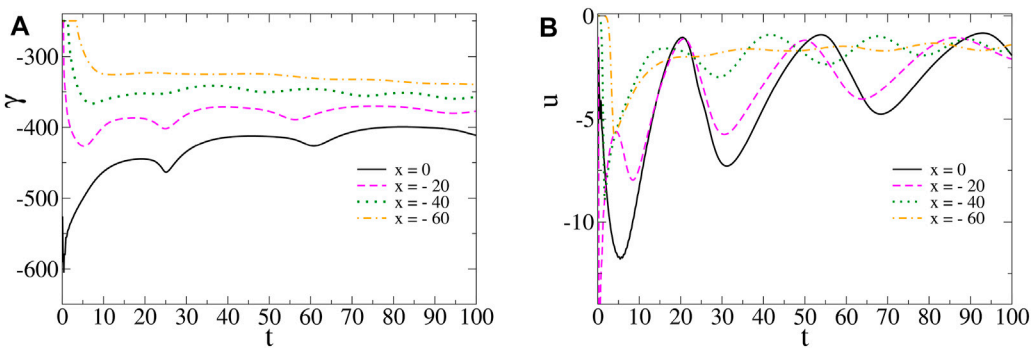

FIGURE 5 | (A) Surface tension $\gamma(x, t)$ and **(B)** horizontal component of the fluid velocity field $u(x, z, t)$ with $z = 0.90L_z$, as a function of time at various spatial locations and for the same parameters values as in **Figure 2**. Aperiodic temporal oscillations emerge and dampen in the course of time with reducing amplitudes as we consider spatial locations further away from the center.

segregated reaction zones along the surface. Each one of them is a source of C production that progressively reduces the surface tension locally as the reaction zones form in the course of time. Such oscillations naturally involve complex spatial dynamics of other observables, such as the product concentration at the surface (c_S) and the horizontal component of the velocity field evaluated at the surface (u_S) (see **Figure 4**). We note that the profiles of c_S have wave-like tails with multiple maxima located at positions close to the ones of the local minima in the surface tension profiles. For short times, the latter are nonmonotonic

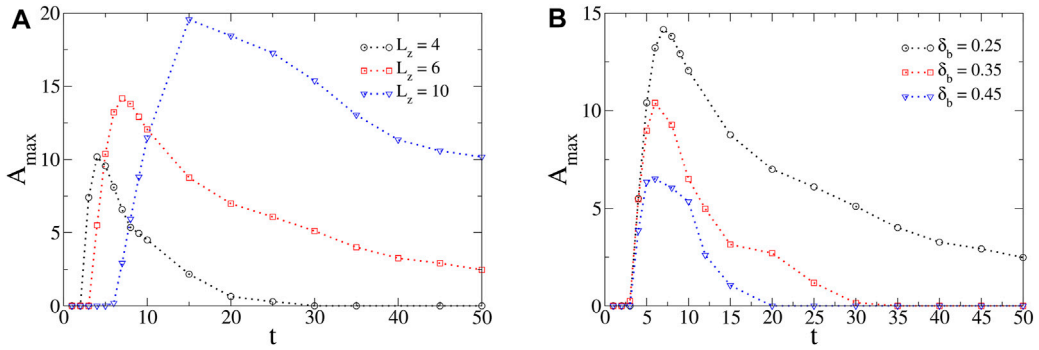

FIGURE 6 | Maximum amplitude A_{max} of oscillations in the course of time for different values of **(A)** L_z and **(B)** δ_b. Unless varied, the values of the model parameters are $M = 250$, $M_c = 500$, $\delta_b = 0.25$, $\delta_c = 0.50$, $\beta = 2$ and $L_z = 6$. When increasing L_z or decreasing δ_b, the maximum amplitude and duration of oscillations in the profiles of surface tension are increased.

with a global minimum and thus, the profiles of u_S have a negative and a positive part associated to the counterclockwise and clockwise convective rolls, respectively. As time evolves, the progressive formation of local extrema in the profiles of surface tension come along with oscillations in the profiles of u_S (u_S indeed oscillates with the gradients of surface tension according to the Marangoni boundary condition, **Eq. 12**), together with bulk vortices in the system as seen in **Figure 3**.

We note that the temporal oscillations of surface tension (**Figure 5A**) and horizontal velocity (**Figure 5B**) are aperiodic with irregular shapes and amplitudes. Such oscillations dampen in the course of time.

4 CONTROL OF THE OSCILLATORY DYNAMICS

As described in **Section 3**, the mechanism of oscillating surface tension profiles requires the front to be (mainly) located at the free surface and to be in motion along the surface. As a result, such oscillations are prevented in the symmetric case (i.e., when $\beta = 1$ and $\delta_b = 1$, $\forall$ M), where two convective rolls of identical intensity leads to a stationary front with surface tension profiles that admit either a global maximum or a global minimum (the symmetric case is described in reference Tiani and Rongy [26]). Hence, oscillations as in **Figure 2** can only be triggered in an asymmetric scheme (i.e., when $\beta \neq 1$ and/or $\delta_b \neq 1$).

If we arbitrary assume $\beta > 1$ (the reverse case $\beta < 1$ can be obtained straightforwardly), then $\gamma_B < \gamma_A$ and the main (biggest) convective roll turns counterclockwise with a surface flow oriented to the left (cf: **Figure 3**) that brings fresh reactants B towards the side of A. In this case, we numerically find that the condition $\delta_b < 1$, i.e. that the species A diffuses faster than B, is necessary for the oscillations to occur. Physically, this condition is expected to play the key role of bringing fresh reactants A towards the side of B to feed the reaction zone as it moves along the surface. This explanation is consistent with the variation of oscillations properties (amplitude and duration) with δ_b as explained below. When $\beta > 1$, the condition $\delta_b < 1$ is therefore found to be essential to initiate and drive the oscillations.

The amplitude and duration of oscillations found in the profiles of surface tension critically depend on the model parameters that modulate both the intensity of convection and the diffusive fluxes of chemical species. To illustrate this, we define the maximum amplitude of the oscillations, A_{max}, as the maximum difference (in absolute value) of surface tension formed in the positive x-direction between a local minimum followed by a local maximum in the corresponding profiles. By following A_{max} in the course of time, the duration of oscillations can also be highlighted (see **Figure 6**).

The layer thickness is a typical control parameter to modulate the intensity of Marangoni-driven flows and thus, the oscillatory dynamics. When decreasing the layer thickness, convection weakens and so does the driving force for the oscillatory process. In the limit $L_z \to 0$, we must recover the RD surface tension profiles that cannot oscillate [28]. Hence, there exists a minimum value for the layer thickness L_z above which convection is strong enough to drive the oscillations (numerically calculated to $L_{z,min} = 2$ for our specific choice of parameters. Physically, convection is more intense by increasing L_z due to the decrease of the influence of the no-slip boundary condition at the bottom. When increasing L_z above this critical value, the maximum of A_{max} reached in time and the duration of the oscillatory dynamics both increase (see **Figure 6A**). Similarly, we find a minimum value for M (numerically calculated to $M_{min} = 200$ for the parameters chosen here) since, by increasing M, the difference of surface tension between the solutions of A and B is increased and so is the intensity of convection. Moreover, when varying δ_b, the relative importance of the diffusive fluxes towards the reaction zone are changed and so are the amplitude and duration of oscillations. In particular, when decreasing δ_b, more species A diffuse towards the side of B feeding the reaction zone as it moves along the surface. More C is therefore produced and the gradients of surface tension are enlarged. Then, the amplitude and duration of oscillations are found to be larger (see **Figure 6B**). Oscillations are prevented above a maximum value of δ_b (numerically evaluated to $\delta_{b,max} = 0.75$ for the chosen parameters). Note

that the threshold values of the model parameters are provided in this paragraph on an indicative basis only.

Thus, the onset of oscillations critically depend on the model parameters. To summarize, by varying one parameter while keeping the other ones fixed as in **Figure 6**, if we take β sufficiently large (more precisely, when $\beta > \beta_{min} > 1$), our numerical results indicate that oscillations emerge when $\delta_b < \delta_{b,max} < 1$, $L_z > L_{z,min}$, $M > M_{min}$, and for intermediate values of δ_c and M_c, where the lower and upper bounds depend on all the model parameters. We have performed the analysis up to $(M, M_c) < 1000$, $\delta_b < 1$ and $\delta_c < 15$, $L_z < 15$, and $1 < \beta < 15$, which defines the range of parameters values tested. We expect that the case $\beta < 1$ could be performed similarly.

5 CONCLUSION AND PROSPECTS

In this work, we have reported an additional mechanism for the emergence of an oscillatory dynamics unique to reactive systems where differential diffusion effects and chemically-driven Marangoni stresses are at play. Such oscillations are explained by segregated reaction zones that progressively form along the free surface in the course of time. Such segregated reaction zones increase the concentration of C at the surface reducing locally the surface tension leading to the observed oscillations in the profiles of surface tension. This mechanism of oscillations is free of chemical or prescribed hydrodynamic instability.

Next, we have shown the critical influence of the model parameters on the properties (amplitude and duration) and on the onset of oscillations. We have also provided a set of conditions on the model parameters for oscillations to occur with the restriction that $M_a = M = M_b$ assumed for simplicity. A natural extension of this work would then be to relax those assumptions to provide a classification of the oscillatory dynamics in the full parameters space with the motivation to guide future experiments. In this context, while our results could be tested in microgravity or thin film experiments where the effects of buoyancy forces (buoyancy-driven convection) can be neglected [27], we could also include such buoyancy effects into the analysis to extend the application scope of our model to more experimental setups. We could then analyze if the presence of buoyancy forces enhances, reduces or prevents the oscillations of surface tension depending in particular on the Rayleigh number of each chemical species, which quantifies the influence of each of them on the solution density. Also, we have assumed the simplest scenario of an isothermal front traveling in adiabatic conditions (no heat loss to the surrounding). Thermal and/or heat loss effects could also be the subject of future interesting works.

As already mentioned in the introductory part, the spatio-temporal oscillations that arise from differential diffusion effects are fundamentally different from the ones described by Budroni et al. [17–19]. In that case, spatio-temporal oscillations in the velocity field and in the concentration profiles are observed when $\beta = 1$ and $\delta_b = 1 = \delta_c$, but there were no spatial oscillation of surface tension (in the sense of the formation and propagation of local extrema in such profiles). Moreover, their mechanism involves an antagonistic effect between the upward relaxation of the front driven by RD processes and the Marangoni downflow that acts to drive the product C in the opposite direction [17,18]. Here, this antagonistic effect is absent. In this sense, our results on the oscillatory dynamics are similar to those found when Marangoni flows are induced across isothermal autocatalytic fronts [12].

We hope that our results will trigger more theoretical and experimental investigations in the growing field of convective effects across traveling fronts.

DATA AVAILABILITY STATEMENT

The original contributions presented in the study are included in the article/Supplementary Material, further inquiries can be directed to the corresponding authors.

AUTHOR CONTRIBUTIONS

LR originally wrote the reaction-diffusion-convection code for autocatalytic fronts [12] which was adapted by RT for bimolecular fronts. The analysis of the numerical results was performed by RT under the supervision of LR. The drafts of this manuscript were written by RT and reviewed by LR. All authors have agreed with the published version of the manuscript.

ACKNOWLEDGMENTS

The authors thank the “Actions de Recherches Concertées” program and the F.R.S.-FNRS for their financial support.

REFERENCES

1. Stern KH. The Liesegang Phenomenon. *Chem Rev* (1954) 54:79–99. doi:10.1021/cr60167a003
2. Kapral R, Showalter K. *Chemical Waves and Patterns*. Dordrecht: Kluwer (1995).
3. Murray JD. *Mathematical Biology*. Berlin: Springer-Verlag (2003).
4. Volpert V, Petrovskii S. Reaction-diffusion Waves in Biology. *Phys Life Rev* (2009) 6:267–310. doi:10.1016/j.plrev.2009.10.002
5. Stern KH. Reaction-Diffusion Model as a Framework for Understanding Biological Pattern Formation. *Chem Rev* (2010) 329:1616.
6. Gálfi L, Rácz Z. Properties of the Reaction Front in an A+B→C type Reaction-Diffusion Process. *Phys Rev A* (1988) 38:3151–4. doi:10.1103/physreva.38.3151
7. Taitelbaum H, Koo Y-EL, Havlin S, Kopelman R, Weiss GH. Exotic Behavior of the Reaction Front in the A+B→C reaction-diffusion System. *Phys Rev A* (1992) 46:2151–4. doi:10.1103/physreva.46.2151
8. Brau F, Schuszter G, De Wit A. Flow Control of A+B→C Fronts by Radial Injection. *Phys Rev Lett* (2017) 118:134101. doi:10.1103/physrevlett.118.134101
9. Horváth D, Petrov V, Scott SK, Showalter K. Instabilities in Propagating Reaction-diffusion Fronts. *J Chem Phys* (1993) 98:6332–43. doi:10.1063/1.465062

10. Tiani R, De Wit A, Rongy L. Surface Tension- and Buoyancy-Driven Flows across Horizontally Propagating Chemical Fronts. *Adv Colloid Interf Sci* (2018) 255:76–83. doi:10.1016/j.cis.2017.07.020
11. De Wit A. Chemo-Hydrodynamic Patterns and Instabilities. *Annu Rev Fluid Mech* (2020) 52:531–55. doi:10.1146/annurev-fluid-010719-060349
12. Rongy L, De Wit A. Steady Marangoni Flow Traveling with Chemical Fronts. *J Chem Phys* (2006) 124:164705. doi:10.1063/1.2186313
13. Budroni MA, Rongy L, De Wit A. Dynamics Due to Combined Buoyancy- and Marangoni-Driven Convective Flows Around Autocatalytic Fronts. *Phys Chem Chem Phys* (2012) 14:14619. doi:10.1039/c2cp41962a
14. Rongy L, Assemat P, De Wit A. Marangoni-driven Convection Around Exothermic Autocatalytic Chemical Fronts in Free-Surface Solution Layers. *Chaos* (2012) 22:037106. doi:10.1063/1.4747711
15. Budroni MA, De Wit A. Dissipative Structures: From Reaction-Diffusion to Chemo-Hydrodynamic Patterns. *Chaos* (2017) 27:104617. doi:10.1063/1.4990740
16. Rana C, De Wit A. Reaction-driven Oscillating Viscous Fingering. *Chaos* (2019) 29:043115. doi:10.1063/1.5089028
17. Budroni MA, Upadhyay V, Rongy L. Making a Simple A+B→C Reaction Oscillate by Coupling to Hydrodynamic Effect. *Phys Rev Lett* (2019) 122:244502. doi:10.1103/physrevlett.122.244502
18. Budroni MA, Polo A, Upadhyay V, Bigaj A, Rongy L. Chemo-hydrodynamic Pulsations in Simple Batch A+B→C Systems. *J Chem Phys* (2021) 154:114501. doi:10.1063/5.0042560
19. Budroni MA, Rossi F, Rongy L. From Transport Phenomena to Systems Chemistry: Chemohydrodynamic Oscillations in A+B→C Systems. *ChemSystemsChem* (2021) 3:e2100023.
20. Smith MK, Davis SH. Instabilities of Dynamic Thermocapillary Liquid Layers. Part 1. Convective Instabilities. *J Fluid Mech* (1983) 132:119–44. doi:10.1017/s0022112083001512
21. Nepomnyashchy AA, Velarde MG, Colinet P. *Interfacial Phenomena and Convection*. Boca Raton: Chapman and Hall/CRC (2002).
22. Kovalchuk N. Spontaneous Oscillations Due to Solutal Marangoni Instability: Air/water Interface. *Cent Eur J Chem* (2012) 10:1423–41. doi:10.2478/s11532-012-0083-5
23. Nepomnyashchy AA, Simanovskii IB. Synchronization of Marangoni Waves by Temporal Modulation of Interfacial Heat Consumption. *Phys Rev Fluids* (2020) 5:094007. doi:10.1103/physrevfluids.5.094007
24. Nazareth RK, Karapetsas G, Sefiane K, Matar OK, Valluri P. Stability of Slowly Evaporating Thin Liquid Films of Binary Mixtures. *Phys Rev Fluids* (2020) 5:104007. doi:10.1103/physrevfluids.5.104007
25. Nepomnyashchy AA, Simanovskii IB. Droplets on the Liquid Substrate: Thermocapillary Oscillatory Instability. *Phys Rev Fluids* (2021) 6:034001. doi:10.1103/physrevfluids.6.034001
26. Tiani R, Rongy L. Influence of Marangoni Flows on the Dynamics of Isothermal A+B→C Reaction Fronts. *J Chem Phys* (2016) 145:124701. doi:10.1063/1.4962580
27. Guyon E, Hulin J-P, Mitescu CD, Petit L. *Physical Hydrodynamics*. Oxford, UK: Oxford University Press (2001).
28. Trevelyan PM, Almarcha C, De Wit A. Buoyancy-driven Instabilities Around Miscible A+B→C Reaction Fronts: a General Classification. *Phys Rev E Stat Nonlin Soft Matter Phys* (2015) 91:023001. doi:10.1103/PhysRevE.91.023001

Conflict of Interest: The authors declare that the research was conducted in the absence of any commercial or financial relationships that could be construed as a potential conflict of interest.

The reviewer SM declared a past collaboration with the author LR to the handling editor. The handling editor FR declared a past co-authorship with the author LR.

frontiers | Frontiers in Physics

ORIGINAL RESEARCH
published: 11 May 2022
doi: 10.3389/fphy.2022.896717

Ants Alter Collective Behavior After Feeding and Generate Shortcut Paths on a Two-Dimensional Foraging Area

Osamu Yamanaka[1], Yusuke Oki[2], Yuta Imamura[2], Yukari Tamura[2], Masashi Shiraishi[1], Shunsuke Izumi[2], Akinori Awazu[2] and Hiraku Nishimori[1]*

[1]*Meiji Institute for Advanced Study of Mathematical Sciences, Meiji University, Nakano, Japan,* [2]*Graduate School of Integrated Sciences for Life, Hiroshima University, Higashi-Hiroshima, Japan*

Ants flexibly change their behavioral modes at various levels, from individuals to whole colonies, based on external stimuli, such as finding a new food source or being attacked by predators. In this study, we investigated mode changes in the foraging behavior of garden ants, *Lasius japonicus.* When extracted pheromone was deposited along a circular path connected to the nest entrance and no food was supplied, a large fraction of the ants continued to walk along the path. In contrast, if a food source was placed on the same circle at the opposite edge to the nest entrance, a large fraction of ants soon came to shuttle directly between the nest and the food source using a shortcut path. We analyzed the process of shifting the foraging path from the initial circular path to the shortcut path, and found that the foragers who reached the food source in the initial stage along the circular pheromone path chose the shortcut path for their homing instead of the circular path; thereafter, the traffic along the shortcut path gradually increased both in the outward and homeward directions. This strongly indicates that the ants changed the foraging mode after the food-intake from the pheromone-following mode to another mode. The present result serves as an example of the switching of collective behavior of animals caused by that of the primarily relying information for individuals according to the input of external stimuli.

Keywords: foraging behavior, pheromone trail, ant, Lasius japonicus, private information, navigation

OPEN ACCESS

Edited by:
Nobuhiko J. Suematsu, Meiji University, Japan

Reviewed by:
Adam Lipowski, Adam Mickiewicz University, Poland
Tomoko Sakiyama, Sōka University, Japan

****Correspondence:***
Masashi Shiraishi
shiraishi.mu@gmail.com

Specialty section:
This article was submitted to Physical Chemistry and Chemical Physics, a section of the journal Frontiers in Physics

Received: *15 March 2022*
Accepted: *22 April 2022*
Published: *11 May 2022*

Citation:
Yamanaka O, Oki Y, Imamura Y, Tamura Y, Shiraishi M, Izumi S, Awazu A and Nishimori H (2022) Ants Alter Collective Behavior After Feeding and Generate Shortcut Paths on a Two-Dimensional Foraging Area. Front. Phys. 10:896717. doi: 10.3389/fphy.2022.896717

1 INTRODUCTION

Ants are typical eusocial insects. Despite their small brain size, ants perform various tasks in a highly organized manner when working together as a colony through autonomously functioning task allocation with no particular leader. To date, various types of collective ant behavior have been investigated. In particular, foraging behavior has been intensively studied because it is the most fundamental task for survival. One of the characteristic features of the foraging process of many ant species is pheromone-mediated trail formation. According to previous studies, pheromone trails are formed using the following procedures [4, 16]: first, scout ants who reach new food sources deposit. Trail pheromone on their way back to the nest. Thereafter, the foragers who have been waiting in the nest respond to the information provided by the returned scout ants and depart to forage by following the pheromone trail to reach the food source. On their way back to the nest, they deposit another trail pheromone, similar to the above-mentioned scouts. Repetition of these processes increases the density of pheromones

along the trail, thereby enabling the colony to effectively carry food to the nest. Information shared among numerous ants through deposition and sensing pheromones is categorized as social information. In contrast, several ant species do not form pheromone trails during foraging. Instead, they rely only on information acquired by the abilities of each individuals, such as the visually obtained route memory to food sources [1, 5, 10, 11, 14] and memory of the required steps to reach the food, which is categorized as private (or personal) information. Another style of foraging without pheromone trail formation involves recruiters showing nest-mates how to reach food sources through tandem running, during which the information exchanged among foragers is categorized as social information. In these ways, ants utilize various types of information in foraging, with the primary information used depending on the species and situation. The combined use of more than one piece of information has been observed in some ant species. For example, the parallel use of remembering the steps required for foragers to reach food sources from the nest (i.e., odometer) and sensing the polarization of sunlight (i.e., sun-compass) enables path integration in desert ants, with which they recognize the temporal location at every moment during foraging [2, 17]. This is a combination of the different types of private information. Another form of combinatory use of multiple information is hierarchical use. For example, in a food-seeking experiment with *Lasius niger*, the ants primarily relied on the stored memory of the feeding location for individuals when the indicated feeding directions conflicted, as opposed to the usual information from the pheromone trail [1, 10]. Also in this study, we investigated the mode changes in the foraging behavior of *Lasius japonicus*, however, unlike the previous studies [3–5], we investigated the mode-change caused by the input of stimulus, i.e. the food intake.

2 MATERIALS AND METHODS

2.1 Experimental Animals

We collected three colonies of *Lasius japonicus* from the Higashi-Hiroshima campus of Hiroshima University. Each colony was housed in a breeding box (30 × 40 cm) containing a plastic nest box (10 × 10 cm). The bottom of each nest box was covered with a layer of plaster. The top of each nest box was covered with cardboard to block light. A rubber tube was connected to the nest box at the entrance. The colonies were queenless, comprising 500–700 workers and a small number of broods. We fed the colonies once every 2 days with 0.5 ml of 1 M sugar solution and once a week with a mealworm. The experiments were performed in a temperature-controlled room, with a light-dark cycle of 12: 12 h and the lights turned on at 8:00. The room windows were covered to prevent natural light. The room contained artificial room lights, different types of lab equipment, and furniture, which would provide visual landmarks for the ants.

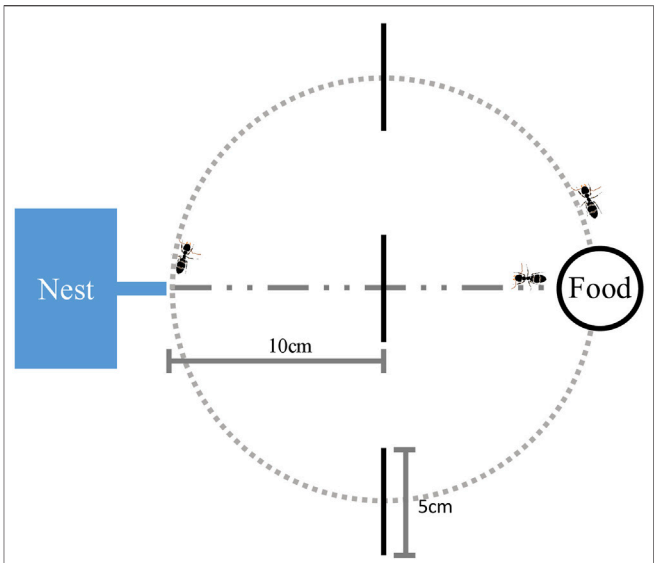

FIGURE 1 | Experimental setup. The dotted line indicates the initial pheromone path, where the trail pheromone was deposited along a circle with a radius of 10 cm. The dash-dotted line indicates the shortcut path. A feeder platform was placed on the edge of the circle and the nest was placed on the other side. The black vertical lines represent the decision lines.

2.2 Pheromone Extraction and Column Chromatography

To obtain trail pheromone during the experimental trials, solutes were extracted from 100 ants using hexane (10 ml) for 3 days. The extract solutes were concentrated to 4 ml in an evaporator. The concentrated solutes were then separated using column chromatography as follows. A column was prepared by packing glass wool and silica gel powder into the tip of a disposable glass Pasteur pipette. First, the extracted solutes were loaded onto the column. Subsequently, the column was eluted with mixture solutes (50 ml per eluent) containing hexane and diethyl ether, and the mixing ratio of each eluent was set stepwise (hexane/diethyl ether ratios of 10:0, 9:1, 7:3, and 5:5). Every 10 ml of the eluate fraction was collected into glass bottles (the bottle was labeled as ID:1–20).

To select an eluate, including the trail pheromone, the eluates of the bottles were examined using a biological assay. We compared the attractiveness of the eluate for three consecutive bottle IDs [i.e., (1,2,3), (2,3,4), (3,4,5)...(18, 19, 20)]. Three solutes were placed along a trident shape on fresh paper, in which each pronged spear comprised one solute in the bottle. We then forced ants to forage on the paper, recorded their foraging behavior with a video camera, and then counted the number of ants walking on each spear for 5 min. Eluates, including the trail pheromone, were selected based on the number of ants following the corresponding spear. The eluate from the bottle was diluted 30–50 times by mixing with hexane and was then used for the subsequent foraging experiments.

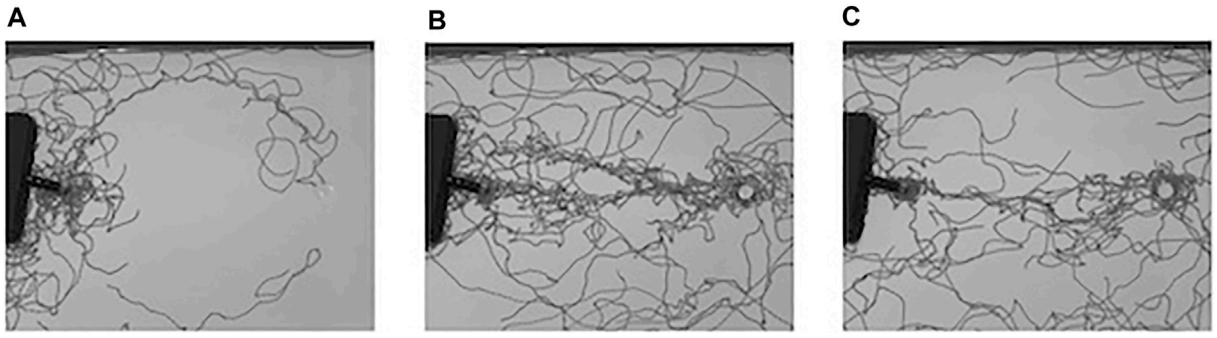

FIGURE 2 | Temporal overlaying of video frames for 60 s from **(A)** 15 s, **(B)** 5 min, and **(C)** 25 min.

2.3 Experimental Setup

We placed a fresh paper over a foraging platform for each trial. We then prepared a pheromone trail that had a circle shape using the selected extracted pheromone. We applied the pheromone trail along the circle with a radius of 10 cm on the paper using a microsyringe as an initial pheromone path. It is known that the ants following the trail tried to find a new path when they reached the point where the two straights crossed [7, 12]. The ants following the circle path could reach the food source without being disturbed because the circle path is smooth. A glass plate was provided as a feeder platform on the edge of the circle, and the nest box was placed on the other side, as shown in **Figure 1**.

Two experiments without a food source and twelve experiments with a food source in total (four subgroups of three colonies) were conducted. The two experiments were set up without sugar solution on the feeder platform to confirm that the ants could follow the initial pheromone path for 60 min. The twelve experiments with a food source were performed in the same place in the room and every few days thereafter. The ants starved during the days between the conducted experiments. The experiments with a food source were recorded for 90 min per trial. The video for all experiments provided images at a resolution of 1280 × 720 at 30 frames/s.

2.4 Video Analysis

The two-dimensional position coordinates for each ant were measured from the recorded video sequences using the background subtraction method. First, every frame in the video sequence was converted to grayscale frames, and then the background image was calculated by storing the highest intensity value of each pixel from the series of preceding frames. Second, we subtracted the background image from all frames to calculate the foreground images. Thus, we binarized the extracted foreground images. Third, we defined the ant position coordinate as the center of the labeled pixel region whose size was between 5 and 100 pixels to retain only ants. Following these three steps, we measured the position of each ant in each frame; however, the relation between the positions in the subsequent frame was unknown. Thus, we defined the nearest positional coordinate in the subsequent frame as the coordinate of the same ant if the magnitude of the difference vector between the coordinates was less than 1 cm. The difference vector between the two coordinates served as a velocity vector for the ant.

Following the above processes, we measured the trajectories of the ants within the two frames and velocity vector sequences, as shown in **Figure 2**. Using the measured information, we classified the outward and homeward ants based on velocity vectors. We quantified the temporal dynamics of the ant traffic flow on decision lines, which were defined at the center of the circle and at the initial pheromone path, as shown in **Figure 1**. We counted the number of ants crossing each decision line for outward and homeward independently as traffic flow, and defined $n_{o,s}$, $n_{h,s}$, $n_{o,i}$, and $n_{h,i}$ as the number of ants crossing the shortcut path for outward and homeward and the initial path for outward and homeward, respectively. In this study, we regarded that the ants went foraging or homed after reaching the food source when they crossed decision lines, respectively, but the ants could cross the outside of the decision lines. To confirm that the ants walked the two paths, we counted all ants crossing the centerline for outward and homeward as n_o and n_s. If $n_{o,s} + n_{o,i} \cong n_o$ and $n_{h,s} + n_{h,i} \cong n_h$, we could assume that the ants in the experiments attended the foraging and homing after finding the food source. In addition, we did not follow all ants' trajectories to confirm that the ants turned around while walking on the two paths without reaching the food source and whether the ants reached the food source or not because of technical difficulty. However, we confirmed that these cases were relatively rare cases while checking the original videos. Each traffic flow was normalized by the total number of traffic flows for each direction, n_o and n_h, and was referred to as the proportion of traffic flow. We compared the proportion of traffic flow between the shortcut path and the initial pheromone path. We referred to the proportion of the traffic flow of ants on the shortcut path as $f_{o,s} = n_{o,s}/n_o$ for outward and $f_{h,s} = n_{h,s}/n_h$ for homeward, and that on the initial pheromone path as $f_{o,i} = n_{o,i}/n_o$ for outward and $f_{h,i} = n_{h,i}/n_h$ for homeward.

2.5 Statistical Analysis

Significant differences in the proportion of traffic flow on the shortcut path and that on the initial pheromone path every 3 min were confirmed using a paired t-test in R software v.3.3.1 [15].

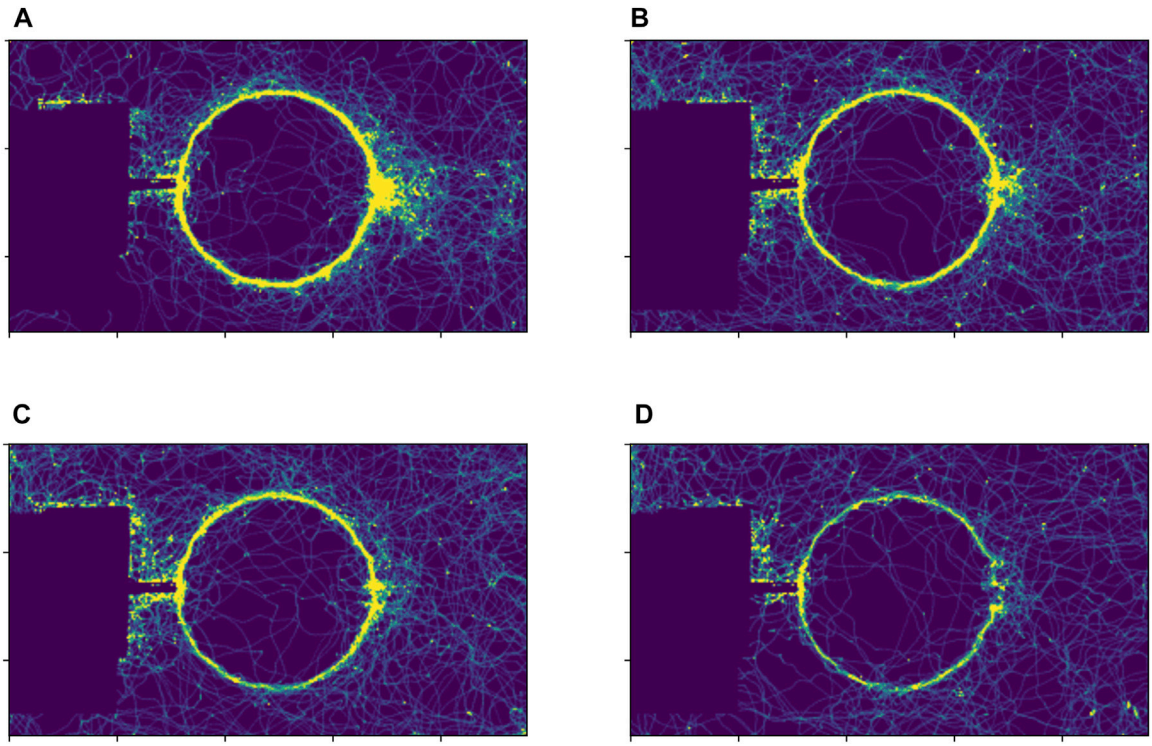

FIGURE 3 | Example of the density of foraging ants in the experiment without a food source: **(A)** an interval from 0 to 3 min, **(B)** an interval from 3 to 6 min, **(C)** an interval from 6 to 9 min, **(D)** an interval from 9 min to 12 min.

3 RESULTS

3.1 Experiments Without a Food Source

We initially set up two experiments to examine whether foragers followed a pheromone trail along a circular path. For this purpose, a pheromone trail was deposited on a circular path without food. In this situation, a large fraction of foragers kept walking on the circular path until the end of the two experiments, both of which continued for 60 min, as shown in **Figure 3**.

3.2 Experiments With a Food Source

Next, the food source was placed on the path, and 12 experiments were conducted in total (four subgroups of three colonies). Within the 12 experiments, we only analyzed the data of the experiments in which the first five ants reached the food source following the initial pheromone trail to investigate the collective behavioral change of the foragers, that is, the primary foraging route changes from the initial pheromone path to the shortcut path. Eight of the 12 experiments satisfied this criterion. Most ants traveled outward from the nest entrance to the food source on the initial pheromone trail during the first 3 minutes. However, there was no statistically significant difference between the number of homeward ants along the initial pheromone path and that along the shortcut path. In addition, we discuss the results of video analysis for all experiments from the start to 45 min, because the foraging ants finished taking the sugar solution at 45 min.

During the next time interval from 3 to 15 min, the fraction of outward ants, $f_{o,s}$, that crossed the decision line, including the shortcut path, monotonically increased, whereas the fraction of outward ants, $f_{o,i}$, that crossed the decision lines, including the initial pheromone path, remained constant, as shown in **Figure 4**. The ratio $f_{o,s}$ also increased, however, $f_{o,s}$ and $f_{o,i}$ did not exhibit significant differences until 18 min ($p > 0.05$), as shown in **Figure 5**. $f_{o,s}$ and $f_{o,i}$ in a 18–21 interval showed a significant difference ($p < 0.05$). In contrast to the outward ants, the number of homeward ants, $f_{h,s}$, that crossed the decision line on the shortcut path was consistently larger than $f_{h,i}$ that crossing the decision line on the initial pheromone path, and $f_{h,s}$ and $f_{h,i}$ were significantly different ($p < 0.01$) except a 15–18 interval ($p > 0.05$). The time series of the number of ants that crossed the decision lines as shown in **Figure 4** revealed that the foraging ants that relied on the initial pheromone path ignored social information and instead used other information. After 3 min, $f_{h,s}$ was approximately 0.7, which was significantly different from $f_{h,i}$ ($p < 0.01$) except a 15–18 interval ($p > 0.05$).

This outcome indicates that the ants preferred to use the shortcut path as the main foraging trail. Notably, the outward foraging ants that walked along the initial pheromone path were retained in a certain fraction, indicating that the pre-set

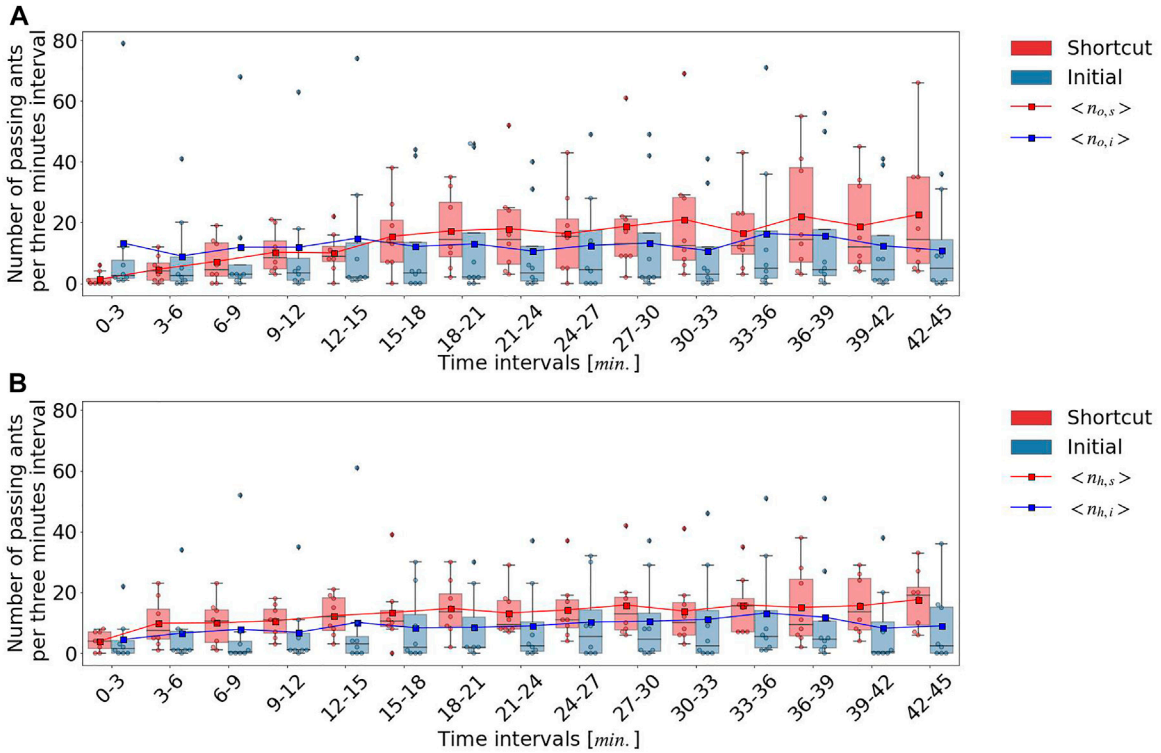

FIGURE 4 | Number of ants passing each decision line per 3 min interval: **(A)** outward ants. **(B)** homeward ants.

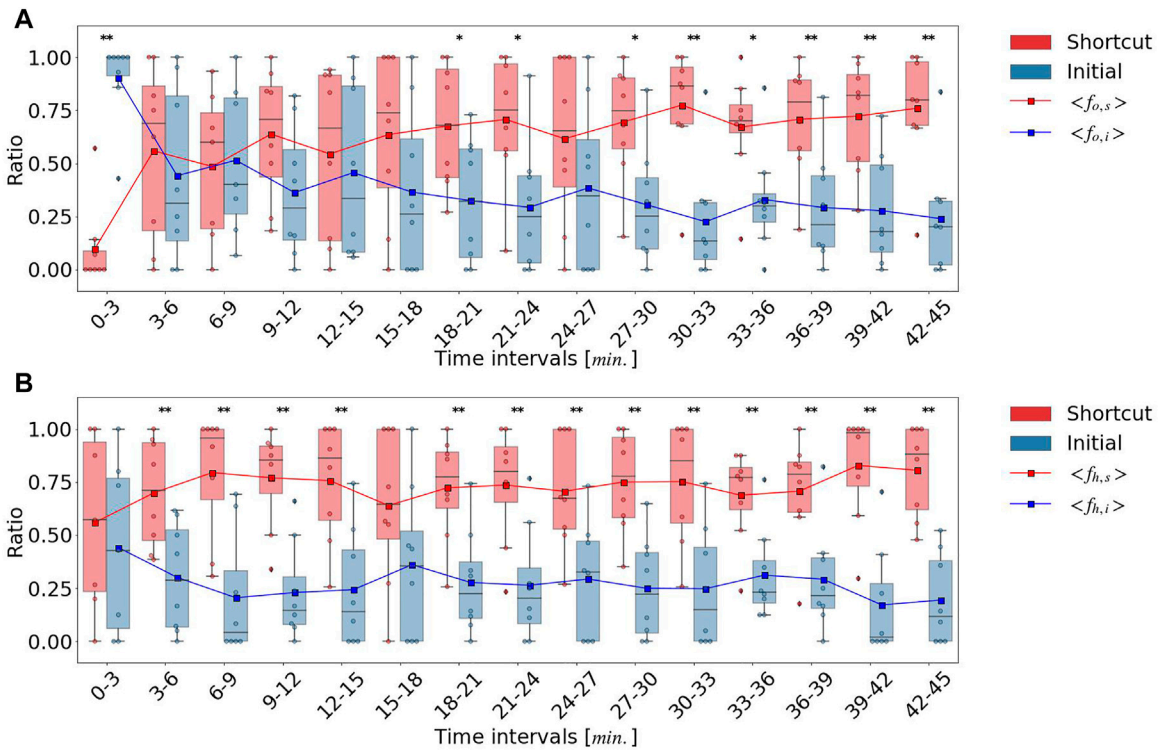

FIGURE 5 | Ratio between the number of ants passing each decision line: **(A)** outward ants. **(B)** homeward ants.

trail pheromone pheromone trail strongly attracted the outward foraging ants.

4 DISCUSSION

We observed that the fed ants collectively tended to switch their foraging behavior mode. The workers that led foraging in the early stages of the experiments walked homeward in areas where no other workers had previously walked. This behavior indicates that the workers independently decided to ignore the trail pheromone and choose to walk across the shortcut path between the food source and their nest entrance.

It is natural to suppose that the workers' decision might be based on some information, which should be the workers' private information because they did not use any social information provided by the pheromone trail and, instead, started to walk to areas for which no social information existed. The possible candidates for the private information which the workers used were their visual information, odometer, or previous memory. In addition, our results indicated that ants may use private information for the homeward journey, which contradicted with the expected behavior based on the hypothesis that ants use pheromones for homing.

Another possible mechanism is the emergence of stochastic effects in the sensitivity of pheromone trails, which allow ants to ignore the established pheromone trail. Based on previous simulation studies, a circular path that is initially set is optimized to a shortcut path in the following steps [4, 6, 8]. First, the ants wander around the vicinity of the circular path and deposit pheromones there. Second, because the ants following the inside of the circular path reach the resources faster than those following the circular path, the trail pheromone on the inside of the circular path becomes more concentrated than that on the circular path. Finally, the primarily used path shifts to the inside of the circular path. By repeating these steps, the primarily used path gradually converges to the shortcut path between the nest and the resource. However, in our experiments, ants discontinuously switched their homeward path from the original pheromone path to the shortcut path. In addition, if the stochastic effects on the sensitivity of the pheromone trail are significant, the ants should spread out in all directions. As the ants headed directly to their nests in our experiment, it is likely that our ants used private information.

Reid et al. [13] evaluated the decision-making mechanism regarding information selection in ants when forced to choose particular information following the removal of the existing information and reported that ants head back to their nest using private information when a pheromone trail is physically blocked. In their study, the appropriate information was externally shut down, and thus, ants were forced to use private information to cover the loss. In contrast, we observed that ants switched the prior homing information from chemical cues to private cues, even though the foraging environment remained unchanged. However, the mechanism for selecting private information without the loss of chemical cues requires further investigation. Our results were consistent with those of Grueter et al. [9], who found that the costs and benefits of information use depend on the context, leading to a change in the primarily used information. In our experiments, the time cost of searching for unknown food sources was high in the outward journey because the pheromone trail was presented and the food source was known. Conversely, relying on private information is beneficial because the time taken for a straight path is less than that for a circular path. The ants that completed the outward journey then acquired up-to-date private information. In summary, the ants succeeded in gaining benefits and decreasing costs by selecting information.

Our data indicate that not only the initial circular pheromone path but the shortcut path also came to work as a pheromone trail with time proceeded. This is because the traffic flow on the shortcut path increased with time. In general, ants on pheromone trails and those who have previously experienced foraging move faster than inexperienced ants or those on unmarked trails [3]. Therefore, subsequent ants could use multiple types of information, potentially increasing the efficiency of ant transport.

In our experiments, we only analyzed the collective foraging behavior of the ants, and thus we indirectly concluded the possibility of private information use in their homeward foraging behavior. The individual ants are small but it still have complex nervous system. That means that the observed behavior might be related to multiple input information. To confirm the origin of their private information, we have to do experiments that strictly control the available cues related to the private information. We conduced the experiments in the laboratory with many instruments which might be used as landmarks to locate their heading direction. It is required to conduct an experiment controlling the visual environment.

DATA AVAILABILITY STATEMENT

The raw data supporting the conclusion of this article will be made available by the authors, without undue reservation.

AUTHOR CONTRIBUTIONS

Conceived and designed the experiments: OY, MS, SI, AA, and HN Performed the experiments: OY, YO, YI, and YT Analyzed the data: OY, MS, and HN Wrote the paper: OY, MS, and HN.

FUNDING

This study was financially supported by Grant-in-Aid for Scientific Research (B) (Grant No. 20H01871), Grant-in-Aid for Transformative Research Areas (A) (Grant No. 21H05297), and the Promotion Project for Development of a Characteristic Joint Research Base of the Ministry of Education, Culture, Sports, Science and Technology (JPMXP0620335886).

REFERENCES

1. Aron S, Beckers R, Deneubourg JL, Pasteels JM. Memory and Chemical Communication in the Orientation of Two Mass-Recruiting Ant Species. *Ins Soc* (1993) 40:369–80. doi:10.1007/bf01253900
2. Collett M, Collett TS. How Do Insects Use Path Integration for Their Navigation? *Biol Cybernetics* (2000) 83:245–59. doi:10.1007/s004220000168
3. Czaczkes TJ, Grüter C, Jones SM, Ratnieks FLW. Synergy between Social and Private Information Increases Foraging Efficiency in Ants. *Biol Lett* (2011) 7:521–4. doi:10.1098/rsbl.2011.0067
4. Czaczkes TJ, Grüter C, Ratnieks FL. Trail Pheromones: an Integrative View of Their Role in Social Insect colony Organization. *Annu Rev Entomol* (2015) 60:581–99. doi:10.1146/annurev-ento-010814-020627
5. Czaczkes TJ, Salmane AK, Klampfleuthner FA, Heinze J. Private Information Alone Can Trigger Trapping of Ant Colonies in Local Feeding Optima. *J Exp Biol* (2016) 219:744–51. doi:10.1242/jeb.131847
6. Deneubourg J-L, Aron S, Goss S, Pasteels JM. The Self-Organizing Exploratory Pattern of the Argentine Ant. *J Insect Behav* (1990) 3:159–68. doi:10.1007/bf01417909
7. Forster A, Czaczkes TJ, Warner E, Woodall T, Martin E, Ratnieks FLW. Effect of Trail Bifurcation Asymmetry and Pheromone Presence or Absence on Trail Choice byLasius nigerAnts. *Ethology* (2014) 120:768–75. doi:10.1111/eth.12248
8. Goss S, Aron S, Deneubourg JL, Pasteels JM. Self-organized Shortcuts in the Argentine Ant. *Naturwissenschaften* (1989) 76:579–81. doi:10.1007/bf00462870
9. Grueter C, Leadbeater E. Insights from Insects about Adaptive Social Information Use. *Trends Ecol Evol* (2014) 29:177–84.
10. Grüter C, Czaczkes TJ, Ratnieks FL. Decision Making in Ant Foragers (Lasius niger) Facing Conflicting Private and Social Information. *Behav Ecol Sociobiol* (2011) 65:141–8.
11. Minoura M, Sonoda K, Sakiyama T, Gunji Y-P. Rotating Panoramic View: Interaction between Visual and Olfactory Cues in Ants. *R Soc Open Sci* (2016) 3:150426. doi:10.1098/rsos.150426
12. Ogihara Y, Yamanaka O, Akino T, Izumi S, Awazu A, Nishimori H. Switching of Primarily Relied Information by Ants: A Combinatorial Study of experiment and Modeling. In: *Mathematical Approaches to Biological Systems*. Berlin, Germany: Springer (2015). p. 119–37. doi:10.1007/978-4-431-55444-8_6
13. Reid CR, Sumpter DJT, Beekman M. Optimisation in a Natural System: Argentine Ants Solve the Towers of Hanoi. *J Exp Biol* (2011) 214:50–8. doi:10.1242/jeb.048173
14. Sakiyama T, Gunji YP. Garden Ant Homing Behavior in a Maze Task Based on Local Visual Cues. *Insect Soc* (2013) 60:155–62. doi:10.1007/s00040-012-0279-x
15. Team RC. *R: A Language and Environment for Statistical Computing* (2013).
16. Wilson EO. A Chemical Releaser of Alarm and Digging Behavior in the Ant Pogonomyrmex Badius (Latreille). *Psyche: A J Entomol* (1958) 65:41–51. doi:10.1155/1958/57483
17. Wittlinger M, Wehner R, Wolf H. The Desert Ant Odometer: a Stride Integrator that Accounts for Stride Length and Walking Speed. *J Exp Biol* (2007) 210:198–207. doi:10.1242/jeb.02657

Conflict of Interest: The authors declare that the research was conducted in the absence of any commercial or financial relationships that could be construed as a potential conflict of interest.

Publisher's Note: All claims expressed in this article are solely those of the authors and do not necessarily represent those of their affiliated organizations, or those of the publisher, the editors and the reviewers. Any product that may be evaluated in this article, or claim that may be made by its manufacturer, is not guaranteed or endorsed by the publisher.

frontiers | Frontiers in Physics

ORIGINAL RESEARCH
published: 19 May 2022
doi: 10.3389/fphy.2022.881384

Analysis of Actomyosin Oscillatory Dynamics Using a Coarse-Grained Model

Miguel Hernández-Del-Valle[1,2,3,4], *Andrea Valencia-Expósito*[5], *Nicole Gorfinkiel*[6], *Maria D. Martín-Bermudo*[5] *and David G. Míguez*[1,2,3,4]*

[1]Centro De Biología Molecular Severo Ochoa, Universidad Autónoma De Madrid, Madrid, Spain, [2]IFIMAC, Fac. De Ciencias, Universidad Autónoma De Madrid, Madrid, Spain, [3]Instituto Nicolás Cabrera, Fac. De Ciencias, Universidad Autónoma De Madrid, Madrid, Spain, [4]Fisica De La Materia Condensada, Fac. De Ciencias, Universidad Autónoma De Madrid, Madrid, Spain, [5]Centro Andaluz De Biología Del Desarrollo, Universidad Pablo De Olavide/CSIC/JA, Sevilla, Spain, [6]Department of Genetics, Physiology and Microbiology, Faculty of Biology, Complutense University of Madrid, Madrid, Spain

Autonomous oscillatory dynamics are ubiquitous at every level in Biology. At the cellular level, one of the most relevant and well characterized examples of periodic behavior is the cyclic assembly and disassembly of actomyosin networks. In *Drosophila*, these oscillations induce the robust contraction and expansion of individual cells required for correct dorsal closure, while in the follicular epithelium that surrounds the germline, periodic contractions of the basal actomyosin network are required for proper elongation of the egg chamber. While some studies suggest that actomyosin oscillations are driven by upstream signaling or mechanochemical features, we have recently proposed that they arise as a systems property from the competition between two well characterized features of the actomyosin machinery: 1) cooperative assembly of actin networks mediated by Actin crosslinker proteins and 2) tension-induced disassembly of actin networks mediated by myosin motors. Here, we perform experiments in amnioserosa and in the follicle cells of *drosophila* and simulations using a coarse-grained model of the actomyosin cortex to characterize the properties of the oscillations and how they depend on different features of the system. We also compare model and experiments to study the dynamics of actomyosin flows and the effect of mechanical coupling between cells in the tissue. In conclusion, our model is a powerful tool to study key features of actomyosin oscillations, from the effect of the individual components to network properties and finally supra-cellular organization of the oscillations at the tissue level.

Keywords: actomyosin, coarse-grained, proteins, oscillations, cytoskeleton, biophyiscs

OPEN ACCESS

Edited by:
Federico Rossi,
University of Siena, Italy

Reviewed by:
Saúl Ares,
National Center for Biotechnology (CSIC), Spain
Ryan McGorty,
University of San Diego, United States

***Correspondence:**
David G. Míguez
david.miguez@uam.es

Specialty section:
This article was submitted to Physical Chemistry and Chemical Physics, a section of the journal Frontiers in Physics

Received: *22 February 2022*
Accepted: *25 April 2022*
Published: *19 May 2022*

Citation:
Hernández-Del-Valle M, Valencia-Expósito A, Gorfinkiel N, Martín-Bermudo MD and Míguez DG (2022) Analysis of Actomyosin Oscillatory Dynamics Using a Coarse-Grained Model. Front. Phys. 10:881384. doi: 10.3389/fphy.2022.881384

1 INTRODUCTION

Many biological systems exhibit oscillatory dynamics. From circadian clocks to gene expression, oscillations have been shown to be underneath many important biological processes, at very different time and spatial scales. At the systems level, periodic dynamics has been shown to modulate the spatial and temporal organization of tissues, as well as to improve the precision in the control of biological processes [1]. This periodicity is very present in morphogenesis (i.e., the formation and organization of tissues during development), and its failure results in severe morphogenetic defects [2, 3]. In this direction, the study of the features that induce and regulate biological oscillations

during developmental processes are of interest to many branches of biology, from regeneration to tissue engineering and cancer biology [4].

Arguably the most studied morphogenetic event that shows an oscillatory behaviour is the dorsal closure in *Drosophila* embryos [5, 6]. In this process, an opening at the dorsal midline of the embryo closes due to the fusion of two sheets of epithelial cells located at both sides of the embryo. An essential part of the process is driven by the cells of the amnioserosa, an epithelial extra-embryonic tissue whose cells exhibit periodic expansions and contractions [7]. As the amplitude of the oscillations in the cells of the amnioserosa increases, they start to internalize concomitant with the closing of the two epithelial sheets [8]. These oscillations are required for proper morphogenesis of the *Drosophila* larva [6, 8, 9], and their disruption results in failure in the process of closure [10].

Using *Drosophila* again as model organism, researchers have shown that oscillations in the basal surface of cells take place during maturation of the oocyte [11]. As the egg chamber increases around 1.7-fold in length, cells in the follicular epithelium (a sheet of cells that coat the oocyte) oscillate in shape with a periodicity of around 6.5 min. Similarly to apical oscillation in amnioserosa, these basal oscillations in the follicular epithelium are required for a correct maturation of the oocyte, and inhibition of the actomyosin contractions blocked the correct elongation of the egg chamber [12].

These cell-autonomous sequential contractions and expansions of the cell shape arise from the oscillations that occur at the level of the cytoskeleton [8]. The cytoskeleton is a dynamic network of protein microfilaments and microtubules in the cytoplasm of cells, ultimately responsible for the shape and mechanical properties of cells. The cytoskeleton is involved in virtually all cellular processes, and therefore, abnormal functioning of the cytoskeleton is linked to many severe diseases, including cardiovascular, neurodegeneration, cancer, cirrhosis, and fibrosis [13].

An essential part of the cytoskeleton mesh is the actomyosin, a protein complex composed of actin and myosin, which is the essential contractile substance of muscle fiber. Actomyosin is characterized by a very well studied set of dynamic properties that arise mainly from the interaction of its two main components: actin and myosin. Globular actin (G-actin) is the most abundant protein in most eukaryotic cells, and it is involved in more protein-protein interactions than any other protein [14]. One of its most important features is its ability to polymerize into long filaments of helical structure composed of several thousand G-actin subunits. These threads called "filamentous" or "F-actin" are very dynamic, and can be rapidly remodelled in the inner cell surfaces as a response to external or internal cues, as a fundamental aspect to cellular life.

Myosin motors are force-generating ATPases, meaning that they can catalyze the decomposition of ATP into ADP, and use the energy released to produce a mechanical force and move along F-actin. Myosin motors are also among the most abundant proteins with regard to biomass, and they are responsible for actin-based cell motility, intracellular transport, and muscle contraction.

Driven by this interaction between F-actin and Myosin, the actomyosin cortex has been characterized as an inherently contractile, highly dynamic structure, with the myosin motor proteins able to pull on actin filaments and remodel the network. In the inner cell membrane of eukaryote cells, the actomyosin complex organizes as a thin film of around 0.2 μm thickness [15], commonly refereed as the actomyosin cortex. Its main function is the control of animal cell morphogenesis [16] as a structural framework, and its assembly and properties are regulated by the interaction of G-actin with actin-membrane linkers [17], such as dystrophin, utrophin, talin, vinculin, integrin and annexins. This family of proteins is responsible for maintaining the cortex tightly attached to the plasma membrane [18], while also affecting strongly its properties and dynamics [19].

The dynamics of the actomyosin cortex are very rich and context dependent, and it is able to exhibit a wide variety of interesting nonlinear properties, such as traveling waves [20] or patterns [21]. It is also the main responsible for the oscillations in cell shape of amnioserosa and follicle cells described above. In brief, as the cortex assemblies, it drives contraction of the inner cell membrane that it is attached to. Then, at some point, the cortex disassembles and the area expands again, and the process of actomyosin assembly begins again.

Although the mechanisms underlying this cyclic process are not fully understood, several models and theoretical approximations have been developed in the last decades that propose potential explanations of its dynamics (see for instance ref [22] for a detailed review of models of dorsal closure). Models can be divided into two main categories, depending on the approach followed: mechanical-based or biochemical-based oscillations. Mechanical-based models assume that the source of oscillations are physical interaction, such as forces, pressure or elastic load [7, 11, 23–28]. Biochemical-based oscillations assume that the source of the oscillations is the nonlinear interactions in the biochemical network [29, 30].

In this direction of biochemical based approaches, we have recently proposed a semi-grand canonical coarse grained model, where some features of the actomyosin cortex are reproduced based on very few well characterized interactions between actin molecules, myosin motors and actin crosslinkers (ACs) [31].

In our model, autonomous periodic assembly and disassembly of the actomyosin cortex arises naturally from the interplay between two well known processes: cooperative F-actin assembly [32, 33] and tension induced disassembly [34–36].

Here, we use our framework to characterize the main parameters that control the dynamics and periodicity of the actomyosin oscillations, its robustness, the properties of the network and other features such as traveling waves and coupling dynamics. The most relevant aspects of the model are described in the Methods section, and a detailed explanation of the full framework can be found in ref. [31]. A scheme of the modeling framework is shown in **Figure 1**. To validate the model predictions, we performed experiments in two tissues of *Drosophila* that exhibit autonomous oscillations in actomyosin levels: follicle cells during marutation of the egg chamber, and cells of the amnioserosa during dorsal closure. Comparison between model predictions and our experimental

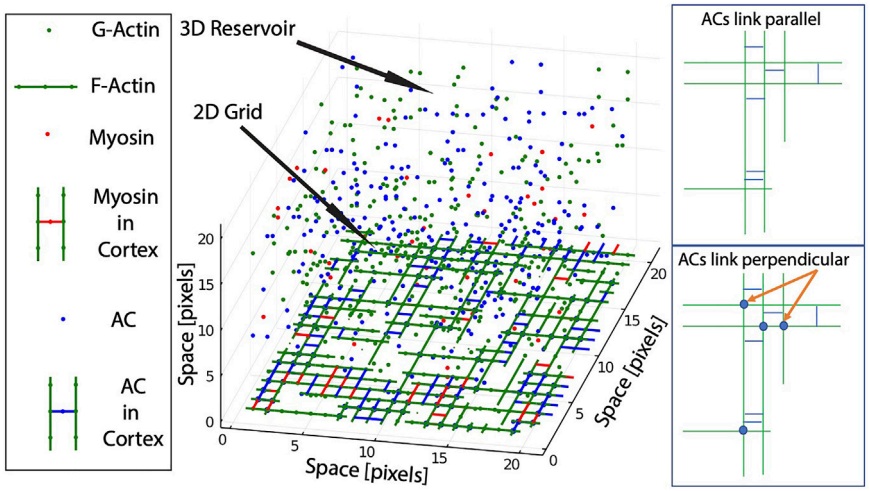

FIGURE 1 | Scheme of the Coarse Grained framework. The model is composed of a two-dimensional grid that represents the inner cellular membrane connected to a three-dimensional reservoir, that represents the cytoplasm. Several molecule types are coexisting and interacting in the framework: G-Actin and F-Actin (green), Actin Crosslinkers ACs (blue), and Myosin (red). Molecules transit between grid and reservoir based on chemical potential (see Methods). Right panels show the effect of different classes of ACs in the link between parallel or perpendicular F-actin.

observations suggest that, despite the highly simplified approach based on very few assumptions, our model is able to recapitulate many important properties of actomyosin oscillatory dynamics.

2 METHODS

2.1 Model Design

In brief, the model is multi-compartment, composed of a two-dimensional grid that represents the inner cellular membrane connected to a three-dimensional reservoir, that represents the cytoplasm. Several molecule types are coexisting and interacting in the framework (G-actin, actin crosslinkers (ACs), and myosin), and can transit between the grid and the reservoir. The total number of molecules for each type (cortex + cytoplasm) remains constant throughout the simulation. For simplicity, diffusion in the cortex and other processes such as rotations are not allowed.

The code is written in Julia language [37], taking advantage of the following libraries: StatsPlots, Dates, KernelDensity, LightGraphs, FFTW, Plots, Random, Printf, Statistics, GLM. Code is available upon request.

Numerical simulations are performed using a Coarse Grained framework developed in house. The model is solved numerically using a Monte-Carlo computational algorithm. The dynamics for each event is accepted or rejected based on the Metropolis method [38]. The probability distribution of the different micro-states of the systems is evaluated statistically using a semi-grand canonical ensemble approach.

In brief, the model works as follows: 1) G-actin molecules in the cortex are allowed to polymerize directionally to form filaments (F-actin). 2) F-actin is then stabilized and linked by ACs, forming meshworks of parallel, anti-parallel and perpendicular filaments. 3) Myosin can bind to F-actin, and produce mechanical force. 4) When bound to two anti-parallel F-actin, the mechanical action of myosin results in tension or stress. 5) When the stress supported by a given F-actin is higher than its attachment to the membrane, the F-actin is released from the cortex to the cytoplasm, and part of its tension is redistributed to the rest of the network. Details and parameters for each of these processes are explained below (a more exhaustive and detailed explanation of the model can be found in ref. [31]).

2.2 Actin Dynamics

At every time step, a location and orientation (horizontal or vertical) in the grid is chosen. If the location is empty, an actin monomer (G-actin) can transition from the cytoplasm to that location in the cortex based on the value $P^+ = e^{-\mu_1}$ μ_1 represents a chemical potential with the following form:

$$\mu_1 = \mu_{1,0} - \gamma_1 * log\frac{N_1}{N_{1,0}} \tag{1}$$

where $\mu_{1,0}$ is a reference potential, $N_{1,0}$ is the total number of actin molecules in the system, N_1 is the number of actin molecules in the grid at a given time point. Parameter γ_1 is a modifier of the slope of the function.

The potential function μ_1 sets the probability of transition of a given molecule from the reservoir to the cortex. The change is accepted or rejected based on the Metropolis method. In the most rigorous definition of the chemical potential in thermodynamics, the units are energy units per molecule), but in the context of semi-grand canonical ensembles, the chemical potential is defined with no units.

To allow crossing of F-actin, each position in the grid can accept one G-actin molecule in vertical orientation and one in horizontal orientation. If insertion is successful, a link between G-actin and the cortex is established, with energy E_1 (mimicking the effect of integrin molecules [19]). In addition, if another G-actin exists directly behind and with the same orientation, a

link between the two molecules is established (with energy E_0), and the filaments grows directionally.

On the contrary, if the location selected is already occupied, removal of the G-actin is evaluated using again the Metropolis method ad the value of $P^- = e^{-E}$, being E the sum of the energy of the links that affect the molecule. Directional de-polymerization is implemented by spontaneous release of the bond of the last G-actin of a F-actin (therefore, $P^- = e^{-E_1}$ in this case).

2.3 Actin Crosslinkers Dynamics

ACs can occupy positions between pixels of the grid, so they can join filaments. Similarly to G-actin, we start by selecting a random location in the grid. If location is between two parallel, anti-parallel or perpendicular filaments, insertion is evaluated based on $P^+ = e^{-\mu_2}$ and the Metropolis method, with μ_2 being a chemical potential for ACs:

$$\mu_2 = \mu_{2,0} - \gamma_2 * log\frac{N_2}{N_{2,0}} \tag{2}$$

If insertion is accepted, links of energy E_2 are established between the AC and the two F-actin.

If the location already has an AC, removal is evaluated based on the value $P^- = e^{-2E_2}$, and the Metropolis method. To study the properties of the actomyosin network, two classes of ACs are used: ACs that only link parallel F-actin, and ACs that can also link perpendicular F-Actin. A scheme of how the two mechanisms of action is shown in **Figure 1** (right panel).

2.4 Myosin Dynamics

Myosin molecules work in our model similarly to ACs, with their own chemical potential μ_3 and their link energy E_3.

$$\mu_3 = \mu_{3,0} - \gamma_3 * log\frac{N_3}{N_{3,0}} \tag{3}$$

When linked to anti-parallel F-actin, myosin adds a certain amount of stress every time step. When the stress accumulated by a filament is higher than the energy attaching it to the cortex, it will be removed, and a fraction of its stress is communicated to the filaments that were connected to it. This way, the stress propagates through the network and it is progressively disassembled. This mechanism is at the core of the oscillatory behavior that we will analyze in the Results section.

2.5 Coupling

Changes in shape of a cell will affect the shape of its neighbors. To implement numerically this spatial coupling, we run simultaneously two numerical simulations corresponding to two neighboring cells (cell i and cell j), and make the value of a given parameter dependent on the total stress tension (TS, the sum of all tension in all filaments of the cell). For the coupling of the potential functions, we define the following function:

$$\mu_{1,j} = \mu_{1,j}^{uncoupled}\left(1 + \alpha\frac{\beta^\gamma}{TS_i^\gamma + \beta^\gamma}\right) \tag{4}$$

Another approach is to modulate the stress in 1 cell by the stress of the neighbour cell (if 1 cells compressed, the other experiences a relaxation in the network tension): to do that, we define the following function:

$$TS_j = TS_j^{uncoupled}\left(1 + \alpha\frac{\beta^\gamma}{TS_i^\gamma + \beta^\gamma}\right) \tag{5}$$

in both previous equations α affects the maximum intensity of the coupling, β affects the inflection point and γ affects the slope. This way, the value of the parameter uncoupled in cell j is recalculated based on the value in the neighbor cell i, using the function that goes from 1 (no effect of neighbour) to α (full effect of neighbour). In all simulations, we use values of $\alpha = 5$, $\gamma = 5$. These values have been chosen to provide an intermediate level of coupling (smaller values show very little effect, higher values suppress the oscillations in both cells). β is set as the half mean value of the total tension, which for the parameters used moves from 0 (minimum of oscillation), to around 10 (maximum total tension at the peak of the oscillation), therefore $\beta = 5$ also.

2.6 Model Calibration

Spatial and temporal calibration of this type of coarse grained models using experimental data is challenging because each interaction in the model often combines many biochemical steps (by design, the model is a very simplified version of the real system, and many molecular interactions are condensed as one simple step). The chemical potential is used as a tool that we use to maintaining a dynamic equilibrium between the molecules in the grid and in the reservoir, therefore it does not have a direct comparison with any experimental value (parameters of the chemical potential are chosen to maintain intermediate levels of cortex occupancy). Finally, bond energies are defined in terms of multiples of RT (being R the universal gas constant). Bonds mediated by ATP hydrolysis are on the order of 30 kJ/mol (RT = 2.47 kJ/mol). The power of Myosin in breaking the network is calibrated based on the time it takes in experiments to disassemble the actomyosin cortex (based on our own reference [30]).

2.7 Experiments

2.7.1 *Drosophila* Stocks and Genetics

Basal Follicle experiments: Flies were grown at 25°C and yeasted for 2 days before dissection. To visualize myosin, we used the Sqh: mCherry stock (see reference [30] for details). The spaghetti squash (Sqh) gene encodes the regulatory myosin light chain of nonmuscle myosin II. For live imaging 1–2-day-old females were fattened on yeast for 48–96 h before dissection. We then dissect ovarioles from ovaries in supplemented Schneider medium (GIBCO-BRL). Culture conditions and time-lapse microscopy are performed as described in [30, 39]. Egg chambers were mounted on a 35-mm glass bottom poly-D-lysine-coated dish (MatTek Corporation) without cover-slip, surrounded by wet tissue paper to preserve humidity around the culturing egg chambers.

Images were acquired on a Leica SP5 MP-AOBS confocal microscope equipped with a 40 × 1, 3 PL APO oil objective and Leica hybrid detectors (standard mode). Time-lapse movies are obtained using a confocal microscope (frame rate = 1/30 s^{-1}). Each frame is a maximal projection of twelve Z-stacks (0.42 μm interval overlapping), to cover the entire basal surface of the cells.

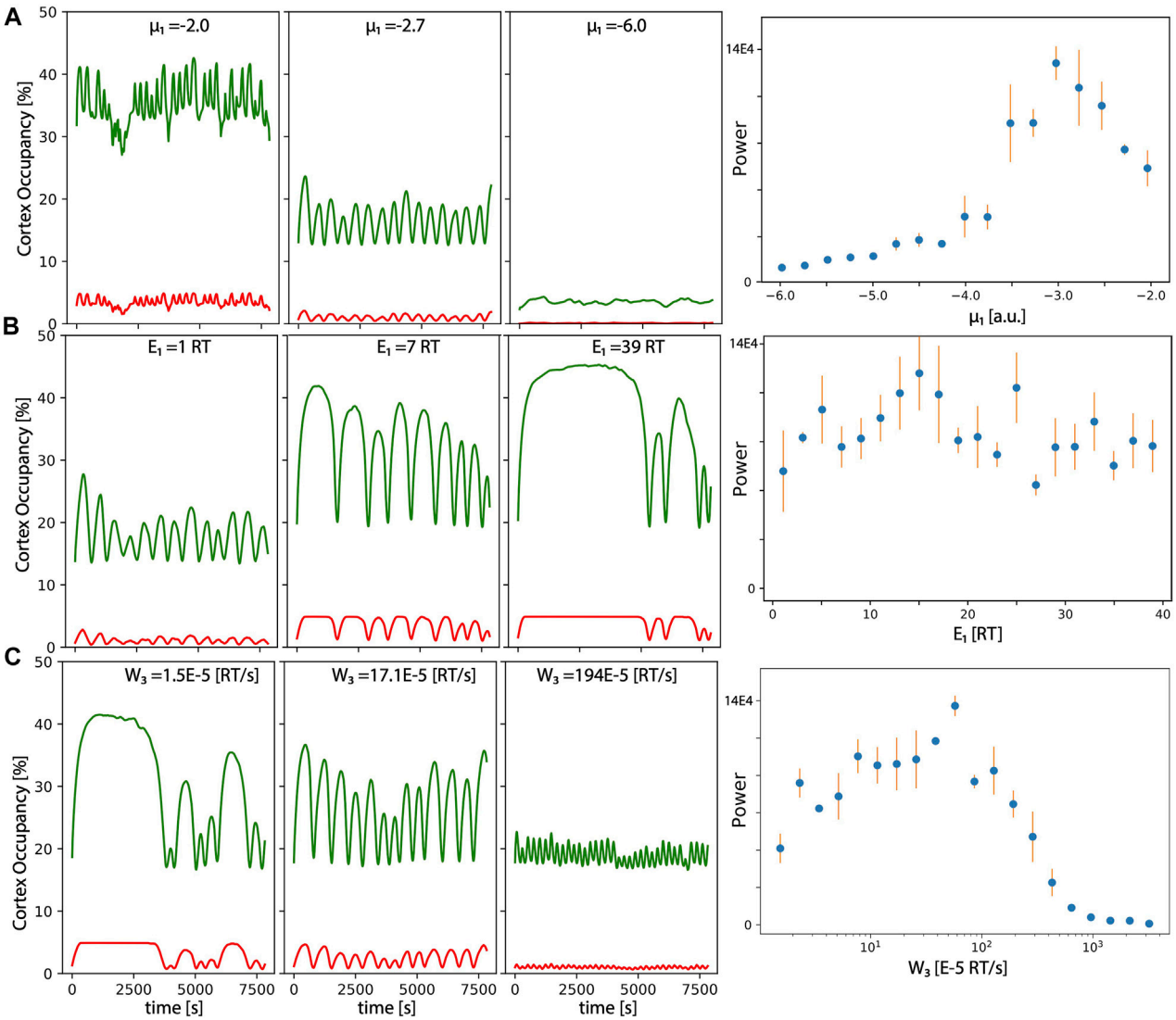

FIGURE 2 | Characterization of the oscillations: Occupancy levels over time of the grid for actin (green) and myosin (red) for different values of the **(A)** reference chemical potential of for G-actin $\mu_{1,0}$, **(B)** link energy E_1, and **(C)** energy per unit of time induced by mechanical force of myosin. Right panels correspond to the amplitude of the maximum of the Fourier transform of the G-actin levels (average over three independent numerical realizations of the model. Error bars correspond to standard deviation).

2.7.2 Amnioserosa Experiments

For the imaging of the amnioserosa during dorsal closure, we used a recombinant fly stock carrying ubiECad- GFP to label cell membranes and zipperCPTI002907 to label Myosin-II (available from Kyoto Stock Center). Stage 12–13 *Drosophila* embryos were dechorionated, mounted in coverslips with the dorsal side glued to the glass and covered with Voltalef oil 10 S (Attachem). The amnioserosa was imaged at 25–28°C. using an inverted LSM710 laser scanning microscope with a 40X oil immersion Plan-Apochromat (NA = 1.3) objective. Imaging was performed with an argon laser and the emitted signal between 495 and 620 nm was collected using spectral detectors. Around 30 z-**Sections 1** μm apart were collected with a frame rate = 1/20 s^{-1}). Signals specific to green fluorescent protein and yellow fluorescent protein were extracted using the linear unmixing tool.

2.7.3 Image Processing and Data Analysis

For cell tracking and automated quantification of intensity levels, we first define the position of center of the cells in each frame manually using FIJI, and track the cell overtime, by identifying cellular characteristics between consecutive frames. Then, Python and OpenCV are used to obtain an average measure of intensity for the red channel (Sqh:mCherry, myosin) inside an area of fixed dimensions, surrounding the center of each cell. A movie of the cell tracking is shown as **Supplementary Movie S5**.

3 RESULTS

3.1 Characterization of Actomyosin Oscillations

To understand the main features and properties of the oscillations in both main components of the actomyosin network (actin and myosin), we start with a characterization of the dependence of the dynamics on the model parameters, to define which aspects of the molecular interaction between actin, myosin and ACs affect the amplitude, period or robustness of the oscillations.

Figure 2A focuses on the effect of the reference chemical potential $\mu_{1,0}$, which regulates the affinity of the G-actin to transit from the cortex to the grid (therefore, it effectively affects the concentration of G-actin in the grid versus the cytoplasm). We can see that oscillations appear for an intermediate value of $\mu_{1,0}$ (low values result in very small amounts of G-actin unable to polymerize, while high values result in too high affinity of G-actin towards the cortex). In this situation, new G-actin enters the grid before the network is fully disassembled, and the system is driven out of the periodic regime towards a dynamic steady state situation (filaments are continuously being assembled and disassembled, but no periodicity arises as a global property of the system.

This is also illustrated in the left panel, where we plot the power of the highest peak of the corresponding Fourier transform of the amount of actin in the cortex overtime, computed for more values of $\mu_{1,0}$ (right panel). The maximum periodicity occurs for values of $\mu_{1,0}$ around −3.

Figure 2B focuses on the effect of the link energy between G-actin and the inner cell membrane E_1 in the period and amplitude of the oscillations. We can see that oscillations are more clear for an intermediate value of E_1 (low values of E_1 result in very unstable filaments; high values of E_1 result in filaments too attached, so myosin cannot produce the sufficient tension to release the filament, so disassembly occurs as a more stochastic and less periodic event). The representation of the maximum power of the Fourier spectrum, shows that the optimal values for periodicity occur around E_1 = 7 RT, but it is more or less maintained for very high and very low values of the same parameter.

Finally, **Figure 2C** represents the effect of the power provided by myosin (W_3), which regulates the energy that a given myosin motor produces per unit of time, once attached to two anti-parallel F-actin. Changes in these parameters seem to strongly affect the period of oscillations, with much longer and higher amplitude bursts as we move towards less power of myosin. This makes sense, since it takes longer to reach the threshold tension to detach a given filament. The longer it takes, more time for the filaments to grow in size and to fill the grid (therefore, amplitude is also increased). Again, optimal periodicity also occurs at intermediate values (see right panel for a maximum peak of the Fourier transform).

A more exhaustive analysis of the robustness of the oscillatory dynamics for each parameter of the model is presented in **Table 1**, where we include a brief statement explaining the biological meaning for each parameter, and the minimum and maximum values for clear and sustained oscillations. Model parameters used to produce this figure and the rest of the figures in the manuscript are liste in **Table 2**.

3.2 Analysis of the Properties of Actomyosin Networks

Since oscillations of the actomyosin cortex are in essence the assembly and disassemble of a interconnected network, we can use this analogy to study the properties of such network from a graph theory perspective. In this approach, we can define F-actin as the nodes of the network, and the links are the molecules capable of attaching to F-actin, i.e., ACs and myosin. This way, a poorly connected network represents a situation where F-actin molecules are linked to a small number of other filaments, while a highly connected network represents a situation where F-actin is linked to multiple other polymers.

To quantify this connectivity, we use the shortest path length L (also called geodesic distance, i.e., the minimum number of links required to connects two nodes in a network), calculated using the Dijkstra algorithm [40]. The average shortest path length $< L >$ corresponds to this value averaged for all shortest paths from each node to each node in the network. For simplicity, we use the maximum connected component size transformed in a simple graph, without weights. To minimize the effect of networks of different sizes, we divide by the average shortest path length $< L_0 >$ for an equivalent network of the same number of nodes and links, but where connections are established randomly. Therefore, high values of $< L/L_0 >$ represent a highly ordered network, while values of $< L/L_0 >$ around 1 represent a network structure similar to random.

Since our inner cell membrane is simplified as a simple square grid of discrete pixels, this will strongly affect the architecture of the network. To study different configurations and different situations of the graph, we first analyze a condition of networks composed of only parallel and anti-parallel F-actin (see Methods and **Figure 1**). This situation illustrates the structure and properties of bundles linked only by Fascin and similar ACs [41].

Figure 3A represents this first scenario. The left panel is a plot comparing the value of $< L/L_0 >$ as a function of time (purple line), with the oscillations in the amount of actin in the cortex (green line). We can see that the value of $< L/L_0 >$ increases and decreases in time, concomitant with the cortex occupancy, suggesting that as the network grows, it differs more from a random-like connectivity (since only parallel and anti-parallel filaments can be connected, two filaments that are placed far away from each other will have a very long L).

If we compute the degree distribution at the point of minimum (central panel) and maximum (right panel) of the oscillation, we see that in both situations, the maximum probability is slightly above two (since F-actin can only bind in this scenario to parallel or anti-parallel neighbors, most of the filaments are only linked to two other F-actin, and only a few filaments are linked to a higher number of F-Actin). The inserts in each panel correspond to spatial representations of the graph at these two time points. The

TABLE 1 | Descriptions and ranges of values for the different parameters.

Parameter Name	Meaning	Range	Units
$\mu_{1,0}$	G-Actin References potential	-4: -2	adimensional
$\mu_{2,0}$	ACs References potential	-10: 0	adimensional
$\mu_{3,0}$	Myosin References potential	-20: 0	adimensional
E_1	G-Actin link energy to inner cell membrane	0: 20 RT	KJ/Mol
E_2	ACs link energy to inner cell membrane	0: 20 RT	KJ/Mol
E_3	Myosin link energy to inner cell membrane	0: 20 RT	KJ/Mol
W_3	Energy introduced by Myosin per second	5e-6: 5e-2 RT	KJ/Mol/s
SF	Stress fraction propagated through the network	0.1: 1	adimensional

TABLE 2 | Values for the parameters used in the panels.

Figure	$N_{1,0}$	$N_{2,0}$	$N_{3,0}$	$\mu_{1,0}$	$\mu_{2,0}$, $\mu_{3,0}$	E_1	E_2, E_3	*SF*	W_3
2A	5,000	3,000	500	label	–5	3	3	1	0.0005
2B	5,000	3,000	500	–3	–5	label	3	1	0.0001
2C	5,000	3,000	500	–3	–5	3	3	1	label
3A,B	5,000	3,000	500	–2	–5	2	3	1	0.001
4A,B	20,000	12,000	2000	–2	–5	label	3	0.25	0.0005
5D,E,F	5,000	3,000	500	–3	–5	5	3	1	0.0005

network develops with few connections per node towards a highly regular configuration at its maximum size (occupancy ≈ 80, % $< L/L_0 > \approx 4$) (the ring form occurs because the boundaries in our model are defined as periodic).

Figure 3B represents the scenario of F-actin being able to link also perpendicularly (see Methods and **Figure 1**). This situation represents the properties of actomyosin networks where ACs are also able to link perpendicular F-actin polymers, mimicking the role of ACs such as the αActinin family [42]. The value of $< L/L_0 >$ (purple line, left panel) again oscillates in time, but now the average shortest distance decreases as the network size increases i.e., as the network grows, it resembles more a random network. This behavior corresponds to the opposite scenario of **Figure 3A**. The explanation for this difference is the following: when the network is beginning to form, the most probable connections are between parallel and anti-parallel filaments (perpendicular filaments can only be joined by their intersection point). These initial connections result in an increase in $< L/L_0 >$, similar to the case in **Figure 3A**. However, as soon as connection between perpendicular filaments appear, $< L/L_0 >$ falls drastically to a value near one, meaning that the average shortest path length is much more similar to what would be expected in a random graph.

This different connectivity impacts how tension and energy is being redistributed in the network, which in the end affects the amplitude of the oscillations (green line, left panel). The addition of perpendicular links results in larger oscillations that become more asymmetric in their shape, compared to smaller and more sinusoidal oscillations in parallel networks (**Figure 3A**, left panel). This asymmetry in the shape of the oscillation occurs because the higher connectivity makes the tension travel faster and further across the network, resulting in a more sudden and organized disassembly.

The central panel in **Figure 3B** shows the degree distribution at the minimum occupancy point, with an average degree slightly above 2 and small clusters being formed (similar to panel A). The right panel in **Figure 3B** corresponds to the maximum point of occupancy, with a much broader distribution (average degree around 6) and a much larger network structure (more connections, see insert for a graphical representation of the network in graph form), resulting in a connectivity very close to random.

3.3 The Model Reproduces Traveling Actomyosin Waves

The actomyosin cortex is an active adaptive material, capable of a wide range of dynamic behaviours, from bulk pulse contractions [26] to anisotropic polarized flows [43–45]. These traveling waves of actomyosin play pivotal roles in cell division, cell motility, and morphogenesis. Wound healing experiments in *Drosophila* show perhaps the clearest example of these cortical flows, with a single pulse of actomyosin filaments assembling from cell to cell toward the margin of the wound [46]. Another key example of actomyosin waves occurs during contraction and protrusion in *Dictyostelium discoideum* [47].

In our previous publication, we have demonstrated how our minimal model is able to reproduce the bulk oscillations of the actomyosin responsible for the periodic contraction of cells. In this section, we take advantage of the fact that our model has been constructed as spatiotemporal to study the conditions that will result in the arising of polarized actomyosin flows.

Figure 4A represents three snapshots of the system for conditions of bulk oscillations. We can see how the cortex transits from full (t_1) to less crowded (t_2) to almost full again (t_3). A time lapse movie of the system for these conditions is

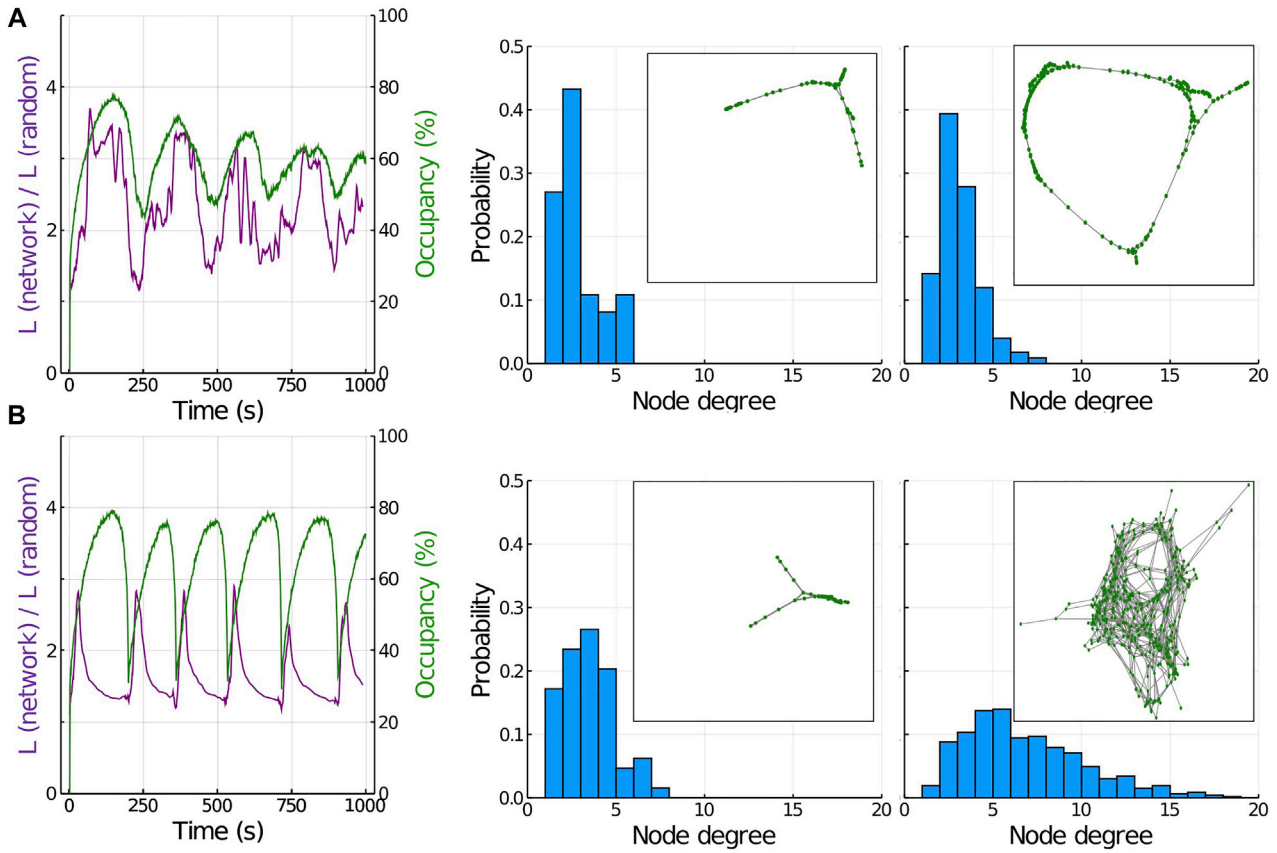

FIGURE 3 | Analysis of the actomyosin network properties. **(A)** Parallel and anti-parallel F-actin networks. Left panel represents the average shortest path length (purple) and occupancy (green) during several oscillations. Central panel represents the degree distribution in a minimum of occupancy (insert is a graphical representation of the network at this time point). Right panel represents the degree distribution when occupancy is at its maximum level (insert is a graphical representation of the network at this time point). **(B)** Perpendicular F-actin networks. Left panel represents the average shortest path length (purple) and occupancy (green) during several oscillations. Central panel represents the degree distribution in a minimum of occupancy (insert is a graphical representation of the network at this time point). Right panel represents the degree distribution when occupancy is at its maximum level (insert is a graphical representation of the network at this time point).

presented as **Supplementary Movie S1**. On the other hand, if we reduce the value of E_1 (**Figure 4B**), instead of bulk oscillations, the system starts to exhibit traveling waves that swipe the system directionally. In this regime, the total occupancy levels do not change so drastically along the simulation, but still we observe oscillations in local levels if we focus on a small region of the system. A time lapse movie of the system for these conditions is presented as **Supplementary Movie S2**.

To further illustrate the difference between these two dynamic regimes, we generated space-time plots (**Figure 4C**), where we pile the intensity levels for the same pixels at different time points of a given simulation. The left panel represents a situation of bulk oscillations, where all the actomyosin is disassembled from the cortex simultaneously. From this plot, it can be seen that the periodicity is highly regular since very early in the simulation, and the collapse of the network is almost instantaneous (illustrated by a red horizontal line).

The right panel corresponds to the situation of low E_1. Now, instead of full sudden collapse of the network, the system transits into a regime where disassemble occurs initially disordered in small clusters that, as time progresses, become more organized in the form of spatio-temporal waves.

Next, we compare these two potential scenarios with the dynamics observed in experiments performed in the basal region of *Drosophila* follicle cells, as well as in amnioserosa cells during dorsal closure (see Methods). In brief, to analyze myosin dynamics in the basal side of *Drosophila* follicle cells, we performed live imaging of egg chambers expressing the *in vivo* marker for myosin, Sqh:mCherry. To analyze myosin dynamics in the apical side of amniserosa cells, we use *Drosophila* embryos stably expressing zipperCPTI002907 to label myosin.

To do this, we recorded time lapse movies and monitor the changes in intensity levels and the spatial redistribution of the actomyosin cortex. **Figure 4D** illustrate the dynamics in the experiments in the form of a space time plot (the full movie for myosin oscillations in follicle cells is presented as **Supplementary Movie S3**, the full movie for myosin oscillations in amnioserosa cells is presented as **Supplementary Movie S4**). To monitor the oscillatory dynamics in the experiments, we compute the levels of myosin

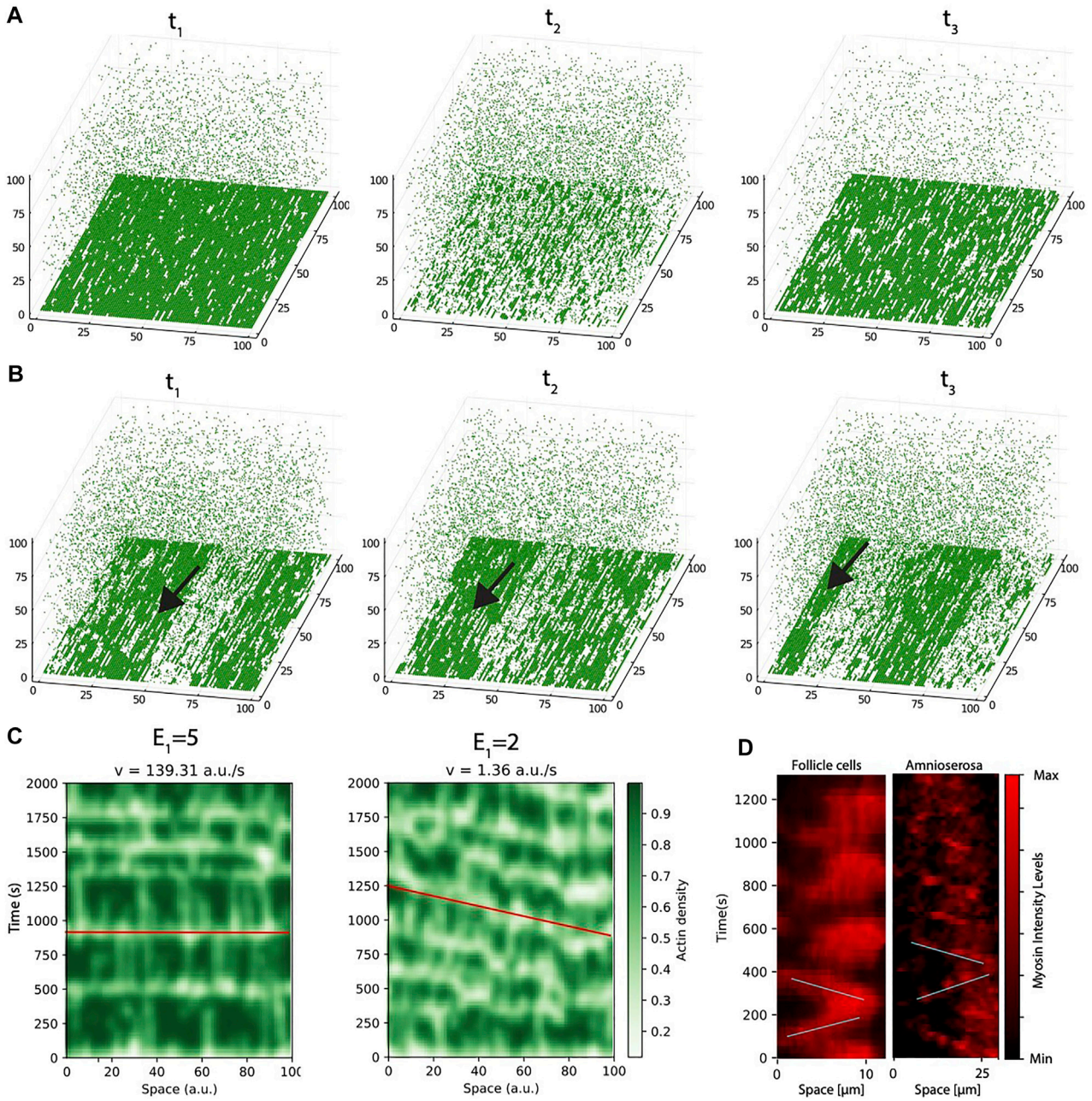

FIGURE 4 | The model reproduces the arising of actomyosin waves. **(A)** Snapshots of the system at three different time points of the same simulation, for conditions of strong link between G-actin and inner cell membrane (E_1 = 5 RT). **(B)** Snapshots of the system at three different time points of the same simulation, for conditions of weak link between G-actin and inner cell membrane (E_1 = 2 RT). Arrow points to a traveling wave, that moves from right to left. **(C)** Space-time plots of the conditions of high (left panel) and low (right panel) values of E_1. The red line is drawn as a guide to the eye to follow the speed of the waves. **(D)** Space-time plots of myosin dynamics for a single cell in Follicle cells (left) and amnioserosa (right) generated using the levels of myosin.

instead of F-actin, because myosin staining allows us to distinguish better single cells (as seen in our previous publications [30], the dynamics of both actin and myosin are very similar).

Left panel in **Figure 4D** corresponds to a single cell quantification of the follicle tissue (**Supplementary Movie S3**). The changes in intensity levels show a dynamic that initially resembles wave-like oscillations (marked with oblique lines as a guide to the eye) but later in time, the dynamics is more bulk-like (there is no clear direction in the assembly and disassembly). On the other hand, in amnioserosa, (right panel, the waves can be clearly distinguished during the 20 min of the experiment (see **Supplementary Movie S4**). Interestingly, although the speed of the waves in both tissues is around the same order (slope of the

lines), the waves are very different in shape (myosin waves in amnioserosa are much thinner, i.e., disassembly occurs almost immediately after assembly, while in basal follicle cell oscillations, the disassemble takes longer, suggesting that tension accumulates more slowly). Based on the model analysis, we hypothesize that both experimental tissues represent different in regions of the phase space: basal follicle cell oscillations are more similar to oscillations of high attachment (**Figure 4A**), while amnioserosa oscillations resemble a situation of low energy attachment. In addition, we have to take into account the inherent experimental differences between both systems (see Methods), and that neighboring cells are also oscillating and probably affecting the dynamics of their neighbours. This effect of the coupling between cells in close proximity is studied in the next section.

3.4 Coupling

There is vast evidence that confirms that actomyosin oscillations are cell autonomous, rather that arising as a dynamic property of the system. On the other hand, since cells are not isolated, but coupled mechanically as part of a larger tissue, it is safe to assume that the dynamics of a given cell will be influenced by the dynamics of their neighbours. Since the integrity of epithelial tissues such as the amnioserosa or follicle cells has to be maintained during morphogenesis, the expansion (or contraction) of a cell in a particular direction has to be coupled with a complementary contraction (or expansion) of its neighbours. In this direction, a clear experimental evidence of the effect of neighbors in the dynamics of the oscillation has been described during wound healing, where the process of cell expansion is simply a result of the absence of tension by the actomyosin, combined with tension being generated in neighboring cells [48].

Previous studies focused on the inter-relation between the changes in cell shape at the tissue level show that the axis of maximum contraction tend to organize in their orientation, showing for the first time a supra-cellular organization during dorsal closure [8]. This is consistent with actomyosin waves that can expand several cell diameters, but authors did not focus on this characterization.

A more detailed studied of the spatiotemporal coordination of the pulses during the invagination of the *Drosophila* ventral furrow, establishing a link between the myosin intensity and the change in area of the cell [49]. Here, authors find that in wild type conditions, the tissue is not governed by force balance, meaning that the reduction in area of a given cell is not affected by peaks in myosin levels in neighboring cells.

To investigate if the mechanical interaction between neighboring cells in the tissue affects in some way the dynamics of the actomyosin cortex, we use again experiments in *Drosophila* follicle cells (see Methods). We perform cell tracking of a set of cells in the tissue and measure the intensity levels of myosin overtime. A time lapse movie of the process is presented as **Supplementary Movie S5**. Next, for each cell, the oscillations are fitted to a sinusoidal function to extract parameters of the dynamics, such as amplitude and phase of the oscillation. Finally, these two parameters are compared between neighbors to identify potential coupling or the existence of supra-cellular organization.

Results of the quantification are summarized in **Figures 5A–C**. Panel A represents a snapshot of the time lapse movie, with the labeled cells part of the analysis. **Figure 5B** corresponds to the oscillation frequency of all the cells analyzed, plotted in levels from blue (low) to red (high frequency). Our data suggests that cells coordinate in the form of arrays with similar frequency of oscillations (illustrated by orange lines). This supra-cellular organization in the form of long lines of cells is similar to the arrays presented in ref [8], and suggest that, a similar organization to the compression and expansion is also taking place at the level of the frequency of oscillation. Interestingly, the frequency values (lower panel) show a distribution that resembles a bimodal shape, but a more extensive analysis (more cells, more movies) will be required to conclude this with mode confidence.

Supra-cellular actomyosin waves should result in spatial coordination in the phase of the oscillations between neighboring cells. This quantification is presented in **Figure 5C**, where the phase relative to cell 0 is represented in a color-bar (restricted to cells with a similar frequency, since comparison of phase is only informative when performed between cells with similar dynamic characteristics). Interestingly, cells closer to our reference cell have a similar phase, while cells further in the tissue oscillate in anti-phase with the reference cell. These results points towards the existence of close coupling in terms of actomyosin levels, suggesting that, despite the lack of coordination in area changes (see ref [49]), the actomyosin levels seem to be coupled between neighbours.

Next, we go back to our model to study potential scenarios for inter-cellular actomyosin coupling that can reproduce the experimental observations. To do that, we generated two parallel numerical simulations of 2 cells simultaneously, and tested different scenarios for the coupling. Details of how the coupling is implemented are described in the Methods section. The first scenario corresponds to coupling in *via* chemical potential. The rationale is that, in a tissue, the contraction of cell *i* should result in expansion of cell *j*. Therefore, an increase in area may correspond to a reduction in local concentration (represented in our model by the reference chemical potential $\mu_{0,i}$). The actin levels of the 2 cells in this situation are represented in **Figure 5E**, where we mark with black and red rectangles the regions where the 2 cells oscillate in phase and anti-phase, correspondingly. Comparing this situation of $\mu_{0,i}$ coupling with **Figure 5D** (no coupling), we cannot see real differences in the phase (rather than an decrease in the frequency of both cells). Increasing the dependence between both cells seems to suppress the oscillations, rather that increasing the synchronization. In addition, to quantify how this coupling we affect the synchronization between the 2 cells, we compute the correlation matrix for each pair of simulations and compare the correlation terms. For the case where no coupling is present, the correlation obtained is -0.02 ± 0.08 (blue bars in right column of **Figure 5D**). When we add the coupling term to the calculation of the chemical potential, the value is similarly low (-0.09 ± 0.17), implying that there is no coupling or that the periods of phase and anti-phase are very similar and cancel each other.

Next, we performed simulations where the coupling is set to occur at the level of the tension. The rationale behind this

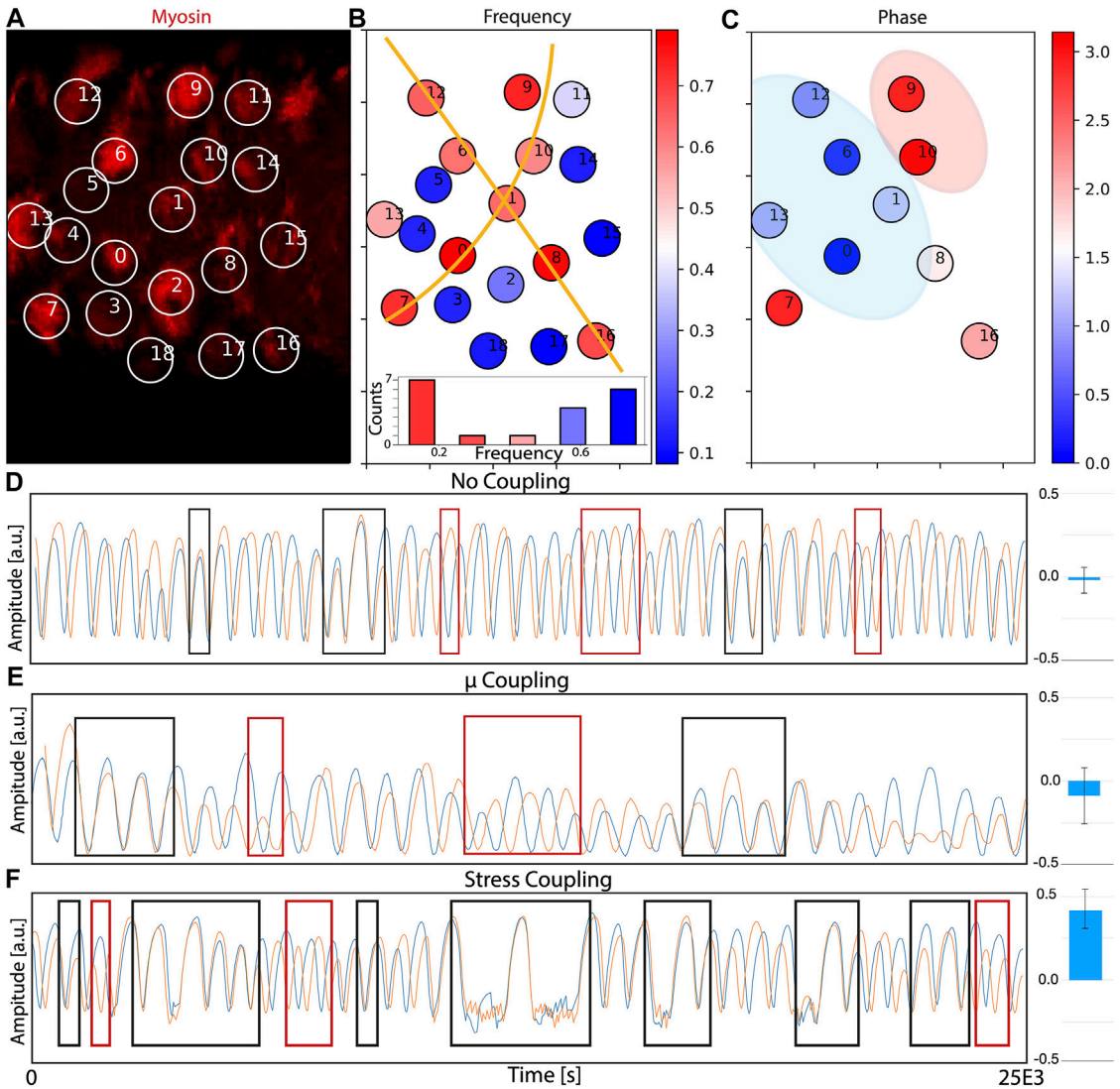

FIGURE 5 | Supra-cellular coordination and coupling of actomyosin oscillations. **(A)** Snapshot of the time-lapse movie used to track myosin levels (red) in different cells. The full movie is shown as **Supplementary Movie S5**. Cells are labeled and the intensity of signal inside the circle is fitted to a sinusoidal function for posterior analysis. Some of the circles appear to be empty because they are at the minimum of the oscillation, but they will become visible in posterior frames. **(B)** Plot of the frequency of the oscillations of each cell. Cells with high frequency of oscillations are colored towards the red. Cells with low frequency are colored towards the blue. The orange lines are drawn as a guide to the eye to help identify supra-cellular organization. A histogram representing the frequency distribution suggest a bimodal organization. **(C)** Comparison of the differences in phase of the oscillations between cells with a similar frequency, taking cell "O" as reference. Cells labeled in blue have similar phase, and cells labeled in red have a dynamics close to full anti-phase. Blue region is used as a mark to the eye to illustrate clusters of cells with similar phase. Red region is used as a mark to the eye to illustrate clusters of cells in anti-phase with cell "O". **(D–F)** Numerical simulations of 2 cells in conditions of **(D)** no coupling, **(E)** coupling *via* chemical potential and **(E)** coupling *via* tension. Black and red rectangles indicate regions of phase and anti-phase synchronization, correspondingly. Blue bars on the left plot the correlation terms of the correlation matrix between pairs (three repeats, bars correspond to the standard deviation).

scenario is the following: since a compression of a cell results in expansion of the neighbor, this expansion may correspond to a release in the local tension of the network (due to local breakup of links between network and inner cell membrane, for instance). The resulting oscillations in this scenario are represented in **Figure 5F**. Compared to the control simulations with no coupling (**Figure 5D**), there seems to appear more regions where locking between the two phases occur. Interestingly, the synchronization is more marked in phase (black rectangles) that in anti-phase (red rectangles), which agrees with the experimental observation that cells in close proximity seem to be oscillating in phase (**Figure 5C**, blue region). Correlation analysis when the systems are coupled through their total stress results in a value of 0.42. ± 0.12, meaning that this approach is causing a more important effect than the previous two (blue bars in right column of **Figure 5D**). Again, higher intensity in the coupling seems to suppress the oscillation, rather than increase the synchronization.

4 DISCUSSION

Coarse Grained simplifications of biological systems allow us to study the properties that arise from molecular interactions, using large amounts of particles and during long periods of time. In addition, the use of a semi-grand canonical ensemble allows us to simulate mixtures of a finite number of entities, an approach much more suitable to models biological systems than the most traditional canonical or grand-canonical ensembles. Coarse Grained approaches are a form of rule-based models, and compared to systems of differential equations, allow direct implementation of compartmentalization, molecule orientation, and other restrictions based on direct experimental observations. Ultimately, coarse grained semi-grand canonical approaches constitute an optimal framework to understand biological processes using computational models.

Here, we use a Coarse Grained model that has been shown to reproduce many features of the actomyosin cortex to study the properties of the emerging actomyosin oscillations. Although the mechanism underlying these oscillations is not fully characterized, it is clear that turnover of the main components is a key aspect in the process [50]. Another main advantage of our model is that turnover is a built-in feature, regulated by potential functions that sets the transport between the two compartments.

The architecture of networks is a key property that determines its dynamics, how information travels, and how force, tension and energy are distributed. In the case of actomyosin networks, their structure is of special importance, because it fully determines force transmission mediated by myosin motors [51], and in consequence, the dynamics of compression (shown beautifully in Refs. [52, 53]). Our framework allows us to directly apply graph theory to characterize the structure of the actomyosin network in the cortex. Our analysis shows that networks generated by both parallel and perpendicular F-actin filaments produce more robust and regular oscillations, due to a faster and more widespread redistribution of energy and tension.

Time-lapse movies of actomyosin oscillations in basal follicle cells show that assembly and disassembly occur almost simultaneously throughout the cell, while in apical oscillations of the amnioserosa, it resembles more a wave-like type of oscillations, that start in one region of the cell and travels directionally. Our model shows that one possibility to transition from bulk to flow oscillations is to reduce the link strength between G-actin and the cortex, mediated by anchor proteins such as the Integrin family of proteins. In a previous publication [31], we over-expressed members of the Integrin family to test the effect of increased attachment. A future interesting experiment will be to reduce Integrin levels and see if we observe a more traveling wave-like behavior.

Finally, it is well established that actomyosin within individual cells can collectively generate tissue-level force during morphogenesis [5]. How this coordination and coupling occurs is not fully understood. Previous studies suggest that oscillations occur mainly in anti-phase between neighboring cells [7], but when cells are part of a tissue with many neighbours, it is simply not possible for each cell in the tissue to be in anti-phase with all of their neighbours.

Our analysis shows that actomyosin oscillations are indeed coupled between short distance neighbours, in both frequency and phase. Unfortunately, our analysis is not able to unequivocally distinguish the existence of supra-cellular actomyosin waves, similarly to the well characterized actomyosin cables [54, 55], the structures that appear during embryonic stem cell colony growth [56] or during wound healing [46], where a single pulse of actomyosin forms around the wound edge and flows toward the margin of the wound.

Our model shows that this coupling can arise based on mechanical interaction, but the conclusions derived from the model are limited because we are only using 2 cells, rather than a tissue where cells have many neighbours. Although many other scenarios can be tested, our results suggests that mechanical coupling can only induce partial synchronization, and that maybe synchronization in the experimental system takes place *via* other mechanisms, such as biochemical communication, for instance.

The whole topic of coupling and the arising of supra-cellular actomyosin organization is very interesting, and an stimulating approach will be to use the model to couple more than 2 cells and observed synchronization and systems organization. To do that, we will need to fully parallelize the framework, and use of high performance workstations or clusters. This effort will be part of future research project from our lab.

In conclusion, our model is able to reproduce many important aspects of actomyosin cortex oscillations, and can be used to explore the role of each main component of the actomyosin cortex. Moreover, the spatial characteristics of the model allow direct comparison with experimental actomyosin flows or the arising of supra-cellular actomyosin organization.

DATA AVAILABILITY STATEMENT

The raw data supporting the conclusions of this article will be made available by the authors, without undue reservation.

AUTHOR CONTRIBUTIONS

MH-D-V performed research and wrote the manuscript. AV-E, MM-B, and NG Performed experiments. DM designed research, provided funding and wrote the manuscript.

FUNDING

DM acknowledges funding to the Spanish Ministerio de Econoíma y Competitividad (BFU2014-53299-P, RTI2018-096953-B-I00), funding to IFIMAC-UAM, through the 'María de Maeztu' Programme for Units of Excellence in R&D from the Spanish Ministerio de Economía y Competitividad (CEX2018-000805-M), and funding from Comunidad de Madrid (PEJD-2018- PRE/BMD-7980). Institutional grants by Fundación Ramón Areces and Banco de Santander to the CBMSO are

also acknowledged. The authors declare that this study received funding from Banco de Santander, via institutional grants. The funder was not involved in the study design, collection, analysis, interpretation of data, the writing of this article or the decision to submit it for publication.

SUPPLEMENTARY MATERIAL

The Supplementary Material for this article can be found online at: https://www.frontiersin.org/articles/10.3389/fphy.2022.881384/full#supplementary-material

REFERENCES

1. Rapp PE. Why Are So Many Biological Systems Periodic? *Prog Neurobiol* (1987) 29:261–73. doi:10.1016/0301-0082(87)90023-2
2. Ray HJ, Niswander L. Mechanisms of Tissue Fusion During Development. *Development* (2012) 139:1701–11. doi:10.1242/dev.068338
3. Clarke DN, Martin AC. Actin-based Force Generation and Cell Adhesion in Tissue Morphogenesis. *Curr Biol* (2021) 31:R667–R680. doi:10.1016/j.cub.2021.03.031
4. Gorfinkiel N. From Actomyosin Oscillations to Tissue-Level Deformations. *Dev Dyn* (2016) 245:268–75. doi:10.1002/dvdy.24363
5. Martin AC, Gelbart M, Fernandez-Gonzalez R, Kaschube M, Wieschaus EF. Integration of Contractile Forces during Tissue Invagination. *J Cell Biol* (2010) 188:735–49. doi:10.1083/jcb.200910099
6. Martin AC, Kaschube M, Wieschaus EF. Pulsed Contractions of an Actin-Myosin Network Drive Apical Constriction. *Nature* (2009) 457:495–9. doi:10.1038/nature07522
7. Solon J, Kaya-Çopur A, Colombelli J, Brunner D. Pulsed Forces Timed by a Ratchet-like Mechanism Drive Directed Tissue Movement during Dorsal Closure. *Cell* (2009) 137:1331–42. doi:10.1016/j.cell.2009.03.050
8. Blanchard GB, Murugesu S, Adams RJ, Martinez-Arias A, Gorfinkiel N. Cytoskeletal Dynamics and Supracellular Organisation of Cell Shape Fluctuations During Dorsal Closure. *Development* (2010) 137:2743–52. doi:10.1242/dev.045872
9. Hayes P, Solon J. Drosophila Dorsal Closure: An Orchestra of Forces to Zip Shut the Embryo. *Mech Development* (2017) 144:2–10. doi:10.1016/j.mod.2016.12.005
10. Pasakarnis L, Frei E, Caussinus E, Affolter M, Brunner D. Amnioserosa Cell Constriction but Not Epidermal Actin Cable Tension Autonomously Drives Dorsal Closure. *Nat Cell Biol* (2016) 18:1161–72. doi:10.1038/ncb3420
11. Koride S, He L, Xiong L-P, Lan G, Montell DJ, Sun SX. Mechanochemical Regulation of Oscillatory Follicle Cell Dynamics in the Developing drosophila Egg Chamber. *MBoC* (2014) 25:3709–16. doi:10.1091/mbc.e14-04-0875
12. He L, Wang X, Tang HL, Montell DJ. Tissue Elongation Requires Oscillating Contractions of a Basal Actomyosin Network. *Nat Cell Biol* (2010) 12:1133–42. doi:10.1038/ncb2124
13. Ramaekers FC, Bosman FT. The Cytoskeleton and Disease. *J Pathol* (2004) 204:351–4. doi:10.1002/path.1665
14. Dominguez R, Holmes KC. Actin Structure and Function. *Annu Rev Biophys* (2011) 40:169–86. doi:10.1146/annurev-biophys-042910-155359
15. Clark AG, Dierkes K, Paluch EK. Monitoring Actin Cortex Thickness in Live Cells. *Biophysical J* (2013) 105:570–80. doi:10.1016/j.bpj.2013.05.057
16. Chugh P, Paluch EK. The Actin Cortex at a Glance. *J Cell Sci* (2018) 131:jcs186254. doi:10.1242/jcs.186254
17. Wang P, Hawkins TJ, Hussey PJ. Connecting Membranes to the Actin Cytoskeleton. *Curr Opin Plant Biol* (2017) 40:71–6. doi:10.1016/j.pbi.2017.07.008
18. Winder SJ, Ayscough KR. Actin-binding Proteins. *J Cell Sci* (2005) 118:651–4. doi:10.1242/jcs.01670
19. Santa-Cruz Mateos C, Valencia-Expósito A, Palacios IM, Martín-Bermudo MD. Integrins Regulate Epithelial Cell Shape by Controlling the Architecture and Mechanical Properties of Basal Actomyosin Networks. *Plos Genet* (2020) 16:e1008717. doi:10.1371/journal.pgen.1008717
20. Masters TA, Sheetz MP, Gauthier NC. F-actin Waves, Actin Cortex Disassembly and Focal Exocytosis Driven by Actin-Phosphoinositide Positive Feedback. *Cytoskeleton* (2016) 73:180–96. doi:10.1002/cm.21287
21. Moore T, Wu SK, Michael M, Yap AS, Gomez GA, Neufeld Z. Self-organizing Actomyosin Patterns on the Cell Cortex at Epithelial Cell-Cell Junctions. *Biophysical J* (2014) 107:2652–61. doi:10.1016/j.bpj.2014.10.045
22. Aristotelous AC, Crawford JM, Edwards GS, Kiehart DP, Venakides S. Mathematical Models of Dorsal Closure. *Prog Biophys Mol Biol* (2018) 137:111–31. doi:10.1016/j.pbiomolbio.2018.05.009
23. Dierkes K, Sumi A, Solon J, Salbreux G. Spontaneous Oscillations of Elastic Contractile Materials with Turnover. *Phys Rev Lett* (2014) 113:148102. doi:10.1103/physrevlett.113.148102
24. Lo WC, Madrak C, Kiehart DP, Edwards GS. Unified Biophysical Mechanism for Cell-Shape Oscillations and Cell Ingression. *Phys Rev E* (2018) 97:062414. doi:10.1103/PhysRevE.97.062414
25. Dureau M, Alessandri A, Bagnerini P, Vincent S. Modeling and Identification of Amnioserosa Cell Mechanical Behavior by Using Mass-spring Lattices. *Ieee/acm Trans Comput Biol Bioinform* (2016) 14:1476–81. doi:10.1109/TCBB.2016.2586063
26. Sedzinski J, Biro M, Oswald A, Tinevez J-Y, Salbreux G, Paluch E. Polar Actomyosin Contractility Destabilizes the Position of the Cytokinetic Furrow. *Nature* (2011) 476:462–6. doi:10.1038/nature10286
27. Machado PF, Blanchard GB, Duque J, Gorfinkiel N. Cytoskeletal Turnover and Myosin Contractility Drive Cell Autonomous Oscillations in a Model of drosophila Dorsal Closure. *Eur Phys J Spec Top* (2014) 223:1391–402. doi:10.1140/epjst/e2014-02197-7
28. Gorfinkiel N. Mechano-chemical Coupling Drives Cell Area Oscillations during Morphogenesis. *Biophysical J* (2013) 104:1–3. doi:10.1016/j.bpj.2012.11.3822
29. Wang Q, Feng JJ, Pismen LM. A Cell-Level Biomechanical Model of drosophila Dorsal Closure. *Biophysical J* (2012) 103:2265–74. doi:10.1016/j.bpj.2012.09.036
30. Valencia-Expósito A, Grosheva I, Míguez DG, González-Reyes A, Martín-Bermudo MD. Myosin Light-Chain Phosphatase Regulates Basal Actomyosin Oscillations during Morphogenesis. *Nat Commun* (2016) 7:10746–11. doi:10.1038/ncomms10746
31. Hernández-del Valle M, Valencia-Expósito A, López-Izquierdo A, Casanova-Ferrer P, Tarazona P, Martín-Bermudo MD, et al. A Coarse-Grained Approach to Model the Dynamics of the Actomyosin Cortex. *BMC Biol* (2022) 20:90–11. doi:10.1186/s12915-022-01279-2
32. Korkmazhan E, Tompa P, Dunn AR. The Role of Ordered Cooperative Assembly in Biomolecular Condensates. *Nat Rev Mol Cell Biol* (2021) 22:647–8. doi:10.1038/s41580-021-00408-z
33. Baumgartner R, Fu H, Song Z, Lin Y, Cheng J. Cooperative Polymerization of α-helices Induced by Macromolecular Architecture. *Nat Chem* (2017) 9:614–22. doi:10.1038/nchem.2712
34. Matsui TS, Kaunas R, Kanzaki M, Sato M, Deguchi S. Non-muscle Myosin Ii Induces Disassembly of Actin Stress Fibres Independently of Myosin Light Chain Dephosphorylation. *Interf Focus.* (2011) 1:754–66. doi:10.1098/rsfs.2011.0031
35. Huang W, Matsui TS, Saito T, Kuragano M, Takahashi M, Kawahara T, et al. Mechanosensitive Myosin Ii but Not Cofilin Primarily Contributes to Cyclic Cell Stretch-Induced Selective Disassembly of Actin Stress Fibers. *Am J Physiology-Cell Physiol* (2021) 320:C1153–C1163. doi:10.1152/ajpcell.00225.2020
36. Sonal KA, Ganzinger KA, Vogel SK, Mücksch J, Blumhardt P, Schwille P. Myosin-II Activity Generates a Dynamic Steady State with Continuous Actin Turnover in a Minimal Actin Cortex. *J Cell Sci* (2018) 132. doi:10.1242/jcs.219899.Jcs219899
37. Bezanson J, Karpinski S, Shah VB, Julia EA. A Fast Dynamic Language for Technical Computing. *arXiv preprint arXiv:1209.5145* (2012).
38. Metropolis N, Ulam S. The Monte Carlo Method. *J Am Stat Assoc* (1949) 44:335–41. doi:10.1080/01621459.1949.10483310
39. Prasad M, Montell DJ. Cellular and Molecular Mechanisms of Border Cell Migration Analyzed Using Time-Lapse Live-Cell Imaging. *Developmental Cel* (2007) 12:997–1005. doi:10.1016/j.devcel.2007.03.021

40. Dijkstra EW. A Note on Two Problems in Connexion with Graphs. *Numer Math* (1959) 1:269–71. doi:10.1007/bf01386390
41. Bashirzadeh Y, Redford SA, Lorpaiboon C, Groaz A, Moghimianavval H, Litschel T, et al. Actin Crosslinker Competition and Sorting Drive Emergent Guv Size-dependent Actin Network Architecture. *Commun Biol* (2021) 4: 1136–11. doi:10.1038/s42003-021-02653-6
42. Sjöblom B, Salmazo A, Djinović-Carugo K. α-Actinin Structure and Regulation. *Cell. Mol. Life Sci.* (2008) 65:2688–701. doi:10.1007/s00018-008-8080-8
43. Rauzi M, Lenne P-F, Lecuit T. Planar Polarized Actomyosin Contractile Flows Control Epithelial junction Remodelling. *Nature* (2010) 468:1110–4. doi:10.1038/nature09566
44. Mayer M, Depken M, Bois JS, Jülicher F, Grill SW. Anisotropies in Cortical Tension Reveal the Physical Basis of Polarizing Cortical Flows. *Nature* (2010) 467:617–21. doi:10.1038/nature09376
45. Vogel SK, Wölfer C, Ramirez-Diaz DA, Flassig RJ, Sundmacher K, Schwille P. Symmetry Breaking and Emergence of Directional Flows in Minimal Actomyosin Cortices. *Cells* (2020) 9:1432. doi:10.3390/cells9061432
46. Antunes M, Pereira T, Cordeiro JV, Almeida L, Jacinto A. Coordinated Waves of Actomyosin Flow and Apical Cell Constriction Immediately after Wounding. *J Cell Biol* (2013) 202:365–79. doi:10.1083/jcb.201211039
47. Ghabache E, Cao Y, Miao Y, Groisman A, Devreotes PN, Rappel WJ. Coupling Traction Force Patterns and Actomyosin Wave Dynamics Reveals Mechanics of Cell Motion. *Mol Syst Biol* (2021) 17:e10505. doi:10.15252/msb.202110505
48. Jayasinghe AK, Crews SM, Mashburn DN, Hutson MS. Apical Oscillations in Amnioserosa Cells: Basolateral Coupling and Mechanical Autonomy. *Biophysical J* (2013) 105:255–65. doi:10.1016/j.bpj.2013.05.027
49. Xie S, Martin AC. Intracellular Signalling and Intercellular Coupling Coordinate Heterogeneous Contractile Events to Facilitate Tissue Folding. *Nat Commun* (2015) 6:7161–13. doi:10.1038/ncomms8161
50. Salbreux G, Charras G, Paluch E. Actin Cortex Mechanics and Cellular Morphogenesis. *Trends Cell Biology* (2012) 22:536–45. doi:10.1016/j.tcb.2012.07.001
51. Murrell M, Oakes PW, Lenz M, Gardel ML. Forcing Cells into Shape: the Mechanics of Actomyosin Contractility. *Nat Rev Mol Cell Biol* (2015) 16: 486–98. doi:10.1038/nrm4012
52. Gardel ML, Shin JH, MacKintosh FC, Mahadevan L, Matsudaira P, Weitz DA. Elastic Behavior of Cross-Linked and Bundled Actin Networks. *Science* (2004) 304:1301–5. doi:10.1126/science.1095087
53. Alvarado J, Sheinman M, Sharma A, MacKintosh FC, Koenderink GH. Molecular Motors Robustly Drive Active Gels to a Critically Connected State. *Nat Phys* (2013) 9:591–7. doi:10.1038/nphys2715
54. Röper K. Supracellular Actomyosin Assemblies during Development. *Bioarchitecture* (2013) 3:45–9. doi:10.4161/bioa.25339
55. Harris TJC. Sculpting Epithelia with Planar Polarized Actomyosin Networks: Principles from drosophila. *Semin Cell Dev Biol* (2018) 81:54–61. doi:10.1016/j.semcdb.2017.07.042
56. Du J, Fan Y, Guo Z, Wang Y, Zheng X, Huang C, et al. Compression Generated by a 3d Supracellular Actomyosin Cortex Promotes Embryonic Stem Cell colony Growth and Expression of Nanog and Oct4. *Cell Syst* (2019) 9:214–20. doi:10.1016/j.cels.2019.05.008

Conflict of Interest: The authors declare that the research was conducted in the absence of any commercial or financial relationships that could be construed as a potential conflict of interest.

Publisher's Note: All claims expressed in this article are solely those of the authors and do not necessarily represent those of their affiliated organizations, or those of the publisher, the editors and the reviewers. Any product that may be evaluated in this article, or claim that may be made by its manufacturer, is not guaranteed or endorsed by the publisher.

frontiers | Frontiers in Physics

ORIGINAL RESEARCH
published: 30 May 2022
doi: 10.3389/fphy.2022.864207

A Twitter-Based Economic Policy Uncertainty Index: Expert Opinion and Financial Market Dynamics in an Emerging Market Economy

*Sevcan Yeşiltaş[1], Anıl Şen[1], Beyza Arslan[1] and Sumru Altuğ[2,3]**

[1]College of Administrative Sciences and Economics, Koç University, Istanbul, Turkey, [2]Department of Economics, American University of Beirut, Beirut, Lebanon, [3]Centre for Economic Policy Research, London, United Kingdom

In this paper, we construct a Twitter-based high-frequency Economic Policy Uncertainty (TEPU) index built on a select set of Twitter user accounts whose tweets are considered to reflect expert opinion on the topic. We study the relationship between the TEPU index and a set of key financial indicators for tracking financial developments in Turkey over the sample period 2013–2021. Based on the results from a vector autoregressive analysis, we find evidence that changes in expert opinion described by fluctuations in the TEPU index interact with fluctuations in financial indicators such as the exchange rate and the stock market index to capture information about high frequency events during our sample period. Second, fluctuations in the TEPU index emerge as a key indicator that helps to predict the country risk premium measured by the CDS spread. We also find evidence that the conditional volatility of the different series reflects salient events that occurred over our sample period.

Keywords: Twitter-based data, economic policy uncertainty, monetary policy, financial markets, Turkey

OPEN ACCESS

Edited by:
Federico Rossi,
University of Siena, Italy

Reviewed by:
Lee A. Smales,
University of Western Australia, Australia
Marcin Wolski,
European Investment Bank, Luxembourg

****Correspondence:***
Sumru Altuğ
sa287@aub.edu.lb

Specialty section:
This article was submitted to Social Physics, a section of the journal Frontiers in Physics

Received: *01 February 2022*
Accepted: *22 April 2022*
Published: *30 May 2022*

Citation:
Yeşiltaş S, Şen A, Arslan B and Altuğ S (2022) A Twitter-Based Economic Policy Uncertainty Index: Expert Opinion and Financial Market Dynamics in an Emerging Market Economy. Front. Phys. 10:864207. doi: 10.3389/fphy.2022.864207

1 INTRODUCTION

On 20 December 2021, the exchange rate hit a record low at 18.36 Turkish Lira (TRY) against the US Dollar (USD) after falling from a value of 8.29 TRY against the USD on September 2021. It rebounded back to a value of 10.78 TRY per USD by 23 December 2021 following the announcement of two foreign-currency indexed saving schemes that link the interest rate received on Turkish lira deposits to fluctuations in the exchange rate.[1] The factors instigating this fall were the removal of two deputy governors and one member of the Monetary Policy Committee (MPC) at the Central Bank of the Republic of Turkey (CBRT) and subsequent cuts in the policy rate of 500 basis points beginning with the MPC meeting on 23 September 2021. These developments were accompanied by large increases in Turkey's CDS spreads on its sovereign bonds as well as significant volatility in its stock market.[2]

In this paper, we construct a daily-frequency Twitter-based Economic Policy Uncertainty (TEPU) index that aims to track such high frequency developments in Turkey's economic and political arena—spanning even a few hours in a given day that cannot be captured through the standard

[1]https://www.ft.com/content/f6c3f33f-356c-47b8-8156-5fe07ffe6237?shareType=nongift.
[2]http://www.aljazeera.com/economy/2021/12/17/turkey-stock-trading-halted-twice-as-lira-crashes-to-new-low.

newspaper–based economic policy uncertainty (EPU) indices [1]. To the best of our knowledge, our paper is the first to test the ability of an EPU index for capturing and conveying information about developments in a highly volatile policy environment for a leading emerging market economy, Turkey.

Earlier [2] constructs an EPU index for Turkey using the Dow Jones' Factiva global news database over the period 1996–2017 and examine the relationship between their EPU index and sectoral data on investment and employment. They argue that their use of mainly foreign newspapers rather than Turkish newspapers as the primary source for this index may be a preferable approach, as foreign newspapers directly capture international perceptions on Turkey's EPU index and foreign news sources span longer periods than Turkish newspapers. [3] and [4] also create EPU indices for Turkey based on the digital archives of several daily Turkish newspapers but none of these analyses go beyond 2018. By contrast, the usage of Twitter data in our analysis facilitates the creation of an EPU index at monthly, weekly and even daily frequencies. The timely character of Twitter data enables us to update our forward-looking TEPU index in real time. This way, our TEPU index captures the effects of the Covid-19 shock of 2020 as well as the fast-moving anomalous developments that occurred in Turkish financial markets during 2021.

From a practical point of view, there are many reasons to make use of Twitter data as an alternative to those extracted from conventional media platforms. In the past decade, the Twitter platform has provided a direct, instantaneous, and network-enhanced channel through which economic policy experts communicate with the public. Economic policy experts can now freely convey their "real-time" opinions on economic and finance matters to a large social network. As Twitter feeds capture a diversity of opinion in a nearly instantaneous fashion that is typically filtered in newspaper articles and reported with a considerable time lag, our TEPU index enables us to account for a variety of different views transmitted within this network in our analysis.

Recent studies in the relevant literature have examined data sets derived from popular social media platforms such as Twitter, Facebook, blogs etc. [5] use the Twitter Application Programming Interface (API) to extract all tweets containing the words "uncertain," "uncertainly," "uncertainties" "uncertainty." and generate an EPU index. They use geotagged tweets and information about users' followers to construct their index based on tweets sent by users located in the US. Utilizing the Twitter accounts of 15 Chilean mass media specialized in or with material devoted to economics, [6] constitute a daily-frequency EPU index for Chile based on Twitter data. Their constructed indices seek to capture the level of general disagreement about economic policies and the current economic situation, respectively, over the period 2012–2019 in Chile.

Our paper differs from these existing studies that are typically based on the use of bulk Twitter data and that potentially suffer from noisy observations. In contrast to these analyses, we use a user list curation process to restrict our analysis to a select group of Twitter users. Using web scraping methods, we are able to extract recent tweets posted by these selected accounts easily and use them to update our TEPU index for capturing the extremely fast daily developments in the Turkish economy in a timely manner.[3] To avoid any bias in TEPU index that might potentially occur due to the selection of user accounts within our user list curation process, we run the bootstrapping algorithm repetitively with different seed lists, which results in the same final candidate list in all repetitions. Furthermore, our bootstrapping algorithm enables us to prevent errors arising from the Turkish language applications of Natural Language Processing (NLP) methods as well as to present a novel approach to the subject of content-based EPU indexing.

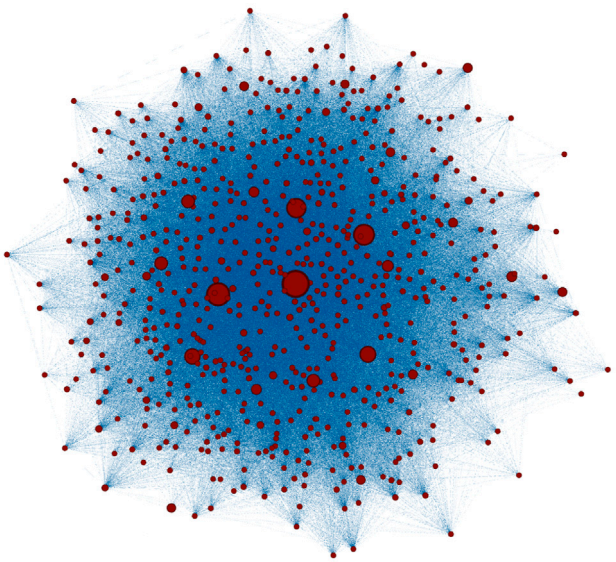

FIGURE 1 | Network of selected Twitter users. Nodes indicate the selected user accounts in Twitter. The size of the nodes reflects the number of their followers.

By implementing the different phases of our bootstrapping algorithm, we obtain a group of selected Twitter users that have expertise in economics and finance. The final candidate list of 661 users is comprised of academics, company executives, politicians, consultants, journalists, portfolio managers, and 218 bureaucrats. **Figure 1** depicts the connections in the network of this selected group. These connections illustrate the following-follower status of the selected user accounts and the size of the nodes shows their relative influence. This figure suggests that there is a very strong interaction among the Twitter users in this group in that they are influenced by each other through their interactions and moreover, influence the public through their high number of followers. Hence, it is reasonable to think of this group as a viable network of Twitter user accounts by which we can capture the role of expert opinion in identifying economic policy uncertainty

[3]In contrast to the Twitter API which has rate limits (see https://developer.twitter.com/en/docs/twitter-api/rate-limitslink), the web scraping method that we use is faster in the extraction of data.

in Turkey. Our approach involves building an EPU index based on the real-time interactions of this network, which allows for a fast-moving way of capturing expert opinion in such a volatile environment.

Turkey offers the case of an emerging market economy where market signals regarding monetary policy have become blurred by the pursuit of unconventional monetary policy as well as policy reversals, especially since 2020. In our analysis, we seek to understand the interaction between our measure of expert opinion summarized by the TEPU index and salient financial indicators for tracking the changes in financial markets that have been occurring in Turkey over the sample period. For this purpose, we derive our results from a Structural Vector Autoregressive (SVAR) analysis model that allows for dynamic inter-relationships in the conditional mean of the different series. We also use a Multivariate Generalized Autoregressive Conditional Heteroscadasticity (M-GARCH) model for understanding the volatility dynamics in the financial series [7]. By conducting a weekly frequency-based analysis, we investigate the full sample that covers the period 2013–2021 as well as several sub-samples to understand the effects of monetary policy changes and unconventional monetary policy being conducted during this period.

Our results show that fluctuations in the TEPU index and financial indicators such as the BIST-100 index and the USD/TRY exchange rate interact to capture information about political and economic developments that occur during the sample period 2013–2021. In particular, the TEPU index and the USD/TRY exchange rate are two key indicators which reflect monetary policy surprises and monetary policy announcements arising from the pursuit of unconventional monetary policy in recent years in Turkey. The TEPU index also emerges as a key predictor of changes in the CDS spread, suggesting that expert opinion itself contains information useful for evaluating the country's risk premium [8]. The fluctuations in the TEPU index together with the USD/TRY exchange rate and the CDS spread also help predict fluctuations in equity markets in Turkey. A novel part of our analysis is that we document how increases in the conditional volatility of one indicator are transmitted to the conditional volatility in the remaining financial indicators. In a tumultuous policy environment similar to the one observed Turkey, we find that the conditional volatility of the different financial indicators respond to salient events that occurred over our sample period.

Our results relate to the literature that has found predictive effects of commodity prices such as oil prices on the economic policy index that, in turn, may affect equity prices for developed countries [9,10] as well as studies for emerging market economies that examine the role of economic policy uncertainty on real outcomes in these economies [11]. Our results differ from these papers in that we focus on a period of large monetary shocks and monetary policy reversals for a major emerging market economy. While we do not provide an analysis of the effects of economic policy uncertainty on real outcomes, our results nevertheless provide novel information about the channels through which economic policy uncertainty impacts high-frequency developments observed in Turkish financial markets.

The remainder of this paper is organized as follows. **Section 2** provides a literature review. **Section 3** explains in detail how we construct the Twitter-based economic policy uncertainty index for Turkey. **Section 4** firstly provides details regarding data used in our econometric analysis and secondly conducts an event analysis to show how our TEPU index relates to important political and economic events over the sample period 2013–2021. It also tracks developments in Turkish financial markets during this period. **Section 5** is devoted to the details of econometric methodology used in the analysis and explains the results. **Section 6** concludes.

2 LITERATURE REVIEW

The question of how households, businesses and policy makers shape their economic activities as a response to any changes in uncertainty has been widely asked in the literature.[4]

A theoretical strand of the related literature aims to identify the channels through which uncertainty can have an impact on economic outcomes. First, a rise in uncertainty encourages households and businesses to delay their costly-to-reverse expenditures. During the times of high uncertainty households are more likely to delay their purchases on durable goods [12]. When the costs of irreversible investments and hiring decisions are high, firms facing high uncertainty tend to adjust and delay the timing of such actions [13]. [14] and [15] show that heightened uncertainty affects investment behavior by creating an option value of waiting. In uncertain times, firms prefer to delay capital expenditures involving sunk costs until more information is revealed.

Second, uncertainty can also have real option effects on employment. [16] suggests that when search frictions are the only costs associated with the reallocation of labor, real option effects of uncertainty are weak if firms can easily reverse their employment decisions. A rise in uncertainty can also encourage firms to adjust on flexible margins such as part-time employment due to the existence of fixed costs of hiring and firing [17]. Third, it is shown that unexpected changes in uncertainty regarding fiscal policy affect economic activity, leading to a sizable adverse effect on output ([18] and [19]). Fourth, uncertainty that works through growth options mechanism might have a positive impact on long run growth. In a recent study, [20] shows that R&D intensive firms can raise their stock value by taking advantage of growth opportunities particularly at times of high uncertainty. Fifth, studies point to financial frictions as one of the key mechanisms through which fluctuations in uncertainty can have an adverse effect on investment by raising risk premiums ([21] and [22]).

Another strand of the literature examines contractionary effects of uncertainty with reference to decreasing household spending. In this vein, [23] model such behavior as a precautionary response to uncertainty and increasing costs of finance arising from risk premium adjustments. Lastly, a group of studies focuses explicitly on economic policy uncertainty and examines the negative impacts of uncertainty derived solely from

[4]See Bloom [57] for a detailed survey on how uncertainty affects economic activity.

policy developments. Among other studies [24–28], and [1] note the depressive effects of uncertainty arising from monetary, fiscal, and regulatory policies on economic aggregates, investment and business cycle volatility. The survey-based evidence shown in [29] suggests that higher trade policy uncertainty since 2017 has dampened U.S. business investment. Moreover, [30] indicate that uncertainty regarding trade policy reduced U.S. business investment by about 1.5% in 2018.

In recent years, many of the empirical studies in the related literature endeavor to develop accurate empirical measures for uncertainty. The reasons for the recent surge in interest range from the ease to accessing online news archives and digital archives of opinionated data, to the availability of firm- and household-level data, to the application of NLP techniques that allows researchers to save memory. A relatively new and growing field aims to develop a measure for economic policy uncertainty by using text search methods. The well-known economic uncertainty index created by [1] is a monthly index for the US economy based on the frequency of a selected list of words in 10 leading US newspapers since 1985.[5] More recently, [31] construct a new uncertainty index, the World Uncertainty Index (WUI), by calculating the frequency of the word "uncertainty" within the country reports released by Economist Intelligence Unit for 143 individual countries including Turkey on a quarterly basis from 1996 onward.

The measurement of economic policy uncertainty and its role in affecting real and financial outcomes have been investigated in numerous empirical studies. Using an SVAR framework, [32] studies the impact of heightened uncertainty that is associated with major economic and political shocks like Cuban Missile crisis, the assassination of JFK, the OPEC I oil-price shock, and the 9/11 terrorist attacks. The simulation results of this study show that uncertainty generates a 1% drop and rebound in output, employment, and productivity growth, leading to powerful real-option effects, which are due to firms using their incentive to delay their investment and hiring decisions. [33] develop a time-varying measure of uncertainty as the conditional volatility of the unforeseeable components of the future values of a set of key macroeconomic variables. They report fewer incidences of uncertainty compared to other approaches such as [32] and find that their measure of uncertainty is bunched around three deep recessions. The results of their Vector Autoregressive (VAR) analysis suggest that macro uncertainty explains 29% of the forecast error variance of industrial production while stock returns explain only 9%. In an application that focuses on regulatory risk, [34] studies the effect of the Financial Regulation Policy Uncertainty (FRPU) index on the behavior of credit spreads together with other macroeconomic variables in both a linear SVAR framework and a nonlinear Smooth Transition VAR (STVAR) model. She finds that an increase in the FPRU index leads to an increase in the cost of external finance as well as persistent decline in real activity. Likewise, using an STVAR model, [35] study the effects of an unanticipated increase in economic policy uncertainty on unemployment in recessions and expansions in the United States. [36] use United States interest rate forecasts from Blue Chip Economic Indicators (BCEI) to construct an uncertainty proxy and examine the inter-relationships among monetary policy uncertainty, monetary policy expectations, core inflation, unemployment, and the federal funds rate in a time-varying VAR framework for the United States.

There are also empirical studies conducted in an emerging market economy context. Following the approach in [32], [11] infer a measure of global uncertainty as periods of spikes in the VXO index, which is the implied volatility on a synthetic 30-days option on the S&P 100 stock index.[6] They examine the impact of their measure of uncertainty on a set of financial and real variables for emerging market economies by conducting an SVAR analysis. They find that an increase in uncertainty is associated with a much more severe decline in investment for a group of 20 emerging market economies which is also more persistent compared to a group of 20 developed economies. They also find a significant decline in consumption due to a rise in uncertainty measured in this way, in contrast to developed economies where consumption does not deviate significantly from its trend in response to such shocks. [3] estimate an SVAR model for Turkey which includes an EPU index, the real exchange rate, the real interest rate and one of three macroeconomic variables among real consumption expenditures, real investment expenditures and real GDP. They find that higher economic policy uncertainty leads to greater declines in investment compared to consumption or real GDP.

There is also an extensive literature that examines the interaction of economic policy uncertainty with financial market indicators. [9] show that the EPU index can help to predict the daily realized stock market volatility on the S&P 500 index both in-sample and out-of-sample for a sample period 1996–2013. [10] examine the effects of oil price shocks arising from oil supply-side shocks measured as changes in world oil production, aggregate demand shocks and oil-market specific shocks on the US EPU index and aggregate United States real stock returns. [37] study the predictability of the US EPU index using a basket of 23 commodity price changes. They show that commodity price changes can be considered as a leading indicator of US EPU index. This arises from the fact that one of the components used to create the US EPU index is given by forecast disagreement among professional forecasters, which becomes more uncertain during periods of oil price changes.

A number of studies have also examined the role of economic policy uncertainty induced by the Covid-19 crisis. [38] investigate multiple economic uncertainty indicators for the United States and United Kingdom before and during the COVID-19 pandemic. According to Choleski-identified VAR models they fit to monthly U.S. data, an uncertainty shock predicts record high drops in industrial production of 12–19% during the Covid-19 pandemic.

[5]The authors of Baker et al. [1] develop indices of economic policy uncertainty for countries around the world. In particular, as of March 2022, the most up-to-date EPU indices are provided for 29 countries in their website: https://www.policyuncertainty.com/all_country_data.html.

[6]They define these events as periods in which the Hodrick–Prescott de-trended VXO series exceeds its mean by more than 1.65 standard deviations. In this way, they obtain six events over the sample period 1990–2010 and generate a measure of uncertainty by weighing these events with the magnitude of the volatility shock.

[39] construct a monthly index for each state in the United States using digital archives of local newspapers. They show that the COVID-19 pandemic drove huge increases in policy uncertainty and unemployment, more so in states with stricter government-mandated lockdowns. Using NLP techniques, [40] develop an economic policy uncertainty index (EPU-NLP) for Canada and the United States. They also construct a so-called EPU-Boolean index following the approach in [1] and find that their EPU-NLP index leads to larger declines in real GDP, employment, industrial production and the TSX Composite index compared to the EPU-Boolean index for Canada over the period 2015–2020 that includes the Covid-19 crisis. Arbatli [41] show that the EPU index rises in Japan in reaction to financial crises, the consumption tax hikes, Brexit, and COVID-19.

3 THE TWITTER-BASED ECONOMIC POLICY INDEX

The need for the perception of opinions, attitudes, emotions, appraisals towards entities such as products, services, organizations, individuals, issues, events, and topics coincides with the rapid growth of social media platforms on the Web. Through multiple platforms including reviews, forum discussions, blogs, microblogs, Twitter, and social networks, we now access digital archives of opinionated data around the world [42].

The number of studies conducting sentiment analysis has proliferated in recent years. For example, [43] investigate public sentiment during the 2008, 2009 election by comparing the measures based on traditional presidential election/approval polls with those based on the text analysis of Twitter data. Sentiment analysis has been widely used in many different fields ranging from computer science, to management science, to health science, and to social sciences such as economics and finance. This increasing popularity of sentiment analysis is due to the fact that opinions shape almost all human activities and have a significant impact on our behaviour [44].

From the perspective of economic analysis, the way agents perceive events, policies and markets, make their choices, and set their expectations heavily depends on how others see and evaluate the world. Therefore, agents generally account for others' opinions when making their decisions. For the same reason, households, firm managers and policymakers become attuned to expert opinion whenever they are uncertain about economic policy.

In this paper we construct a measure for economic policy uncertainty based on a select group of Twitter accounts whose tweets are considered to reflect expert opinion in the area of economic policy by the general public. In line with the related literature on social media interactions,[7] we analyze the interaction of the Twitter accounts of economic policy experts with other accounts in Twitter through the number of their followers. The select group of Twitter users consists of ministers, parliamentarians, academicians, bureaucrats, journalists, and private sector professionals that are considered to have capability to provide expert opinion on economic policy. The assessment of economic policy uncertainty by these selected experts is similar, in some ways, to the assessment of risk and uncertainty by the US economists questioned in the highly regarded Survey of Professional Forecasters that is conducted by the Federal Reserve Bank of Philadelphia.[8]

With the increased capacity of Twitter to provide up-to-date documentary on world events, it is inevitably getting harder to extract useful information from the bulk data generated daily by users.[9] As mentioned in the Introduction, our paper differs from existing studies that use bulk Twitter data. Instead we implement a user list curation process. This alternative approach allows us to restrict our analysis to a select group of Twitter accounts. By doing so, we are able to update our TEPU index and to capture the daily developments in the Turkish economy in a timely manner. To verify that our TEPU index does not suffer from any bias that might potentially arise from the above-mentioned selection of Twitter accounts, we use a bootstrapping algorithm that we run repetitively with different seed lists, which results in the same final candidate list in all repetitions.

3.1 The Selection of Twitter Users

In the related literature researchers use several different methods to identify whether the content is about the "economy," "policy" and/or "uncertainty" to construct a measure of economic policy uncertainty. Among others, for example [5] extract all tweets from Twitter API data that contains the words "uncertain," "uncertainly," "uncertainties," "uncertainty.", whereas [40] use NLP methods to determine content. In our paper, we implement a user list curation process that closely follows [45, 46]. This provides us with three advantages: First, it enables us to remove tweets with only a weak impact on public opinion and eliminate the need for scaling noisy data created by bulk retrieval methods.[10] Second, it prevents errors arising from the Turkish language applications of NLP methods. Third, it presents a novel approach to the subject of content-based EPU indexing.

[7]Using three measures of influence including in-degree, retweets and mentions, Cha, Haddadi, Benevenuto and Gummadi [58] investigate the dynamics of user influence across topics and time based on these notions. One of their findings shows that influence is typically gained through concerted effort such as limiting tweets to a single topic. Verweij [59] studies the interactions between a group of Dutch journalists and politicians and show that contacts on Twitter are driven by the need for finding and spreading news, as opposed to religious or ideological identity of parties and media.

[8]The European Central Bank conducts the same survey to obtain the forecasts of the economists located in Euro Area. See https://www.philadelphiafed.org/surveys-and-data/real-time-data-research/survey-of-professional-forecasters and https://www.ecb.europa.eu/stats/ecb_surveys/survey_of_professional_forecasters/html/index.en.html for further details on these surveys.

[9]Turkey has 16.25 million active Twitter users, ranking as the seventh country in the world as of October 2021, see https://www.statista.com/statistics/242606/number-of-active-twitter-users-in-selected-countries/.

[10]Likewise, Storyful, a news and intelligence agency, devotes significant time to manually curate content on social networks such as Twitter and YouTube with the aim of filtering news, or newsworthy content, from the vast quantities of noisy data on these platforms.

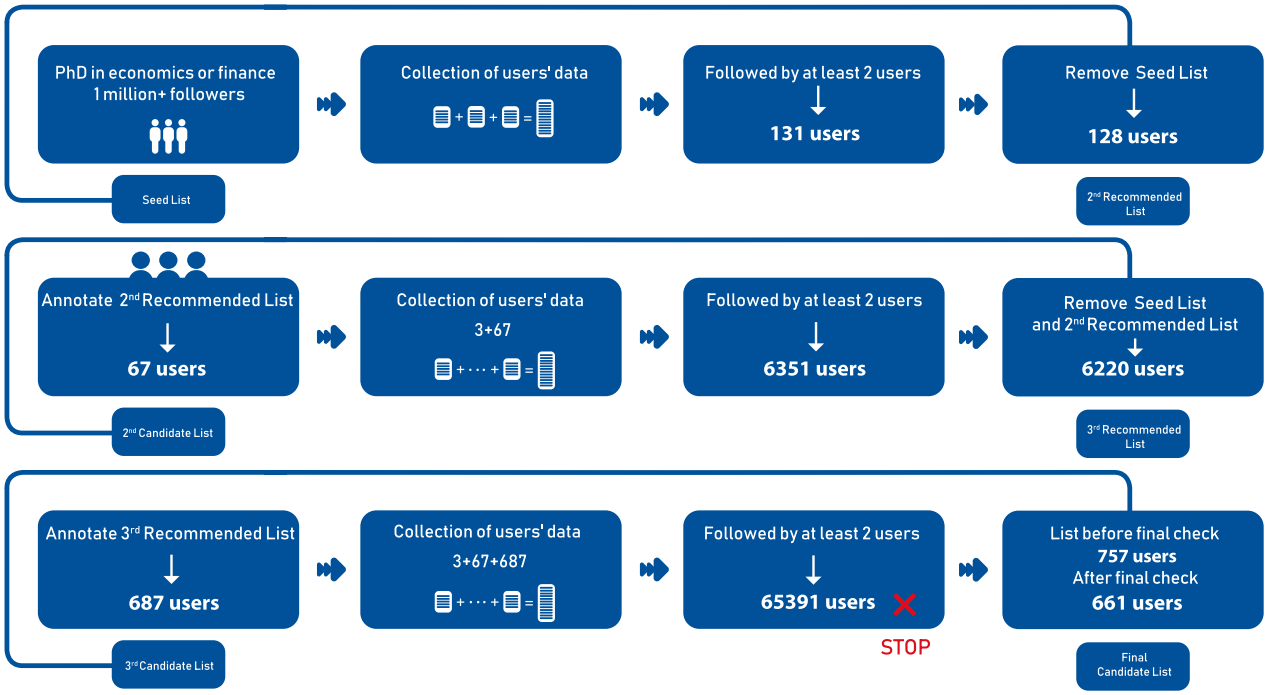

FIGURE 2 | The phases of bootstrapping algorithm.

TABLE 1 | Descriptive statistics of the selected Twitter user accounts.

Occupation/Variable	Mean	Std	Min	Max
Academicians (# 170)				
Number of Followers	54,529.1	283,969	93	3,260,269
Number of Followings	1,080.7	1,092.6	0	5,684
Number of Tweets	9,757.8	14,385.3	33	105,827
Registration Date	2013	2.9	2009	2020
Parliamentarians & Bureaucrats (# 50)				
Number of Followers	322,652	547,982	777	2,723,161
Number of Followings	909.8	1,026.3	1	4,158
Number of Tweets	13,829.7	22,551.5	205	153,345
Registration Date	2012	2.2	2009	2018
Journalists (# 129)				
Number of Followers	59,856.5	139,654	234	825,779
Number of Followings	1,076.5	1,088.9	15	7,911
Number of Tweets	14,531	19,958.4	28	127,223
Registration Date	2011	2.4	2008	2019
Private Sector Professionals (# 312)				
Number of Followers	28,080.7	69,974.3	31	571,834
Number of Followings	977.9	1,193.6	3	8,443
Number of Tweets	11,384.4	20,312.1	37	216,277
Registration Date	2012	2.51	2007	2020

NOTES: *This table provides descriptive statistics of the selected Twitter user accounts retained in the final candidate list.*

Our bootstrapping algorithm consists of three distinct list types:

Seed list: The initial list is used to initialize the process, serving as a nucleus in the bootstrapping algorithm [45]. This list is not called first, second etc. as it is only used to initialize the process.
Recommended List: This list is prepared to be annotated, purified from the users in the seed list and the recommended list formed in the previous phase. These lists are named according to which phase they are formed, first, second, etc.
Candidate List: This list is comprised of experts in economics and finance, according to the annotation results of the recommended list formed in the previous phase. These lists are named according to which phase they are formed, second, final, etc.

As illustrated in **Figure 2** we implement three phases to obtain the final candidate list of Twitter accounts whose tweets are used to construct our TEPU index. In what follows, we provide the details of these phases:

- **First Phase**:
  [−] We constitute our initial list that contains a small number of Twitter accounts that have been considered to belong to experts on the matters of economics and finance by the Turkish community.[11] The users in the initial list are required to satisfy the following criteria:
  (i) to hold a PhD degree in economics or finance
  (ii) to possess the highest number of followers (1 million plus).[12]
  [−] The selection results in an initial list of three users. We name this list the seed list as shown in **Figure 2**.
  [−] We constitute a list of 131 users that corresponds to those followed by at least 2 of the Twitter accounts available in the seed list.[13] We then remove the first three users that we name as the seed list from these 131 users.
  [−] Following the annotation process suggested by Giachanou and Crestani [47],[14] the profiles of 128 Twitter accounts are manually annotated by three different human annotators to identify those belonging to the experts in the field of economics and finance. Additionally, we delete users who closed their Twitter accounts during the course of our study or post only personal tweets.
  [−] This results in a list of 67 users that we name as the 2^{nd} candidate list.
- **Second Phase**:
  [−] We combine the seed list and the 2^{nd} candidate list, which yields us a merged list of 70 users.
  [−] We constitute a list of 6,351 users that corresponds to those followed by at least 2 of the Twitter accounts available in this merged list.
  [−] From these 6,351 users we remove the users of the seed list and the 2^{nd} recommended list, yielding us the 3^{rd} recommended list of 6,220 users.
  [−] We implement the above-mentioned annotation process and the cleaning filter. This results in a list of 687 users that we name as the 3^{rd} candidate list.
- **Third Phase**:
  [−] We combine the seed list, the 2^{nd} candidate list, and the 3^{rd} candidate list, which yields us a merged list of 757 users.
  [−] We constitute the list that corresponds to those followed by at least 2 of the user accounts available in this merged list. At this point, the human annotators fail to manually annotate the profiles of 65,391 users to label who are experts in the field of economics and finance. Therefore three different human annotators proceed by annotating the profiles of randomly chosen users among 65,391 users.
  [−] During this annotation process, we observe that these users are not representative of experts compared to those retained in the earlier phases, hence we end the algorithm at this point.
  [−] As before, we delete users who closed their Twitter accounts during the course of our study or who post only personal tweets.
  [−] This results in the list of 661 users that we use to construct our TEPU index. We name this list as the final candidate list.

To validate our approach, we implement the above-mentioned phases using the following alternative seed lists: 1) the Twitter accounts that are followed by 16 Twitter accounts who have more than 500,000 followers, and 2) the Twitter accounts that are followed by 7 randomly selected Twitter accounts out of the 16 Twitter accounts who have more

[11]Due to the nature of the bootstrapping algorithm, it is immaterial how many people are included in the initial list. It may differ according to the country one focuses on and the selection criteria that is implemented. In our case, we want to restrict our initial list to a select set of people who are expected to be the most influential on public sentiment. This way of identification of influential experts builds on the insights of Weng, Lim, Jiang and He [60] where an influential *twitterer* is defined as one with certain authority within her social network. To this end, we start with an initial list that comprises of Twitter accounts of three experts in the field of economics and finance that have the highest number of followers.
[12]In addition to this "in-degree" measure of user influence, the two of these three experts are ranked as the first two *twitterers* in the Turkish community in 2021 in terms of number of retweets, see https://twitter.com/adbaanalytics/status/1487045047644299 26 for further statistics released by Adba Analytics, a digital consumer research agency.
[13]This restriction goes in line with the "homophily" phenomenon. The analysis of Weng et al. [60] shows that "homophily" does exist in Twitter data, implying that the "following" relationships between *twitterers* are related to their topical similarity.
[14]Similarly, Saif, Fernandez, He and Alani [61] construct a data set, namely, the Stanford Twitter Sentiment Gold (STS-Gold) that has been used for Twitter Sentiment Analysis. This data set contains 2,034 tweets which are automatically annotated with sentiment labels. This data set also contains 58 entities manually annotated by three different human annotators.

TABLE 2 | Dictionary of keywords.

Category	Subcategory	Turkish Term	English Term
Economy		ekon/iktisat	econ/economics
		işsizlik	unemployment
		yabancı yatırımcı	foreign investor
		dış yatırım	foreign investment
		bankacılık	banking system
Policy	Fiscal policy	Hazine	Treasury
		Hazine ve Maliye Bakanlığı	Ministry of Treasury and Finance
		bütçe açı ğı	budget deficit
		regülasyon	regulation
		devlet harcamaları	government spending
		devlet büçesi	government budget
		devalüasyon	devaluation
		devlet borcu	government debt
		mali teşvik	fiscal stimulus
		dış borç	external debt
		mali disiplin	fiscal discipline
	Monetary Policy	Merkez Bankası	Central Bank
		faiz	Interest
		FED	FED
		IMF	IMF
		açık piyasa işlemleri	open market operations
		ortodoks	orthodox policies
		parasal sıkılaşma	monetary tightening
		para politikası	monetary policy
		parasal genişleme	monetary expansion
		Avrupa Merkez Bankası	European Central Bank
		ihtiyat akçesi	precautionary saving
		para arzı	money supply
		euro	euro
		dolar	US Dollar
		döviz	foreign exchange
		enflasyon	inflation
	Trade Policy	ithalat	exports
		ihracat	imports
		cari açık	current account deficit
		belirsiz	uncertain
Uncertainty		kriz	crisis
		zarar	loss
		eksik	insufficient
		TBMM	Turkish Grand National Assembly
		Covid-19	Covid-19
		saray	presidential palace
Economic Situation		kurultay	convention
		parlamento	parliament
		güçler ayrılığı	separation of powers
		tüzük	charter
		düzenleme	rule-based arrangement

NOTES: *This table provides the dictionary of keywords that we search within the Turkish-language tweets posted by 661 Twitter accounts retained in the final candidate list. We obtain this dictionary by identifying any words that begin with the corresponding Turkish term listed in each subcategory of the EPU index.*

than 500,000 followers. Both seed lists yield two final lists of users that are identical to the final candidate list of 661 users obtained using the reference seed list.

Table 1 presents descriptive statistics of the selected Twitter user accounts categorized by occupation.[15] This table reports the number of followers, followings and tweets, and the registration date corresponding to each occupation. These statistics show that in the sample period 2013–2021, on average, parliamentarians and bureaucrats are the most-followed users whereas they don't follow people as much as users in other three categories do. Further, on average, experts in all these four categories post at least around 10,000 tweets, suggesting that they seem to actively use the Twitter platform for transmitting their opinions to the public in our sample period. In particular, starting with the seed list of three Twitter user accounts belonging to the most-followed experts in the field of economics and finance in the Turkish community, we obtain a network of users that not only capture the influence of these people on public opinion but also their interaction with other users that they follow.

3.2 Constructing the Daily TEPU Index

To construct the TEPU index, we focus on the sample period from 1 January 2013 to 22 December 2021 because this period coincides with the onset of many events associated with political and economic uncertainty in Turkey.

We use the same search procedure developed by [1]. We treat the Twitter data-based series as if they are extracted from a single newspaper. We use the Twitter API to obtain all of the "following" lists of users. Using the web scraping with *Python*, we extract the full tweet content that the users posted within the specified time interval. We exclude retweets in the calculation of our TEPU index to avoid duplicates. We transform the letters in the tweets into lower case and use English characters throughout.

[1] use a list of words that captures the policy uncertainty characteristics of advanced economies. However, in our search process, we include the set of words that are considered more relevant for emerging market economies as in [6] and [2]. **Table 2** shows the Turkish and English versions of the words that we search for. In each tweet posted by these selected 661 Twitter accounts in the period 2013–2021, we search for keywords and record the word count data. We normalize the raw word count data using the standardization procedure outlined in [1]. In particular, we first count the keywords at the daily frequency.[16] Second, we compute the value M which corresponds to the mean value of the daily series for the entire period from 1 January 2013 to 22 December 2021 and multiply the daily series by its own normalizing factor, 100/M.

4 THE TEPU INDEX AND FINANCIAL MARKETS

4.1 Data

In addition to the daily TEPU index, we make use of daily data on the selected financial indicators that we use to track developments in Turkish financial markets over the period 2013–2021.

First, we use the Chicago Board Option Exchange (CBOE) Volatility Index (VIX) to proxy for global risk perceptions. The VIX is a real-time index that represents the market's expectation of near-term price changes on the S&P 500 Index (SPX). It is measured as the implied volatility on SPX options, which provides a way to gauge market sentiment, and in particular, the degree of fear among market participants. We obtain the end-of-day VIX values from the Federal Reserve Bank of St Louis Economic Database (FRED). The Credit Default Swap (CDS) spread is an indicator that measures the risk of default on Turkey's sovereign debt. Equivalently, the CDS spread represents the annual premium (the CDS "fee" or "spread") to be paid to the lender against the risk of default. If the number of years of the loan is not specified in the contract, calculations are made according to the 5-years CDS Spread. The Bloomberg Terminal provides the daily 5-years CDS spread series, which we measure as basis points on US dollar-denominated CDS contracts. The spot USD/TRY exchange rate and the BIST-100 index are obtained from Yahoo! Finance. The first represents units of the domestic currency, namely the Turkish lira, per US dollar. The latter measures the performance of the top 100 stocks traded on the Istanbul Stock Exchange entitled as Borsa Istanbul.[17]

The daily series are reported as opening, closing, high and low values. In our analysis we use their closing values. We aggregate the resulting daily series into weekly series to be used in our analysis over the period 2013w1 and 2021w51.

4.2 Event Analysis

In what follows, we conduct an event analysis to show how our TEPU index relates to important political and economic events that have occurred in Turkey in the sample period 2013–2021.

Table 3 records both domestic and foreign events that may have been associated with changes in economic policy uncertainty in Turkey. It considers the timeline of events by making a distinction between political announcements versus the immediate reaction of financial markets. This table indicates episodes of political uncertainty in the weeks or months preceding such events as national elections or referendums whereas it indicates the exact date associated with monetary policy announcements and surprises. As a visual device, **Figure 3** plots the daily TEPU index from 1 January 2013 to 22 December 2021 and tracks the evolution of economic policy uncertainty for Turkey. Some of the events associated with spikes

[15]In the final candidate list of 661 users, 4 users are identified as both academician and parliamentarian/bureaucrat based on their personal information reported in their Twitter accounts.

[16]To correct for intra-week variation in the number of tweets, we scale the daily TEPU index by the average number of tweets for each day of the week during the year 2017.

[17]According to the 2020/26 numbered notification of Borsa Istanbul published on 4 April 2020, especially from BIST-30 and BIST-100, two zeros were removed from the BIST Equity Indexes as of Monday 27 July 2020 and the index value has continued to be displayed as two digits after the comma. In order to have a consistent format in these series, we divide the values before 27 July 2020 by 100.

TABLE 3 | Timeline of events.

Year	Date	Event
2013	28 May	Gezi Parkı Protests
	18 September	Fed maintains the pace of stimulus in the face of uncertainty about the US economy
	17–25 December	Corruptions allegations against members of the government
2014	29 January	CBRT MPC increases its weekly repurchase rate from 4.5 to 10%
2015	April	Uncertainty about elections scheduled for June 2015
	7 June	General elections
	26 August	General elections are re-scheduled for 1 November 2015
	October	Uncertainty about early elections scheduled for 1 November 2015
	16 December	FED FOMC increases the Federal Funds rate from 0.25 to 0.50% ending 7 years of near zero interest rates
2016	22 May	Resignation of Prime Minister Ahmet Davutoğlu
	15 July	15 July Coup Attempt
	21 September	FED FOMC leaves the Federal Funds rate unchanged at 0.50%
2017	January	Upcoming constitutional amendment in Turkey
	16 April	Constitutional amendment referendum
2018	May	Political uncertainty about early elections on June 24
	10 August	Black Friday Currency Shock
	13 September	CBRT MPC increases its weekly repurchase rate of 17.75% by 625 basis points to 24%
2019	6 July	CBRT Governor Murat Çetinkaya is replaced by Governor Murat Uysal
	31 July	FED reduces the target range for its overnight lending rate from 2.25 to 2%
2020	11 March	The first Covid-19 case is observed in Turkey
	24 September	CBRT MPC increases its policy rate of 8.25% by 200 basis points to 10.25%
	7 November	CBRT Governor Murat Uysal is replaced by Governor Naci Ağbal
	19 November	CBRT MPC increases its policy rate of 10.25% by 475 basis points to 15%
	24 December	CBRT MPC increases its policy rate of 15% by 200 basis points to 17%
2021	20 March	CBRT Governor Naci Ağbal is replaced by Governor Şahap Kavcıoğlu
	23 September	CBRT MPC reduces its policy rate of 19% by 100 basis points to 18%
	14 October	Two deputy governors and one member of the CBRT MPC are dismissed from their positions
	21 October	CBRT MPC reduces policy rate of 18% by 200 basis points to 16%
	18 November	CBRT MPC reduces policy rate of 16% by 100 basis points to 15%
	16 December	CBRT MPC reduces policy rate of 15% by 100 basis points to 14%

Source: Authors' elaboration.

in economic policy uncertainty have already been documented by earlier papers [3,4].[18] In common with these papers, we find that beginning in 2013, some of the most significant events refer to the occurrence of the Gezi Protests, which erupted due to a disagreement regarding the usage of a municipal park and turned into nation-wide protests against the government, as well as the revelation of corruption allegations against various members of the government during 17–25 December 2013. The TEPU index rises before significant political events such as the national elections which were held on 24 June 2015 and re-scheduled for 1 November 2015. The TEPU index spikes during the failed coup attempt of 15 July 2016. There is also evidence of a general increase in uncertainty in the periods preceding the presidential referendum of 16 April 2017 as well as in the few weeks immediately preceding the elections under the new presidential system that took place on 24 June 2018.

As a further way of illustrating the impact of economic policy uncertainty for Turkey, **Figure 4** considers two measures of risk assessment by foreign and domestic agents together with our TEPU index. This figure displays the behavior of the TEPU index together with two other indicators that summarize the risk

[18]For the period 2000–2018, Topçu and Oran [4] find that most of the uncertainty in Turkey over the period 2000–2018 arises from events that trigger political uncertainties such as elections and the changes in policy that these may induce.

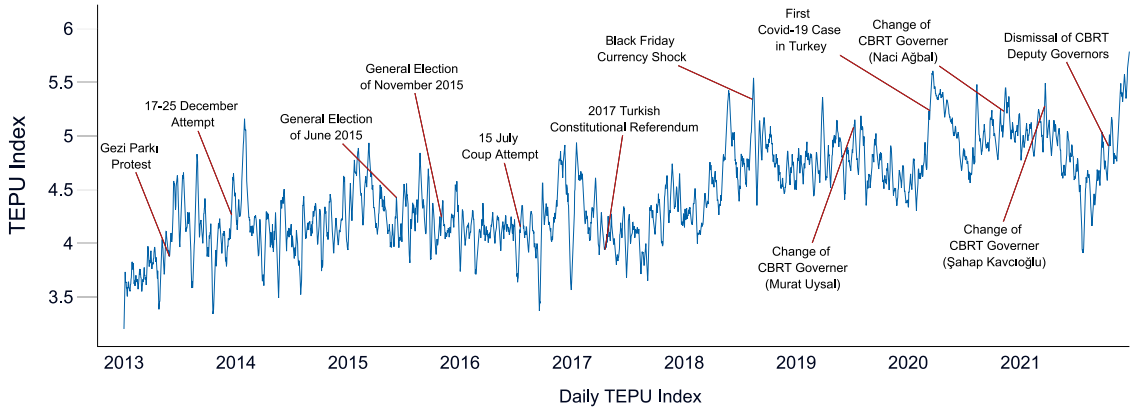

FIGURE 3 | The daily TEPU index. This figure plots 7-day moving average of logarithm of TEPU index from January 1, 2013 to December 22, 2021. We provide the details on the construction of this index in **Section 3**.

perceptions of foreign investors, namely, the VIX, as well as a measure of country risk premium for Turkey, namely, its CDS spread, over the entire sample period from January 2013 to December 2021. As a significant regularity, we note that the TEPU index moves in tandem with both of these indicators. The TEPU index and the CDS spread, in particular, display a tendency to increase together especially over the period since 2018. One of the major events in 2018 is the Black Friday currency shock and the CBRT's subsequent decision to increase its policy rate by 625 basis points. As **Figure 4** shows, this event is captured by the increase in both the TEPU index and the CDS spread for Turkey in August 2018. Following a sharp depreciation in the Turkish lira from 4 TRY per USD to 7 TRY per USD, the Turkish lira recovers after the large policy rate increase by the CBRT. In July 2019 there is an increase in Turkey's CDS spread concurrently with a spike in the TEPU index that occurs in response to the replacement of Governor Murat Çetinkaya by Governor Murat Uysal.

In March 2020, we observe a large increase in the VIX in response to the onset of the Covid-19 crisis, which is also reflected in a significant increase in Turkey's CDS spread. As it is well-known, the VIX captures changes in the risk perceptions of foreign investors due to exogenous shocks, external monetary and financial conditions, and developments specific to emerging market economies including the Turkish economy. In this regard, the correlation between the VIX and the TEPU index partially reflects the fact that the Turkish economy is vulnerable to episodes of divergence between its policy actions relative those of the US, as argued by Kalemli-Özcan [48]. This is due to its dependence on international capital flows for financing its current account deficit. By contrast, Turkey's CDS spread tends to capture a systematic assessment of the uncertainty and risk premium associated with long-term prospects for the Turkish economy. This is evidenced by its sharp rise around the August 2018 currency shock as well as the Covid-19 shock, which tends to persist until the end of 2020. These movements are accompanied by significant increases in the TEPU index as well.

Uncertainty about policy changes as measured by the TEPU index rises sharply in March 2021 when Governor Naci Ağbal, a central official known for his orthodox views on monetary policy, is replaced as governor of the CBRT by Governor Şahap Kavcıoğlu. In response to this event, the daily value of the USD/TRY exchange rate jumps from 7.305 TRY per USD to 8.0954 TRY per USD, indicating a 10% depreciation of the Turkish lira. Turkish bond and stock markets also witness their largest capital outflow of $1.9 billion since 2006.[19] As a consequence, the BIST-index falls by around 8% on 21 March 2021, the day following the dismissal of Governor Naci Ağbal. These developments are also reflected in an increase in Turkey's CDS spread and a smaller increase in the VIX in March 2021.

After September 2021, the effects of the unconventional monetary policy being espoused in Turkey begin to manifest themselves. As **Table 3** shows, consecutive decreases in the CBRT's policy rate are implemented between 23 September 2021 to 16 December 2021. During this period, the CBRT MPC reduces its policy rate by 500 basis points, the last cut of 100 basis points occurring after a MPC meeting on 16 December 2021. These changes lead to an unprecedented increase in the TEPU index. Turkey's CDS spread shows a tendency to increase rapidly with the TEPU index, rising from a value of around 388 up until the second week of September 2021 to 578 by 17 December 2021.

During this period, Turkey's exchange rate also follows a highly volatile pattern, with the value of the Turkish lira falling by around 120% against the US dollar in a spiraling fashion until the end of December 2021 when the introduction of new foreign-exchange linked saving schemes help to stem the rout. The volatility in the foreign exchange rate market is also accompanied by volatility in Turkey's stock market, as trading is suspended twice on all listed stocks as the BIST-100 index falls by more than 7%. Countervailing this effect, stock prices nevertheless recover as investors in Turkey

[19]http://www.bloomberg.com/news/articles/2021-04-01/turkey-s-central-bank-revamp-spurs-biggest-outflows-in-15-years.

seek to take advantage of the price discount on stocks in Turkish lira to protect their savings.[20]

5 ECONOMETRIC METHODOLOGY

In this section, we consider the dynamic inter-relationships among fluctuations in the TEPU index and a set of key financial indicators for Turkey, including the CDS spread, the BIST-100 stock index and the USD/TRY exchange rate, for the sample period comprising 1 January 2013 to 22 December 2021. In this analysis, we do not seek to jointly model the dynamics of the VIX with the remaining variables, instead considering its lagged values as exogenous control variables.[21]

Consider a standard VAR of the form

$$\mathbf{y}_t = A_1\mathbf{y}_{t-1} + A_2\mathbf{y}_{t-2} + \cdots + A_p\mathbf{y}_{t-p} + C_1\mathbf{x}_{t-1} + \cdots + C_q\mathbf{x}_{t-q} + \mathbf{u}_t, \tag{5.1}$$

where $\mathbf{y}_t$ is the $K \times 1$ vector for $K = 4$ comprising the TEPU index and the three domestic financial variables and $\mathbf{x}_t = (1, \mathrm{VIX}_t)'$. In this expression, $A_i, i = \ldots, p$ denote $K \times K$ matrices of autoregressive coefficients, p the lag length of the VAR, C_i, $i = 1, \ldots, q$ the $K \times 2$ matrices of coefficients for the exogenous variables, and q their lag length. Here $\mathbf{u}_t$ denotes a $K \times 1$ vector of innovations with mean $E(\mathbf{u}_t) = 0$ and an unconditional variance-covariance matrix $E(\mathbf{u}_t\mathbf{u}_t') = \Sigma$ and $\mathrm{E}(\mathbf{u}_t\mathbf{u}_s) = 0$ for $s \neq t$. In general, the elements of $\mathbf{u}_t$ will be contemporaneously correlated, i.e., $\sigma_{i,j} \neq 0$. Hence, we cannot consider experiments where we hold, say $u_{i,t}$ constant and let $u_{j,t}$ vary for $i \neq j$. In what follows, we implement an SVAR approach to identify the structural shocks. Consider the representation $A\mathbf{u}_t = B\boldsymbol{\varepsilon}_t$, where A is a lower triangular matrix with ones on its diagonal, B is a diagonal matrix and $\boldsymbol{\varepsilon}_t$ is a vector of orthogonalized innovations. In this expression, $\boldsymbol{\varepsilon}_t \sim N(0, I)$ and $E(\boldsymbol{\varepsilon}_t\boldsymbol{\varepsilon}_s') = 0$. Here the matrix A captures the contemporaneous relations between observable variables and the variance-covariance matrix of the errors $\mathbf{u}_t$ and satisfies $\Sigma = A^{-1}BB'(A^{-1})'$.

In our analysis, we impose a recursive ordering to identify the structural shocks in the estimated SVAR model. In the literature, alternative indices of economic policy uncertainty have typically been placed first based on the notion that shocks to this variable have a contemporaneous impact on the remaining variables while none of the other variables are assumed to have a contemporaneous impact on it. In our analysis, we place the CDS spread first to allow for possible contemporaneous effects from it to affect the TEPU index and the remaining variables. Likewise, each of the remaining variables will have a contemporaneous effect on the variables listed after them but will not affected by them contemporaneously.

5.1 Estimates of the SVAR Model

To estimate the SVAR model, we first test the different series for unit roots based on the Augmented Dickey-Fuller (ADF) test. We cannot reject the null hypothesis of a unit root for the USD/TRY exchange rate and the BIST-100 stock index, suggesting that they are non-stationary. On the other hand, the TEPU index, the VIX and the CDS spread are shown to be trend-stationary.

We use the HP-filter to remove time-varying trends in the different series. While implementing the HP-filter has been criticized as being *ad hoc* and for inducing spurious dynamics into the series to which it is applied [49], the so-called Hamilton regression filter which uses the residuals from an h-step ahead regression of a variable on values of itself at time t and earlier is also known to extract specific frequencies of the time series [50]. [51] provide a so-called boosted version of the HP filter which they argue can "remove trend mechanisms that involve integrated processes, deterministic drifts, and structural breaks," which are the most common types of trend processes observed in economic and financial data.[22] We adjust the HP-filter for the weekly frequency of observations using the approach in [52].

In what follows, we estimate an SVAR model with three lags of the endogenous variables and 4 lags of the VIX. Our choice is based on the AIC, while selection criteria such as the SBIC and HQIC which favor more parsimonious specifications choose a lag length of 2. Based on diagnostic tests for the behavior of the SVAR model, we find that evidence of stability in the conditional mean equations in that all of the estimated eigenvalues are inside the unit circle. This suggests that the system we are estimating is stable. Second, the Lagrange Multiplier test for autocorrelation [53] suggests that the absence of serial correlation in the residuals of the SVAR model for almost all lags up to lag 24.[23]

In our analysis, we make use of the SVAR model to conduct Granger causality tests to understand the dynamic inter-relationships among the different series. Granger causality tests provide a way for examining the predictive power of one variable $y_{i,t}$ for another given by $y_{j,t}$. More formally, let $y_{i,t}(h|I_t)$ be the optimal (minimum Mean Square Error (MSE)) h-step predictor of the process $y_{i,t}$ at origin t, based on the information in I_t. Denote the corresponding forecast MSE by $\Xi_{y_i}(h|I_t)$. The process $y_{j,t}$ is said to cause $y_{i,t}$ in Granger's sense if $\Xi_{y_i}(h|I_t) < \Xi_{y_j}(h|I_t \{y_{j,s}|s \leq t\})$ for at least one $h = 1, 2, \ldots..$[24] In our analysis, we use the multivariate version of Granger causality tests to test for the predictability of one variable by another, after controlling for the effects of other potentially relevant variables [54]. In a multivariate VAR context, a test of Granger causality involves a test of zero restrictions on a subset of the coefficients of the VAR [54,55].

Table 4 shows the results of Granger causality tests among expert opinion represented by the TEPU index and Turkey's

[20]http://www.reuters.com/markets/stocks/turkish-stocks-open-down-after-sharp-friday-selloff-2021-12-20/.

[21]To the extent that the variables in our study reflect the domestic dynamics of financial markets in Turkey, especially at the weekly frequency, inclusion of the VIX as an endogenous variable is unlikely to yield information about its comovement with the remaining variables.

[22]The boosting involves applying the HP-filter multiple times based on stopping criteria from a machine-learning algorithm.

[23]We include 4 lags of the VIX, as it helps to reduce the autocorrelation in the residuals from the estimated SVAR.

[24]In this definition, $I_t\{y_{j,s}|s \leq t\}$ is all of the information relevant for predicting $y_{i,t}$ except for information in current and past values of $y_{j,t}$. Thus, $y_{i,t}$ can be predicted more efficiently if the information in the past and present of the y_j process is taken into account, then $y_{j,t}$ is said to cause $y_{i,t}$ in Granger's sense. See Lutkepol [54], pp. 41–42.

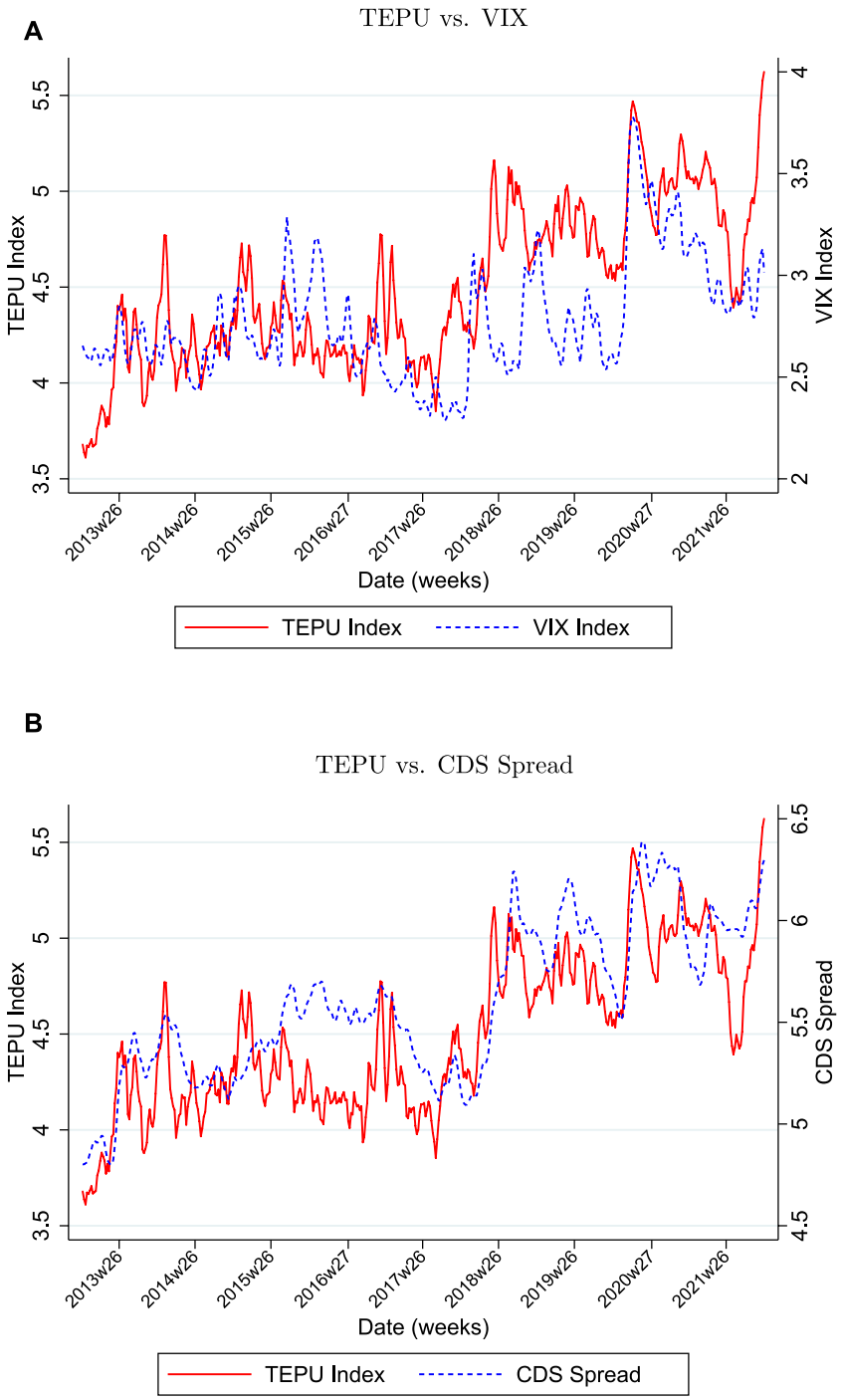

FIGURE 4 | The comparison of the TEPU index versus VIX and CDS spread. **(A)** TEPU vs. VIX **(B)** TEPU vs. CDS Spread. This figure plots 4-week moving average of the logarithm of the TEPU index against the logarithms of VIX and CDS spread in sub-panels (a)–(b), respectively. See **Section 4.1** for further details. Sample period: 2013w1-2021w51.

financial indicators for three different sample periods. These results show that the TEPU index and financial indicators such the USD/TRY exchange rate and the BIST-100 stock index interact with and influence each other at the weekly frequency. This may have to do with their high-frequency movements in a shallow financial market where news gets transmitted rapidly to economic agents and markets. While lagged values of fluctuations in the exchange rate help to predict both fluctuations in the stock market index and the TEPU index, changes in the TEPU index also help to predict the changes in the exchange rate and in the stock index. These results hold, on the whole, for the three samples that we consider, though

they are weaker for the samples ending in 2019 and 2017. The bi-directional relationship between the USD/TRY exchange rate and the TEPU index is among the strongest and holds for all three sample periods. This may occur if fluctuations in the USD/TRY exchange rate transmit signals about monetary policy announcements and other unanticipated policy changes to economic agents, which are then incorporated into expert opinion. On the other hand, changes in expert opinion represented by the TEPU index may also influence the exchange rate through the social media activities of economic experts.

Table 4 also provides information about the determinants of changes in Turkey's CDS spread. As it is well-known, the CDS spread tends to capture a systematic assessment of the uncertainty and risk premium associated with long-term prospects for a given country. **Table 4** shows that changes in the TEPU index emerges as the key predictor for changes in the CDS spread for the samples ending in 2021 and 2019. In a related analysis, [8] create a real-time News-implied Sovereign Risk Index (NSRI) for over 100 countries by applying text search methods to socioeconomic, political and financial news.[25] They show that lagged changes in this index are a significant predictor of changes in a country's CDS spread, especially at the monthly frequency, after controlling for the effects of other domestic and global macro-economic variables. Thus, as in [8], changes in expert opinion about economic policy issues help to predict movements in the CDS spread. Nevertheless, there are some differences between the approach followed by these authors and ours. While [8] implement a panel data analysis based on a bi-variate relation between the CDS spread and their news-based measure of sovereign risk, we find that dynamic inter-relationships among changes in expert opinion and other financial indicators help to determine changes in Turkey's country risk premium based on a multivariate analysis. This further provides evidence about the interactive relationship between expert opinion represented by the TEPU index and the different financial indicators in our analysis.[26]

We can relate our results to the literature that studies the interaction of economic policy uncertainty with other financial indicators. Using monthly data, [10] argue that oil prices and economic policy uncertainty are inter-related and influence both stock returns and stock market volatility in that a positive oil-market specific shock raises economic policy uncertainty and reduces real stocks returns. Thus, the endogenous response of economic policy uncertainty amplifies the direct effects of oil price shocks. Likewise, [8] find that spikes in their NSRI "are negatively associated with same-week market returns, which reverses over the next week, indicating that investors might overreact to default risk news." They further find that the reaction of equity markets in countries that face binding fiscal constraints is more pronounced and persistent. In our analysis, we find that the CDS spread helps predict fluctuations in equity markets. This may occur if expectations about the future of the Turkish economy and hence, its country risk premium, signify changes in the profitability of investing in Turkey.[27]

TABLE 4 | Granger causality tests.

	CDS_t	$TEPU_t$	$BIST-100_t$	USD/TRY_t
Sample period: 2013–2021				
CDS_t	-	0.844	0.076	0.554
$TEPU_t$	0.0	-	0.021	0
$BIST-100_t$	0.300	0.783	-	0.089
USD/TRY_t	0.357	0.052	0	-
All	0.001	0.011	0.001	0
Sample period: 2013–2019				
CDS_t	-	0.116	0.027	0.226
$TEPU_t$	0.001	-	0.039	0.0
$BIST-100_t$	0.681	0.291	-	0.402
USD/TRY_t	0.937	0.247	0.022	-
All	0.020	0.017	0.008	0.0
Sample period: 2013–2017				
CDS_t	-	0.071	0.084	0.875
$TEPU_t$	0.191	-	0.314	0.032
$BIST-100_t$	0.261	0.103	-	0.150
USD/TRY_t	0.823	0.011	0.105	-
All	0.224	0.008	0.160	0.016

NOTES: *In **Table 4** the entries show the p-values for the test of the null hypothesis that the indicators listed in the rows do not Granger cause the indicators listed in the columns. See **Section 4.1** for further details on these series.*

5.2 Volatility Dynamics

As we discussed in **Section 4**, there has been considerable volatility in the sample period that we are analyzing. To make this notion precise, **Table 5** provides estimates of a GARCH(1,1) model specified as $\sigma_{ii,t} = \tilde{\mu}_i + \tilde{\gamma}_i u^2_{ii,t-1} + g_i \sigma_{ii,t},\ i = 1, \ldots, 4$, where $\sigma_{ii,t}$ is the conditional variance of the residuals from the i^{th}

[25]They implement machine learning algorithms such as topic modelling and text similarity to identify sovereign default risk concerns in newspaper articles. They consider the world stock market index from MSCI, the US EPU index from Baker et al. [1], the US macroeconomic activity index, namely Aruoba-Diebold-Scotti (ADS) of Aruoba, Diebold and Scotti [62] from the Federal Reserve Bank of Philadelphia, and the VIX as controls.

[26]We also create Impulse Response Functions (IRFs) to trace the dynamic response of the different series to each of the structural innovations. These IRFs show that a one-standard deviation shock to the TEPU index tends to increase the CDS spread and the USD/TRY exchange rate while a similar shock to the USD/TRY exchange rate increases the TEPU index. Finally, contemporaneous changes in the CDS spread are reflected in declines in the BIST-100 index and increases in the USD/TRY exchange rate and the TEPU index. These results are available upon request.

[27]In our analysis, we use the nominal values of the USD/TRY exchange rate and the BIST-100 index. To check the robustness of our results, we also create real values of the USD/TRY exchange rate and the BIST-100 index over our sample period. However, the price level series required to convert nominal values to real values is available only at the monthly frequency. Hence, we divide the (levels) of the nominal series by the monthly series on Consumer Price Index (2003 = 100) released by the Turkish Statistical Agency (TURKSTAT); see https://data.tuik.gov.tr/Kategori/GetKategori?p=Enflasyon-ve-Fiyat-106. The correlations between the real and nominal monthly series for HP-filtered versions of each of the two financial indicators - the stock index and the exchange rate - are both around 0.98, suggesting that any inflationary bias induced in the relevant nominal series is filtered out through the time-varying trend created by the HP-filter.

TABLE 5 | Estimates of conditional heteroscedasticity.

Panel (a): Univariate GARCH(1,1) model									
Variable	**Parameter**	**Estimate**	**p-Value**	**Parameter**	**Estimate**	**p-Value**	**Parameter**	**Estimate**	**p-Value**
σ^2_{CDS}	$\tilde{\mu}_1$	0.003	0.0	$\tilde{\gamma}_1$	0.129	0.002	g_1	–0.158	0.373
σ^2_{TEPU}	$\tilde{\mu}_2$	0.032	0.004	$\tilde{\gamma}_2$	0.111	0.033	g_2	0.282	0.218
$\sigma^2_{BIST-100}$	$\tilde{\mu}_3$	0.0002	0.106	$\tilde{\gamma}_3$	0.111	0.001	g_3	0.659	0.0
$\sigma^2_{USD/TRY}$	$\tilde{\mu}_4$	0.5E-04	0.0	$\tilde{\gamma}_4$	0.295	0.0	g_4	0.536	0.0
Panel (b): Diagonal VECH Model									
σ^2_{CDS}	$\mu_{1,1}$	0.003	0.0	$\gamma_{1,1}$	0.171	0.015	-	-	-
$\sigma_{CDS,BIST-100}$	$\mu_{2,1}$	–0.001	0.0	$\gamma_{2,1}$	0.112	0.047	-	-	-
$\sigma_{CDS,USD/TRY}$	$\mu_{3,1}$	0.0005	0.0	$\gamma_{4,1}$	0.236	0.008	-	-	-
$\sigma^2_{BIST-100}$	$\mu_{2,2}$	0.0006	0.0	$\gamma_{3,3}$	0.160	0.003	-	-	-
$\sigma_{BIST-100,USD/TRY}$	$\mu_{3,2}$	–0.0002	0.0	$\gamma_{4,3}$	0.214	0.0	-	-	-
$\sigma^2_{USD/TRY}$	$\mu_{3,3}$	0.0002	0.0	$\gamma_{4,4}$	0.432	0.002	-	-	-

Notes: p-values are for the Wald test of $p(z > z_{stat})$.

equation in an unrestricted VAR for the CDS spread, TEPU index, BIST-100 index, USD/TRY exchange rate series, taking as given the lagged values of the VIX as exogenous control variables. The estimates of γ_i show the ARCH(1) term is significantly different from zero for all the four series considered in **Table 5**. The series on the BIST-100 index and the USD/TRY exchange rate also display significant GARCH(1) coefficients.[28]

To capture such conditional heteroscedasticity in the residuals, we estimate an M-GARCH model over the main sample period. In this specification, the error terms of the SVAR satisfy $\mathbf{u}_t = H_t^{1/2}\boldsymbol{\varepsilon}_t$ while the time-varying conditional variance of the original SVAR model is assumed to follow a Choleski decomposition as

$$E_t\left(\mathbf{u}_t\mathbf{u}_t'\right) = \Sigma_{t|t-1} = H_t^{1/2}\left(H_t^{1/2}\right)', \tag{5.2}$$

where $\Sigma_{t|t-1}$ is the variance covariance of the residuals at time t, given information at time $t-1$ denoted by I_{t-1} and the elements of H_t are given by $h_{ij,t}$ for $i,\ j = 1, \ldots$. Hence, $\boldsymbol{\varepsilon}_t$ is an i.i.d random vector with mean $E(\boldsymbol{\varepsilon}_t) = 0$, $E_t(\boldsymbol{\varepsilon}_t\boldsymbol{\varepsilon}_t') = I$ and $E_t(\boldsymbol{\varepsilon}_t\boldsymbol{\varepsilon}_s') = 0$ for $s \neq t$. In this representation, we have not specified the distribution of the innovations $\boldsymbol{\varepsilon}_t$. As [54] states, even if the conditional distribution for $\mathbf{u}_t$ is normal, the unconditional distribution will generally be non-normal. In particular, it will have more mass around zero and in the tails than the normal distribution and, hence, it can produce occasional extreme observations relative to the normal distribution.

The dynamics of the M-GARCH model embodied in the matrix H_t are very rich and may be modeled in alternative ways. The multivariate GARCH model may be written as

$$vech(\mathbf{H}_t) = \gamma_0 + \sum_{i=1}^{m}\Gamma_i vech\left(\mathbf{u}_{t-i}\mathbf{u}_{t-i}'\right) + \sum_{j=1}^{q}G_j vech\left(\mathbf{H}_{t-j}\right) \tag{5.3}$$

where *vech* denotes the half-vectorization operator which stacks the columns of a square matrix from the diagonal downwards in a vector, γ_0 is a $(1/2)K(K+1)$ -dimensional vector of constants and the Γ_j, G_j are $(1/2)K(K+1) \times (1/2)K(K+1)$ coefficient matrices. A diagonal multivariate GARCH(1) process is one in which the matrices Γ_1 and D_1 are diagonal so that the conditional covariances $h_{ij,t}$ satisfy $h_{ij,t} = \mu_{ij} + \gamma_{ij}u_{i,t-1}u_{j,t-1} + g_{ij}h_{ij,t-1}$. In this case, each conditional covariance depends on its own past but not on the past of the other conditional variances and covariances.[29]

In the estimation of the M-GARCH model, we model the conditional volatility in the different series by considering ARCH processes for the conditional variances and covariances that depend only on the second moments of the past shocks in the relevant equation as $h_{ij,t} = \mu_{i,j} + \gamma_{i,j}u_{i,t-1}u_{j,t-1}$ for $i,\ j = 1, \ldots, K$. Due to the highly nonlinear framework implied by the DVECH model, we were unable to estimate a system that includes the TEPU index. Instead, we consider a 3-variable system comprised of the CDS spread, the BIST-100 index, and the USD/TRY exchange rate series, taking the VIX as a control variable.[30] The lag length is given by $p = 3$ in the conditional mean equation and a ARCH(1) specification is used to model the conditional heteroscedasticity in the error terms. Panel (b) of **Table 5** shows that the ARCH coefficients $\gamma_{i,i}$ for $i = 1, 2, 3$ for the conditional variances of the CDS spread, the BIST-100 index and USD/TRY exchange rate are estimated to be significantly different from zero. Moreover, we find evidence that the volatility of the different series are related to each other (the coefficients $\gamma_{2,1}$, $\gamma_{3,1}$ and $\gamma_{3,2}$ are estimated to be significantly different from zero).

Figure 5 displays the predicted values of the conditional variances for the main sample period from 1 January 2013 to 22 December 2021. From Panel (a) of this figure, we observe volatility clusters in the behavior of the conditional volatility of

[28]If we allow for a t-distribution with 4 degrees of freedom as the distribution of the error terms in the GARCH(1,1) model, there is less evidence in favor of the significant ARCH(1) terms. However, these are still significant for the USD/TRY exchange rate and marginally significant for the CDS spread and TEPU index.

[29]This yields the DVECH model studied by Bollerslev, Engle and Wooldridge [63]. Other versions of the M-GARCH model are considered by Baba, Engle, Kraft and Kroner [64].

[30]An asymmetric version of the M-GARCH model is used by de Goeij and Marquering [65] to analyse dynamics for the conditional variances and covariances of bond and stock returns for the US.

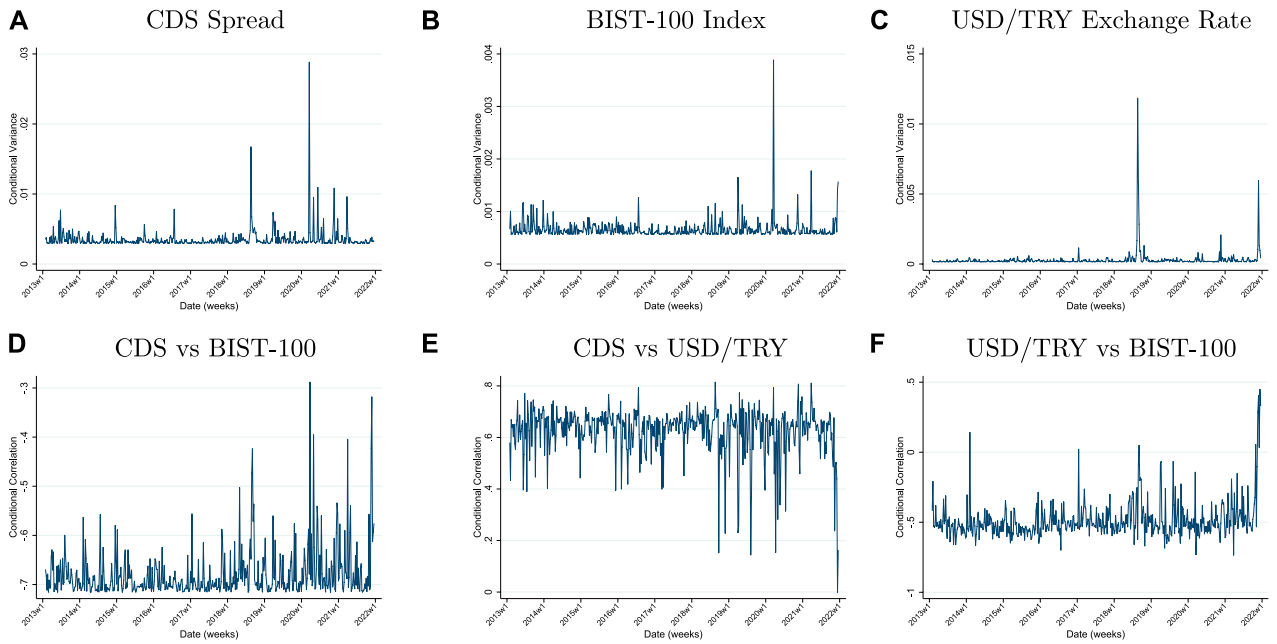

FIGURE 5 | Conditional variances and correlations. **(A)** CDS Spread. **(B)**BIST-100 Index. **(C)** USD/TRY Exchange Rate. **(D)** CDS vs BIST-100. **(E)** CDS vs USD/TRY. **(F)** USD/TRY vs BIST-100. Sample covers the period 2013w1-2021w51.

the CDS spread, which reflects the events that we catalogued in **Section 4.2**. In particular, the Black Friday shock of August 2018, the Covid-19 shock as well as the impacts of the unconventional monetary policy being increasingly pursued during 2020 and 2021 register as increases in the conditional volatility of the CDS spread. For the BIST-100 index, the major source of volatility is the Covid-19 shock of March 2020. By contrast, the August 2018 foreign exchange shock registers as the most important source of volatility for the conditional variance of the USD/TRY exchange rate. The December 2021 exchange rate shock also appears as an important shock to this conditional variance. However, the overall effect of the December 2021 shock on the USD/TRY exchange rate turns out to be smaller compared to the Black Friday shock of August 2018 due to the fact that the time-varying trend in the exchange rate has been increasing over the sample period.

Put differently, this discrepancy in the relative magnitudes of the two above-mentioned volatility shocks might stem from differences in their nature. We may view the Black Friday shock of August 2018 as being exogenous in the sense that it was partly the result of political tensions between the Trump administration and the government of Turkey. Hence, market participants did not anticipate it beforehand and failed to revise their expectations of its effect on the Turkish lira. By contrast, the December 2021 exchange rate shock seems to be endogenous in that it occurred in an environment where the pursuit of unconventional monetary policies was increasingly being espoused by different government officials. As the repeated interest rate cuts eroded the value of the Turkish lira throughout the last 3 months of 2021, the 20 December 2021 shock, though large in absolute magnitude, was most likely incorporated into the expectations of market participants as another shock against a backdrop of deteriorating sentiment regarding the value of Turkey's national currency.

Another way to examine the volatility behavior of changes in the TEPU index and the remaining financial indicators is to examine their conditional covariance. To ensure that the conditional covariance is not dominated by the estimates of the conditional variances, we calculate the conditional correlation between changes in the exchange rate and the CDS spread. The conditional correlations are defined as $\rho_{ij,t} = h_{ij,t}/(\sqrt{(h_{ii,t})}\sqrt{(h_{jj,t})})$. Panel (a) of **Figure 5** shows that the conditional correlations of the CDS spread with the BIST-100 index are among the highest for the Covid-19 shock of March 2020 and for the December 2021 exchange rate shock. Likewise, Panel (c) shows that the largest spikes in the conditional correlations between changes in the USD/TRY exchange rate and BIST-100 index are due to the December 2021 exchange rate shock. On the other hand, the conditional correlations between the CDS spread and the USD/TRY exchange rate, though always positive, reveal an inverted shape: this is due to the effect of the conditional variance of the USD/TRY exchange rate, which tends to swamp the magnitude of the conditional covariance.

6 CONCLUSION

In this paper, we construct a Twitter-based high frequency economic policy uncertainty index for Turkey over the period 2013–2021 by using a select set of Twitter accounts whose tweets are considered to reflect expert opinion on

economic policy issues in Turkey. This index may be used to track the evolution of economic policy uncertainty for a key emerging market economy, namely, Turkey. The timely character of Twitter data enables us to update our forward-looking TEPU index to follow rapidly changing movements in financial markets through changes in expert opinion and to understand how expert opinion itself is affected by financial indicators in a volatile policy environment.

As in other related research [8], expert opinion as represented by the TEPU index is a key indicator that helps to predict the country risk premium measured by the CDS spread. We further find evidence that the CDS spread itself may be useful for predicting changes on equity markets in Turkey. These two findings suggest a close connection between expert opinion, measures of the domestic risk premium and profit opportunities in an emerging market economy context. Finally, as an additional contribution, we relate the sources of conditional volatility in the CDS spread together with the USD/TRY exchange rate and BIST-100 stock index to salient events that occurred over the sample period 2013–2021.

That economic policy uncertainty stemming from such policy changes will have deleterious effects on investment by private firms in key emerging market economies is well-established; for a recent example, see [56] who aims to quantify the impact of heightened uncertainty associated with the sanctions regime of 2014 on investment behavior by non-financial privately-held firms in Russia. By analyzing a current episode of policy uncertainty that arises from political and economic events in Turkey, we provide a road-map for understanding the effects of economic policy uncertainty for other key emerging market economies which are historically prone to uncertainty and volatility.

DATA AVAILABILITY STATEMENT

The raw data supporting the conclusion of this article will be made available by the authors, without undue reservation.

AUTHOR CONTRIBUTIONS

All authors listed have made a substantial, direct, and intellectual contribution to the work and approved it for publication.

ACKNOWLEDGMENTS

This research is supported by TUBITAK Grant No: 118K268. We are grateful to Cem Çakmaklı for helpful comments. We thank Elif Güneş for her superb research assistance

REFERENCES

1. Baker SR, Bloom N, Davis SJ. Measuring Economic Policy Uncertainty*. *Q J Econ* (2016) 131(4):1593–636. doi:10.1093/qje/qjw024
2. Jirasavetakul L-BF, Spilimbergo A. *Economic Policy Uncertainty in Turkey*. IMF Working Papers 18/272, International Monetary Fund; Washington, DC (2018).
3. Sahinoz S, Erdogan Cosar E. Economic Policy Uncertainty and Economic Activity in Turkey. *Appl Econ Lett* (2018) 25(21):1517–20. doi:10.1080/13504851.2018.1430321
4. Topçu G, Oran J. Measuring Economic Policy Uncertainty in Turkey. *Ijepee* (2021) 14(3):288–305. doi:10.1504/ijepee.2021.114962
5. Baker SR, Bloom N, Renault T. *Twitter-Derived Measures of Economic Uncertainty* (2021). Available at: https://www.policyuncertainty.com/media/Twitter Uncertainty 5 13 2021.pdf.
6. Becerra JS, Sagner A. *Twitter-Based Economic Policy Uncertainty Index for Chile*. Technical Report 883. Santiago, Chile: Working Papers of the Central Bank of Chile (2020).
7. Laurent S, Bauwens L, Rombouts J. Multivariate GARCH Models: A Survey. *J Appl Econom* (2006) 21(1):79–109.
8. Dim C, Koerner K, Wolski M, Swart S. *News-based Sovereign Default Risk*. European Investment Bank Working Paper 2022/06 (2022). doi:10.2867/661002
9. Liu L, Zhang T. Economic Policy Uncertainty and Stock Market Volatility. *Finance Res Lett* (2015) 15(C):99–105. doi:10.1016/j.frl.2015.08.009
10. Kang W, Ratti RA. Oil Shocks, Policy Uncertainty and Stock Market Return. *J Int Financial Markets, Institutions Money* (2013) 26(C):305–18. doi:10.1016/j.intfin.2013.07.001
11. Carrière-Swallow Y, Céspedes LF. The Impact of Uncertainty Shocks in Emerging Economies. *J Int Econ* (2013) 90(2):316–25. doi:10.1016/j.jinteco.2013.03.003
12. Eberly JC. Adjustment of Consumers' Durables Stocks: Evidence from Automobile Purchases. *J Polit Economy* (1994) 102(3):403–36. doi:10.1086/261940
13. Bernanke BS. Irreversibility, Uncertainty, and Cyclical Investment. *Q J Econ* (1983) 98(1):85–106. doi:10.2307/1885568
14. Dixit A. Entry and Exit Decisions under Uncertainty. *J Polit Economy* (1989) 97(3):620–38. doi:10.1086/261619
15. Dixit RK, Dixit AK, Pindyck RS. *Investment under Uncertainty*. Princeton, NJ: Princeton University Press (1994).
16. Schaal E. Uncertainty and Unemployment. *Econometrica* (2017) 85(6):1675–721. doi:10.3982/ecta10557
17. Valletta RG, Bengali L, Van der List C. Cyclical and Market Determinants of Involuntary Part-Time Employment. *J Labor Econ* (2020) 38(1):67–93. doi:10.1086/704496
18. Fernández-Villaverde J, Guerrón-Quintana P, Kuester K, Rubio-Ramírez J. Fiscal Volatility Shocks and Economic Activity. *Am Econ Rev* (2015) 105(11):3352–84. doi:10.1257/aer.20121236
19. Johannsen BK. When Are the Effects of Fiscal Policy Uncertainty Large? In: *Finance and Economics Discussion Series 2014-40*. Washington, DC: Board of Governors of the Federal Reserve System (U.S.) (2014).
20. Kraft H, Schwartz E, Weiss F. Growth Options and Firm Valuation. *Eur Financial Manage* (2018) 24(2):209–38. doi:10.1111/eufm.12141
21. Christiano LJ, Motto R, Rostagno M. Risk Shocks. *Am Econ Rev* (2014) 104(1):27–65. doi:10.1257/aer.104.1.27
22. Gilchrist S, Sim JW, Zakrajšek E. *Uncertainty, Financial Frictions, and Investment Dynamics*. NBER Working Paper w20038. Cambridge, MA: National Bureau of Economic Research (2014).
23. Pástor Ľ, Veronesi P. Political Uncertainty and Risk Premia. *J Financial Econ* (2013) 110(3):520–45. doi:10.1016/j.jfineco.2013.08.007
24. Friedman M. The Role of Monetary Policy. *Am Econ Rev* (1968) 58:1–17.
25. Rodrik D. Policy Uncertainty and Private Investment in Developing Countries. *J Develop Econ* (1991) 36(2):229–42. doi:10.1016/0304-3878(91)90034-s
26. Higgs R. Regime Uncertainty: Why the Great Depression Lasted So Long and Why Prosperity Resumed after the War. *Independent Rev* (1997) 1(4):561.
27. Hassett KA, Metcalf GE. Investment with Uncertain Tax Policy: Does Random Tax Policy Discourage Investment. *Econ J* (1999) 109(457):372–93. doi:10.1111/1468-0297.00453

28. Altug S, Demers FS, Demers M, Demers M. The Investment Tax Credit and Irreversible Investment. *J Macroeconomics* (2009) 31(4):509–22. doi:10.1016/j.jmacro.2009.01.001
29. Altig D, Bloom N, Davis SJ, Meyer B, Parker N. *Tariff Worries and US Business Investment, Take Two*. Federal Reserve Bank of Atlanta Macro Blog Post. Atlanta, GA: Policy HUB (2019).
30. Caldara D, Iacoviello M, Molligo P, Prestipino A, Raffo A. The Economic Effects of Trade Policy Uncertainty. *J Monetary Econ* (2020) 109:38–59. doi:10.1016/j.jmoneco.2019.11.002
31. Ahir H, Bloom N, Furceri D. *The World Uncertainty Index*. Stanford University (2018). Available at SSRN: https://ssrn.com/abstract=3275033 (Accessed October 29, 2018).
32. Bloom N. The Impact of Uncertainty Shocks. *Econometrica* (2009) 77(3):623–85. doi:10.3386/w13385
33. Jurado K, Ludvigson SC, Ng S. Measuring Uncertainty. *Am Econ Rev* (2015) 105(3):1177–216. doi:10.1257/aer.20131193
34. Nodari G. Financial Regulation Policy Uncertainty and Credit Spreads in the US. *J Macroeconomics* (2014) 41:122–32. doi:10.1016/j.jmacro.2014.05.006
35. Caggiano G, Castelnuovo E, Figueres JM. Economic Policy Uncertainty and Unemployment in the United States: A Nonlinear Approach. *Econ Lett* (2017) 151(C):31–4. doi:10.1016/j.econlet.2016.12.002
36. Doehr R, Martínez-García E. *Monetary Policy Uncertainty and Economic Fluctuations at the Zero Lower Bound*. Globalization Institute Working Paper 412. Federal Reserve Bank of Dallas (2021). Available at: http://doi.org/10.24149/gwp412.
37. Wang Y, Zhang B, Diao X, Wu C. Commodity Price Changes and the Predictability of Economic Policy Uncertainty. *Econ Lett* (2015) 127:39–42. doi:10.1016/j.econlet.2014.12.030
38. Altig D, Baker S, Barrero JM, Bloom N, Bunn P, Chen S, et al. Economic Uncertainty before and during the COVID-19 Pandemic. *J Public Econ* (2020) 191:104274. doi:10.1016/j.jpubeco.2020.104274
39. Baker SR, Davis SJ, Levy JA. *State-Level Economic Policy Uncertainty*. Working Paper 2022-21. Chicago, IL: Becker Friedman Institute for Economics at UChicago (2022).
40. Qureshi S, Chu B, Demers FS, Demers M. *Using Natural Language Processing to Measure COVID-19-Induced Economic Policy Uncertainty for Canada and the US*. Carleton Economics Working Papers (CEWP) 22-01. Ottawa, Canada: Carleton University (2022).
41. Arbatli Saxegaard EC, Davis SJ, Ito A, Miake N, Miake N. Policy Uncertainty in Japan. *J Jpn Int Economies* (2022) 64:101192. doi:10.1016/j.jjie.2022.101192
42. Liu B. *Sentiment Analysis: Mining Opinions, Sentiments, and Emotions*. Cambridge University Press (2020).
43. O'Connor B, Balasubramanyan R, Routledge BR, Smith NA. From Tweets to Polls: Linking Text Sentiment to Public Opinion Time Series. In: *Fourth International AAAI Conference on Weblogs and Social Media* (2010).
44. Zhang L, Wang S, Liu B. Deep Learning for Sentiment Analysis: A Survey. *Wiley Interdiscip Rev Data Mining Knowledge Discov* (2018) 8(4):e1253. doi:10.1002/widm.1253
45. Greene D, Reid F, Sheridan G, Cunningham P. *Supporting the Curation of Twitter User Lists* (2011). *arXiv preprint arXiv:1110.1349*.
46. Greene D, Sheridan G, Smyth B, Cunningham P. Aggregating Content and Network Information to Curate Twitter User Lists. In: *Proceedings of the 4th ACM RecSys Workshop on Recommender Systems and the Social Web* (2012). p. 29–36. doi:10.1145/2365934.2365941
47. Giachanou A, Crestani F. Like it or Not. *ACM Comput Surv* (2016) 49(2):1–41. doi:10.1145/2938640
48. Kalemli-Özcan S. *US Monetary Policy and International Risk Spillovers*. National Bureau of Economic Research Working Papers w26297. Cambridge, MA: National Bureau of Economic Research (2019). Available at: http://doi.org/10.3386/w26297.
49. Cogley T, Nason JM. Effects of the Hodrick-Prescott Filter on Trend and Difference Stationary Time Series: Implications for Business Cycle Research. *J Econ Dyn Control* (1995) 19(1-2):253–78. doi:10.1016/0165-1889(93)00781-x
50. Schuler YS. *On the Cyclical Properties of Hamilton's Regression Filter*. Discussion Papers 03/2018. Frankfurt, Germany: Deutsche Bundesbank (2018). Available at: http://dx.doi.org/10.2139/ssrn.3127430.
51. Phillips PCB, Shi Z. Boosting: Why You Can Use the HP Filter. *Int Econ Rev* (2021) 62(2):521–570. doi:10.1111/iere.12495
52. Ravn MO, Uhlig H. On Adjusting the Hodrick-Prescott Filter for the Frequency of Observations. *Rev Econ Stat* (2002) 84(2):371–6. doi:10.1162/003465302317411604
53. Johansen S. *Likelihood-Based Inference in Cointegrated Vector Autoregressive Models*. Oxford University Press (1995).
54. Lutkepol H. *New Introduction to Multiple Time Series Analysis*. Berlin: Springer (2005).
55. Lütkepohl H, Martin K. *Applied Time Series Econometrics*. Cambridge: Cambridge University Press (2004).
56. Altug S, Yeşiltaş S. *Investment under Stormy Skies: The Case of Russian Firms during 2004-2016*. CEPR Discussion Papers 16646. London, UK: Centre for Economic Policy Research (2021).
57. Bloom N. Fluctuations in Uncertainty. *J Econ Perspect* (2014) 28(2):153–76. doi:10.1257/jep.28.2.153
58. Cha M, Haddadi H, Benevenuto F, Gummadi K. Measuring User Influence in Twitter: The Million Follower Fallacy. In: *Proceedings of the International AAAI Conference on Web and Social Media* (2010) 4(1):10–17. Available at: https://ojs.aaai.org/index.php/ICWSM/article/view/14033.
59. Verweij P. Twitter Links between Politicians and Journalists. *Journalism Pract* (2012) 6(5-6):680–91. doi:10.1080/17512786.2012.667272
60. Weng J, Lim E-P, Jiang J, Qi H. TwitterRank: Finding Topic-Sensitive Influential Twitterers. In: *Proceedings of the Third ACM International Conference on Web Search and Data Mining*. New York, NY, USA: WSDM '10 Association for Computing Machinery (2010). p. 261–70.
61. Saif H, Fernandez M, He Y, Alani H. Evaluation Datasets for Twitter Sentiment Analysis: A Survey and A New Dataset, the STS-Gold. In: *1st Interantional Workshop on Emotion and Sentiment in Social and Expressive Media: Approaches and Perspectives from AI (EESEM 2013)*; 2013 December 3; Turin, Italy (2013). Available at: http://www.di.unito.it/patti/essem13/index.html.
62. Aruoba SB, Diebold FX, Scotti C. Real-time Measurement of Business Conditions. *J Business Econ Stat* (2009) 27(4):417–27. doi:10.1198/jbes.2009.07205
63. Bollerslev T, Engle RF, Wooldridge JM. A Capital Asset Pricing Model with Time-Varying Covariances. *J Polit Economy* (1988) 96(1):116–31. doi:10.1086/261527
64. Baba Y, Engle RF, Kraft DF, Kroner KF. *Multivariate Simultaneous Generalized ARCH*. San Diego: mimeo, Department of Economics, University of California (1990).
65. de Goeij P, Marquering W. Modeling the Conditional Covariance between Stock and Bond Returns: A Multivariate GARCH Approach. *J Financial Econom* (2004) 2(4):531–64. doi:10.1093/jjfinec/nbh021

Conflict of Interest: The authors declare that the research was conducted in the absence of any commercial or financial relationships that could be construed as a potential conflict of interest.

frontiers | Frontiers in Chemistry

ORIGINAL RESEARCH
published: 08 July 2022
doi: 10.3389/fchem.2022.881691

Periodic Motion in the Chaotic Phase of an Unstirred Ferroin-Catalyzed Belousov Zhabotinsky Reaction

Florian Wodlei, Mihnea R. Hristea and Giuseppe Alberti*

Living Systems Research, Klagenfurt, Austria

The Belousov Zhabotinsky reaction, a self-organized oscillatory color-changing reaction, can show complex behavior when left unstirred in a cuvette environment. The most intriguing behavior is the transition from periodicity to chaos and back to periodicity as the system evolves in time. It was shown that this happens thanks due to the decoupling of reaction, diffusion and convection. We have recently discovered that, as the so-called chaotic transient takes place, periodic bulk motions in form of convective cells are created in the reaction solution. In this work we investigated this phenomenon experimentally by changing cuvette size and reaction volume, in order to allow different types of convection patterns to appear. So far, we have observed single and double convection cells in the system. There are indications that the convection patterns are connected to the duration of the chaotic phase. A simplified mathematical model confirms the form and dynamics of the observed convection cells and explains the connection between chemical chaos and hydrodynamical order.

Keywords: BZ reaction, ferroin-catalyzed, chaotic transient, periodic patterns, convection cells

OPEN ACCESS

Edited by:
Federico Rossi,
University of Siena, Italy

Reviewed by:
Sumana Dutta,
Indian Institute of Technology Guwahati, India
Pier Luigi Gentili,
Università degli Studi di Perugia, Italy

****Correspondence:***
Florian Wodlei
florian.wodlei@ilsr.at

Specialty section:
This article was submitted to Physical Chemistry and Chemical Physics, a section of the journal Frontiers in Chemistry

Received: *22 February 2022*
Accepted: *24 May 2022*
Published: *08 July 2022*

Citation:
Wodlei F, Hristea MR and Alberti G (2022) Periodic Motion in the Chaotic Phase of an Unstirred Ferroin-Catalyzed Belousov Zhabotinsky Reaction. Front. Chem. 10:881691. doi: 10.3389/fchem.2022.881691

INTRODUCTION

The Belousov Zhabotinsky (BZ) is a typical example of a chemical oscillator that shows self-organizing behaviour at different levels. It is the most thoroughly studied oscillatory reaction system in homogeneous phase in chemistry. At the same time, due to its complexity, not all aspects of its dynamics are yet understood. After its discovery by Boris P. Belousov (Belousov, 1959) in the 1950s and the thorough investigation by Anatol M. Zhabotinsky and other colleagues (Zhabotinsky, 1964; Korzukhin Zhabotinsky, 1965; Zaikin and Zhabotinsky, 1970) it became famous in the 70s where major achievements were gained in trying to understand its reaction mechanism (Field et al., 1972; Noyes et al., 1972; Field and Noyes, 1974a; Field and Noyes, 1974b).

The BZ reaction is a periodic bromination of an organic species in acidic environment and in the presence of a catalytic color indicator in liquid phase. Convection and diffusion play an important role in liquid phase systems. It is possible to observe beautiful periodic color oscillations when the reaction is carried out in well stirred batch reactor to hinder diffusion and convection. The formation of chemical waves can be observed in a Petri dish where the development of convective motion is suppressed.

The BZ reaction is not the only chemical oscillator but the first found in homogeneous phase (Scott, 1993; Tyson and Levin, 1994). Subsequently, many other systems, showing similar oscillatory and self-organizing properties, were discovered in both biology and chemistry. In biology the majority of oscillatory reactions are related to the so called biological clocks, for example, those that occur during the cell cycle (Chance et al., 1973; Goldbeter, 1996). For instance, an interesting system

in biology is that of the Min protein system found in *E. Coli*. This system ensures the proper spatial and temporal regulation of chromosomal segregation and division prior to cell division. The Min proteins spontaneously form chemical surface waves on artificial flat membrane *in vitro* (Loose et al., 2008) that show high similarity to those observed in the BZ reaction. Nowadays in chemistry we know many systems that show oscillatory and self-organizing properties. In particular, the cetrimonium bromide (CTAB)/dichloromethane system shows especially beautiful self-organization. More specifically, it is a biphasic system where oscillations of the surface tension occur at the interface between CTAB and dichloromethane (Pimienta et al., 2004). Even though their origin is different, they show a surprisingly similar shape to the ones seen in a BZ reaction. When only one little drop of dichloromethane is added to a CTAB solution, it is possible to observe highly organized patterns, such as oscillations of the drop diameter (Antoine et al., 2016; Wodlei et al., 2018). As in the BZ reaction, convection plays a crucial role in this system too.

Such similarities are no coincidence; rather they are the fulfilment of certain conditions that allow periodic behavior to occur. Irving Epstein and colleagues, for example, were actively searching for such oscillators and successfully constructed one following these conditions (Epstein and Pojman, 1998).

At present, researchers employ the BZ reaction not only to investigate and better understand its dynamics, but for many different applications. It is used in elastomechanical gels to generate periodical motion (Deb et al., 2014), to create binary operations in non-convectional computing (Adamatzky and Costello, 2007; Adamatzky, 2019), to mimic neural dynamics (Gentili et al., 2017) and to implement chemical automata to mention only a few (Dueñas-Díez and Pérez-Mercader, 2021).

In this study we investigate the dynamics of the BZ reaction when left unstirred in a batch reactor. Due to the fact that the system is liquid and unstirred, its dynamics will be not only governed by the reaction kinetics, but also by diffusion and convection. In this case the reaction dynamics becomes more complex. In addition to the periodic color change, a phase of aperiodic color change appears for a limited time that transits back to periodicity. The appearance of this chaotic transient led some researchers to even call this behavior a "re-birth" (Onuma et al., 2011), even though the system never reaches thermodynamic equilibrium during the chaotic phase. More specifically, the reaction system is undergoing a transition to an aperiodic phase from which it returns to periodicity after several hours. This behavior was first discovered by Rustici et al. in a Cerium-catalyzed (Rustici et al., 1996) and later also in a Ferroin-catalyzed version (Rossi et al., 2009) of the BZ reaction. Rustici et al. (Rustici et al., 1998) also demonstrated that the transition to chaos follows a Ruelle-Takens-Newhouse (RTN) scenario (Newhouse et al., 1978).

An unstirred BZ reaction behaves in a more complex manner due to the fact that convections of different origins are not hindered by the homogenizing effect of stirring and are free to develop instead. Therefore the resulting dynamics is an interplay between diffusion, convection and (local) kinetics.

Chaotic behavior is not found only in unstirred batch reactors but also in open constantly stirred tank reactors (CSTR), where the reaction solution flows in and out with a specific flow rate. In this case, the appearance of chaos is totally dependent on the flow rate. High flow rates are connected with chaos (Gyorgyi et al., 1992).

The appearance of chaos in an unstirred BZ reaction, on the other hand, shows strong relations to the complex coupling that happens in this system between chemical kinetics, diffusion and convection. The effect of convection on the chaotic phase was demonstrated by Budroni et al. (2017) by varying the solution viscosity. An increased viscosity hinders the formation of convection; the duration of the chaotic phase in such systems could be reduced, even until the complete disappearance of the chaotic transient. It was proven that the temperature has an effect too (Masia et al., 2001). Variation in temperature, between 0 and 8°C, leads the system from periodicity to chaos. Thus, temperature affects the coupling between chemical kinetics, diffusion and convection in a similar way. Marchettini et al. (2010) theoretically showed that the consumption of the chemical species is at the origin of the decoupling of reaction kinetics, diffusion and convection.

Our group discovered that this unstirred dynamics can also be affected by applying a limited stirring phase immediately following the first periodic phase. By doing so, the duration of the chaotic phase is shortened (Wodlei and Hristea, 2013).

Convective motion in the BZ reaction was mainly investigated in the shallow configuration, in order to study the spatial patterns by varying, for example, the layer depths (Rossi et al., 2012). To study the temporal dynamics, either constantly stirred tank reactors (CSTR) or stirred standard cuvettes were used. Due to the homogeneity of the reaction solution the system is usually examined with spectrophotometers. Even though the homogeneity in an unstirred batch configuration is not always given, the majority of the studies carried out were conducted in standard photometric cuvettes and investigated by using spectrophotometers. So far, to our knowledge, convective motion in the BZ reaction was never studied in a cuvette configuration. This might be due to the fact that the convection dynamics in a filled standard cuvette shows only very slow upwards and downwards motions, hardly visible to the eye. However, convective motion was observed in another system, in a cuvette configuration. Gentili et al. investigated color oscillations and waves due to hydrodynamic convective motion in a solution of a thermoreversible photochromic spiro-oxazine (Gentili and Micheau, 2019).

EXPERIMENTAL METHODS

A BZ reaction in a cuvette configuration is usually investigated in a spectrophotometer. A concentrated light beam is sent through a point in the middle of the cuvette and the absorbance/transmission is registered by a photo diode or another type of sensor. Such measurements can give great insight into the dynamics that occur in homogeneous reaction solutions. A constant stirring of the solution does usually guarantee its

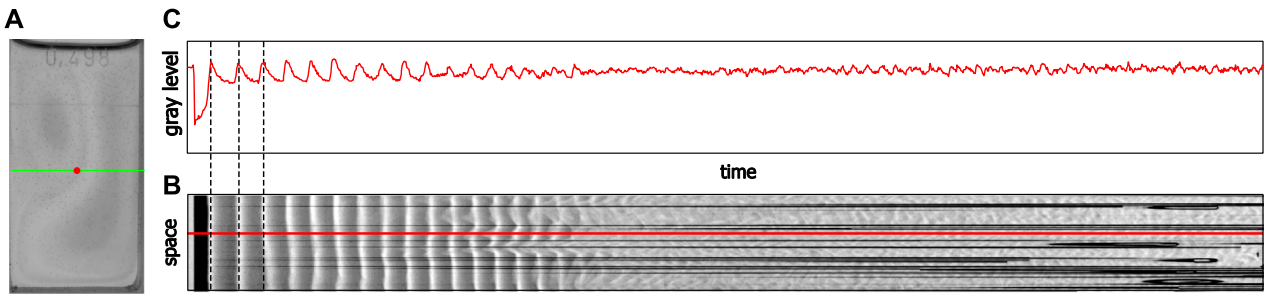

FIGURE 1 | Extraction of time series from video data, **(A)** shows a video image of the BZ reaction in a special cuvette, **(B)** shows a space–time plot for the green cross-section line in **(A)**, **(C)** shows the gray level value profile along the red line in **(B)** corresponding to the change in gray level at the red point shown in **(A)**.

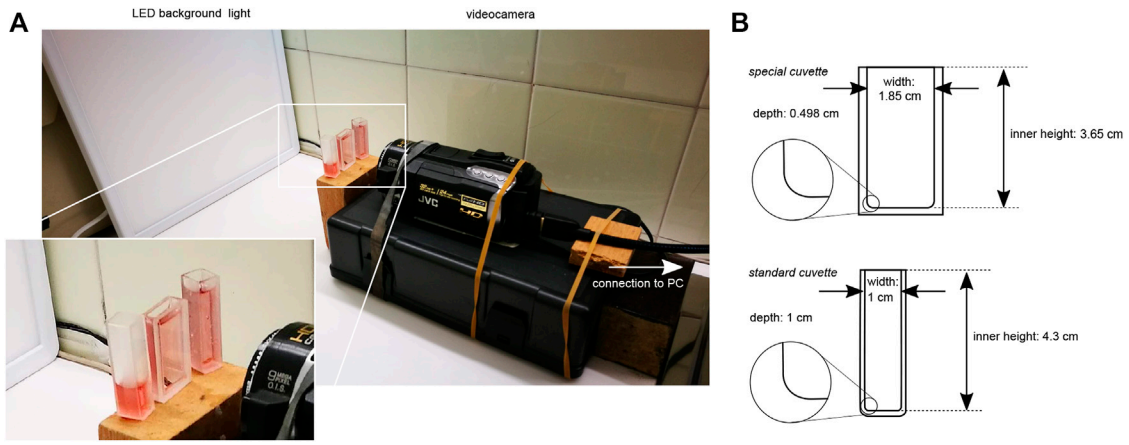

FIGURE 2 | Optical setup, **(A)** shows the arrangement of the LED backlight, photo spectroscopic quartz cuvettes and the video camera; inset shows a zoom on the cuvettes, **(B)** shows the schemes of the cuvettes with their dimensions; insets show the curved inside corners.

homogeneity. In an unstirred BZ reaction such a homogeneity is generally not achieved, and therefore a spectrophotometric analysis can only provide a certain amount of insight into the reaction dynamics. To record the entire cuvette we used a video camera instead of a spectrophotometer, which allowed us to record the spatial dynamics of an unstirred BZ reaction. Additionally, we could extract from the video data time series by creating space–time plots from cross-section lines along the width of the cuvette. Since we are interested in the dynamics of a given point (see **Figure 1A**, red point) which corresponds to a line in the space-time plot (see **Figure 1B**, red line) we translated the shades of gray back into gray level values and obtained a time series (see **Figure 1C**). These time series are similar to those obtained by a spectrophotometer. Due to the sensitivity of the sensor chip of the video camera these time series correspond to a wavelength of around 450 nm. For more details, see the **Supplementary Material S1**.

Materials and Instruments

An optical setup consisting of a ceiling LED panel (B.K.Licht 18 W LED Panel, 2,400 lm, 4000 K white light) as background light and a video camera (JVC Everio HM400) was used to record the dynamics of the reaction. The filled cuvettes of different types were placed in the focal point of the camera in front of the backlight (see **Figure 2**).

Preparation of the Solution

All chemicals were commercial grade reactants (Sigma-Aldrich) and were used without further purification. All solutions were prepared with laboratory reagent grade distilled water. The four following aqueous stock solutions with their specific concentrations were prepared by weight, using an analytical balance: malonic acid (MA) 2 M, sodium bromate ($NaBrO_3$) 1 M, sulfuric acid (H_2SO_4) 2 M, sodium bromide (NaBr) 1 M. The ferroin solution with a concentration of 0.025 M was used without further dilution.

The reaction solution was prepared by adding the following volumes of the stock solutions and of distilled water with a micropipette, in a volumetric flask: 1.5 ml distilled water, 1.265 ml MA solution, 0.675 ml $NaBrO_3$ solution, 3 ml H_2SO_4 solution, 0.12 ml NaBr solution and 0.1 ml ferroin solution. The resulting solution then was stirred for 15 min at a high stirring rate before being poured into the spectrophotometric quartz cuvettes of different volumes and geometries. All experiments were performed at a constant room temperature of 22°C.

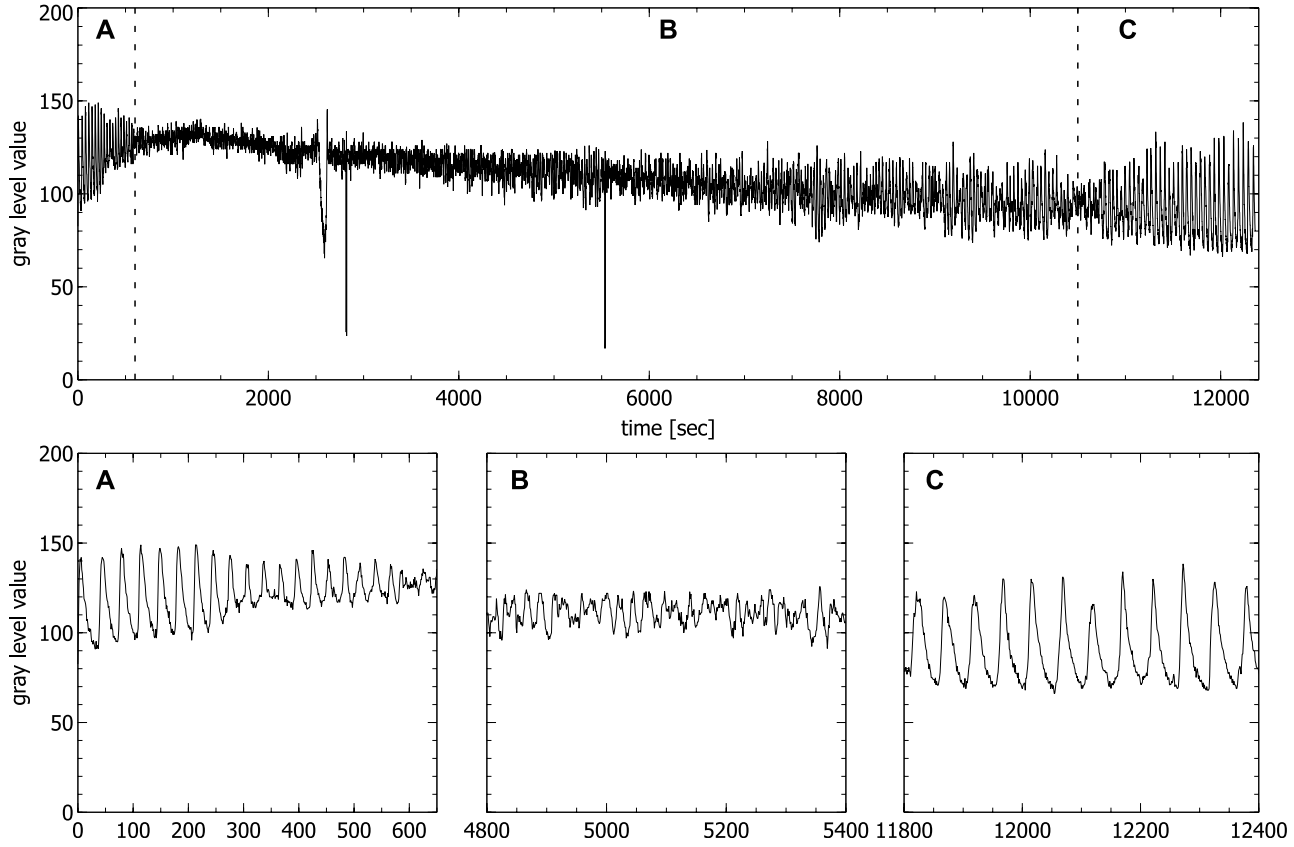

FIGURE 3 | Oscillations of the concentration of the ferriin concentration extracted from video data of an unstirred BZ reaction carried out in a fully filled standard cuvette (spikes in the time series correspond to the passage of bubbles). Panels **A–C** show the enlargement of the areas **A–C** in the upper part corresponding to the first periodic **(A)**, the chaotic **(B)** and the second periodic phase **(C)**, respectively.

EXPERIMENTAL RESULTS AND DISCUSSION

Figure 3 shows a typical time series of a ferroin-catalyzed BZ reaction in unstirred batch conditions, obtained from video data of an open, 3 ml filled standard quartz cuvette (1 × 1 × 4.5 cm). Similar time series produced by spectrophotometric measurements of unstirred BZ reaction in unstirred batch conditions were also obtained by others (Rustici et al., 1996; Rossi et al., 2009; Marchettini et al., 2010).

The typical transition from a region of periodic (see **Figure 3A**) to a region of aperiodic oscillations (see **Figure 3B**) and back again to periodic oscillations (see **Figure 3C**) is clearly visible. Only the beginning of the second periodic phase is shown, since our interest is in the aperiodic phase. The second periodic phase itself can last up to 8 h before the reaction reaches thermodynamic equilibrium. It has been shown that the phase of aperiodic oscillations shows two distinct features of deterministic chaos, namely a broadband spectrum in the frequency domain and positive maximal Lyapunov exponents (Rossi et al., 2009). We have analyzed the aperiodic regime of the time series shown in **Figure 3**, obtained from video data and we also got a broadband spectrum in the frequency domain and a positive maximal Lyapunov exponent calculated with the TISEAN Nonlinear Time Series Analysis package (Kantz and Schreiber, 2004), comparable to the one obtained by Rossi et al. (Rossi et al., 2009) (for details, see **Supplementary Material S1**). For that reason, from now on we will name the region of aperiodic oscillations *chaotic* phase.

The results reported here were obtained from a series of seven experiments conducted under the same conditions. For each experiment the BZ reaction solution was prepared as described above and poured into two standard cuvettes (1 × 1 × 4.5 cm), one partially filled (1.3 ml), the other one fully (3 ml), and one fully filled (3 ml) slimmer but broader special cuvette (1.85 × 0.498 × 3.65 cm) that were all already placed in a simple optical setup (see **Figure 2**).

Even though the same conditions were used for all the experiments, slight unavoidable variations in the initial conditions of the concentrations and the temperature led to small differences in the evolution of the reaction. The observed oscillation period of the first periodic phase is the same in all cuvettes from a given mother solution independent of the reaction volume or shape (e.g. 35.33 ± 0.5 s), while the oscillation period between different mother solution with the same apparent initial conditions can vary up to 30% (i.e. 35.33 s ± 0.46 s vs.

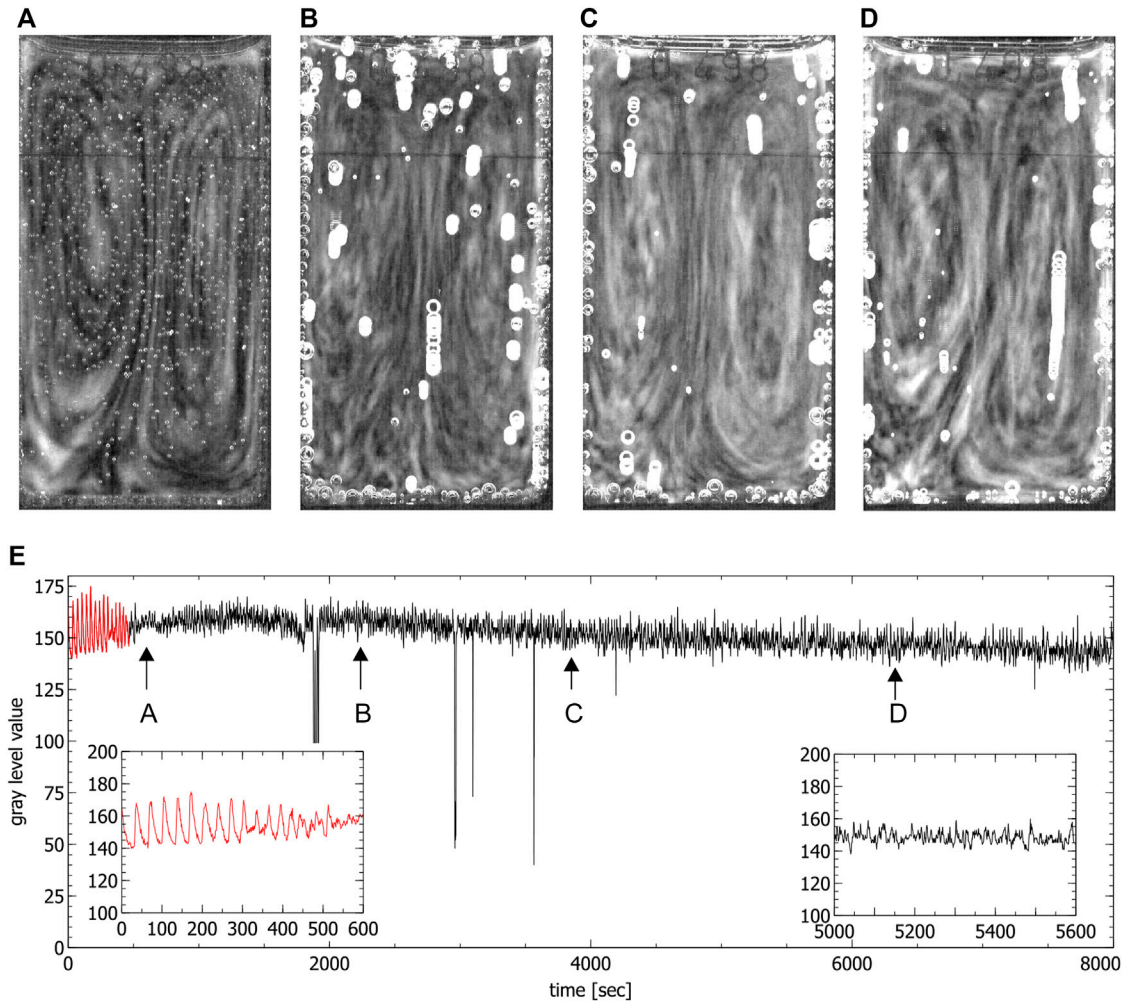

FIGURE 4 | Convection cells in the special cuvette during the chaotic phase. **(A–D)** show the presence of two convection cells (liquid moves up in the middle and down on the left and right side). Images were obtained by averaging over 60 s, **(E)** shows the time series extracted from the video data where the red part corresponds to the periodic phase. Arrows indicate the times where the images **(A–D)** were created (spikes in the time series correspond to the passage of bubbles). Insets show the periodic phase (left) and part of the chaotic phase (right) magnified.

25.48 ± 0.16 s). This variation can be understood in terms of the uncertainty of the micropipette that leads to an uncertainty in the concentrations of around 1% and temperature variation of maximal 1°C, knowing that the oscillation period depends on the initial concentration of the reactants and the temperature. The observed convection patterns are also sensitive to these slight variations, even though the general dynamics is unaffected by them.

All the experiments conducted were accompanied by a "bubble phase" that started soon after pouring the substances in the cuvettes and lasted between 30 and 40 min. In this phase bubbles formed at the glass walls of the cuvettes and moved upwards when they reached a certain size. These gas bubbles are composed of carbon monoxide and carbon dioxide (Onel et al., 2007). The additional volume created by the bubbles led to an apparent volume increase of the reaction solution, following by its decrease after the most of the bubbles were released. Due to this formation of gas during the whole duration of the reaction the cuvette could not be closed as it would have been necessary to avoid evaporation.

During the chaotic phase ordered convective motions were visible in the partially filled standard cuvettes, where one convection cell formed (see **Figure 6**) and in the special cuvette, where two convection cells formed (see **Figure 4**). A first estimation of the magnitude of the convection velocity gives a value range of 0.5–0.6 mm/s (calculated in the experiment shown in **Figure 4**). The convection cells stayed stable throughout the whole chaotic phase. Only in some of the experiments conducted in the special cuvette one of the two convection cells became more dominant while the second one got reduced in size. This situation was not stable and there was a continuous switching between two convection cells of the same size and two of different sizes.

In the fully filled standard cuvette only up- and downwards convective motions were observed (see **Figure 5**). The fact that in this case no clear convection cells were visible seems to be

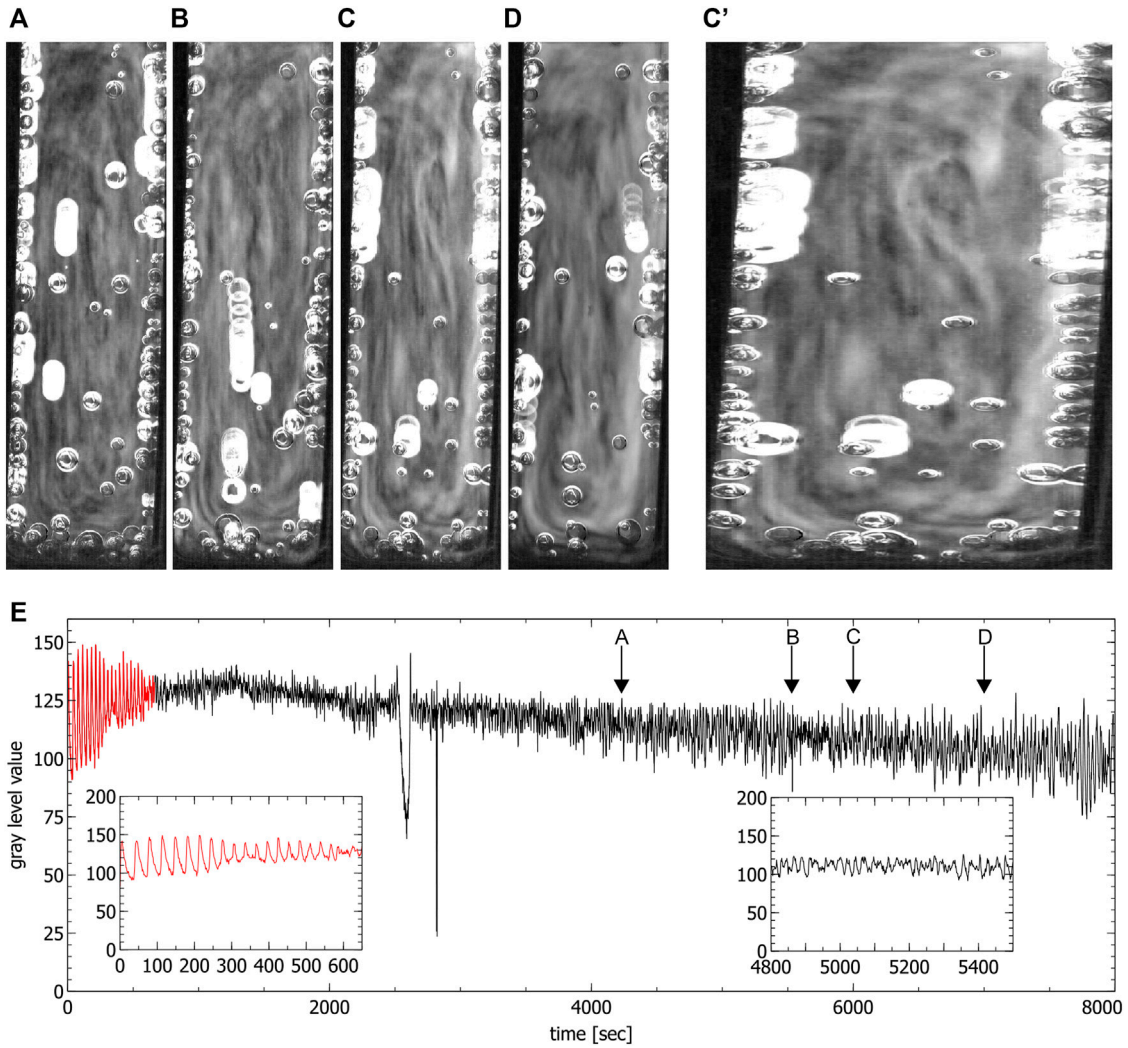

FIGURE 5 | Convection cells in a fully filled standard cuvette during the chaotic phase. **(A–D)** show the up and down motion inside the liquid. Images were obtained by averaging over 60 s **(C')** shows subfigure **(C)** stretched for better visibility, **(E)** is the time series extracted from the video data where the red part corresponds to the periodic phase. Insets show the periodic phase (left) and part of the chaotic phase (right) magnified (spikes in the time series correspond to the passage of bubbles). Arrows indicate the times where the images **(A–D)** were created.

connected to the ratio between the height and the width of the reaction solution which in this case did not favor the formation of convection cells. By only partially filling the cuvettes, the reaction volume is reduced, this ratio changes and the formation of one single convection cell could be observed which confirms this assumption (see in **Figure 6**).

The appearance of ordered spatial structures in the chaotic phase in the special cuvette was unexpected. A Fast Fourier Transform (FFT) analysis and the calculation of the maximal Lyapunov exponents of the corresponding aperiodic time series of this cuvette indicates the presence of deterministic chaos. The analysis was conducted in the timeframes indicated by the arrows in **Figure 4E**. As expected, a broad band spectrum was found (see **Figures 7A–D**) and the corresponding maximal Lyapunov exponents were all positive (λ_A = 0.001178 ± 0.000276, λ_B = 0.005099 ± 0.000249, λ_C = 0.0009 ± 0.000271 and λ_D = 0.001432 ± 0.000266). This confirms indeed the chaoticity of this phase from a local chemical point of view. Nevertheless, from a global hydrodynamical point of view, the phase is spatially ordered.

For comparison, a Fast Fourier Transform (FFT) analysis was also conducted on the periodic phases of the time series in the special cuvette for the first periodic phase (see **Figure 7E**) and for the beginning of the second periodic phase (see **Figure 7F**). The FFT spectrum of the first periodic phase shows a characteristic main frequency and its harmonics. The FFT spectrum of the beginning of the second periodic phase, on the other hand, shows three incommensurable frequencies and its harmonics, indicating the transition from chaos back to periodicity.

Convection cells can form, for different reasons, in liquid and gaseous phases and their form and dynamics depend,

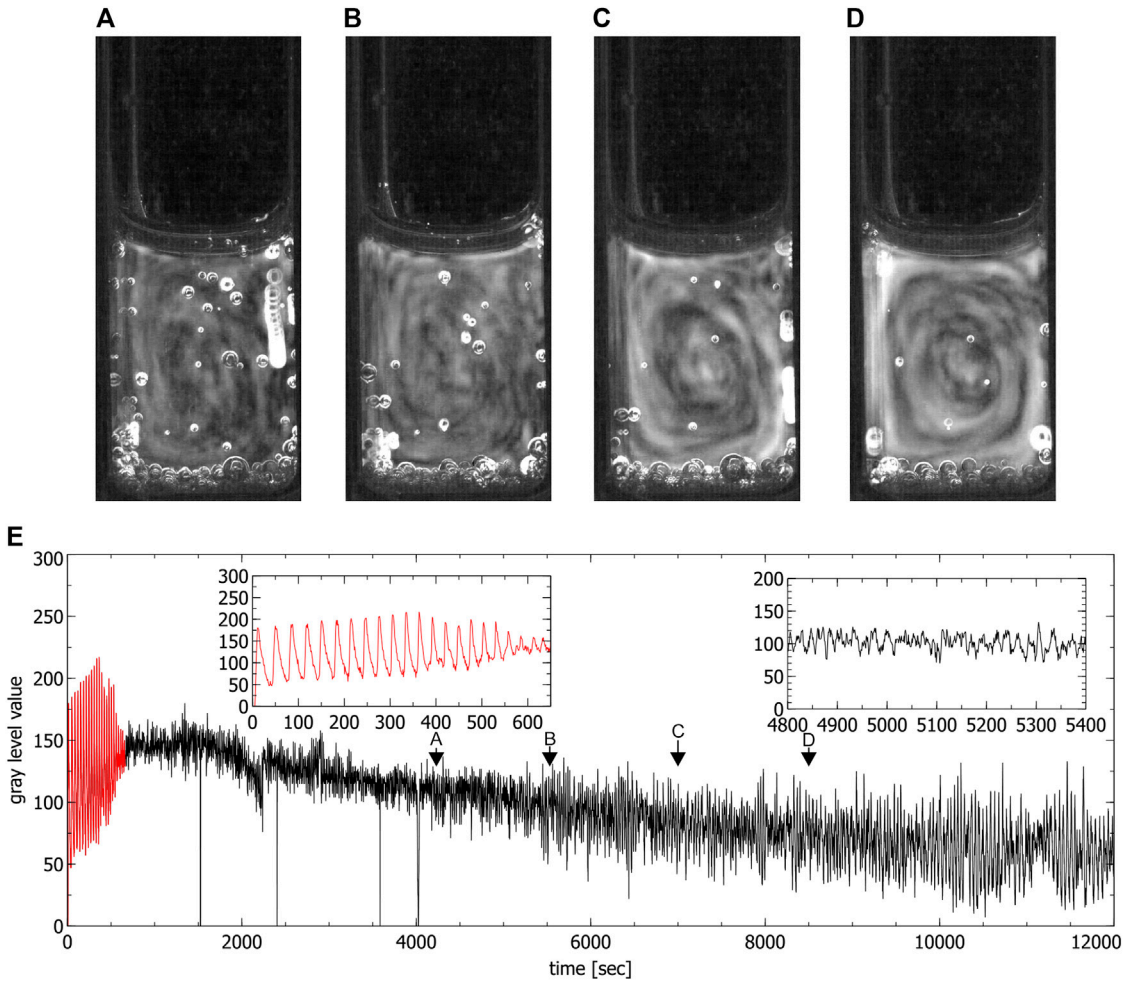

FIGURE 6 | Convection cells in a partly filled standard cuvette during the chaotic phase. **(A–D)** show the presence of one convection cell (liquid moves anti-clockwise). Images were obtained by averaging over 60 s, **(E)** is the time series extracted from the video data where the red part corresponds to the periodic phase. Insets show the periodic phase (left) and part of the chaotic phase (right) magnified (spikes in the time series correspond to the passage of bubbles). Arrows indicate times where the images **(A–D)** were created.

respectively, on the properties of the liquid or gas. The fact that in our case the cuvettes could not be closed allows the evaporation of the reaction solution. Subsequently surface tension gradients are created, potentially inducing convections in the bulk phase according to a thermo-capillary Marangoni effect. Even though such an effect becomes weaker with the depths of the liquid layer (Rongy and De Wit, 2007; Rossi et al., 2012), it could play a role in our system. On the other hand, the different densities of the reaction products within the reaction solution could create density gradients big enough to trigger Rayleigh-Bénard convections. Most likely the convection cells observed in our system are an interplay of both effects, where the partially evaporation of the solvent induces a convective motion, which enhances and amplifies already existing Rayleigh-Bénard convections induced by density gradient of the reaction products. This idea is also supported by the appearance of similar convection cells in the work of Gentili et al. (2014). Nevertheless, to get a better picture on the origin of the convection cells in our system, further research is needed.

The fact that chemical chaos and convective motion are connected in the unstirred BZ reaction was already mentioned in the introduction and is confirmed by experiments and theoretical models (Masia et al., 2001; Marchettini et al., 2010; Budroni et al., 2017). The possibility of the coexistence of chemical chaos and hydrodynamical order in form of ordered convective motion is surprising and needs further analysis and modelling.

A first explanation of this coexistence could come from the decoupling of reaction kinetics, diffusion and convection within an unstirred BZ reaction, i.e. the change in relative importance of reaction kinetics, diffusion and convection throughout the evolution of the system (Marchettini et al., 2010).

It is possible to imagine that an increase in importance of convective motion could lead to a “de-synchronization” of the

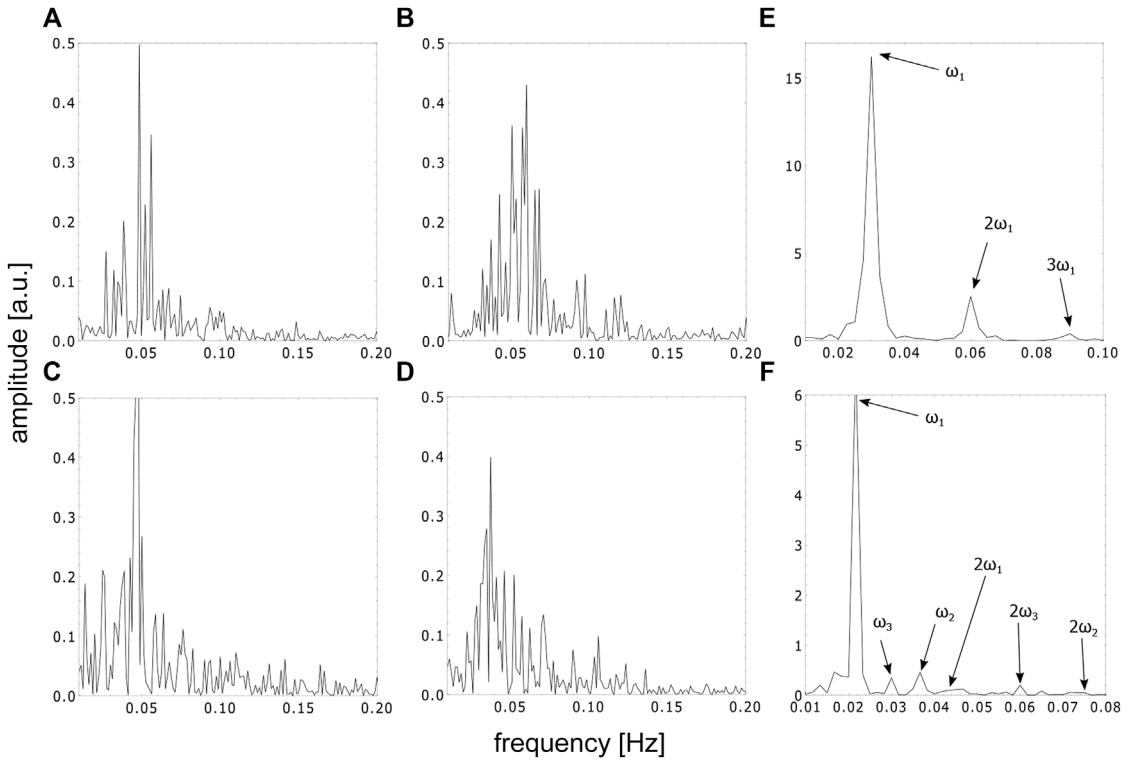

FIGURE 7 | FFT spectra of the time series in the special cuvette in different phases, **(A–D)** represent the FFT spectra of the time series in the aperiodic phase corresponding to the timeframes shown in **Figures 4A–D**, **(E)** represents the FFT spectra of the first periodic and **(F)** represents the beginning of the second periodic phase, respectively.

locally in-phase oscillations of the bulk phase. In other words, the relative increase of convection might lead to a mixing of the bulk solution and could therefore increase already existing small gradients in the concentration of the reactants of the system, leading to small "patches" in the solution that change color at different times in an asynchronous way. This relative increase of hydrodynamical effects over chemical dynamics in the chaotic phase is also confirmed in our experiments by the fact that the observed magnitude of the convection velocity is about 30 times faster than the velocity by which the color changes. This is also the reason why the convections becomes visible to the eye. The transition back to periodicity occurs when the hydrodynamical effects become again less important in respect to the chemical kinetics and diffusion.

Apart from the observations described above, we also discovered an interesting phenomenon. There are indications that the chaotic phase lasts longer when clear convection cells are visible. This would mean that the transition back to periodicity is accompanied by the decrease of hydrodynamical order.

To better understand the complex dynamics happening in the system, we investigated the problem also theoretically. By combining the classical equation for reaction and diffusion with the Navier-Stokes equation in a Boussinesq approximation, we developed a simple model. Within this model it was possible to qualitatively confirm the experimental observed behavior.

THEORETICAL MODEL

In order to describe mathematically the above presented phenomena, we took into account the main processes which occur in the reaction cuvette. Firstly, we must consider the chemical reactions leading to localized inhomogeneities of the concentrations and the density. As a consequence, two other effects take place, namely the diffusion and convection of the liquid. In this model we neglect both the surface tension and the evaporation at the free upper surface of the liquid. The three processes taken into consideration are described by combining the classical differential equations for diffusion and reaction kinetics and the Navier-Stokes equation in a Boussinesq approximation (Glansdorf and Prigogine, 1971; Landau and Lifshitz, 2007) which are given by.

$$\frac{\partial c_i}{\partial t} + \left(\vec{u}\,\nabla\right)c_i = D_i\,\Delta c_i + f_i\,(c), \tag{1a}$$

$$\frac{\partial \vec{\Omega}}{\partial t} + \left(\vec{u}\,\nabla\right)\vec{\Omega} = \nu\Delta\vec{\Omega} + \left(\vec{\Omega}\,\nabla\right)\vec{u} - \vec{\Omega}\left(\nabla\,\vec{u}\right) - \nabla\times\left(\frac{\nabla P}{\rho}\right). \tag{1b}$$

Here, c_i are the concentrations of the representative reactants, $c_1 = [HBrO_2]$, $c_2 = [Fe^{3+}]$ and $c_3 = [BrO_3^-]$, with the corresponding chemical reactions rates $f_i(c)$ which are given by.

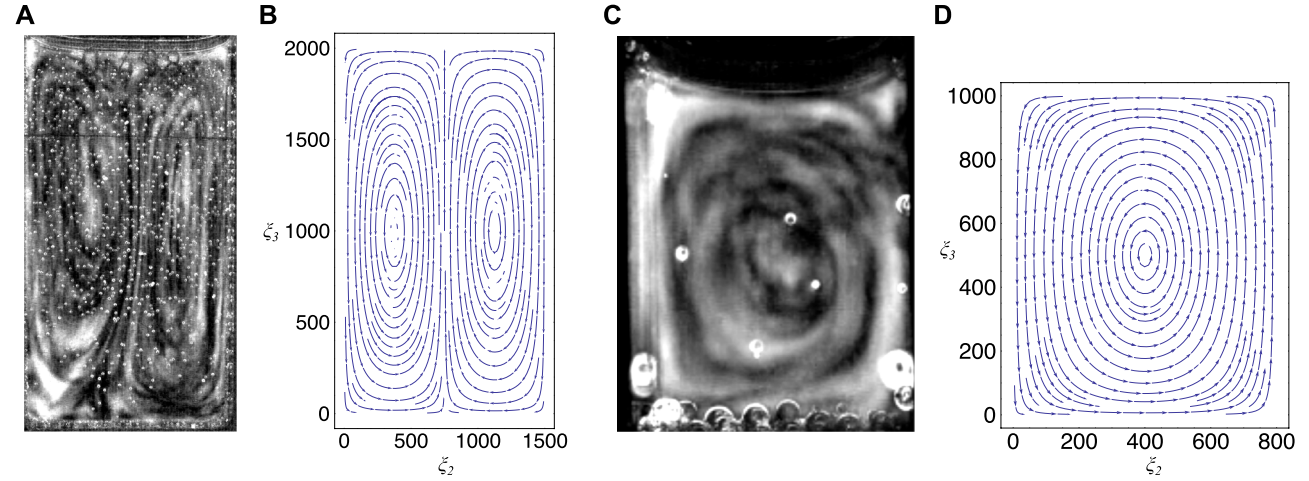

FIGURE 8 | Comparison between experiment and theory, **(A)** shows the convection cells developed in a special cuvette in the chaotic phase (see also **Figure 2A**), **(B)** shows a stream plot that indicates the field lines of the velocity field given in **formula (3)** by using the values given in the text, **(C)** shows the convection cells developed in a partly filled standard cuvette (see also **Figure 6D**), **(D)** shows a stream plot that indicates the field lines of the velocity field given by the three-dimensional extension of the model (for details, see text).

$$f_1(c_1, c_2, c_3) = \frac{1}{\epsilon}\left(\frac{qc_3 - c_1}{qc_3 + c_1} f\, c_2 + c_1 c_3 - c_1^2\right), \tag{2a}$$

$$f_2(c_1, c_2, c_3) = c_3\, c_1 - c_2, \tag{2b}$$

$$f_3(c_1, c_2, c_3) = c_1\left(\frac{1}{2}c_1 - c_3\right) - \frac{q\, f\, c_2\, c_3}{c_1 + qc_3}. \tag{2c}$$

Eq. 2 are derived from the adapted Oregonator equations (Marchettini et al., 2010) where ϵ, q and f are kinetic parameters. Furthermore, $\vec{u}$ and $\vec{\Omega} = \nabla\times\vec{u}$ represent, respectively, the fluid velocity and its vorticity, whereas P and ρ are, respectively, the pressure and the density of the bulk. Because of the incompressibility of the bulk, the term $\nabla\vec{u}$ vanishes in **Eq. 1b**. The estimation of the Reynolds number, with respect to the whole cuvette, is about 5.52. Although this value is bigger than 1, it is much smaller than the typical values (of the order of 10^7). Consequently, in a first approximation it is reasonable to neglect the nonlinear term in $\vec{u}$ in the Navier-Stokes **Eq. 1b** in order to simplify the equation. Furthermore the Boussinesq approximation (adapted for the concentration instead of the temperature (Marchettini et al., 2010)) was applied and a linear analysis around the steady state was performed (for details, see **Supplementary Material S1**). We obtained an expression for the velocity field for the lowest modes given by

$$(u_2, u_3) = \pi\chi\left(\frac{1}{b}\sin\left(\frac{2\pi\xi_2}{a}\right)\cos\left(\frac{\pi\xi_3}{b}\right), -\frac{2}{a}\cos\left(\frac{2\pi\xi_2}{a}\right)\sin\left(\frac{\pi\xi_3}{b}\right)\right) \tag{3}$$

where u_2 and u_3, ξ_2 and ξ_3 are the dimensionless y- and z-component of the velocity field as well as the dimensionless y- and the z-coordinate, respectively. a and b in this formula represent the dimensions of the liquid in the cuvette. The function χ is independent of the dimensionless coordinates. We also obtained an algebraic relation between reaction related parameters and those related to the hydrodynamics given by

$$\frac{c_3^*}{\epsilon} = \pi^2\frac{1 + \delta_2\pi^2\left(\frac{4n^2}{a^2} + \frac{m^2}{b^2}\right)}{1 + f + \delta_2\pi^2\left(\frac{4n^2}{a^2} + \frac{m^2}{b^2}\right)}\left(\frac{4n^2}{a^2} + \frac{m^2}{b^2}\right), \tag{4}$$

where c_3^* and δ_2 are, respectively, the steady state approximation of the concentration of $[BrO_3^-]$ and the dimensionless diffusion coefficient of ferriin. n and m are the modes of the harmonic functions of the velocity field.

The foregoing expression enables us to qualitatively compare the hydrodynamic chaos with the chemical order. The smaller the numbers n and m are, the clearer is the structure of the convection pattern and the more ordered is the flow. The variation interval of c_3^* is strongly affected by **formula (4)**. The value of c_3^* can be indirectly calculated relating to the original Oregonator model and gives the range

$$c_3^* \in \left(2\times10^{-4}, 1.0355\right) \tag{5}$$

for the appearance of oscillations (using $f \in (0.5, 2.4)$ as found by Scott (Scott, 1993)). The threshold value found by Marchettini et al. (Marchettini et al., 2010) for the concentration $\overline{c_3}$ is $\overline{c_3} \approx 0.95$ and thus is comparable to what we found in this study (for details, see **Supplementary Material S1**).

In our case, for $n = m = 1$ (hydrodynamic order) and for $a = 1500$, $b = 2000$ and $\delta_2 = 0.558$, $c_3^* \in (6\times10^{-8}, 1.23\times10^{-7})$, thus outside of the chemical order. By increasing the values of n and m, i.e. increasing the hydrodynamic disorder, the value of c_3^* moves within the range of chemical order. For $n = 100$ and $m = 1$ this is already the case, $c_3^* \in (5.6\times10^{-4}, 1.22\times10^{-3})$. These results prompt qualitatively that the hydrodynamic order is indeed connected to chemical chaos, as seen from the experimental results. **Figure 8** compares the real dynamics in the special cuvette with the velocity

field calculated according to the obtained **formula (3)** using the above initially mentioned values for n, m, a, b and δ_2. We stress the fact that **formula (3)** and its implications occur only within a 2-dimensional model, applicable only for the slim special cuvette.

To model the dynamics in the standard cuvette we extended the procedure to the three-dimensional case. This case is partially different from the two-dimensional one, even though the results are only slightly different from **formula 3** and **formula 4**. In this three-dimensional case a single convection cell, as observed experimentally, may be obtained using the lowest modes in the slightly different equation for the velocity field (**Figure 8D** shows the velocity field for this case by using the dimensions $a = 800$ and $b = 1000$ that correspond to a partly filled standard cuvette) (for details, see **Supplementary Material S1**). Within this simple model the number of convection cells depend only on the boundary conditions chosen and not on the ratio between the width and the height of the cuvette as one would expect from a more sophisticated model.

CONCLUSION

The behavior of an unstirred BZ reaction in a batch configuration is more complex than it is in constantly stirred tank reactors or in Petri dishes. This is due to the complex coupling between reaction kinetics, convection and diffusion. In both cases either convection and diffusion or convection only is suppressed. Normally, a BZ reaction in a batch configuration is investigated in a spectrophotometer, where possible inhomogeneities or convective motions in the bulk solution cannot be seen.

In this work we focused on these inhomogeneities and we investigated the convective motion created in the chaotic phase in an unstirred BZ reaction in a cuvette configuration. The ordered convective cells observed in specific cuvette geometries were investigated in respect to the local chemical kinetics in the reaction solution. Surprisingly, we discovered that this ordered hydrodynamical structures are correlated to the chaotic nature of the local chemical kinetics. As a first explanation of this correlation, we assume that the formed convection cells lead to a "de-synchronization" of the previously homogeneous color oscillations moving the system into a chaotic phase. With the simple mathematical model presented here we were able to indirectly confirm the same qualitative results, i.e. that a connection between chemical chaos and hydrodynamical order in such systems exists.

DATA AVAILABILITY STATEMENT

The original contributions presented in the study are included in the article/**Supplementary Material**, further inquiries can be directed to the corresponding author.

AUTHOR CONTRIBUTIONS

FW has conducted the experiments and performed the data analysis and the data treatment. MR and GA have elaborated the analytical model. The drafts of this manuscript were written by FW and reviewed by MR and GA. All authors have agreed with the published version of the manuscript.

ACKNOWLEDGMENTS

We thank Bao Tang who, by asking an important question on the solution dynamics in the chaotic phase, inspired us to do this very specific research. We thank also Véronique Pimienta for helpful comments and Jessica Franco for her support. We thank Michela DiLullo for the review of the English text and Cristina Huamán for typing the second part of the supplementary material. We wish to express special thanks to our reviewers for their valuable comments and efforts towards improving our article.

SUPPLEMENTARY MATERIAL

The Supplementary Material for this article can be found online at: https://www.frontiersin.org/articles/10.3389/fchem.2022.881691/full#supplementary-material

Supplementary Material S1 | Details on the data treatment and analysis and the theoretical model used in the main article.

Supplementary Material S2 | Video of the full dynamics of an unstirred ferroin-catalyzed BZ reaction in a special cuvette (200x faster than real time).

REFERENCES

Adamatzky, A. (2019). A Brief History of Liquid Computers. *Phil. Trans. R. Soc. B* 374, 20180372. doi:10.1098/rstb.2018.0372

Adamatzky, A., and Costello, B. d. L. (2007). Binary Collisions Between Wave-Fragments in a Sub-Excitable Belousov-Zhabotinsky Medium. *Chaos, Solit. Fractals* 34, 307–315. doi:10.1016/j.chaos.2006.03.095

Antoine, C., Irvoas, J., Schwarzenberger, K., Eckert, K., Wodlei, F., and Pimienta, V. (2016). Self-Pinning on a Liquid Surface. *J. Phys. Chem. Lett.* 7, 520–524. doi:10.1021/acs.jpclett.5b02724

Belousov, B. P. (1959). A Periodically Acting Reaction and its Mechanism (In Russian). *Collection of Articles on Radiation Medicine. Moscow: Medgiz* 1, 145.

Budroni, M. A., Calabrese, I., Miele, Y., Rustici, M., Marchettini, N., and Rossi, F. (2017). Control of Chemical Chaos Through Medium Viscosity in a Batch Ferroin-Catalysed Belousov-Zhabotinsky Reaction. *Phys. Chem. Chem. Phys.* 19, 32235–32241. doi:10.1039/c7cp06601e

B. Chance, A. K. Gosh, and E. K. Pye (Editors) (1973). *Biological and Biochemical Oscillators* (Cambridge, MA: Academic Press).

Deb, D., Kuksenok, O., Dayal, P., and Balazs, A. C. (2014). Forming Self-Rotating Pinwheels From Assemblies of Oscillating Polymer Gels. *Mat. Horiz.* 1, 125–132. doi:10.1039/c3mh00083d

Dueñas-Díez, M., and Pérez-Mercader, J. (2021). Native Chemical Computation. A Generic Application of Oscillating Chemistry Illustrated with the Belousov-Zhabotinsky Reaction. A Review. *Front. Chem.* 9, 611120. doi:10.3389/fchem.2021.611120

Epstein, I. R., and Pojman, J. A. (1998). *An Introduction to Nonlinear Chemical Dynamics: Oscillations, Waves, Patterns, and Chaos*. Oxford: Oxford University Press.

Field, R. J., Koros, E., and Noyes, R. M. (1972). Oscillations in Chemical Systems. II. Thorough Analysis of Temporal Oscillation in the Bromate-Cerium-Malonic Acid System. *J. Am. Chem. Soc.* 94, 8649–8664. doi:10.1021/ja00780a001

Field, R. J., and Noyes, R. M. (1974). Oscillations in Chemical Systems. IV. Limit Cycle Behavior in a Model of a Real Chemical Reaction. *J. Chem. Phys.* 60, 1877–1884. doi:10.1063/1.1681288

Field, R. J., and Noyes, R. M. (1974). Oscillations in Chemical Systems. V. Quantitative Explanation of Band Migration in the Belousov-Zhabotinskii Reaction. *J. Am. Chem. Soc.* 96, 2001–2006. doi:10.1021/ja00814a003

Gentili, P. L., and Micheau, J. C. (2019). Light and Chemical Oscillations: Review and Perspectives. *J. Photochem. Photobiol. C Photochem. Rev.* 2019, 100321.

Gentili, P. L., Dolnik, M., and Epstein, I. R. (2014). "Photochemical Oscillator": Colored Hydrodynamic Oscillations and Waves in a Photochromic System. *J. Phys. Chem. C* 118, 598–608. doi:10.1021/jp407393h

Gentili, P. L., Giubila, M. S., Germani, R., Romani, A., Nicoziani, A., Spalletti, A., et al. (2017). Optical Communication Among Oscillatory Reactions and Photo-Excitable Systems: UV and Visible Radiation Can Synchronize Artificial Neuron Models. *Angew. Chem. Int. Ed.* 56, 7535–7540. doi:10.1002/anie.201702289

Glansdorf, P., and Prigogine, I. (1971). *Thermodynamic Theory of Structure, Stability and Fluctuations*. Hoboken, NJ: Wiley-Interscience.

Goldbeter, A. (1996). *Biochemical Oscillations and Cellular Rhythms*. Cambridge: Cambridge University Press.

Gyorgyi, L., Field, R. J., Noszticzius, Z., McCormick, W. D., and Swinney, H. L. (1992). Confirmation of High Flow Rate Chaos in the Belousov-Zhabotinskii Reaction. *J. Phys. Chem.* 96, 1228–1233. doi:10.1021/j100182a038

Kantz, H., and Schreiber, T. (2004). *Nonlinear Time Series Analysis*. Cambridge: Cambridge University Press.

Korzukhin, M. D., and Zhabotinsky, A. M. (1967). "Mathematical Modeling of Chemical and Ecological Self-Oscillatory Systems" (In Russian) in *Oscillatory Processes in Biological and Chemical Systems*. Editors G. M. Frank (Moscow: Nauka).

Landau, L., and Lifshitz, E. (2007). *Lehrbuch der Theoretischen Physik, Vol. VI, Hydrodynamik*. Frankfurt, Germany: Harry Deutsch Verlag.

Loose, M., Fischer-Friedrich, E., Ries, J., Kruse, K., and Schwille, P. (2008). Spatial Regulators for Bacterial Cell Division Self-Organize into Surface Waves *In Vitro*. *Science* 320, 789–792. doi:10.1126/science.1154413

Marchettini, N., Antonio Budroni, M., Rossi, F., Masia, M., Liria Turco Liveri, M., and Rustici, M. (2010). Role of the Reagents Consumption in the Chaotic Dynamics of the Belousov-Zhabotinsky Oscillator in Closed Unstirred Reactors. *Phys. Chem. Chem. Phys.* 12, 11062–11069. doi:10.1039/c0cp00109k

Masia, M., Marchettini, N., Zambrano, V., and Rustici, M. (2001). Effect of Temperature in a Closed Unstirred Belousov-Zhabotinsky System. *Chem. Phys. Lett.* 341, 285–291. doi:10.1016/s0009-2614(01)00474-2

Newhouse, S., Ruelle, D., and Takens, F. (1978). Occurrence of Strange Axiom A Attractors Near Quasi Periodic Flows on Tm,m ≧ 3. *Commun. Math. Phys.* 64, 35–40. doi:10.1007/bf01940759

Noyes, R. M., Field, R., and Koros, E. (1972). Oscillations in Chemical Systems. I. Detailed Mechanism in a System Showing Temporal Oscillations. *J. Am. Chem. Soc.* 94, 1394–1395. doi:10.1021/ja00759a080

Onel, L., Wittmann, M., Pelle, K., Noszticzius, Z., and Sciascia, L. (2007). The Source of the Carbon Monoxide in the Classical Belousov–Zhabotinsky Reaction. *J. Phys. Chem. A* 111, 7805–7812. doi:10.1021/jp073512+

Onuma, H., Okubo, A., Yokokawa, M., Endo, M., Kurihashi, A., and Sawahata, H. (2011). Rebirth of a Dead Belousov-Zhabotinsky Oscillator. *J. Phys. Chem. A* 115, 14137–14142. doi:10.1021/jp200103s

Pimienta, V., Lavabre, D., Buhse, T., and Micheau, J.-C. (2004). Correlation Between Electric Potential and Interfacial Tension Oscillations in a Water–Oil–Water System. *J. Phys. Chem. B* 108, 7331–7336. doi:10.1021/jp0374859

Rongy, L., and De Wit, A. (2007). Marangoni Flow Around Chemical Fronts Traveling in Thin Solution Layers: Influence of the Liquid Depth. *J. Eng. Math.* 59, 221–227. doi:10.1007/s10665-007-9144-8

Rossi, F., Budroni, M. A., Marchettini, N., and Carballido-Landeira, J. (2012). Segmented Waves in a Reaction-Diffusion-Convection System. *Chaos* 22, 037109. doi:10.1063/1.4752194

Rossi, F., Budroni, M. A., Marchettini, N., Cutietta, L., Rustici, M., and Liveri, M. L. T. (2009). Chaotic Dynamics in an Unstirred Ferroin Catalyzed Belousov-Zhabotinsky Reaction. *Chem. Phys. Lett.* 480, 322–326. doi:10.1016/j.cplett.2009.09.018

Rustici, M., Branca, M., Brunetti, A., Caravati, C., and Marchettini, N. (1998). Inverse Ruelle-Takens-Newhouse Scenario in a Closed Unstirred Cerium-Catalysed Belousov-Zhabotinsky System. *Chem. Phys. Lett.* 293, 145–151. doi:10.1016/s0009-2614(98)00781-7

Rustici, M., Branca, M., Caravati, C., and Marchettini, N. (1996). Evidence of a Chaotic Transient in a Closed Unstirred Cerium Catalyzed Belousov-Zhabotinsky System. *Chem. Phys. Lett.* 263, 429–434. doi:10.1016/s0009-2614(96)01249-3

Scott, S. K. (1993). *Chemical Chaos*. Oxford: Clarendon Press.

Tyson, J. J. (1994). "What Everyone Should Know About the Belousov-Zhabotinsky Reaction," in *Frontiers in Mathematical Biology*. Editor S. A. Levin (Berlin, Heidelberg: Springer Berlin Heidelberg), 569–587. doi:10.1007/978-3-642-50124-1_33

Wodlei, F., and Hristea, M. R. (2013). Effect of Limited Stirring on the Belousov Zhabotinsky Reaction. *Proc. Eur. Conf. Complex Syst.* 2012, 29–34. doi:10.1007/978-3-319-00395-5_5

Wodlei, F., Sebilleau, J., Magnaudet, J., and Pimienta, V. (2018). Marangoni-Driven Flower-Like Patterning of an Evaporating Drop Spreading on a Liquid Substrate. *Nat. Commun.* 9, 820. doi:10.1038/s41467-018-03201-3

Zaikin, A. N., and Zhabotinsky, A. M. (1970). Concentration Wave Propagation in Two-Dimensional Liquid-Phase Self-Oscillating System. *Nature* 225, 535–537. doi:10.1038/225535b0

Zhabotinsky, A. M. (1964). Periodic Progress of Oxidation of Malonic Acid in Solution (Investigation of the Kinetics of the Reaction of Belousov) (In Russian). *Biophysics* 9, 306–311.

Conflict of Interest: The authors declare that the research was conducted in the absence of any commercial or financial relationships that could be construed as a potential conflict of interest.

The handling editor FR declared a past co-authorship with the author FW.

frontiers | Frontiers in Chemistry

ORIGINAL RESEARCH
published: 05 August 2022
doi: 10.3389/fchem.2022.915217

Controlling Nonlinear Dynamics of Milling Bodies in Mechanochemical Devices Driven by Pendular Forcing

A. Polo[1], *M. Carta*[2], *F. Delogu*[2], *M. Rustici*[1] *and M. A. Budroni*[1]*

[1]*Dipartimento di Chimica e Farmacia, Università Degli Studi di Sassari, Sassari, Italy,* [2]*Dipartimento di Ingegneria Meccanica, Chimica, e Dei Materiali, Università Degli Studi di Cagliari, Cagliari, Italy*

Understanding the dynamics of milling bodies is key to optimize the mixing and the transfer of mechanical energy in mechanochemical processing. In this work, we present a comparative study of mechanochemical reactors driven by harmonic pendular forcing and characterized by different geometries of the lateral borders. We show that the shape of the reactor bases, either flat or curved, along with the size of the milling body and the elasticity of the collisions, represents relevant parameters that govern the dynamical regimes within the system and can control the transition from periodic to chaotic behaviors. We single out possible criteria to preserve target dynamical scenarios when the size of the milling body is changed, by adapting the relative extent of the spatial domain. This allows us to modulate the average energy of the collisions while maintaining the same dynamics and paves the way for a unifying framework to control the dynamical response in different experimental conditions. We finally explore the dynamical and energetic impact of an increasingly asymmetric mechanical force.

Keywords: transition to chaos, forced-damped oscillators, modeling of mechanochemical systems, mechanochemistry, ball-mill grinding

OPEN ACCESS

Edited by:
Rabih Sultan,
American University of Beirut, Lebanon

Reviewed by:
Angelo Facchini,
IMT School for Advanced Studies Lucca, Italy
Marco Masia,
University of Vienna, Austria

***Correspondence:**
M. A. Budroni
mabudroni@uniss.it

Specialty section:
This article was submitted to Physical Chemistry and Chemical Physics, a section of the journal Frontiers in Chemistry

Received: *07 April 2022*
Accepted: *20 June 2022*
Published: *05 August 2022*

Citation:
Polo A, Carta M, Delogu F, Rustici M and Budroni MA (2022) Controlling Nonlinear Dynamics of Milling Bodies in Mechanochemical Devices Driven by Pendular Forcing. Front. Chem. 10:915217. doi: 10.3389/fchem.2022.915217

1 INTRODUCTION

Mechanochemistry is emerging with increasing strength as a powerful approach to the synthesis of fine chemical compounds (Friscic, 2012; James et al., 2012; Balaz et al., 2013; Boldyreva, 2013; Wang, 2013; Rightmire and Hanusa, 2016; Do and Friščić, 2017; Tan and García, 2019; Friscic et al., 2020; Porcheddu et al., 2020). In contrast with conventional chemistry in solution, which makes use of heat and light to activate and drive the chemical reaction, mechanochemical transformations are caused by the application of mechanical forces to solid phases (Thiessen et al., 1967; Butyagin, 1971; Thiessen, 1979; Boldyrev, 1983; Avvakumov, 1986; Heinicke, 1986; Michalchuck et al., 2020).

In light of the common use of manual and mechanical grinding throughout human history, and starting from the XIX century in particular (Takacs, 2013), the mechanical activation of chemistry does not represent a novelty in itself. However, the possibility to carry out chemical reactions under solventless conditions, or with a significant reduction of solvent phase, is extremely appealing now that attention to green chemistry issues is unavoidable and impossible to procrastinate (Galant et al., 2022). The evidence that mechanical processing can also open synthetic routes to chemicals and materials that cannot be prepared by more conventional

methods further explains why mechanochemistry is currently experiencing vigorous growth (Gomollon-Bel, 2019;[1]).

Amongst the mechanical processing methods, ball milling is a popular choice. Contrary to the mechanochemistry of individual molecules, which requires extremely refined manipulation methods (Boldyreva, 2013), ball milling is an easy method for mechanical processing of granular materials (Thiessen et al., 1967; Tan and García, 2019; Friscic et al., 2020; Porcheddu et al., 2020). Widely available in a variety of sizes and designs, ball milling devices are equipped with one or more reactors that contain one or more balls. The balls collide with each other and with the reactor walls as the vessel is shaken in mono-axial, pendular or rotational modes, crushing and deforming at relatively high strain rates the powder particles trapped between the colliding surfaces (Tan and García, 2019; Friscic et al., 2020). The local non-hydrostatic mechanical stresses generated during the impact can finally result in the activation of chemical reactions depending on the intensity of mechanical forces and the physical and chemical properties of the processed material (Thiessen et al., 1967; Tan and García, 2019; Friscic et al., 2020; Porcheddu et al., 2020).

Despite the interest attracted by mechanical processing in the past 50 years, the understanding of how the mechanical energy translates into chemical reactivity is still unsatisfactory. Accordingly, new theoretical tools to understand how to design, control, and predict the development of these processes are needed (Carta et al., 2020; Carta et al., 2021).

As the activation and the progress of a given mechanochemical transformation crucially depend on the conditions experienced by powder particles at collisions and by their effective mixing, one informative approach relies on the study of the dynamics of the milling bodies responsible for dragging the powder and driving collisions.

In the past, various attempts have been made in this direction for the most widespread ball milling devices (Burgio et al., 1991; Abdellaoui and Gaffet, 1995; Courtney, 1996; Magini et al., 1996; Feng et al., 2004; Cleary et al., 2006; Sinnott et al., 2006; Boschetto et al., 2013; Broseghini et al., 2016; Zhao and Shaw, 2017). The dynamics of milling balls in the SPEX Mixer/Mill 8,000 device have also been studied in detail within a deterministic framework (Watanabe et al., 1995; Delogu et al., 1998; Concas et al., 2006). In agreement with experimental results, numerical simulations showed how balls' trajectories and collisions at the reactor walls are sensitive to the collision elasticity degree (Rustici et al., 1996; Delogu et al., 1998; Delogu et al., 2000), which can control the transition from periodic to chaotic behaviors in the temporal displacement of the ball (Caravati et al., 1999; Manai et al., 2002). From the spatial viewpoint, these chaotic regimes showed a fingerprinting multifractal topology in the location and recurrence of collisions on the reactor walls (Budroni et al., 2014; Budroni et al., 2017).

The onset of chaotic behaviors can greatly favor an effective mixing of the granular medium inside the medium (King, 1998; Aref et al., 2017), and it is, indeed, useful for isolating parametric conditions where these regimes can occur. In this context, we propose a comparative study and classification of mill body dynamics inside reactors driven by harmonic pendular motion, which represents one class of commonly used mechanochemical devices. We focus on two different geometries of reactors characterized either by flat or curved lateral borders (the latter system has never been explored in this perspective). Moreover, two possible designs of the reactors are considered, either with the mechanical arm driving the periodic motion allocated at the center of the reactor (symmetric forcing) or at different distances from it (asymmetric forcing). Symmetric and asymmetric forcing can induce different transfer and dissipation of the energy within the reactor as well as impact spatio-temporal dynamics of the milling body, which has never been deepened. We first explore the onset of dynamical scenarios of the two geometries driven by a symmetric forcing in response to the variation of the collision elasticity and the milling body size. The latter critically impacts mechanochemical processing and is mostly chosen in experiments by following empirical methods and trial-error procedures, hence without any theoretical reference. On the basis of these first results, we check the existence of a guiding criterion to predict the typology of dynamical regimes on the basis of the relative size of the reactor and the milling body. This represents a contribution on the way towards a unifying parametrization of mechanochemical devices, which could help the reproducibility and the scaling-up of the results of mechanical processing, which are carried out in a plethora of different experimental conditions (Gil-González et al., 2021). We finally investigate systematically the effect of an asymmetric forcing on the milling body dynamics.

2 MECHANOCHEMICAL DEVICES DRIVEN BY PENDULAR FORCING: MODELS

We analyzed systems where the mechanical forcing is transferred to a milling body via a harmonic pendular motion of the reactor. Since in a previous paper we verified that the main dynamical features of these milling body dynamics are preserved in a 2-dimensional description, we focused our attention on this reduced framework. We considered the most common geometries for these classes of devices, as illustrated schematically in **Figure 1**. The first presents a rectangular shape with flat bases, defining a spatial domain $\Omega_f = w_f \times 2h$, where w_f and h are the reactor width and semi-height, respectively. The other geometry is characterized by semicircular lateral borders (bases) of radius h, such that the related spatial domain writes $\Omega_c = l_c \times 2h + \pi h^2$. The milling disc has a radius r_d. The reactor is driven by the displacement of a mechanical arm of length R, which can be mounted at a variable distance from the reactor center as controlled by parameters l_l and l_r, giving the right and left border distance from the reactor center, respectively. In the flat-base model, the system width is thus $w_f = l_l + l_r$, while $w_c = l_l + l_r + 2h$ holds for the curved-base case (i.e., $l_c = l_l + l_f$). When $l_l \neq l_r$ the milling disc experiences an asymmetric force.

[1]https://www.cost.eu/stories/mechanochemistry-pushes-more-sustainable-processes.

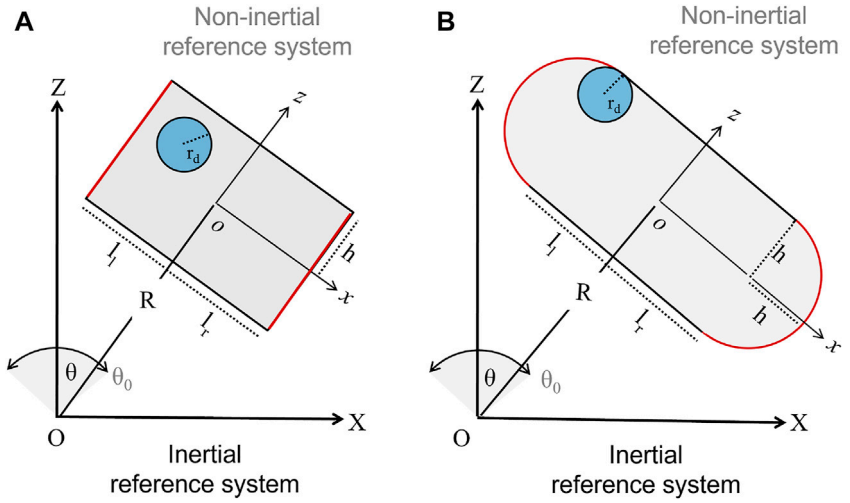

FIGURE 1 | Sketches of two 2-dimensional ball-milling devices driven by harmonic pendular motion (X, Z) and (x, z) represent the inertial and non-inertial reference frames, respectively. Panel **(A)** illustrates a reactor with flat bases (in red) of width $l_f = l_l + l_r$ and height $2h$, sustained by a mechanical arm of length R. l_l and l_r regulate the distance of the arm from the reactor center, and when the left and right sides of the reactor are different, $l_l \neq l_r$, the system experiences an asymmetric forcing. The mechanical treatment is performed by a rigid disc of radius r_d. The oscillatory motion is described by the angle θ, with maximal amplitude $\theta_0 = \pi/12$, and frequency $\nu = 18$ Hz. Panel **(B)** shows a reactor characterized by curved bases of curvature radius h, width $l_c = l_l + l_r + 2h$ and height $2h$.

The periodic angular motion of the reactor on the vertical plane follows $\theta = \theta_0 \cos(\omega t)$, where θ_0 is the maximal angular amplitude and $\omega = 2\pi\nu$ gives the oscillation frequency. Two Cartesian reference frames can be used to reconstruct the reactor motion and the disc dynamics: the inertial system of coordinates (X, Z), which is centered at the lower end of the mechanical arm, and the non-inertial reference of coordinates (x, z), whose origin coincides with the geometrical center of the reactor, where the x axis is orthogonal to the mechanical arm. This non-inertial reference frame undergoes rigid displacement with the reactor.

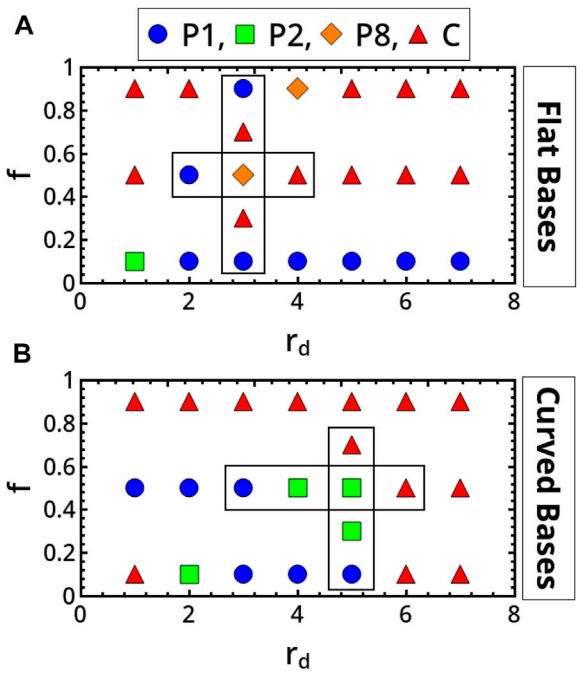

FIGURE 2 | Classification in the parameter spaces spanning the restitution coefficient, f, and the disc radius, r_d, of the main scenarios characterizing the milling body dynamics in flat-base **(A)** and curved-base **(B)** geometries. P1, P2, P8 and C identify period-1, period-2, period-8 and chaotic regimes, respectively.

The motion of each point in the system can be described and transformed from the non-inertial to the inertial coordinate system through the following systems of equations:

$$X = x\cos\theta + (z + R)\sin\theta, \tag{1}$$

$$Z = -x\sin\theta + (z + R)\cos\theta \tag{2}$$

and

$$x = X\cos\theta + Z\sin\theta, \tag{3}$$

$$z = X\sin\theta + Z\cos\theta - R. \tag{4}$$

In the absence of external forces, the disc follows a rectilinear motion started by the impact with a reactor wall.

$$X^b(t + ht) = X^b(t) + V_x^b(t)\,ht, \tag{5}$$

$$Z^b(t + ht) = Z^b(t) + V_z^b(t)\,ht, \tag{6}$$

where $\mathbf{V^b}(\mathbf{t}) = (V_x^b(t), V_z^b(t))$ is the disc velocity in the inertial reference frame at time t, which can be obtained by differentiation of **Eqs 1** and **2**, and ht is the integration time step. The integration is performed by using the Euler algorithm. At each step, the inertial reference frame coordinates of the disc $(X_b(t), Z_b(t))$ are updated by applying **Eq. 5**, and, from that, the disc coordinates in the non-inertial reference frame $(x_b(t)\ z_b(t))$ can also be calculated.

Whenever $\mathbf{x_b} = (x_b, z_b) \notin \Omega$ (i.e., the distance of the disc from the reactor walls is smaller than r_d), a collision occurs and the non-inertial component of the disc velocity normal to the impacted surface is instantaneously reversed, modulated by the restitution

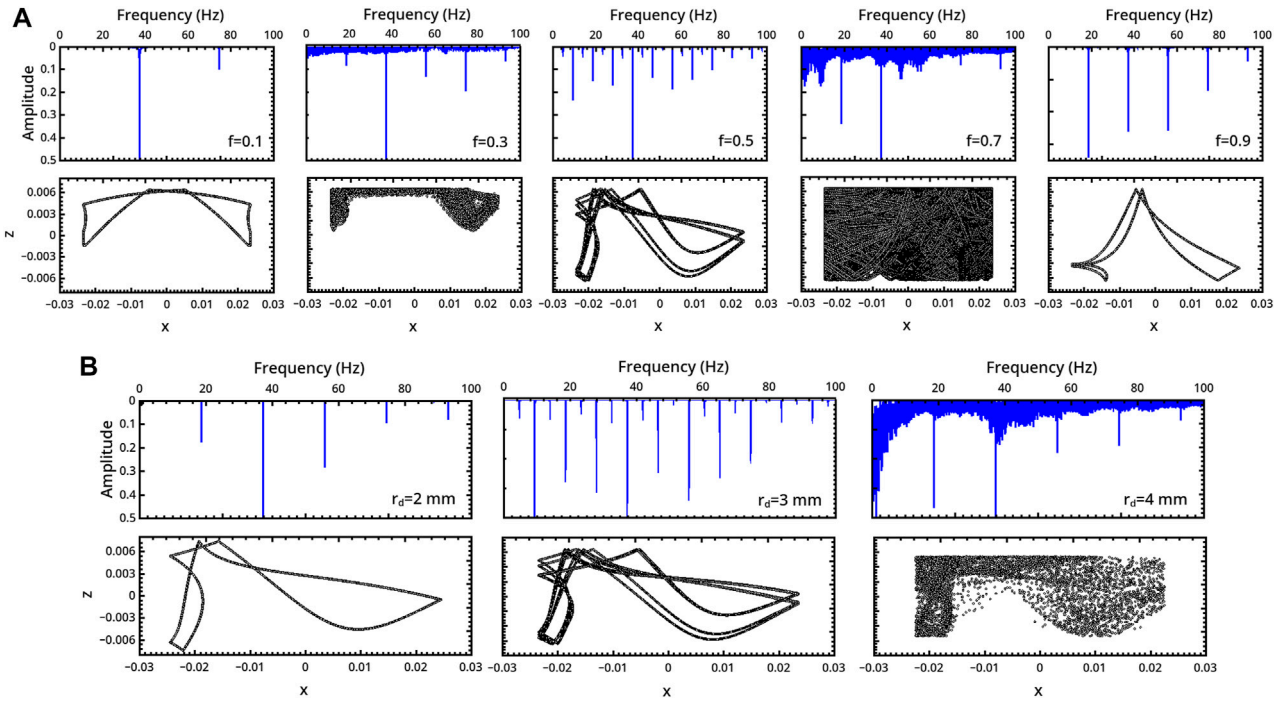

FIGURE 3 | Characterization of the milling body dynamics in a flat-base geometry as a function of **(A)** the restitution coefficient f (r_d = 3 mm) and **(B)** the milling disc radius r_d (f = 0.5). For each regime, we report the trajectory (bottom) and the FFT of the related series describing the vertical displacement of the milling disc in time (top).

coefficient *f*. *f* ranges between 0 and 1, giving the inelastic and elastic limits, respectively. This mimics the effect of the powder undergoing a transformation inside the mechanochemical device on the collision efficiency. The term "collision" here identifies any event where the milling disc is at the reactor walls, including slipping phenomena.

As a whole, the dynamics of the milling body describes a forced-damped oscillator, where the impacts with the periodically moving reactor and friction at the walls feature the forcing and the damping contributions to the disc dynamics, respectively. In a sense, our problem features a complicated variant of the classical bouncing ball system (Tufillaro and Albano, 1986).

The duration of any given collision is limited to a single time step. Coherently with this aspect, the integration time step is set smaller than 10^{-5} s (we used $ht = 10^{-7}$ s), which is also consistent with experimental data (Delogu et al., 1998) and the Hertzian theory of impacts (Love, 1944; Timoshenko and Goodier, 1970).

It is finally worth noticing that the acceleration experienced by the disc with the oscillation frequency at use is one order of magnitude larger than the gravitational acceleration, and this, together with the shortness of the disc's mean free path, allows us to consider negligible the gravitational contribution to the disc motion.

3 RESULTS AND DISCUSSION

3.1 Flat vs. Curved Bases

We first investigate the influence of the different shapes of the reactor lateral borders (either flat or curved) on the disc dynamics. To make the comparison between the two geometries as homogeneous as possible, we fixed the reactors' height to $2h$ and adapted their width in order to get the same spatial domain $\Omega_f = \Omega_c$. As a reference, we assumed the values of typical devices with semicircular bases ($w_c + 2h$ = 57 mm and h = 9.4 mm), which are smaller than common Spex-mill apparatuses characterized by flat borders and already characterized in previous work (Caravati et al., 1999; Manai et al., 2002; Budroni et al., 2014). Equivalent areas of the spatial domains Ω_f and Ω_c are thus obtained via the relation $w_f = (2l_c + \pi h)/2$.

To facilitate the comparison of the two systems, we classified the possible behaviors in the parameter spaces spanning the restitution coefficient, f, and the disc radius, r_d. From previous studies and preliminary simulations, these parameters remained the most relevant from the dynamical viewpoint, and a numerical benchmark on the effect of these parameters could be useful for practical purposes. The other parameters governing the mechanics of the system were fixed to typical values for these devices $\theta_0 = \pi/12$, ν = 18.6 Hz, R = 0.122 m. Simulations were run for 50 s and the resulting trajectories were analyzed from a dynamical viewpoint.

To get an integrated dynamical and energetic view, we also evaluated the average number of collisions on the reactor lateral borders (bases), $\langle \text{Collisions} \rangle = N_b^{(d)}/t$ (where $N_b^{(d)}$ is the number of collisions on the bases and t the total simulation time) as well as the mean energy, $\langle E \rangle_{rel}$, averaged over the total number of collisions, $N_t^{(d)}$.

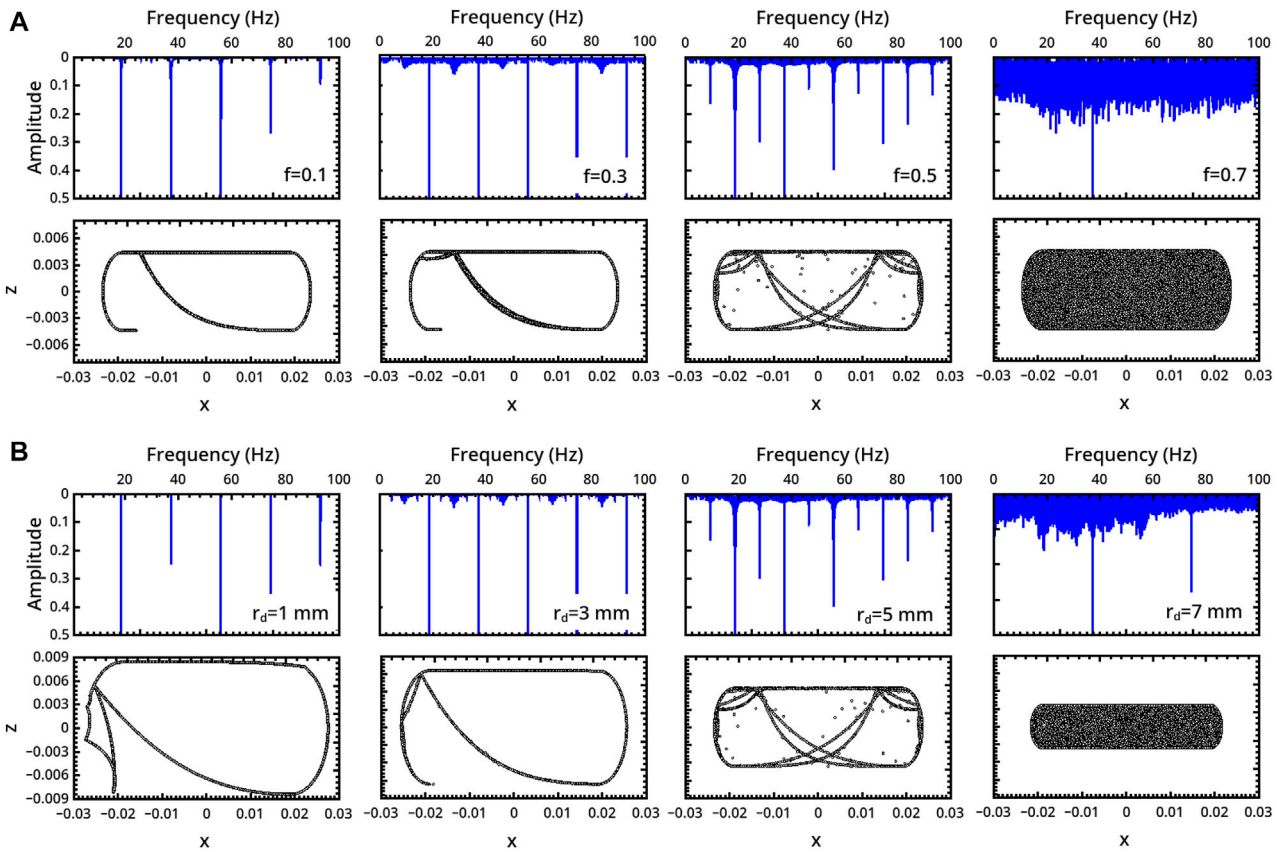

FIGURE 4 | Characterization of the milling body dynamics in a curved-base geometry as a function of **(A)** the restitution coefficient f (r_d = 5 mm) and **(B)** the milling disc radius r_d (f = 0.5). For each regime, we report the trajectory (bottom) and the FFT of the time series describing the vertical displacement of the milling disc (top).

$$\langle E \rangle = \frac{m_d}{2N_t^{(d)}} \sum_{i=1}^{N_t^{(d)}} \left(v_i^{(d)}\right)^2, \tag{7}$$

where m_d is the disc mass and $v_i^{(d)}$ is the related velocity at the ith collision. In our numerical framework, the disc is a material point with an effective size given by r_d, which can influence the dynamics and velocity profile of the disc, while its mass is not explicitly controlled by a parameter. However, we can define the mean collision energy in relation to that of a reference disc with radius r_f (we used r_f = 1 mm) and the same density, ρ (such that $m_d = \pi\rho r_d^2$ and $m_f = \pi\rho r_f^2$):

$$\langle E \rangle_{rel} = \frac{\langle E \rangle_d}{\langle E \rangle_f} = \frac{N_t^{(f)} r_d^2}{N_t^{(d)} r_f^2} \frac{\sum_{i=1}^{N_t} \left(v_i^{(d)}\right)^2}{\sum_{i=1}^{N_t} \left(v_i^{(f)}\right)^2}, \tag{8}$$

where $N_t^{(f)}$ and $v_i^{(f)}$ are the total number of collisions and the ith collision velocity of the reference disc, respectively. Each simulation was started by locating the milling disc in the center of the non-inertial reference system. Changes in the initial position of the disc do not affect the asymptotic dynamical regime unless the system is marginally close to chaotic conditions.

Figure 2 gives a global overview of the typical scenarios pertaining to the two systems, which clearly differ both in qualitative and quantitative terms.

Periodic regimes dominate the dynamics of the reactor with flat bases in inelastic conditions (low f). For this geometry, transitions from periodic to aperiodic behaviors can be observed by increasing the restitution coefficient (see for example, the back and forth scenario framed in **Figure 2A** for r_d = 3 mm). This route to chaos (and back to regular periodicity) is illustrated in **Figure 3**, where we report the trajectories of the disc in the reactor along with the Fast Fourier Transforms (FFTs) of the vertical displacement of the disc in time ([2]). The transition is characterized by the alternation of periodic and aperiodic regimes which occurs in narrow windows of the control parameters (insignificant changes from the experimental viewpoint). Although a period-doubling scenario seems to regulate the transition, it was difficult to refine the whole sequence of bifurcations. Coarsely, by increasing f from 0.1 to

[2]While the horizontal component of the disc displacement is essentially Imposed by the working frequency of the devise, the vertical Displacement confers emergent features to the global dynamics (see **Figure 1** of the **Supplementary Material**).

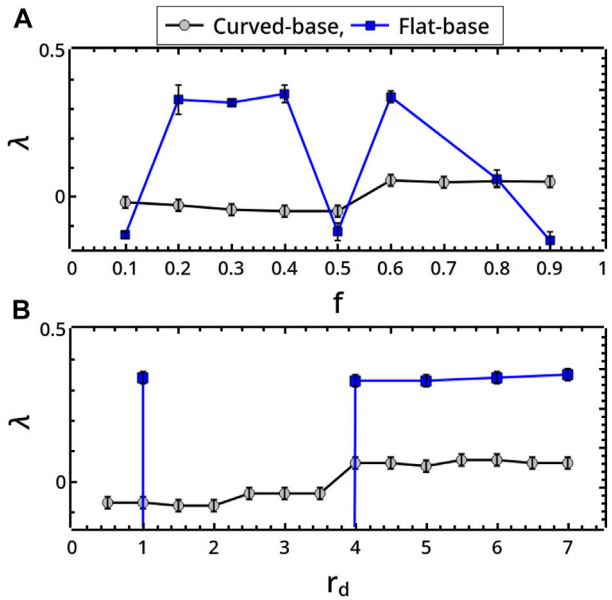

FIGURE 5 | Exponential divergence, λ, characterizing milling body trajectories in the flat- and curved-base geometries when changing **(A)** the restitution coefficient f (r_d = 5 mm) and **(B)** the milling disc radius r_d (f = 0.5). λ was obtained through the formula $\|\delta(t)\| \simeq \|\delta_0\| e^{\lambda t}$, by calculating the distance $\|\delta(t)\|$ at any time t between two trajectories starting from infinitesimally distant conditions $\|\delta_0\| \to 0$ (here $\|\delta_0\| \sim 10^{-7}$ mm) for $t \gg 1$ (here after 50 s) (Kantz and Schreiber, 1997).

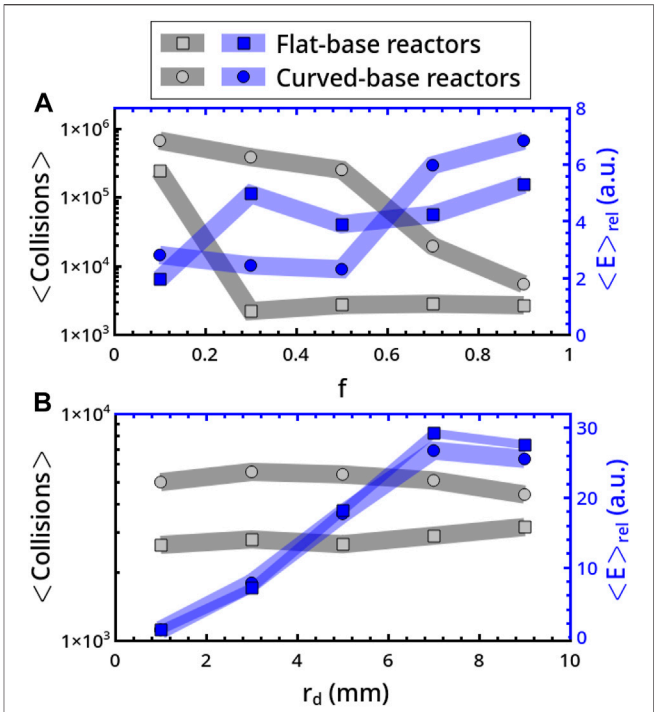

FIGURE 6 | Analysis of the average number of collisions on the reactor bases, ⟨Collisions⟩ (in gray-black), and relative energy per collision, $\langle E \rangle_{rel}$ (in blue). $\langle E \rangle_{rel}$ was evaluated in relation to a disc of radius rd = 5 mm, to which we attributed unitary mass. ⟨Collisions⟩ and $\langle E \rangle_{rel}$ are characterized as a function of f (r_d = 3 mm) in panel A and r_d (f = 0.9) in panel B. Squares and circles refer to flat- and curved-base reactors, respectively.

0.3, the system switches from a period-1 (P1) behavior (characterized by a main frequency twice the working frequency of the device) to a chaotic regime. The last regime shows the fingerprinting broad-band FFT profile of chaotic scenarios, with the same dominant frequency as the preceding periodic regime. We further analyzed the aperiodic dynamics by calculating the progressive divergence of two disc trajectories starting from infinitesimally distant initial positions, $\|\delta_0\| \sim 10^{-7}$ mm, with the formula $\|\delta(t)\| \simeq \|\delta_0\| e^{\lambda t}$ for $t \gg 1$. Although not calculated from the true phase-space, λ can give a rough estimation of the maximal Lyapunov exponent of the system (Strogatz, 1994; Kantz and Schreiber, 1997), whose positive values are a signature of chaotic regimes. Approaching chaos, λ goes from small negative values to positive values as reported in **Figure 5A**.

In the inelastic range $f \in (0.1, 0.3)$, the milling disc spends most of the time in the upper part of the reactor. The related trajectories show a symmetric pattern with respect to the central x = 0 axis in the periodic regime, which transmutes into an asymmetric shape in the chaotic one.

The system undergoes a bifurcation to period-8 (P8) dynamics by further increasing f to 0.5 (see the frequency-halving in the related FFT), which preludes a new chaotic regime at f = 0.7. Elastic conditions (f = 0.9) bring the system back to a P1 periodicity compatible with the forcing frequency.

The dynamics of the disc is also very sensitive to the disc radius, and a transition from periodicity to chaos can be observed when r_d is increased from 2 to 4 mm (with f = 0.5). Here also a period-doubling scenario can be inferred, though not all progressive regimes were isolated.

The asymmetric patterns drawn by the disc motion within the spatial domain can be reflected with respect to the axis x = 0 by reversing the initial direction of the external angular forcing.

In the system with curved bases, aperiodic dynamics are found not only in the elastic domain but also for low values of f (see also **Figure 2** of the **Supplementary Material**). Again, the system can evolve from periodicity to chaotic regimes following a period-doubling-like pathway when f or r_d are varied as framed in **Figure 2B**, explicitly illustrated in **Figure 4** and characterized by computing the exponent λ in **Figure 5B**.

For both kinds of reactors, periodic regimes correspond to highly ordered trajectories where the milling disc explores a very restricted portion of the available area. However, while in flat-base reactors impacts take place in a few points of the reactor walls, curved-base geometries favor a displacement along the reactor borders dragged by the reactor motion.

This explains why the number of collisions experienced by the disc in the curved-base systems is, in general, much larger than that observed in flat-base reactors. In **Figures 6A,B** we report the dependence upon f and r_d of the average number of collisions on the reactor bases, ⟨Collisions⟩ (in gray-black), and the relative energy, $\langle E \rangle_{rel}$ (in blue). In flat-base reactors (circles), ⟨Collisions⟩ shows a sharp drop-down as f is increased beyond the strongly inelastic condition 0.1 (r_d = 5 mm), while a smoother decreasing

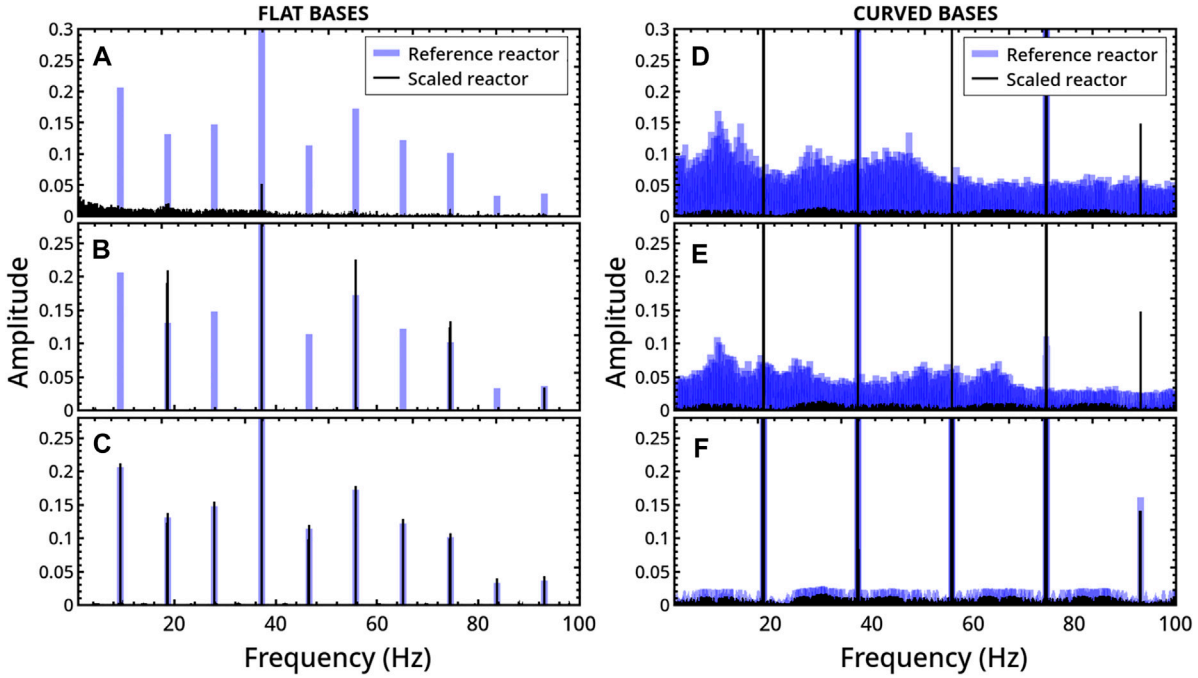

FIGURE 7 | Comparison between the milling disc dynamics obtained by changing the reactor size with the milling disc radius in flat-base (left) and curved-base (right) geometries, keeping fixed the ratio $Q = \Omega_c/(\pi(r_d)^2) = \Omega_c/(\pi(r_d)^2)$ ($f = 0.5$). The reference systems, in blue, are characterized by $r_d^1 = 3$ mm, $\Omega_f^1 = 53$ mm × 18.8 mm = Ω_c^1 =38.2 mm × 18.8 mm + π (9.4 mm)^2 while the scaled reactors, in black, have $r_d^2 = 1.5r_d^1$ =4.5 mm, $\Omega_f^2 = \Omega_c^2 = 2.25\Omega_f^1 = 2.25\Omega_c^1$. The comparison between the reference and scaled systems is performed by using the Fast Fourier Transforms of the *z*-displacement of the milling disc over time. The change of the reactor size is operated in three different ways: **(A–D)** Case 1: scaling the dimensions without preserving the reactor aspect ratio keeping $R = 122$ mm ($\Omega_f^2 = 53$ mm × 42.3 mm; Ω_c^2 = 104.4 mm × 18.8 mm + π(9.4 mm)^2); **(B–E)** case 2: scaling the dimensions by the same factor of the disc radius, preserving the aspect ratio of the reactor and keeping $R = 122$ mm (Ω_f^2 = 79.45 mm × 28.2 mm; Ω_c^2 =57.3 mm × 28.2 mm + π(14.1 mm)^2); **(C-F)** case 3: scaling the whole system proportionally, including the mechanical arm (Ω_f^2 = 78.45 mm × 28.2 mm; Ω_c^2 =57.3 mm × 28.2 mm + π(14.1 mm)^2; R = 183 mm).

trend pertains to curved-base reactors (**Figure 6A**). For both reactor types, ⟨Collisions⟩ is less sensitive to a variation of r_d and the corresponding trends are essentially constant. The trends for $\langle E \rangle_{rel}$ of the two geometries are comparable both in qualitative and quantitative terms. The increasing trend with r_d is described by **Eq. 8** and is related to the disc mass, which increases correspondingly.

In practical terms, curved-base reactors provide a more efficient mixing, showing wider regions of the parameter space where chaotic dynamics can be accessed and a larger number of collisions, which corresponds to a higher probability of inducing a transformation, but there is a negligible gain in energetic terms as compared to flat-base reactors.

3.2 Scaling the Reactor Size

The reactors with different shapes of the lateral borders show divergent dynamics even if the sizes of the milling body and the reactor, as well as all the other mechanical parameters, are the same. However, given the dependence of the dynamics of the two reactors on the size of the milling body, we checked whether systems with the same basis type and the same ratio of the reactor size to that of the milling body converge to analogous regimes. The rationale is that discs with an analogous free space to move, under the same mechanical forcing, could give a similar dynamical response. If this is the case, the dimensionless ratio $Q = \Omega_f/(\pi(r_d)^2) = \Omega_c/(\pi(r_d)^2)$ can feature a simplified and unifying parameter to control the dynamics.

We thus explored separately the dynamics of symmetrically forced reactors with either flat or curved bases, keeping fixed Q. Specifically, we compared the behaviors of systems where a constant Q is obtained by varying the reactor dimensions (*i*) without keeping the reactor aspect ratio (i.e., changing at will the width and the height of the reactor with the length of the mechanical arm, R, fixed) (case 1), (*ii*) preserving the aspect ratio of the reactor by scaling its dimensions by the same factor (with R fixed) (case 2), and (*iii*) scaling the whole system proportionally, including the length of the mechanical arm (case 3).

We first comment on the general case 1. **Figure 7A** shows a representative parallel between the dynamical regimes of two systems with flat bases, one being 2.25 times larger than the other, including the disc area. In particular, there are superimposed the FFTs of the temporal series describing the disc displacement along the vertical axis, *z*. An analogous comparison is reported for reactors with curved bases in **Figure 7D** (related trajectories can be found in **Figure 3** of the **Supplementary Material**). In both cases, preserving Q does not translate into analogous regimes. In the example with flat base reactors, the regular periodicity characterizing the "small" reactor changes into an aperiodic scenario in the scaled reactor. *Viceversa*, a transition from

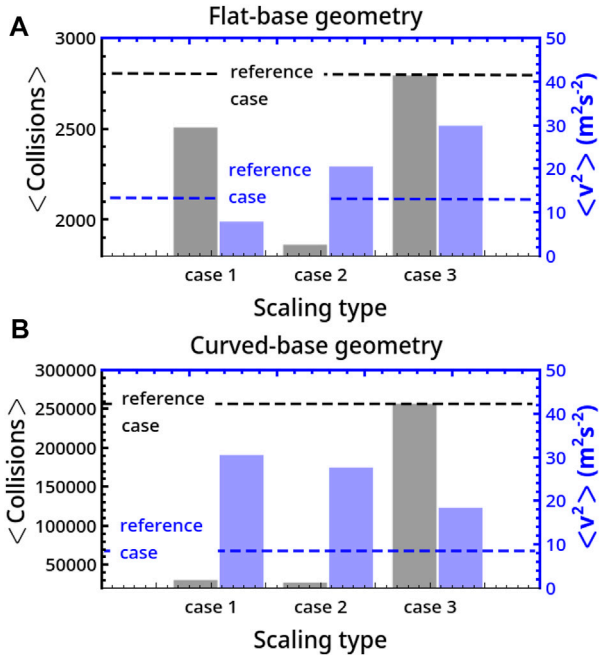

FIGURE 8 | Comparison of the average number of collisions on the basis, ⟨Collisions⟩, and mean squared velocity per collision, $\langle v^2 \rangle$, for different scaling (cases 1, 2, and 3) of the system size. Panel A and B describe results for flat- and curved-base geometries.

strongly aperiodic to period-1 behavior is observed in the curved-base system. In general, we found that the discrepancy between the dynamics of reference and scaled systems holds from both qualitative and quantitative viewpoints for different combinations of f and r_d (becoming much more prominent when approaching elastic conditions, see **Figure 2** of the **Supplementary Material**), and also by increasing the horizontal instead of the vertical dimension.

A similar comparison between systems where the reactor dimensions are scaled proportionally while maintaining the aspect ratio does not indicate any dynamical matching (see an example in **Figures 7B,E**), unless the mechanical arm is also scaled by the same scale factor, which is shown in **Figures 7C,F**. In this last case, the trajectory described by the disc within the two scaled reactors follows the same scaled path (see **Figure 4** of **Supplementary Material**) and, as a consequence, the Fourier analysis leads to overlapping results.

In **Figure 8** we can observe that both in flat- and curved-base reactors, the average number of collisions on the bases ⟨Collisions⟩ is maximal for the reference reactor (case 3 coincides with this). By contrast, the average energy per collision will be larger in scaled systems not only because of the increment in the mass of the milling body but also because of an increment in the mean squared velocity of the disc, $\langle v^2 \rangle$. In particular, in flat reactors, apart from case 1, $\langle v^2 \rangle$ is larger in the scaled reactors than in the smaller reference system, with $\langle v^2 \rangle_{\text{case 2}} < \langle v^2 \rangle_{\text{case 3}}$ while in curved-base geometries $\langle v^2 \rangle$

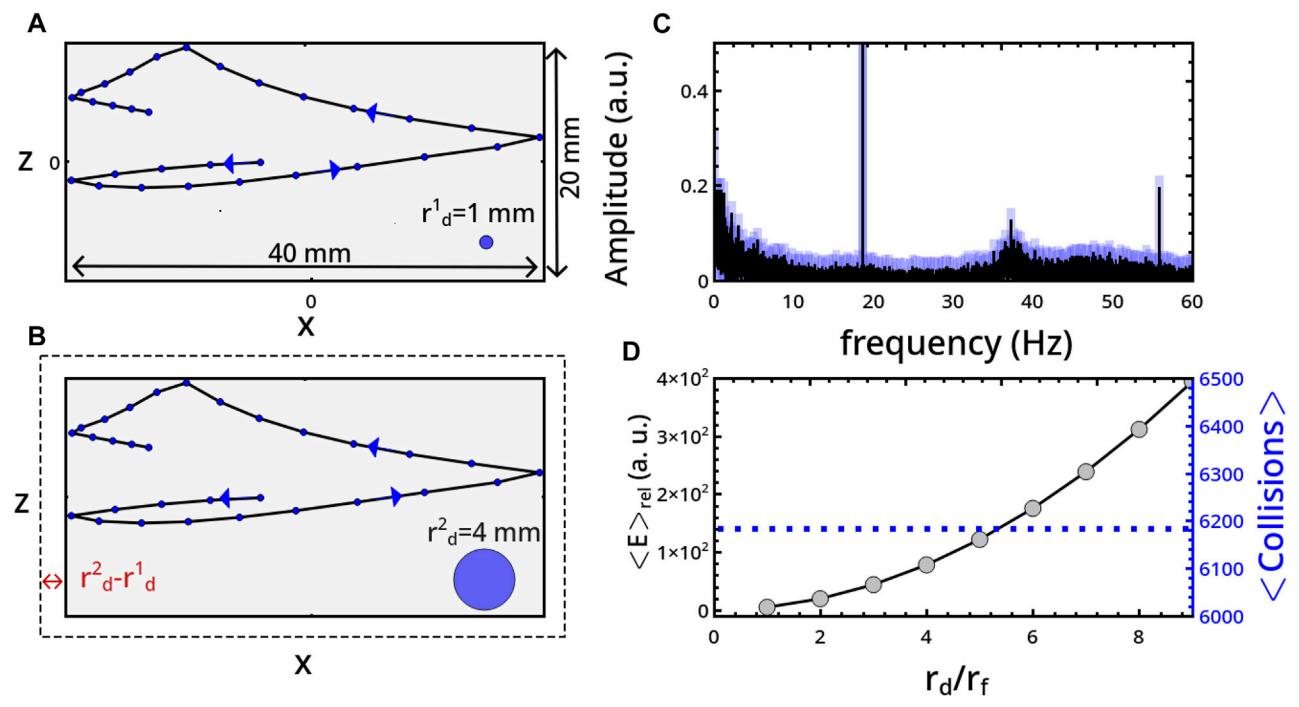

FIGURE 9 | Comparison between the milling disc dynamics obtained with $r_d = 1$ mm **(A)** and $r_d = 4$ mm **(B)** (i.e., $\epsilon = 3$ mm), by adapting the spatial domain from $\Omega_f =$ 20, ×, 40 mm to $\Omega_f = 26 \times 46$ mm, according to **Eqs 9**, **10**. f is fixed to 0.5. **(C)** Comparison between the FFTs of the x-displacement of the milling disc in time. **(D)** Average number of collisions on the bases, ⟨Collisions⟩, and average relative energy per collision, $\langle E \rangle_{rel}$, with respect to the reference energy of a milling disc with radius $r_f = 1$ mm.

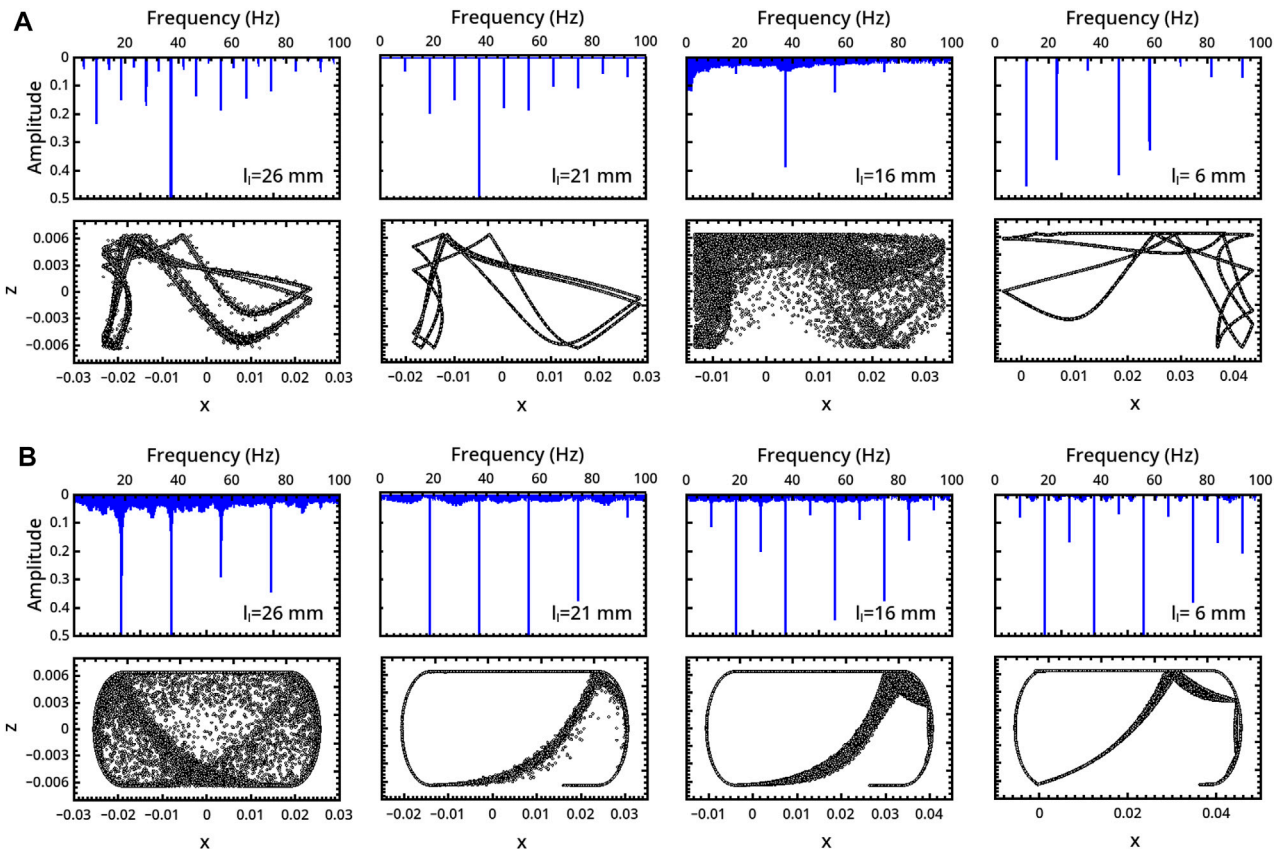

FIGURE 10 | Characterization of the milling body dynamics in **(A)** flat- and **(B)** curved-base geometries as a function of the mechanical arm location, l_l. For each regime, we report the trajectory (bottom) and the FFT of the time series describing the vertical displacement of the milling disc (top).

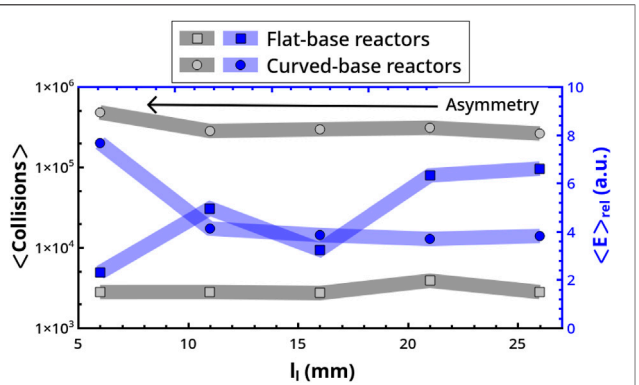

FIGURE 11 | Dependence of ⟨Collisions⟩ and $\langle E \rangle_{rel}$ on the forcing asymmetry as controlled by the mechanical arm location, l_l.

follows the order $\langle v^2 \rangle_{\text{case 1}} > \langle v^2 \rangle_{\text{case 2}} > \langle v^2 \rangle_{\text{case 3}} > \langle v^2 \rangle_{\text{reference case}}$.

Another way to relate the dynamics of the milling body to the spatial domain available relies on simple geometrical arguments. Since the conditions for collisions are based on the distance r_d of the disc center from the borders, when r_d increases by, ϵ, collision conditions remain unaltered if the dimensions of the reactor are increased by the same quantity ϵ at each side in the flat-base and if the reactor half-height increases to $h + \epsilon$ in the curved-base systems. In other words, the dynamics of a disc with a radius r_d^1 will be the same of a milling disc with r_d^2, if the reactor dimensions change from $(w^1 \times 2h^1)$ to

$$w^2 = w^1 + 2\epsilon, \tag{9}$$

$$2h^2 = 2h^1 + 2\epsilon, \tag{10}$$

$$(\text{with}\, \epsilon = r_d^2 - r_d^1),,$$

in flat-base geometry, and to

$$h^2 = h^1 + 2\epsilon, \tag{11}$$

in geometries with curved bases. These equivalence criteria, allowing to adapt the system size to a change in the disc radius in order to get the same dynamics, are applied to the representative systems shown in **Figure 9**. There are reported small portions of the spatial trajectories of a milling disc moving in a flat-base symmetrically-forced reactor when r_d changes from 1 mm (panel (a)) to 4 mm (panel (b)) and, consequently, $\Omega_f = 20, \times, 40$ mm is varied to $\Omega_f = 26 \times 46$ mm ($f = 0.5$). The resulting dynamics are identical and show overlapping FFTs of the temporal x-displacement in **Figure 9C**. Analogous results were also found for curved-base reactors (see **Figure 5** of the **Supplementary Material**).

If, in this way, the dynamical regime of the milling body is preserved, things vary from the energetic viewpoint due to the increase of the disc mass. Assuming a constant density of the disc and verified that the velocity distribution does not change while adapting the reactor size, the average energy per collision will only depend upon r_d. In particular, $\langle E \rangle_{reb}$ measuring the average energy per collision of a disc with radius r_d with respect to that of a reference radius r_f, follows $\langle E \rangle_{rel} \sim (r_d)^2/(r_f)^2$ as shown in **Figure 9D**, where $r_f = 1$ mm. Notice how the total number of collisions remains constant while varying r_d. This picture introduces a degree of freedom in the control of the system by which a desired regime can be modulated in intensity while maintaining unaltered the dynamical features.

3.3 Symmetrical vs. Asymmetrical Forcing

We finally explored the impact of an asymmetric forcing imposed on the disc when the mechanical arm is placed at different distances from the reactor center, for instance, decreasing l_l in favor of l_r. The results for the two reactor geometries under consideration are summarized in **Figure 10**, where we report different dynamics observed by progressively decreasing l_l (increasing l_r) by steps of 5 mm from the centered allocation, which is $l_l = 26$ mm (the case $f = 0.5$ and $r_d = 3$ mm is considered).

In the flat-base system (**Figure 10A**), the system firstly undergoes a transition from a P8 (l_l = 26 mm) to a P4 (l_l = 21 mm) periodicity, and then a chaotic regime for l_l = 16 mm occurs. Pushing further the geometrical asymmetry (l_l = 6 mm) the dynamics recovers a P1 behavior characterized by a main frequency which is half of the device forcing frequency.

In reactors with curved bases (**Figure 10B**), the asymmetry shows a "simplifying" effect in dynamical terms, inducing a transition from an initial chaotic regime for the centered arm to different kinds of periodicity: P1 (with the same devise working frequency) for $l_l = 21$ mm, P2 for $l_l = 16$ mm and P4 for $l_l = 6$ mm.

As shown in **Figure 11**, in both geometries the average number of collisions on the bases is not substantially affected by the asymmetric position of the mechanical arm. However, the two reactor types follow opposite trends in energetic terms, with the average relative energy of the collisions decreasing with the asymmetry of the forcing (i.e., decreasing l_l) in flat-base reactors. The opposite is true in curved-base reactors. A correlation between the typology of the dynamical regimes and collision energy can hardly be established. We can just point out that chaotic regimes correspond to a decrement of $\langle E \rangle_{rel}$.

4 CONCLUDING REMARKS

The geometry of the reactor used in ball-milling approaches can profoundly impact the outcome of a mechanical process by affecting the dynamics of the milling body, which rules the powder dragging, mixing, and concretely transfers the mechanical energy to induce physico-chemical transformations at collision with other milling bodies or with the reactor walls.

In this work we have focused our attention on the dynamics of one milling body driven by a harmonic pendular force within two different geometries, namely reactors with flat and curved bases, which are among the most common devices in use. By using a 2-dimensional description of these systems, we have probed the dynamical response of a milling body to the variation of relevant parameters such as the milling body size and the restitution coefficient. These parameters present experimental interest and turn out to critically control the transition from periodic to chaotic behaviors in both the geometries considered, following period-doubling-like routes. Parametric regions where the systems show chaotic behaviors and, hence, potentially more efficient mixing, are observed in curved-base reactors, where aperiodic dynamics dominate in the presence of nearly elastic conditions and are also found in inelastic conditions. Although the energetic profiles of the two geometries as a function of the control parameters considered are essentially overlapping, curved-base reactors are characterized by a larger number of collisions, which could translate into a higher probability of inducing a transformation. A direct correspondence between the dynamic type and the energetics of the system cannot be established. In both systems, the number of collisions is larger in periodic inelastic conditions as these favor the slipping of the milling body on the reactor walls.

A more general criterion for controlling the dynamics within the systems relies on a suitably small change in the relative size of the reactor and that of the milling body. Here we identified two possible ways to maintain a given dynamic when the milling body size is varied: *i*) scaling the reactor size, including the length of the mechanical arm, of the same factor of the milling body size variation; *ii*) augmenting the reactor width and height by the same increment (or decrement) of the milling body radius. In both cases, a desired regime can be modulated in intensity (i.e., the collision energy can be either increased or decreased) while maintaining unaltered the dynamical features.

An asymmetric force on the milling body, which can be imposed by changing the position of the mechanical arm with respect to the reactor center, can also play a critical role in controlling the transition from periodic to chaotic regimes.

DATA AVAILABILITY STATEMENT

The raw data supporting the conclusion of this article will be made available by the authors without undue reservation.

AUTHOR CONTRIBUTIONS

FD and MB conceived this work. AP, MC, and MB ran simulations and analyzed and interpreted data. All the authors contributed to the editing of the manuscript.

FUNDING

This work was supported by Attrazione e mobilità dei ricercatori, Linea 2 (Attrazione dei Ricercatori), and funding by University of Sassari (Fondo di Ateneo per la ricerca 2020). MC performed her activity within the framework of the International PhD in Innovation Sciences and Technologies at the Università degli Studi di Cagliari, Italy.

ACKNOWLEDGMENTS

MB gratefully acknowledges funding from Programma Operativo Nazionale (PON) Ricerca e Innovazione 2014–2020, Asse I Capitale Umano, Azione I.2 A.I.M.

SUPPLEMENTARY MATERIAL

The Supplementary Material for this article can be found online at: https://www.frontiersin.org/articles/10.3389/fchem.2022.915217/full#supplementary-material

REFERENCES

Abdellaoui, M., and Gaffet, E. (1995). The Physics of Mechanical Alloying in a Planetary Ball Mill: Mathematical Treatment. *Acta Metallurgica Materialia* 43, 1087–1098. doi:10.1016/0956-7151(95)92625-7

Aref, H., Blake, J. R., Budišić, M., Cardoso, S. S. S., Cartwright, J. H. E., Clercx, H. J. H., et al. (2017). Frontiers of chaotic advection. *Rev. Mod. Phys.* 89, 025007. doi:10.1103/RevModPhys.89.025007

Avvakumov, E. G. (1986). *Mechanical Methods for Activation of Chemical Processes*. Novosibirsk: Nauka.

Balaz, P., Achimovicova, M., Balaz, M., Billik, P., Cherkezova-Zheleva, Z., Manuel Criado, J., et al. (2013). *Chem. Soc. Rev.* 42, 7571.

Boldyrev, V. V. (1983). *Experimental Methods in the Mechanochemistry of Solid Inorganic Materials*. Novosibirsk: Nauka.

Boldyreva, E. (2013). Mechanochemistry of Inorganic and Organic Systems: what Is Similar, what Is Different? *Chem. Soc. Rev.* 42, 7719. doi:10.1039/c3cs60052a

Boschetto, A., Bellusci, M., La Barbera, A., Padella, F., and Veniali, F. (2013). Kinematic Observations and Energy Modeling of a Zoz Simoloyer High-Energy Ball Milling Device. *Int. J. Adv. Manuf. Technol.* 69, 2423–2435. doi:10.1007/s00170-013-5201-9

Broseghini, M., Gelisio, L., D'Incau, M., Azanza Ricardo, C. L., Pugno, N. M., and Scardi, P. (2016). Modeling of the Planetary Ball-Milling Process: The Case Study of Ceramic Powders. *J. Eur. Ceram. Soc.* 36, 2205–2212. doi:10.1016/j.jeurceramsoc.2015.09.032

Budroni, M. A., Baronchelli, A., and Pastor-Satorras, R. (2017). *Phys. Rev. E* 95 (5), 052311. doi:10.1103/physreve.95.052311

Budroni, M. A., Pilosu, V., Delogu, F., and Rustici, M. (2014). Multifractal Properties of Ball Milling Dynamics. *CHAOS* 24 (2), 023117. doi:10.1063/1.4875259

Burgio, N., Iasonna, A., Magini, M., Martelli, S., Padella, F., Burgio, N., et al. (1991). Mechanical Alloying of the Fe–Zr System. Correlation between Input Energy and End Products. *Il Nuovo Cimento D.* 13, 459–476. doi:10.1007/bf02452130

Butyagin, P. Y. (1971). Kinetics and Nature of Mechanochemical Reactions. *Usp. Khim.* 40, 1935. doi:10.1070/rc1971v040n11abeh001982

Caravati, C., Delogu, F., Cocco, G., and Rustici, M. (1999). Hyperchaotic Qualities of the Ball Motion in a Ball Milling Device. *CHAOS* 9, 219–226. doi:10.1063/1.166393

Carta, M., Colacino, E., Delogu, F., and Porcheddu, A. (2020). Kinetics of Mechanochemical Transformations. *Phys. Chem. Chem. Phys.* 22, 14489–14502. doi:10.1039/d0cp01658f

Carta, M., Delogu, F., and Porcheddu, A. (2021). A Phenomenological Kinetic Equation for Mechanochemical Reactions Involving Highly Deformable Molecular Solids. *Phys. Chem. Chem. Phys.* 23, 14178–14194. doi:10.1039/d1cp01361k

Cleary, P. W., Sinnott, M., and Morrison, R. (2006). Analysis of Stirred Mill Performance Using DEM Simulation: Part 2 - Coherent Flow Structures, Liner Stress and Wear, Mixing and Transport. *Miner. Eng.* 19, 1551–1572. doi:10.1016/j.mineng.2006.08.013

Concas, A., Lai, N., Pisu, M., and Cao, G. (2006). Modelling of Comminution Processes in Spex Mixer/Mill. *Chem. Eng. Sci.* 61, 3746–3760. doi:10.1016/j.ces.2006.01.007

Courtney, T. H. (1996). *Mat. Trans. JIM* 36, 119.

Delogu, F., Monagheddu, M., Mulas, G., Schiffini, L., and Cocco, G. (2000). *Int. J. Non-Equilib. Process.* 11, 235.

Delogu, F., Mulas, G., Monagheddu, M., Schiffini, L., and Cocco, G. (1998). *Int. J. Non-Eq. Proc. (IJNEP)* 11, 235.

Do, J.-L., and Friščić, T. (2017). Mechanochemistry: A Force of Synthesis. *ACS Cent. Sci.* 3, 13–19. doi:10.1021/acscentsci.6b00277

Feng, Y. T., Han, K., and Owen, D. R. J. (2004). Discrete Element Simulation of the Dynamics of High Energy Planetary Ball Milling Processes. *Mater. Sci. Eng. A* 375-377, 815–819. doi:10.1016/j.msea.2003.10.162

Friscic, T., Mottillo, C., and Titi, H. M. (2020). Mechanochemistry for Synthesis. *Angew. Chem. Int. Ed.* 59, 1018. doi:10.1002/anie.201906755

Friscic, T. (2012). Supramolecular Concepts and New Techniques in Mechanochemistry: Cocrystals, Cages, Rotaxanes, Open Metal–Organic Frameworks. *Chem. Soc. Rev.* 41, 3493. doi:10.1039/C2CS15332G

Galant, O., Cerfeda, G., McCalmont, A. S., James, S. L., Porcheddu, A., Delogu, F., et al. (2022). *ACS Sust. Chem. Eng.* 10, 1430–1439.

Gil-González, E., Rodríguez-Laguna, M. d. R., Sánchez-Jiménez, P. E., Perejón, A., and Pérez-Maqueda, L. A. (2021). Unveiling Mechanochemistry: Kinematic-Kinetic Approach for the Prediction of Mechanically Induced Reactions. *J. Alloys Compd.* 866, 158925. doi:10.1016/j.jallcom.2021.158925

Gomollon-Bel, F. (2019). *Chem. Int.* 49, 12.

Heinicke, G. (1986). *Tribochemistry*. Berlin: Akademie Verlag.

James, S. L., Adams, C. J., Bolm, C., Braga, D., Collier, P., Friščić, T., et al. (2012). Mechanochemistry: Opportunities for New and Cleaner Synthesis. *Chem. Soc. Rev.* 41, 413–447. doi:10.1039/c1cs15171a

Kantz, H., and Schreiber, T. (1997). *Nonlinear Time Series Analysis*. Cambridge: Cambridge University Press.

King, G. (1998). Towards a Science of Mixing. *Phys. World* 11 (11), 23–24. doi:10.1088/2058-7058/11/11/24

Love, E. H. (1944). *A Treatise on the Mathematical Theory of Elasticity*. 4th ed. New York: Dover.

Magini, M., Iasonna, A., and Padella, F. (1996). Ball Milling: an Experimental Support to the Energy Transfer Evaluated by the Collision Model. *Scr. Mater.* 34, 139. doi:10.1016/1359-6462(95)00465-3

Manai, G., Delogu, F., and Rustici, M. (2002). Onset of Chaotic Dynamics in a Ball Mill: Attractors Merging and Crisis Induced Intermittency. *CHAOS* 12, 601–609. doi:10.1063/1.1484016

Michalchuck, A. A. L., Boldyreva, E. V., Belenguer, A. M., Emmerling, F., and Boldyrev, V. V. (2020). *Front. Chem.* 9, 685789.

Porcheddu, A., Colacino, E., De Luca, L., and Delogu, F. (2020). Metal-Mediated and Metal-Catalyzed Reactions under Mechanochemical Conditions. *ACS Catal.* 10, 8344–8394. doi:10.1021/acscatal.0c00142

Rightmire, N. R., and Hanusa, T. P. (2016). Advances in Organometallic Synthesis with Mechanochemical Methods. *Dalton Trans.* 45, 2352–2362. doi:10.1039/c5dt03866a

Rustici, M., Mulas, G., and Cocco, G. (1996). Detecting Chaotic Attractors in a Ball Milling Process. *Msf* 225-227, 243–248. doi:10.4028/www.scientific.net/msf.225-227.243

Sinnott, M., Cleary, P. W., and Morrison, R. (2006). Analysis of Stirred Mill Performance Using DEM Simulation: Part 1- Media Motion, Energy Consumption and Collisional Environment. *Miner. Eng.* 19, 1537–1550. doi:10.1016/j.mineng.2006.08.012

Strogatz, S. H. (1994). *Nonlinear Dynamics and Chaos: With Applications to Physics, Biology, Chemistry, and Engineering*. Boulder, Colorado, USA: Westview Press.

Takacs, L. (2013). The Historical Development of Mechanochemistry. *Chem. Soc. Rev.* 2013. doi:10.1039/C2CS35442J

Tan, D., and García, F. (2019). Main Group Mechanochemistry: from Curiosity to Established Protocols. *Chem. Soc. Rev.* 48, 2274–2292. doi:10.1039/c7cs00813a

Thiessen, K. P. (1979). *Z. Phys. Chem. Leipz.* 260, 403. doi:10.1515/zpch-1979-0159

Thiessen, P. A., Meyer, K., and Heinicke, G. (1967). *Grundlagen der Tribochemie*. Berlin: Akademie Verlag.

Timoshenko, S. P., and Goodier, J. N. (1970). *Theory of Elasticity*. New York: McGraw-Hill.

Tufillaro, N. B., and Albano, A. M. (1986). Chaotic Dynamics of a Bouncing Ball. *Am. J. Phys.* 54, 939–944. doi:10.1119/1.14796

Wang, G.-W. (2013). Mechanochemical Organic Synthesis. *Chem. Soc. Rev.* 42, 7668. doi:10.1039/c3cs35526h

Watanabe, R., Hashimoto, H., and Geun Lee, G. (1995). *Mater. Trans. JIM* 36, 2. doi:10.2320/matertrans1989.36.102

Zhao, X., and Shaw, L. (2017). Modeling and Analysis of High-Energy Ball Milling through Attritors. *Metall Mat Trans A* 48, 4324–4333. doi:10.1007/s11661-017-4195-6

Conflict of Interest: The authors declare that the research was conducted in the absence of any commercial or financial relationships that could be construed as a potential conflict of interest.

Publisher's Note: All claims expressed in this article are solely those of the authors and do not necessarily represent those of their affiliated organizations, or those of the publisher, the editors, and the reviewers. Any product that may be evaluated in this article, or claim that may be made by its manufacturer, is not guaranteed or endorsed by the publisher.

Advantages of publishing in Frontiers

OPEN ACCESS
Articles are free to read for greatest visibility and readership

FAST PUBLICATION
Around 90 days from submission to decision

HIGH QUALITY PEER-REVIEW
Rigorous, collaborative, and constructive peer-review

TRANSPARENT PEER-REVIEW
Editors and reviewers acknowledged by name on published articles

Frontiers
Avenue du Tribunal-Fédéral 34
1005 Lausanne | Switzerland

Visit us: www.frontiersin.org
Contact us: frontiersin.org/about/contact

REPRODUCIBILITY OF RESEARCH
Support open data and methods to enhance research reproducibility

DIGITAL PUBLISHING
Articles designed for optimal readership across devices

FOLLOW US
@frontiersin

IMPACT METRICS
Advanced article metrics track visibility across digital media

EXTENSIVE PROMOTION
Marketing and promotion of impactful research

LOOP RESEARCH NETWORK
Our network increases your article's readership